

G. Bard Ermentrout
David H. Terman

INTERDISCIPLINARY
APPLIED MATHEMATICS

35

Mathematical Foundations of Neuroscience

Interdisciplinary Applied Mathematics

Volume 35

Editors

**S.S. Antman J.E. Marsden
L. Sirovich S. Wiggins**

Geophysics and Planetary Sciences

Imaging, Vision, and Graphics

D. Geman

Mathematical Biology

L. Glass, J.D. Murray

Mechanics and Materials

R.V. Kohn

Systems and Control

S.S. Sastry, P.S. Krishnaprasad

Problems in engineering, computational science, and the physical and biological sciences are using increasingly sophisticated mathematical techniques. Thus, the bridge between the mathematical sciences and other disciplines is heavily traveled. The correspondingly increased dialog between the disciplines has led to the establishment of the series: *Interdisciplinary Applied Mathematics*.

The purpose of this series is to meet the current and future needs for the interaction between various science and technology areas on the one hand and mathematics on the other. This is done, firstly, by encouraging the ways that mathematics may be applied in traditional areas, as well as point towards new and innovative areas of applications; and, secondly, by encouraging other scientific disciplines to engage in a dialog with mathematicians outlining their problems to both access new methods and suggest innovative developments within mathematics itself.

The series will consist of monographs and high-level texts from researchers working on the interplay between mathematics and other fields of science and technology.

Interdisciplinary Applied Mathematics

For further volumes:
<http://www.springer.com/series/1390>

G. Bard Ermentrout • David H. Terman

Mathematical Foundations of Neuroscience

G. Bard Ermentrout
University of Pittsburgh
Dept. Mathematics
301 Thackeray Hall
Pittsburgh, Pennsylvania 15260
USA
bard@pitt.edu

David H. Terman
Ohio State University
Dept. Mathematics
231 W. 18th Ave.
Columbus, Ohio 43210
USA
terman@math.ohio-state.edu

Editors

S.S. Antman
Department of Mathematics
and
Institute for Physical Science
and Technology
University of Maryland
College Park, MD 20742, USA
ssa@math.umd.edu

J.E. Marsden
Control and Dynamical Systems
Mail Code 107-81
California Institute of Technology
Pasadena, CA 91125, USA
marsden@cds.caltech.edu

L. Sirovich
Division of Applied Mathematics
Brown University
Providence, RI 02912, USA
chico@camelot.mssm.edu

S. Wiggins
School of Mathematics
University of Bristol
Bristol BS8 1TW, UK
s.wiggins@bris.ac.uk

ISSN 0939-6047

ISBN 978-0-387-87707-5 e-ISBN 978-0-387-87708-2

DOI 10.1007/978-0-387-87708-2

Springer New York Dordrecht Heidelberg London

Library of Congress Control Number: 2010929771

Mathematics Subject Classification (2010): 37N25; 92C20; 92C05

© Springer Science+Business Media, LLC 2010

All rights reserved. This work may not be translated or copied in whole or in part without the written permission of the publisher (Springer Science+Business Media, LLC, 233 Spring Street, New York, NY 10013, USA), except for brief excerpts in connection with reviews or scholarly analysis. Use in connection with any form of information storage and retrieval, electronic adaptation, computer software, or by similar or dissimilar methodology now known or hereafter developed is forbidden.

The use in this publication of trade names, trademarks, service marks, and similar terms, even if they are not identified as such, is not to be taken as an expression of opinion as to whether or not they are subject to proprietary rights.

Printed on acid-free paper

Springer is part of Springer Science+Business Media (www.springer.com)

Preface

One can say that the field of computational neuroscience started with the 1952 paper of Hodgkin and Huxley in which they describe, through nonlinear partial differential equations, the genesis of the action potential in the giant axon of the squid. These equations and the methods that arose from this combination of modeling and experiments have since formed the basis for nearly every subsequent model for active cells. The Hodgkin–Huxley model and a host of simplified equations that are derived from it have inspired the development of new and beautiful mathematics. Dynamical systems and computational methods are now being used to study activity patterns in a variety of neuronal systems. It is becoming increasingly recognized, by both experimentalists and theoreticians, that issues raised in neuroscience and the mathematical analysis of neuronal models provide unique interdisciplinary collaborative research and educational opportunities.

This book is motivated by a perceived need for an overview of how dynamical systems and computational analysis have been used in understanding the types of models that come out of neuroscience. Our hope is that this will help to stimulate an increasing number of collaborations between mathematicians and other theoreticians, looking for interesting and relevant problems in applied mathematics and dynamical systems, and neuroscientists, looking for new ways to think about the biological mechanisms underlying experimental data.

The book arose out of several courses that the authors have taught. One of these is a graduate course in computational neuroscience that has students from the disciplines of psychology, mathematics, computer science, physics, and neuroscience. Of course, teaching a course to students with such diverse backgrounds presents many challenges. However, the course provides many opportunities to encourage students, who may not normally interact with each other, to collaborate on exercises and projects. Throughout the book are many exercises that involve both computation and analysis. All of the exercises are motivated by issues that arise from the biology.

We have attempted to provide a comprehensive introduction to the vocabulary of neuroscience for mathematicians who are just becoming interested in the field, but who have struggled with the biological details. Anyone who wants to work in computational neuroscience should learn these details as this is the only way one can be sure that the analysis and modeling is actually saying something useful to

biologists. We highly recommend the reader study this material in more detail by consulting one of the many excellent books devoted primarily to neuroscience. Such books include those by Kandel et al. [144] and Johnston and Wu [139].

We have also tried to provide background material on dynamical systems theory, including phase plane methods, oscillations, singular perturbations, and bifurcation analysis. An excellent way to learn this material is by using it, together with computer simulations, to analyze interesting, concrete examples. The only prerequisites are a basic knowledge of calculus, knowledge of a little linear algebra (matrices, eigenvalues), and understanding of some basic theory of ordinary differential equations. Much of the mathematics is at the level of Strogatz [255].

The book is organized from the bottom up. The first part of the book is concerned with properties of a single neuron. We start with the biophysics of the cell membrane, add active ion channels, introduce cable theory, and then derive the Hodgkin–Huxley model. Chapter 2 is concerned with the basic properties of dendrites. We then introduce dynamical systems theory, using a simple neuron model to illustrate the basic concepts. We return to the biology in Chap. 4, where we discuss the variety of ion channels which have been found in neurons. Chapters 5 and 6 are devoted to bursting oscillations and propagating action potentials, respectively. Here, we use many of the dynamical systems techniques to describe mechanisms underlying these behaviors. The second part of the book is concerned with neuronal networks. In Chap. 7, we describe synaptic channels, which are the primary way that neurons communicate with each other. Chapters 8 and 9 discuss two different approaches for studying networks. First, we assume weak coupling and use phase-response methods. We then demonstrate how one can analyze firing patterns in neuronal networks using fast/slow analysis. In Chap. 10, we discuss the role of noise in neuron models. Here, we briefly introduce the reader to the mathematical theory of stochastic differential equations. Finally, in Chaps. 11 and 12 we discuss firing rate models and spatially distributed networks.

There is far more material in this book than could be covered in a one-semester course. Furthermore, some of the material is quite advanced. A course in computational neuroscience slanted toward mechanisms and dynamics could easily be made out of the first five chapters along with Chap. 7. These chapters would cover most of the basics of single-cell modeling as well as introduce students to dynamical systems. The remainder of such a course could include selections from Chaps. 8–12. For example, Chap. 11 contains firing rate models, with many applications provided in Sect. 11.3. Parts of Chap. 12 could comprise the remainder of the course.

For more mathematically inclined students, the elementary dynamics chapter (Chap. 3) could be skipped and the more technical chapters could be emphasized. There is lovely nonlinear dynamics in Chaps. 5, 6, 8, and 9, which along with the earlier chapters could form the core of a mathematical neuroscience course.

There are several recent books that cover some of the same material as in the present volume. *Theoretical Neuroscience* by Dayan and Abbott [53] has a broader range of topics than our book; however, it does not go very deeply into the mathematical analysis of neurons and networks, nor does it emphasize the dynamical systems approach. A much more similar book is *Dynamical Systems*

in Neuroscience by Izhikevich [136]. This book emphasizes the same approach as we take here; however, the main emphasis of *Dynamical Systems in Neuroscience* is on single-neuron behavior. We cover a good deal of single-neuron biophysics, but include a much larger proportion of theory on systems neuroscience and applications to networks. There are many specific models and equations in this text. The forms of these models and their parameters are available at <http://www.math.pitt.edu/~bard/bardware/neurobook/allodes.html>.

Pittsburgh, PA
Columbus, OH

G. Bard Ermentrout
David H. Terman

Contents

1	The Hodgkin–Huxley Equations	1
1.1	The Resting Potential	1
1.2	The Nernst Equation	3
1.3	The Goldman–Hodgkin–Katz Equation.....	5
1.4	Equivalent Circuits: The Electrical Analogue	8
1.5	The Membrane Time Constant	11
1.6	The Cable Equation	13
1.7	The Squid Action Potential	16
1.8	Voltage-Gated Channels	18
1.9	Hodgkin–Huxley Model	20
1.10	The Action Potential Revisited	25
1.11	Bibliography	27
1.12	Exercises	28
2	Dendrites	29
2.1	Multiple Compartments	29
2.2	The Cable Equation	33
2.3	The Infinite Cable	34
2.4	Finite and Semi-infinite Cables.....	36
2.5	Branching and Equivalent Cylinders	38
2.6	An Isolated Junction	40
2.7	Dendrites with Active Processes.....	42
2.8	Concluding Remarks	45
2.9	Bibliography	45
2.10	Exercises	45
3	Dynamics	49
3.1	Introduction to Dynamical Systems	49
3.2	The Morris–Lecar Model	49
3.3	The Phase Plane	51
3.3.1	Stability of Fixed Points	52
3.3.2	Excitable Systems	53
3.3.3	Oscillations	55

3.4	Bifurcation Analysis	56
3.4.1	The Hopf Bifurcation	56
3.4.2	Saddle–Node on a Limit Cycle	58
3.4.3	Saddle–Homoclinic Bifurcation	60
3.4.4	Class I and Class II	62
3.5	Bifurcation Analysis of the Hodgkin–Huxley Equations	63
3.6	Reduction of the Hodgkin–Huxley Model to a Two-Variable Model	66
3.7	FitzHugh–Nagumo Equations	69
3.8	Bibliography	70
3.9	Exercises	70
4	The Variety of Channels	77
4.1	Overview	77
4.2	Sodium Channels	78
4.3	Calcium Channels	80
4.4	Voltage-Gated Potassium Channels	82
4.4.1	A-Current	83
4.4.2	M-Current	85
4.4.3	The Inward Rectifier	86
4.5	Sag	87
4.6	Currents and Ionic Concentrations	88
4.7	Calcium-Dependent Channels	90
4.7.1	Calcium Dependent Potassium: The Afterhyperpolarization	90
4.7.2	Calcium-Activated Nonspecific Cation Current	93
4.8	Bibliography	95
4.9	Exercises	95
4.10	Projects	100
5	Bursting Oscillations	103
5.1	Introduction to Bursting	103
5.2	Square-Wave Bursters	105
5.3	Elliptic Bursting	111
5.4	Parabolic Bursting	114
5.5	Classification of Bursters	117
5.6	Chaotic Dynamics	118
5.6.1	Chaos in Square-Wave Bursting Models	118
5.6.2	Symbolic Dynamics	121
5.6.3	Bistability and the Blue-Sky Catastrophe	123
5.7	Bibliography	125
5.8	Exercises	126

6 Propagating Action Potentials	129
6.1 Traveling Waves and Homoclinic Orbits	130
6.2 Scalar Bistable Equations	132
6.2.1 Numerical Shooting	135
6.3 Singular Construction of Waves	136
6.3.1 Wave Trains	139
6.4 Dispersion Relations	139
6.4.1 Dispersion Kinematics	141
6.5 Morris–Lecar Revisited and Shilnikov Dynamics	141
6.5.1 Class II Dynamics	142
6.5.2 Class I Dynamics	143
6.6 Stability of the Wave	145
6.6.1 Linearization	146
6.6.2 The Evans Function	147
6.7 Myelinated Axons and Discrete Diffusion	149
6.8 Bibliography	151
6.9 Exercises	152
7 Synaptic Channels	157
7.1 Synaptic Dynamics	158
7.1.1 Glutamate	161
7.1.2 γ -Aminobutyric Acid	162
7.1.3 Gap or Electrical Junctions	164
7.2 Short-Term Plasticity	164
7.2.1 Other Models	167
7.3 Long-Term Plasticity	168
7.4 Bibliography	169
7.5 Exercises	169
8 Neural Oscillators: Weak Coupling	171
8.1 Neural Oscillators, Phase, and Isochrons	172
8.1.1 Phase Resetting and Adjoints	174
8.1.2 The Adjoint	177
8.1.3 Examples of Adjoints	178
8.1.4 Bifurcations and Adjoints	181
8.1.5 Spike-Time Response Curves	186
8.2 Who Cares About Adjoints?	187
8.2.1 Relationship of the Adjoint and the Response to Inputs	187
8.2.2 Forced Oscillators	189
8.2.3 Coupled Oscillators	193
8.2.4 Other Map Models	199
8.3 Weak Coupling	202
8.3.1 Geometric Idea	203
8.3.2 Applications of Weak Coupling	205

8.3.3	Synaptic Coupling near Bifurcations	206
8.3.4	Small Central Pattern Generators	208
8.3.5	Linear Arrays of Cells	213
8.3.6	Two-Dimensional Arrays.....	217
8.3.7	All-to-All Coupling.....	219
8.4	Pulse-Coupled Networks: Solitary Waves	223
8.4.1	Integrate-and-Fire Model.....	226
8.4.2	Stability	229
8.5	Bibliography	229
8.6	Exercises	229
8.7	Projects	238
9	Neuronal Networks: Fast/Slow Analysis	241
9.1	Introduction	241
9.2	Mathematical Models for Neuronal Networks	242
9.2.1	Individual Cells	242
9.2.2	Synaptic Connections	243
9.2.3	Network Architecture	245
9.3	Examples of Firing Patterns	246
9.4	Singular Construction of the Action Potential	249
9.5	Synchrony with Excitatory Synapses.....	254
9.6	Postinhibitory Rebound	258
9.6.1	Two Mutually Coupled Cells.....	258
9.6.2	Clustering	260
9.6.3	Dynamic Clustering	260
9.7	Antiphase Oscillations with Excitatory Synapses	262
9.7.1	Existence of Antiphase Oscillations	263
9.7.2	Stability of Antiphase Oscillations	266
9.8	Almost-Synchronous Solutions.....	269
9.8.1	Almost Synchrony with Inhibitory Synapses	269
9.8.2	Almost Synchrony with Excitatory Synapses	271
9.8.3	Synchrony with Inhibitory Synapses	274
9.9	Slow Inhibitory Synapses	275
9.9.1	Fast/Slow Decomposition	275
9.9.2	Antiphase Solution	276
9.9.3	Suppressed Solutions	278
9.10	Propagating Waves	278
9.11	Bibliography	282
9.12	Exercises	282
10	Noise.....	285
10.1	Stochastic Differential Equations.....	287
10.1.1	The Wiener Process	288
10.1.2	Stochastic Integrals	289
10.1.3	Change of Variables: Itô's Formula	289

10.1.4	Fokker–Planck Equation: General Considerations	290
10.1.5	Scalar with Constant Noise	293
10.1.6	First Passage Times	295
10.2	Firing Rates of Scalar Neuron Models	299
10.2.1	The Fokker–Planck Equation	299
10.2.2	First Passage Times	303
10.2.3	Interspike Intervals	306
10.2.4	Colored Noise	307
10.2.5	Nonconstant Inputs and Filtering Properties	309
10.3	Weak Noise and Moment Expansions	310
10.4	Poisson Processes	314
10.4.1	Basic Statistics	314
10.4.2	Channel Simulations	317
10.4.3	Stochastic Spike Models: Beyond Poisson	319
10.5	Bibliography	321
10.6	Exercises	321
10.7	Projects	326
11	Firing Rate Models	331
11.1	A Number of Derivations	332
11.1.1	Heuristic Derivation	332
11.1.2	Derivation from Averaging	336
11.1.3	Populations of Neurons	338
11.2	Population Density Methods	341
11.3	The Wilson–Cowan Equations	344
11.3.1	Scalar Recurrent Model	346
11.3.2	Two-Population Networks	346
11.3.3	Excitatory–Inhibitory Pairs	350
11.3.4	Generalizations of Firing Rate Models	356
11.3.5	Beyond Mean Field	359
11.4	Some Methods for Delay Equations	361
11.5	Exercises	363
11.6	Projects	365
12	Spatially Distributed Networks	369
12.1	Introduction	369
12.2	Unstructured Networks	370
12.2.1	McCulloch–Pitts	370
12.2.2	Hopfield’s Model	371
12.2.3	Designing Memories	373
12.3	Waves	375
12.3.1	Wavefronts	376
12.3.2	Pulses	379

12.4	Bumps	383
12.4.1	The Wilson–Cowan Equations	384
12.4.2	Stability	387
12.4.3	More General Stability	388
12.4.4	More General Firing Rates	389
12.4.5	Applications of Bumps	390
12.5	Spatial Patterns: Hallucinations	394
12.6	Exercises	399
References		407
Index		419

Acknowledgments

I am deeply grateful for the opportunity to have learned from and worked with so many brilliant teachers, collaborators, and students. Thanks to them all. I especially thank Donald Aronson, for his encouragement to study mathematical biology, Charles Conley, whose mathematical insights pervade this book, and John Rinzel, for helping to pave the way into mathematical neuroscience. I would also like to thank those who proofread and commented on earlier versions of the book. These include Euiwoo Lee, Sungwoo Ahn, Choongseok Park, Michael Rempe, Josic Kresimir, Robert McDougal, and Hossein Abbassian. Finally, thank you to the National Science Foundation for its continued support. I dedicate the book to my family Effat, Sarah, and Rochelle for their love, patience and support.

– David H. Terman, The Ohio State University, 2009

This book would not have been possible without the input of many students and colleagues. Jack Cowan, Hugh Wilson, and John Rinzel had a keen appreciation for how mathematics could provide insight into the working of the nervous system and, as my teachers, they conveyed to me their knowledge and enthusiasm. I am grateful for their efforts. I also want to thank the many students who took various versions of courses I have taught on mathematical neuroscience and who provided valuable feedback. In particular, I want to thank Jon Rubin, Brent Doiron, Sergio Verduzco, and Kreso Jozic for comments on the many partial drafts of the book. Any mistakes belong to me. I dedicate the book to my family, Ellen, Kyle, and Jordan, for their patience with me over the years (and for putting up with the endless series of bad puns and pointless stories). Finally, because I promised my nephew, B.S. King, I will also dedicate the book to all the other “Bards” out there.

– G. Bard Ermentrout, The University of Pittsburgh, 2009

Chapter 1

The Hodgkin–Huxley Equations

1.1 The Resting Potential

All living cells have an electrical voltage, or potential difference, between their inside and outside. Since the cell's membrane is what separates the inside from the outside, this potential difference is referred to as the *membrane potential*. In mathematical terms, the membrane potential V_M is defined as

$$V_M = V_{\text{in}} - V_{\text{out}},$$

where V_{in} is the potential on the inside of the cell and V_{out} is the potential on the outside. This will change during an action potential, for example.

The *resting potential* refers to the potential across the membrane when the cell is at rest. A typical neuron has a resting potential of about -70 mV . An *inward current* corresponds to a positively charged ion, such as Na^+ , entering the cell. This raises the membrane potential; that is, it brings the membrane potential closer to zero. In this case, the cell is said to be *depolarized*. An *outward current* corresponds to a positively charged ion, such as K^+ , leaving the cell or a negatively charged ion, such as Cl^- , entering the cell. In this case, the cell becomes *hyperpolarized*.

The potential difference arises from differences in the concentrations of various ions within and outside the cell. The maintenance of the potential difference also involves the transport of ions across the cell membrane and the selective permeability of the membrane to these ions. The principal ions found on either side of the cell membrane are Na^+ , K^+ , and Cl^- . The concentration of K^+ ions inside a cell is about 10 times that in the extracellular fluid, whereas the concentrations of Na^+ and Cl^- are much higher outside the cell than inside.

The lipid bilayer of the cell membrane is a poor conductor of ionic current because it is not permeable to ions. However, the membrane does contain channel proteins that allow for the ions to move through it. There are two types of ion channels in the membrane: gated and nongated. Nongated channels are always open, whereas gated channels can open and close and the probability of opening often depends on the membrane potential; these are referred to as *voltage-gated channels*. Gated channels are typically selective for a single ion. The *permeability* of the

membrane to a particular ion depends on the number of open channels selective for that ion. Most gated channels are closed at rest; hence, the nongated ion channels are primarily responsible for establishing the resting potential. An action potential is generated when gated channels open allowing for the flux of ions across the cell membrane.

Because of concentration differences, when the appropriate channels are open, Na^+ and Cl^- ions tend to diffuse into the cell, whereas K^+ ions tend to diffuse outward. Note that ions do not simply diffuse in or out of an open channel until the concentration of that ion on either side of the cell is zero. This is because of the electric field created by separation of positive and negative charges across the cell membrane.

Suppose, for example, the cell is permeable only to K^+ . The concentration gradient of K^+ moves K^+ ions out of the cell. However, the continued efflux of K^+ builds up an excess of positive charge on the outside of the cell and leaves behind an excess of negative charge on the inside. The negative charge consists mostly of impermeable organic anions A^- . This buildup of charge acts to impede the further efflux of K^+ , so eventually an equilibrium is reached. At this equilibrium, the electrical and chemical driving forces are equal and opposite (Fig. 1.1). The membrane potential at which K^+ ions are in equilibrium across the membrane is called the K^+ *Nernst, equilibrium, or reversal potential*.

In the next section, we shall derive the following expression for the K^+ Nernst potential:

$$E_K = -\frac{RT}{zF} \ln \frac{[K^+]_{\text{in}}}{[K^+]_{\text{out}}} \quad (1.1)$$

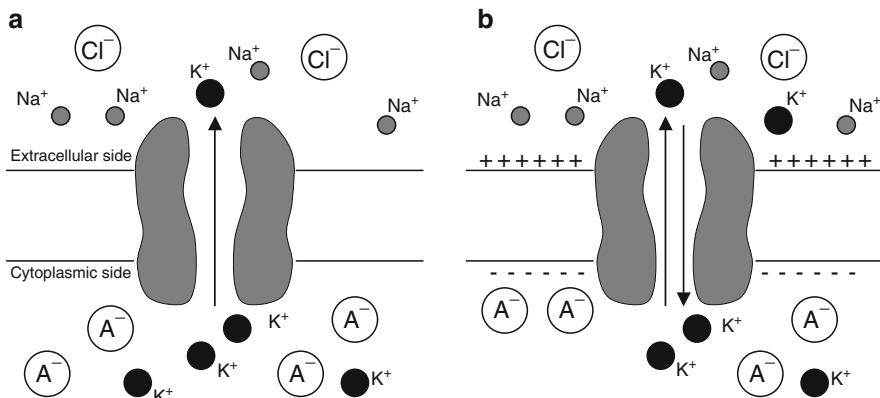


Fig. 1.1 The K^+ flux is determined by both the K^+ concentration gradient and the electrical potential across the membrane. (a) For a cell that is permeable only to K^+ , the concentration gradient of K^+ moves K^+ ions out of the cell. (b) The continued efflux of K^+ builds up an excess of positive charge on the outside and an excess of negative charge on the inside. At equilibrium, the electrical and chemical driving forces are equal and opposite

Here, E_K is the K^+ Nernst potential, R is the gas constant, T is the absolute temperature in kelvin, z is the valence of K^+ , F is Faraday's constant, and $[K^+]_{\text{out}}$ and $[K^+]_{\text{in}}$ are the concentrations of K^+ ions outside and inside the cell. A similar formula holds for the Na^+ and Cl^- Nernst potentials.

Neurons at rest are permeable to Na^+ and Cl^- in addition to K^+ . Because of their concentration differences, Na^+ and Cl^- ions move into the cell and K^+ ions move outward. The influx of Na^+ ions tends to depolarize the cell, whereas the efflux of K^+ and the influx of Cl^- have the opposite effect. The resting potential of the cell is the potential at which there is a balance between these fluxes. It depends on the concentrations of the ions both inside and outside the cell, as well as the permeability of the cell membrane to each of the ions. We note that at rest, many more K^+ and Cl^- channels than Na^+ channels are open; hence, the cell's resting potential is determined primarily by the K^+ and Cl^- Nernst potentials. In the following sections, we shall derive the *Goldman–Hodgkin–Katz (GHK) equation*, which gives an explicit expression for how the resting potential depends on the concentrations, both inside and outside, of ions and the permeabilities of the membrane to the ions.

For a cell to maintain a constant resting potential, the efflux of K^+ ions must balance the influx of Na^+ ions (here we are ignoring Cl^- ions). That is, the charge separation across the membrane must be constant. If these steady ion leaks continued unopposed, then K^+ ions within the cell would become depleted, whereas the concentration of Na^+ ions inside the cell would increase. This would eventually result in a loss of the ionic gradients, necessary for maintaining the resting potential. The dissipation of ionic gradients is prevented by active pumps that extrude Na^+ ions from the cell while taking in K^+ . The Na^+-K^+ pump is an integral membrane protein that exchanges three Na^+ ions for two K^+ ions. This is probably the most important ion transporter in biological membranes; however, there are many other proteins in the membrane that are capable of pumping ions from one side of the membrane to the other.

1.2 The Nernst Equation

Here we derive the Nernst equation and, in Sect. 1.3 we derive the GHK equation. Recall that if the membrane is permeable to only one ion, then that ion's Nernst potential is the resting potential at which the electrical and chemical driving forces balance. The GHK equation is, in some sense, a generalization of the Nernst equation in which we assume the membrane is permeable to more than just one ion. The GHK equation determines the resting potential at which the electrical and chemical forces, generated by each of these ions, balance each other. The first step in deriving these equations is to derive the *Nernst–Planck* equation.

In what follows, let $[C](x)$ be the concentration of some ion and $V(x)$ the potential at the point x across the membrane. Then, Fick's law of diffusion says that the diffusive flux, J_{diff} , is given by

$$J_{\text{diff}} = -D \frac{\partial [C]}{\partial x}.$$

The diffusion constant, D , has units of square centimeters per second and the concentration is in molecules per cubic centimeter, so the diffusive flux has units of molecules per square centimeter second. (Think of the flux as movement across the two-dimensional cell surface.) The direction of movement is from high concentrations to low concentrations. The diffusion constant (empirically measured) depends on the size of the molecule and the medium in which it is diffusing. A typical value for ions such as K^+ , Cl^- , and Na^+ is $2.5 \times 10^{-6} \text{ cm}^2/\text{s}$. Calcium ion has a diffusion constant about an order of magnitude less.

The other physical force that is responsible for the passive movement of ions is the electrical drift described by the microscopic version of Ohm's law:

$$J_{\text{drift}} = -\mu z[C] \frac{\partial V}{\partial x}.$$

The electric field, $E \equiv -\partial V / \partial x$, is the gradient of the potential V (measured in volts) and thus has units of volts per centimeter. z is the valence of the ion ($\pm 1, \pm 2$, etc.). The parameter μ is the mobility and has dimensions of square centimeters per volt second and $[C]$ is the concentration. The higher the concentration, the greater the drift. Note that the drift has the same dimensions as the diffusive flux.

The total flux across the membrane is given by the sum of the diffusive flux and the electrical drift:

$$J_{\text{total}} = -D \frac{\partial [C]}{\partial x} - \mu z[C] \frac{\partial V}{\partial x}.$$

Einstein's relation connects the mobility with the diffusion coefficient:

$$D = \frac{kT}{q}\mu,$$

where k is Boltzmann's constant (J/K), T is the absolute temperature, and q is the charge (measured in coulombs). Thus, we can write the total flux as

$$J_{\text{total}} = -\frac{\mu k T}{q} \frac{\partial [C]}{\partial x} - \mu z[C] \frac{\partial V}{\partial x}.$$

It is convenient to convert this equation, which is in terms of the number of individual molecules, into its molar equivalent, by dividing by Avogadro's number. It is also convenient to introduce RT/F , where R is the ideal gas constant and F is Faraday's constant, instead of kT/q . (A list of these constants is given at the end of the next section.) This will yield the flux per mole. Multiplying this flux by the valence and Faraday's constant yields a current flux

$$I = - \left(u z R T \frac{\partial [C]}{\partial x} + u z^2 F [C] \frac{\partial V}{\partial x} \right)$$

measured in amperes per square centimeter. The quantity u is the molar mobility, μ/N_A . This equation is the *Nernst–Planck equation*.

The Nernst equation is obtained by setting the current equal to zero. That is, for a given ionic species, at equilibrium, the diffusion and electric effects balance:

$$I = - \left(uzRT \frac{\partial [C]}{\partial x} + uz^2 F [C] \frac{\partial V}{\partial x} \right) = 0.$$

As an exercise, it is left to the reader to prove this implies the *Nernst equation*:

$$V_{\text{eq}} \equiv V_{\text{in}} - V_{\text{out}} = - \frac{RT}{zF} \ln \frac{[C]_{\text{in}}}{[C]_{\text{out}}}. \quad (1.2)$$

That is, the equilibrium (or Nernst) potential, which occurs when all the fluxes balance, depends on the logarithm of the ratio of the concentrations of the ions inside and outside the cell.

To illustrate how to use the Nernst equation to compute an equilibrium potential, note that in a typical mammalian cell, there is 140 mM K⁺ inside the cell and 5 mM outside. At room temperature, 37°C, $RT/F = 26.73$ mV. Hence, the equilibrium potential of potassium is

$$-62 \log \frac{140}{5} = -89.7 \text{ mV}.$$

1.3 The Goldman–Hodgkin–Katz Equation

The Nernst–Planck equation describes the movement of charged ions in aqueous media. However, the cell membrane has thickness and there may be energy barriers or blocking sites within the channel. In this case, the ions flowing through the open channel may not obey the Nernst–Planck equation and we must model the complex behavior within the membrane to get a true picture of the flux across the cell. This type of biophysics is beyond the details that are needed for this book, but the resulting equation does play a role in later parts. Thus, we will present a shortened derivation of a simplification of what happens within the membrane. Goldman, Hodgkin, and Katz came up with this simplified model called the *constant-field equation*. They assumed (1) the electric field across the lipid membrane is constant, (2) the Nernst–Planck equation holds within the membrane, and (3) the ions all move independently.

Let V_M be the total potential across a membrane of width l and let $V(x)$ be the potential at the point x across the membrane. Since the electric field is constant, $E = -V_M/l$. This implies that $dV/dx = V_M/l$. The mobility of ions within the membrane will be different from that in the aqueous solution; denote this mobility by u^* . Finally, let β be the ratio of the ion solubility within the membrane to the ion

solubility in the aqueous solution. Thus, if $[C]$ is the aqueous concentration, then $\beta[C]$ is the membrane concentration. With these assumptions, the Nernst–Planck equation for current across the membrane is

$$I = -u^* z^2 F \beta [C] \frac{V_M}{l} - u^* z R T \beta \frac{d[C]}{dx}, \quad 0 < x < l.$$

This is just a first-order linear ordinary differential equation for $[C]$ subject to the *two* boundary conditions

$$[C](0) = [C]_{\text{in}}, \quad [C](l) = [C]_{\text{out}}.$$

One cannot, in general, solve a first-order equation with two boundary conditions. However, the current I is unknown, so choosing this correctly will allow us to find a solution that satisfies both boundary conditions. We leave this elementary exercise for the reader. The result is

$$I = \frac{u^* z^2 F V_M \beta}{l} \left(\frac{[C]_{\text{out}} e^{-\xi} - [C]_{\text{in}}}{e^{-\xi} - 1} \right),$$

where

$$\xi = \frac{z V_M F}{R T}.$$

This expression is often written in terms of the permeability,

$$P \equiv \frac{\beta u^* R T}{l F};$$

that is,

$$I = P z F \xi \left(\frac{[C]_{\text{out}} e^{-\xi} - [C]_{\text{in}}}{e^{-\xi} - 1} \right). \quad (1.3)$$

The permeability has dimensions of centimeters per second. Thus, the dimensions are in terms of current per unit area. Equation (1.3) is called the constant-field equation.

This is the current due to a single ionic species. The current vanishes at the equilibrium or Nernst potential of the ionic species. A current–voltage (I – V) plot is a common plot. If the inside and outside concentrations are identical, then the I – V plot is linear. For $[C]_{\text{out}} > [C]_{\text{in}}$ (respectively, $[C]_{\text{out}} < [C]_{\text{in}}$) the I – V plot is concave down (respectively concave up). The reader is encouraged to plot the current as a function of the voltage for different concentration ratios. If the concentrations are quite different on the inside and outside, then the I – V curve is *strongly rectifying*. This means the magnitude of the current depends strongly on whether or not the potential is above or below the equilibrium.

Given several ionic species, the total current is just a sum of the individual currents. This is a consequence of assumption 3, which says that the ions do not interact. Suppose there are three permeable ions, K^+ , Na^+ , and Cl^- with corresponding currents, I_K , I_{Na} , and I_{Cl} . At equilibrium, the total current, $I = I_K + I_{Na} + I_{Cl}$, vanishes; that is, $I = 0$. The potential at which this occurs is

$$V_M = \frac{RT}{F} \ln \frac{P_K[K^+]_{out} + P_{Na}[Na^+]_{out} + P_{Cl}[Cl^-]_{in}}{P_K[K^+]_{in} + P_{Na}[Na^+]_{in} + P_{Cl}[Cl^-]_{out}}, \quad (1.4)$$

where the P_j 's are the permeabilities of each of the three ionic species. This is a generalization of the Nernst equilibrium discussed above and is called the *Goldman–Hodgkin–Katz (GHK) equation*. With one species, the equation reduces to the Nernst potential. For example, in the squid axon, the ratios of the permeabilities, at rest, are $P_K : P_{Na} : P_{Cl} = 1 : 0.03 : 0.1$. The ion concentrations inside the cell are, respectively, for K^+ , Na^+ , and Cl^- , 400, 50, and 40 mM, whereas outside the cell they are 10, 460, and 540 mM. Thus, at room temperature, the equilibrium or resting potential is -74 mV.

Table 1.1 Typical ion concentrations in cells (from Johnston and Wu [139])

Ion	Inside (mM)	Outside (mM)	Equilibrium potential (mV),
			$E_i = \frac{RT}{zF} \ln \frac{[C]_{out}}{[C]_{in}}$
Frog muscle			$T = 20^\circ C$
K^+	124	2.25	$58 \log \frac{2.25}{124} = -101$
Na^+	10.4	109	$58 \log \frac{109}{10.4} = +59$
Cl^-	1.5	77.5	$-58 \log \frac{77.5}{1.5} = -99$
Ca^{2+}	10^{-4}	2.1	$29 \log \frac{2.1}{10^{-4}} = +125$
Squid axon			$T = 20^\circ C$
K^+	400	20	$58 \log \frac{20}{400} = -75$
Na^+	50	440	$58 \log \frac{440}{50} = +55$
Cl^-	40–150	560	$-58 \log \frac{560}{40-150} = -66$ to -33
Ca^{2+}	10^{-4}	10	$29 \log \frac{10}{10^{-4}} = +145$
Mammalian cell			$T = 37^\circ C$
K^+	140	5	$62 \log \frac{5}{140} = -89.7$
Na^+	5–15	145	$62 \log \frac{145}{5-15} = +90 - (+61)$
Cl^-	4	110	$-62 \log \frac{110}{4} = -89$
Ca^{2+}	10^{-4}	2.5–5	$31 \log \frac{2.5-5}{10^{-4}} = +136 - (+145)$

Table 1.2 Elementary constants

N_A	6.022×10^{23} mol (Avogadro's number)
k	1.380658×10^{-23} J/K (Boltzmann's constant)
R	8.31451 J/(mol K) (ideal gas constant)
e	1.602177×10^{-19} C (electron charge)
F	96,485.3 C/mol (Faraday's constant)
ϵ_0	8.85×10^{-12} F/m (permittivity constant)
K	Kelvin (degrees centigrade +273.16)
L	Liter
N	Newton
J	Joule (N m); 1 J = 0.238845 cal
V	Volt (J/C)
C	Coulomb
A	Ampere (C/s)
Ω	Ohm (V/A)
S	Siemens (A/V)
F	Farad (s A/V or C/V)

1.4 Equivalent Circuits: The Electrical Analogue

We saw in Sect. 1.3 that the electrical properties of cells are determined by the ionic species that move through the membrane. Currents flow according to the permeabilities of ion channels and concentration gradients across the cell membrane. However, all of our discussion so far has been in a steady-state environment. The GHK equation does not determine how the membrane potential changes in response to changes in the permeabilities. For this reason, it cannot be used to understand how these changes in permeabilities may generate an action potential. A very useful way to describe the behavior of the membrane potential is in terms of electrical circuits; this is commonly called the *equivalent circuit model*. The circuit consists of three components: (1) conductors or resistors, representing the ion channels; (2) batteries, representing the concentration gradients of the ions; and (3) capacitors, representing the ability of the membrane to store charge. The equivalent circuit model leads to both an intuitive and a quantitative understanding of how the movement of ions generates electrical signals in the nerve cell.

We first consider a membrane that is only permeable to potassium. The equivalent circuit is shown in Fig. 1.2. The lipid bilayer that constitutes the cell membrane has dielectric properties and as such behaves in much the same manner as a capacitor. Recall that capacitors store charge and then release it in the form of currents. The relationship between the charge stored and the potential is given by

$$q = C_M V_M; \quad (1.5)$$

that is, the total charge q is proportional to the potential V_M with a proportionality constant C_M called the *membrane capacitance*. Note that the total capacitance depends on the total area of the dielectric; thus, larger neurons have a larger total capacitance than smaller ones. The capacitance per square centimeter is called the *specific membrane capacitance* and will be denoted as c_M . Hence, the total

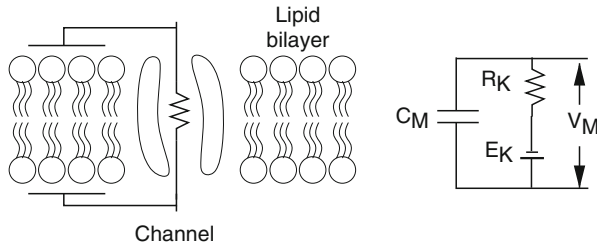


Fig. 1.2 The cell membrane showing the insulating lipid bilayer and a K^+ channel, which allows current to flow. The equivalent electrical circuit is shown on the right

membrane capacitance C_M is the specific membrane capacitance c_M times the total surface area of the cell. In general, the specific membrane capacitance may depend on the potential; however, for most cell membranes, the specific membrane capacitance is very close to $1 \mu\text{F}/\text{cm}^2$.

Since current is the time derivative of charge, we can differentiate (1.5), divide by the cell's area, and obtain an expression for the specific capacitance current:

$$i_{\text{cap}} = c_M \frac{dV_M}{dt}. \quad (1.6)$$

This gives the capacitance current per unit area. We will denote the total capacitance current as I_{cap} .

In the equivalent circuit, K^+ channels are represented as a conductor in series with a battery. If \hat{g}_K is the conductance of a single K^+ channel, then, using Ohm's law, the ionic current through this channel is

$$\hat{I}_K = \hat{g}_K(V_M - E_K). \quad (1.7)$$

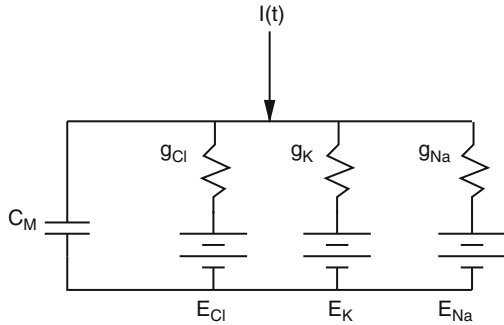
Here, E_K is the potential generated by the battery; this is given by the K^+ Nernst potential. The *driving force* is $V_M - E_K$. Now suppose there are N_K K^+ channels in a unit area of membrane. These can all be combined into the single equivalent circuit shown in Fig. 1.2. The conductance per unit area, or specific membrane conductance (S/cm^2), is given by $g_K = N_K \times \hat{g}_K$ and the specific membrane resistance ($\Omega \text{ cm}^2$) is $r_K \equiv 1/g_K$. Since the Nernst potential depends only on the concentration gradient of K^+ , and not on the number of K^+ channels, it follows that the K^+ current, per unit area, is given by

$$I_K = g_K(V_M - E_K) = \frac{V_M - E_K}{r_K}. \quad (1.8)$$

Kirchhoff's current law states that the total current into the cell must sum to zero. Together with the equivalent circuit representation, this leads to a differential equation for the membrane potential:

$$0 = i_{\text{cap}} + I_K = c_M \frac{dV_M}{dt} + \frac{V_M - E_K}{r_K} \quad (1.9)$$

Fig. 1.3 Equivalent circuit for a membrane with three channels



or

$$c_M \frac{dV_M}{dt} = -\frac{V_M - E_K}{r_M} = -g_K(V_M - E_K). \quad (1.10)$$

Figure 1.3 shows an equivalent circuit with three parallel conductances and a current source, $I(t)$. Here the capacitance current must be equal to the sum of the ionic currents and the current source. As before, the capacitance current, per unit area, is given by (1.6) and the ionic current, per unit area, is given by

$$i_{\text{ion}} = -g_{\text{Cl}}(V_M - E_{\text{Cl}}) - g_K(V_M - E_K) - g_{\text{Na}}(V_M - E_{\text{Na}}). \quad (1.11)$$

The current source is not typically expressed as current per unit area, so we must divide $I(t)$ by the total surface area of the neuron, A . It then follows that

$$c_M \frac{dV_M}{dt} = -g_{\text{Cl}}(V_M - E_{\text{Cl}}) - g_K(V_M - E_K) - g_{\text{Na}}(V_M - E_{\text{Na}}) + I(t)/A. \quad (1.12)$$

Note that we can rewrite this equation as

$$c_M \frac{dV_M}{dt} = -\frac{(V_M - E_R)}{r_M} + I(t)/A, \quad (1.13)$$

where

$$E_R = (g_{\text{Cl}}E_{\text{Cl}} + g_KE_K + g_{\text{Na}}E_{\text{Na}})r_M$$

is the cell's resting potential and

$$r_M = \frac{1}{g_{\text{Cl}} + g_K + g_{\text{Na}}}$$

is the specific membrane resistance.

For a passive membrane in which the conductances and currents are all constant, V_M will reach a steady state:

$$V_{ss} = \frac{g_{\text{Cl}}E_{\text{Cl}} + g_KE_K + g_{\text{Na}}E_{\text{Na}} + I/A}{g_{\text{Cl}} + g_K + g_{\text{Na}}}.$$

In the absence of the applied current, the steady-state potential is a weighted sum of the equilibrium potentials of the three currents. This is similar to the GHK equation (1.4), in which the contribution to the resting potential by each ion is weighted in proportion to the permeability of the membrane to that particular ion. Note, however, that in the equivalent circuit model, the equilibrium is a linear weighted sum of the equilibrium potentials, whereas in the GHK equation, the sum is nonlinear.

We remark that membrane conductance and permeability are related concepts; however, they are not the same. The permeability depends on the state of the membrane, whereas conductance depends on both the state of the membrane and the concentration of the ions. The permeability to K^+ , for example, may be high if there are a large number of open K^+ channels. However, if the concentration of K^+ ions is low on both sides of the membrane, then the K^+ conductance will be low.

1.5 The Membrane Time Constant

In this section, we consider how a passive, isopotential cell responds to an applied current. This will help explain how each component of the electrical circuit contributes to changes in the membrane potential. The cell is said to be *passive* if its electrical properties do not change during signaling. Such a cell cannot generate an action potential; however, it is important to understand how a cell's passive, or constant, properties influence changes in the membrane potential before considering active signaling. Moreover, many dendrites do not have gated channels, so their behavior is influenced primarily by their passive properties. The cell is said to be *isopotential* if the membrane potential is uniform at all points of the cell; that is, the membrane potential depends only on time. To simplify the analysis, we will consider a spherical cell with radius ρ .

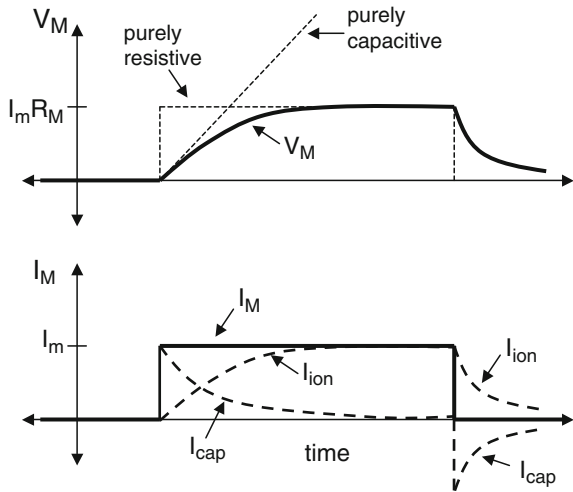
Suppose this cell is injected with an applied current, $I(t)$, that is turned on at $t = 0$ to some constant value, I_0 , and turned off at $t = T$. Here, we assume $I_0 > 0$; however, this is really not necessary. Note that for an isopotential cell, the injected current distributes uniformly across the surface. It follows that for a spherical cell, the current flowing across a unit area of the membrane is

$$I_M(t) = \frac{I(t)}{4\pi\rho^2} = \begin{cases} \frac{I_0}{4\pi\rho^2} & \text{if } 0 < t < T \\ 0 & \text{otherwise.} \end{cases} \quad (1.14)$$

As before, suppose c_M is the specific membrane capacitance, r_M is the specific membrane resistance, and E_R is the cell's resting potential. To simplify things, we take $E_R = 0$ so that V_M measures the deviation of the membrane potential from rest. From (1.13), the membrane potential satisfies the ordinary differential equation

$$c_M \frac{dV_M}{dt} = -\frac{V_M}{r_M} + I_M(t). \quad (1.15)$$

Fig. 1.4 The change of membrane potential in response to a step of current. The membrane potential is shown with a *solid line*. The *dashed lines* show the time courses of the purely capacitive and resistive elements. The *bottom panel* shows the time course of the total membrane current, the ionic current, and the capacitive current



If the cell starts at rest, then the solution of this linear equation satisfies

$$V_M(t) = \frac{r_M I_0}{4\pi\rho^2} \left(1 - e^{-\frac{t}{\tau_M}} \right) \quad \text{for } 0 < t < T, \quad (1.16)$$

where $\tau_M \equiv c_M r_M$ is the *membrane time constant* and

$$V_M(t) = V_M(T) e^{-\frac{t}{\tau_M}} \quad \text{for } t > T. \quad (1.17)$$

The solution is shown in Fig. 1.4. Once the current is turned on, the membrane potential asymptotically approaches the steady-state value $r_M I_0 / (4\pi\rho^2)$. The approach is exponential with the time constant τ_M . The membrane time constant also determines the rate at which the membrane potential decays back to rest after the current is turned off. The steady-state membrane potential satisfies

$$I_0 \frac{r_M}{4\pi\rho^2} \equiv I_0 R_{\text{INP}}, \quad (1.18)$$

where R_{INP} is the *input resistance* of the cell. Note that if the input current changes by ΔI , then the steady-state membrane potential changes by $R_{\text{INP}} \Delta I$; that is, the input resistance is the slope of the $I-V$ curve obtained by plotting the steady-state voltage against the injected current.

The initial rise in membrane potential is determined primarily by the membrane capacitance. Initially, the voltage across the resistor and that across the capacitor are both zero. From Ohm's law, it follows that initially no current flows through the resistor and all the current is due to the capacitor. Because of the capacitive current, the potential across the capacitor, and hence the membrane potential, will become

more positive. As V_M increases, the membrane potential difference begins to drive current across the membrane resistance, resulting in less current across the capacitor. Eventually, the membrane potential reaches a value where all the membrane current flows through the resistor. This value is given by $V_M = I_0 R_{\text{INP}}$.

Figure 1.4 also shows responses in which there are purely resistive or purely capacitive elements. If there is no membrane capacitance, then V_M satisfies

$$V_M(t) = r_M I_M(t). \quad (1.19)$$

That is, V_M jumps to the steady-state potential, $I_0 R_{\text{INP}}$, as soon as the injected current is turned on and it jumps back to rest as soon as the current is turned off. If there is only a capacitive element, then the membrane potential changes linearly as long as there is an applied current.

1.6 The Cable Equation

We have, so far, considered the passive properties of an isopotential cell. This analysis may be used to describe signaling within the cell body, which can be approximated by a sphere. However, it is clearly not appropriate for studying electrical properties of the axon or dendrites. These are better approximated by cylinders that are not isopotential. A subthreshold voltage signal that is initiated at one point along the axon or dendrite will decrease in amplitude with distance from the point of initiation. It is important to understand how the geometry of the cell affects the spread of the signal. The signal may, for example, correspond to synaptic input from another neuron. Understanding how geometry affects the spread of the signal will help determine whether the synaptic input will cause the cell to fire an action potential. Here, we assume the membrane is passive, so the analysis is more applicable to dendrites than to axons. However, as we shall describe later, the passive spread of current flow helps determine the velocity of propagating action potentials in the axon.

We consider a cell that is shaped as a long cylinder, or cable, of radius a . We assume the current flow is along a single spatial dimension, x , the distance along the cable. In particular, the membrane potential depends only on the x variable, not on the radial or angular components. The cable equation is a partial differential equation that describes how the membrane potential $V_M(x, t)$ depends on currents entering, leaving, and flowing within the neuron. The equivalent circuit is shown in Fig. 1.5. In what follows, we will assume $R_e = 0$, so that the extracellular space is isopotential. This assumption is justified if the cable is in a bath with large cross-sectional area.

We first consider the axial current flowing along the neuron due to voltage gradients. Note that the total resistance of the cytoplasm grows in proportion to the length of the cable and is inversely proportional to the cross-sectional area of the cable. The specific intracellular resistivity, which we denote as r_L , is the constant of proportionality. Hence, a cable of radius a and length Δx has a total resistance of

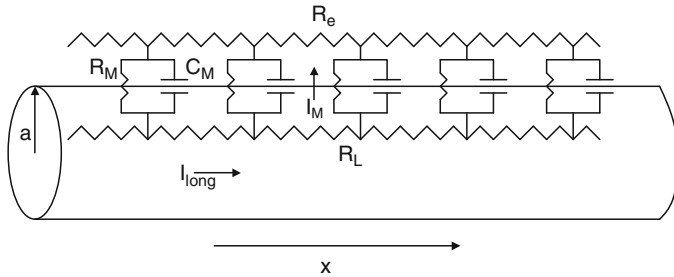


Fig. 1.5 Equivalent circuit for a uniform passive cable. I_{long} is the current along the inside of the cable, I_M is the current across the membrane, R_L is the resistance of the cytoplasm, R_e is the resistance of the extracellular space, R_M is the membrane resistance, and C_M is the membrane capacitance

$R_L = r_L \Delta x / (\pi a^2)$. It follows from Ohm's law that at any point x , the decrease in V_M with distance is equal to the current times the resistance. That is,

$$V_M(x + \Delta x, t) - V_M(x, t) = -I_{\text{long}}(x, t)R_L = -I_{\text{long}}(x, t) \frac{\Delta x}{\pi a^2} r_L. \quad (1.20)$$

There is a minus sign because of the convention that positive current is a flow of positive charges from left to right. If voltage decreases with increasing x , then the current is positive. In the limit $\Delta x \rightarrow 0$,

$$I_{\text{long}}(x, t) = -\frac{\pi a^2}{r_L} \frac{\partial V_M}{\partial x}(x, t). \quad (1.21)$$

Let i_{ion} be the current per unit area due to ions flowing into and out of the cell. Then the total ionic current that flows across a membrane of radius a and length Δx is given by $I_{\text{ion}} = (2\pi a \Delta x) i_{\text{ion}}$.

Recall that the rate of change of the membrane potential is determined by the capacitance. The total capacitance of a membrane is equal to the specific membrane capacitance c_M multiplied by the total surface area of the membrane. Hence, for a cable of radius a and length Δx , the total capacitance is given by $C_M = (2\pi a \Delta x) c_M$ and the amount of current needed to change the membrane potential at a rate $\partial V_M / \partial t$ is

$$I_{\text{cap}}(x, t) = (2\pi a \Delta x) c_M \frac{\partial V_M}{\partial t}. \quad (1.22)$$

From Kirchhoff's law, the change in intracellular axial current is equal to the amount of current that flows across the membrane. Hence,

$$I_{\text{cap}}(x, t) + I_{\text{ion}}(x, t) = -I_{\text{long}}(x + \Delta x, t) + I_{\text{long}}(x, t), \quad (1.23)$$

from which it follows that

$$(2\pi a \Delta x) c_M \frac{\partial V_M}{\partial t} + (2\pi a \Delta x) i_{\text{ion}} = \frac{\pi a^2}{r_L} \frac{\partial V_M}{\partial x} (x + \Delta x, t) - \frac{\pi a^2}{r_L} \frac{\partial V_M}{\partial x} (x, t).$$

We divide both sides of this equation by $2\pi a \Delta x$ and let $\Delta x \rightarrow 0$ to obtain the cable equation:

$$c_M \frac{\partial V_M}{\partial t} = \frac{a}{2r_L} \frac{\partial^2 V_M}{\partial x^2} - i_{\text{ion}}. \quad (1.24)$$

For a passive cable, in which the resting potential is assumed to be zero,

$$i_{\text{ion}} = V_M(x, t) / r_M, \quad (1.25)$$

where r_M is the specific membrane resistance. Then (1.24) becomes

$$c_M \frac{\partial V_M}{\partial t} = \frac{a}{2r_L} \frac{\partial^2 V_M}{\partial x^2} - \frac{V_M}{r_M}. \quad (1.26)$$

We can rewrite this equation as

$$\tau_M \frac{\partial V_M}{\partial t} = \lambda^2 \frac{\partial^2 V_M}{\partial x^2} - V_M, \quad (1.27)$$

where

$$\lambda = \sqrt{\frac{ar_M}{2r_L}} \quad \text{and} \quad \tau_M = c_M r_M \quad (1.28)$$

are the *space* or *length constant* and the *membrane time constant*, respectively. Note that the space constant depends on the geometry of the cable, that is, the cable's diameter; however, the time constant does not.

Later, we shall give a detailed analysis of solutions to the cable equation and properties of passive dendrites. For now, it is instructive to consider steady-state solutions. Suppose, for example, we consider a semi-infinite cable (defined for $x > 0$) and we inject a step of current, I_0 , at $x = 0$. As $t \rightarrow \infty$, the solution $V_M(x, t)$ approaches a steady-state solution $V_{ss}(x)$ that does not depend on time. Setting $\frac{\partial V_M}{\partial t} = 0$ in (1.27), we find that V_{ss} satisfies

$$\lambda^2 \frac{d^2 V_{ss}}{dx^2} - V_{ss} = 0. \quad (1.29)$$

To solve this equation, we need boundary conditions. Recall from (1.21) that

$$I_0 = -\frac{\pi a^2}{r_L} \frac{\partial V_M}{\partial x}.$$

It follows that V_{ss} must satisfy the boundary condition

$$\frac{dV_{ss}}{dx}(0) = -\frac{r_L}{\pi a^2} I_0. \quad (1.30)$$

The solution of (1.29) and (1.30) is

$$V_{ss}(x) = \frac{\lambda r_L}{\pi a^2} I_0 e^{-x/\lambda}. \quad (1.31)$$

Note that the membrane potential decays exponentially. The distance at which the potential has decayed to $1/e$ is the space constant λ . Since the space constant is proportional to the square root of the cable's radius, we conclude that thicker axons or dendrites have larger space constants than narrower processes. That is, thicker processes transmit signals for greater distances. As we discuss later, this is important because it influences the ability of the neuron to spatially summate incoming synaptic potentials. Moreover, the electrotonic, or passive, conductance plays an important role in the propagation of the action potential. Thicker cells with a larger space constant are more easily excited and are able to generate faster action potentials.

The input resistance is defined to be the steady-state membrane potential, evaluated at $x = 0$, divided by the injected current. That is,

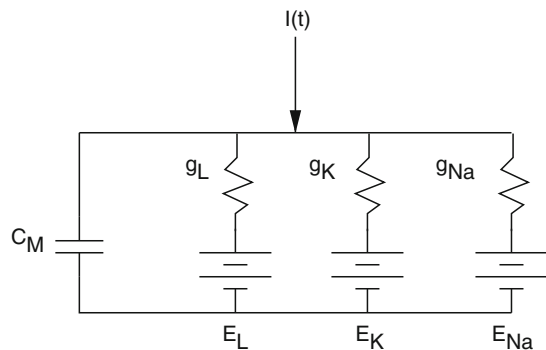
$$R_{inp} = V_{ss}(0)/I_0 = \frac{r_L \lambda}{\pi a^2} = \frac{1}{\pi a^{3/2}} \sqrt{r_M r_L / 2}. \quad (1.32)$$

Note that the input resistance of the cable varies with the $-3/2$ power of the cable radius. Therefore, the input conductance is directly proportional to the $3/2$ power of the cable radius. The input resistance is important because it is something that can be measured experimentally. Since it is also possible to measure the space constant λ , one can compute r_M and r_L from experimental data.

1.7 The Squid Action Potential

We have so far viewed the membrane as a passive cable. However, linear cables cannot transmit information over long distances unless the cable has an enormous diameter. For example, the squid axon is more than 5 cm long, has a diameter of about a 0.5 mm, a resting membrane resistance of $r_M = 700 \Omega \text{ cm}^2$, and a transmembrane resistance of $r_L = 30 \Omega \text{ cm}$. Thus, the space constant for the squid axon is $\lambda = 5.4 \text{ mm}$. This is an order of magnitude smaller than the length. If the potential at one end of the axon is held at 120 mV above rest, then the potential at the other end is about 10 μV above the rest, a 10,000-fold decrement. For neural signals to reach any distance, there must be another way to carry them so that they do not degrade.

Fig. 1.6 Equivalent circuit underlying the Hodgkin–Huxley equations



Nature has solved this problem by inserting *voltage-gated* channels into the membranes of many cell types. These channels are proteins which selectively let different ionic species into the cell. Furthermore, the permeability of the channels depends on the local environment near the channel. In particular, for voltage-gated channels, whether the channel is open or closed depends on the local potential near the channel. It is the opening and closing of voltage-gated channels that is responsible for the generation of the action potential that propagates along the axon.

Hodgkin and Huxley (1952) were the first to provide a comprehensive, quantitative description of the regenerative currents generating the action potential. The choice of the squid axon was fortuitous since the electrical properties rely primarily on Na^+ and K^+ ions. Consider the equivalent circuit shown in Fig. 1.6 and assume the cell is isopotential. Then the membrane potential satisfies

$$C_M \frac{dV}{dt} = -g_{\text{Na}}(V - E_{\text{Na}}) - g_{\text{K}}(V - E_{\text{K}}) - g_L(V - E_L).$$

Here, we write V instead of V_M and $I_L \equiv g_L(V - E_L)$ is called the *leak current*. It corresponds to passive flow of ions through nongated channels. The leak conductance, g_L , is constant. Since most nongated channels are permeable to K^+ ions, E_L is close to E_K . The conductances g_{Na} and g_{K} may change with time since these correspond to the opening and closing of Na^+ and K^+ channels, respectively. At rest, g_K is about 30-fold bigger than g_{Na} , so the resting state is near E_K at about -65 mV . Suppose we could increase the conductance of g_{Na} 100-fold, then the resting potential would be much closer to the Nernst potential of Na^+ , which is about $+55 \text{ mV}$. Thus, the amplification of the potential, such as during an action potential, involves changes in the relative conductances of the dominant ionic species. Hodgkin and Huxley's insight was that voltage-gated channels provide the substrate for this dynamic regulation of the conductances.

The basic mechanisms underlying action potentials are the following (Fig. 1.7). At rest, most of the Na^+ channels are closed, so the membrane potential is determined primarily by the K^+ Nernst potential. If the cell is depolarized above some threshold, then Na^+ channels open and this further depolarizes the cell. This allows

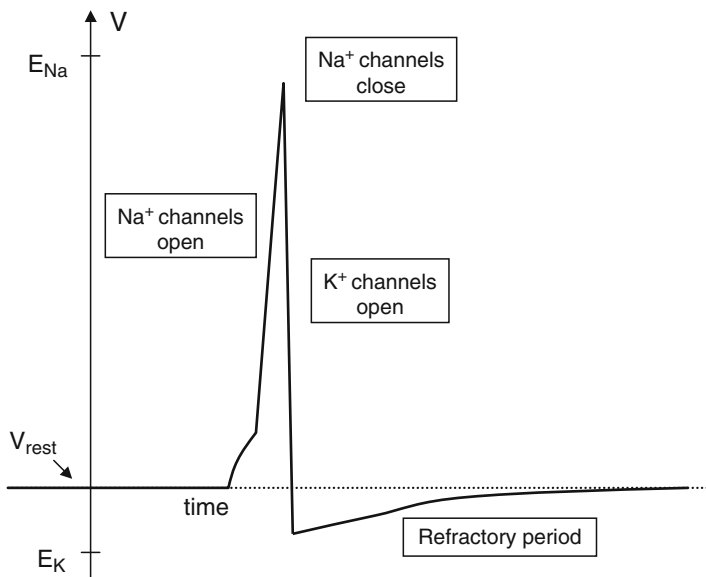


Fig. 1.7 The action potential. During the upstroke, Na^+ channels open and the membrane potential approaches the Na^+ Nernst potential. During the downstroke, Na^+ channels are closed, K^+ channels are open, and the membrane potential approaches the K^+ Nernst potential

even more Na^+ channels to open, allowing more Na^+ ions to enter the cell and forcing the cell toward the Na^+ Nernst potential. This is the upstroke of the action potential. The Na^+ channel is transient, so even when they are depolarized, the Na^+ channels eventually shut down. In the meantime, the depolarization opens K^+ channels and K^+ ions exit the cell. This hyperpolarizes the cell as the membrane potential moves toward the K^+ equilibrium potential. Until the voltage-gated K^+ channels close up again, the membrane is refractory. During this time, pumps exchange excess Na^+ ions inside the cell with excess K^+ ions outside the cell.

Only a very small change in the concentration of Na^+ ions is needed to generate an action potential. From the exercises, we find that approximately 53 million Na^+ ions must diffuse across the membrane to depolarize it from -60 to $+50$ mV. This influx of Na^+ ions represents only a 0.012% change in the internal Na^+ concentration, which is typically around 12 mM. Hence, changes in local charge separation, not in concentration, are required for an action potential.

1.8 Voltage-Gated Channels

In the Hodgkin–Huxley model, each channel is viewed as a transmembrane protein that forms a pore through which ions can diffuse down their concentration gradients. The pores have gates that can be either open or closed; the probability that a

gate is open or closed depends on the membrane potential. The gate model can be summarized by the diagram



where C and O correspond to the closed and open states, respectively, and $\alpha(V)$ and $\beta(V)$ are the voltage-dependent rate constants at which a gate goes from the closed to the open and from the open to the closed states, respectively. If we let m be the fraction of open gates, then $1 - m$ is the fraction of closed gates, and, from the law of mass action,

$$\frac{dm}{dt} = \alpha(V)(1 - m) - \beta(V)m = (m_\infty(V) - m)/\tau(V), \quad (1.34)$$

where

$$m_\infty(V) = \frac{\alpha(V)}{\alpha(V) + \beta(V)} \quad \text{and} \quad \tau(V) = \frac{1}{\alpha(V) + \beta(V)}. \quad (1.35)$$

It is easy to solve this equation if V is constant. The solution starting at $m(0)$ is

$$m(t) = m_\infty(V) + (m(0) - m_\infty(V))e^{-t/\tau(V)}.$$

Note that the solution approaches the steady-state $m_\infty(V)$ at a rate determined by the time constant $\tau(V)$.

One must obtain expressions for the voltage-dependent rate constants α and β . In the Hodgkin–Huxley model, these functions were derived by fitting the data. Borg-Graham [17] and others have suggested a simple formulation based on thermodynamics. The idea is that the probability of opening or closing a channel depends exponentially on the potential. Thus,

$$\alpha(V) = A_\alpha \exp(-B_\alpha V) \quad \text{and} \quad \beta(V) = A_\beta \exp(-B_\beta V). \quad (1.36)$$

From this, we find that

$$m_\infty(V) = \frac{1}{1 + \exp(-(V - V_h)/V_s)},$$

where V_h and V_s are constants. We leave as an exercise the calculation of these constants in terms of the constants A and B . The time constant, $\tau(V)$, will generally be a skewed bell-shaped function of V . If $B_\beta = -B_\alpha$, then $\tau(V)$ is a hyperbolic secant.

1.9 Hodgkin–Huxley Model

We are now ready to derive the Hodgkin–Huxley model for the propagation of an action potential along the squid’s giant axon. We view the axon as a cylinder of fixed radius, a , so the membrane potential depends on the spatial variable x and time t . Here, we assume there are voltage-gated K^+ and Na^+ channels and a leak current. Then balancing currents, as in (1.23), we have

$$I_L = I_{\text{cap}} + I_{\text{ion}} \quad (1.37)$$

or, using (1.6) and (1.24),

$$\frac{a}{2r_L} \frac{\partial^2 V_M}{\partial x^2} = c_M \frac{\partial V_M}{\partial t} + I_K + I_{\text{Na}} + I_L. \quad (1.38)$$

If each ionic current is ohmic, then this can be written as

$$c_M \frac{\partial V_M}{\partial t} = \frac{a}{2r_L} \frac{\partial^2 V_M}{\partial x^2} - g_K(V_M - E_K) - g_{\text{Na}}(V_M - E_{\text{Na}}) - g_L(V_M - E_L). \quad (1.39)$$

To complete the model, we need to describe how one computes the membrane conductances g_K , g_{Na} , and g_L . Note that the voltage-gated conductances g_K and g_{Na} change with time during an action potential.

Hodgkin and Huxley used two experimental methods to separate the ionic currents and compute how the K^+ and Na^+ conductances depend on voltage. The first was a simple feedback circuit called the *voltage clamp* that allows the experimenter to hold the membrane potential at a constant or holding level V_C . The voltage clamp does so by injecting a current into the axon that is equal and opposite to the current flowing through the voltage-gated channels. Electrical details can be found in the book by Johnston and Wu [139]. Note that the voltage clamp separates the total membrane current into its ionic and capacitive components. Recall that the capacitive current satisfies $I_{\text{cap}} = C_M dV_M/dt$. If the membrane potential is fixed at some constant, then the capacitive current must be zero. Moreover, the total current can be made spatially uniform by inserting a highly conductive axial wire inside the fiber; the axon is then said to be *space-clamped*. In this case, $\frac{\partial^2 V_M}{\partial x^2} = 0$. It then follows that any changes in current must be due to either the leak or the opening and closing of voltage-gated membrane channels.

We first consider how the voltage clamp can be used to determine the leak conductance, g_L . Note that most of the voltage-gated channels are closed at rest. Moreover, if we hyperpolarize the cell, then we may assume all of the voltage-gated channels are closed. It follows that if the membrane potential is clamped at some sufficiently strong hyperpolarized level, then the total current is given by the leak; that is,

$$I_M \approx g_L(V_C - E_L).$$

From this equation, we can easily solve for g_L .

Fig. 1.8 Numerically computed voltage-clamp experiment. The membrane potential is stepped from rest to 0 mV. This results in an inward current followed by an outward current. The separate K^+ and Na^+ currents are also shown

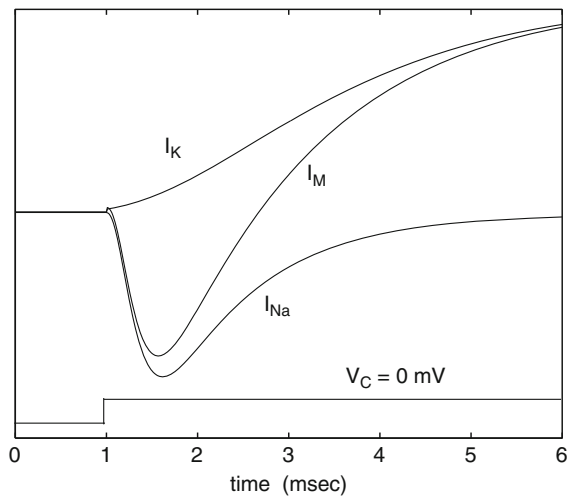


Figure 1.8 shows the results of a (numerically computed) voltage-clamp experiment when the membrane potential is clamped at 0 mV. Note that there is an inward current followed by an outward current. This result suggests the depolarizing voltage step turns on two voltage-gated channels. The inward current is due to the influx of Na^+ ions, whereas the outward current is due to the outward flow of K^+ ions. It is not clear, however, how these two separate ions contribute to the total membrane current. For this it is necessary to isolate the two voltage-gated currents.

Hodgkin and Huxley were able to isolate the K^+ current by replacing Na^+ ions in the external bathing solution with a larger, impermeant cation. This eliminated the inward Na^+ current. Now there are dozens of compounds that selectively block different currents, many derived from natural toxins. (For example, tetrodotoxin, which blocks Na^+ channels, comes from the Pacific puffer fish, a tasty, if slightly dangerous, Japanese delicacy called fugu.) Once Na^+ has been removed, the voltage clamp can be used to determine how I_K depends on the membrane potential. That is, one holds the membrane potential at various levels and determines the time course of the total membrane current I_M . If Na^+ is removed, then the K^+ current is computed by subtracting the leak current from I_M .

It is also now possible to block K^+ channels using the drug tetraethylammonium. This was not available to Hodgkin and Huxley; however, if I_K and I_L are known, then one computes I_{Na} simply by subtracting I_K and I_L from I_M . Once these currents have been determined, we can calculate the I_K and I_{Na} conductances using Ohm's law. That is,

$$g_K(t) = \frac{I_K(t)}{(V_M - E_K)} \quad \text{and} \quad g_{Na}(t) = \frac{I_{Na}(t)}{(V_M - E_{Na})}. \quad (1.40)$$

Figure 1.9 shows the I_K and I_{Na} conductances for different levels of the holding potential. Note that g_{Na} turns on more rapidly than g_K . Moreover, the Na^+ channels

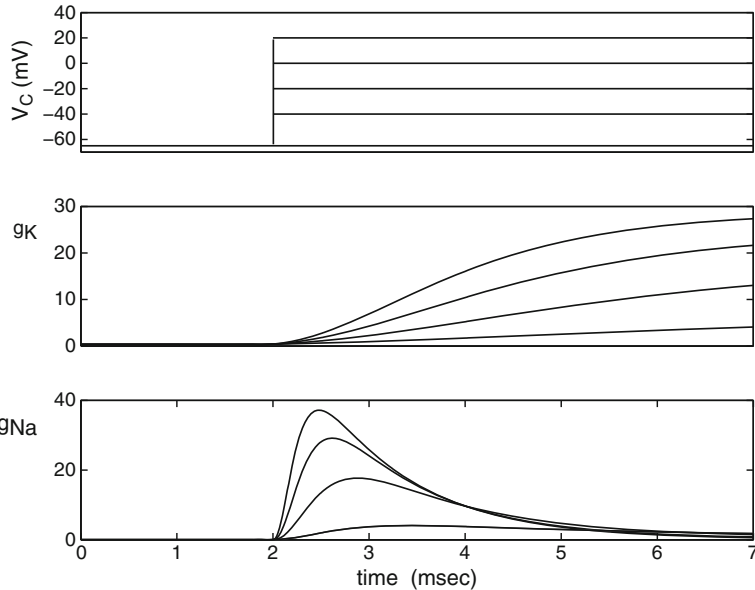


Fig. 1.9 Numerically computed voltage-clamp experiment. The membrane potential is stepped to different values and the resulting K^+ and Na^+ conductances are computed

begin to close before the depolarization is turned off, whereas the K^+ channels remain open as long as the membrane is depolarized. This suggests the Na^+ channel can exist in three states: resting, activated, and inactivated. When the cell is depolarized, the Na^+ channels switch from the resting (closed) to the activated (open) state. If the depolarization is maintained, then the channel switches to the inactivated (closed) state.

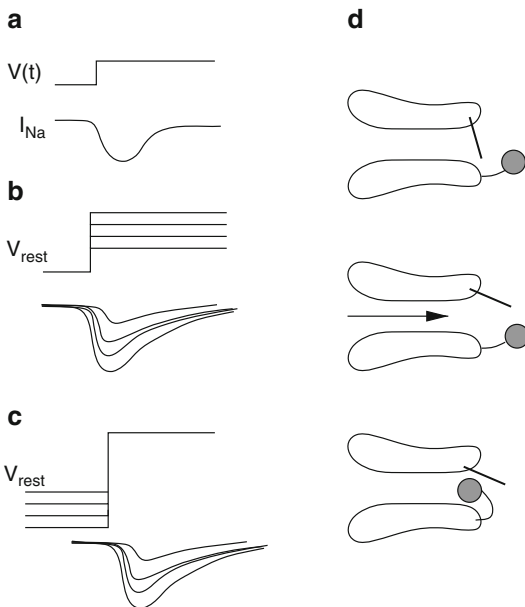
A physical interpretation of the Na^+ channel is shown in Fig. 1.10. There are two gates in the Na^+ channel: a fast one (the activation gate), represented by the line, and a slow one (the inactivation gate), represented by the ball. Both gates must be open for the channel to conduct Na^+ ions. At rest, the activation gate is closed and the inactivation gate is open. When the membrane is depolarized, the activation gate opens, which allows Na^+ into the cell. The inactivation gate (ball) closes at the higher potential, so the flow of Na^+ is transient. Hodgkin and Huxley used a more complicated voltage-clamp protocol, first stepping to a fixed voltage and then applying brief voltage steps to probe the fast activation and slow inactivation gates. Details can be found in [144].

Using the voltage-clamp data, Hodgkin and Huxley derived expressions for the K^+ and Na^+ conductances. They proposed that

$$g_{\text{K}} = \bar{g}_{\text{K}} n^4 \quad \text{and} \quad g_{\text{Na}} = \bar{g}_{\text{Na}} m^3 h, \quad (1.41)$$

where \bar{g}_{K} and \bar{g}_{Na} are maximum conductances and n , m , and h are gating variables that take values between 0 and 1. Hence, n^4 represents the probability that a K^+

Fig. 1.10 The Hodgkin–Huxley Na^+ channel. (a–c) Voltage-clamp dynamics. (d) Physical model of the channel. If the voltage step is small (d, top) then the Na^+ channel’s activation gate (line) is closed but the inactivation gate (ball) is open. At intermediate steps (d, middle), both gates are partially open. For large steps (d, bottom), the activation gate is open and the inactivation gate is closed



channel is open: the K^+ channel has four independent components, all of which are identical. The probability that the sodium activation gate is open is m^3 and the probability that the sodium inactivation gate is open is h . Each of the gating variables satisfies a first-order differential equation of the form (1.34). That is, they satisfy equations of the form

$$\begin{aligned}\frac{dn}{dt} &= \alpha_n(V)(1-n) - \beta_n(V)n = (n_\infty(V) - n)/\tau_n(V), \\ \frac{dm}{dt} &= \alpha_m(V)(1-m) - \beta_m(V)m = (m_\infty(V) - m)/\tau_m(V), \\ \frac{dh}{dt} &= \alpha_h(V)(1-h) - \beta_h(V)h = (h_\infty(V) - h)/\tau_h(V).\end{aligned}$$

If $X = n, m$, or h , then

$$X_\infty(V) = \frac{\alpha_X(V)}{\alpha_X(V) + \beta_X(V)} \quad \text{and} \quad \tau_X(V) = \frac{1}{\alpha_X(V) + \beta_X(V)}. \quad (1.42)$$

To match the data, Hodgkin and Huxley chose the following parameters and gating functions: $\bar{g}_{\text{Na}} = 120 \text{ mS/cm}^2$, $\bar{g}_{\text{K}} = 36 \text{ mS/cm}^2$, $\bar{g}_{\text{L}} = 0.3 \text{ mS/cm}^2$, $E_{\text{Na}} = 50 \text{ mV}$, $E_{\text{K}} = -77 \text{ mV}$, $E_{\text{L}} = -54.4 \text{ mV}$,

$$\begin{aligned}\alpha_n(V) &= 0.01(V + 55)/(1 - \exp(-(V + 55)/10)), \\ \beta_n(V) &= 0.125 \exp(-(V + 65)/80), \\ \alpha_m(V) &= 0.1(V + 40)/(1 - \exp(-(V + 40)/10)),\end{aligned}$$

$$\begin{aligned}\beta_m(V) &= 4 \exp(-(V + 65)/18), \\ \alpha_h(V) &= 0.07 \exp(-(V + 65)/20), \\ \beta_h(V) &= 1/(1 + \exp(-(V + 35)/10)).\end{aligned}$$

In Fig. 1.11, we plot the *activation curves* $n_\infty(V)$, $m_\infty(V)$, and $h_\infty(V)$ along with $\tau_n(V)$, $\tau_m(V)$, and $\tau_h(V)$. Note that n_∞ and m_∞ are increasing functions that approach 0 for hyperpolarizing currents and approach 1 for depolarizing currents. Hence, n and m become activated when the membrane is depolarized. On the other hand, $h_\infty(V)$ is a decreasing function, so the Na^+ channels inactivate when the membrane is depolarized. It is also important to note that $\tau_m(V)$ is considerably smaller than τ_n or τ_h . Hence, Na^+ channels activate much faster than they inactivate or K^+ channels open. In Fig. 1.12, we show the response of m , h , and n to a step in voltage.

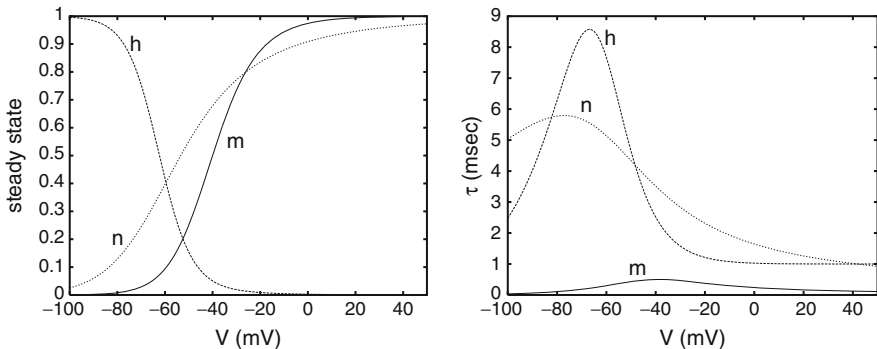


Fig. 1.11 Hodgkin–Huxley functions. *Left* the steady-state opening of the gates and *right* the time constants

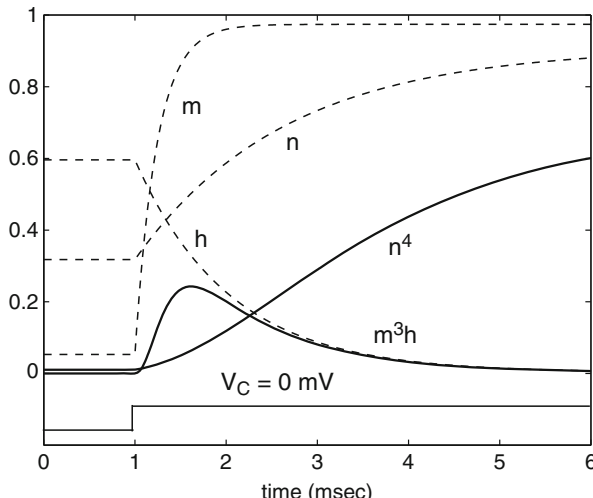


Fig. 1.12 Response of the activation and inactivation variables m , h , and n to a step in voltage

1.10 The Action Potential Revisited

In summary, the Hodgkin–Huxley model is a system of four differential equations; there is one equation for the membrane potential and three equations for channel gating variables. In the case of a space-clamped squid axon, we write these equations as

$$\begin{aligned} c_M \frac{dV}{dt} &= -\bar{g}_{Na} m^3 h (V - E_{Na}) - \bar{g}_K n^4 (V - E_K) - \bar{g}_L (V - E_L), \\ \frac{dn}{dt} &= \phi [\alpha_n(V)(1-n) - \beta_n(V)n], \\ \frac{dm}{dt} &= \phi [\alpha_m(V)(1-m) - \beta_m(V)m], \\ \frac{dh}{dt} &= \phi [\alpha_h(V)(1-h) - \beta_h(V)h]. \end{aligned} \quad (1.43)$$

Here, we added a parameter ϕ ; this is the *temperature factor*. It is important to realize that the temperature at which an experiment is done can be very important. Since channels are stochastic in nature, they are sensitive to the temperature, so the rates of switching states depend exponentially on the temperature. Higher temperatures cause faster switching. Thus, there is a factor

$$\phi = Q_{10}^{(T-T_{base})/10}. \quad (1.44)$$

Q_{10} is the ratio of the rates for an increase in temperature of 10°C. For the squid giant axon, $T_{base} = 6.3^\circ\text{C}$ and $Q_{10} = 3$.

Figure 1.13 shows solutions of these equations in response to different levels of steps in currents. Note that there is “all-or-none” behavior: When the applied current is below some threshold, the membrane potential returns quickly to the rest; when the current is above some threshold, there is an action potential. If the applied current is sufficiently large and held for a sufficiently long time, then the model generates a periodic response.

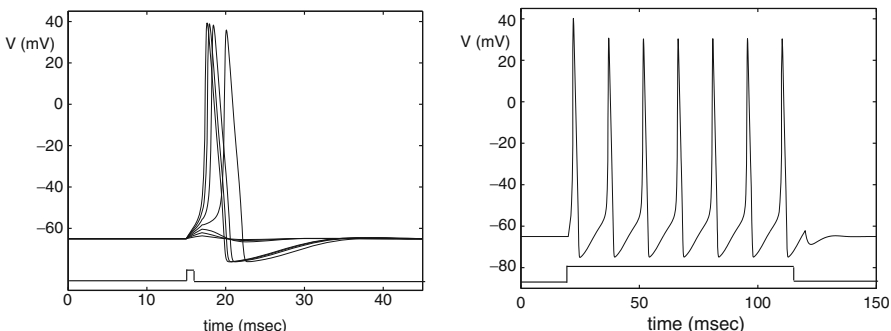


Fig. 1.13 Responses of the Hodgkin–Huxley model to applied currents. *Left* transient responses showing “all-or-none” behavior and *right* sustained periodic response

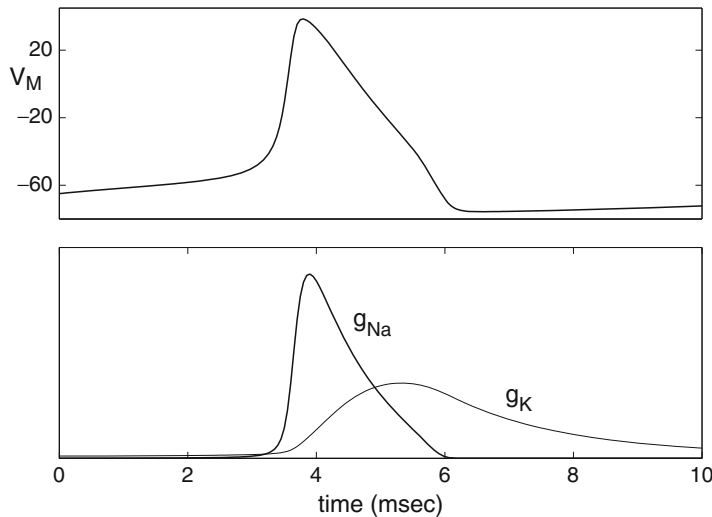


Fig. 1.14 Solution of the Hodgkin–Huxley equations showing an action potential. Also shown are the Na^+ and K^+ conductances

Figure 1.14 shows an action potential along with plots of the Na^+ and K^+ conductances, g_{Na} and g_K . Here, we start with the cell at rest and then depolarize the cell by 10 mV at $t = 0$. The cell then generates a single action potential. In Sect. 1.8, we described the events underlying the action potential in terms of the inward and outward flow of Na^+ and K^+ ions. Here, we give a more “mathematical” explanation in terms of the behavior of the dependent variables in the differential equations.

When we depolarize the cell, we change the values of the activation curves: $n_\infty(V)$ and $m_\infty(V)$ increase, whereas $h_\infty(V)$ decreases. Since n , m , and h tend toward their activation curves, it follows that n and m initially increase, whereas h decreases. That is, K^+ channels open, whereas Na^+ channels both activate and inactivate. However, τ_m is much smaller than both τ_h and τ_n . It follows that the Na^+ channels activate much faster than they inactivate or K^+ channels open. Therefore, the Na^+ conductance, $g_{\text{Na}} = \bar{g}_{\text{Na}} m^3 h$, increases faster than $g_K = \bar{g}_K n^4$.

The increase in the Na^+ conductance leads to a large increase in the Na^+ current, $I_{\text{Na}} = g_{\text{Na}}(V - E_{\text{Na}})$. As long as the cell is near rest, the driving force $V - E_{\text{Na}}$ is large (recall that $E_{\text{Na}} \approx +55$ mV). Hence, the Na^+ current will dominate the equation for the membrane potential and V will increase toward the Na^+ Nernst potential. As V increases, $m_\infty(V)$ increases further, leading to further increase in Na^+ activation.

As V increases toward E_{Na} , Na^+ channels inactivate. This is because $h \rightarrow h_\infty(V) \approx 0$. Moreover, the Na^+ driving force $V - E_{\text{Na}}$ decreases. For both reasons, the Na^+ current turns off. Meanwhile, the K^+ channel activates because $n \rightarrow n_\infty(V) \approx 1$. Moreover, the K^+ driving force $V - E_K$ becomes very large.

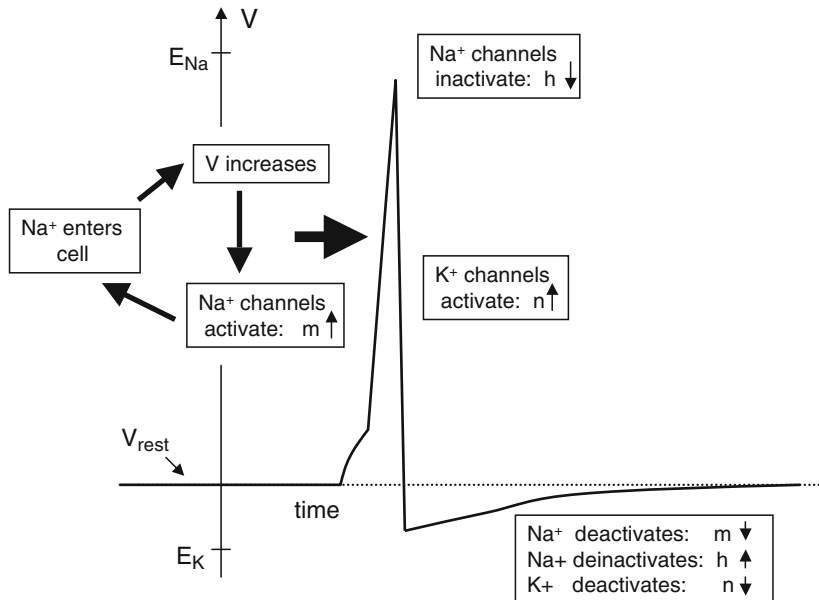


Fig. 1.15 Mechanisms underlying the action potential

It follows that eventually, the K^+ current dominates and the membrane potential must fall back toward the K^+ Nernst potential. This corresponds to the downstroke of the action potential.

After the action potential (Fig. 1.15), the cell is hyperpolarized with $m_\infty \approx 0$, $n_\infty \approx 0$, and $h_\infty \approx 1$. After some time, m , n , and h approach their steady-state values and the cell returns to rest.

1.11 Bibliography

There are many standard neuroscience textbooks that present the biological aspects covered in this chapter in much more detail. These textbooks include those by Kandel et al. [144], Hille [122], and Martin [192]. The reader is also highly recommended to look at Hodgkin and Huxley's original papers [124]. A review of these papers, along with a short review of the history leading up to them, is given in Rinzel [229]. Excellent textbooks which emphasize modeling and quantitative approaches are those of Johnston and Wu [139], Koch [156], Jack et al. [137], Izhikevich [136], and Dayan and Abbott [54]. Keener and Sneyd [148] and Fall et al. [83] give detailed introductions to mathematical aspects of cellular biophysics.

1.12 Exercises

- Suppose the external potassium in a mammalian cell is increased by a factor of 10. What is the new value of E_K ?
- At 10°C a cell contains 80 mM sodium inside and has only 100 mM sodium outside. What is the equilibrium potential for sodium?
- Compute the resting potential for the mammalian cell using the same permeabilities as were used for the squid axon and the ion concentrations listed in Table 1.1.
- Derive the Nernst equation (1.2) from the Nernst–Planck equation by setting the current to zero and integrating with respect to x across the membrane.
- Compute the calcium equilibrium potential for a mammalian cell assuming that the extracellular concentration is 5 mM and the intracellular concentration is 10^{-4} mM.
- Complete the derivation the constant-field equation (1.3) from the linear Nernst–Planck equation.
- Derive the GHK equation (1.4) from the constant-field equation.
- Consider the GHK equation and plot the I – V relation for different values of the inside and outside concentrations. Show that for $[C]_{\text{out}} > [C]_{\text{in}}$ (respectively $[C]_{\text{out}} < [C]_{\text{in}}$) the I – V plot is concave down (respectively up).
- Consider a passive, spherical cell with radius 0.003 cm^2 , a resting membrane potential of -65 mV , a membrane capacitance of $1 \mu\text{F}/\text{cm}^2$, and a membrane resistance of $R_M = 700 \Omega \text{ cm}^2$. Suppose the cell is injected with an applied current of $5 \text{ nA}/\mu\text{m}^2$ for 2 s and then the current is turned off. What is the membrane potential at $t = 1$, $t = 2$, and $t = 3$?
- Suppose a passive axon has a diameter of 0.5 mm, a resting membrane resistance of $R_M = 700 \Omega \text{ cm}^2$, and a transmembrane resistance of $R_L = 30 \Omega \text{ cm}$. Compute the space constant. If the axon is 5 cm long and one end of the axon is held at 120 mV above rest, then what is the potential at the other end?
- (Johnston and Wu [139], page 12) The membrane capacitance of a typical cell is $1 \mu\text{F}/\text{cm}^2$ and the concentration of ions inside and outside the cell is about 0.5 M. Calculate the fraction of uncompensated ions on each side of the membrane required to produce 100 mV in a spherical cell with a radius of 25 μm .
- Numerically solve the Hodgkin–Huxley equations. Start the system at rest and, at some later time, inject an applied current to generate an action potential. Plot the time courses of the Na^+ and K^+ conductances, as well as the gating variables m , h and n .
- Numerically perform space-clamp experiments. That is, start the Hodgkin–Huxley model at rest and, at some later time, change the membrane potential and keep it as some “clamped” level. Plot the Na^+ and K^+ conductances for when the membrane potential is stepped to different values.

Chapter 2

Dendrites

We now present mathematical theories for describing dendrites. Dendrites are very important for many reasons. Indeed, the majority of the total membrane area of many neurons is occupied by the dendritic tree. Dendrites enable neurons to connect to thousands of other cells, far more than would be possible with just a soma, as there is a huge membrane area to make connections. Dendrites may direct many subthreshold postsynaptic potentials toward the soma, which summates these inputs and determines if the neuron will fire an action potential. In addition to the treelike structure of dendrites, many dendrites have additional fine structures at the ends of the branches called *spines*. During development, animals that are raised in rich sensory environments have more extensive dendritic trees and more spines.

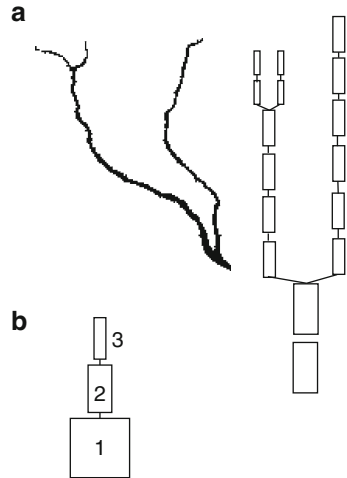
Here, we will mainly discuss classical models for dendritic structure, activity, and function. There has been tremendous progress recently in understanding the role dendrites play in, for example, learning and neuronal computations, and the classical view of dendrites is changing. Dendrites were originally thought, for example, to be passive, in which the conductances and currents are constant; however, it is now recognized that dendrites may have active voltage-gated channels and these may greatly influence the firing properties of the neuron and how the neuron responds to synaptic inputs. At the end of this chapter, we will briefly describe more recent developments in understanding dendritic function.

2.1 Multiple Compartments

A very useful way to treat complicated dendritic structures is the compartmental approach. Here, one divides the dendritic tree into small segments or compartments that are all linked together. Examples are shown in Fig. 2.1. Each compartment is assumed to be isopotential and spatially uniform in its properties. Differences in voltage and nonuniformity in membrane properties, including diameter, occur between compartments rather than within them.

As a simple example, consider a two-compartment model in which each compartment is viewed as an isopotential cylinder with radius a_i and length L_i . Let V_i be the membrane potential of the i th compartment and let c_i and r_{Mi} be the corresponding

Fig. 2.1 (a) Branched dendrite converted to a series of cylinders for modeling.
 (b) Simple three-compartment model



specific membrane capacitance and specific membrane resistivity, respectively. We assume each compartment has an electrode current and the total electrode current is given by $I_{\text{electrode}}^i$. Finally, we assume the intracellular, or longitudinal, resistivity is given by r_L .

Now the capacitive and ionic currents for each compartment must be balanced by the longitudinal and electrode currents. That is,

$$i_{\text{cap}}^i + i_{\text{ion}}^i = i_{\text{long}}^i + i_{\text{electrode}}^i, \quad (2.1)$$

where i_{cap}^i and i_{ion}^i are the capacitive and ionic currents per unit area of membrane for compartment i . As before,

$$i_{\text{cap}}^i = c_i \frac{dV_i}{dt} \quad \text{and} \quad i_{\text{ion}}^i = \frac{V_i}{r_{Mi}} \quad (2.2)$$

if we assume the resting potential is 0. To compute i_{long}^i , we need to determine the total axial resistance. Note that the total resistance between the centers of the two compartments is simply the sum of the two resistances of the half-cylinders that separate the compartment centers. That is, the total resistance is given by

$$R_{\text{long}} = \frac{r_L L_1}{2\pi a_1^2} + \frac{r_L L_2}{2\pi a_2^2}. \quad (2.3)$$

Using Ohm's law, we can write the expressions for the current from compartment i to compartment j as

$$i_{\text{long}}^{1,2} = g_{1,2}(V_2 - V_1) \quad \text{and} \quad i_{\text{long}}^{2,1} = g_{2,1}(V_1 - V_2). \quad (2.4)$$

The coupling terms $g_{1,2}$ and $g_{2,1}$ are obtained by inverting (2.3) and dividing by the surface area of the compartment of interest. That is,

$$g_{1,2} = \frac{a_1 a_2^2}{r_L L_1 (a_2^2 L_1 + a_1^2 L_2)}$$

and

$$g_{2,1} = \frac{a_2 a_1^2}{r_L L_1 (a_2^2 L_1 + a_1^2 L_2)}.$$

Finally, to compute $i_{\text{electrode}}^i$, we divide the total electrode currents by the surface areas of the compartments. That is,

$$i_{\text{electrode}}^i = \frac{I_{\text{electrode}}^i}{A_i},$$

where $A_i = 2\pi a_i L_i$ is the surface area of compartment i .

Putting this all together, we find that the equations for two connected cylinders are

$$\begin{aligned} c_1 \frac{dV_1}{dt} + \frac{V_1}{r_{M1}} &= g_{1,2}(V_2 - V_1) + \frac{I_{\text{electrode}}^1}{A_1}, \\ c_2 \frac{dV_2}{dt} + \frac{V_2}{r_{M2}} &= g_{2,1}(V_1 - V_2) + \frac{I_{\text{electrode}}^2}{A_2}. \end{aligned} \quad (2.5)$$

If instead of using conductances, $g_{i,j}$, we use $r_1 = 1/g_{1,2}$ and $r_2 = 1/g_{2,1}$ then we can express this system as

$$\begin{aligned} c_1 \frac{dV_1}{dt} + \frac{V_1}{r_{M1}} &= \frac{V_2 - V_1}{r_1} + i_1, \\ c_2 \frac{dV_2}{dt} + \frac{V_2}{r_{M2}} &= \frac{V_1 - V_2}{r_2} + i_2, \end{aligned} \quad (2.6)$$

where $i_i = I_{\text{electrode}}^i / A_i$.

We can now explore the effects of two compartments on the input resistance of the “cell.” Suppose we inject current into cell 1 only. Moreover, each cylinder is identical, with the same length and radius. Then, $r_1 = r_2 \equiv r$. What is the input resistance due to the coupling? To find this, we must compute the steady-state potential due to the coupling. Without loss in generality, define $r_M = r_{M1} = r_{M2}$. A simple bit of algebra shows that

$$V_1/i_1 = \frac{r_M(r + r_M)}{r + 2r_M}$$

and thus the ratio of the coupled to the uncoupled input resistance is

$$\frac{R_{\text{input,coupled}}}{R_{\text{input,uncoupled}}} = 1 - \frac{r_M}{r + 2r_M};$$

that is, the input resistance decreases. To get the same increment in potential, the current required for the coupled system is more than that required for the uncoupled system because some current is drained away by the second compartment.

In a similar way, we can derive a compartmental model for a general treelike structure. A general algorithm for computing the correct equations is

- For each cylinder, j , with radius and length a_j and L_j in micrometers, compute the surface area, $A_j = 2\pi a_j L_j$, and the axial resistance factor, $Q_j = L_j / (\pi a_j^2)$.
- The membrane capacitance is $C_j = c_j A_j \times 10^{-8}$ and the membrane resistance is $R_j = (r_M j / A_j) \times 10^8$.
- The coupling resistance between compartments j and k is $R_{jk} = \frac{r_L}{2}(Q_j + Q_k) \times 10^4$.
- The equations are then

$$C_j \frac{dV_j}{dt} = -\frac{V_j}{R_j} + \sum_{k \text{ connected } j} \frac{V_k - V_j}{R_{jk}} + I_j.$$

The factors of $10^{\pm 8}$ and 10^4 are the conversion from micrometers to centimeters. For example, consider a two-compartment model with (1) compartment 1 having a length of $200 \mu\text{m}$ and radius of $30 \mu\text{m}$ and (2) compartment 2 having a length of $20 \mu\text{m}$ and radius of $20 \mu\text{m}$. Then, $R_1 = 2.65 \times 10^7 \Omega$, $C_1 = 3.77 \times 10^{-10} \text{ F}$, $R_2 = 3.98 \times 10^8 \Omega$, $C_2 = 2.52 \times 10^{-11} \text{ F}$, and $R_{\text{long}} = 4.34 \times 10^4 \Omega$. Thus,

$$10 \frac{dV_1}{dt} = -V_1 + 611(V_2 - V_1), \quad 10 \frac{dV_2}{dt} = -V_2 + 9,181(V_2 - V_1),$$

where time is in milliseconds and the coupling coefficients are dimensionless. Note how the ratio of the coupling strengths is the same as the reciprocal of the area ratios. The bigger compartment has a much greater effect on the smaller compartment than vice versa.

We also remark that the standard units used in most compartmental models are microfarads per square centimeter, millisiemens per square centimeter, and microamperes per square centimeter for the capacitance, conductance, and applied current, respectively. Experimentalists do not generally know the current density, but only the total current injected. Typical currents injected into a cell are of the order of less than 1 nA.

To generate arbitrary compartmental models, one needs only to compute the length, diameter, and the connectivity of the cylinders that make up the dendritic tree. The program NEURON [33] enables an experimentalist to input a digitized picture of a neuron and the program will automatically produce a compartmental model of the neuron by linking together many cylinders.

2.2 The Cable Equation

Mathematically, dendrites and axons are regarded as continuous media rather than a series of compartments. Previously, we derived the cable equation for a simple cable in which the radius along the cable was assumed to be constant. Here we derive the cable equation for more general geometries. This is done by considering the limit as the number of compartments in an approximation of it tends to infinity.

Suppose the cable is defined on the interval $(0, \ell)$ with a circular cross-section and diameter $d(x)$. We break the cable into n pieces and define $x_j = jh$ where $h = \ell/n$. Each piece has a surface area $A_j = \pi d_j h$ where $d_j = d(x_j)$, and cross-sectional area, $\pi d_j^2/4$. Let c_M and r_M denote the specific membrane capacitance and resistance, and let r_L be the longitudinal resistance. Then, neglecting the end points, the voltage satisfies:

$$c_M A_j \frac{dV_j}{dt} = -\frac{V_j}{r_M/A_j} + \frac{V_{j+1} - V_j}{4r_L h / (\pi d_{j+1}^2)} + \frac{V_{j-1} - V_j}{4r_L h / (\pi d_j^2)}.$$

Note that we use the larger diameter for the transmembrane resistance; in simulations, the average of the two would be preferred. Dividing by h the coupling term simplifies to:

$$\frac{\pi}{h} \left(\frac{d_{j+1}^2(V_{j+1} - V_j)}{4r_L h} - \frac{d_j^2(V_j - V_{j-1})}{4r_L h} \right).$$

As $h \rightarrow 0$, this goes to the diffusion operator:

$$\frac{\pi}{4r_L} \frac{\partial}{\partial x} \left(d^2(x) \frac{\partial V}{\partial x} \right).$$

Thus, (dividing by $\pi d(x)$) the cable equation has the form:

$$c_M \frac{\partial V}{\partial t} = -\frac{V}{r_M} + \frac{1}{4r_L d(x)} \frac{\partial}{\partial x} \left(d^2(x) \frac{\partial V}{\partial x} \right). \quad (2.7)$$

We remark that the term

$$\frac{\pi d_j^2(V_{j-1} - V_j)}{4r_L h}$$

has dimensions of current and in the limit as $h \rightarrow 0$ is called the *longitudinal current*:

$$I_L = -\frac{\pi d^2(x)}{4r_L} \frac{\partial V}{\partial x}. \quad (2.8)$$

If one is interested only in the passive cable and $d(x) = d$ is constant, then it is convenient to multiply both sides by r_M obtaining the linear cable equation:

$$\tau \frac{\partial V}{\partial t} = -V + \lambda^2 \frac{\partial^2 V}{\partial x^2} \quad (2.9)$$

where

$$\lambda = \sqrt{\frac{dr_M}{4r_L}} \quad (2.10)$$

is the space constant. Since λ depends on the diameter of the cable, this parameter depends on the geometry of the cable. The quantity $\tau = r_M c_M$ is the time constant and is independent of geometry. For example, if $c_M = 1 \mu\text{F}/\text{cm}^2$, $r_M = 20,000 \Omega \text{ cm}^2$, $r_L = 100 \Omega \text{ cm}$, and the diameter of the cable is $2 \mu\text{m}$, then $\tau = 20 \text{ ms}$ and $\lambda = 1 \text{ mm}$.

2.3 The Infinite Cable

We first consider the infinite cable, so $-\infty < x < \infty$, with some applied current:

$$\tau \frac{\partial V}{\partial t} + V(x, t) - \lambda^2 \frac{\partial^2 V}{\partial x^2} = r_M I(x, t). \quad (2.11)$$

The current, $I(x, t)$ has units of microamperes per square centimeter. Additionally, we also must provide an initial voltage distribution, $V(x, 0) = V_0(x)$. We will solve this using Fourier transforms and then write the solution in terms of a *Green function*. Let

$$\begin{aligned}\hat{V}(k, t) &= \int_{-\infty}^{\infty} e^{-ikx} V(x, t) dx, \\ \hat{V}_0(k) &= \int_{-\infty}^{\infty} e^{-ikx} V_0(x) dx, \\ \hat{I}(k, t) &= \int_{-\infty}^{\infty} e^{-ikx} I(x, t) dx\end{aligned}$$

denote the Fourier transforms of V , V_0 , and I . Then, \hat{V} satisfies the differential equation

$$\begin{aligned}\frac{d\hat{V}}{dt} + (1 + \lambda^2 k^2) \hat{V} / \tau &= r_M \hat{I} / \tau, \\ \hat{V}(0) &= \hat{V}_0,\end{aligned}$$

where we have dropped the k dependence for simplicity. This is a linear first-order ordinary differential equation, so we can write the solution

$$\hat{V}(k, t) = e^{-(1+\lambda^2 k^2)t/\tau} \hat{V}_0(k) + (r_M / \tau) \int_0^t e^{-(1+\lambda^2 k^2)(t-s)/\tau} \hat{I}(k, s) ds.$$

Recalling that the inverse Fourier transform is

$$V(x, t) = \frac{1}{2\pi} \int_{-\infty}^{\infty} e^{ikx} \hat{V}(k, t) dk,$$

we find that $V(x, t)$ is given by

$$V(x, t) = \int_{-\infty}^{\infty} G(x - y, t) V_0(y) dy + \frac{r_M}{\tau} \int_0^t \int_{-\infty}^{\infty} G(x - y, t - s) I(y, s) dy ds,$$

where

$$G(x, t) = \frac{1}{\sqrt{4\pi\lambda^2 t/\tau}} e^{-t/\tau} e^{-x^2/(4\lambda^2 t/\tau)}. \quad (2.12)$$

Note that $G(x, t)$ has dimensions of λ^{-1} .

Suppose $V_0(x) = 0$ (that is, the membrane is at rest) and at $t = 0$, the membrane is perturbed by a delta function in space and time. That is, $I(x, t) = I_0 \delta(x) \delta(t)$. Then,

$$V(x, t) = \frac{r_M I_0}{\tau \lambda \sqrt{4\pi t/\tau}} \exp\left(-\frac{\tau x^2}{4\lambda^2 t}\right) \exp\left(-\frac{t}{\tau}\right). \quad (2.13)$$

In the exercises you are asked to analyze this. One interesting point is that at each spatial location x , the function $V(x, t)$ reaches its maximum at $t^*(x)$. You can obtain this expression using calculus and show that for x large, $t^*(x) \approx \tau x / 2\lambda$; that is, the voltage is a rapidly decaying “wave.”

For another example, consider an infinite cable with a step of constant applied current at a single point: $I(x, t) = I_0 \delta(x)$. Plugging this into (2.12), we find that

$$\begin{aligned} V(x, t) &= \frac{r_M I_0 \lambda}{4} \left[e^{-(x/\lambda)} \operatorname{erfc}\left(\frac{x\sqrt{\tau}}{2\lambda\sqrt{t}} - \sqrt{t/\tau}\right) \right. \\ &\quad \left. - e^{(x/\lambda)} \operatorname{erfc}\left(\frac{x\sqrt{\tau}}{2\lambda\sqrt{t}} + \sqrt{t/\tau}\right) \right], \end{aligned} \quad (2.14)$$

where

$$\operatorname{erfc}(x) = \frac{2}{\sqrt{\pi}} \int_x^{\infty} e^{-y^2} dy.$$

Note that $\operatorname{erfc}(0) = 1$, $\operatorname{erfc}(\infty) = 0$, and $\operatorname{erfc}(-\infty) = 2$. If we let $t \rightarrow \infty$ in (2.15), then $V(x, t)$ approaches the steady-state solution:

$$V_{ss}(x) = \frac{r_M I_0}{4\lambda} e^{-|x|/\lambda}.$$

Often a cable is described in terms of its *electrotonic length*, which is $L = \ell/\lambda$, where ℓ is the physical length and λ is the space constant.

2.4 Finite and Semi-infinite Cables

For the infinite cable, the only physically reasonable boundary condition is that $V(x) \rightarrow 0$ as $|x| \rightarrow \infty$. However, for the finite and semi-infinite cables, there are several interesting boundary conditions that are often used:

- *Sealed end*, where no current can pass and so the longitudinal current $I_L = 0$. It then follows from (2.8) that $\frac{\partial V}{\partial x}(0) = 0$.
- *Current injected at one end*, where a current of magnitude $I(t)$ is injected at, say, the end $x = 0$. In this case, $\frac{\partial V}{\partial x}(0) = \frac{4r_L}{\pi d^2} I(t)$.
- *Voltage clamp*, in which the voltage is clamped to some fixed level, so $V(0) = V_c$, a constant.
- *Short circuit or open end*, where the voltage is clamped to 0.
- *Lumped soma*, where we regard the soma as a single compartment attached to the nerve cable. Suppose the soma has total resistance R_s and capacitance C_s . Then, the boundary condition at $x = 0$ is

$$\frac{V(0, t)}{R_s} + C_s V_t(0, t) - \frac{\pi d^2}{4r_L} V_x(0, t) = 0.$$

Note that the general steady-state equation $0 = -V + \lambda^2 V_{xx}$ has solutions of the equivalent forms:

$$\begin{aligned} V(x) &= A_1 e^{-x/\lambda} + A_2 e^{x/\lambda}, \\ V(x) &= B_1 \cosh((l-x)/\lambda) + B_2 \sinh((l-x)/\lambda), \\ V(x) &= C_1 \cosh(x/\lambda) + C_2 \sinh(x/\lambda). \end{aligned}$$

The constants are determined from the boundary conditions. First consider the semi-infinite cable. This has a solution of the form $V(x) = A \exp(-x/\lambda)$. Suppose we inject current I_0 into the end of the cable. Recall that the longitudinal current is $I_0 = -(\pi d^2 / 4r_L) dV/dx$. Thus, we find that

$$A = \frac{4\lambda I_0 r_L}{\pi d^2}.$$

Recall that the *input resistance*, R_{inp} , of a cable is the ratio of the steady-state potential divided by the current injected. Thus, for the semi-infinite cable,

$$R_{\text{inp}} = V(0)/I(0) = \frac{4\lambda r_L}{\pi d^2} = \frac{2\sqrt{r_M r_L}}{\pi d^{3/2}},$$

and the input conductance is given by

$$G_{\text{inp}} = 1/R_{\text{inp}} = \frac{\pi d^{3/2}}{2\sqrt{r_M r_L}}.$$

For finite cables, it is convenient to use dimensionless space, $X = x/\lambda$, and the electrotonic length, $L = \ell/\lambda$. Assume the voltage at $X = 0$ is V_0 . Then, the general solution of the steady-state equation is

$$V(X) = V_0 \frac{\cosh(L - X) + B_L \sinh(L - X)}{\cosh L + B_L \sinh L},$$

where B_L is an arbitrary constant. This general solution is equivalent to asserting that the boundary condition at $X = 0$ is V_0 and that at $X = L$

$$B_L V(L) + \frac{dV}{dX}(L) = 0.$$

The free parameter, B_L , is the ratio of the terminal conductance for the cable, G_L , to that of the semi-infinite cable, G_{inp} . That is, $B_L = G_L/G_{\text{inp}}$.

For example, if we want the sealed-end condition at $X = L$, we take $B_L = 0$ so that

$$V(X) = V_0 \frac{\cosh(L - X)}{\cosh L}.$$

If we want the open-end condition, we take $B_L = \infty$ so that

$$V(X) = V_0 \frac{\sinh(L - X)}{\sinh L}.$$

If we choose $B_L = 1$, then

$$V(X) = V_0 e^{-X},$$

which is precisely the solution for the semi-infinite cable.

From these equations for the membrane potential, we can compute the input resistance and input conductance of a finite-length cable. For example, consider the sealed-end condition at $X = L$. Suppose a current, I_0 , is injected into the other end at $X = 0$. Then, the input resistance is given by

$$R_{\text{inp}} = V(0)/I_0 = V_0/I_0.$$

Now,

$$I_0 = -\frac{1}{\lambda r_L} \frac{\partial V}{\partial X} = \frac{V_0}{\lambda r_L} \frac{\sinh(L - X)}{\cosh(L)}.$$

It follows that

$$I_0 = \frac{V_0}{\lambda r_L} \tanh(L) \text{ at } X = 0.$$

Hence,

$$R_{\text{inp}} = \frac{\lambda r_L}{\tanh(L)} \quad \text{and} \quad G_{\text{inp}} = \frac{\tanh(L)}{\lambda r_L}.$$

2.5 Branching and Equivalent Cylinders

The infinite cable and the finite cable are simple idealizations of the multibranched structure of true neurons. Here, we briefly look at branch points and describe the Rall model for dendrites. Figure 2.2 shows a simple branched dendritic structure. Consider the cable with diameter d_0 , length ℓ_0 , and space constant λ_0 which branches at $x = x_1$ into two semi-infinite cables with diameters d_1 and d_2 and space constants λ_1 and λ_2 . The cable equation for such a structure can be solved on the individual segments coupled with continuity of the voltages and the conservation of current. Under certain constraints on the geometry, we can attain a stronger result than continuity of the voltage and its derivative that is important physically and allows us to significantly simplify the problem. With these constraints on the geometry, we will show that having the branch point at x_1 is exactly equivalent to extending branch d_0 to infinity.

Conservation of current implies that the current leaving branch d_0 equals the sum of the currents entering branches d_1 and d_2 . That is,

$$\frac{\pi d_0^2}{4r_L} V'_0(x_1) = \frac{\pi d_1^2}{4r_L} V'_1(x_1) + \frac{\pi d_2^2}{4r_L} V'_2(x_1). \quad (2.15)$$

Here, we assume the material properties of the cables are the same; only their geometry differs. Now, if we let $V_0 \equiv V_0(x_1) = V_1(x_1) = V_2(x_1)$, then

$$V_1(x) = V_0 e^{-(x-x_1)/\lambda_1} \quad \text{and} \quad V_2(x) = V_0 e^{-(x-x_1)/\lambda_2}$$

for $x > x_1$. Moreover, if $V_{\text{eq}}(x)$ is the membrane potential of the cable obtained by extending branch d_0 to infinity, then

$$V_{\text{eq}}(x) = V_0 e^{-(x-x_1)/\lambda_0}.$$

Plugging these into (2.15), and recalling that $\lambda_j \propto \sqrt{d_j}$, we find that we can collapse the three cables 0, 1, and 2 into a single semi-infinite cable with diameter d_0 if

$$d_0^{\frac{3}{2}} = d_1^{\frac{3}{2}} + d_2^{\frac{3}{2}}. \quad (2.16)$$

Rall was the first to recognize that if (2.16) is satisfied and the material properties of the cables are the same, then the three cables 0, 1, and 2 can be collapsed into an *equivalent cylinder*. For a complex structure, starting at the ends, we can recursively

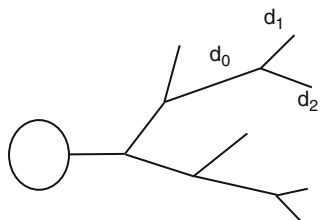


Fig. 2.2 A simple dendritic tree

simplify the model to a single semi-infinite cylinder. In the previous example, we considered only two branches at the branch point; however, we could have had any number of branches at each branch point as long as

$$d_p^{\frac{3}{2}} = \sum d_D^{\frac{3}{2}},$$

where d_p is the diameter of the parent dendrite and d_D are the diameters of the daughter dendrites. If this condition holds at every branch point and the material properties of the cables are the same, then the entire dendritic tree can be reduced to an equivalent semi-infinite cable.

We have so far assumed the branches attached to the final branch point extend to infinity; that is, they correspond to semi-infinite cables. A similar analysis holds if we assume all of the branches have finite lengths. Here, we must assume all dendrites end at the same electrotonic length. Recall that the electrotonic length of a cable of length ℓ and space constant λ is ℓ/λ . Suppose, for example, cables 1 and 2 shown in Fig. 2.2 have lengths ℓ_1 and ℓ_2 . If we assume $\ell_1/\lambda_1 = \ell_2/\lambda_2$, then we can collapse the three cables 0, 1, and 2 into a single cable of diameter d_0 and electrotonic length equal to $\ell_0/\lambda_0 + \ell_1/\lambda_1 = \ell_0/\lambda_0 + \ell_2/\lambda_2$.

Example:

In Fig. 2.3, we depict a dendritic tree consisting of several branches with their lengths and diameters in micrometers. Can this dendritic tree be reduced to an equivalent cylinder? What is the electrotonic length? What is the input conductance? Assume sealed ends for all terminal dendrites and assume $r_M = 2,000 \Omega \text{ cm}^2$ and that $r_L = 60 \Omega \text{ cm}$.

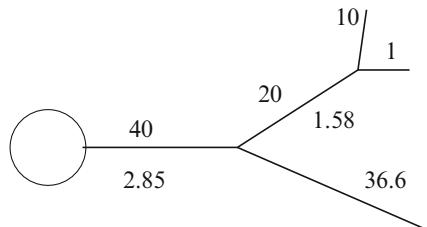
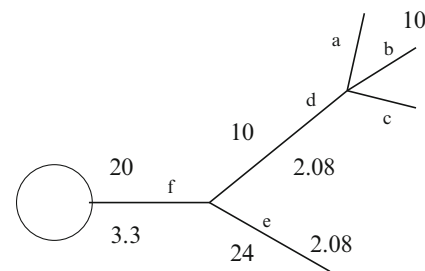


Fig. 2.3 Example of the Rall reduction to an equivalent cylinder

Answer:

$$d_a^{3/2} + d_b^{3/2} + d_c^{3/2} = 1 + 1 + 1 = 3 = 2.08^{3/2} = d_d^{3/2},$$

$$d_d^{3/2} + d_e^{3/2} = 3 + 3 = 6 = 3.3^{3/2} = d_f^{3/2}$$

so the 3/2 rule is obeyed. Clearly a , b , and c are all the same electrotonic length. The space constants are

$$\lambda_a = \lambda_b = \lambda_c = \sqrt{d_a r_M / 4r_L} = 289 \mu\text{m},$$

$$\lambda_d = \lambda_e = \sqrt{d_e r_M / 4r_L} = 416 \mu\text{m},$$

$$\lambda_f = \sqrt{d_f r_M / 4r_L} = 524 \mu\text{m}.$$

Thus, the total electrotonic length of a , b , and c with d is

$$L_{abcd} = \frac{\ell_a}{\lambda_a} + \frac{\ell_d}{\lambda_d} = \frac{10}{289} + \frac{10}{416} = 0.0586,$$

and

$$L_e = \frac{\ell_e}{\lambda_e} = \frac{24}{416} = 0.0576,$$

which are close enough to be considered equal (2% difference). Thus, we can combine the whole thing into an equivalent cylinder. The total electrotonic length is then

$$L = L_f + L_e = L_f + L_{abcd} = \frac{\ell_f}{\lambda_f} + L_e = 0.096 \approx 0.1.$$

Finally, the input conductance is

$$G_{\text{inp}} = G_\infty \tanh L = \frac{\pi d^{3/2}}{2\sqrt{r_L r_M}} \tanh L,$$

which is

$$G_{\text{inp}} = \frac{\tanh(0.1)(3.14159)(3.3 \times 10^{-4})^{3/2}}{2\sqrt{2000 \times 60}} = 2.7 \times 10^{-9} \text{ S}.$$

2.6 An Isolated Junction

The equivalent cylinder is a very useful method for reducing the analysis of complex dendritic trees to a simpler model. However, there are limitations. For example, one must assume the so-called 3/2 law (see (2.16)) is satisfied. Another difficulty is related to the problem of determining the response of the dendritic tree to an

injected current. Consider, for example, the simple dendritic tree shown in Fig. 2.2. If the injection site is at d_0 , then the principal initial cylinder, then the equivalent cylinder will determine the membrane potential responses at this and the daughter dendrites. However, if the injection site is along the daughter dendrites, then to use the equivalent circuit, one must assume the current is spread out evenly along all of the daughter dendrites that emerge from the same junction point. One cannot use the equivalent circuit if only one of the daughter dendrites receives input and the others receive no input.

In this section, we consider a single isolated junction of three semi-infinite cables with a point source of current injection. We do not assume the 3/2 law holds. We note that a considerably more general analysis for dendritic trees with complex geometries is given in [222].

We consider the branched cable shown in Fig. 2.4. The three cables are denoted as C_0 , C_1 , and C_2 . Assume the diameters and specific membrane resistance of the cables are d_i and r_{Mi} , $i = 0, 1, 2$, respectively. Let r_L be the longitudinal resistivity. We assume the junction point is at $x = 0$. Finally, we assume there is an electrode current at an isolated point, y , along C_0 (here, $y < 0$).

We derive the steady-state solution to this problem. Except at the junction and the injection points, each membrane potential $V_i(x)$ satisfies the steady-state cable equation:

$$\lambda_i^2 \frac{\partial^2 V_i}{\partial x^2} - V_i = 0,$$

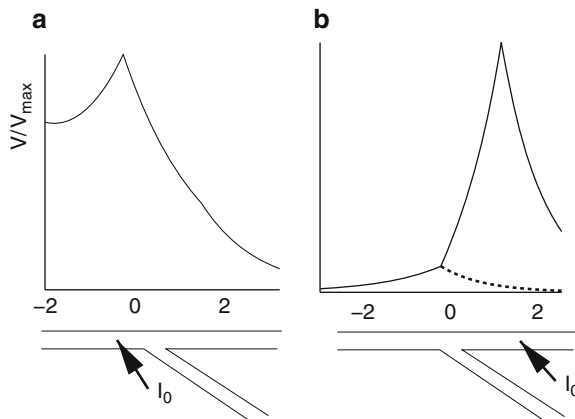


Fig. 2.4 The membrane potential along three cables branched at an isolated junction for a current injected at one point. The thick branch has a radius of $2 \mu\text{m}$ and an electrotonic length constant of 1 mm . The thin cables have a radius of $1 \mu\text{m}$ and an electrotonic length constant of $2^{-1/2} \text{ mm}$. (a) Current injected along the thick cable. The solid curve for $x < 0$ shows the voltage along the thick branch where current is being injected. The curve for $x > 0$ shows the potential for both thin cables, which are identical. (b) Current injected along one of the thin cables. The solid curve for $x > 0$ shows the potential along the cable where the current is injected and the dashed curve for $x > 0$ shows the potential along the cable where the injection does not occur. The solid curve for $x < 0$ shows the potential for the thick cable

where

$$\lambda_i = \sqrt{\frac{d_i r_{Mi}}{4r_L}}$$

is the space constant of the corresponding cable. We now need to determine the boundary conditions that must be satisfied. At the junction point, the three membrane potentials must be equal; moreover, the flow of current must be conserved. Hence,

$$V_0(0) = V_1(0) = V_2(0) \quad \text{and} \quad \sum d_i^2 \frac{dV_i}{dx}(0) = 0.$$

At the electrode site, the injection current is conserved and spreads toward (decreasing x) or away from (increasing x) the junction point. Recall that the longitudinal current is given by (2.8). It follows that the boundary condition at the junction point is

$$\frac{dV_0}{dx}(y^-) - \frac{dV_0}{dx}(y^+) = \frac{4r_L}{\pi d_0^2} I_0,$$

where I_0 is the total electrode current and the two terms on the left-hand side represent the left-handed and right-handed derivatives of V_0 at y , respectively.

We leave it as an exercise to demonstrate that the solution of this problem is given by

$$\begin{aligned} V_0(x) &= \frac{I_0 R_{\lambda_0}}{2} [\exp(-|y - x|/\lambda_0) + (2p_0 - 1) \exp(-(|y| - |x|)/\lambda_0)], \\ V_1(x) &= p_1 I_0 R_{\lambda_1} \exp(-x/\lambda_1 - |y|/\lambda_0), \\ V_2(x) &= p_2 I_0 R_{\lambda_2} \exp(-x/\lambda_2 - |y|/\lambda_0), \end{aligned} \quad (2.17)$$

where, for $i = 0, 1, 2$,

$$p_i = \frac{d_i^{3/2}}{d_0^{3/2} + d_1^{3/2} + d_2^{3/2}} \quad \text{and} \quad R_{\lambda_i} = \frac{4r_L \lambda_i}{\pi d_i^2}.$$

An example is shown in Fig. 2.4. If the injection site is along the thickest dendrite, then this has little effect on the attenuation of the potential along the thin branches. However, if the injection site is along one of the thinner dendrites, then the thick dendrite has a much greater effect on the attenuation between the two thinner branches.

2.7 Dendrites with Active Processes

We have, so far, primarily considered passive dendrites in which all of the conductances and currents are constant. However, it is now recognized that neurons may have active voltage-gated conductances along the dendritic trees and these active

conductances may have a profound influence on the neuron's firing properties and the neuron's response to synaptic inputs. We note that active channels are typically unevenly distributed along the dendrites, so, for example, there may be a higher distribution of, say, sodium channels in the proximal region near the soma than in the distal region far from the soma. A useful way to model neurons with active dendrites is to use the multicompartment approach. Here, we present an example of this due to Pinsky and Rinzel [215].

Pinsky and Rinzel developed a two-compartment model for CA3 hippocampal pyramidal neurons in a guinea pig. This work was motivated by an earlier, considerably more complex model of Traub [270], which consisted of 19 compartments. The reduced Pinsky–Rinzel model contained elements of the full model which were thought to be essential and was capable of reproducing many of the important stimulus–response properties of the Traub model. By considering a minimal reduced model, Pinsky and Rinzel were able to explain how interactions between the somatic and dendritic compartments generate bursting with unusual waveforms which do not seem to arise in single-compartment models. The reduced model is also considerably easier to implement computationally.

A schemata of the two-compartment model is shown in Fig. 2.5. Motivated by Traub's model, Pinsky and Rinzel restricted the fast spiking currents to the soma, whereas most of the calcium and calcium-modulated currents lie in the dendritic-like compartment. The somatic-like compartment has two voltage-dependent currents, an inward sodium current and an outward delayed-rectifier potassium current. The dendritic compartment has three voltage-dependent currents. There is a fast calcium current and two types of potassium currents: a calcium-activated potassium current and a potassium afterhyperpolarization. Electrotonic coupling between the compartments is modeled using two parameters, g_c and p , where g_c represents the strength of coupling and p represents the percentage of total area in the somatic-like compartment. Finally, the model includes terms for applied current to the soma and dendrite.

The model can generate bursting activity for appropriate values of the parameters. Figure 2.6 shows the waveform of the spiking activity during a burst. This type

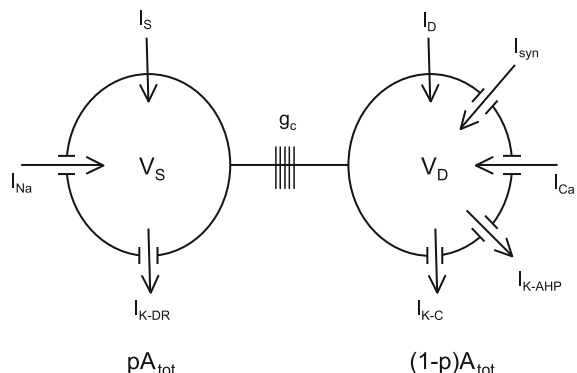
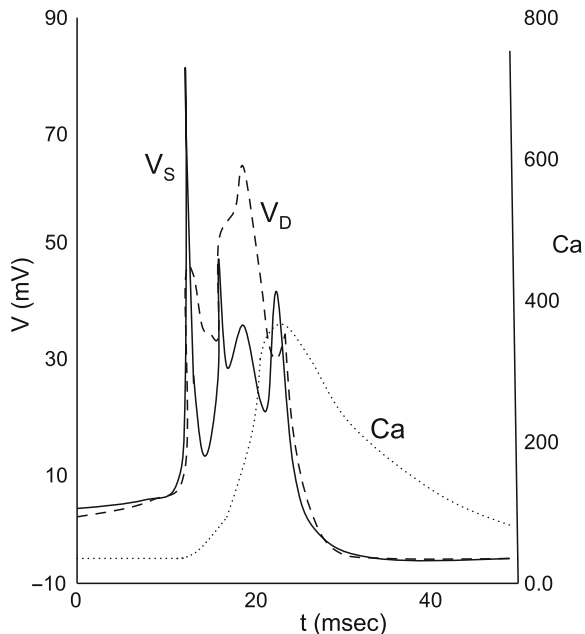


Fig. 2.5 A two-compartment model showing applied currents and outward and inward currents from and to soma and dendrite compartments. Here, A_{tot} is the total cell membrane area. (Redrawn from [215])

Fig. 2.6 Voltage and calcium traces of a bursting solution in the two-compartment model



of activity does not typically arise in single-compartment models; it results from interactions between the two compartments. Here, we step through how this burst is generated; a more complete and detailed description is given in [215].

The burst shown in Fig. 2.6 results from electrotonic interactions between the soma and the dendrite with significant coupling current that flows back and forth, alternately providing depolarizing or hyperpolarizing current to each compartment. The burst sequence is initiated by a somatic sodium spike. This is because I_{Na} is activated at lower voltages than I_{Ca} . The leading sodium action potential depolarizes the dendrite through the spread of electrotonic current. The soma then repolarizes, but only partially. This causes the dendritic membrane potential to fall below the threshold for calcium spike generation, thereby delaying the full dendritic spike. During this repolarization phase, current flows into the soma from the dendrite, which then initiates a second somatic spike. The second somatic spike stops the drain of coupling current from the dendrite, enabling the dendrite to undergo a full I_{Ca} -mediated voltage spike with accompanying rapid increase in calcium. The dendritic spike then provides depolarization which drives soma activity. We note that the calcium dendritic spikes are considerably broader than the somatic spikes. The broad dendritic spike leads to strong stimulation of the soma, which leads to damped, high-frequency spiking. The dendritic calcium spike, and hence the burst, is terminated by the calcium-dependent potassium current. This builds up on a slow timescale during the dendritic spiking activity. Hence, the burst duration is primarily determined by the amount of time required for calcium to build up. Both of these currents must decrease before a somatic action potential can be initiated.

2.8 Concluding Remarks

In this chapter, we have only touched on certain aspects of dendritic processing. It is now recognized that dendrites may play an active role determining how a neuron's firing pattern and how the neuron responds to synaptic inputs. Dendrites have been implicated in numerous functions, including direction selectivity [10, 97, 193], by which a neuron responds to images that move in a preferred direction but not in the opposite direction, and coincidence detection [1]. The classical view is that information flows from the dendrites to the soma; however, it is now clear that in many neurons the presence of excitable ionic currents in the dendrites allows for dendritic action potentials that travel in the opposite direction. Moreover, the spatial distribution of active channels in the dendrites may vary, so individual portions of the dendritic tree may act as independent subunits, each performing separate computations. Each of these issues provides exciting opportunities for mathematical modeling. London and Häusser [185] gave a recent review of dendritic computation.

2.9 Bibliography

Much of the pioneering work on the modeling of dendrites was done by Wilfred Rall. Reviews of this material can be found in Rall [221] and Koch and Segev [157]. The book by Segev et al. [243] was written in honor of Rall and contains many of his original papers, along with commentaries by leading researchers in this field. Other textbooks include those of Jack et al. [137], Tuckwell [274], Johnston and Wu [139], and Koch [156].

2.10 Exercises

- Derive the differential equations for the three-compartment model shown in Fig. 2.1b, where you can take $r_M = 10,000 \Omega \text{ cm}^2$, $c_M = 1 \mu \text{ F/cm}^2$, and $r_L = 100 \Omega \text{ cm}$. The compartments have dimensions $(\ell_j, \rho_j) = (50, 25), (100, 15), (80, 10)$, respectively. Compute the input resistance for a current applied to compartments 1 and 3 (the “soma” and the “distal dendrite”).
- Consider three identical compartments coupled in a chain by the same coupling resistance:

$$C \frac{dV_1}{dt} = -\frac{V_1}{R} + (V_2 - V_1)/R_{\text{couple}} + I,$$

$$C \frac{dV_2}{dt} = -\frac{V_2}{R} + (V_3 - 2V_2 + V_1)/R_{\text{couple}},$$

$$C \frac{dV_3}{dt} = -\frac{V_3}{R} + (V_2 - V_3)/R_{\text{couple}}.$$

Compute the input resistance. What do you think happens with more and more compartments?

3. Consider an semi-infinite array of compartments with only the first one receiving injected current. Can you prove

$$V_1/I_1 = \frac{R}{1 + \frac{R}{R_{\text{couple}}} (1 - \mu)},$$

where

$$\mu = 1 + z - \sqrt{z^2 + 2z}, \quad z = \frac{R}{2R_{\text{couple}}}?$$

(Here is a hint. Show that the steady-state voltages satisfy

$$V_{j+1} - 2(1+z)V_j + V_{j-1} = 0$$

except for $j = 1$. The general solution to this difference equation is just $V_j = A\mu_1^j + B\mu_2^j$, where μ_1 and μ_2 are roots of $\mu^2 - 2(1+z)\mu + 1 = 0$. One of these roots, say, μ_2 , is greater than 1, so as $j \rightarrow \infty$ you had better choose $B = 0$. Choose A so that the correct equation for V_1 holds:

$$0 = -\frac{V_1}{R} + \frac{V_2 - V_1}{R_{\text{couple}}} + I.$$

4. Consider a general N -compartment model for a passive neuron with current injected into some or all of the compartments. This will obey the following differential equation:

$$C_j \frac{dV_j}{dt} = I_j + \sum_k g_{jk}(V_k - V_j) - g_{L,j}(V_j - V_{\text{leak}}).$$

Suppose $g_{jk} \geq 0$, $C_j > 0$, and $g_{L,j} > 0$. Prove there is a unique equilibrium point for this and that it is asymptotically stable. (Hint: This is a diagonally dominant system.)

5. Consider the infinite linear array of cells

$$\tau \frac{dV_1}{dt} = V_0 - V_1 + \beta(V_2 - V_1),$$

$$\tau \frac{dV_j}{dt} = -V_j + \beta(V_{j+1} - 2V_j + V_{j-1}).$$

Find the steady-state solution for this. [Hint: The second group of equations has the form $V_{j+1} = V_j(2 + 1/\beta) - V_{j-1}$, which is a finite difference equation.]

The general solution to such equations is $V_j = C_1 r_1^j + C_2 r_2^j$.]

6. Consider a single-compartment model with a sinusoidal current:

$$C \frac{dV}{dt} = -g_L(V - V_{\text{leak}}) + I_0 \sin \omega t.$$

Find the steady-state solution to this equation.

7. Consider the single-compartment model

$$C \frac{dV}{dt} = I - g_L(V - V_{\text{leak}}) - g(t)(V - V_{\text{syn}}),$$

where $g(t) = 0$ except when $t \in [t_1, t_2]$, where it is \bar{g} . Solve this equation assuming the cell starts from rest. For what values of V_{syn} does $V(t)$ increase above rest?

8. (a) Plot profiles of $V(x, t)$ for the response of an infinite cable (2.13) at different spatial locations as a function of time. (b) Compute the time at which $V(x, t)$ reaches its maximum and show that for x large it is asymptotically linear in x . (c) Compute the maximum value of the voltage for each spatial position.
9. Compute the steady-state response of the cable to a sustained periodic input. That is, $I(x, t) = I_0 \sin(\omega t) \delta(x)$. [Hint: Everything will be easier if you write the current as proportional to $\exp(i\omega t)$ and use the linearity of the cable to assume a solution of the form $v(x) \exp(i\omega t)$. Then use the steady-state infinite cable result.] Compute the phase shift as a function of the distance from the source. Plot the amplitude at $x = 0$ as a function of the frequency. Determine how quickly the amplitude falls off with distance as a function of frequency.
10. Solve the cable equation $\tau v_t = -v + v_{xx} + I(x, t)$ on the finite interval $0 < x < L$ subject to the boundary conditions $v(0) = 0$ and $v_x(L) = 0$. [Hint: You could compute a Green function for this, or you could expand it in an eigenfunction expansion by solving $v'' = \beta v$ with $v(0) = 0$ and $v'(L) = 0$.]
11. Consider a cable with electrotonic length L and a sealed end at $x = L$. Suppose $V(0) = V_0$. Show that the input conductance at $X = 0$ is

$$G_L = G_\infty \tanh L.$$

12. Prove the homogeneous solution to equation

$$\frac{1}{d(x)} \frac{d}{dx} \left(\frac{d^2(x) dV}{dx} \right) = V(x) \quad (2.18)$$

with boundary conditions $dV/dx(0) = 0$ and $V(L) = 0$ has no nonzero solutions. [Hint: Without loss of generality, you can assume $V(0) > 0$. Show that $V(x)$ must be concave up in the interval $(0, L)$.]

13. Numerically compute the solution to (2.18) with $d(x) = 1 - cx/L$, where $c < 1$, $V(0) = 1$ and $V'(L) = 0$. Compare the solutions for $c = 0$ with those for $c = 0.95$ when $L = 10$. Try $c = -0.5$ (corresponding to a fattening cable).
14. Do the equivalent cylinder reduction to the bottom dendrite in Fig. 2.3.
15. *Advanced exercise.* Consider a cable with three currents, as shown in Fig. 1.6. Suppose the concentrations of the ions are those given for the squid axon in Table 1.1 and that the permeabilities are $P_K = 1$, $P_{Cl} = 0.1$, and $P_{Na} = 0.03$. Suppose the temperature is 20°C. Let $I(V)$ denote the total current as defined by (1.3). Simulate the response to the cable

$$c_M \frac{\partial V}{\partial t} = -I(V) + K \frac{\partial^2 V}{\partial x^2}$$

to a current step at $x = 0$. You can make $C_m = 1$, $K = 1$ without loss of generality since these just set the time and space scales. Compare this with the passive linear conductance cable model. Convince yourself that there is very little difference. In particular, you might want to solve the steady-state boundary value problem for, say, $V(0) = V_0$ and $V_x(L) = 0$. You cannot do this analytically, but numerical solutions should be fairly simple.

Chapter 3

Dynamics

3.1 Introduction to Dynamical Systems

Dynamical systems theory provides a powerful tool for analyzing nonlinear systems of differential equations, including those that arise in neuroscience. This theory allows us to interpret solutions geometrically as curves in a phase space. By studying the geometric structure of phase space, we are often able to classify the types of solutions that a model may exhibit and determine how solutions depend on the model's parameters. For example, we can often predict if a model neuron will generate an action potential, determine for which values of the parameters the model will produce oscillations, and compute how the frequency of oscillations depends on the parameters.

In this chapter, we introduce many of the basic concepts of dynamical systems theory using a reduced two-variable model: the Morris–Lecar equations. Although this model is considerably simpler than the Hodgkin–Huxley equations, it still exhibits many important features of neuronal activity. For example, the Morris–Lecar model generates action potentials, there is a threshold for firing, and the model displays sustained oscillations at elevated levels of an applied current. By considering a reduced model, we can more easily explain the geometric mechanisms underlying each of these phenomena. Moreover, we can introduce important mathematical concepts such as phase space analysis, bifurcation theory, oscillations, and stability theory. Each of these concepts plays a fundamental role in the analysis of more complex systems discussed throughout the book.

3.2 The Morris–Lecar Model

One of the simplest models for the production of action potentials is a model proposed by Kathleen Morris and Harold Lecar. The model has three channels: a potassium channel, a leak, and a calcium channel. In the simplest version of

the model, the calcium current depends instantaneously on the voltage. Thus, the Morris–Lecar equations have the form

$$\begin{aligned} C_M \frac{dV}{dt} &= I_{\text{app}} - g_L(V - E_L) - g_K n(V - E_K), \\ &\quad -g_{\text{Ca}} m_\infty(V)(V - E_{\text{Ca}}) \equiv I_{\text{app}} - I_{\text{ion}}(V, n), \\ \frac{dn}{dt} &= \phi(n_\infty(V) - n)/\tau_n(V), \end{aligned} \quad (3.1)$$

where

$$\begin{aligned} m_\infty(V) &= \frac{1}{2}[1 + \tanh((V - V_1)/V_2)], \\ \tau_n(V) &= 1/\cosh((V - V_3)/(2V_4)), \\ n_\infty(V) &= \frac{1}{2}[1 + \tanh((V - V_3)/V_4)]. \end{aligned}$$

Here, V_1 , V_2 , V_3 , and V_4 are parameters chosen to fit voltage-clamp data.

The solutions shown in Fig. 3.1 demonstrate that the Morris–Lecar model exhibits many of the properties displayed by neurons. Here, the parameters are listed in Table 3.1 under the Hopf case. Figure 3.1a demonstrates that the model is *excitable* if $I_{\text{app}} = 60$. That is, there is a stable constant solution corresponding to the resting state of the model neuron. A small perturbation decays to the resting state, whereas a larger perturbation, above some threshold, generates an action potential. The solution $(V_1(t), n_1(t)) \equiv (V_R, n_R)$ is constant; V_R is the resting state of the model neuron. The solution $(V_2(t), n_2(t))$ corresponds to a subthreshold response. Here, $V_2(0)$ is slightly larger than V_R and $(V_2(t), n_2(t))$ decays back to rest. Finally,

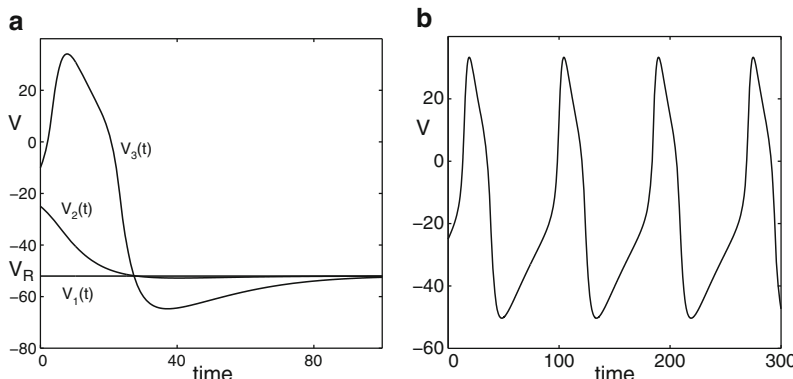


Fig. 3.1 Solutions of the Morris–Lecar equations. Parameters are listed in Table 3.1, the Hopf case. **(a)** A small perturbation from rest decays to the resting state, whereas a larger perturbation generates an action potential. Here, $I_{\text{app}} = 60$. **(b)** A periodic solution of the Morris–Lecar equations. Here, $I_{\text{app}} = 100$

Table 3.1 Morris–Lecar parameters; the current, I_{app} , is a parameter

Parameter	Hopf	SNLC	Homoclinic
ϕ	0.04	0.067	0.23
g_{Ca}	4.4	4	4
V_3	2	12	12
V_4	30	17.4	17.4
E_{Ca}	120	120	120
E_K	−84	−84	−84
E_L	−60	−60	−60
g_K	8	8	8
g_L	2	2	2
V_1	−1.2	−1.2	−1.2
V_2	18	18	18
C_M	20	20	20

SNLC saddle-node on a limit cycle

$(V_3(t), n_3(t))$ corresponds to an action potential. Here, we start with $V_3(0)$ above some threshold. There is then a large increase of $V_3(t)$, followed by $V_3(t)$ falling below V_R and then a return to rest.

Figure 3.1b shows a periodic solution of the Morris–Lecar equations. The parameter values are exactly the same as before; however, we have increased the parameter I_{app} , corresponding to the applied current. If we increase I_{app} further, then the frequency of oscillations increases; if I_{app} is too large, then the solution approaches a constant value.

In the following, we will show how dynamical systems methods can be used to mathematically analyze these solutions. The analysis is extremely useful in understanding when this type of model, for a given set of parameters, displays a particular type of behavior. The behavior may change as parameters are varied; an important goal of bifurcation theory, which we describe later, is to determine when and what types of transitions take place. Our introduction to dynamical systems will be brief and we will only discuss those topics needed for the rest of the book. Readers interested in learning more about dynamical systems should consult one of the books listed in Sect. 3.8.

3.3 The Phase Plane

It will be convenient to write (3.1) as

$$\begin{aligned} \frac{dV}{dt} &= f(V, n), \\ \frac{dn}{dt} &= g(V, n). \end{aligned} \tag{3.2}$$

The phase space for this system is simply the (V, n) plane; this is usually referred to as the *phase plane*. If $(V(t), n(t))$ is a solution of (3.2), then at each time t_0 , $(V(t_0), n(t_0))$ defines a point in the phase plane. The point changes with time, so the entire solution $(V(t), n(t))$ traces out a curve (or trajectory or orbit) in the phase plane.

Of course, not every arbitrarily drawn curve in the phase plane corresponds to a solution of the differential equations. What is special about solution curves is that the velocity vector at each point along the curve is given by the right-hand side of (3.2). That is, the velocity vector of the solution curve $(V(t), n(t))$ at a point (V_0, n_0) is given by $(V'(t), n'(t)) = (f(V_0, n_0), g(V_0, n_0))$. This geometric property – that the vector $(f(V, n), g(V, n))$ always points in the direction that the solution is flowing – completely characterizes the solution curves.

Two important types of trajectories are *fixed points* (sometimes called *equilibria* or *rest points*) and *closed orbits*. At a fixed point, $f(V_R, n_R) = g(V_R, n_R) = 0$; this corresponds to a constant solution. Closed orbits correspond to periodic solutions. That is, if $(v(t), n(t))$ represents a closed orbit, then there exists $T > 0$ such that $(V(t), n(t)) = (V(t + T), n(t + T))$ for all t .

A useful way to understand how trajectories behave in the phase plane is to consider the *nullclines*. The V -nullcline is the curve defined by $V' = f(V, n) = 0$ and the n -nullcline is where $n' = g(V, n) = 0$. Note that along the V -nullcline, the vector field $(f(V, n), g(V, n))$ points either up or down, and along the n -nullcline, vectors point either to the left or to the right. Fixed points are where the two nullclines intersect. The nullclines divide the phase plane into separate regions; in each of these regions, the vector field points in the direction of one of the four quadrants: (1) $f > 0, g > 0$; (2) $f < 0, g > 0$; (3) $f < 0, g < 0$; or (4) $f > 0, g < 0$.

3.3.1 Stability of Fixed Points

One can determine the stability of a fixed point by considering the linearization of the vector field at the fixed point. The linearization of (3.2) at a fixed point (V_R, n_R) is the matrix

$$M = \begin{bmatrix} \frac{\partial f}{\partial V}(V_R, n_R) & \frac{\partial f}{\partial n}(V_R, n_R) \\ \frac{\partial g}{\partial V}(V_R, n_R) & \frac{\partial g}{\partial n}(V_R, n_R) \end{bmatrix}.$$

The fixed point is stable if both of the eigenvalues of this matrix have a negative real part; the fixed point is unstable if at least one of the eigenvalues has a positive real part. For the Morris–Lecar equations, the linearization is given by

$$M = \begin{bmatrix} -\frac{\partial I_{\text{ion}}(V_R, n_R)}{\partial V}/C_M & -g_K(V_R - E_K)/C_M \\ \phi n'_\infty(V_R)/\tau_n(V_R) & -\phi/\tau_n(V_R) \end{bmatrix} \equiv \begin{bmatrix} a & b \\ c & d \end{bmatrix}.$$

Moreover,

$$\begin{aligned} a &\equiv -\frac{\partial I_{\text{ion}}(V_R, n_R)}{\partial V} \Big/ C_M \\ &= (-g_L - g_K n_R - g_{\text{Ca}} m_\infty(V_R) + (E_{\text{Ca}} - V_R) g_{\text{Ca}} m'_\infty(V_R)) / C_M. \end{aligned}$$

We now find conditions on the nonlinear functions in (3.1) for when the fixed point is stable.

Suppose the equilibrium voltage lies between E_K and E_{Ca} , a reasonable assumption. Then $b < 0$, $c > 0$, and $d < 0$ in the linearization. Only a can be either negative or positive and the only term contributing to the positivity of a is the slope of the calcium activation function, $m_\infty(V)$. If $a < 0$, then the fixed point is asymptotically stable since the trace of M is negative and the determinant is positive. (Recall that the trace is the sum of the eigenvalues and the determinant is the product of the eigenvalues.) Note that the slope of the V -nullcline near the fixed point is given by $-a/b$. Since $b < 0$, it follows that if this slope is negative, then the fixed point is stable; that is, if the fixed point lies along the left branch of the V -nullcline, then it is stable (see Fig. 3.2).

Now suppose the fixed point lies along the middle branch of the V -nullcline, so $a > 0$. Note that the slope of the n -nullcline, $-c/d$, is always positive. If the slope of the V -nullcline is greater than the slope of the n -nullcline (i.e., $-a/b > -c/d$), then $ad - bc < 0$. In this case, the determinant is negative and the fixed point is an unstable saddle point. In contrast, if the slope of the n -nullcline is greater than that of the V -nullcline, then the fixed point is a node or a spiral. In this case, the stability of the fixed point is determined by the trace of M : the fixed point is stable if $a + d < 0$ and it is unstable if $a + d > 0$. Since $a > 0$ and $d = -\phi/\tau_n(V_R)$, it follows that the fixed point is unstable if ϕ is sufficiently small. Note that ϕ governs the speed of the potassium dynamics.

3.3.2 Excitable Systems

Recall that for the parameters given in Table 3.1 for the Hopf case, the system is *excitable* if $I_{\text{app}} = 60$. As Fig. 3.1a demonstrates, a small perturbation in voltage from the resting state decays back to rest, whereas a sufficiently large perturbation in voltage continues to increase and generates an action potential.

Phase plane analysis is very useful for understanding what separates the firing of an action potential from the subthreshold return to rest in this model. The projection of the solutions shown in Fig. 3.1a onto the phase plane are shown in Fig. 3.2a. This figure also shows the V -nullcline and the n -nullcline. Note that the V -nullcline separates points along trajectories in which $V' < 0$ and $V' > 0$. In particular, V increases below the V -nullcline and V decreases above the V -nullcline. We further note that the V -nullcline is “cubic.” This suggests a perturbation from rest that lies to the “left” of the middle branch of the V -nullcline will return quickly to rest, whereas

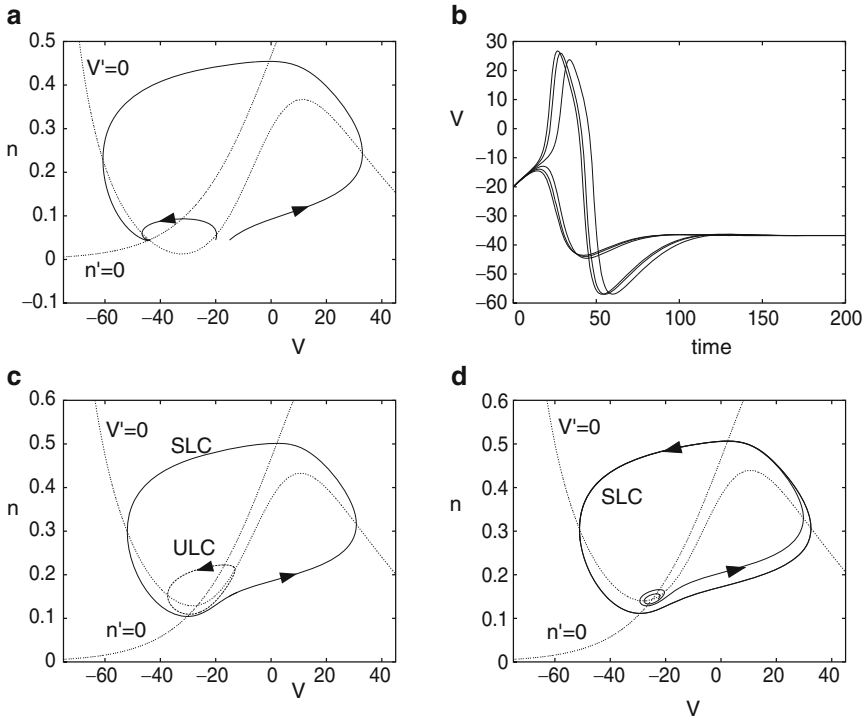
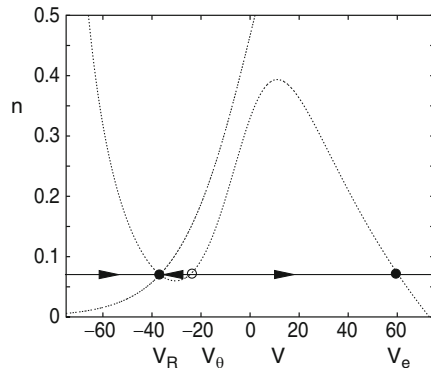


Fig. 3.2 Phase planes and voltage traces for the Morris–Lecar model in the Hopf regime. (a) $I_{\text{app}} = 60$; an excitable system with threshold at about -20 mV . Nullclines are included as well. (b) Starting at $n = n_{\text{rest}}$ and varying V from -20 to -20.1 mV leads to graded action potentials. (c) $I_{\text{app}} = 90$ showing bistability between a stable limit cycle (SLC) and a fixed point, separated by the unstable limit cycle (ULC). (d) $I_{\text{app}} = 100$, the fixed point is unstable and only a limit cycle remains

a perturbation that lies to the “right” of the middle branch of the V -nullcline will initially display an increase in membrane potential, corresponding to an action potential, before returning to rest. Therefore, the middle branch of the V -nullcline in some sense separates the firing of an action potential from the subthreshold return to rest.

This analysis can be made more precise if we assume the parameter ϕ is small. Looking at Table 3.1, we can see that ϕ is relatively smaller in the Hopf case than in the other two cases. For small ϕ , n will not change much, so let us hold it at rest. Figure 3.3 shows the phase plane with a horizontal line drawn through the fixed point. If n does not change much, then the dynamics are governed by the behavior on the phase line $n = n_R$. Since the V -nullcline intersects this line at three points, there are three equilibria for the system when n is held constant. The resting state (and true equilibrium of the full system) V_R is stable. There are two additional equilibria (which are not equilibria of the full model, just the model when n is held at its resting value): V_θ , which is unstable, and V_c , which is stable. On this line, if the voltage is

Fig. 3.3 Threshold construction for the Morris–Lecar model



perturbed past V_θ , then it will jump to the right fixed point, V_e . Otherwise, it will decay to rest, V_R . This shows that for small ϕ , the “threshold” voltage for generating an action potential is roughly the intersection of the horizontal line through the resting state and the middle branch of the V -nullcline. Since experimentalists can only move the voltage through current injection, we can use this to estimate the magnitude of a current pulse needed to cross the threshold (see Exercise 2).

We note that the peak of the action potential occurs at some latency after the initial perturbation, but this latency can never become very large. The action potential itself is graded and takes on a continuum of peak values, as shown in Fig. 3.2b. If ϕ is not “small” and it is increased, then the spike amplitudes are even more graded than those shown in Fig. 3.2b. Recall that ϕ is related to the temperature of the preparation. Thus, increasing the temperature of a neuron should lead to a much less sharp threshold distinction and graded action potentials. Indeed, Cole et al. [42] demonstrated this in the squid axon.

3.3.3 Oscillations

We expect the phase plane to change if a parameter in the equations changes. Figure 3.2d shows the phase plane corresponding to the periodic solution shown in Fig. 3.1b. Here, $I_{\text{app}} = 100$. Note that the periodic solution corresponds to a closed curve or *limit cycle*. In general, whenever we wish to find periodic solutions of some model, we look for closed orbits in phase space. In Fig. 3.2d, there is a unique fixed point; this is where the nullclines intersect. This fixed point is unstable, however.

If we change I_{app} to 90, then the model is *bistable*, and the phase plane is shown in Fig. 3.2c. Note that there exist both a stable fixed point and a stable limit cycle. Small perturbations from rest will decay back to the stable fixed point, whereas large perturbations will approach the stable periodic solution. Note that there also exists an unstable periodic solution. This orbit separates those initial conditions that approach the stable fixed point from those that approach the stable limit cycle.

It is often difficult to show that a given model exhibits stable oscillations, especially in higher-dimensional systems such as the Hodgkin–Huxley model. Limit cycles are global objects, unlike fixed points, which are local. To demonstrate that a given point is on a periodic solution, one must follow the trajectory passing through that point and wait to see if the trajectory returns to where it started. This is clearly not a useful strategy for finding periodic solutions. A powerful method for locating oscillatory behavior is bifurcation theory, which we describe in Sect. 3.4.

3.4 Bifurcation Analysis

Bifurcation theory is concerned with how solutions change as parameters in a model are varied. For example, in the previous section we showed that the Morris–Lecar equations may exhibit different types of solutions for different values of the applied current I_{app} . If $I_{\text{app}} = 60$, then there is a stable fixed point and no oscillations, whereas if $I_{\text{app}} = 100$, then the fixed point is unstable and a stable limit cycle exists. Using bifurcation theory, we can classify the types of transitions that take place as we change parameters. In particular, we can predict for which value of I_{app} the fixed point loses its stability and oscillations emerge. There are, in fact, several different types of bifurcations; that is, there are different mechanisms by which stable oscillations emerge. The most important types of bifurcations can be realized by the Morris–Lecar model. These are described next.

3.4.1 The Hopf Bifurcation

In Fig. 3.4, we chose the parameters as in Table 3.1 for the Hopf regime and show the *bifurcation diagram* for the Morris–Lecar equations as I_{app} is varied. For each value of I_{app} , there is a unique fixed point, $(V_R(I_{\text{app}}), n_R(I_{\text{app}}))$. In Fig. 3.4a, we plot V_R versus I_{app} . The fixed point is stable for $I_{\text{app}} < 94 \equiv I_1$ and $I_{\text{app}} > 212 \equiv I_2$; otherwise, it is unstable. A *Hopf bifurcation* occurs at $I_{\text{app}} = I_1$ and $I_{\text{app}} = I_2$. By this we mean the following. Recall that a fixed point is stable if all of the eigenvalues of the linearization have a negative real part; the fixed point is unstable if at least one of the eigenvalues has a positive real part. The fixed point loses stability, as a parameter is varied, when at least one eigenvalue crosses the imaginary axis. If the eigenvalues are all real numbers, then they can cross the imaginary axis only at the origin in the complex plane. However, if an eigenvalue is complex, then it (and its complex conjugate) will cross the imaginary axis at some point that is not at the origin. This latter case corresponds to the Hopf bifurcation and it is precisely what happens for the example we are considering. In this example, $(I_1, V_R(I_1), n_R(I_1))$ and $(I_2, V_R(I_2), n_R(I_2))$ are called *bifurcation points*. Sometimes, I_1 and I_2 are also referred to as bifurcation points. The *Hopf bifurcation theorem* states that (if certain technical assumptions are satisfied) there must exist values of the parameter I_{app}

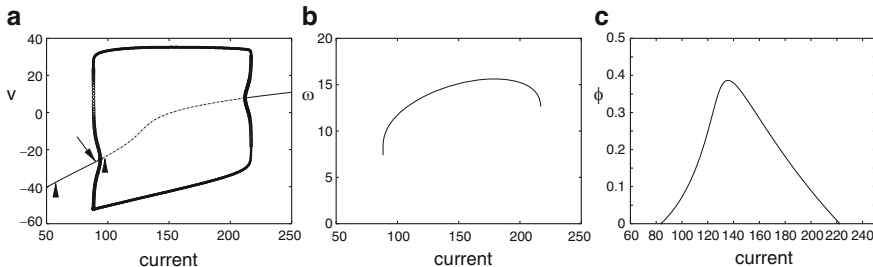


Fig. 3.4 Bifurcation diagram for the Morris–Lecar model in the Hopf regime. (a) Voltage as a function of current. The curves above and below the fixed-point curve correspond to the maximum and minimum voltages along periodic orbits. Solid curves represent stable solutions and dashed curves represent unstable solutions. Arrows shown at $I_{app} = 60, 90$, and 100 correspond to the solutions shown in Fig. 3.2a, c, and d, respectively. (b) Frequency (Hz) versus current. (c) Two-parameter bifurcation showing the curve of Hopf bifurcations as ϕ and I_{app} vary

near I_1 and I_2 such that there exist periodic solutions that lie near the fixed points $(V_R(I_{app}), n_R(I_{app}))$. A more precise statement of the Hopf bifurcation theory can be found in numerous texts on dynamical systems.

The curves in Fig. 3.4a represent fixed points and periodic solutions of the Morris–Lecar model. This diagram was generated using the numerical software program XPPAUT. The curve above the fixed-point curve represents the maximum voltages on the periodic orbits and the curve below the fixed-point curve represents the minimum voltages. The solid curves represent stable solutions and the dashed curves represent unstable solutions. The bifurcation diagram shows many interesting and important features. Note that the periodic solutions near the two bifurcation points are unstable. These unstable, small-amplitude periodic solutions lie on the same side of the bifurcation points as the stable fixed points. These are both examples of *subcritical Hopf bifurcations*. At a *supercritical Hopf bifurcation*, the small-amplitude periodic solutions near the Hopf bifurcation point are stable and lie on the side opposite the branch of stable fixed points.

If $88.3 < I_{app} < I_1$ or $I_2 < I_{app} < 217$, then the Morris–Lecar model is bistable. For these values of I_{app} , there exist both a stable fixed point and a stable periodic solution. The phase plane for $I_{app} = 90$ is shown in Fig. 3.2c. Note that small perturbations of initial conditions from the resting state will decay back to rest; however, large perturbation from rest will generate solutions that approach the stable limit cycles.

Figure 3.4b shows the frequency of the stable periodic solutions versus current. Note that the frequency lies in a narrow range between 7 and 16 Hz. In particular, the frequency does not approach zero as I_{app} approaches the bifurcation points. This is a general property of periodic solutions that arise via the Hopf bifurcation. In Sect. 3.4.2, we shall consider another mechanism for the generation of stable limit cycles. In that mechanism, the frequency does approach zero.

Finally, we can ask what happens if we change the speed of the potassium kinetics. Figure 3.4c shows a two-parameter diagram with ϕ along the vertical axis and

I_{app} along the horizontal axis. This shows the locus of Hopf bifurcations in these two parameters. For fixed values of ϕ below about 0.4, there are two currents at which the Hopf bifurcation occurs. Inside the curve, the resting state is unstable. One can numerically show that the Hopf bifurcation is subcritical outside the interval $124.47 < I_{\text{app}} < 165.68$; inside this interval, the bifurcation is supercritical. The reader can choose, for example, $\phi = 0.35$ and show that both Hopf bifurcations are supercritical; the only oscillations are stable and have small amplitude.

3.4.2 Saddle–Node on a Limit Cycle

The Hopf bifurcation is the best known mechanism through which one can go from a stable fixed point to an oscillation. Importantly, the fixed point persists through the bifurcation. Furthermore, the limit cycles which bifurcate are of *small amplitude* and are local, in the sense that they lie close to the branch of fixed points (although, as we saw in the Morris–Lecar model, the bifurcation is subcritical at low currents and thus bifurcating periodic orbits are unstable). Another mechanism through which an oscillation can emerge from a fixed point is called a *saddle–node on a limit cycle* (SNLC). It is also called a *saddle–node on an invariant circle* (SNIC). This is an example of a global bifurcation.

The behavior of the Morris–Lecar model with these parameters is quite different, as is shown in Fig. 3.5. First, unlike in Fig. 3.2b, the action potentials appear to occur with arbitrary delay after the end of the stimulus. Second, the shape of the action potentials is much less variable. The reason for this can be understood by looking at the phase plane in Fig. 3.5b. Unlike the Hopf case, here there are three fixed points, only one of which (labeled N) is stable. The middle fixed point is a saddle point (labeled S). Thus, the linearized system at this fixed point has one positive and one negative eigenvalue. Associated with these eigenvalues are the stable and unstable manifolds. These manifolds consist of trajectories that approach the saddle point in either forward or backward time, respectively. The two branches of the unstable manifold, Σ^+ , form a loop with the stable node N and the saddle point S . This loop in the plane constrains the spike shape; since trajectories cannot cross, any trajectory starting outside the loop must remain outside it. Thus, the spike height cannot fall below a certain level. More importantly, the stable manifold, Σ^- , forms a hard threshold that is precisely determined. This contrasts with the pseudothreshold we saw in the Hopf case. Any perturbation which drives the potential to the right of Σ^- results in a spike and any perturbation which drives the potential to the left of Σ^- leads to a return to rest without a spike.

Figure 3.5 also explains the delay in firing. Suppose a stimulus drives the voltage to a point exactly on the stable manifold Σ^- . Then, the trajectory will go to the saddle point, where it will remain. The closer a perturbation gets to Σ^- (but to the right of it), the longer the delay to the spike. Indeed, the spike with the longest delay in Fig. 3.5a stays at a nearly constant voltage close to the value at the saddle point before finally firing.

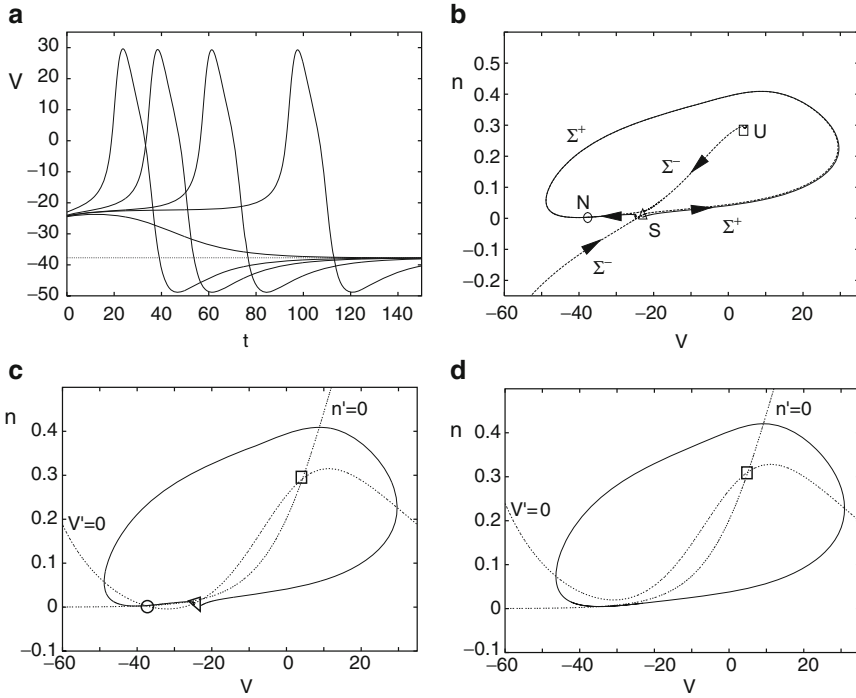


Fig. 3.5 Dynamics of the Morris–Lecar model with saddle–node dynamics. **(a)** The delay to spiking can be arbitrary but the spike height is invariant. For the different plots, we start with different initial conditions. **(b, c)** Phase plane explaining **(a)**. The fixed points N , S , and U are, respectively a stable node (the resting state), a saddle point, and an unstable node. Σ^\pm are the stable (−) and unstable (+) manifolds of S . **(d)** There exists a stable limit cycle for sufficient current; the nullclines are also shown

Like the Hopf case, as current is increased, the model fires repetitively. A typical limit cycle is shown in Fig. 3.5d. Figure 3.6a shows the bifurcation diagram as the current is increased. The steady-state voltage shows a region where there are three equilibria for I_{app} between about -15 and $+40$. Only the lower fixed point is stable. As I_{app} increases, the saddle point and the stable node merge together at a saddle–node bifurcation, labeled SN_2 . When $I_{\text{app}} = I_{\text{SN}_2}$, the invariant loop formed from Σ^+ becomes a homoclinic orbit; that is, it is a single trajectory that approaches a single fixed point in both forward and backward time. This type of homoclinic orbit is sometimes called a *saddle–node homoclinic orbit* or a SNIC. As I_{app} increases past $I_{\text{app}} = I_{\text{SN}_2}$, the saddle point and node disappear; the invariant loop formed from Σ^+ becomes a stable limit cycle. The branch of limit cycles persists until it meets a branch of unstable periodic solutions emerging from a subcritical Hopf bifurcation.

Figure 3.6b shows the frequency of the oscillations as a function of the current. Unlike in Fig. 3.4b, the frequency for this model can be arbitrarily low and there is a

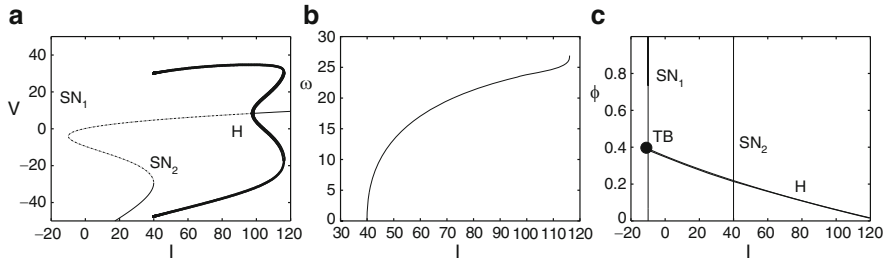


Fig. 3.6 Bifurcation for the Morris–Lecar model with saddle–node dynamics. (a) Voltage versus current showing saddle–node (SN_1 , SN_2) and Hopf (H) bifurcations. (b) Frequency as a function of current. (c) Two-parameter bifurcation diagram showing the curves of Hopf and saddle–node bifurcations as the rate, ϕ , of the potassium channel varies. The Hopf curve meets the leftmost saddle–node curve at a double-zero eigenvalue characterizing a Takens–Bogdanov bifurcation (TB)

much greater dynamic range. Note that the nullclines in Fig. 3.5c can be very close to touching each other and thus create a narrow channel where the flow is extremely slow. This suggests why the frequency of firing can be arbitrarily low. Moreover, as $I_{app} \rightarrow I_{SN_2}$, the limit cycles approach a homoclinic orbit. We expect that the frequency should approach zero as $I_{app} \rightarrow I_{SN_2}$. In an exercise later, the reader is asked to show that the frequency scales as the square root of $I_{app} - I_{SN_2}$ and to develop the theta model.

3.4.3 Saddle–Homoclinic Bifurcation

By changing the rate of the potassium channel, ϕ , we can alter the dynamics of the model so that the SNIC is replaced by another type of global bifurcation; this is called a *saddle–homoclinic bifurcation*. In both types of bifurcations, the frequency of oscillations approaches zero as the current approaches the bifurcation value. However, there are important differences.

Since ϕ only changes the rate of n , it has no effect on the number and values of the fixed points, only their stability. Figure 3.7 shows the bifurcation diagram for the model when ϕ is increased from 0.067 to 0.23. As before, the fixed points are lost at a saddle–node bifurcation. The Hopf bifurcation on the upper branch occurs at a much lower value of current than in Fig. 3.6, but the Hopf bifurcation is still subcritical. The main difference is that the stable branch of periodic orbits does not terminate on the saddle–node as in Fig. 3.6. Rather it terminates on an orbit that is homoclinic to one of the saddle points along the middle branch of fixed points. Like the SNIC, this homoclinic orbit has an infinite period. However, the periods of the limit cycles approach infinity quite differently from before. One can show that the period scales as

$$T \sim \ln \frac{1}{I_{app} - I_{Hc}},$$

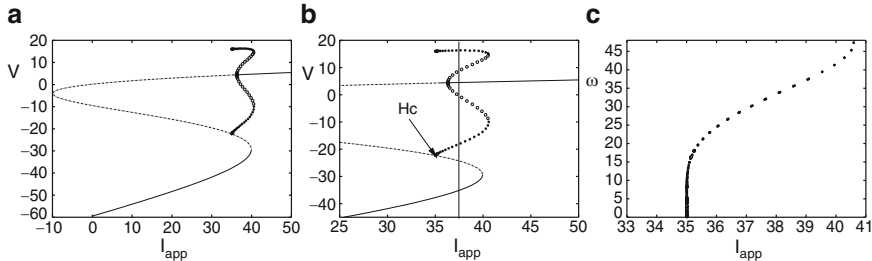


Fig. 3.7 Bifurcation for the Morris–Lecar model with increased ϕ . (a) Voltage versus current. (b) Zoom in of (a) showing the homoclinic orbit (H_c). The vertical line at $I_{\text{app}} = 37$ shows tristability. (c) Frequency versus current; note the much steeper approach to I^* than in Fig. 3.6

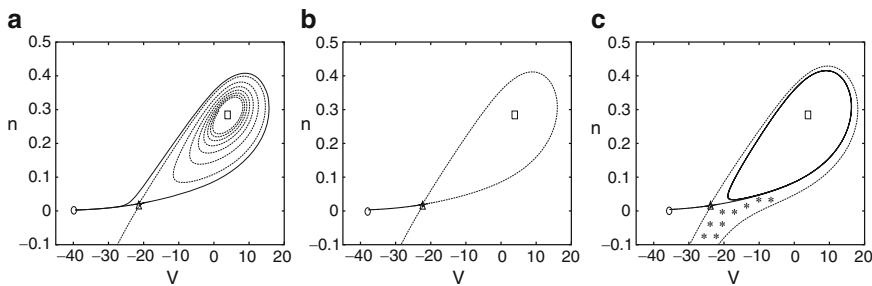


Fig. 3.8 Phase plane for the Morris–Lecar system near the homoclinic bifurcation showing (a) $I_{\text{app}} < I_{\text{Hc}}$, (b) $I_{\text{app}} \approx I_{\text{Hc}}$, and (c) $I_{\text{app}} > I_{\text{Hc}}$. Perturbations from rest that lie in the starred region shown in (c) will approach the stable limit cycles

where I_{Hc} is the current at which there is a saddle–homoclinic orbit. The frequency T^{-1} approaches zero much more rapidly than in the SNIC case.

Figure 3.8 shows the phase plane for the membrane model near the critical current, I_{Hc} . There are three fixed points. The lower-left fixed point is always stable, the middle point is a saddle, and the upper-right point is an unstable spiral. For $I_{\text{app}} < I_{\text{Hc}}$ (Fig. 3.8a), the right branch of the unstable manifold of the saddle wraps around and returns to the stable fixed point. The upper branch of the stable manifold wraps around the spiral (in negative time). Note that the unstable manifold passes on the outside of the stable manifold. In Fig. 3.8b, the stable and unstable manifolds meet and form the homoclinic orbit at $I_{\text{app}} = I_{\text{Hc}}$. For $I_{\text{app}} > I_{\text{Hc}}$, the unstable manifold passes *inside* the stable manifold and wraps around a stable limit cycle. Thus, this model has a regime of bistability where there is a stable fixed point and a stable periodic orbit. Unlike the bistability in the Hopf case, the stable limit cycle does not surround the stable fixed point. In the Hopf case, an unstable periodic orbit acted to separate the stable fixed point from the stable limit cycle. For the present set of parameters, the stable manifold of the middle fixed point separates the two stable states. To get onto the limit cycle, it is necessary to perturb the potential into

the starred region in Fig. 3.8c. Consider a brief current pulse which perturbs the voltage. If this pulse is weak, then the system returns to rest. If it is very strong and passes the starred region, then the model will generate a single spike and return to rest. However, for intermediate stimuli (like the baby bear’s porridge – just right), the system will settle onto the stable limit cycle.

Finally, we look closely at the bifurcation diagram (Fig. 3.7b). Near $I_{\text{app}} = 37$, there are two stable fixed points as well as a stable limit cycle. Thus, the model is actually “tristable.” The reader is urged to explore this aspect of the model more carefully as an exercise.

3.4.4 Class I and Class II

The Morris–Lecar model illustrates several important features of neuronal firing. Three different mechanisms for switching from rest to repetitive firing were illustrated. In particular, the most common mechanisms are through the Hopf and SNIC bifurcations. In the 1940s, Hodgkin classified three types of axons according to their properties. He called these classes I and II, with class III being somewhere in-between the first two classes which we describe:

- Class I.* Axons have sharp thresholds, can have long latency to firing, and can fire at arbitrarily low frequencies.
- Class II.* Axons have variable thresholds, short latency, and a positive minimal frequency.

From this description, we can see that these two classes fall neatly into the dynamics of the SNIC and the Hopf bifurcations, respectively. Rinzel and Ermentrout [230] were the first to note this connection. Now there are many papers which classify membrane properties as class I or class II and mean SNIC and Hopf bifurcation dynamics, respectively.

Tateno et al. [259] have characterized regular spiking neurons (excitatory) and fast spiking neurons (inhibitory) in rat somatosensory cortex using this classification. (Note that many authors call the dynamics type I and type II instead of class I and class II.) Figure 3.9 shows some properties of cortical neurons. Regular spiking neurons appear to be class I; the minimal frequency is close to zero. Note that regular spiking neurons do not seem to have subthreshold oscillations (not shown). In contrast, fast spiking neurons appear to be class II; they have a minimum frequency of around 15 Hz. They also exhibit subthreshold oscillations. Near the critical current, they seem to switch back and forth between rest and firing. This suggests the possibility of a narrow range of bistability consistent with the subcritical Hopf bifurcation.

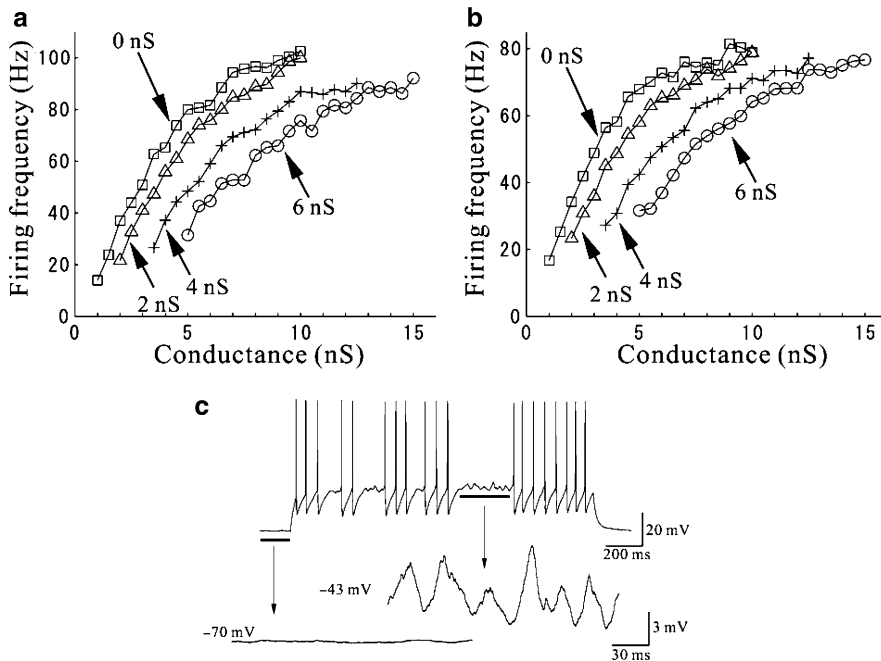


Fig. 3.9 Properties of regular spiking and fast spiking neurons in cortex. (a) Firing rate versus the AMPA receptor-type conductance for regular spiking neurons. Each curve represents a different level of GABA-type conductance. [Note that these cells have spike-frequency adaptation, so the interspike interval is not constant. Thus, this shows the interspike interval after several spikes as well as the steady state.] (b) Same as (a) for fast spiking neurons. (c) Mixture of spikes and subthreshold oscillations near the critical current for fast spiking neurons. (From [259])

3.5 Bifurcation Analysis of the Hodgkin–Huxley Equations

We now consider the space-clamped Hodgkin–Huxley model (1.43). In Chap. 2, we discussed the response to a brief current pulse. Figure 1.13 shows the effects of a brief current pulse at amplitudes ranging from 1 to $5 \mu\text{A}/\text{cm}^2$. There appears to be a very sharp transition between an action potential and a minimal response. A constant current can induce the membrane to oscillate repeatedly as seen in the right panel in Fig. 1.13.

We can get a more global picture of the dynamics of the equations by looking at a bifurcation diagram. Figure 3.10a shows the behavior of the voltage as a function of the applied current, I_{app} . Lines represent fixed points and circles represent periodic orbits. The frequency of the oscillations is shown in Fig. 3.10c. The range is from about 40 Hz to about 150 Hz.

Note that there is a unique equilibrium point for all I_{app} . At $I_{\text{app}} \approx 10$, the resting state loses stability at a Hopf bifurcation. At a large value of $I_{\text{app}} \approx 154$ there is another Hopf bifurcation. From the figure, it seems clear that the bifurcation

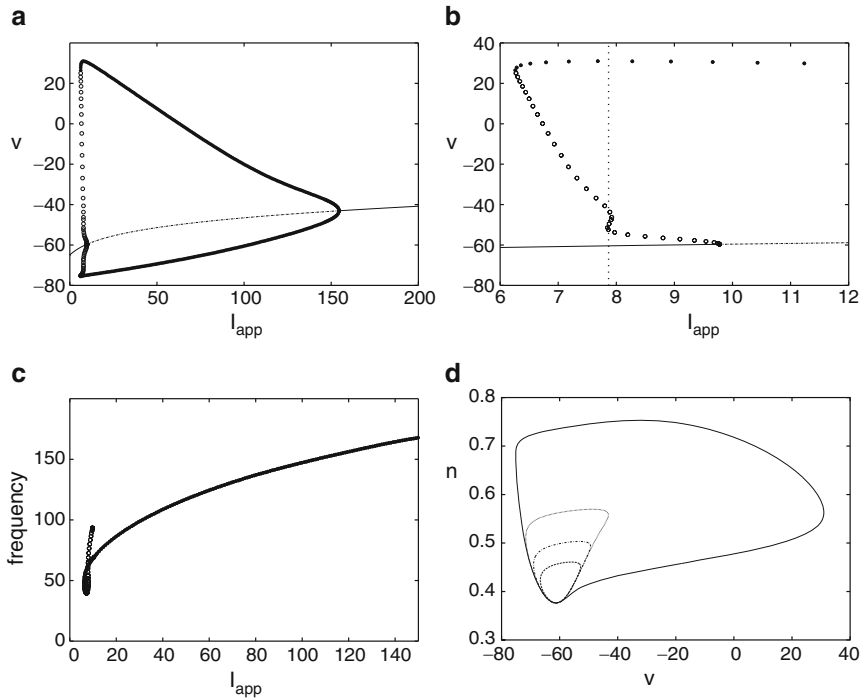


Fig. 3.10 Bifurcation diagram for the Hodgkin–Huxley model. (a) V versus I_{app} , the applied current. (b) Expanded view of (a). (c) Frequency as a function of current. (d) (V, n) -phase plane projection showing four different limit cycles

is subcritical at the low current and supercritical at the high current. At the lower Hopf bifurcation, there is a subcritical branch of unstable periodic orbits. Hence, the transition from resting behavior to oscillations is class II.

Figure 3.10b shows a blowup of the region near this Hopf bifurcation. Evidently, there are values of I_{app} near 7.88 where there are *four* different limit cycles. Figure 3.10d shows the projection of these limit cycles in the (V, n) -plane. Guckenheimer and Oliva [112] provide convincing numerical evidence for chaotic behavior near this lower current value. The chaos that they compute is *unstable*, so it will not be observed in simulations. For large values of current, the resting state stabilizes again through a supercritical Hopf bifurcation.

The apparent fact that there is a unique equilibrium point for all I_{app} has never been rigorously proved for the Hodgkin–Huxley equations. At equilibrium, each of the gating variables m , n , and h can be written as a function of V , so we find

$$\begin{aligned} I_{\text{app}} &= \bar{g}_L(V - E_L) + \bar{g}_{\text{Na}}m_\infty^3(V)h_\infty(V)(V - E_{\text{Na}}) \\ &\quad + \bar{g}_Kn_\infty^4(V)(V - E_K) \equiv F(V). \end{aligned} \tag{3.3}$$

The statement that there is a unique equilibrium is a statement that $F(V)$ is monotonic for all V . Since this monotonicity depends very much on the details of the steady-state gate functions, it is not likely that any general theory of the monotonicity of F exists. We leave it as an exercise to show that if $|V|$ is large enough, then there is a unique value of I_{app} for which there exists an equilibrium.

If we assume the function $F(V)$ is monotonic, then it is possible to rigorously prove the existence of the two Hopf bifurcation points. Troy [272] proved under fairly general assumptions that there are two values of I_{app} at which the resting state loses stability at a pair of imaginary eigenvalues. Thus, from the Hopf bifurcation theorem, he was able to conclude that there is a branch of periodic solutions emerging from the fixed points. A rigorous proof of the direction of the bifurcation remains an open question.

Troy's proof relies on an analysis of the linearized equations and application of Hurwitz's criteria to the characteristic polynomial. We can sketch out some of the details. Troy's assumption that the function $F(V)$ is monotonic implies that for each I_{app} there is a unique V that satisfies (3.3). Furthermore, this implies that there are never any zero eigenvalues of the linear system. The linearization about the fixed point leads to a matrix with a very special form. It is zero except along the diagonal, across the first row, and down the first column:

$$M = \begin{pmatrix} -F_V & -F_m & -F_h & -F_n \\ \phi m'_\infty / \tau_m & -\phi / \tau_m & 0 & 0 \\ \phi h'_\infty / \tau_h & 0 & -\phi / \tau_h & 0 \\ \phi n'_\infty / \tau_n & 0 & 0 & -\phi / \tau_n \end{pmatrix}.$$

The characteristic polynomial for such matrices (which are called *mammillary* because they resemble a mammal with many suckling babies; here the voltage is the mother and the gates are the babies) is easy to compute and the result is a fourth-order polynomial of the form

$$P_M(\lambda) = \lambda^4 + a_3\lambda^3 + a_2\lambda^2 + a_1\lambda + a_0.$$

The coefficients are messy, but straightforward to compute. The Hopf bifurcation occurs when there are purely imaginary roots. The Routh–Hurwitz criterion provides the simplest test for this condition (see the digression that follows). For a fourth-order polynomial, there will be a Hopf bifurcation if $a_0 > 0$, $a_3 > 0$, $a_3a_2 - a_1 > 0$, and $R \equiv a_3a_2a_1 - a_1^2 - a_3^2a_0$ vanishes. Thus, Troy used assumptions for the shapes of the gating functions to prove there is a Hopf bifurcation by showing that the quantity R changes sign.

Digression: The Routh–Hurwitz Criterion

Consider the polynomial

$$P(\lambda) = \lambda^n + a_{n-1}\lambda^{n-1} + \cdots + a_1\lambda + a_0. \quad (3.4)$$

The Routh–Hurwitz determinants provide a simple way to tell if the real parts of the roots of P are negative. We define $a_n = 1$ and $a_j = 0$ for $j > n$ or for $j < 0$. We will form a series of matrices containing the coefficients a_j :

$$\begin{aligned} H_1 &= a_{n-1}, \\ H_2 &= \begin{bmatrix} a_{n-1} & 1 \\ a_{n-3} & a_{n-2} \end{bmatrix}, \\ H_3 &= \begin{bmatrix} a_{n-1} & 1 & 0 \\ a_{n-3} & a_{n-2} & a_{n-1} \\ a_{n-5} & a_{n-4} & a_{n-3} \end{bmatrix}, \end{aligned}$$

and so on up to H_n . Each matrix is square and the first column contains every other coefficient, a_{n-1}, a_{n-3}, \dots . The roots of $P(\lambda)$ have negative real parts if and only if $\det H_j > 0$ for $j = 1, \dots, n$. For example:

$$\begin{aligned} n = 1. \quad &a_0 > 0 \\ n = 2. \quad &a_0 > 0 \text{ and } a_1 > 0 \\ n = 3. \quad &a_0 > 0, a_2 > 0, a_1 a_2 - a_0 > 0 \\ n = 4. \quad &a_0 > 0, a_3 > 0, a_3 a_2 - a_1 > 0, a_3 a_2 a_1 - a_1^2 - a_3^2 a_0 > 0 \end{aligned}$$

We note the following:

- $\det H_n = a_0 \det H_{n-1}$, so this means $a_0 > 0$ is necessary. If $a_0 = 0$, then there is a zero eigenvalue.
- If $\det H_{n-1} = 0$, $a_0 > 0$, and $\det H_j > 0$ for $j < n-1$, then there are imaginary roots.

These two criteria allow us to determine where possible saddle–node (eigenvalue 0) and Hopf (imaginary eigenvalues) bifurcations occur.

End of digression

3.6 Reduction of the Hodgkin–Huxley Model to a Two-Variable Model

We have seen that two-dimensional models, such as the Morris–Lecar equations, exhibit many important features of the more complicated Hodgkin–Huxley equations. The Morris–Lecar equations generate action potentials, there is a threshold for firing, and, depending on parameters, there are several mechanisms for the generation of oscillatory behavior. In this section, we shall describe two ways in which dynamical systems methods can be used to formally reduce the four-dimensional Hodgkin–Huxley model to a two-dimensional system of equations. Reduction methods will be very useful in later sections when we consider networks of neurons.

Rinzel [226] developed a simple method based on two observations. The first is that $\tau_m(V)$, the voltage-dependent time constant for the gating variable m , is much

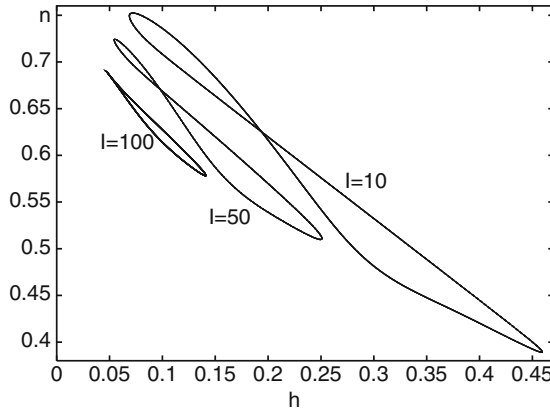


Fig. 3.11 Projection of limit cycles in Hodgkin–Huxley equations in the (n, h) -plane

smaller than both τ_h and τ_n . Because τ_m is small, $m(t)$ is very close to $m_\infty(V(t))$. If we replace m by $m_\infty(V)$ in the voltage equation, then this reduces the Hodgkin–Huxley model by one equation. The second observation, first made by Krinskii and Kokoz [164], is that $(n(t), h(t))$ lies nearly along a line $n = b - rh$, where b and r are constants. Figure 3.11 shows these curves at three different currents. The slope and the intercept depend somewhat on the current, but Rinzel ignored this. Hence, we replace n by $b - rh$ in the voltage equation and obtain the reduction to a two-dimensional model. We leave the analysis of this model as an exercise.

A common method for comparing parameters which have different units is to render the model in terms of dimensionless variables. Kepler et al. [150] described a method for comparing the timescales of all the gating variables. Each voltage-dependent gate $x(t)$ satisfies an equation of the form

$$x' = (x_\infty(V) - x)/\tau_x(V).$$

The functions $x_\infty(V)$ are monotonic, so they are invertible. Thus, Kepler et al. introduced a new variable V_x for each gate, where $x(t) = x_\infty(V_x(t))$. They obtained an equivalent dynamical system, but now every variable has the dimensions of voltage. The equivalent potentials satisfy

$$\frac{dV_x}{dt} = \frac{x_\infty(V) - x_\infty(V_x)}{\tau_x(V)x'_\infty(V_x)},$$

where $x'_\infty(V_x)$ is the derivative of x_∞ with respect to V . Now, we must simulate the equations in these new variables and this allows us to compare the amplitudes and the time courses of the responses of all the variables. Figure 3.12a shows a plot of the equivalent potentials for the four-variable Hodgkin–Huxley equations. From the figure, it looks as if V_m and V have roughly the same temporal dynamics, whereas

V_h and V_n have similar time courses. Thus, we create a reduced model by setting $V_m = V$ and $V_n = V_h$. There are two possible reduced models: use the dynamics of V_h and set $n = n_\infty(V_h)$ or use the dynamics of V_n and set $h = h_\infty(V_n)$. We leave the latter case to the reader and consider the (V, V_h) system.

The two-dimensional (V, V_h) system has the following form:

$$\begin{aligned} \frac{dV}{dt} &= I_{\text{app}} - \bar{g}_{\text{Na}} m_\infty^3(V) \bar{h}_\infty(V_h)(V - E_{\text{Na}}) \\ &\quad - \bar{g}_{\text{K}} n_\infty^4(V_h)(V - E_{\text{K}}) - g_L(V - E_L), \\ \frac{dV_h}{dt} &= \frac{h_\infty(V) - h_\infty(V_h)}{\bar{\tau}_h(V, V_h)}, \end{aligned}$$

where $\bar{\tau}_h$ is the effective time constant, $\tau_h(V)h'_\infty(V_h)$. Figure 3.12b shows the bifurcation diagram for the reduced system. It cannot have any more fixed points than the full system since both have identical equilibria. There is a subcritical Hopf bifurcation at roughly $I_{\text{app}} = 6.8$ which is slightly lower than that for the original Hodgkin–Huxley equations. What is strikingly different is that the reduced model continues to oscillate at an extremely large applied current. The second Hopf bifurcation does not occur until $I_{\text{app}} = 267$, much higher than in the original

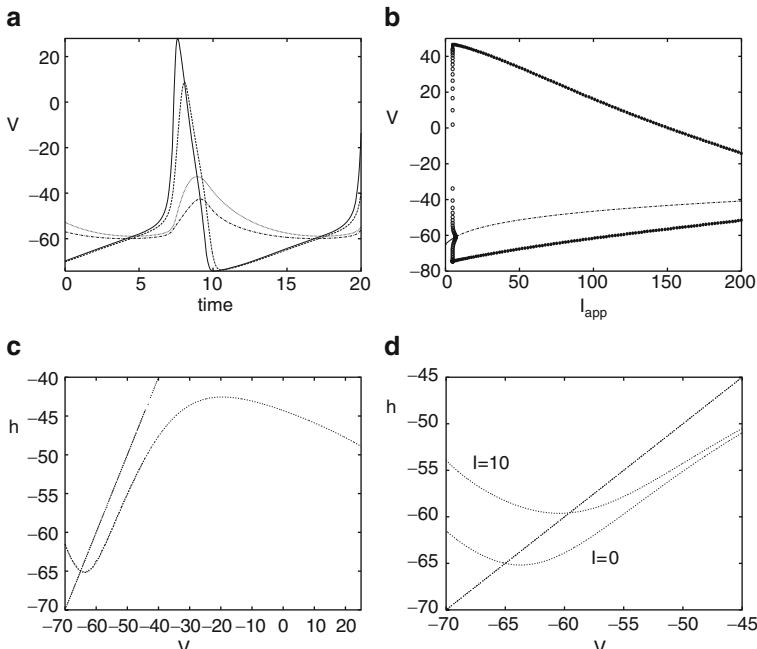


Fig. 3.12 Equivalent potentials for the Hodgkin–Huxley model. **(a)** The voltages of the four variables. **(b)** Bifurcation diagram for the (V, V_h) system, **(c)** Phase plane at rest. **(d)** Phase plane showing how the fixed point moves to the middle branch as I_{app} increases

four-variable system. The phase plane is shown for $I_{\text{app}} = 0$ in Fig. 3.12c. A convenient aspect of the equivalent potential method is that the V_h -nullcline is just $V = V_h$. The V -nullcline has a cubic form which is typical in many neural models and absolutely necessary to get oscillations.

3.7 FitzHugh–Nagumo Equations

The simplified (V, n) version of the Hodgkin–Huxley equations and the Morris–Lecar equations share a common feature insofar as their nullclines are concerned. The V -nullcline has a cubic shape, whereas the recovery nullcline is a monotonically increasing function of the voltage. In 1961, FitzHugh [89] developed a simplified model which captures the essence of the cubic nature of the V -nullcline and has many of the properties of the more complicated models that we have already discussed. Because of its pivotal importance in the literature (particularly, the mathematical literature), we discuss it briefly at this point. We leave as an exercise the numerical and qualitative analysis of these equations. The equations (called the FHN equations) have the form

$$\frac{dV}{dt} = V(V - a)(1 - V) - w + I, \quad (3.5)$$

$$\frac{dw}{dt} = \epsilon(V - \gamma w), \quad (3.6)$$

where $0 < a < 1$, $\epsilon > 0$, and $\gamma \geq 0$. The actual model is based on a modification of the van der Pol equation:

$$\begin{aligned} C \frac{dV}{dt} + F(V) + J &= 0, \\ L \frac{dJ}{dt} &= V. \end{aligned}$$

The van der Pol equation arises from an electrical circuit with a linear capacitor, linear inductor, and nonlinear resistor in parallel. C is the capacitance, L the inductance, $F(V)$ a nonlinear current depending on the voltage, V , across the capacitor, and J the current through the inductor. By adding a driving current and the additional $-\gamma w$, FitzHugh created a model for the action potential. At about the same time, Nagumo and colleagues developed a similar model.

The FHN equations have been used to model many physiological systems from nerve to heart to muscle and is a favorite model for the study of excitability. In most applications, ϵ is small, so the recovery variable is much slower than the voltage. When $I = 0$ and γ is small enough, there is a unique fixed point at the origin. As I increases, this fixed point becomes unstable through a Hopf bifurcation and a limit cycle emerges. We will provide an extensive exercise later for examining the behavior of this popular and much studied model.

3.8 Bibliography

An excellent reference for an introduction to dynamical systems is Strogatz [255]. More advanced textbooks include those of Guckenheimer and Holmes [111], Perko [212], and Kuznetsov [167]. FitzHugh [89] was perhaps the first to use phase plane analysis to study the Hodgkin–Huxley and reduced models. Much of the analysis in this chapter builds on the paper by Rinzel and Ermentrout [230], who carefully described geometric methods, including phase planes and bifurcation theory, applied to reduced neuronal models. They also recognized the relationship between class I and class II excitability and the geometric properties of different types of bifurcations. Izhikevich [135] covers most of the material described in this chapter, but in more detail.

3.9 Exercises

There are a number of exercises on simplified neural models which are popular in the literature. Rather than discussing these in the text, we have chosen to leave them as an extended set of exercises. In later chapters, we will refer to these models and their properties. Thus, it would be a good idea to do those related to the leaky integrate and fire and quadratic integrate and fire models.

1. Show that the gating functions used by Morris and Lecar are derived from the Boltzmann model.
2. Near rest, the potential of the Morris–Lecar system can be approximated by its linearization:

$$C_M \frac{dV}{dt} = I(t) - a C_M (V - V_R),$$

where a is as computed above. Suppose I is a square pulse of current with duration T and magnitude I_0 . Estimate the value of I_0 needed to evoke an action potential assuming that one will occur if V crosses V_t (see Fig. 3.3). Sketch the critical value I_0 as a function of T . This is called the *strength-duration curve*. The minimum strength needed to elicit a response is called the *rheobase* and the stimulus duration needed to elicit an action potential when the stimulus is twice the strength of the rheobase is called the *chronaxie*. Compute the rheobase and chronaxie using this estimate. Numerically determine them as well.

3. Simulate the Morris–Lecar model with the homoclinic parameters and $I = 36$ corresponding the phase plane in Fig. 3.8c. (a) Starting at rest, give a 5-ms current pulse sufficient to produce a single spike. Weaken the current pulse to perturb the model to the stable limit cycle. (b) Set $I = 38$. This corresponds to the vertical line in Fig. 3.7b where there is tristability. Starting at rest, is it possible to inject a single pulse of current to get the system to go from the lower resting state to the upper resting state? If not, figure out a stimulation sequence that will let you go from rest to the upper state.

4. *Exploring the FHN model I.* The fixed points of this model satisfy $w = V/\gamma$ and $I = V/\gamma - V(V - a)(1 - V) \equiv h(V)$. The latter is a cubic. It can have at most three roots. Differentiating $h(V)$ and setting this to zero allows us to find local maxima and minima. (a) Find these as a function of a and γ . Show that $\gamma > 3/(1 - a + a^2) \equiv \gamma^*(a)$ for such extrema to exist. Next, set V to these roots and use this to find values of I where there are saddle-node bifurcations. This summarizes the steady-state behavior of the model. (b) Consider the case when $\gamma < \gamma^*(a)$ so that there is only a single root. Since there is one root, there can be no bifurcation at a zero eigenvalue as I varies. Thus, the only way to lose stability is a Hopf bifurcation. Show that the trace of the linearization is

$$T = -3V^2 + (2 + a)V - a - \epsilon.$$

Show that there are two values of V such that the trace vanishes as long as $3\epsilon < a^2 - a + 1$. These correspond to two distinct values of current ($I = h(V)$) at which there is a Hopf bifurcation.

5. *Exploring the FHN model II.* (a) Choose $\epsilon = 0.02$, $\gamma = 1$, and $a = 0.1$. For $I = 0$ show that the system is excitable, that is, show that there is an action potential if the voltage is taken sufficiently past threshold. (b) Compute the bifurcation diagram and look at the frequency–current plot. Notice that the bifurcation is nearly vertical. Compute several limit cycles along the nearly vertical branch. Notice how they hug the middle branch of the nullcline. This is an example of a phenomenon called a *canard* and is common in systems with a small parameter (e.g., ϵ).
 6. *The integrate and fire model.* A classic approximation for the firing of a cell is the leaky integrate and fire model [174]. This model has the form

$$\tau \frac{dV}{dt} = -(V - V_R) + R_M I, \quad (3.7)$$

where R_M is the membrane resistance, τ the time constant, and V_R the resting potential. In addition to this linear equation, there is a nonlinear reset condition. If $V(t^-) = V_{\text{spike}}$, then an action potential occurs and $V(t)$ is reset to V_{reset} . In many cases, an additional condition is imposed in which V is prevented from firing for a period, T_{ref} , the “refractory” period. Assume $V_R < V_{\text{spike}}$ and $V_{\text{reset}} < V_{\text{spike}}$. Find the critical value of I , I_{\min} , under which the leaky integrate and fire model fires repetitively. Compute the F – I curve; the firing rate as a function of the applied current for $I > I_{\min}$. Show that for large values of I , the firing rate is linear with respect to I when $T_{\text{ref}} = 0$.

7. *Spike response model.* Consider the leaky integrate and fire model with a time-dependent current, $I(t)$:

$$\tau \frac{dV}{dt} = I(t) - V(t) - A \sum_j \delta(t - t_j),$$

where $A = \tau(V_{\text{spike}} - V_{\text{reset}})$. We have formally included the reset into the equations by adding the delta function term. The values t_j are the times for which $V(t)$ crosses V_{spike} from below; that is, the spike times. Integrate this equation to convert it to the following form:

$$V(t) = V(0)e^{-t/\tau} + \sum_j \eta(t - t_j) + \int_0^t k(t-s)I(s)ds,$$

where

$$\eta(t) = H(t)(V_{\text{reset}} - V_{\text{spike}})e^{-t/\tau}$$

and

$$k(t) = \frac{1}{\tau}e^{-t/\tau}.$$

Here, H is the Heaviside step function. Gerstner et al. [99] considered classes of models like this where η takes a more general form. These models are called *spike response models*. For example, $\eta(t)$ could include an additional spike frequency adaptation term, for example,

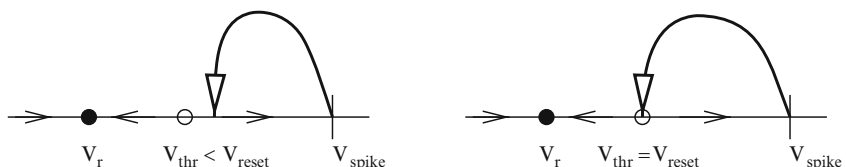
$$\eta(t) = H(t)[k_1 e^{-t/\tau} + k_2 e^{-t/\tau_a}].$$

Unfortunately, once these extra terms are added, it becomes difficult to compute even the steady-state firing rate. Later in the book, we will use this formulation to compute the velocity of waves in networks of coupled integrate and fire models.

8. In the Morris–Lecar model with class I dynamics (the SNIC), the potential near the bifurcation satisfies the following differential equation:

$$\frac{dV}{dt} = a(I - I_{\text{SN}}) + b(V - V_{\text{SN}})^2, \quad (3.8)$$

where a and b are positive numbers that can be determined from the actual dynamics (see [167]). (What are the physical dimensions of a, b ?) This is called the *quadratic integrate and fire* model. (a) By integrating this equation, show that V can go to infinity in finite time. When $V(t)$ goes to infinity, we say that a spike has been generated. (b) Suppose $I < I_{\text{SN}}$ and find the fixed points for this, V_{rest} and V_{thr} , corresponding to the stable and unstable fixed points,



respectively. Suppose $V(0) > V_{\text{thr}}$. Compute the time to spiking as a function of $V(0) - V_{\text{thr}}$. (c) Show that if $I > I_{\text{SN}}$, then $V(t)$ goes to infinity no matter what the initial condition is. In particular, compute the time it takes to reach infinity if $V(0) = -\infty$. (d) Let

$$V(t) = V_{\text{SN}} + \frac{c}{b} \tan(\theta/2).$$

where c^{-1} has dimensions of time. Show that $\theta(t)$ satisfies

$$\frac{d\theta}{dt} = c(1 - \cos \theta) + \frac{ab}{c}(1 + \cos \theta)[I - I_{\text{SN}}]. \quad (3.9)$$

This is called the *theta model*. Ermentrout and Kopell [72] showed that this was the normal form for a system near a saddle-node limit cycle bifurcation. Sketch the phase line for this when $I < I_{\text{SN}}$, $I = I_{\text{SN}}$, and $I > I_{\text{SN}}$. Compute the F - I curve when $c = 1$.

9. A variant of the quadratic integrate and fire model truncates the spike and the reset. [175] first suggested the model

$$\tau \frac{dV}{dt} = a(V - V_R)(V - V_{\text{thr}}) + R_M I \quad (3.10)$$

with the condition that if $V(t) = V_{\text{spike}} > V_{\text{thr}}$, then $V(t)$ is reset to V_{reset} . When $I = 0$, V_r is the resting state and V_{thr} is the threshold. If $V(0) > V_{\text{thr}}$, then the model will spike. (a) Compute the F - I curve for this model. Note that it is somewhat different from the quadratic integrate and fire in (3.8) owing to the finite reset.

(b) Suppose $V_{\text{reset}} > V_{\text{thr}}$. Then, this model is bistable for $I = 0$ or I is sufficiently small and has a fixed point near V_r and a periodic solution. As $V_{\text{reset}} \rightarrow V_{\text{thr}}^+$, the period goes to infinity and this model has the equivalent of a homoclinic orbit. (see the diagram above.) Compute the period as a function of $V_{\text{reset}} - V_{\text{thr}}$. (c) Now suppose $V_R < V_{\text{reset}} < V_{\text{thr}}$. As I increases, either the stable resting state will reach V_{reset} from below or the unstable fixed point will reach V_{reset} from above and form a homoclinic. Find conditions for the latter scenario and sketch the bifurcation diagram as I varies. Compare this with the diagram for the Morris–Lecar model in parameter set 3. From this exercise, it should be clear that the quadratic integrate and fire model has much richer dynamics than the leaky integrate and fire model precisely because it has a true spiking threshold which is different from the value of the actual spike.

10. Karbowski and Kopell [145] introduced a linear model:

$$\tau \frac{dV}{dt} = R_M I + a|V|, \quad (3.11)$$

where $a > 0$ is parameter. (a) Show that this is qualitatively like (3.10). How does the firing rate scale near $I = 0$? (b) One can define a class of scalar neural models by considering

$$\tau \frac{dV}{dt} = R_M I + f(V).$$

Suppose $f(V) = |V|^p$, where $p > 1$. The model spikes when $V(t)$ reaches infinity, in which case the neuron is reset to negative infinity. What is the firing rate of such a neuron for I large? That is, how does it scale with p ? For example, we know that when $p = 2$, the firing rate scales like the square root of I .

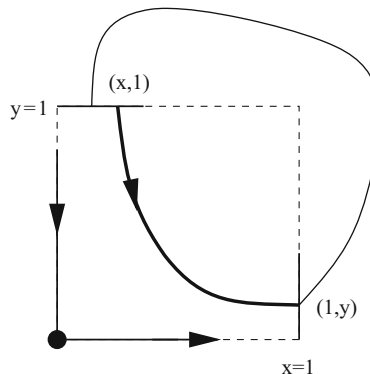
11. A class of models related to the theta model are called *ring* models [75, 291]. These are models for excitable activity which lies on the unit circle:

$$\frac{dx}{dt} = f(x) + I,$$

where $f(x + 2\pi) = f(x)$ is a bounded periodic function. For certain ranges of I , the system has two fixed points: a saddle and a node. The saddle point acts as a threshold. Since $f(x)$ is bounded, for I large enough, there are periodic solutions to the equation and thus there is repetitive firing. Suppose $f(x)$ is $C^2[0, 2\pi]$ and periodic. Write an expression for the period of the oscillations when there is repetitive firing. Discuss the mechanism from going from a stable resting state to repetitive firing. Can there ever be bistability?

12. Fourcaud et al. [91] introduced the exponential integrate and fire model:

$$C \frac{dV}{dt} = -g_L(V - V_L) + a \exp(bV) + I.$$



Set $g_L = 0$ and assume a , b , and C are positive. Find an expression for the firing rate as a function of I in terms of an integral. Show that if a and b are positive, then for I large enough, the solution of the ordinary differential equation blows up in finite time. Obtain an estimate for how fast it blows up by ignoring the linear terms, $g_L(V - E_L)$. That is, the blowup time is roughly

$$\int_0^\infty \frac{dV}{I + a \exp(bV)}.$$

Evaluate this as a function of I .

13. *Period near a homoclinic.* This is actually an exercise in dynamical systems, but is instructive in that it shows the period of the homoclinic orbit. Assume the origin is a saddle point with eigenvalues $-\mu$ and ν , the y -axis is the stable manifold, and the x -axis is the unstable manifold. Moreover, $\mu > \nu > 0$. Consider a point $(1, y)$ on the little interval at $x = 1$. This is mapped onto the little interval at $y = 1$, via $(1, y) \rightarrow (ay + b, 1)$. The parameter a is positive and will not really matter. The parameter b is the distance from the homoclinic orbit. Note that if $b = 0$, then $(1, 0) \rightarrow (0, 1)$ is the homoclinic orbit. Starting at $(x_0, 1)$, we follow the linear dynamics

$$x' = \nu x; \quad y' = -\mu y.$$

This maps the $y = 1$ interval onto the $x = 1$ interval. Thus, we obtain a map from $(1, y_{\text{old}}) \rightarrow (1, y_{\text{new}})$. (a) Show that the map of the y values is

$$y_{\text{new}} = (ay_{\text{old}} + b)^r,$$

where $r = \mu/\nu > 1$. For b sufficiently small, show that $y = b^r + o(b^r)$ is a fixed point. Show that the fixed point is stable. (b) Since the map from $x = 1$ to $y = 1$ is instant, the period is the time it takes to go from $y = 1$ to $x = 1$. Show that at the fixed point

$$T \sim -\frac{1}{\nu} \log b.$$

(Note: This relies on the fact that $r > 1$. If $r < 1$, then the fixed point will be unstable and so the periodic orbit will also be unstable.)

Chapter 4

The Variety of Channels

We have discussed several types of active (voltage-gated) channels for specific neuron models. The Hodgkin–Huxley model for the squid axon consisted of three different ion channels: a passive leak, a transient sodium channel, and the delayed rectifier potassium channel. Similarly, the Morris–Lecar model has a delayed rectifier and a simple calcium channel (with no dynamics). Hodgkin and Huxley were smart and supremely lucky that they used the squid axon as a model to analyze the action potential, as it turns out that most neurons have dozens of different ion channels. In this chapter, we briefly describe a number of them, provide some instances of their formulas, and describe how they influence a cell’s firing properties. The reader who is interested in finding out about other channels and other models for the channels described here should consult <http://senselab.med.yale.edu/modeldb/default.asp>, which is a database for neural models.

4.1 Overview

We briefly describe various ion channels in this section. Most of the voltage-gated channels follow the usual formulation of the delayed rectifier, the calcium model, and the transient sodium current we have already discussed. However, there are several important channels which are gated by the internal calcium concentration, so we will describe some simple models for intracellular calcium handling.

All of the channels that we describe below follow the classic Hodgkin–Huxley formulation. The total current due to the channel is

$$I_{\text{channel}} = m^p h^q I_{\text{drive}}(V),$$

where m and h are dynamic variables lying between 0 and 1, p and q are nonnegative integers, and V is the membrane potential. Thus, the channel current is maximal when m and h are both 1. By convention, h will generally inactivate (get smaller) with higher potentials of the cell and m will activate. Not all channels have both activation and inactivation. For example, the Hodgkin–Huxley potassium channel and both the Morris–Lecar calcium and potassium channels have no inactivation. The Hodgkin–Huxley sodium channel has both activation and inactivation.

The drive current generally takes two possible forms corresponding to the linear model or the constant field model, respectively:

$$I_{\text{lin}} = g_{\max}(V - V_{\text{rev}}) \quad (4.1)$$

and

$$I_{\text{cfe}} = P_{\max} \frac{z^2 F^2}{RT} V \left(\frac{[C]_{\text{in}} - [C]_{\text{out}} e^{-\frac{zVF}{RT}}}{1 - e^{-\frac{zVF}{RT}}} \right). \quad (4.2)$$

The constant g_{\max} has units of siemens per square centimeter and the constant P_{\max} has units of centimeters per second, so the driving current has dimensions of amperes per square centimeter.

The gates m and h generally satisfy equations of the form

$$\frac{dx}{dt} = a_x(1-x) - b_x x$$

or

$$\frac{dx}{dt} = (x_{\infty} - x)/\tau_x,$$

where the quantities a_x , b_x , x_{∞} , and τ_x depend on voltage or some other quantities. The functional forms of these equations often take one of the following three forms:

$$\begin{aligned} F_e(V, A, B, C) &= A e^{(V-B)/C}, \\ F_l(V, A, B, C) &= A \frac{(V-B)}{1 - e^{(V-B)/C}}, \\ F_h(V, A, B, C) &= A / (1 + e^{-(V-B)/C}). \end{aligned}$$

Generally speaking, most of the voltage-gated ion channels can be fit with functions of the form

$$x_{\infty}(V) = \frac{1}{1 + e^{(V-V_T)/k}} \quad (4.3)$$

and

$$\tau_x(V) = \tau_{\min} + \tau_{\text{amp}} / \cosh \frac{V - V_{\max}}{\sigma}. \quad (4.4)$$

4.2 Sodium Channels

Roughly speaking, there are two types of sodium currents: the transient or fast sodium current and the persistent or slow sodium current. We have already described the former when we discussed the Hodgkin–Huxley model. The fast sodium current is found in the soma and axon hillocks of many neurons. The persistent (slow) sodium current (which activates rapidly; the “slow” in its name refers to inactivation) has been implicated as underlying both subthreshold and suprathreshold firing

in many neurons by adding a small depolarizing current which keeps them active. The fast sodium current used in the Hodgkin–Huxley equations is not suitable for neurons in the brains of mammal; instead, modelers often use a model that is due to Roger Traub [269]. The equations for this channel and all others in this chapter can be found online.

As an example of the utility of the persistent sodium channel we will introduce a simple model of the pre-Bötziinger complex, a group of neurons responsible for generating the respiratory pacemaker oscillations in the brainstem. (That is, these are the cells that make us breathe.) Here, the persistent sodium channel and its inactivation play a crucial role in generating the pacemaker potential for the oscillation [55]. The model has the form

$$\begin{aligned} C_m \frac{dV}{dt} &= -g_L(V - E_L) - g_K n^4 (V - E_K) - g_{Na} m_\infty(V)^3 (1 - n)(V - E_{Na}) \\ &\quad - g_{Nap} w_\infty(V) h(V - E_{Na}), \\ \frac{dn}{dt} &= (n_\infty(V) - n)/\tau_n(V), \\ \frac{dh}{dt} &= (h_\infty(V) - h)/\tau_h(V). \end{aligned}$$

Note that for the fast sodium channel, the inactivation has been replaced by $1 - n$ as in the Rinzel reduction of the Hodgkin–Huxley equations (see Sect. 3.6). The variable h now corresponds to inactivation of the persistent sodium channel. The key feature in this model is that the inactivation of the persistent sodium current has a time constant of 10 s. Figure 4.1a shows a simulation of this model for 40 s. The voltage oscillates at a period of about 6 s, which is commensurate with the 10-s time constant for inactivation of the persistent sodium channel. In Chap. 5, we will explore the role of the persistent sodium channel in producing the bursts. Here, we restrict our discussion to the pacemaker duties of the persistent sodium channel.

Butera et al. [30, 31] showed that one of the key parameters in inducing the bursting is the leak potential E_L . If $E_L = -65$ mV, then the system exhibits stable resting behavior. By shifting this parameter from -65 to -60 mV, they obtained the pattern shown in Fig. 4.1a. If we block the transient sodium channel by setting $g_{Na} = 0$, then we can look at the bifurcation diagram of the “spikeless” model as a function of E_L . Figure 4.1b shows the voltage as a function of the leak current. There are two Hopf bifurcations: a subcritical bifurcation at about -60 mV and a supercritical bifurcation at about -54 mV. Thus, for a range of leak potentials there is a slow pacemaker potential. We can further understand this by noting that the variable h is much slower than (V, n) . If we set $n = n_\infty(V)$, then this leads to a two-dimensional system in (V, h) , the phase plane of which we show in Fig. 4.1c. At $E_L = -62$ mV, there is a single stable fixed point. As E_L increases, the V -nullcline moves down and intersects the h -nullcline in the middle branch. Since h is very slow, this leads to a relaxation oscillation shown in the phase plane and in Fig. 4.1d. The period of the pacemaker potential is about twice that of the full model (in Fig. 4.1a). This is because the spikes produced by the full model cause more inactivation of the persistent sodium channel.

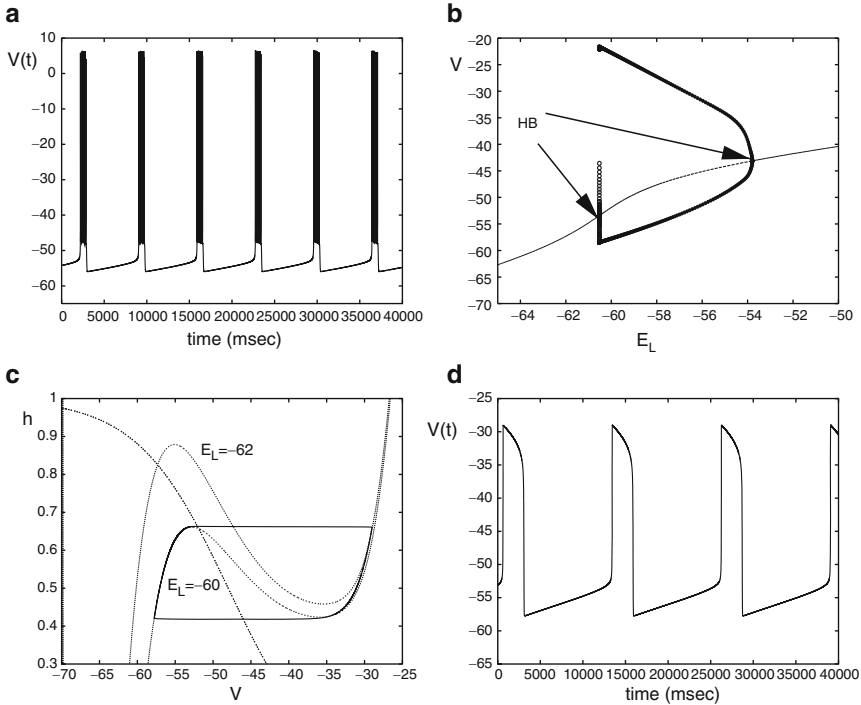


Fig. 4.1 The persistent sodium channel provides the pacemaker current for the model pre-Botzinger cell. **(a)** Potential with $E_L = -60$ mV for the full bursting model. **(b)** Bifurcation diagram with the fast sodium channel blocked showing the onset of pacemaker oscillations at the Hopf bifurcation. **(c)** Phase plane with $n = n_\infty(V)$ showing relaxation oscillation. **(d)** Potential of the simple relaxation model

4.3 Calcium Channels

Calcium channels are quite similar to sodium channels in their form, function, and dynamics. However, because the concentration of calcium in the cell is very low (e.g., of the order of 10^{-8} M), the small amount of calcium coming into the cell from the channel opening can drastically alter the driving potential. Thus, many modelers (but no theoreticians!) use the constant-field equation (CFE) (4.2) rather than the simple ohmic drive (4.1). Using the CFE model requires an extra equation for the intracellular calcium concentration, but this is often ignored. The CFE just adds a nonlinearity to the current with little effect on the dynamics.

We can divide calcium channels into roughly two classes (although experimentalists describe many more): (1) T-type calcium currents $I_{Ca,T}$, which are low-threshold but inactivate, and (2) L-type calcium currents, $I_{Ca,L}$ which have a high threshold and do not inactivate. $I_{Ca,T}$ is fast and both the activation and the inactivation are voltage-dependent. This current is responsible for bursting in many neurons, particularly in the thalamus, where it plays the dominant role in producing

oscillatory activity during sleep [58, 59]. $I_{\text{Ca,L}}$ is responsible for spikes in some cells (such as the Morris–Lecar model). It does, in fact, inactivate, but the inactivation is calcium- rather than voltage-dependent.

The T-current has some interesting properties, such as the ability to produce rebound bursts and subthreshold oscillations. Let us see some of these features. We will look at a simple model in which the spiking currents (sodium and potassium) are blocked so that all that is left is the T-current and the leak:

$$\begin{aligned} C \frac{dV}{dt} &= I_0 - g_L(V - E_L) - I_T, \\ \frac{dh}{dt} &= (h_\infty(V) - h)/\tau_h(V), \\ I_T &= m_\infty(V)^2 h I_{\text{cfe}}(V, [Ca]_o, [Ca]_i), \\ m_\infty(V) &= 1/(1 + \exp(-(V + 59)/6.2)), \\ h_\infty(V) &= 1/(1 + \exp((V + 83)/4)), \\ \tau_h(V) &= 22.7 + 0.27/(\exp((V + 48)/4) + \exp(-(V + 407)/50)). \end{aligned} \quad (4.5)$$

To simplify the analysis of this model, we have set the activation variable m to its steady state $m_\infty(V)$. Full parameters for the model are given online. What sets the behavior for this model is the resting potential. Various neural modulators (chemicals which alter the behavior of neurons in a quasiconstant manner) set the resting potential from either relatively depolarized at, say, -60 mV to relatively hyperpolarized at -80 mV. The inactivation h has a half-activation at -83 mV in the present model, so if the resting potential is -60 mV, then $h \approx 0$. This means no amount of depolarizing current can activate the current. In the sensory literature, when the thalamic neurons are depolarized like this, the network is said to be in “relay” mode. Inputs to the thalamus are transmitted as if the cell were just a nonlinear spiker like we have already encountered. However, if the network is hyperpolarized, then inactivation of the T-current, h , will be much larger and a subsequent stimulus will lead to an explosive discharge of the neuron.

Suppose the leak is set so that the resting potential is around -60 mV. Figure 4.2a shows the response of the model to brief depolarizing and hyperpolarizing pulses. At -60 mV, the T-current is completely inactivated, so the response to depolarizing pulses is the same as it would be if the current were not there. In this simplified model, the result is a passive rise in voltage followed by a passive decay. However, if the same membrane is provided with a brief and strong hyperpolarizing stimulus, it responds with a calcium action potential when released from the stimulus. This is called *rebound* and is a classic property of cells with a T-type calcium current. Figure 4.2b provides a geometric explanation for rebound. At rest, the membrane sits at the lower-right fixed point. At this point $h \approx 0$. A hyperpolarizing input moves the V -nullcline upward; if the hyperpolarization is maintained, the trajectory will move toward the new fixed point (upper-left circle.) If, instead, the hyperpolarization is transient, then when the stimulus is removed, the V -nullcline moves to its original position. Since h is slow compared with V , the potential will rapidly move horizontally to reach the right branch of the V -nullcline, leading to the calcium spike.

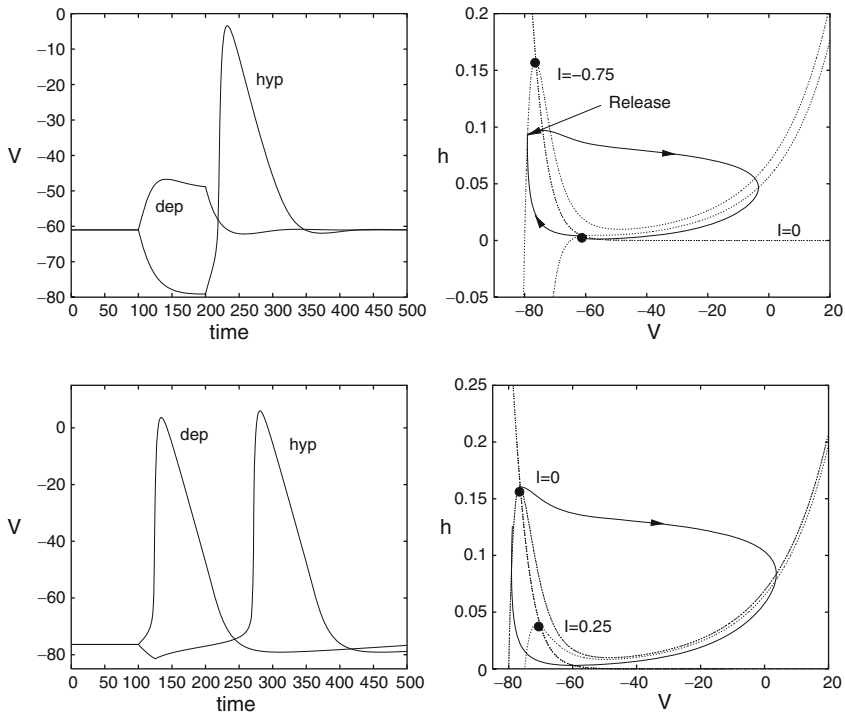


Fig. 4.2 Properties of the T-type calcium current

In contrast, consider the system when the leak is -80 mV . Then, the resting state is about -78 mV and the T-current inactivation, h , is no longer negligible. Figure 4.2c shows that a small depolarizing input is now sufficient to elicit a calcium action potential. Similarly, a small hyperpolarizing input will also result in the firing of an action potential. Figure 4.2d provides an explanation for why depolarization will work in this case. Depolarization lowers the V -nullcline, allowing the trajectory to jump to the right branch of the nullcline and produce a spike.

The T-current also provides a mechanism for subthreshold calcium oscillations which can be pacemakers for bursting like the persistent sodium current. In Exercise 2, you are asked to find these oscillations and give a geometric explanation for them.

4.4 Voltage-Gated Potassium Channels

There is no doubt that the greatest variety of channels is found among those which involve potassium. We have already seen the workhorse for spiking, the delayed rectifier, in the Hodgkin–Huxley model, the Butera model of the pre-Botzinger

complex, and the Morris–Lecar model. The delayed rectifier is rather fast and has only an activation gate. Potassium channels provide the main repolarizing force for nerve cells. If they are fast, then the cells are allowed to rapidly repolarize, so very fast spike rates are possible. If they are slow, they cause the spike rate to slow down with sustained depolarization, an important form of adaptation. In addition to the voltage-gated potassium channels which we describe here, there are also calcium-gated potassium channels which perform similar roles.

4.4.1 A-Current

The Hodgkin–Huxley model was based on a quantitative analysis of the squid axon. In 1971, Connor and Stevens [45] introduced an alternative model for action potentials in the axons of crab legs. The transient sodium current and the delayed rectifier were similar to those in the Hodgkin–Huxley model although they were faster. In addition, Connor and Stevens introduced a transient potassium current, the *A-current*. Like the transient sodium current, this current has both an activation and an inactivation gate:

$$I_A = g_A a^3 b(V - E_A).$$

The reversal potential E_A is close to that of the delayed rectifier. The activation variable a increases with voltage, whereas the inactivation variable b decreases; $b_\infty(V)$ has a half-activation at about -78 mV. (The full Connor–Stevens model is given online.) One consequence of having this current is that it induces a delay to spiking when the cell is relatively hyperpolarized. Intuitively, the reason for this is that when the cell is somewhat hyperpolarized, b will be large. Depolarization engages a and thus there will be a large potassium current. However, when the membrane is depolarized, $b_\infty(V)$ will be small, so b will decrease, leading to a gradual loss of the A-current. The neuron will spike only when this current is sufficiently small. Thus, the A-current causes a delay to spiking. Figure 4.3a shows an example of the delay to spiking due to the A-current.

One of the most interesting dynamic consequences of the A-current in the Conner–Stevens model is that it converts the transition to repetitive firing from class II (like the Hodgkin–Huxley model) to class I. Recall that for a class II neuron, the transition from resting behavior to oscillations is via a Hopf bifurcation; moreover, the steady-state voltage–current (I – V) relationship is monotonic. For a class I neuron, the transition to oscillations is via a saddle–node on an invariant circle (SNIC) bifurcation and the I – V relationship is nonmonotonic.

The A-current provides a means to make the I – V relationship nonmonotonic since the steady-state current,

$$I_{A,ss} = g_A a_\infty(V)^3 b_\infty(V)(V - E_A),$$

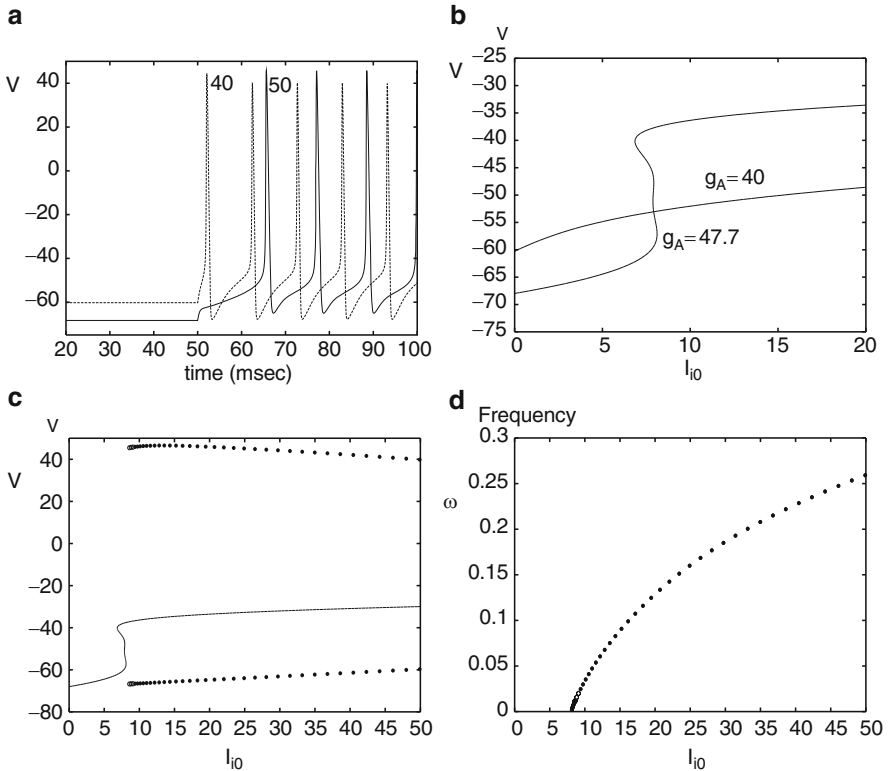


Fig. 4.3 Connor–Stevens model. (a) Delay to spiking depends on the A-current. The *dashed curve* shows $g_K = 27.7$ and $g_A = 40$, and the *solid curve* shows $g_K = 17.7$ and $g_A = 50$. (b) Steady-state I – V curve with two different amounts of A-current. (c) Full bifurcation diagram for the Connor–Stevens model with default parameters. (d) Frequency–current curve for the Connor–Stevens model showing class I behavior

is nearly zero. Thus, if the majority of the potassium current is A-type rather than the delayed rectifier current, then the steady-state I – V curve will be dominated by the sodium current.

To explore this idea in more detail, we consider the Connor–Stevens model keeping the maximal total potassium conductance constant: $g_A + g_K = g_{\text{total}} = 67.7$. The choice of 67.7 for the total is so that the Connor–Stevens model is our default, $g_K = 20$ and $g_A = 47.7$. Figure 4.3b shows the steady-state I – V curve for the standard Connor–Stevens parameters and also for when the A-current is reduced to 40 while the delayed rectifier is increased to 27.7. It is clear that the I – V curve is monotonic with the reduced A-current, so class I (SNIC) dynamics is impossible. Figure 4.3c shows the bifurcation diagram for the standard Connor–Stevens model as current is injected. A branch of periodic orbits emerges at high applied currents at a supercritical Hopf bifurcation (not shown). This branch terminates via a SNIC on the steady-state I – V curve. The frequency is shown in Fig. 4.3d and as predicted by

the general theory has a square-root shape and vanishes at the critical current. We point out that the steady-state I - V curve in the standard parameter regime is not a simple “cubic” as in the Morris–Lecar model. Rather, there are values of the applied current where there are five fixed points. Rush and Rinzel [239] were the first to notice this. The phenomenon occurs over a very narrow range of values of g_A . In Exercise 5, you are asked to explore the behavior of the system with slightly different values of g_A .

4.4.2 M-Current

There are several slow potassium currents which are responsible for a phenomenon known as spike-frequency adaptation. That is, this slow low-threshold outward current gradually reduces the firing rate of a neuron which has been depolarized sufficiently to cause repetitive firing. The M-current and related slow potassium currents are able to stop neurons from firing if they are strong enough and thus can provide an effective brake to runaway excitation in networks.

Figure 4.4 shows an example of spike-frequency adaptation in a simple cortical neuron model due to Destexhe and Paré [57]. The left-hand graphic shows the voltage as a function of time when the current is instantaneously increased to $6 \mu\text{A}/\text{cm}^2$. The initial interspike interval is short but over time this lengthens. Figure 4.4b shows the instantaneous frequency (reciprocal of the initial interspike interval) as a function of the spike number. The frequency drops from 130 to 65 Hz over about 1 s.

The M-current does far more than just slow down the spike rate. Because it is active at rest (the threshold is -30 mV), the M-current can have profound effects on the steady-state behavior. Figure 4.5a shows the bifurcation diagram of steady states as the conductance of the M-current (g_m) is increased. With no M-current, the model has a SNIC bifurcation to a limit cycle, so it is a class I membrane. For

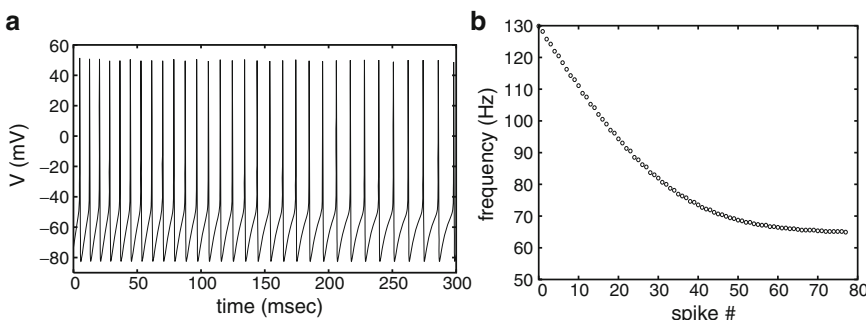


Fig. 4.4 Spike-frequency adaptation from the M-type potassium current. The model is from Destexhe and Paré [57] and represents a cortical pyramidal neuron. The applied current is $6 \mu\text{A}/\text{cm}^2$ and $g_M = 2 \text{ mS}/\text{cm}^2$. (a) Voltage and (b) instantaneous frequency versus spike number

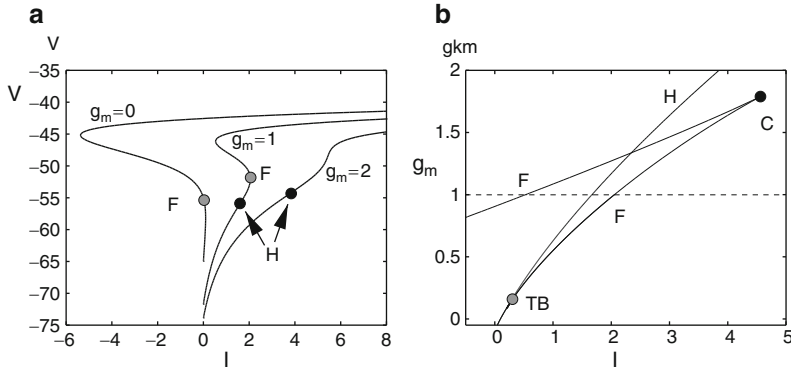


Fig. 4.5 Effects of M-current on equilibria. (a) Steady state as a function of current at three values of g_m . With no M-current, the neuron is class I and oscillations are borne via a saddle-node on an invariant circle along the fold curve F . With large enough M-current ($g_m = 2$), oscillations are borne via a Hopf (H) bifurcation and the fold points no longer exist since there is a unique equilibrium point. For intermediate values, the folds still exist, but the Hopf bifurcation occurs on the lower branch of fixed points. (b) Two-parameter diagram. The twofold curves (F) meet at a cusp point (C) near $I = 4.8$ and $g_m = 1.8$. There is a curve of Hopf points (H) which terminates at a Takens–Bogdanov (TB) point when the Hopf curve meets a fold curve. The dashed line corresponds to $g_m = 1$; as I increases, there is first a Hopf point and then the fold. At $g_m = 0$, no Hopf point is encountered and when $g_m = 2$, there are no folds

larger values of g_m (Destexhe and Paré used $2 < g_m < 5$) the resting state loses stability at a Hopf bifurcation, so the membrane is class II. The transition from class I to class II occurs for $g_m = 1$ where the fold points (saddle-nodes) remain but the lower branch of fixed points loses stability at a Hopf bifurcation. Figure 4.5b shows a two-parameter bifurcation diagram of this system where the applied current and g_m vary. As g_m increases, the two fold points merge at a cusp point (labeled C) and for g_m larger, there is only a single fixed point. Additionally, there is a curve of Hopf points which terminates on the rightmost fold point at a Takens–Bogdanov point. In some sense, the Takens–Bogdanov point marks the transition from class I to class II excitability. The global picture is complex. For example, when $g_m = 0$, there is a single branch of periodic solutions terminating at the fold point via a SNIC. However, when $g_m = 1$, a branch of periodic solutions must bifurcate from the Hopf point. This branch must somehow either merge with the SNIC branch or disappear. The interested reader could attempt to put together a plausible global picture as a project. (The reader could also consult [136], p 197.)

4.4.3 The Inward Rectifier

The inward rectifier is hyperpolarization-activated. That is, if the neuron is hyperpolarized enough, the current is activated, further hyperpolarizing the model. This

implies the possibility for bistability in the hyperpolarizing direction. The current has the form

$$I_{\text{Kir}} = g_{\text{Kir}} h(V)(V - E_K),$$

where

$$h(V) = 1/(1 + \exp((V - V_{\text{th}})/k)).$$

Typical values for the parameters are $V_{\text{th}} = -85$ mV and $k = 5$ mV. With a leak current the steady-state current satisfies

$$I = g_L(V - E_L) + g_{\text{Kir}} h(V)(V - E_K).$$

Differentiating this equation, we obtain

$$\frac{dI}{dV} = g_L + g_{\text{Kir}} h(V) + g_{\text{Kir}} h'(V)(V - E_K).$$

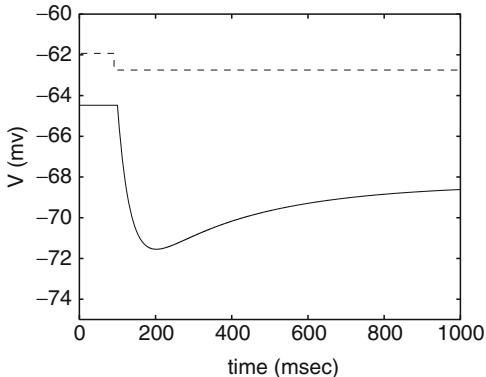
The first two terms are positive. However, if $V > E_K$, then since $h'(V) < 0$, it is possible that this last term can be large and negative enough so that the I - V curve is cubic-like. Necessary conditions are that $E_K < V_{\text{th}}$ and k must be small enough. Once there is bistability, it is possible to generate oscillations. Izhikevich [136] points out that if you add a delayed rectifier potassium current, then it is possible to generate oscillations *with two potassium currents!* Given the fact that this current can induce bistability, this is not surprising. In Exercise 8, you can give this a try. Another way to induce oscillations in this model is to assume there is extracellular potassium accumulation. This will result in the reversal potential for potassium becoming more positive, inactivating the channel. Thus, there will be negative feedback to a bistable system and possibly oscillations; see Exercise 9.

4.5 Sag

We end our discussion of voltage-gated channels with a description of the so-called sag current, I_h . This is a slow inward current with a reversal potential of between -43 and 0 mV, but which requires hyperpolarization to become active; that is, the activation curve decreases monotonically. The ions involved are a mixture of sodium and potassium ions, so the reversal potential lies between that of sodium and that of potassium. The sag current is implicated as a pacemaker in many different systems [158, 186]. It also plays an important role in dendritic computations [203, 277]. There are several models for this current; some have a single component and others have multiple components. The simplest model is due to Huguenard and McCormick [131]:

$$I_h = g_h y(V + 43), \quad (4.6)$$

Fig. 4.6 The sag (I_h) current causes a slow repolarization of the potential to hyperpolarizing steps. (Parameters are those from McCormick et al. [131])



where

$$\begin{aligned}\frac{dy}{dt} &= (y_\infty(V) - y)/\tau_y(V), \\ y_\infty(V) &= 1/(1 + \exp((V - V_{th})/k)), \\ \tau_y(V) &= \tau_0 \operatorname{sech}((V - V_m)/b).\end{aligned}$$

The time constant τ_0 varies from 50 ms to over 1,000 ms. (Note that the function $\tau_y(V)$ used by McCormick et al. is more complicated than the present version, but they are almost identical in shape.) Figure 4.6 shows how the sag gets its name. Hyperpolarizing the membrane causes the potential to drop and thus activates the sag current, which then repolarizes the membrane. In Exercise 10, you combine this current with I_{Kir} from Sect. 4.4.3 to obtain a slow pacemaker oscillation.

4.6 Currents and Ionic Concentrations

So far, we have assumed the ionic concentrations both inside and outside the cell are held constant. This is usually a good assumption except for the calcium ion. Because the internal free calcium levels are very low in a cell (10^{-4} mM), the entry of calcium through voltage-gated channels can substantially contribute to the intracellular calcium. Indeed, calcium is a very important signaling molecule and it often sets up complex reaction cascades within the cell. These reactions have both long-term and short-term effects on the cell. Thus, it is useful to understand how to model the flow of calcium due to voltage-gated channels. In certain pathological cases, the buildup of extracellular potassium can also have profound effects on neurons. Since the normal extracellular medium has quite a low level of potassium, if many neurons are firing simultaneously, they are releasing large amounts of potassium into the medium. The surrounding nonneuronal cells (glia) buffer the potassium concentration, but this process can be slow.

Consider a current due to some ionic species I_X . Suppose this is a positive ion. The current is typically measured in units of microamperes per square centimeter. Recall that an ampere is a coulomb of charge per second. We need to convert this current to a concentration flux which has dimensions of millimolar. Recall that 1 M is 1 mol/L, or 1 mol per 1,000 cm³. Faraday's constant, 96,485 C/mol, is just what we need. Suppose the valance of the ion is z . Then, $I_X/(zF)$ gives us the transmembrane flux in units of micromolar per centimeter per second. To convert this into a concentration flux, we suppose the ions collect in a thin layer of depth d (in microns) near the surface of the cell. Thus, the change in concentration is $I_X/(zdF)$. Finally, we want our units of concentration to be in millimoles per liter per millisecond. Noting that 1 L is 1,000 cm³, we find that the total in(out)flux of an ion is

$$f_X = 10I_X/(zFd), \quad (4.7)$$

where $F = 96,485$, d is the depth in microns, and I_X is the current in microamperes per square centimeter.

Having defined the flux of ions moving through the cell, we need to write equations for the total concentration of the ion, X :

$$\frac{dX}{dt} = \pm f_X - \delta(X),$$

where $\delta(X)$ is the decay of ion X through uptake or buffering. Which sign should we take for the flux? If we are interested in the intracellular concentration, then we take the negative sign and if we are interested in extracellular concentrations, we take the positive sign. The simplest form for the decay is

$$\delta_P(X) = (X - X_0)/\tau,$$

which means in absence of the ionic current, X tends to X_0 . Another common form is

$$\delta_M(X) = \frac{K_1 X}{K_h + X},$$

which is a passive buffering model due to the reaction



where Y is the inactivated form of X . We finally note that the flux term f_X can have a factor multiplying it to account for buffering [84]. Thus, for intracellular ion accumulation, we can write

$$\frac{dX}{dt} = -\gamma I_X - \delta(X), \quad (4.8)$$

where the parameter γ takes into account the buffering and depth of the membrane pool.

The main ion of interest is calcium. Wang [282] used $\gamma = 0.002 \text{ } \mu\text{M} (\text{ms } \mu\text{A})^{-1} \text{cm}^2$ to produce a 200 nM influx of calcium per spike. This amount is based on careful measurements reported in [120] in cortical pyramidal neurons. Wang also used a simple decay for calcium, $\delta(X) = X/\tau$, where for the dendrite, $\tau = 80 \text{ ms}$.

4.7 Calcium-Dependent Channels

The main reason to track calcium is that there are several important channels whose behavior depends on the amount of intracellular calcium. The two most important such channels are $I_{\text{K,Ca}}$, the calcium-dependent potassium current, and I_{can} , the calcium-dependent inward current. The former current appears in many neurons and is responsible for slow afterhyperpolarizations (AHPs) and spike-frequency adaptation. It is often referred to as the AHP current. The calcium-activated nonspecific cation (CAN) current can last for many seconds and causes sustained depolarization. It has been implicated in graded persistent firing [64] and in the maintenance of discharges by olfactory bulb granule cells [116]. To model these currents, we need to keep track of the calcium. Thus, (1) there must be a source of calcium and (2) we need to track it via (4.8).

4.7.1 Calcium Dependent Potassium: The Afterhyperpolarization

A typical model for $I_{\text{K,Ca}}$ is due to Destexhe et al. [61]:

$$I_{\text{K,Ca}} = g_{\text{K,Ca}} m^2 (V - E_{\text{K}}), \quad (4.9)$$

$$\frac{dm}{dt} = (m_\infty(c) - m)/\tau_m(c), \quad (4.10)$$

$$m_\infty(c) = \frac{c^2}{K^2 + c^2}, \quad (4.11)$$

$$\tau_m(c) = \max(\tau_{\min}, \tau_0/(1 + (c/K)^2)). \quad (4.12)$$

Typically, $K = 0.025 \text{ mM}$, $\tau_{\min} = 0.1 \text{ ms}$, and τ_0 varies. In [61] τ_0 was around 40 ms, but values as high as 400 ms can be found in the literature. A simple way to incorporate this model into one which has a calcium channel is to assume it depends instantly on the calcium concentration,

$$m = m_\infty(c),$$

so to incorporate this current into a spiking model one need only add an instantaneous calcium channel (if one is not present), the calcium dynamics, and the

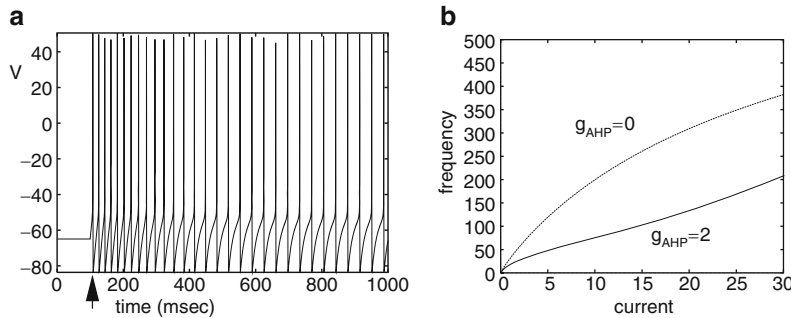


Fig. 4.7 Calcium-dependent potassium channel. (a) Spike-frequency adaptation showing decrease in frequency over time. (b) Steady-state firing rate with and without adaptation

instantaneous AHP current. As with all the models, the equations for this are found online. Figure 4.7a shows the behavior of the firing rate over time when this current is added to the Morris–Lecar model. The onset of spiking is unaffected by the presence of this current because it turns on only when the cell is spiking (and calcium enters the cell). Thus, unlike the M-current, the AHP current cannot alter the stability of the resting state.

One very interesting effect of the AHP is shown in Fig. 4.7b. It is not surprising that the AHP current lowers the frequency–current curve. However, it also tends to make the curve more linear. This point was first described in [282] for a model similar to that depicted above. We now attempt to explain the origin of this linearization effect [68]. We will first formulate this problem rather abstractly and then consider a full biophysical model.

Suppose the unadapted neuron is able to fire at arbitrarily low rates and that the derivative of the firing rate function tends to infinity as the threshold for firing is approached. Let z be the degree of adaptation in the model and suppose $z = \alpha f$, where f is the firing rate. The adaptation acts negatively on the total current injected into the neuron; thus,

$$f(I) = F(I - gz),$$

where $F(I)$ is the unadapted firing rate function and g is some constant. Since $z = \alpha f$, this leads us to

$$f(I) = F(I - g\alpha f). \quad (4.13)$$

Differentiating this with respect to I and rearranging, we obtain

$$\frac{df}{dI} = \frac{F'(I - g\alpha f)}{1 + g\alpha F'(I - g\alpha f)}.$$

For large F' , we see that

$$\frac{df}{dI} \approx \frac{1}{\alpha g},$$

showing that it is approximately linear. If we suppose $F(I) = A\sqrt{I}$ so that the neuron has a class I firing rate curve, we can exactly solve for f :

$$f(I) = -\kappa + \sqrt{\kappa^2 + A^2 I}, \quad (4.14)$$

where $\kappa = A^2 \alpha g / 2$. For small I , the prominent nonlinearity in the firing rate curve disappears and the slope at the origin of the firing rate curve is finite. Thus, for currents near threshold, the firing rate is nearly linear.

What does this simple calculation have to do with the full biophysical model? We can exploit the slow dynamics of adaptation to justify (4.13). For simplicity, we assume the conductance of the adaptation is linear rather than the nonlinear model we used as an illustration. Consider

$$C \frac{dV}{dt} = I - I_{\text{fast}} - gz(V - E_K), \quad (4.15)$$

$$\frac{dz}{dt} = \epsilon[q(V)(1 - z) - z]. \quad (4.16)$$

Here, I_{fast} represents all the “fast” currents which are responsible for spiking. There are three keys to the analysis: (1) ϵ is very small; (2) the fast system has class I dynamics; (3) the width of the spikes does not change very much as a function of the firing rate. Figure 4.7b shows that the present model is class I. The interested reader can verify that the spike width is nearly independent of the frequency. Finally, we have chosen the calcium time constant to be 300 ms, which is at least an order of magnitude slower than any of the other dynamics. (We remark that the calculations that follow will be often used to justify the simplified firing rate dynamics of biophysical models in Chap. 11.)

4.7.1.1 Slow–Fast Analysis

Since ϵ is small, we can treat z as a constant as far as the dynamics of the fast variables is concerned. Thus, we can examine (4.15) using I and z as parameters. Since $gz(V - E_K)$ is essentially a constant hyperpolarizing current (when z is fixed), we expect that if we inject enough current into the cell, it will fire. We also expect that the onset of firing will be a SNIC at some critical current, $I_{\text{SN}}(z)$, depending on z . A numerical analysis of the model illustrated in Fig. 4.7 shows that

$$I_{\text{SN}}(z) \approx I_0 + gI_1 z.$$

Recall that the firing rate of class I neurons is (at least near the bifurcation) a square-root function of the distance from the saddle-node:

$$f(I, z) = A\sqrt{I - I_{\text{SN}}(z)} \approx A\sqrt{I - I_0 - gI_1 z}. \quad (4.17)$$

Thus, if $I < I_{SN}$, then the neuron does not fire and if $I > I_{SN}$, the neuron fires at a rate dependent on the distance from the saddle-node. Note that the function f need not be exactly a square root. However, we do assume it depends only on the distance from the saddle-node and that the saddle-node value is a linear function of the degree of adaptation. Now we turn to the slow equation (4.16). We assume the function $q(V)$ is such that if the neuron does not fire an action potential, then $q(V) = 0$. Thus, at rest, $q = 0$ and $z = 0$. Since the adaptation in this section is *high-threshold*, the subthreshold membrane behavior will have no effect on the degree of adaptation. Now, suppose the neuron is firing with period T . Then (4.16) is a scalar periodically driven equation:

$$\frac{dz}{dt} = \epsilon[q(V(t))(1 - z) - z].$$

Since ϵ is small, we can use the method of averaging [111] and replace z by its average Z :

$$\frac{dZ}{dt} = \epsilon \langle q \rangle (1 - Z) - Z,$$

where

$$\langle q \rangle = \frac{1}{T} \int_0^T q(V(t)) dt.$$

Now, we invoke the hypothesis that the spike width is independent of the frequency. Since $q(V)$ is zero except during a spike and the spike width is independent of the frequency, the above integral simplifies to

$$\langle q \rangle = \frac{c}{T}.$$

Here, c is the integral of $q(V(t))$, a frequency-independent constant. But $1/T$ is just the frequency and this is given by (4.17). Thus, we obtain a closed equation for the degree of adaptation:

$$\frac{dZ}{dt} = \epsilon \left[cA\sqrt{I - I_0 - I_1 Z} (1 - Z) - Z \right]. \quad (4.18)$$

The steady states for this equation will yield the steady-state $F-I$ curve. However, one has to solve a cubic equation to get the steady states, so it is not analytically tractable (but see Exercise 11).

4.7.2 Calcium-Activated Nonspecific Cation Current

The CAN channel is similar in many ways to the AHP except that it produces an inward (depolarizing) current which can make the neuron fire quite actively. The

CAN current can be modeled very much like the AHP, so we model the CAN current simply as

$$I_{\text{CAN}} = g_{\text{CAN}} m_{\text{CAN}}^p (V - E_{\text{CAN}}).$$

The gate m_{CAN} obeys dynamics much like that of the AHP:

$$\frac{dm_{\text{CAN}}}{dt} = (q(c)(1 - m_{\text{CAN}}) - m_{\text{CAN}})/\tau_{\text{CAN}},$$

where $q(c)$ is some monotonic function of the calcium. The reversal potential, E_{CAN} , ranges from -20 mV to near the calcium reversal potential. Typically, $q(c) = \alpha(c/c_0)^2$. The CAN current has been implicated in sustained firing of many neurons, notably those in the entorhinal cortex [64]. A simple illustration of sustained firing due to the CAN current is shown in Fig. 4.8. We use the Destexhe–Paré spiking model for the generation of action potentials and add a small amount of the CAN current:

$$I_{\text{Can}} = g_{\text{can}} m_c (V + 20),$$

where

$$\frac{dm_c}{dt} = 0.005[Ca]^2(1 - m_c) - m_c/3000.$$

Since the spiking model does not have any calcium channels, we suppose the synaptic stimulation of the model produces a square pulse of calcium of width 50 ms and magnitude 1 mM (see Chap. 6). The results of three pulses at $t = 200, 700, 1200$ shows the long-lasting graded persistent activity. (This model is quite naive and cannot maintain the firing rate since the CAN current eventually decays. One way to rectify this is to have calcium channels in the model for spiking which will then provide positive feedback. Problems related to this are explored below in one of the exercises/projects.)

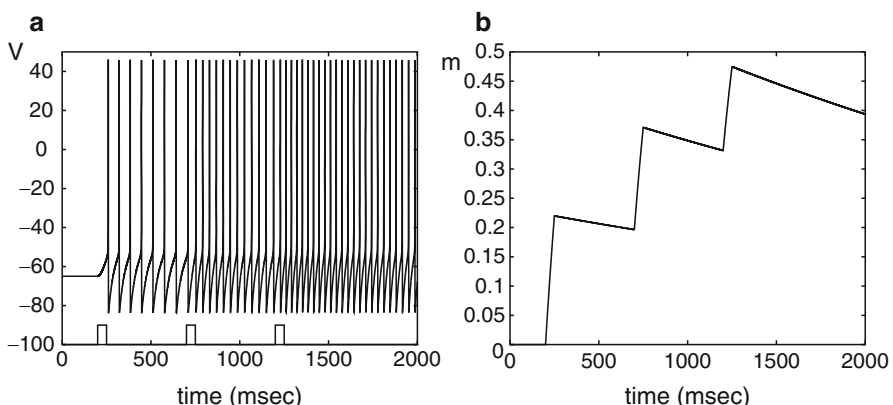


Fig. 4.8 The calcium-activated nonspecific cation (CAN) current can explain long-lasting persistent activity. **(a)** The voltage of a spiking model with three calcium stimuli. **(b)** The gate for the CAN current

4.8 Bibliography

There are thousands of papers in the neurophysiology literature that describe specific computational models for the channels here as well as dozens of other channels. A good place to start is the book by Huguenard and McCormick [131]. Biophysical intuition on what many of these channels do to the firing of the neuron is provided in [140]. The ModelDB Web page (<http://senselab.med.yale.edu/senselab/ModelDB/default.asp>) can be searched by specific current and contains hundreds of models. Most of the models are in the scripting language NEURON [33]. Equations for all of rechannels in this chapter and all of reexercises can be found online.

4.9 Exercises

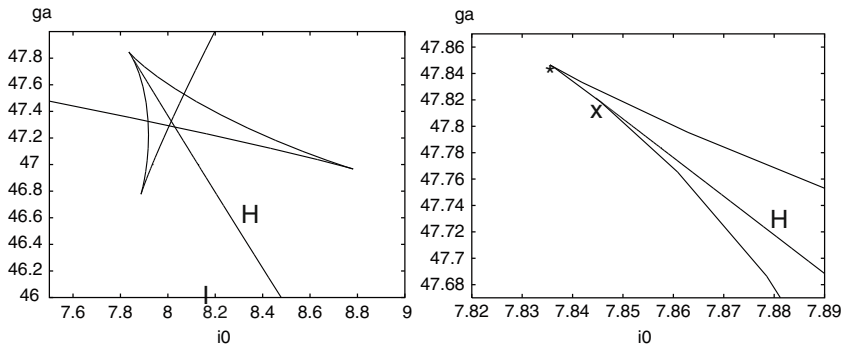
1. On the basis of what you have seen in the Morris–Lecar system, one might guess that there is the possibility of getting oscillations in the Butera model when the fast sodium channel is blocked and the inactivation of the persistent sodium channel is held constant (that is, $dh/dt = 0$). Thus, the model could be reduced to a planar system in V, n :

$$\begin{aligned} C_m \frac{dV}{dt} &= -g_L(V - E_L) - g_K n^4 (V - E_K) - g_{NaP} w_\infty(V) h(V - E_{Na}), \\ \frac{dn}{dt} &= (n_\infty(V) - n)/\tau_n(V). \end{aligned}$$

Compute the bifurcation diagram of this using h as a parameter at a variety of different values of E_L . Conclude that there can be no oscillations for this. How would you change the shape of $n_\infty(V)$ to generate oscillations in this model?

2. Compute the bifurcation diagram of the T-current model using E_L as a parameter starting it at -60 mV and decreasing it to -85 mV. Simulate the model when there are calcium oscillations.
3. Add sodium and potassium currents to the T-current model using the equations online for `cat-spike.ode`. Show that when the resting potential is depolarized ($E_L = -65$), the application of sufficient depolarizing current leads to a train of action potentials. Show the analogues of Fig. 4.2a and c for the spiking model.
4. The T-type calcium current was shown to be capable of oscillations and rebound depending on the leak current. Explore the L-type calcium current, which has calcium-dependent inactivation. The model equations for this are given online. The activation is set to its steady state so that the resulting model is planar. Explore the bifurcation to periodic solutions as a function of the applied current. Compute the bifurcation diagram as I_0 , the applied current, is increased.
5. The Connor–Stevens model has its parameters balanced at a nearly critical value in that there are many complicated bifurcations which can occur nearby.

This has not been systematically explored, although Rush and Rinzel mentioned the unusual behavior. Use the Connor–Stevens model in which the A-current and delayed rectifier current are balanced so that their total maximal conductance is fixed. (That is, let $g_K = 67.7 - g_A$ in the Connor–Stevens model.) The standard values are $g_A = 47.7$ and $g_K = 20$. (a) Change the model so that $g_A = 48.7$ and $g_K = 19$. Compute the bifurcation diagram and show that there are at most three fixed points. (b) Change $g_A = 47.4$ and $g_K = 20.3$. Compute the bifurcation diagram as a function of the current. Show that there is a small range of currents where there are two stable fixed points. Now, use the parameters g_A and I_0 to create a two-parameter diagram of fold points and Hopf points. You should find something that looks like the left figure below. There are three cusp points corresponding to the coalescence of fold points. There is also a curve of Hopf points which terminates on one to the folds at a Takens–Bogdanov point. An expanded view is shown on the right. Thus, the standard parameters for the Connor–Stevens model are quite weird!



6. Compute the $F-I$ curve for the Destexhe–Paré model with $g_m = 0$ and with $g_m = 5$ and compare the two.
7. Create a figure like Fig. 4.4b for the Destexhe–Paré model ($I = 6$, $g_m = 2$) and try to fit the data to a function of the form

$$F = F_{ss} + (F_{\text{inst}} - F_{ss})\lambda^{n-1},$$

where F_{ss} is the steady-state firing rate, F_{inst} is the instantaneous rate, λ is a parameter, and n is the initial interspike interval number. The parameters F_{ss} and F_{inst} characterize the degree of adaptation and the parameter λ characterizes the timescale of adaptation.

8. Make a neural oscillator using the inward rectifier and a delayed rectifier model of the form

$$I_K = g_K n^4 (V - E_K),$$

where

$$\frac{dn}{dt} = (1/(1 + \exp(-(V - a)/b)) - n)/\tau.$$

You should try to pick a , b , and τ so that the model oscillates. Do not worry if the choices of a are quite low values. Use $g_{\text{Kir}} = 0.5$, $E_K = -90$, $E_L = 60$, $g_L = 0.05$, and V_{th}, k as in the text.

9. *Inward rectifier and potassium accumulation.* Let

$$I_K = g_K m_\infty(V)(V - E_K),$$

where

$$m_\infty(V) = 1/[1 + \exp((V + 71)/0.8)]$$

and

$$E_K = 85 \log_{10} K_{\text{out}}.$$

Consider the model with external potassium accumulation with passive uptake:

$$\begin{aligned} C \frac{dV}{dt} &= I - g_L(V - E_L) - I_K, \\ \tau \frac{dK_{\text{out}}}{dt} &= \alpha I_K + K_0 - K_{\text{out}}, \end{aligned}$$

where $K_0 = 0.1$, $\alpha = 0.2$, $g_L = 0.1$, and $g_K = 0.1$. Sketch the phase plane for various hyperpolarizing currents. Show that if you choose I in some small range and τ to be sufficiently large, you will obtain oscillations in the potential. (Hint: Show that the V -nullcline can be cubic and that it can intersect the K_{out} -nullcline in the middle branch. Then, increase τ until this fixed point is unstable.)

10. Consider a combination of the sag current and the inward rectifier. Parameters should be taken from the model online. Draw the phase plane and integrate the equations. Change the sag model from the McCormick parameters to the Migliore parameters. Does the model still generate subthreshold oscillations? Compute the bifurcation diagram for the model using I as a parameter. How is the oscillation born and how does it die?
11. Suppose Z is small in (4.18) so that the equation is well approximated by

$$\frac{dZ}{dt} = \epsilon [cA\sqrt{I - I_0 - gI_1 Z} - Z].$$

Find the steady states of Z and obtain the F - I curve from this.

12. Repeat the calculations for the slow-adaptation model by explicitly computing the averaged quantities for the theta model:

$$\begin{aligned} \frac{d\theta}{dt} &= 1 - \cos \theta + (1 + \cos \theta)[I - gz], \\ \frac{dz}{dt} &= \epsilon [\delta(\theta - \pi) - z]. \end{aligned}$$

The right-hand side of z says that each time θ crosses π , z is increased by an amount ϵ . Numerically compute the F - I curve for this model with different

values of g (say, 0, 1, 5). Since the firing rate of the unadapted theta model is known exactly (see Exercise 8, Chap. 3.), you should try to fit the numerically computed F - I curves to (4.14).

13. A model related to that in the previous exercise adds spike adaptation to the quadratic integrate-and-fire model. The simplest form of this model is

$$\begin{aligned} V' &= I + V^2 - u, \\ u' &= a(bV - u), \end{aligned} \quad (4.19)$$

along with reset conditions such that when $V = V_{\text{spike}}$, V is reset to c and u is increased by d . By rescaling V , you can set $V_{\text{spike}} = 1$ with no loss in generality. (Do this.) The variable u plays several roles in this model. If $a = 0$, then it can have no effect on the local behavior of the rest point. However, if $a \neq 0$, the adaptation can change the stability of rest. Touboul [268] provided a complete analysis of this model as well as generalizations to other nonlinearities.

- (a) Suppose there is a resting state, (\bar{V}, \bar{u}) . Linearize about the resting state and find the parameters (a, b, I) where there is a saddle-node bifurcation, a Hopf bifurcation, and where the two bifurcations merge at a Takens–Bogdanov point. This is not surprising as the next part of this exercise will show.
- (b) The Takens–Bogdanov bifurcation occurs when there is a double-zero eigenvalue which has geometric multiplicity 1. The Takens normal form for this bifurcation takes the form

$$\frac{dw}{dt} = z + \beta w + w^2, \quad \frac{dz}{dt} = \alpha + w^2.$$

Let $r = w - z$ and write equations for the new (r, w) system. Next, let

$$\begin{aligned} x &= w + \frac{\beta + 1}{2}, \\ z &= \frac{r}{\beta + 1} + \frac{\alpha + (\beta + 1)^2/2}{\beta + 1}, \end{aligned}$$

yielding

$$\frac{dx}{dt} = -(\beta + 1)z + x^2 + k, \quad \frac{dy}{dt} = x - y,$$

where

$$k = \alpha + (\beta + 1)^2/4.$$

Thus, the local dynamics of the quadratic integrate-and-fire model with spike adaptation is the same as that of the normal form. Note that we can get rid of the parameter a by rescaling time and V, z in (4.19). You should attempt this.

- (c) The F - I curve of this model cannot be analytically derived even when $a = 0$, nor can we use AUTO or other bifurcation tools to obtain the F - I curve

since the reset condition makes the equations discontinuous. However, we can pose this as a boundary value problem which *is* smooth and so can be computed with AUTO. We suppose there is a repetitively firing solution with period P . This means $V(0) = c$ and $V(P) = 1$. Thus, the boundary conditions for V are specified. We also require that $u(0) = u(P) + d$ since u is increased whenever V crosses 1. Since the period is unknown, we rescale time, $t = Ps$, and thus have the following equations:

$$\begin{aligned} V' &= P(V^2 + I - u), \\ u' &= Pa(bV - u), \\ V(0) &= c, \\ V(1) &= 1, \\ u(0) &= u(1) + d. \end{aligned}$$

There are *three* boundary conditions, but only two differential equations. However, there is a free parameter P which can allow us to solve the equations. For example, take $(a, b, c, d) = (0.1, 1, -0.25, 0.5)$ and $I = 1$ and you will find a repetitive spiking solution with $u(0) = 1.211$ and period $P = 5.6488$. Try this, and then use AUTO or some other method to compute the F - I curve. The analysis of the resting state that you did above should tell you the lowest possible current for repetitive firing.

14. Izhikevich [134] adapted the quadratic integrate-and-fire model with linear adaptation (4.19) to look more like a biophysical model. The model has four free parameters as well as the current. The equations are

$$\begin{aligned} \frac{dV}{dt} &= 0.04V^2 + 5V + 140 + I - u, \\ \frac{du}{dt} &= a(bV - u) \end{aligned} \tag{4.20}$$

along with the reset conditions if $V = 30$ then $V = c$ and $u = u + d$. Find a change of variables which converts (4.20) to (4.19). Izhikevich suggested the following sets of parameters (a, b, c, d, I) for various types of neurons. Try these and classify the behavior: $(0.02, 0.2, -65, 6, 14)$, $(0.02, 0.2, -50, 2, 15)$, $(0.01, 0.2, -65, 8, 30)$, $(0.2, 0.26, -65, 0)$, and let I vary in this example. For each of these, start with $I = 0$ and then increase I to the suggested value. Can you derive a method for numerically following a bursting solution as a function of some parameter? (It is likely you will have to fix the number of spikes in a burst.)

15. Sakaguchi and Tobiishi [240] devised a simple model for a one-variable bursting neuron. The equation is as follows:

$$C \frac{dV}{dt} = \alpha(V_0 - V + DH(V - V_T)), \tag{4.21}$$

where $H(X)$ is the step function. There are two reset conditions. If V crosses V_T from below, then V is boosted to V_1 . If V crosses V_{T2} from above, V is reset to V_2 . Sakaguchi used $\alpha = 0.035$, $C = 2$, $V_0 = 30$, $D = 5$, $V_T = -35$, $V_1 = 50$, $V_2 = -50$, and $V_{T2} = 40$. Compute the period of the Sakaguchi burster for these parameters. What are the conditions on the various resets and thresholds for this model to have sustained periodic behavior?

4.10 Projects

In this section, we lay out some projects that could be used in a classroom setting.

1. *Artificial respiration.* The Hering–Breuer reflex is a phenomenon through which it has been shown that mechanical deformation of the lungs can entrain the respiratory pattern generator. Use the full Butera model as your simple pacemaker. This pacemaker provides the motor output for the inspiratory phase of breathing. The ventilator provides both inflation and deflation. Inflation is known to inhibit the motoneuron pools for inspiration, so assume the ventilator provides periodic inhibitory input. Explore the range of frequencies and patterns of entrainment and the conditions under which there is 1:1 locking.

2. *Calcium feedback and bistability.* Consider a spiking model

$$C \frac{dV}{dt} = -I_L - I_{\text{Na}} - I_{\text{Kdr}} - I_{\text{Ca}} - I_{\text{Can}} + I(t),$$

where you can use the Destexhe–Paré model of the leak, sodium, and potassium currents. Choose a very small instantaneous high-threshold calcium current as was done for the calcium-dependent potassium current. Add calcium dynamics and a CAN current. Try to adjust the parameters so that a sufficient stimulus generates sustained firing. If you give a very strong stimulus, you should be able to get more calcium into the system and thus increase the CAN current. This may lead you to believe that you can get graded persistent firing. But simulations should convince you that the best you can get is bistability. Can you design a model (even an abstract one) which has many fixed points and thus admits a variety of steady-state firing rates? (Hint: See [93, 184, 260].)

3. *Bifurcation analysis of the adaptive exponential integrate-and-fire model (aEIF).* Brette and Gerstner [22] proposed the following simple two-variable integrate-and-fire model

$$\begin{aligned} C \frac{dV}{dt} &= I - g_L(V - E_L) + g_L \Delta_T e^{(V-V_T)/\Delta_T} - w, \\ \tau_w \frac{dw}{dt} &= a(V - E_L) - w \end{aligned}$$

with the provision that when $V(t) = 20$, it is reset to V_r and w is increased by an amount b . A lengthy project would be to study the local behavior of this model using combined analytical and computational methods. For example, find the saddle-node and Hopf bifurcations. Brette and Gerstner fit this model to a detailed biophysical model with parameters $C = 281 \text{ pF}$, $g_L = 20 \text{ nS}$, $E_L = -70.6 \text{ mV}$, $V_T = -50.4 \text{ mV}$, $\Delta_T = 2 \text{ mV}$, $\tau_w = 144 \text{ ms}$, $a = 4 \text{ nS}$, and $b = 0.0805 \text{ nA}$. Note the units, w is a current and V is a voltage. The time constant of the cell at rest is roughly 9 ms.

Chapter 5

Bursting Oscillations

5.1 Introduction to Bursting

Many neurons exhibit much more complicated firing patterns than simple repetitive firing. A common mode of firing in many neurons and other excitable cells is bursting oscillations. This is characterized by a silent phase of near-steady-state resting behavior alternating with an active phase of rapid, spikelike oscillations. Examples of bursting behavior are shown in Fig. 5.1. Note that bursting arises in neuronal structures throughout the central nervous system. Bursting activity in certain thalamic cells, for example, is implicated in the generation of sleep rhythms, whereas patients with parkinsonian tremor exhibit increased bursting activity in neurons within the basal ganglia. Cells involved in the generation of respiratory rhythms within the pre-Botzinger complex also display bursting oscillations.

At least two biophysical mechanisms are required to produce bursting: a mechanism responsible for the generation of spiking and a separate mechanism underlying the slow modulation, responsible for the switch between the silent and active phases. The spikes are action potentials and typically arise from interactions between an inward sodium current and an outward potassium current. To generate the slow modulation, there must be another process that slowly builds up (or possibly decays) during the spiking phase and then decays (builds up) during the silent phase. This process typically involves an ionic current which either activates or inactivates at a rate slower than the other currents.

A classic example of an ionic current underlying the slow modulation is the calcium-dependent potassium current I_{KCa} . Calcium enters the cell during the active spiking phase and this leads to activation of the I_{KCa} current. Once this outward current is sufficiently large, the cell can no longer sustain spiking activity and the active phase terminates. During the silent phase, calcium leaves the cell and calcium-dependent potassium channels close. Spiking resumes once I_{KCa} is sufficiently small. This is just one of many mechanisms that may underlie the slow modulation. In this example, an outward current slowly activates, because of the buildup of calcium, and this eventually terminates the spiking phase. Another possibility is that an inward current slowly inactivates, thereby weakening spiking activity. An example of such a current is the persistent sodium current I_{NaP} and this mechanism underlies bursting in models for cells in the pre-Botzinger complex.

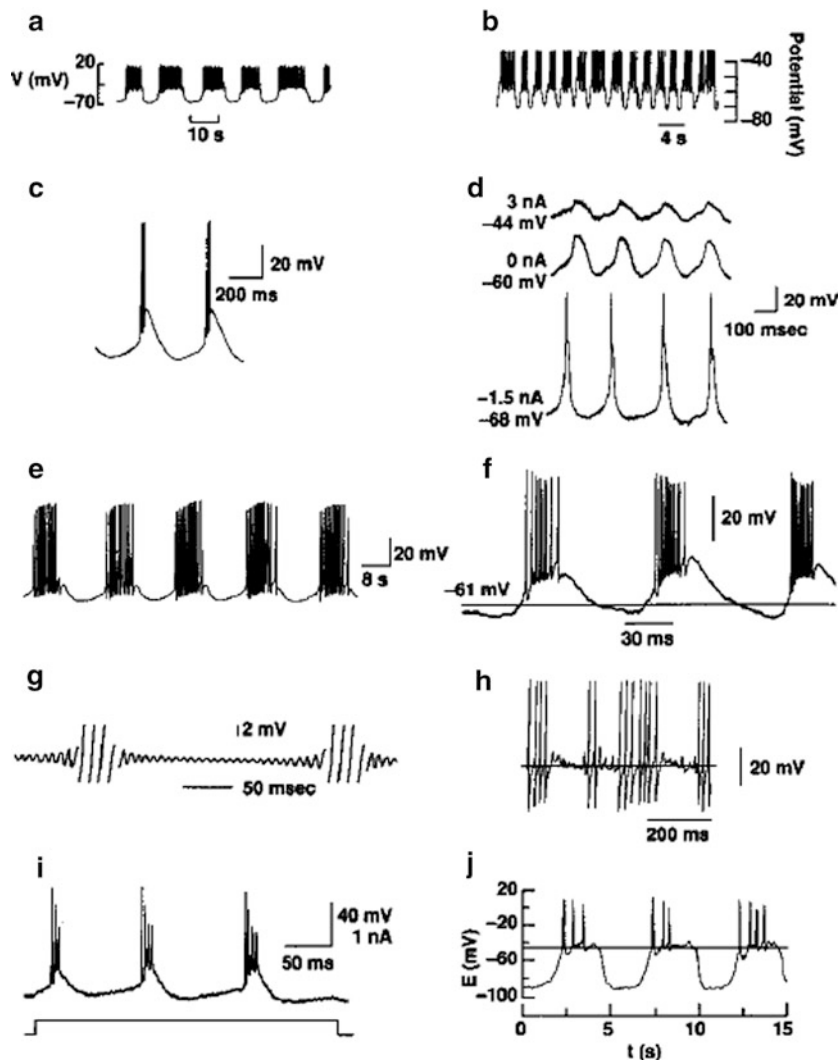


Fig. 5.1 Bursting patterns seen in different neurons. (From Wang and Rinzel [285])

The examples shown in Fig. 5.1 demonstrate that the firing properties of bursting cells may be quite different. There has been considerable effort to classify mechanisms underlying bursting oscillations. Mathematical classifications have been in terms of geometric properties of the corresponding phase-space dynamics. Note that bursting cannot happen in a two-variable model such as the Morris–Lecar equations. This is because each spike corresponds to a loop in phase space and trajectories cannot cross each other in a two-dimensional phase plane. Hence, a minimal model for bursting must include at least three dependent variables.

Models for bursting typically involve multiple timescales and can often be written as

$$\begin{aligned}\frac{dx}{dt} &= f(x, y), \\ \frac{dy}{dt} &= \epsilon g(x, y),\end{aligned}\tag{5.1}$$

where $\epsilon > 0$ is a small singular parameter. Here, $x \in R^n$ are fast variables responsible for spike generation and $y \in R^m$ are slow variables responsible for the slow modulation of silent and active phases. Note that if $\epsilon = 0$, then y is constant. We denote the first equation in (5.1), with y is constant, as the fast subsystem. During the silent phase, a bursting trajectory passes near a manifold of fixed points of the fast subsystem, whereas during the active phase of repetitive spikes the trajectory passes near a manifold of periodic solutions of the fast subsystem. The slow processes modulate the fast dynamics between these two phases. Different classes of bursting oscillations are distinguished by the mechanisms by which the bursting trajectory switches between the silent and active phases. This is closely related to the global bifurcation structure of the fast subsystem with the slow variables treated as parameters.

Models for bursting may exhibit other types of oscillatory activity, as well as more exotic behavior, including chaotic dynamics. Geometric dynamical systems methods are extremely useful in determining what sorts of solutions may arise and how the solutions depend on parameters. The models contain multiple timescales and this often leads to very interesting issues related to the theory of singular perturbations. Transitions from one type of behavior to another usually involve global bifurcations. Homoclinic orbits, for example, often play an important role in the generation of bursting activity: the active phase of rapid oscillations may either begin or end (or both) as the bursting trajectory crosses near a homoclinic point in phase space. At these points, standard singular perturbation methods may break down, so more delicate analysis is required.

5.2 Square-Wave Bursters

Perhaps the best-studied form of bursting is so-called *square-wave bursting*. This class of bursting was first considered in models for electrical activity in pancreatic β cells; these play an important role in the release of insulin. Another example of square-wave bursters is respiratory generating neurons within the pre-Botzinger complex.

An example of a square-wave burster is shown in Fig. 5.2. Note that the active phase of repetitive firing occurs at membrane potentials considerably more depolarized than during the silent phase. Another feature of square-wave bursting is that the frequency of spiking slows down during the active phase. These firing properties reflect geometric properties of the trajectory in phase space corresponding to the

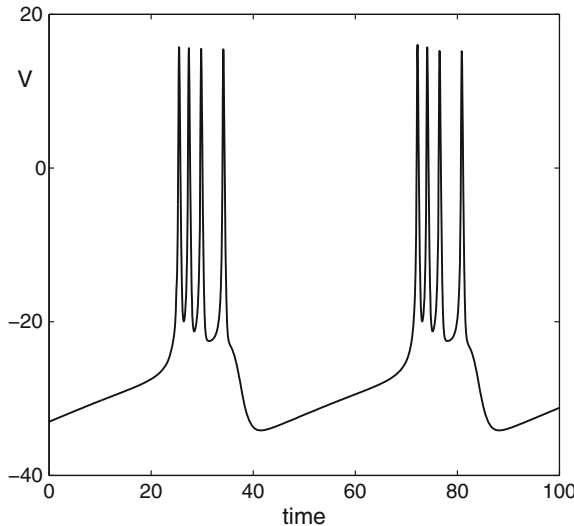


Fig. 5.2 Square-wave bursting. Note that the active phase of repetitive firing is at membrane potentials more depolarized than during the silent phase. Moreover, the frequency of spiking slows down at the end of the active phase

bursting solution. In fact, it is these geometric properties which uniquely characterize square-wave bursters and distinguish them from other classes of bursters.

We have already noted that bursting cannot arise in two-variable models. There is simply not enough room in a two-dimensional phase plane to generate the repetitive spiking. However, it is rather simple to generate bursting activity if we periodically drive a two-variable model. Consider, for example, the Morris–Lecar equations (3.1) with parameters given in Table 3.1 for the homoclinic regime. The bifurcation diagram, with bifurcation parameter I_{app} , is shown in Fig. 5.3. The set of fixed points forms an S-shaped curve. There is a branch of periodic orbits which originates at a subcritical Hopf bifurcation along the upper branch of fixed points and terminates at an orbit homoclinic to the middle branch of fixed points. (The fact that the Hopf bifurcation is subcritical is not important here.) Moreover, there is an I_{app} interval between $I_{\text{app}} = I_{\text{HOM}}$ and $I_{\text{app}} = I_{\text{SN}}$ for which the model is bistable: there are stable resting states along the lower branch of fixed points and stable, more depolarized, limit cycles. When $I_{\text{app}} = I_{\text{HOM}}$, there is a homoclinic orbit and when $I_{\text{app}} = I_{\text{SN}}$, there is a saddle–node bifurcation. Now suppose I_{app} slowly varies back and forth across this interval. Because of the bistability, it is easy to see how a hysteresis loop is formed in which the membrane potential alternates between resting and spiking activity. Note that the frequency of firing slows down near the termination of the active phase. This is because the active phase ends as the solution crosses the homoclinic orbit.

This example provides a simple mechanism, and geometric interpretation, for square-wave bursting. However, this mechanism is unsatisfactory since we im-

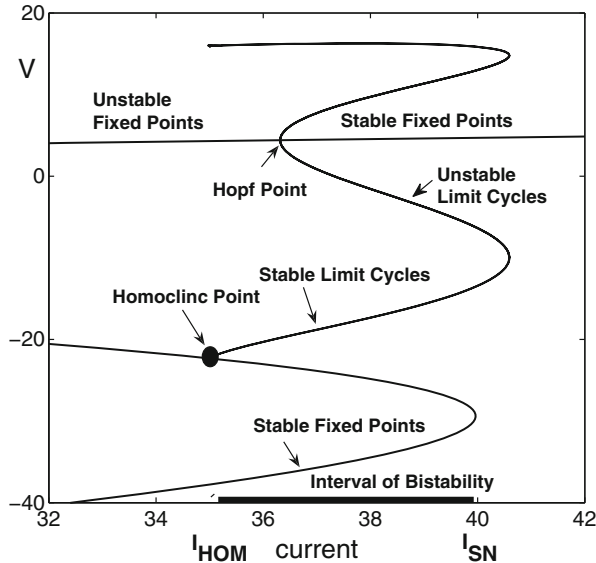


Fig. 5.3 A bifurcation diagram of the Morris–Lecar equations, homoclinic case. The set of fixed points form an S-shaped curve (not all of which is shown). A branch of limit cycles originates at a Hopf point and terminates at a homoclinic orbit. There is an interval of applied currents for which the system displays bistability

posed an external, periodic applied current. What we really wish to understand is autonomous bursting, that is, bursting that arises owing to interactions among intrinsic properties of the cell. One way to achieve autonomous square-wave bursting is to again consider the Morris–Lecar model except now we redefine I_{app} to be a dynamic dependent variable that decreases during the active phase of repetitive firing and increases during the silent phase. This example demonstrates the basic principle that slow negative feedback together with hysteresis in the fast dynamics underlie square-wave bursting.

Many different ionic current mechanisms could produce the slow negative feedback. Here, we construct an autonomous model for square-wave bursting by starting with the Morris–Lecar model (3.1) and adding a calcium-dependent potassium current. The complete model can be written as

$$\begin{aligned}
 C_M \frac{dV}{dt} &= -g_L(V - E_L) - g_K n(V - E_K) \\
 &\quad - g_{Ca} m_\infty(V)(V - E_{Ca}) - I_{KCa} + I_{app}, \\
 \frac{dn}{dt} &= \phi(n_\infty(V) - n)/\tau_n(V), \\
 \frac{d[Ca]}{dt} &= \epsilon(-\mu I_{Ca} - k_{Ca}[Ca]), \tag{5.2}
 \end{aligned}$$

where the calcium-dependent potassium current I_{KCa} is given by

$$I_{\text{KCa}} = g_{\text{KCa}}z(V - E_K). \quad (5.3)$$

Here, g_{KCa} is the maximal conductance for this current and z is the gating variable with a Hill-like dependence on the near-membrane calcium concentration, $[\text{Ca}]$. Hence,

$$z = \frac{[\text{Ca}]^p}{[\text{Ca}]^p + 1}.$$

For simplicity, we set the Hill exponent $p = 1$. The third equation in (5.2) represents the balance equation for $[\text{Ca}]$. The parameter μ is used for converting current into a concentration flux and involves the ratio of the cell's surface area to the calcium compartment's volume. The parameter k_{Ca} represents the calcium removal rate and ϵ is the ratio of free to total calcium in the cell. Since calcium is highly buffered, ϵ is small, so the calcium dynamics is slow. We shall refer to the first two equations in (5.2) as the fast subsystem and the third equation as the *slow equation*.

Note that I_{KCa} is an outward current. If its conductance $g_{\text{KCa}}z$ is large, then the cell is hyperpolarized and the cell exhibits steady-state resting behavior. If, on the other hand, this conductance is small, then the cell can fire action potentials. Figure 5.4 shows the bifurcation diagram of (5.2), in which z is the bifurcation parameter. Note that the curve of fixed points is now Z-shaped, not S-shaped. There is a branch of limit cycles that begins at a subcritical Hopf point and terminates at an orbit homoclinic to the middle branch of fixed points. Finally, there is an interval of z values for which the fast subsystem exhibits both a stable fixed point and a stable limit cycle.

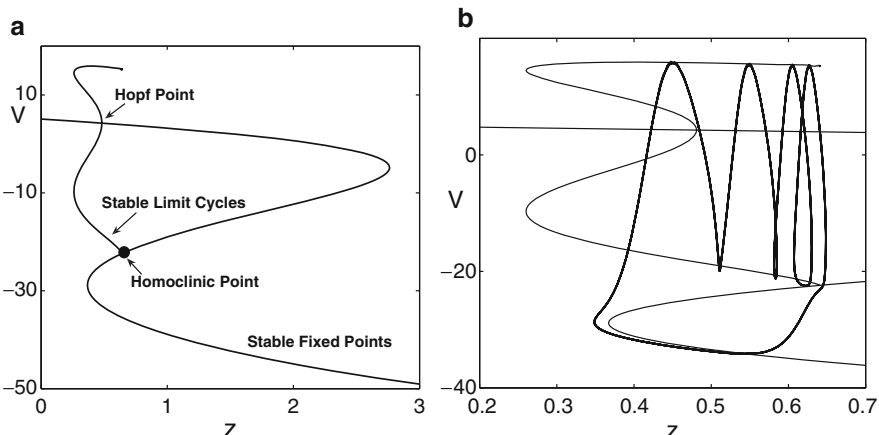


Fig. 5.4 (a) Bifurcation diagram of the fast subsystem for square-wave bursters. (b) The projection of the bursting trajectory onto the bifurcation diagram

Table 5.1 Bursting parameters

Parameter	Square wave	Elliptic	Parabolic
V_1	-1.2	-1.2	-1.2
V_2	18	18	18
V_3	12	2	12
V_4	17.4	30	17.4
E_{Ca}	120	120	120
E_K	-84	-84	-84
E_L	-60	-60	-60
g_K	8	8	8
g_L	2	2	2
g_{Ca}	4	4.4	4
g_{KCa}	0.75	1	1
C_m	1	1	1
I_{app}	45	120	65
ϕ	4.6	0.8	1.33
ϵ	0.1	0.04	0.01
k_{Ca}	1	1	1
μ	0.02	0.01667	0.025
τ_s, g_{CaS}			0.05, 1

Now the full system exhibits square-wave bursting, as shown in Fig. 5.2. Parameter values are given in Table 5.1. When the membrane is firing, intracellular calcium slowly accumulates, turning on the outward I_{KCa} current. When this current is sufficiently activated, the membrane can no longer maintain repetitive firing, thus terminating the active phase. During the silent phase, the intracellular calcium concentration decreases, thereby closing calcium-dependent potassium channels. Once enough outward channels are closed, the cell may resume firing.

The projection of the bursting solution onto the bifurcation diagram of the fast subsystem is shown in Fig. 5.4b. During the silent phase, the solution trajectory lies close to the lower branch of fixed points of the fast subsystem. The silent phase ends when the trajectory reaches the saddle-node of fixed points, at which point the trajectory jumps close to the branch of stable limit cycles of the fast subsystem. While the membrane is spiking, the solution remains close to this branch until it crosses the homoclinic orbit of the fast subsystem. The trajectory is then forced to jump down to the lower branch of fixed points and this completes one cycle of the bursting trajectory.

This example illustrates some of the basic features of square-wave bursting. We now consider a more general class of fast/slow systems and describe in more detail what geometric properties are needed to generate square-wave bursting. In general, square-wave bursting can arise in a system of the form (5.1) in which there are at least two fast variables and one slow variable. To obtain square-wave bursting, we must make assumptions regarding both the bifurcation structure of the fast subsystem and the slow dynamics. To describe these assumptions, we consider a three-variable model of the form

$$\begin{aligned} v' &= f(v, w, y), \\ w' &= g(v, w, y), \\ y' &= \epsilon h(v, w, y, \lambda). \end{aligned} \quad (5.4)$$

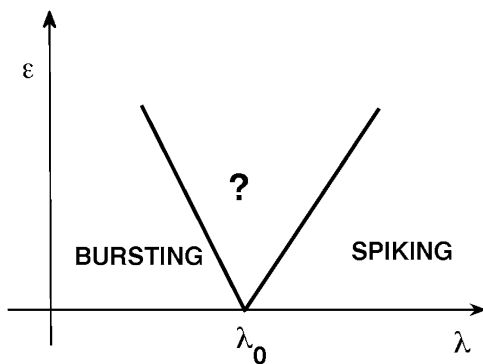
In the third equation in (5.4), λ represents a fixed parameter. Later, we discuss complex bifurcations that arise when λ is varied. What distinguishes square-wave bursting is the bifurcation diagram of the fast subsystem: the set of fixed points of the fast subsystem forms a Z-shaped (or possibly S-shaped) curve and there is a branch of stable limit cycles that terminates at a homoclinic orbit. The fixed points along the lower branch are stable with respect to the fast subsystem, whereas those fixed points along the middle branch are saddles with one stable and one unstable direction. The branch of limit cycles terminates at an orbit homoclinic to one of these saddles. In what follows, we denote the curve of fixed points of the fast subsystem as C_{FP} and the branch of stable limit cycles as P .

Assumptions are also needed for the slow dynamics. The slow variable y must decrease during the silent phase and increase during the active phase. (Here, we are assuming that the set of fixed points of the fast subsystem is Z-shaped, not S-shaped.) Note that the y -nullsurface $\{h = 0\}$ is two-dimensional. We assume this surface intersects C_{FP} at a single point that lies along the middle branch of C_{FP} below the homoclinic point. Moreover, $h > 0$ above $\{h = 0\}$ and $h < 0$ below $\{h = 0\}$. This allows for y to slowly increase (decrease) while the bursting solution is in the active (silent) phase. Note that the point where the y -nullsurface intersects C_{FP} is a fixed point of the full system (5.4) with $\epsilon > 0$.

It is important that the slow nullsurface $\{h = 0\}$ intersects C_{FP} below the homoclinic point; in particular, the nullsurface must lie between the lower branch of C_{FP} and the branch of stable limit cycles P . If this condition is not satisfied, then the system may exhibit other types of solutions. For example, suppose $\{h = 0\}$ intersects the lower branch of C_{FP} . This point of intersection will be a stable fixed point of (5.4), corresponding to a resting state of the neuron. If, on the other hand, $\{h = 0\}$ intersects C_{FP} along its middle branch above the homoclinic point, then (5.4) may exhibit a stable limit cycle which lies near P . This type of solution is often referred to as either *continuous* or *tonic spiking*.

Rigorous results concerning the existence and stability of bursting oscillations and continuous spiking are presented in [263]. To describe these results, we suppose there exists λ_0 such that if $\lambda < \lambda_0$, then $\{h = 0\}$ intersects C_{FP} along its middle branch below the homoclinic point, whereas if $\lambda > \lambda_0$, then $\{h = 0\}$ intersects C_{FP} along its middle branch above the homoclinic point. The results in [263] state that if ϵ is sufficiently small, then (5.1) exhibits bursting oscillations for $\lambda < \lambda_0$ and continuous spiking for $\lambda > \lambda_0$, just as expected. However, it is important to realize that how small ϵ needs to be depends on how close λ is to λ_0 . In particular, $\epsilon \rightarrow 0$ as $\lambda \rightarrow \lambda_0$. This is illustrated in Fig. 5.5. Note that there is a wedge-shaped region emanating from $(\lambda, \epsilon) = (\lambda_0, 0)$ where we cannot conclude whether there exists bursting or spiking. Numerical studies and rigorous analysis have shown that as λ varies across this wedge-shaped region, between the bursting and continuous spiking regimes, the bifurcation structure of solutions must be very complicated.

Fig. 5.5 Dependence of bursting oscillations and continuous spiking with respect to ϵ and λ . Bursting exists if $\lambda < \lambda_0$ and spiking exists if $\lambda > \lambda_0$. However, how small ϵ must be depends on how close λ is to λ_0 . There is a wedge-shaped region in which chaotic dynamics exist



In particular, there will be solutions in which the number of spikes per burst varies considerably. Further discussion of chaotic dynamics in models for bursting oscillations will be given later.

5.3 Elliptic Bursting

Square wave is only one type of bursting. Examples of two other types are shown in Fig. 5.6; these are commonly known as *elliptic* and *parabolic* bursters. Elliptic bursters exhibit small-amplitude oscillations during the silent phase and the amplitude of the spikes gradually waxes and wanes. An important feature of elliptic bursters is that the frequency of spikes first increases and then decreases during the active phase. Both elliptic and parabolic bursters arise in models for neuronal activity and other excitable systems. Elliptic bursters arise in models for thalamic neurons, rodent trigeminal neurons, certain neurons within the basal ganglia, and 40-Hz oscillations. Parabolic bursting is found in models for *Aplysia* R-15 neurons.

Elliptic bursting can arise in a system of the form (5.1) in which there are two fast variables and one slow variable. Parabolic bursting, on the other hand, requires at least two slow variables. What characterizes each class of bursting are the properties of the bifurcation diagram of the fast subsystem in which the slow variables are considered as bifurcation parameters.

The elliptic burster shown in Fig. 5.6 is a solution of (5.2) and (5.3) with parameter values given in Table 5.1. As before, we denote the first two equations in (5.2) as the fast subsystem and the third equation, for calcium, as the slow equation. The bifurcation diagram of the fast subsystem is shown in Fig. 5.7; the bifurcation parameter is the slow variable [Ca]. Note that the fast subsystem exhibits bistability: there are a range of values of [Ca] for which there exist both a stable fixed point and a stable limit cycle. Bistability is also an important feature of square-wave bursting. An important difference, however, between square-wave and elliptic bursting is that for elliptic bursting the curve C_{FP} of fixed points of the fast subsystem need not be Z-shaped; there may be only one fixed point of the fast subsystem for each

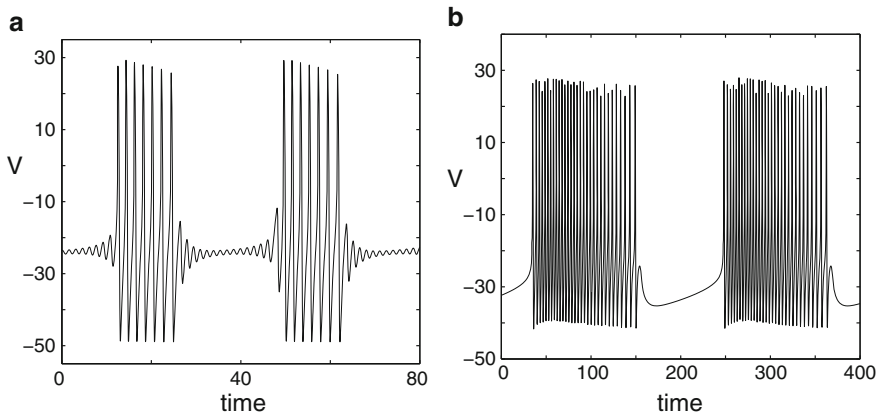


Fig. 5.6 (a) Elliptic burster. Note the subthreshold oscillations. (b) Parabolic bursting. The frequency of spiking first increases and then decreases during the active phase

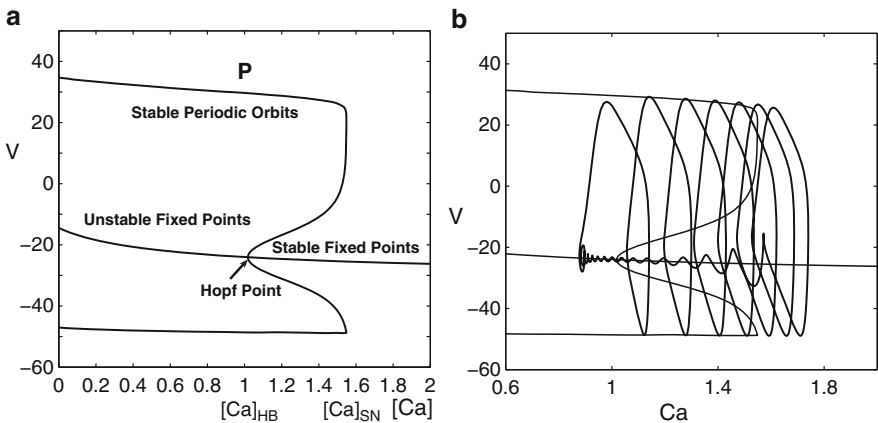


Fig. 5.7 (a) Bifurcation diagram associated with elliptic bursting. The projection of the elliptic bursting trajectory onto the bifurcation diagram is shown in (b)

value of $[Ca]$. The branch of periodic solutions P now originates at a subcritical Hopf bifurcation along C_{FP} . Suppose the Hopf point is at $[Ca] = [Ca]_{HB}$. Then, the fixed points of the fast subsystem are stable for $[Ca] > [Ca]_{HB}$ and unstable for $[Ca] < [Ca]_{HB}$. Since the Hopf bifurcation is subcritical, the branch of periodic orbits which bifurcates from the Hopf point is unstable. This branch “turns around” at some $[Ca] = [Ca]_{SN} > [Ca]_{HB}$, giving rise to a stable branch of limit cycles for $[Ca] < [Ca]_{SN}$. There are two limit cycles for $[Ca]_{HB} < [Ca] < [Ca]_{SN}$, one of which is stable and the other is unstable. The two limit cycles come together at $[Ca] = [Ca]_{SN}$, where there is a fold or saddle-node bifurcation of limit cycles. This is where that active phase of the bursting trajectory terminates.

To obtain bursting, we must make some assumptions regarding the slow variable dynamics so that $[Ca]$ decreases during the silent phase and (on average) increases during the active phase. In what follows, we define $h(V, n, [Ca])$ so that the right-hand side of the third equation in (5.2) can be written as

$$\frac{d[Ca]}{dt} = \epsilon h(V, n, [Ca]).$$

We hypothesize that $h(V, n, [Ca]) < 0$ near C_{FP} . During the silent phase, the bursting solution evolves near the stable portion of C_{FP} , with $[Ca]$ decreasing, until it passes the Hopf point, beyond which the fixed points along C_{FP} are no longer stable. Note, however, that the trajectory does not jump up to the active phase immediately after crossing the Hopf point. The slow variable $[Ca]$ may traverse a distance that is $O(1)$ with respect to ϵ past the Hopf point before jumping up. This type of delayed behavior or slow passage past a Hopf point has been studied extensively in the singular perturbation literature (see, for example, [7]).

We next consider the active phase. We cannot expect that $h(V, n, [Ca]) > 0$ near all of P , as was the case for square-wave bursting. This follows from geometric considerations. For square-wave bursting, the two-dimensional surface $\{h = 0\}$ separates the curve C_{FP} and the cylindrical-shaped surface P . For elliptic bursting, C_{FP} lies “inside” P , so $\{h = 0\}$ cannot separate them. Since $h < 0$ near C_{FP} , it follows that we must expect that $h < 0$ near at least some part of P , that is, $[Ca]$ must decrease during some portion of the active phase. The best we can hope for is that there is a net increase of $[Ca]$ as the bursting trajectory passes near P .

To make this more precise, we consider the average increase or decrease of $[Ca]$ along the bursting trajectory. For each fixed $[Ca] \leq [Ca]_{SN}$, let $(v_{[Ca]}(t), n_{[Ca]}(t))$ denote the periodic solution along the outer branch of P and let $T([Ca])$ be the corresponding period. Then

$$\bar{h}([Ca]) = \frac{1}{T([Ca])} \int_0^{T([Ca])} h(v_{[Ca]}(t), n_{[Ca]}(t), [Ca]) dt$$

represents the average of h along this fixed limit cycle. We assume $\bar{h}([Ca]) > 0$ for each $[Ca] < [Ca]_{SN}$. This assumption implies that in the limit $\epsilon \rightarrow 0$, the net change in $[Ca]$ during the active phase is positive. Thus, during the active phase, $[Ca]$ slowly increases, on average, until the bursting solution passes the fold along P . The fast dynamics then forces the trajectory back toward C_{FP} and a new silent phase begins.

Both square-wave and elliptic bursting depend on bistability and hysteresis. An important difference is how the active phase is initiated and terminates. For square-wave bursting, the silent phase ends at a saddle-node of fixed points and the active phase ends at a homoclinic orbit of the fast subsystem. For elliptic bursting, the silent phase ends when there is a slow passage through a Hopf bifurcation and the active phase ends at a saddle-node of limit cycles. These contrasting mechanisms reflect differences in firing properties. For square-wave bursting, the frequency of spiking slows down at the end of each active phase; for elliptic bursting, there are subthreshold oscillations during each silent phase.

5.4 Parabolic Bursting

Both square-wave and elliptic bursting can be achieved in a system with only one slow variable. Moreover, both depend on bistability of the fast dynamics. Parabolic bursting, on the other hand, requires at least two slow variables and does not arise from a hysteresis phenomenon. The parabolic burster shown in Fig. 5.6b satisfies the equations

$$\begin{aligned} C_m \frac{dV}{dt} &= -I_L - I_K - I_{Ca} - I_{KCa} - I_{Cas} + I_{app}, \\ \frac{dn}{dt} &= \phi(n_\infty(V) - n)/\tau_n(V), \\ \frac{d[Ca]}{dt} &= \epsilon(\mu I_{Ca} - [Ca]), \\ \frac{ds}{dt} &= \epsilon(s_\infty(V) - s)/\tau_s, \end{aligned} \quad (5.5)$$

where I_L , I_K , I_{Ca} , and I_{KCa} are leak, potassium, calcium, and calcium-dependent potassium currents, respectively, as described in (5.2) and (5.3). Here, we have added a new calcium current

$$I_{Cas} = g_{Cas}s(V - E_{Ca}) \quad (5.6)$$

which depends on the gating variable s . Here, $s_\infty(V) = 0.5(1 + \tanh(V - 12)/24)$. Parameter values are given in Table 5.1. Note that in this model there are two fast variables, V and n , and two slow variables, $[Ca]$ and s .

A geometric model for parabolic bursting is the following. Consider a system of the form (5.1) where $x \in R^n$, $n \geq 2$, and $y = (y_1, y_2) \in R^2$. (Here, (y_1, y_2) corresponds to $([Ca], s)$.) There are now two slow variables, namely, y_1 and y_2 . We first describe the bifurcation structure of the fast subsystem with both slow variables considered as parameters. We then discuss the properties which the slow dynamics must satisfy.

The bifurcation diagram of the fast subsystem is illustrated in Fig. 5.8, where we plot one component of the fast variable, corresponding to the membrane potential. In Fig. 5.8a, we fix one of the slow variables to be constant and compute the bifurcation diagram with the other slow variable as a parameter. Note that there is a Z-shaped curve of fixed points and a branch of periodic orbits that originates at a subcritical Hopf point and terminates at a saddle-node on an invariant circle (SNIC). If we allow both slow variables to vary, as shown in Fig. 5.8b, then the set of fixed points and the branch of limit cycles become surfaces, whereas there is a curve of Hopf points, as well as SNICs. The fixed points along the lower branch are assumed to be stable fixed points of the fast subsystem. In Fig. 5.8b, we also show the maximum and minimum values of the fast variable along each of these periodic solutions along with the projection of the parabolic bursting solution shown in Fig. 5.6b. In Fig. 5.9,

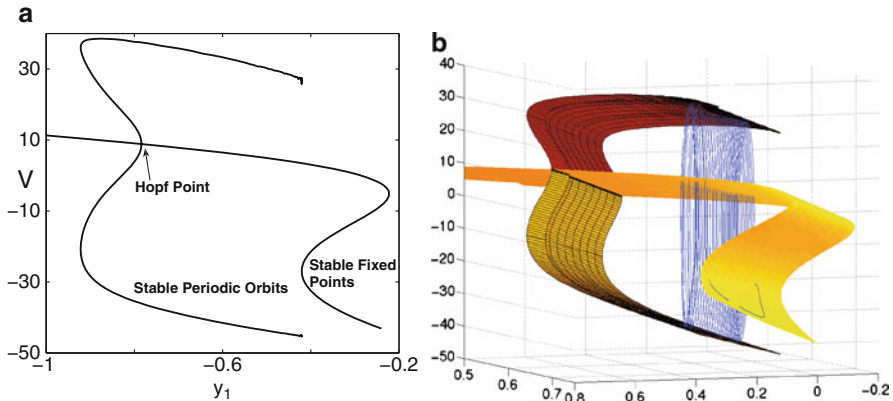


Fig. 5.8 Bifurcation diagram of the fast subsystem for parabolic bursting. (a) One of the slow variables is fixed. Note that the branch of periodic orbits ends at a saddle-node on an invariant circle (SNIC). (b) With both slow variables as bifurcation parameters, the sets of fixed points and limit cycles form surfaces. Also shown is the projection of the bursting trajectory onto the bifurcation diagram

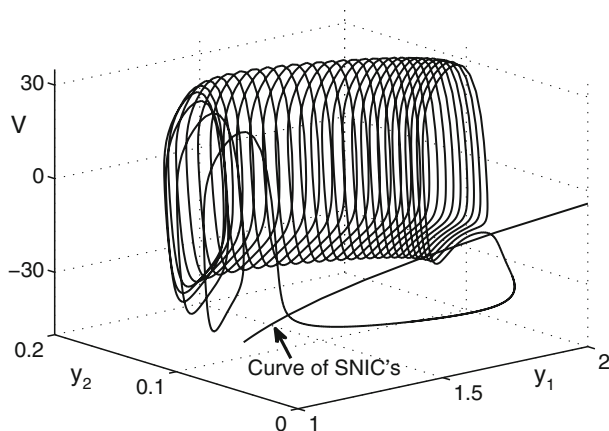


Fig. 5.9 Projection of the parabolic bursting solution onto (V, y_1, y_2) -space. There is a curve in the slow (y_1, y_2) -plane corresponding to SNICs. This curve separates the regions where the fast subsystem exhibits spiking and resting behavior

we show regions in the slow phase plane where the fast dynamics exhibit spiking and stable resting behavior along with the projection of the bursting solution. Note that these regions do not overlap; that is, the fast dynamics do *not* exhibit bistability. The spiking and resting regions are divided by a curve at which the fast dynamics exhibit a SNIC; this curve also corresponds to the fold of the fixed-point surface.

The existence of a parabolic bursting solution also requires hypotheses regarding the slow dynamics. There must be a mechanism by which the slow variables drift

back and forth between the spiking and resting regions. In what follows, we exploit the singular nature of the fast/slow system to obtain reduced equations for just the slow variables y_1 and y_2 . This is done in two steps, one for the silent phase and one for the active phase. The method we describe here is quite general and can be applied to any bursting model of the form (5.1).

First consider the silent phase. We change to the slow timescale $\tau = \epsilon t$ in (5.1) and then set $\epsilon = 0$ to obtain

$$\begin{aligned} 0 &= f(x, y), \\ \frac{dy}{d\tau} &= g(x, y). \end{aligned} \tag{5.7}$$

The first equation in (5.7) simply states that during the silent phase the (singular) solution lies along the lower branch of the fixed-point surface. If we write this branch as $x = \Phi(y)$, then the second equation in (5.7) becomes

$$\frac{dy}{d\tau} = g(\Phi(y), y). \tag{5.8}$$

This is then the reduced system for the evolution of the slow variables during the silent phase.

To obtain the reduced equations for the evolution of the slow variables in the active phase, we use the method of averaging. Suppose $y = (y_1, y_2)$ lies in the region where there exists a stable limit cycle of the fast subsystem. Let $x_y(t)$ be the corresponding periodic solution of the fast subsystem, with period $T(y)$, and consider the averaged quantity

$$\bar{g}(y) = \frac{1}{T(y)} \int_0^{T(y)} g(x_y(t), y) dt.$$

The evolution of the slow variables during the active phase is then given by the averaged equations

$$\frac{dy}{d\tau} = \bar{g}(y). \tag{5.9}$$

Parabolic bursting corresponds to the existence of a closed curve in the slow (y_1, y_2) phase plane which passes through both the region of stable fixed points and the region of stable limit cycles. While passing through the silent and active regions, the curve must satisfy (5.8) and (5.9), respectively.

The active phase of the bursting solution both begins and ends along a curve of homoclinic bifurcations. Since the limit cycles have frequencies which approach infinity at the homoclinic bifurcations, the interspike interval is longer at both the beginning and the end of each burst. This accounts for the parabolic nature of the period of fast oscillations.

5.5 Classification of Bursters

We have now described three types of bursters. Other types are possible and do, in fact, arise in important applications. There has been considerable effort to classify the types of bursters, beginning with Rinzel, who was the first to analyze bursting models using fast/slow geometric methods. He described square-wave, parabolic, and elliptic bursting and this classification scheme was extended by Bertram et al. [15]. Izhikevich [132] has given a complete topological classification of bursters arising from codimension-1 bifurcations; he identified 120 different topological types. All of these classification schemes are based on the bifurcation structure of the fast subsystem in which the slow variables are considered to be bifurcation parameters. Different types of bursters correspond to different ways in which there can be transitions between resting behavior and repetitive spiking. Since resting behavior and repetitive spiking correspond to branches of stable equilibria and periodic limit cycles of the fast subsystem, it follows that different classes of bursters represent different bifurcations of these branches. For example, square-wave bursting corresponds to a saddle-node, or fold, bifurcation of the branch of stable fixed points and a saddle-homoclinic bifurcation of the branch of stable limit cycles of the fast subsystem. It follows that to classify bursters, we need to understand all possible codimension-1 bifurcations of equilibria and limit cycles.

It turns out that there are just four types of bifurcations of equilibria and four types of bifurcations of limit cycles. Hence, there are 16 types of bursting in which the resting state is a stable equilibrium point and its spiking state is a stable limit cycle. The four bifurcations of equilibria are saddle-node (fold), SNIC, supercritical Hopf, and subcritical Hopf. The four types of bifurcations of limit cycles are SNIC, saddle-homoclinic orbit, supercritical Hopf, and fold cycle. In Izhikevich's classification scheme, each type of bursting is named according to *bifurcation of equilibria/bifurcation of limit cycle*. Hence, the square-wave burster is denoted as *fold/homoclinic*, whereas an elliptic burster is referred to as *subHopffold cycle*.

An example of a bursting type not discussed earlier is shown in Fig. 5.10. Here, the branch of stable fixed points of the fast subsystem ends at a saddle-node

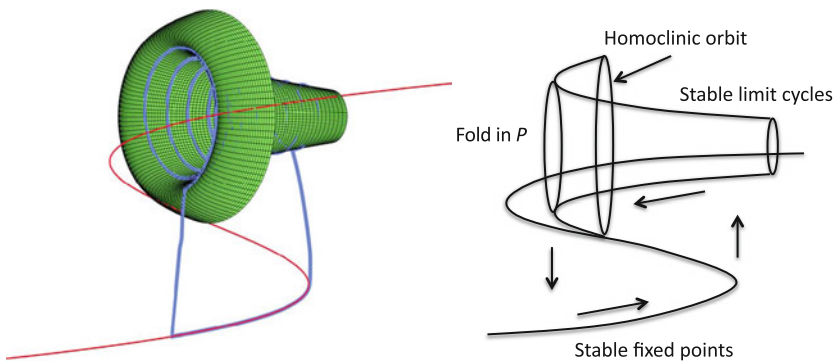


Fig. 5.10 Top hat bursting

bifurcation (fold) and the branch of stable limit cycles of the fast subsystem ends at a fold limit cycle bifurcation. Note that the branch of limit cycles that bifurcates from the homoclinic orbit is unstable with respect to the fast subsystem. This branch “turns around” at the fold limit cycle bifurcation to form the branch of stable limit cycles. Bertram et al. referred to this as *type IV* bursting; it corresponds to a fold/fold cycle in Izhikevich’s classification scheme. This type of bursting was first discovered in the Chay–Cook model for bursting in pancreatic β cells. It also arises in a model for a leech heart interneuron and in a model for synaptically coupled pre-Botzinger cells, where it was referred to as *top hat* bursting.

5.6 Chaotic Dynamics

5.6.1 Chaos in Square-Wave Bursting Models

Even three-variable minimal bursting models can exhibit complex dynamics as parameters are varied. There are at least two ways in which square-wave bursters, for example, may generate chaotic behavior. As the singular perturbation parameter ϵ decreases, the number of spikes per bursts increases. The process of adding a spike may be quite complicated. It was shown in [262] that chaotic dynamics may arise during this transition. For example, Fig. 5.11a and c shows solutions of (5.2) in which there are three and two spikes per burst. The parameters are given in Table 5.1, with $\epsilon = 0.0072$ and $\epsilon = 0.0073$, respectively. For the solution shown in Fig. 5.11b, $\epsilon = 0.00721998$. Note that there are bursts which possess two, three, and four spikes. The pattern of spikes per burst does not appear to repeat in a periodic manner. We note that this mechanism for chaotic dynamics only arises for a very small range of parameter values. It was shown in [262] that the size of this range is of the order $e^{-k/\epsilon}$ for some $k > 0$. This is indeed very small, so the chaos is probably not of much biological interest.

A second mechanism for chaos arises during the transition from bursting to continuous spiking. Figure 5.12 shows four solutions of (5.2); the parameters are chosen as in Table 5.1, except for k_{Ca} . In Fig. 5.12, we set $k_{Ca} = 1, 1.225, 1.228$, and 1.3, respectively. Note that as we increase k_{Ca} , the system appears to transition from exhibiting periodic bursting, chaotic bursting, chaotic spiking, and finally periodic spiking. For the chaotic bursting shown in Fig. 5.12b, some bursts are much longer than others; the occurrence of long or short bursts appears to be random.

A standard way to analyze oscillatory behavior, including chaos, is in terms of a Poincaré return map. We start with a given periodic bursting orbit and then consider a two-dimensional cross section \mathcal{S} that is transverse to the flow; i.e., trajectories cross \mathcal{S} at a nonzero angle. Then the Poincaré map is defined from some subset of \mathcal{S} back to \mathcal{S} as follows. For each $p_0 \in \mathcal{S}$, let $\gamma(t, p_0)$ be the solution starting at p_0 . If p_0 is sufficiently close to the original periodic orbit, then this trajectory must eventually cross \mathcal{S} at some time $T_0 > 0$. The Poincaré map is defined as $\pi(p_0) = \gamma(T_0, p_0)$. This is where the solution starting at p_0 “returns” to the cross section.

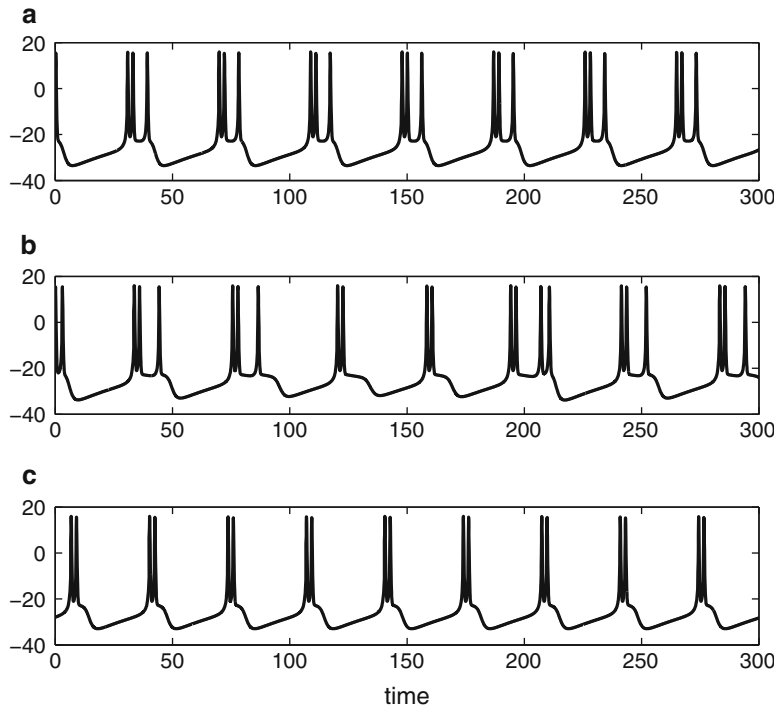


Fig. 5.11 Chaotic dynamics may arise during the transition of adding spikes. As we increase ϵ , the number of spikes per burst will decrease from, for example, (a) three to (c) two. As (b) demonstrates, during this transition there may exist solutions in which the number of spikes per burst is not constant

Consider the example illustrated in Fig. 5.12c. Here, the solution exhibits repetitive firing that is not regular. We compute a Poincaré map by recording the values of n and $[Ca]$ each time that V decreases through 0. For this model, the recorded values of n are all about 0.35; however, the value for calcium varies between 1.4 and 1.65. The solution is approximately represented by the time series of values for calcium, $[Ca]_1, [Ca]_2, \dots$. We can generate a one-variable map whose solutions approximate this time series as follows. With initial conditions $V = 0$ and $n = 0.35$, we specify a value for calcium, and then integrate the full differential equations until V crosses 0 again, obtaining the next value for calcium. This is then the Poincaré map, which we denote as $y = F([Ca])$, and is shown in Fig. 5.13. From the figure, it is evident that there is an intersection of the line $y = [Ca]$ and $y = F([Ca])$. This means there is a single concentration of calcium $[Ca]^*$ to which the trajectory returns after one cycle. This corresponds to a periodic solution to the model equations. If $|F'([Ca]^*)| > 1$, as is the case here, then the periodic solution is unstable. This type of map is characteristic of dynamics that have chaotic behavior. Further analysis of the map is presented in the exercises.

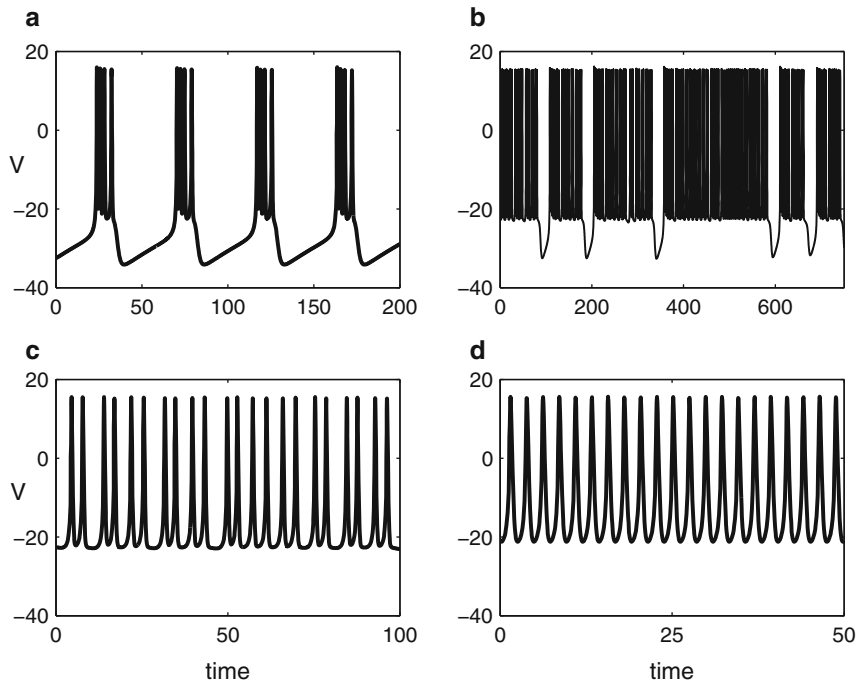


Fig. 5.12 A chaotic burst arising during the transition between bursting and continuous spiking. As we increase the parameter k_{Ca} , the model may exhibit (a) regular bursting, (b) chaotic bursting, (c) chaotic spiking, and (d) continuous spiking

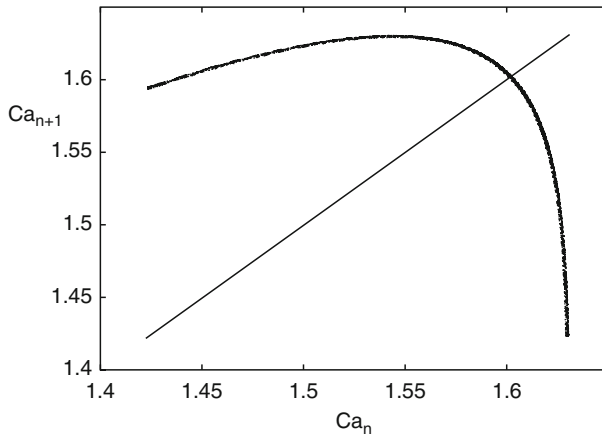


Fig. 5.13 Poincaré map

5.6.2 Symbolic Dynamics

In the preceding section, we saw that the complex dynamics that arise during the transition from bursting to continuous spiking in square-wave bursting models can be described in terms of a one-dimensional map. This description must be an approximation of the full dynamics since the model has three dependent variables and the Poincaré section, along with the return map, must be two-dimensional. Terman [263] analyzed this two-dimensional map and rigorously demonstrated that chaotic dynamics must arise during the transition from bursting to continuous spiking; moreover, the dynamics can be described in terms of symbolic dynamics. Here, we will present the main result given in [263].

To state this result, we need to recall some basic properties of two-dimensional maps and how they relate to symbolic dynamics. The most famous two-dimensional map that exhibits complex dynamics is the Smale-horseshoe map, which we will now quickly describe. A more detailed discussion of this map can be found in [263].

Let \mathcal{S} be the unit square in \mathbb{R}^2 . Then the Smale-horseshoe map is a map, which we denote as π , from \mathcal{S} to \mathbb{R}^2 . The construction of this map consists of two steps, as shown in Fig. 5.14. First we contract \mathcal{S} by an amount μ in the horizontal direction and expand \mathcal{S} in the vertical direction by an amount λ . Here, $0 < \mu < 1$ and $\lambda > 1$. The second step is to fold the resulting rectangle so that $\pi(\mathcal{S}) \cap \mathcal{S}$ consists of two vertical rectangles as shown in the figure.

Although the Smale-horseshoe map is easy to define, it is not at all clear if it has any interesting properties. Note, for example, that not every point in \mathcal{S} is mapped back into \mathcal{S} . It is not obvious if there is any point x_0 whose entire orbit $\{\pi^k(x_0) : k = 0, \pm 1, \pm 2, \dots\}$ lies entirely in \mathcal{S} . In what follows, we let

$$\Lambda = \{x_0 : \pi^k(x_0) \in \mathcal{S} \text{ for all } k\}.$$

We can also ask if there are any fixed points or periodic orbits of π ; that is, does there exist $x_0 \in \mathcal{S}$ and an integer k such that $\pi^k(x_0) = x_0$? If there do exist periodic orbits, then how many are there? Or, does there exist an orbit in \mathcal{S} that

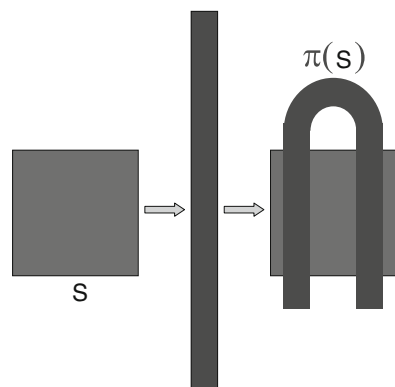


Fig. 5.14 The Smale horseshoe. The square \mathcal{S} is stretched in the vertical direction, contracted in the horizontal direction and then folded. The intersection of $\pi(\mathcal{S})$ with \mathcal{S} forms two vertical strips

is not periodic; that is, does there exist $x_0 \in S$ such that $\pi^k(x_0) \in S$ for every integer k but $\pi^k(x_0) \neq x_0$ unless $k = 0$? It turns out that this map does indeed have infinitely many periodic orbits and uncountably many aperiodic orbits. There is a very eloquent way to prove this result and this involves symbolic dynamics.

Let Σ be the set of all bi-infinite sequences of two symbols; that is,

$$\Sigma = \{a_i : i = 0, \pm 1, \pm 2, \dots\}, \text{ where } a_i = 0 \text{ or } 1.$$

Consider the shift map $\sigma : \Sigma \rightarrow \Sigma$ defined as follows. Suppose $\mathbf{a} = \{a_i\}$ and $\sigma(\mathbf{a}) = \mathbf{b}$, where $\mathbf{b} = \{b_i\}$. Then $b_i = a_{i-1}$. That is, σ shifts the indices of \mathbf{a} . Now σ defines a dynamical system on Σ and it is easy to see that this dynamical system contains infinitely many periodic orbits. For example, if

$$\mathbf{a} = \{\dots 0 1 0 1 0 1 \dots\},$$

then the orbit $\{\sigma^k(\mathbf{a})\}$ has period 2. It is also easy to see that there are uncountably many aperiodic orbits. This is left as an exercise.

A remarkable fact is that Σ and Λ are topologically equivalent. There is a one-to-one correspondence between points in Σ and points in Λ ; moreover, there is a one-to-one correspondence between orbits generated by σ and orbits generated by π . It follows that π has a countably infinite number of periodic orbits and uncountably many aperiodic orbits.

To state the result concerning chaotic dynamics in square-wave bursting models, we will need to consider more complex two-dimensional maps. These are shown in Fig. 5.15. We start with two squares, denoted as S_1 and S_2 . Each square is expanded, contracted, folded, and mapped into \mathbb{R}^2 as shown in the middle-horseshoe map in Fig. 5.15. Here, $\pi(S_1)$ intersects both S_1 and S_2 in a single vertical strip; $\pi(S_2)$ intersects S_1 in a vertical strip but does not intersect S_2 . This map also generates symbolic dynamics; however, the symbolic dynamics is somewhat different from that generated by the Smale-horseshoe map. A description of the symbolic dynamics

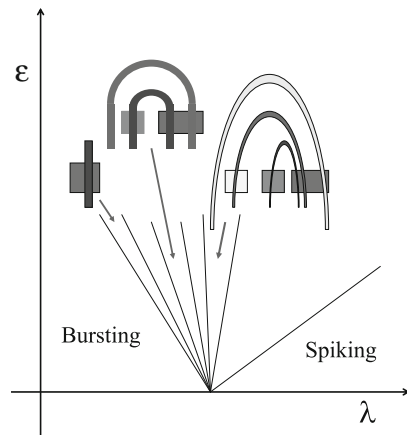


Fig. 5.15 The transition from bursting to spiking in the square-wave bursting model. If one fixes $\epsilon > 0$ and increases λ , then there is a series of increasingly more complex global bifurcations in which the system exhibits symbolic dynamics

is given in [177]. Finally, we will need to consider generalizations of this map. These are also shown in Fig. 5.15. For each integer $K > 1$, there are K squares; each rectangle is contracted, expanded, folded, and then mapped as shown. We denote the map corresponding to K rectangles as π_K . These maps generate increasingly more complicated symbolic dynamics.

We can now describe the main result given in [177]. Consider the (λ, ϵ) parameter plane shown in Fig. 5.15. Recall that there is a wedge-shaped region, arising from $(\lambda, \epsilon) = (\lambda_0, 0)$, in which we could not conclude whether the system exhibits bursting or continuous spiking. Then there are infinitely many wedge-shaped regions that emanate from $(\lambda_0, 0)$, as shown in Fig. 5.15. There is a return map $\pi(\lambda, \epsilon)$ such that in each odd sector, S_{2K-1} , the map gives rise to dynamics topologically equivalent to π_K . Hence, as we fix $\epsilon > 0$ to be sufficiently small and increase λ from the bursting to the spiking regions, then the system must undergo a series of increasingly more complicated global bifurcations. We note that each sector may only be defined for ϵ sufficiently small. Hence, each horizontal line segment with ϵ constant may intersect only finitely many sectors. However, the number of sectors which the line segment $\epsilon = \epsilon_0$ intersects becomes unbounded as $\epsilon_0 \rightarrow 0$.

5.6.3 Bistability and the Blue-Sky Catastrophe

Shilnikov et al. [245] described a mechanism in which a model can exhibit co-existence of both stable continuous spiking and stable bursting oscillations. The system also generates chaotic dynamics, through a mechanism known as the *blue-sky catastrophe*. The mechanism underlying bistability between spiking and bursting is shown in Fig. 5.16. Note that the fast subsystem has the bifurcation structure of the fold/fold or top hat burster. This bifurcation structure is actually not that crucial for what follows; a square-wave burster would work just as well. Here, we consider the top hat burster, since this is what was used in the original papers.

For bistability, what is important is that there are two periodic orbits of the full system that lie close to the branch of limit cycles of the fast subsystem (see Fig. 5.16a). One of these periodic orbits is stable, whereas the other is unstable. The unstable periodic orbit is a saddle with a two-dimensional stable manifold. Trajectories which lie on one side of this manifold will approach the stable periodic orbit and exhibit continuous spiking, whereas trajectories that lie on the other side will display bursting. To explain the geometry in more detail, we need to say more about the fast subsystem and how it is perturbed if the singular perturbation parameter is positive.

Consider a fast/slow system of the form (5.1) in which there are two fast variables and one slow variable; that is, $x \in R^2$ and $y \in R^1$. Suppose the set of fixed points of the fast subsystem forms a Z-shaped curve whose left knee is at $y = y_{LK}$. Moreover, there is a branch of stable limit cycles of the fast subsystem, which we denote as \mathcal{P} . Recall that, for $\epsilon > 0$ but small, the dynamics near \mathcal{P} is determined by the averaged equations. That is, let $x_y(t)$ denote the limit cycle of the fast subsystem for some

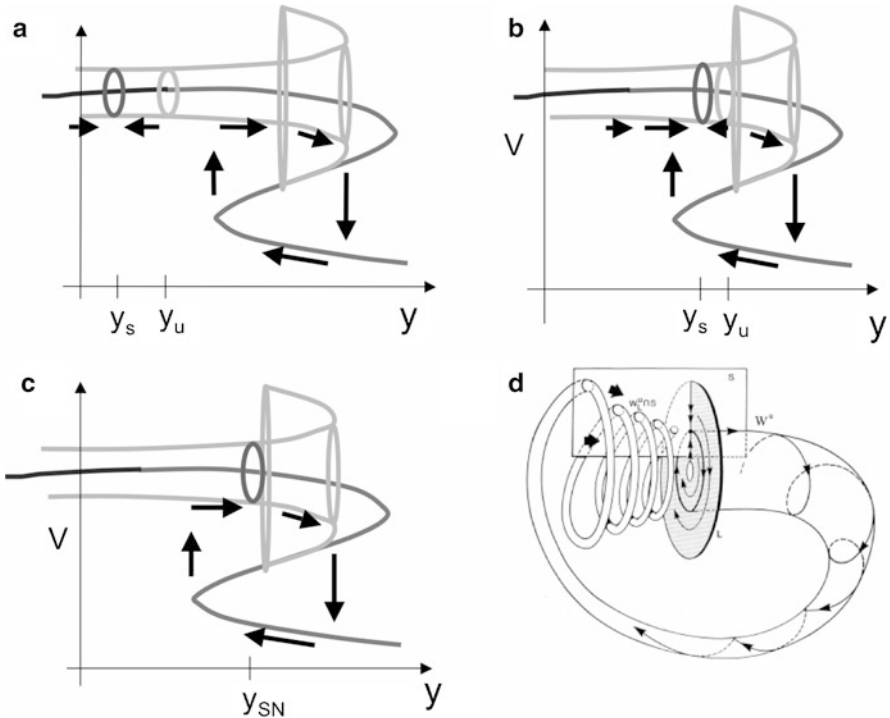


Fig. 5.16 (a) Bistability of bursting and spiking. There are stable and unstable limit cycles of the full system that lie close to \mathcal{P} , the branch of periodic solutions of the fast subsystem. The stable manifold of the unstable limit cycle separates those orbits approaching the bursting solution from those that exhibit continuous spiking. (b) The periodic orbits lie to the right of the left knee. Bursting is no longer exhibited; however, there are orbits heteroclinic between the two limit cycles. (c) and (d) A blue-sky catastrophe occurs if the two limit cycles form a saddle-node bifurcation

y and suppose this periodic orbit has period $T(y)$. Then the evolution of the slow variable near \mathcal{P} for $\epsilon > 0$ is determined by the averaged equation

$$\frac{dy}{d\tau} = \bar{g}(y) \equiv \frac{1}{T(y)} \int_0^{T(y)} g(x_y(t), y) dt. \quad (5.10)$$

Here, $\tau = \epsilon t$ is the slow time variable. A fixed point of this equation corresponds to a periodic solution of the full system. If $\bar{g}(y_0) = 0$, then there is a periodic solution $\gamma_\epsilon(t) = (x_\epsilon(t), y_\epsilon(t))$ of the full system (5.1) such that $|y_\epsilon(t) - y_0| = O(\epsilon)$ for all t and ϵ sufficiently small. This periodic solution is stable, with respect to the full system, if $\bar{g}'(y_0) < 0$ and is unstable if $\bar{g}'(y_0) > 0$. In general, a solution $(x(t), y(t))$ with $|y(0) - y_0|$ small will first evolve according to the fast dynamics to near \mathcal{P} and then evolve according to the slow averaged equation either toward or away from $\gamma_\epsilon(t)$.

Suppose $\bar{g}'(y_0) > 0$ so that $\gamma_\epsilon(t)$ is unstable. Then the stable manifold of γ_ϵ separates those solutions that drift to the left from those that drift to the right. To understand this stable manifold further, consider the case $\epsilon = 0$. The local stable manifold of $\gamma_0(t) = (x(y_0; t), y_0)$ is the set of points in the plane $\{y = y_0\}$ that lie close to \mathcal{P} . (By *local* we mean near the periodic orbit.) It follows that for $\epsilon > 0$, the two-dimensional local stable manifold of $\gamma_\epsilon(t)$ lies very close, i.e., $O(\epsilon)$, to the plane $\{y = y_0\}$.

One can now see how the model can display both stable spiking and stable bursting. Suppose the averaged equation has both a stable and an unstable fixed point at $y_s < y_u$, respectively. Fix $\epsilon > 0$ and denote the corresponding periodic solutions of the full system as $\gamma_s(t)$ and $\gamma_u(t)$. We further assume $y_u < y_{LK}$ so that the left knee lies to the “right” of the unstable periodic orbit. The two-dimensional stable manifold of $\gamma_u(t)$ divides phase space into two regions. Trajectories in the region $y < y_u$ will approach \mathcal{P} and then drift toward γ_s , whereas trajectories in the region $y > y_u$ will drift away from γ_u toward the fold in \mathcal{P} . Once these trajectories cross the fold, they will be forced down toward the branch of stable fixed points of the fast subsystem. Since $y_{LK} > y_u$, a stable bursting oscillation will result.

Chaotic dynamics can arise in this model as follows. Suppose as some parameter changes, the positions of y_u and y_s change. In particular, suppose both move to the right so that at some parameter value $y_s > y_{LK}$. This is shown in Fig. 5.16b. In this case, if a trajectory begins near \mathcal{P} in the region where $y > y_u$, then this solution will drift away from γ_u toward the fold in \mathcal{P} , fall down to the silent phase, and eventually jump back up. Since $y_s > y_{LK}$, the trajectory will approach γ_s as $t \rightarrow \infty$. We note that this solution will approach γ_u as $t \rightarrow -\infty$. This corresponds to an orbit that is heteroclinic between the two periodic orbits.

We now suppose as a parameter changes the stable and unstable periodic orbits come together at a saddle-node of periodic bifurcation. This is shown in Fig. 5.16c. In this case, there will be orbits that are homoclinic to the saddle-node periodic orbit. A more detailed diagram of this is shown in Fig. 5.16d. Once the periodic orbit near \mathcal{P} disappears, the system exhibits bursting oscillations. However, it has been demonstrated that the bursting is chaotic. The dynamics illustrated in Fig. 5.16 has been called the “blue-sky catastrophe” and the behavior described in this section has been observed in neuronal models. Details can be found in [245].

5.7 Bibliography

Rinzel [227, 228] was the first to classify bursting oscillations using fast/slow analysis and to consider their geometric properties in phase space. He described square-wave, parabolic, and elliptic bursting, and this classification scheme was extended by others, including Bertram [15]. A complete classification of bursting oscillations was given by Izhikevich [132]; a detailed description of his classification scheme is presented in his book [135], where there is also a discussion of possible roles of bursting oscillations in neuronal computations.

Several authors have studied the transitions between resting behavior, bursting, and continuous spiking. References include Ermentrout and Kopell [72], Terman [177, 262, 263], Destexhe and Gaspard [56], Shilnikov and Cymbalyuk [245], and Medvedev [198].

A recently published book edited by Coombes and Bressloff [47] contains many review articles pertaining to various aspects of bursting oscillations.

5.8 Exercises

1. Consider the Hindmarsh–Rose model [123]:

$$\begin{aligned} x' &= y - x^3 + 3x^2 - z + I, \\ y' &= 1 - 5x^2 - y, \\ z' &= r(4(x + 1.6) - z), \end{aligned} \tag{5.11}$$

where $r = 0.001$ and $I = 2$. This should give bursting oscillations. What kind of bursting is it? Draw the bifurcation diagram of the fast subsystem with the slow variable z as the bifurcation parameter.

2. Consider the FitzHugh–Rinzel model [228]:

$$\begin{aligned} v' &= v - v^3/3 - w + y + I, \\ w' &= 0.08(0.7 + v - 0.8w), \\ z' &= \epsilon(-0.775 - v - y), \end{aligned} \tag{5.12}$$

where $\epsilon = 0.0001$ and $I = 0.3125$. This should give bursting oscillations. What kind of bursting is it? Draw the bifurcation diagram of the fast subsystem with the slow variable z as the bifurcation parameter.

3. Consider model (5.2) with the parameters for square-wave bursting given in Table 5.1. Simulate this model to generate square-wave bursting. How many spikes are there during each bursting cycle? Change a single parameter so that there are now twice as many spikes per burst. Change this same parameter so that the number of spikes per burst is not a single integer, but changes from burst to burst. Now change another parameter so that the model exhibits continuous spiking. Change this same parameter so that the duty cycle of bursting is twice as large as it was originally. (By *duty cycle* we mean the ratio of the time the solution spends in the spiking phase and the entire period.)
4. As in the previous exercise, consider model (5.2) with the parameters for square-wave bursting given in Table 5.1. Compute the bifurcation diagram of the fast subsystem (as shown in Fig. 5.4). Plot the projection of the bursting solution onto this bifurcation diagram (as shown in Fig. 5.4b). Choose $z_1 < z_2 < z_3 < z_4 < z_5$ so that the saddle-node bifurcation of periodic orbits is at $z = z_1$, the “left” saddle-node bifurcation of fixed points is at $z = z_2$, the Hopf bifurcation is at

- $z = z_3$, the homoclinic orbit is at $z = z_4$, and the “right” saddle–node bifurcation of fixed points is at $z = z_5$. Draw the two-dimensional (v, w) phase planes for values of z that satisfy (a) $z < z_1$, (b) $z_1 < z < z_2$, (c) $z_2 < z < z_3$, (d) $z_3 < z < z_4$, (e) $z_4 < z < z_5$, and (f) $z_5 < z$.
5. Consider model (5.2) with the parameters for elliptic bursting given in Table 5.1. Compute the bifurcation diagram of the fast subsystem (as shown in Fig. 5.7). Plot the projection of the bursting solution onto this bifurcation diagram (as shown in Fig. 5.7b). Choose $z_1 < z_2$ so that the Hopf bifurcation is at $z = z_1$ and the saddle–node bifurcation of periodic orbits is at $z = z_2$. Draw two-dimensional (v, w) phase planes for values of z that satisfy (a) $z < z_1$, (b) $z_1 < z < z_2$, and (c) $z_2 < z$.
 6. Consider model (5.5) with the parameters for parabolic bursting given in Table 5.1. Here, there are two slow variables $[Ca]$ and s . Consider the two-dimensional (v, n) fast subsystem, fix $s = 0$, and compute the bifurcation diagram with $z = \frac{[Ca]}{1+[Ca]}$ as the bifurcation parameter. You should see something similar to Fig. 5.8a. There should be a SNIC bifurcation for some value of z . Use XPPAUT to compute the two-parameter (z, s) bifurcation diagram for the location of the SNIC. Plot the projection of the bursting solution onto this two-parameter slow phase plane (see Fig. 5.9).
 7. *Poincaré map.* Consider the square-wave bursting model and choose parameters so that it exhibits nice continuous spiking. Compute the Poincaré map defined in Sect. 4.6.1 (see Fig. 5.13). Now change the parameters so that it goes into bursting. Identify the parameters where periodic doubling bifurcations of the Poincaré map take place. Find the parameter values where the map is chaotic.
 8. *Bistability of the fast subsystem.* Start with a square-wave burster and solve it until the solution is in the silent phase. Now introduce a short perturbation to “kick” it into the spiking regime. How long is the subsequent burst of spiking activity? How does the length of the spiking activity depend on the phase at which the perturbation was introduced? Next, introduce the perturbation while the bursting solution is spiking so that the perturbation kicks the solution into the silent phase. How does the length of the subsequent silent phase depend on the phase at which the perturbation was introduced? Do the same thing for elliptic bursters. Justify your answers using fast/slow analysis.
 9. *Smale horseshoe.*
 - (a) Prove the Smale-horseshoe map exhibits a countable number of periodic orbits and uncountably many aperiodic orbits.
 - (b) How many periodic orbits are there with period N ?
 - (c) Prove there is a dense orbit.

Chapter 6

Propagating Action Potentials

Neurons need to communicate over long distances. This is accomplished by electrical signals, or action potentials, that propagate along the axon. We have seen that linear cables cannot transmit information very far; neural signals are able to reach long distances because there exist voltage-gated channels in the cell membrane. The combination of ions diffusing along the axon together with the nonlinear flow of ions across the membrane allows for the existence of an action potential that propagates along the axon with a constant shape and velocity.

One of the great successes of the Hodgkin–Huxley model is that it exhibits the propagating action potential; moreover, it accurately predicts the speed of the action potential. We remark that the Hodgkin–Huxley equation is a system of a nonlinear partial differential equation coupled with three ordinary differential equations. It is not at all clear how Hodgkin and Huxley were able to numerically solve these equations to compute the speed of the propagating action potential.

Mathematically, the Hodgkin–Huxley model is an example of a system of reaction–diffusion equations. The propagating action potential corresponds to a traveling wave solution; that is, it is a solution that “moves” with constant shape and velocity. Motivated to a large part by the Hodgkin–Huxley model, there was a flowering of papers in the mid 1970s and 1980s in which mathematicians developed sophisticated techniques to rigorously analyze the existence, uniqueness, and stability properties of traveling wave solutions to reaction–diffusion equations.

In this chapter, we will begin by describing a geometric way to think about the propagating action potential. As we shall see, the traveling wave corresponds to a homoclinic orbit of a system of ordinary differential equations. Hodgkin and Huxley numerically computed the speed of the wave by considering this system of ordinary differential equations and we shall briefly describe how Hodgkin and Huxley did this. We will then describe mathematical methods for analyzing the existence and stability properties of traveling waves. Here, we will consider reduced models such as the Morris–Lecar equations. We will also consider periodic wave trains and models for myelinated axons and discrete diffusion.

Although much of the excitement over propagation of action potentials down an axon has waned (particularly among neuroscientists), the exact same equations and ideas are relevant for the dynamics of the membrane potential in active dendrites. In Chap. 2, most of our analysis was predicated on the notion that dendrites

obey the linear cable equation. However, better experimental techniques (which allow neuroscientists to record currents on dendrites) point to strong experimental evidence that dendrites contain many voltage-gated currents and, like axons, can propagate potentials with little attenuation [141,142,188,201,202]. Thus, the mathematics in this chapter is quite relevant to questions which are being actively pursued by neuroscientists.

6.1 Traveling Waves and Homoclinic Orbits

The propagating action potential corresponds to a traveling wave solution of the Hodgkin–Huxley model. By this we mean the following. We rewrite the Hodgkin–Huxley model from Chap. 2 as

$$\begin{aligned} C_m \frac{\partial V}{\partial t} &= \frac{4d}{R_i} \frac{\partial^2 V}{\partial x^2} - I_{\text{ion}} + I, \\ \frac{\partial \Gamma}{\partial t} &= \alpha_\Gamma(V)(1 - \Gamma) - \beta_\Gamma(V)\Gamma, \end{aligned} \quad (6.1)$$

where $\Gamma = m, h$, or n . Figure 6.1a shows a simulation of the action potential down a 10-cm axon with a diameter of 1 mm. The time between the two action potentials at 6 and 7 cm is about 8 ms, so the velocity of this action potential is 1.25 m/s. The spatial profile looks just like the temporal profile in backward time and scaled by the velocity, as shown in Fig. 6.1b. The propagating action potential thus corresponds to a solution of (6.1) that “travels” with constant shape and velocity; that is, it is a *traveling wave solution*. If we denote the shape of the wave as $\hat{V}(x)$ and the speed of the wave as c , then the traveling wave solution satisfies $V(x - ct, t) = \hat{V}(x)$.

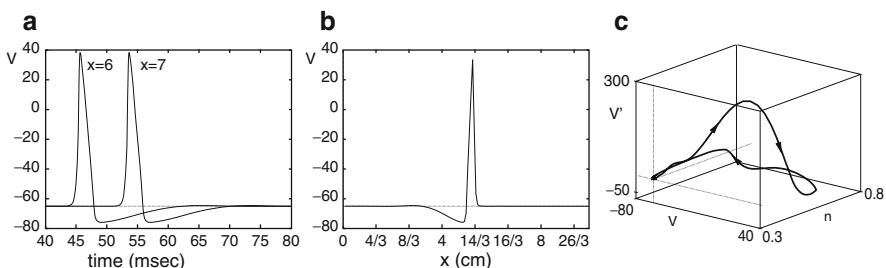


Fig. 6.1 Action potential for the Hodgkin–Huxley equations. Discretization of the nonlinear partial differential equation for a 10-cm axon into 150 segments. $R_i = 100 \Omega \text{ cm}$ and $d = 0.1 \text{ cm}$. (a) Voltage at $x = 6 \text{ cm}$ and $x = 7 \text{ cm}$, showing the velocity is about 1.25 m/s. (b) Spatial profile at $t = 20 \text{ ms}$. (c) Three-dimensional trajectory of the wave at grid point 50; the axes are the voltage derivative, the potassium gating variable, and the voltage

Suppose we change coordinates and replace x by $\xi = x - ct$. For convenience, we will also write V instead of \hat{V} . Then, the new equations are

$$\begin{aligned} C_m \frac{\partial V}{\partial t} &= C_m c \frac{\partial V}{\partial \xi} + \frac{4d}{R_i} \frac{\partial^2 V}{\partial \xi^2} + I - I_{\text{ion}}, \\ \frac{\partial \Gamma}{\partial t} &= c \frac{\partial \Gamma}{\partial \xi} + \alpha_\Gamma(V)(1 - \Gamma) - \beta_\Gamma(V)\Gamma, \end{aligned} \quad (6.2)$$

where, again, $\Gamma = m, h$, or n . A traveling wave is thus a time-independent solution in ξ and satisfies a system of ordinary differential equations. We will consider an infinite domain. Then, the traveling wave solution must also satisfy the boundary conditions $V(\xi = \pm\infty) = V_{\text{rest}}$.

It will be more convenient to write (6.2) as a first-order system; that is, we set $\frac{dV}{d\xi} = U$. Then, time-independent solutions of (6.2) satisfy the following system of five first-order ordinary differential equations:

$$\begin{aligned} \frac{dV}{d\xi} &= U, \\ \frac{dU}{d\xi} &= \frac{R_i}{4d}(I_{\text{ion}} - I - cC_m U), \\ \frac{d\Gamma}{d\xi} &= -(\alpha_\Gamma(V)(1 - \Gamma) - \beta_\Gamma(V)\Gamma)/c. \end{aligned}$$

The solution must also satisfy the boundary conditions

$$(V, U, m, h, n)(\pm\infty) = (V_{\text{rest}}, 0, m_\infty(V_{\text{rest}}), h_\infty(V_{\text{rest}}), n_\infty(V_{\text{rest}})).$$

If follows that the propagating action potential corresponds to a *homoclinic orbit* of (6.3). Figure 6.1c shows a projection of this orbit in the coordinates $(V, n, c \frac{dV}{d\xi})$.

This system is parameterized by c and one only expects homoclinic orbits to exist for discrete values of c . This is because homoclinic orbits are generically codimension-1 bifurcations – any perturbation of the system, including changing the wave speed c – should destroy the homoclinic orbit. The mathematical question is to prove there *is* such a c for which there is a homoclinic orbit. Once the homoclinic has been found, we have to determine whether it is a stable stationary solution to (6.2). We generally expect that for parameters near the homoclinic orbit, there are periodic orbits with arbitrarily long periods in the spacelike variable ξ . Furthermore, in some cases, we can find very complex dynamics for (6.3).

Hodgkin and Huxley did not attempt to numerically solve the full partial differential equation (6.1) as they did not have the necessary computing equipment (we can now do it in less than a few seconds on a laptop!). Rather, they used a shooting procedure to estimate the speed of the wave. What they did was to first fix a value of c and find a solution that decays to rest as $\xi \rightarrow -\infty$. Denote this solution as $\hat{V}(\xi, c)$. They then needed to find a value of c for which $\lim_{\xi \rightarrow +\infty} \hat{V}(\xi, c_0) = 0$.

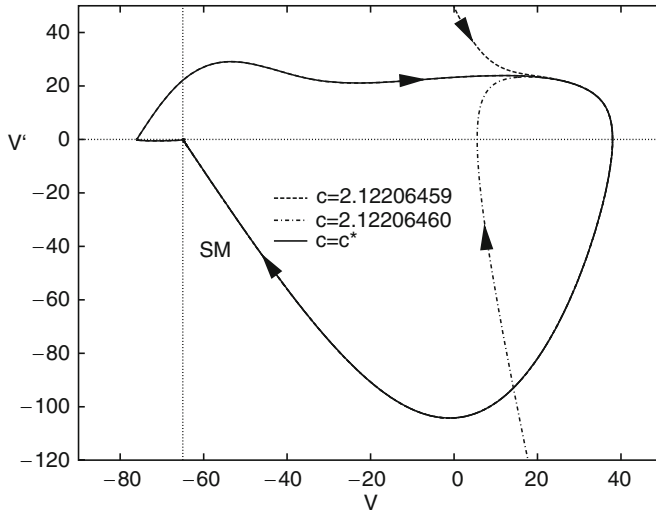


Fig. 6.2 Numerical shooting for the Hodgkin–Huxley traveling wave equations. Shooting is from the one-dimensional stable manifold (SM) by integrating backward in time. For c too low, the stable manifold goes off the top and for c too high, it goes out the bottom

For most values of c , the solution $\hat{V}(\xi, c)$ satisfies either $\lim_{\xi \rightarrow +\infty} V(\xi, c) = +\infty$ or $\lim_{\xi \rightarrow +\infty} V(\xi, c) = -\infty$. If one finds two values of c , say, c_1 and c_2 , such that $\lim_{\xi \rightarrow +\infty} V(\xi, c_1) = -\infty$ and $\lim_{\xi \rightarrow +\infty} V(\xi, c_2) = +\infty$, then there must be a value c_0 between c_1 and c_2 for which $\lim_{\xi \rightarrow +\infty} \hat{V}(\xi, c_0) = 0$; that is, $\hat{V}(\xi, c_0)$ is a homoclinic orbit and c_0 is the speed of the traveling wave. Using an iteration scheme, Hodgkin and Huxley used this idea to estimate the speed of the wave. Figure 6.2 shows an example of numerical shooting to find the homoclinic orbit.

6.2 Scalar Bistable Equations

There have been numerous papers in which mathematical methods were developed to rigorously analyze the existence and stability of traveling waves. Most of these studies considered simplified neuronal models such as the FitzHugh–Nagumo or the Morris–Lecar equations. These studies also often assumed the recovery dynamics $[(h, n)$ in the Hodgkin–Huxley equations] is slow. One then lets the rates of these equations go to zero and this leads to a singular perturbation problem. The basic idea is to then piece together a traveling wave or periodic orbit. This basic idea has also been used to analyze the stability of the wave.

We will discuss some of these methods in detail. However, before considering a two-dimensional example, we first review the general theory of bistable scalar reaction–diffusion equations. This theory will be important in the construction of

traveling waves in higher-dimensional systems. Moreover, by considering a simpler example, we can more easily introduce some of the geometric constructions that will be needed later.

Consider the following equation defined on the real line:

$$\frac{\partial u}{\partial t} = f(u) + \frac{\partial^2 u}{\partial x^2}, \quad -\infty < x < \infty. \quad (6.3)$$

We assume, for now, $f(u) = u(1-u)(u-\alpha)$, where $0 < \alpha < 1/2$. Then, 0 and 1 are stable equilibria for the equation $du/dt = f(u)$ and α is an unstable equilibrium. We would like to find traveling wave solutions to (6.3) which join the two stable states. That is, we want a solution of the form $u(x, t) = U(\xi)$, $\xi = x - ct$, that satisfies

$$\lim_{\xi \rightarrow -\infty} U(\xi) = 1 \quad \text{and} \quad \lim_{\xi \rightarrow +\infty} U(\xi) = 0.$$

Here, c is the velocity of the wave. Note that $U(\xi)$ satisfies the ordinary differential equation

$$-c \frac{dU}{d\xi} = f(U) + \frac{d^2 U}{d\xi^2}. \quad (6.4)$$

We rewrite this as the first-order system

$$\begin{aligned} \frac{dU}{d\xi} &= Y, \\ \frac{dY}{d\xi} &= -cY - f(U). \end{aligned} \quad (6.5)$$

We want to show that there exists a unique value of c , which we denote as c^* , for which there is a solution that satisfies the boundary conditions

$$\lim_{\xi \rightarrow -\infty} (U(\xi), Y(\xi)) = (1, 0) \quad \text{and} \quad \lim_{\xi \rightarrow +\infty} (U(\xi), Y(\xi)) = (0, 0).$$

Hence, we need to show that there is a (unique) value of the wave speed c for which (6.5) exhibits a heteroclinic orbit. One proves the existence of a heteroclinic orbit using a standard shooting argument. Here, we will only outline the geometric construction and leave details to the reader as exercises.

Note that for every value of c , the fixed points at $(0, 0)$ and $(1, 0)$ are saddles. Both the stable and the unstable manifold of each of these fixed points have dimension 1. A heteroclinic orbit corresponds to a trajectory that lies in both the unstable manifold of $(1, 0)$ and the stable manifold of $(0, 0)$. The phase planes of (6.3) for $c = 0$ and c very large are shown in Fig. 6.3. Note that when $c = 0$, the unstable manifold of $(1, 0)$ lies “below” the stable manifold of $(0, 0)$ (in the region $0 < U < 1$), whereas if c is very large, then the opposite is true. Since these manifolds depend in a continuous way on the parameter c , one can show that there must exist at least one value of c for which the manifolds “cross.” This then corresponds to the heteroclinic orbit, or traveling wave solution of (6.3). In the exercises, you are asked to fill in the details and prove the wave speed is uniquely determined.

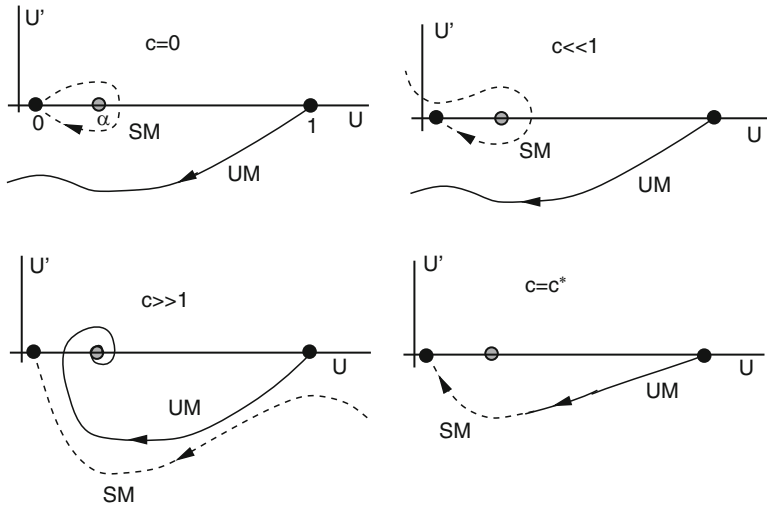


Fig. 6.3 Existence of a traveling front for the scalar bistable equation. If $c = 0$, then the system is integrable and we can derive explicit formulas for the trajectories in phase space. For small c , the unstable manifold of the right fixed point (UM) falls below the stable manifold of the left-fixed point (SM). For large c , the opposite is true. For a single intermediate value of $c = c^*$, the manifolds intersect, creating a heteroclinic orbit

We note that this construction does not depend on the precise form of $f(u)$. More generally, we may assume f is any smooth ‘‘cubic-shaped’’ function such that $f(0) = f(1) = 0$, $f'(0) < 0$, and $f'(1) < 0$. (In fact, we do not even need f to be ‘‘cubic shaped’’; it may have an arbitrary number of zeros.) Then the shooting argument outlined above can be used to demonstrate the existence of the traveling wave solution.

A key point of interest for us is how c depends on f . Multiply (6.4) by $dU/d\xi$ and integrate over the real line:

$$\begin{aligned} -c \int_{-\infty}^{\infty} (dU(\xi)/d\xi)^2 d\xi &= \int_{-\infty}^{\infty} (dU(\xi)/d\xi) f(U(\xi)) d\xi \\ &\quad + \int_{-\infty}^{\infty} (dU(\xi)/d\xi) (d^2 U/d\xi^2) d\xi. \end{aligned}$$

Since $U(\xi)$ is monotonic, we let $u = U(\xi)$ be a new variable. Then, $du = (dU/d\xi)d\xi$, so the first integral on the right-hand side is now $-\int_0^1 f(u)du$. The second integral vanishes since

$$(dU/d\xi)(d^2 U/d\xi^2) d\xi = \frac{1}{2} d \left(\frac{dU}{d\xi} \right)^2,$$

which integrates to zero because $dU/d\xi(\pm\infty) = 0$. Thus, we have

$$c \int_{-\infty}^{\infty} (U'(\xi))^2 d\xi = \int_0^1 f(u) du. \quad (6.6)$$

Since the first integral in (6.6) is positive, this shows that the sign of the velocity, c , is the same as the area of f between the two stable equilibria. What does this mean intuitively? Suppose that the middle root α is close to 0. Then, the region where $f(u)$ is negative, $(0, \alpha)$, is small compared with the region where f is positive. Thus the integral will be positive and the wave will move to the right, converting the medium from the 0-state to the 1-state. On the other hand, if α is close to 1, then the area will be negative, the velocity will be negative, the wave will move to the left, and the 1-state will be converted to the 0-state. Finally, if the positive and negative areas balance exactly, the velocity of the wave will be zero. The case of more than two-stable equilibria can be handled similarly and under fairly general circumstances; there can be multiple wavefronts with multiple speeds joining these fixed points.

6.2.1 Numerical Shooting

How do we obtain the velocity c numerically? Let us write the traveling wave equations as a system:

$$U' = Y, \quad Y' = -cY - f(U).$$

Consider the fixed point at $(1, 0)$. The linearization is

$$A \equiv \begin{pmatrix} 0 & 1 \\ -f'(1) & -c \end{pmatrix}.$$

Since $f'(1) < 0$, the determinant of A is negative, so the fixed point is a saddle and the eigenvalues are

$$\lambda^{\pm} = \frac{-c \pm \sqrt{c^2 - 4f'(1)}}{2}.$$

The unstable manifold is a tangent to the eigenvector corresponding to λ^+ , which is simply $[1, \lambda^+]^T$. Thus, we take initial conditions, $(U, Y) = (1 - a, -a\lambda^+)$, where a is a small positive number. We then integrate the equations until the trajectory crosses either the U -axis or the Y -axis. If the U -axis is hit, then c is too big, whereas if the Y -axis is hit, c is too small. In the exercises, we have you try your hand at shooting for the problem $f(u) = u(u - \alpha)(1 - u)$.

6.3 Singular Construction of Waves

We now describe the construction of a traveling pulse for the equation

$$\begin{aligned}\frac{\partial v}{\partial t} &= f(v, w) + \frac{\partial^2 v}{\partial x^2}, \\ \frac{\partial w}{\partial t} &= \epsilon g(v, w),\end{aligned}$$

where ϵ is a small positive number. We will consider a general class of nonlinear functions f and g . We assume the v -nullcline, $\{f(v, w) = 0\}$, is a cubic-shaped curve; moreover, $f > 0$ ($f < 0$) below (above) this nullcline. We further assume the w -nullcline, $\{g(v, w) = 0\}$, is a monotonically increasing function that intersects the v -nullcline at precisely one point, which we denote as (v_r, w_r) . Moreover, this point lies along the left branch of the cubic-shaped v -nullcline. Finally, we assume $g > 0$ ($g < 0$) below (above) the w -nullcline. Note that (v_r, w_r) corresponds to a stable (resting) state of the kinetic equations

$$\begin{aligned}\frac{dv}{dt} &= f(v, w), \\ \frac{dw}{dt} &= \epsilon g(v, w).\end{aligned}\tag{6.7}$$

We remark that these assumptions are satisfied for many two-variable models for neurons, including the FitzHugh–Nagumo equations and the Morris–Lecar equations.

A traveling wave solution is a solution of the form $(v(x, t), w(x, t)) = (V(\xi), W(\xi))$, where $\xi = x + ct$. As before, c is the (yet to be determined) wave speed; (V, W) now corresponds to the profile of the wave. We note that we have now chosen $\xi = x + ct$ instead of $\xi = x - ct$ as was done in the preceding section. The wave is now “moving” to the left.

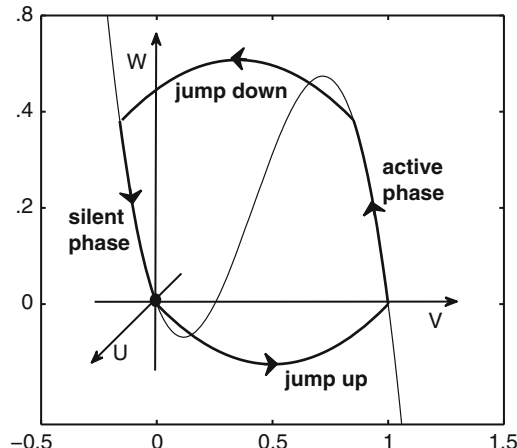
The traveling wave equations are

$$\begin{aligned}\frac{dV}{d\xi} &= U, \\ \frac{dU}{d\xi} &= cU - f(V, W), \\ \frac{dW}{d\xi} &= \frac{\epsilon}{c}g(V, W)\end{aligned}\tag{6.8}$$

together with the boundary conditions

$$\lim_{\xi \rightarrow \pm\infty}(V, U, W)(\xi) = (v_r, 0, w_r).\tag{6.9}$$

Fig. 6.4 Singular construction of the traveling pulse. During the jump up, the singular solution lies in the plane $\{w = 0\}$. The active phase lies along the right branch of the cubic in the plane $\{U = 0\}$ and the silent phase lies along the left branch of this cubic. The jump down lies in a plane $\{w = \text{constant}\}$ where the constant is chosen so that the speed of the back of the pulse is the same as that of the front



Hence, we seek values of c for which there exists an orbit homoclinic to the fixed point $(v_r, 0, w_r)$. There may, in fact, be at least two waves. This was demonstrated for the FitzHugh–Nagumo model by Hastings, Carpenter, and Conley. It has been demonstrated that the wave with the greater speed is the stable one and this is what we will concentrate on. In a later section, we will consider the stability of this wave.

We demonstrate the existence of a homoclinic orbit using methods from the geometric theory of singular perturbations. The idea is to formally set $\epsilon = 0$ and construct a singular homoclinic trajectory. Once we construct the singular trajectory, we worry about proving that this trajectory is perturbed to an actual homoclinic orbit for $\epsilon > 0$. The singular trajectory will consist of four pieces; these correspond to the jump up from the silent to the active phase, the active phase, the jump down to the silent phase, and the return to rest in the silent phase (see Fig. 6.4). We note that the jumps up and down take place on a fast timescale ξ , whereas the active phase and the return to rest take place on a slower timescale $\eta = \epsilon\xi$. It will be important to exploit this separation of timescales in the construction of the singular orbit.

It will be convenient to introduce some notation. Recall that the curve $\{(V, W) : f(V, W) = 0\}$ is cubic-shaped. For fixed W , let $(V_L(W), W)$ and $(V_R(W), W)$ be the points that lie on the left and right branches of the cubic, respectively. (Here, we are assuming W lies below the local maximum of the cubic.) Note that $V_L(w_r) = v_r$, since (v_r, w_r) is a fixed point of the kinetic equation (6.7).

We first consider the jump up to the active phase. Let $\epsilon = 0$ in (6.8); this leads to the reduced system

$$\begin{aligned} V' &= U, \\ U' &= cU - f(V, W), \\ W' &= 0. \end{aligned} \tag{6.10}$$

Note that W must be constant. For the jump up, we take $W \equiv w_r$ and (6.10) becomes just the traveling equation for the scalar equation. From the discussion in the

previous section, we know that there exists a unique value of c , which we denote as c^* , for which there exists a unique heteroclinic orbit of (6.10) that connects $(v_r, 0, w_r)$ along the left branch of the cubic nullcline to $(V_R(w_r), 0, w_r)$ along the right branch. This heteroclinic orbit corresponds to the jump-up piece of the full singular orbit and c^* corresponds to the ($\epsilon = 0$) velocity of the traveling pulse. For the remainder of the analysis, we assume $c = c^*$.

We next consider the active phase. Here, we introduce in (6.8) the slow variable $\eta = \epsilon\xi$ and then set $\epsilon = 0$ to obtain the reduced system

$$\begin{aligned} 0 &= U, \\ 0 &= cU - f(V, W), \\ \frac{dW}{d\eta} &= \frac{1}{c}g(V, W). \end{aligned} \tag{6.11}$$

The first two equations state that this piece of the singular orbit lies on the cubic nullcline $f(V, W) = 0$ and the third equation gives the rate at which the orbit evolves along the cubic. For the active phase, the singular orbit lies on the right branch of the cubic beginning at the point $(V_R(w_r), 0, w_r)$ (see Fig. 6.4).

Now consider the jump down. Once again we use the fast timescale and consider the reduced system (6.10) with $c = c^*$. Now W is constant, say, W_{jd} , along this piece; however, it is not clear how we should choose this constant. Analysis similar to that given in the preceding section demonstrates for each such W that lies below the local maximum of the cubic, there exists a wave speed $c(W)$ for which there exists a solution of (6.10) that approaches $(V_R(W), 0, W)$ along the right branch as $\xi \rightarrow -\infty$ and approaches $(V_L(W), 0, W)$ along the left branch as $\xi \rightarrow +\infty$. Now the pulse must maintain a constant width, so the speed of the jump up and that of the jump down must be the same. That is, we must choose the position of the jump down so that $c(W_{jd}) = c^*$. This condition determines W_{jd} uniquely. We remark that this condition may not be satisfied. In this case, the jump down is at the local maximum of the v -nullcline. Such systems admit traveling waves for a continuum of velocities. For some models, it is possible to compute W_{jd} explicitly. In the exercises, the reader is asked to do this for the FitzHugh–Nagumo equations in which $f(v, w) = v(1 - v)(v - \alpha) - w$.

Finally, we consider the return to rest. Here, we use the slow timescale η and consider the reduced system (6.11). This piece of the singular orbit lies along the left branch of the cubic, as shown in Fig. 6.4, and approaches the resting state as $\xi \rightarrow \infty$.

Note that during the active phase, the traveling wave lies along the right branch of the cubic V -nullcline; moreover, the slow variable W satisfies (6.11). From this we can compute the width, Ξ , of the action potential. Using the slow variable η , we find that

$$\Xi = c^* \int_{w_r}^{W_{jd}} \frac{dw}{g(V_R(w), w)}.$$

For the membrane models that we have considered, $g(v, w) = \epsilon(w_\infty(v) - w)/\tau(v)$. If $w_\infty(v)$ is very sharp, then $w_\infty(v_R(w))$ will be close to 1. Assuming $\tau(v)$ does not vary much along the right branch of the cubic nullcline, we can approximate $g(V_R(w), w)$ by $(1 - w)/\tau_R$, where τ_R is a constant. Then, it is easy to show that the width of the action potential is

$$\Xi = \tau_R c^* \ln \frac{1 - w_r}{1 - W_{jd}}.$$

6.3.1 Wave Trains

How do we compute the periodic wave trains for this model? Basically, the method is relatively easy. Instead of jumping from w_r , we jump at a slightly higher value of w , say, w_P . Thus, we first compute a jump from $V_L(w_P)$ to $V_R(w_P)$. This will have a smaller velocity than the solitary pulse (why?); call it c_P . As before, we need to find a jump-back point, w_Q , such that the velocity of the wave from $V_R(w_Q)$ to $V_L(w_Q)$ matches c_P . Then we compute the dynamics on the left branch until w reaches w_P and the process repeats. The up-jump and down-jump are relatively fast compared with the evolution time of w along the two branches. Thus, the actual period of these wave trains is

$$\Xi_P \approx \frac{c_P}{\epsilon} \left[\int_{w_P}^{w_Q} \frac{dw}{g(V_R(w), w)} + \int_{w_Q}^{w_P} \frac{dw}{g(V_L(w), w)} \right].$$

6.4 Dispersion Relations

In general, if a dynamical system has a homoclinic orbit for a special parameter value, then for parameters nearby we expect to find periodic orbits. What do such orbits correspond to in (6.2)? Consider the following “experiment.” We initiate an action potential at one end of a semi-infinite cable. Then, after a period of time, we initiate another one, and so on. This will asymptotically produce a traveling wave train. Denote the temporal period by T , the spatial separation between the successive action potentials by P , and assume the wave train travels at velocity c . Note that c , P , and T are not independent of each other: $P = cT$, since the spatial period is dictated by the velocity and the temporal period. The velocity c will not be the same as the velocity of the homoclinic orbit (solitary action potential) because successive action potentials travel on a cable which may be refractory from the prior activity. As we will see below, this can lead to either lower values of c or, surprisingly, higher values of c . Thus, we expect that c will be a function of T (or P). This notion is well known from nonlinear wave theory. The spatial and temporal frequencies ($1/P$ and $1/T$) are related through the so-called *dispersion*

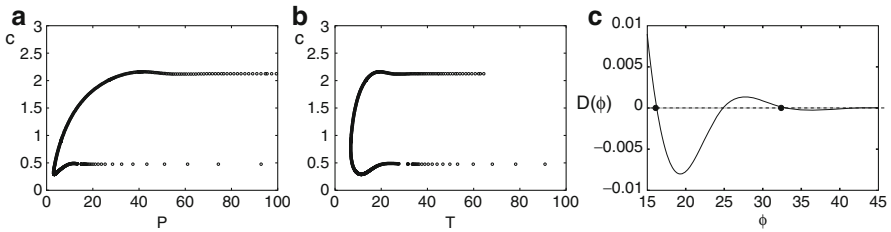


Fig. 6.5 Dispersion relations for the Hodgkin–Huxley equation. (a) The full dispersion relation showing velocity versus period, P . (b) The temporal dispersion relation showing velocity versus the temporal period $T = P/c$. (c) The function $D(\phi) = 1/c(\phi) - 1/c_\infty$

relation. Traditionally, in mathematical neuroscience, the relationship is given by $c = c(P)$, the spatial period between waves. A way to think about this is to suppose we make the axon into a ring. A periodic wave train with spatial period P is a solitary wave propagating around the ring with circumference P .

The dispersion relationship is very important since it tells us how the axon responds to multiple stimuli. As with the homoclinic orbit, it is possible to numerically compute the dispersion relationship by looking for a periodic orbit and varying c , the speed. Figure 6.5a shows the dispersion relationship for the Hodgkin–Huxley equations. There are several important points to note. There is a minimum period, P^* , below which waves do not seem to exist. This means there is a limit to how closely spaced action potentials can be on the axon – not surprising, given the refractoriness (recovery from the hyperpolarization). For each $P > P^*$, there are two possible speeds, one is fast and the other slow. What is perhaps most interesting is that the velocity exhibits damped oscillations around the solitary wave speed c_∞ . This means for some spatial periods, the waves move *faster* than the solitary wave. The reason for this is complex, but we can provide a bit of intuition. Consider the recovery to rest after the wave has passed. This is dominated by the behavior of the linearization of (6.3) at rest. We note that this linearization has a single negative eigenvalue and all the remaining eigenvalues have positive real parts. Two of these eigenvalues are complex, $\alpha \pm i\beta$, so we expect that there will be some damped oscillations on return to rest. (Note that we shoot backward in ξ , the traveling coordinate, so the oscillations are damped rather than growing.) This means the membrane potential shows damped oscillations near rest, for example,

$$V(\xi) \approx V_{\text{rest}} + Ae^{\alpha\xi} \cos \beta\xi$$

for ξ large and negative. This implies that for some values of ξ , $V(\xi)$ is larger than V_{rest} , so it takes less current to produce an action potential. Thus, waves which are spaced close to the characteristic length $2\pi/\beta$ would have the added “boost” and would travel faster.

6.4.1 Dispersion Kinematics

Rinzel and Maginu [231] came up with a clever method for studying multiple waves along axons without using the full neuron model. The idea is to use the dispersion relation to compute the instantaneous velocity of an action potential which is a certain distance (in space or time) from an initial impulse. Suppose an initial pulse is initiated at $x = 0$ and at time t_1 . Then, the time at which this first impulse reaches a point x is $T_1(x) = t_0 + x/c_\infty$, where c_∞ is the speed of the solitary pulse. Suppose we introduce a new spike at $x = 0$ at time t_2 . The instantaneous velocity of this new spike at $x = 0$ will depend on the time since the last spike occurred at $x = 0$; that is, $t_2 - t_1$. Rinzel and Maginu suggested the instantaneous velocity should be approximated by $c(t_2 - t_1)$, where $c(T)$ is the velocity of a wave with *temporal period* T . [If one has the dispersion curve as a function of the spatial period, P , divide this by $c(P)$ to get the temporal period.] Figure 6.5b replots the data from Fig. 6.5a to show the temporal dispersion relationship for the Hodgkin–Huxley equations. Given this Rinzel–Maginu approximation, the time at which a second action potential reaches a point x will evolve as

$$\frac{dT_2}{dx} = \frac{1}{c(T_2(x) - T_1(x))}. \quad (6.12)$$

The time interval, $\phi \equiv T_2(x) - T_1(x)$, between two action potentials initiated at $x = 0$ will evolve (in space, x) as

$$\frac{d\phi}{dx} = \frac{1}{c(\phi)} - \frac{1}{c_\infty} \equiv D(\phi). \quad (6.13)$$

If $D(\phi)$ has a zero(s), $\bar{\phi}$, then the time difference between the two action potentials will lock at these zeros. Figure 6.5c shows a plot of $D(\phi)$ and two zeros of this function. Viewed as an evolution equation, we see that if $D'(\phi) < 0$, then the timing difference is stable. Intuitively, this says the following. Suppose ϕ is slightly larger than $\bar{\phi}$ so that $D(\phi) < 0$. This means $c(\phi) > c_\infty$, so the trailing action potential will speed up and the temporal difference, ϕ , decreases. The case of multiple action potentials is easily analyzed by assuming the only action potential which matters is the preceding one. The timing of the $(j + 1)$ th action potential will depend only on the time since the j th action potential,

$$\frac{dT_{j+1}}{dx} = \frac{1}{c(T_{j+1} - T_j)}.$$

6.5 Morris–Lecar Revisited and Shilnikov Dynamics

Here, we will briefly describe additional properties of traveling wave solutions for the Morris–Lecar equations. In particular, we point out that these properties depend on whether the model cells exhibit class I or class II dynamics.

6.5.1 Class II Dynamics

The Morris–Lecar model is two-dimensional, so the analysis of propagating action potentials leads to a three-dimensional dynamical system of the form

$$\begin{aligned}\frac{dV}{dt} &= U, \\ \frac{dU}{dt} &= -U/c - f(V, W), \\ \frac{dW}{dt} &= -g(V, W)/c.\end{aligned}\tag{6.14}$$

We start as in Chap. 3, with the Morris–Lacar model with class II dynamics. There is a unique fixed point, $(v_r, 0, w_r)$, which has a one-dimensional stable manifold and a two-dimensional unstable manifold. Figure 6.6a shows the dispersion relation for the Morris–Lecar model in this regime. As expected, it looks very similar to Fig. 6.2b as both types of cells are class II. At $I = 80$, the linearization of (6.14) at the fixed point has eigenvalues $-\nu$ and $\mu \pm i\omega$, with $\nu > \mu > 0$. Thus, we can apply a very powerful theorem from dynamical systems due to Shilnikov. This theorem implies that if (6.14) has a homoclinic orbit for $c = c^*$, and if the linearization of the fixed point has a real eigenvalue, r , and a pair of complex conjugate eigenvalues, $\alpha \pm i\beta$, with r and α of opposite signs and $0 < |\alpha| < |r|$, then there must exist infinitely many periodic orbits for values of c near c^* . Furthermore, the system contains so-called Smale-horseshoe dynamics (see Chap. 5). This implies very complex behavior. Indeed, we can expect very complicated sequences of action potentials to persist on the axon. (An interesting project would be to use the kinematics of the dispersion relationship to find some of these complex orbits.)

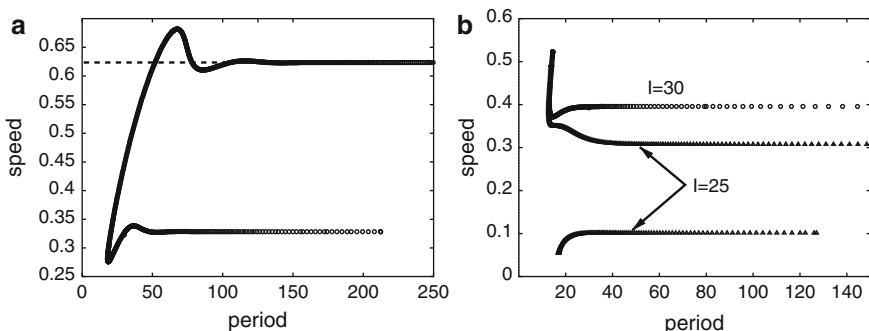


Fig. 6.6 Dispersion relation for the Morris–Lecar model. (a) Class II dynamics showing characteristic damped oscillatory form with fast and slow connected wave branches ($I = 80$). (b) Class I dynamics showing disconnected fast and slow waves (slow waves for $I = 30$ are on the $c = 0$ axis.)

We note that Shilnikov-type dynamics may also exist for the FitzHugh–Nagumo model:

$$\begin{aligned}\frac{\partial v}{\partial t} &= \frac{\partial^2 v}{\partial x^2} + f(v) - w + I, \\ \frac{\partial w}{\partial t} &= \epsilon(v - kw),\end{aligned}$$

where $f(v) = v(1 - v)(v - a)$, $0 < a < 1$, $\epsilon > 0$, and $k \geq 0$. Here, we assume $I = k = 0$. Hastings [118] and Carpenter [34] proved the existence of traveling wave solutions (or homoclinic orbits) for this model when the recovery variable ϵ is sufficiently small. However, it is easy to show that when the recovery is very slow, then all the eigenvalues of the linearized system are real. Thus, one cannot obtain Shilnikov-type dynamics in this case. However, Hastings [119] proved the homoclinic orbit exists when the recovery is fast enough such that the linearized system does have complex eigenvalues. In a related paper, Feroe [87] showed the existence of the Shilnikov structure for the piecewise-linear McKean model, $f(v, w) = I - v + H(v - a) - w$, where H is the Heaviside step function. Finally, Evans et al. [81] proved a theorem similar to the Shilnikov theorem and applied it to the question of double-impulse solutions. They showed that if the return to the fixed point is damped-oscillatory, then there are double-pulse solutions and that if the return is monotonic, then there are no such solutions.

6.5.2 Class I Dynamics

Surprisingly, no one has looked at the propagation of action potentials in class I membranes, except in a scalar case. Figure 6.6b shows the dispersion relationship for the Morris–Lecar equations with class I dynamics at two different currents. At $I = 30$, there is only a fast branch of waves. At $I = 25$, there is a new slow branch of waves. The explanation of this is somewhat complicated and not suitable for a textbook. Rather than go through the details, we consider the scalar model for an excitable medium.

Class I excitability is characterized by dynamics which lies on a circle. Figure 6.7a shows the phase space for simple scalar dynamics which is equivalent to the θ -model:

$$\frac{dV}{dt} = f(V),$$

where V lives on the circle of radius 1 and $f(V)$ is 2π -periodic. We assume $f(V)$ has two roots in $[0, 2\pi]$ and denote the unique root r , where $f(r) = 0$ and $f'(r) < 0$. Ermentrout and Rinzel [76] considered

$$\frac{\partial V}{\partial t} = \frac{\partial^2 V}{\partial x^2} + f(V),$$

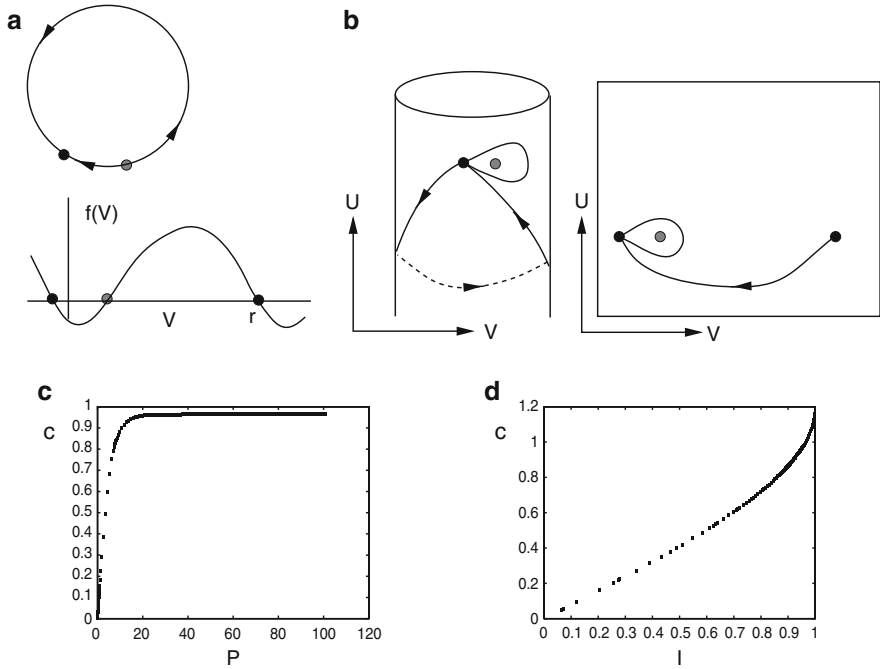


Fig. 6.7 Ermentrout–Rinzel excitable model. **(a)** The dynamics lies on a *circle*; the nonlinearity is periodic with period 2π and has two fixed points. **(b)** The phase space of the traveling wave equations is a *cylinder*. For $c = c_\infty > 0$, there is a “big” homoclinic which wraps around the cylinder; for $c = 0$, there is also a small homoclinic. These are depicted on the unfolded cylinder; the “big” homoclinic is now a heteroclinic joining $(2\pi + r, 0)$ to $(r, 0)$ where $f(r) = 0$ and $f'(r) < 0$. **(c)** Dispersion relation for $f(V) = I - \cos(V)$ when $I = 0.95$. **(d)** Velocity of the large periodic wave as I varies

where $V(x, t) \in S^1$, the unit circle. In traveling coordinates, we obtain

$$-cV' = V'' + f(V),$$

the dynamics of which lie on a cylinder. There are two types of homoclinic solutions: a “big” homoclinic orbit and a “small” homoclinic orbit. Figure 6.7b shows these solutions as well as their projections onto the unfolded cylinder. The small homoclinic occurs when $c = 0$, for then the dynamics is

$$V'' = -f(V),$$

which is an integrable equation. That is, all solutions lie on a curve defined by

$$E = (V')^2/2 + F(V),$$

where $F'(V) = f(V)$ and E is constant. There is a family of periodic orbits (inside the small homoclinic) whose period varies between p_{\min} and ∞ . This branch of solutions for $c = 0$ corresponds to the “slow” branch of solutions we have seen in other models. The “big” homoclinic is actually a heteroclinic orbit joining r and $r - 2\pi$. But in the cylindrical phase space, these two points are the same point, so, projected on the cylinder, the solution is a homoclinic orbit. The theory of bistable reaction–diffusion equations provides the existence of a unique value of c for the heteroclinic orbit.

6.6 Stability of the Wave

Perhaps the most influential work done concerning the stability of traveling wave solutions of nerve impulse equations was that done by John Evans. In a series of four papers, he developed a general mathematical framework in which to study a general class of models that include the Hodgkin–Huxley equations. In his fourth paper, Evans constructed a complex analytic function, now called the Evans function, with the property that eigenvalues of the equations linearized about the traveling wave correspond to zeros of the *Evans function*. Using other properties developed by Evans, this implies that the stability of the traveling wave is determined by computing the roots of the Evans function. Here, we will briefly describe issues surrounding stability of waves and define the Evans function. Defining the Evans function is not that hard; what is difficult is to compute the Evans function and say something concrete about the eigenvalues. Jones [143] applied the Evans function to the FitzHugh–Nagumo equations and completed the rigorous proof of the stability of the traveling wave solution. Another stability proof was given by Maginu [189].

Here, we consider the FitzHugh–Nagumo equations and we denote the traveling wave solution as $(V(\xi), W(\xi))$, $\xi = x + ct$. For stability, we need to consider the initial value problem

$$\begin{aligned} v_t &= v_{xx} + f(v) - w, \\ w_t &= \epsilon(v - kw), \\ (v(x, 0), w(x, 0)) &= (v_0(x), w_0(x)). \end{aligned} \tag{6.15}$$

It is not completely obvious how one should define asymptotic stability of the traveling wave. Intuitively, we would like to say that the wave is asymptotically stable if we start with initial data that is “close” to the wave, then the corresponding solution will asymptotically approach the wave as $t \rightarrow \infty$. One issue is how do we define “close”; that is, what norm or function space should we use? This turns out not to be a problem and any reasonable norm, such as the supremum norm, works. A more serious issue is that the traveling wave is, in fact, not unique; every translate of a traveling wave is also a traveling wave. That is, if $(V(\xi), W(\xi))$ is a traveling wave solution, then so is $(V(\xi + \xi_0), W(\xi + \xi_0))$ for any constant ξ_0 . Now if we take our initial data to be $(V(\xi + \xi_0), W(\xi + \xi_0))$ with ξ_0 very small, then the initial data

lies very close to the original traveling wave; however, the solution with this initial data does not approach the original traveling wave as $t \rightarrow \infty$. In general, the best that we can hope for is that a perturbation of a traveling wave solution will approach some translate of the original traveling wave solution. With this in mind, we define asymptotic stability as follows. By $\|\cdot\|$ we mean the usual supremum or L^∞ norm.

Definition: The traveling wave $(V(\xi), W(\xi))$ is asymptotically stable if for each $\delta_0 > 0$ there exists $\delta_1 > 0$ and ξ_0 such that if $\|(V(x), W(x)) - (v_0(x), w_0(x))\| < \delta_1$, then $\|(V(x + ct), W(x + ct)) - (v(x, t), w(x, t))\| < \delta_0$ for all $t > 0$. Moreover, $\lim_{t \rightarrow \infty} \|(V(x + ct + \xi_0), W(x + ct + \xi_0)) - (v(x, t), w(x, t))\| = 0$.

6.6.1 Linearization

A common approach to proving the stability of the wave is to use the method of linearization. In fact, this is one of the few mathematical methods available to treat the initial value problem for the system of partial differential equations (6.15). The first step in applying this method is to reduce the issue of stability to an eigenvalue problem. This is done as follows. We first change to the moving coordinate frame $\xi = x + ct$. In this new variable, (6.15) becomes

$$\begin{aligned} v_t &= v_{\xi\xi} - cv_\xi + f(v) - w, \\ w_t &= \epsilon(v - kw) - cw_\xi, \\ (v(\xi, 0), w(\xi, 0)) &= (v_0(\xi), w_0(\xi)). \end{aligned} \tag{6.16}$$

Note that the traveling wave $(V(\xi), W(\xi))$ is a steady solution of this system. We then look for solutions of (6.16) that are perturbations of the traveling wave. In particular, we look for solutions of the form

$$(v(\xi, t), w(\xi, t)) = (V(\xi) + p(\xi)e^{\lambda t}, W(\xi) + r(\xi)e^{\lambda t}).$$

This solution either grows or decays (in time) with rate λ . If we plug a solution of this form into (6.16), “linearize” around the traveling wave, drop higher-order terms, use the fact that the traveling wave is a steady solution, and let $q = p'$, then we find that $(p(\xi), q(\xi), r(\xi))$ must solve the eigenvalue problem

$$\begin{aligned} p' &= q \\ q' &= cq + (\lambda - f'(V(\xi)))p + r \\ r' &= \frac{\epsilon}{c}(p - kr) - \frac{\lambda}{c}r. \end{aligned} \tag{6.17}$$

Note that we are interested in solutions of (6.17) that satisfy the boundary conditions

$$\lim_{\xi \rightarrow \pm\infty} (p, q, r)(\xi) = (0, 0, 0). \tag{6.18}$$

Now λ is an eigenvalue if there exists a bounded, nonzero solution of (6.17) that satisfies the boundary conditions (6.18). We note that $\lambda = 0$ must be an eigenvalue because every translation of the wave is also a wave; in particular, $(p, q, r) = (V', V'', W')$ is the corresponding eigenvector. Evans proved if all the remaining eigenvalues are in the left-half complex plane (and 0 is a simple eigenvalue), then the traveling wave is asymptotically stable.

6.6.2 The Evans Function

Here, we will show how to define the Evans functions for a broad class of reaction–diffusion systems. Unfortunately, this class does not include the nerve impulse equations, for reasons we point out below. Our discussion will at least give a taste for how such a function is defined and why it has the properties that it does. It is not too difficult to extend this definition to nerve impulse equations; however, this becomes somewhat technical so we simply refer the interested reader to [143].

We consider a general class of reaction–diffusion equations of the form:

$$U_t = DU_{xx} + F(U). \quad (6.19)$$

Here, $U(x, t) \in R^n$ and $F : R^n \rightarrow R^n$ is sufficiently smooth. We assume D is an n -dimensional diagonal matrix with nonzero, positive entries along the diagonal. Note that this rules out the nerve impulse equations since these do not have diffusion in the recovery variables. We assume $U = A$ and $U = B$ are fixed points (that is, $F(A) = F(B) = 0$) and there is a traveling wave solution $V(\xi)$ of (6.19), with speed c , which connects A with B . Note that we do not rule out $A = B$.

As before, we change to a moving coordinate frame, $\xi = x + ct$, and consider perturbations of the wave of the form $p(\xi)e^{\lambda t}$. This leads to an eigenvalue problem of the form:

$$\begin{aligned} p' &= q, \\ q' &= D^{-1}\{cq + (\lambda - F'(V))\}p. \end{aligned} \quad (6.20)$$

Then, λ is an eigenvalue if there is a nontrivial solution (eigenfunction) $(p(\xi), q(\xi))$ of (6.20) that satisfies

$$\lim_{\xi \rightarrow \pm\infty}(p, q)(\xi) = (0, 0). \quad (6.21)$$

Note that an eigenfunction is a pair of (complex) functions that satisfy (6.20) and decays at $\pm\infty$. To define the Evans function, we consider the two sets of solutions that decay at either $+\infty$ or $-\infty$. That is, let

$$\begin{aligned} \mathcal{E}^+(\lambda) &= \{\text{solutions of (6.20) such that } \lim_{\xi \rightarrow +\infty}(p(\xi), q(\xi)) = (0, 0)\}, \\ \mathcal{E}^-(\lambda) &= \{\text{solutions of (6.20) such that } \lim_{\xi \rightarrow -\infty}(p(\xi), q(\xi)) = (0, 0)\}. \end{aligned}$$

It is obvious that λ is an eigenvalue if the intersection of $\mathcal{E}^+(\lambda)$ and $\mathcal{E}^-(\lambda)$ is nontrivial. It is important to realize that $\mathcal{E}^+(\lambda)$ and $\mathcal{E}^-(\lambda)$ are linear subspaces. This is because (6.20) is linear. A standard result from the theory of linear ordinary differential equations implies that the dimension of each of these linear subspaces is n . We choose a basis for each of these linear subspaces. That is, suppose

$$\mathcal{E}^+(\lambda) = \text{span}\{Q_1^+(\xi, \lambda), \dots, Q_n^+(\xi, \lambda)\}$$

and

$$\mathcal{E}^-(\lambda) = \text{span}\{Q_1^-(\xi, \lambda), \dots, Q_n^-(\xi, \lambda)\}.$$

Note that each Q_j^+ and Q_j^- is a $2n$ -dimensional vector. We next form the $2n \times 2n$ -dimensional matrix in which the first n columns are Q_1^+, \dots, Q_n^+ and the next n columns are Q_1^-, \dots, Q_n^- . We denote this matrix by $\mathcal{M}(\xi, \lambda)$.

We are now ready to define the Evans function. Let

$$\mathcal{D}(\lambda) = \det \mathcal{M}(\xi_0, \lambda), \quad (6.22)$$

where ξ_0 is some arbitrary point (say, 0).

Now the Evans function is certainly well defined. Evans proved this function has many important properties. Perhaps the most important property is that λ is an eigenvalue if and only if $\mathcal{D}(\lambda) = 0$. This is actually trivial to prove. The proof is simply:

$$\mathcal{D}(\lambda) = 0$$

if and only if $\det \mathcal{M}(\xi_0, \lambda) = 0$,

if and only if the rows of $\mathcal{M}(\lambda, \lambda)$ are linearly dependent,

if and only if there exist constants c_1, c_2, \dots, c_{2n} such that

$$c_1 Q_1^+ + c_2 Q_2^+ + \cdots + c_n Q_N^+ + c_{n+1} Q_1^- + c_{n+2} Q_2^- + \cdots + c_{2n} Q_n^- = 0,$$

if and only if

$$c_1 Q_1^+ + c_2 Q_2^+ + \cdots + c_n Q_N^+ = -(c_{n+1} Q_1^- + c_{n+2} Q_2^- + \cdots + c_{2n} Q_n^-),$$

if and only if $\mathcal{E}^+(\lambda)$ and $\mathcal{E}^-(\lambda)$ have nonzero intersection,

if and only if λ is an eigenvalue.

Another important property of the Evans function is that it is analytic. Moreover, if λ is a zero of \mathcal{D} , then the order of this zero is equal to the algebraic multiplicity of λ as an eigenvalue. These two properties are considerably more difficult to prove.

Although it is straightforward to define the Evans function, it is quite challenging to actually compute this function in any given example. For stability, one needs to prove there are no roots of \mathcal{D} in the right-half plane, there are no roots on the imaginary axis except at the origin (because of translation), and zero is a simple eigenvalue. Methods that have been developed for computing \mathcal{D} go well beyond the scope of this book.

6.7 Myelinated Axons and Discrete Diffusion

Many vertebrate axons are covered by a fatty substance called myelin which serves to both insulate the axons and decrease the membrane capacitance. Myelin consists of the membranes of glial cells which wrap around the axons to make a thick layer. At regularly spaced intervals, the *nodes of Ranvier*, the axon is exposed to the extracellular medium and there is a high density of sodium channels. The increased transmembrane resistance implies that little current leaks out along the myelinated portions of the axon, so we can expect the velocity of propagation to be greatly enhanced (see below).

Let a_1 denote the diameter of the axon and a_2 denote the diameter of the myelinated axon. Dayan and Abbott [54] showed that the total capacitance due to the myelination is

$$\frac{1}{c_m} = \frac{\ln(a_2/a_1)}{2C_m\pi d_m L},$$

where L is the length of the myelinated region, C_m is the usual material constant for capacitance, and d_m is the thickness of a cell layer. Because of the large transmembrane resistance and small capacitance, the potential in the myelinated membrane satisfies the diffusion equation

$$\frac{c_m}{L} \frac{\partial V}{\partial t} = \frac{4\pi a_1^2}{R_L} \frac{\partial^2 V}{\partial x^2}, \quad (6.23)$$

where R_L is the transmembrane resistivity. Dividing by c_m/L , this is the diffusion equation with $D = 4a_1^2 \ln(a_2/a_1)/(2C_m R_L d_m)$. The larger the diffusion coefficient, the faster the propagation. Suppose we fix the outer diameter, a_2 . Then, we can ask what inner diameter maximizes the diffusion coefficient. It is easy to show that this occurs when $a_1 = a_2 \exp(-1/2) \approx 0.6a_2$. At the optimal diameter, $D = K a_2^2$, so the velocity of propagation (which scales as \sqrt{D}) scales linearly with diameter. The velocity of propagation for unmyelinated axons scales as the square root of the diameter.

Figure 6.8 shows a cartoon of a myelinated axon with nodes of Ranvier spaced a distance L apart. We assume the nodes are sufficiently small so that they are

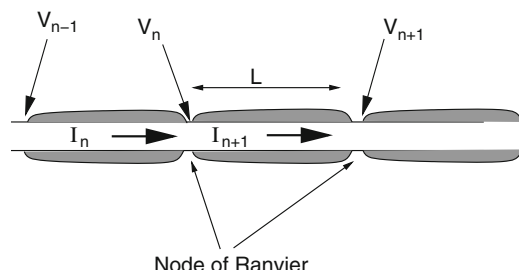


Fig. 6.8 Myelinated axon. Currents in the myelinated region are confined to the axial direction. Potentials at the nodes are governed by active currents

isopotential. Let V_n denote the potential at a node. The transmembrane conductance and the capacitance of myelinated regions are roughly 100-fold smaller than those of the unmyelinated portions of the axon (the nodes of Ranvier). Thus, there is a sense in which we can regard the myelinated axon as a collection of discrete active nodes separated by a purely resistive medium. Take the limit as $c_m \rightarrow 0$ in (6.23). Then $V_{xx} = 0$ between nodes $n - 1$ and n . The voltage at $x = 0$ and $x = L$ must match the voltage at the nodes. Thus, the potential is linear between nodes: $V(x) = V_{n-1} + (V_n - V_{n-1})x/L$. The current flowing into node n is proportional to the gradient of the voltage in the myelinated segments. Thus, at node n , the voltage satisfies

$$AC_m \frac{dV_n}{dt} = -AI_{\text{ionic}}(V_n, \dots) + I_n - I_{n+1}, \quad (6.24)$$

where A is the area of membrane exposed at the node, and the longitudinal current [recall (2.8)]

$$I_n = -\frac{4a_1^2}{R_l} \frac{\partial V}{\partial x} = 4\pi a_1^2 \frac{(V_n - V_{n-1})}{R_l L}.$$

The area A is $\pi\mu a_1$, where μ is the length of the node. Dividing through by the area, we obtain

$$C_m \frac{dV_n}{dt} = -I_{\text{ionic}}(V_n, \dots) + D(V_{n+1} - 2V_n + V_{n-1}), \quad (6.25)$$

where $D = 4a_1/(R_l L \mu)$. Thus, the continuous axon equation, in the presence of myelin, becomes a discrete system of differential equations. Surprisingly, this is much more difficult to analyze, even in the simple bistable case. A traveling wave, if it exists, satisfies $V_{n+1}(t) = V_n(t - \tau)$; that is, translating by one space unit results in a time shift of τ . The speed of the wave is thus L/τ since L is the distance between nodes. With the traveling wave ansatz, we must solve the differential-delay equations:

$$\begin{aligned} C_m \frac{dV}{dt} &= D[V(t + \tau) - 2V(t) + V(t - \tau)] - I_{\text{ionic}}(V, w, \dots) \\ \frac{dw}{dt} &= g(V, w), \end{aligned}$$

where w represents the gating variables, calcium, etc. In the scalar bistable case, we set $f(V) = -I_{\text{ionic}}(V)$ and assume $f(V)$ has three roots, $V_{\text{rest}}, V_{\text{thr}}$, and V_{ex} , the resting state, the threshold, and the excited state. We seek solutions to the delay equation where $V(-\infty) = V_{\text{ex}}$ and $V(+\infty) = V_{\text{ex}}$. There have been a few results for this problem [35, 297].

Keener and Sneyd [148] offered the following approximate analysis. Approximate $V(t + \tau) - 2V(t) + V(t - \tau)$ by $\tau^2 V''$ so that we have to solve

$$C_m V' = f(V) + \frac{\tau^2}{L\mu} \frac{4a_1}{R_l} V'',$$

with τ an unknown parameter. To compare this with the continuous cable, we contrast the term multiplying V'' with that in (2.7). We introduce the new space-like variable $\xi = \sqrt{L\mu}/\tau$. Then, the traveling wave equation is

$$C_m \frac{\sqrt{L\mu}}{\tau} V_{\xi\xi} = f(V) + \frac{4a_1}{R_l} V_{\xi\xi}.$$

Let c be the traveling wave speed of the unmyelinated axon. Then, we can immediately identify $c = \sqrt{L\mu}/\tau$, so

$$c_{\text{myelin}} = L/\tau \approx \sqrt{\frac{L}{\mu}} c.$$

Since μ is often $1 \mu\text{m}$ and L is around $100 \mu\text{m}$, the increase in velocity of myelinated axons can be almost 10 times that of unmyelinated axons. In practice, the factor is closer to 6, but we have made a rather crude approximation here.

6.8 Bibliography

There have been a great number of papers devoted to a rigorous treatment of propagating waves in reaction–diffusion models, including nerve impulse equations. Two of the most influential papers concerning scalar reaction–diffusion equations were those by Aronson and Weinberger [6] and Fife and McLeod [88].

As we have described in this chapter, the propagating action potential corresponds to a homoclinic orbit in phase space. Conley [44] developed a very powerful topological method (known as the Conley index) for rigorously proving the existence of heteroclinic and homoclinic orbits, as well as other invariant sets such as periodic orbits. This approach was used by Carpenter [34] to prove the existence of homoclinic orbits for the Hodgkin–Huxley model. Hastings [118] also considered this problem, using a topological shooting argument. Analysis of homoclinic orbits often involves fast/slow analysis and methods from geometric singular perturbation theory. A seminal paper on geometric singular perturbation theory was that of Fenichel [86].

The most influential papers concerning the stability of the traveling wave solution were those by Evans [80], who developed what is now known as the Evans function. In these papers, Evans developed the mathematical machinery needed to begin to analyze the stability of the waves; however, he did not consider whether the traveling wave solution of a specific nerve impulse equation is stable. This step was carried out for the FitzHugh–Nagumo model by Jones [143]. The Evans function has also been used to study integrodifferential equations that arise as neuronal models; see, for example, Zhang [296] and Coombes [48].

6.9 Exercises

1. Consider the scalar equation (6.3) with $f(u) = u(1 - u)$. Prove there exists c^* such that a traveling wave solution $U(x - ct)$ exists for all wave speeds $c \geq c^*$. Here, $U(\xi)$ should satisfy $U(-\infty) = 1$, $U(+\infty) = 0$ and $U(\xi) > 0$ for all ξ . What is the precise value of c^* ?
2. Consider the scalar equation (6.3) with $f(u) = -u + H(u - a)$, where H is the Heaviside step function and $0 < a < 1/2$. In this case, one can construct the traveling wave solution explicitly and find a formula for the wave speed. This is done as follows. Note that (6.5) consists of two linear systems: one for $U < a$ and the other for $U > a$. One can solve each of these systems explicitly in terms of exponentials. For each a and $c > 0$, find a solution, $U_+(a, c)(\xi)$, of the system for $U > a$ such that $U(0) = a$ and $\lim_{\xi \rightarrow -\infty} U(\xi) = 1$. Then find a solution, $U_-(a, c)(\xi)$, of the system for $U < a$ such that $U(0) = a$ and $\lim_{\xi \rightarrow +\infty} U(\xi) = 0$. Now fix a and derive a formula for the wave speed by assuming the derivatives of these two solutions match up at $U = a$; that is, $U'_+(0) = U'_-(0)$. Plot the wave speed, c , versus the parameter a ? What happens to the wave speed as (a) $a \rightarrow 0$ and (b) $a \rightarrow 1/2$.
3. Prove the traveling wave solution of the bistable equation (6.3) exists for a unique value of the wave speed. In what sense is the traveling wave unique?
4. Draw the phase plane corresponding to the equation $U'' + f(U) = 0$, where $f(U) = U(1 - U)(U - \alpha)$, $0 < \alpha < 1/2$. [Hint: Consider the total energy function $E(U, Y) = Y^2/2 + F(U)$, where $Y = U'$ and

$$F(U) = \int_0^U f(s)ds.$$

Show that $E(U, Y)$ is constant along trajectories in the phase plane.]

5. Consider the scalar equation (6.3) where $f(u) = u(a-u)(u-b)(u-c)(u-d)$, where $a < b < c < d$. Note that the equation $u' = f(u)$ has three stable fixed points, at $u = 0$, b , and d . Show that there is a traveling wave solution such that $U(-\infty) = b$ and $U(+\infty) = 0$. Moreover, there is another traveling wave solution $U(-\infty) = d$ and $U(+\infty) = b$. Denote the speeds of these waves as c_{b0} and c_{db} , respectively. Prove there exists a traveling wave solution such that $U(-\infty) = d$ and $U(+\infty) = 0$ if and only if $c_{b0} \leq c_{db}$. How does the speed of this third wave compare with the speeds of the other two waves?
6. *Aglantha digitale*, a lovely jellyfish (see Fig. 6.9), has an interesting axon [187]. When the animal is moving through the water, slow-moving spikes are generated in the axon, but when it is trying to escape, the animal produces fast action potentials. The slow waves occur at a lower threshold stimulus, have low amplitude, and are produced by a calcium spike. The fast waves are generated by a high-threshold sodium current. One way to think about this behavior theoretically is to study the initiation of the spike by looking at a model with no recovery. That is, imagine a tristable system in which there are five fixed points, three of which are stable and two unstable. The slow wave is a front from rest

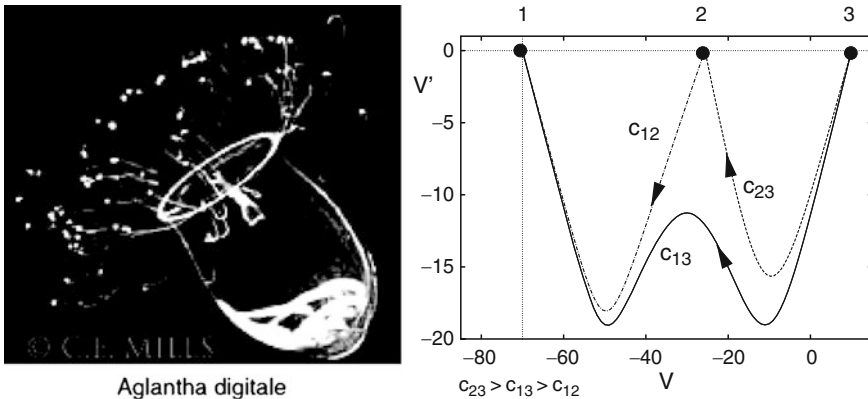


Fig. 6.9 The jellyfish *Aglantha digitale* and the phase plane for a tristable system. The three heteroclinic orbits corresponding to the three wavefronts are shown. Here, $c_{12} < c_{13} < c_{23}$

to the middle stable fixed point. The fast wave is a front from rest to the highest fixed point. Consider the simple model

$$V_t = V_{xx} + I_{\text{ion}}(V),$$

where

$$I_{\text{ion}}(V) = g_L(V - E_L) + g_{\text{Ca}}m_1(V)(V - E_{\text{Ca}}) + g_{\text{Na}}m_2(V)(V - E_{\text{Na}})$$

and each $m_j(V)$ is of the form $m_j(V) = 1/(1 + \exp(-(V - V_{tj})b_j))$. Assume $E_L = -70$, $E_{\text{Na}} = 55$, and $E_{\text{Ca}} = 150$. Find values of the other parameters so that I_{ion} has five zeros. Arrange these zeros so that there are the requisite traveling fronts. Figure 6.9 shows our attempt at this. The figure shows three different fronts at three different speeds.

7. Here is a cool trick. Let $f(u) = Au(u - \alpha)(1 - u)$, where $\alpha \in (0, 1/2)$, and consider the traveling front equation

$$-cu' = f(u) + u'',$$

where $u(-\infty) = 1$ and $u(+\infty) = 0$. Also consider the equation

$$u' = -bu(1 - u).$$

Find a value of b and of c so that the solution to the second equation is a solution to the first. Thus, find an exact expression for the wave speed. Solve the second equation by quadrature to get a closed-form expression for the wavefront! Plot the wave speed, c , versus the parameter α . What happens to the wave speed as $\alpha \rightarrow 0$ and $\alpha \rightarrow 1/2$?

8. Consider the equation $v_t = v_{xx} + f(v) - w$, where $f(v) = v(1-v)(v-\alpha)$, $0 < \alpha < 1/2$, and w is constant. Note that there is a range of w for which there are three fixed points; we denote the left, middle, and right fixed points as $(v_L(w), w)$, $(v_M(w), w)$, and $(v_R(w), w)$, respectively. For what values of w does there exist a traveling wave solution such that $\lim_{\xi \rightarrow -\infty} V(\xi) = v_R(w)$ and $\lim_{\xi \rightarrow \infty} V(\xi) = v_L(w)$? How does the wave speed depend on w ? For what value of w is the wave speed zero? For what value of w does the speed of this wave equal c_* , the wave speed of the scalar equation, defined in Sect. 6.2. This gives the value of W_{jd} , defined in Sect. 3.3.
9. Consider the FitzHugh–Nagumo equations (6.15) with $k > 0$ and $I = 0$. Note that if k is sufficiently large, then the traveling wave equations have three fixed points. One of these is at the origin \mathcal{O} and we denote the fixed point on the right branch of the cubic as q_0 . Construct a singular heteroclinic orbit of the traveling wave equations which connects \mathcal{O} at $\xi = -\infty$ to q_0 at $\xi = +\infty$. For what values of the wave k does there exist a singular heteroclinic orbit that connects q_0 to \mathcal{O} ? For what values of k does there exist a singular orbit homoclinic to the origin?
10. Consider the FitzHugh–Nagumo equations (6.15) with $k = I = 0$. Construct singular periodic orbits. The orbit should “jump up” from the left to the right branch of the cubic nullcline for some fixed value of w , lie along the right and left branches of this cubic during the active and silent phases, respectively, and jump down from the right to the left branch of the cubic at some other fixed value of w . The values of w for the jump up and jump down need to be chosen so that the velocities of the front and back parts of the wave match. For what values of w is there the jump up? How do the speeds of the waves depend on these values of w ?
11. Simulate the reduced Hodgkin–Huxley cable model using $m = m_\infty(V)$ and $h = 0.8 - n$. Deduce that the velocity of an action potential is about 2–3 times faster than that of a full model. Why do you think this is?
12. Consider the Morris–Lecar model with no potassium,

$$C_m \frac{dV}{dt} = \frac{d^2V}{dx^2} - g_L(V - E_L) - g_{Ca}m_\infty(V)(V - E_{Ca}) + I,$$

with parameters as in Chap. 4. Choose the injected current, I , so that this equation is bistable. How does the velocity of the wavefront depend on I ? Now, in the original Morris–Lecar model, m is a dynamic variable, but we have set it to its steady state. Study the velocity of the wavefronts for the Morris–Lecar model,

$$\begin{aligned} C_m \frac{dV}{dt} &= \frac{d^2V}{dx^2} - g_L(V - E_L) - g_{Ca}m(V - E_{Ca}) - I, \\ \frac{dm}{dt} &= \epsilon(m_\infty(V) - m), \end{aligned}$$

as ϵ increases.

13. Use shooting to estimate the velocity of an action potential for the FitzHugh–Nagumo equations. Try to find the slow-velocity wave and then use continuation software (such as AUTO) to draw the dispersion relation.
14. What is the velocity of an action potential using the Hodgkin–Huxley dynamics for an axon of diameter $d = 0.1\text{ cm}$ and axial resistance $R_i = 100\Omega\text{ cm}^2$?
15. Consider the traveling wave equations (6.8) for the FitzHugh–Nagumo equations (6.15) with $I = 0$. Show that if $b > 0$ is sufficiently small, then the linearization at the origin has two negative eigenvalues and one positive eigenvalue. Thus, there is a two-dimensional stable manifold and a one-dimensional unstable manifold.
16. Analyze the traveling wave equations (6.8) for the FitzHugh–Nagumo equations (6.15) with $k > 0$ and show that the resting state can become unstable as I increases. [Hint: Assume the resting state is at $V = \bar{V}$ and show that a Hopf bifurcation occurs when $f'(\bar{V}) = k$. Then solve this last equation for two values of \bar{V} and plug these values into the expression for the resting state. This yields two values of I , thus showing there are two possible Hopf bifurcation points. Find a relationship between a and k guaranteeing that these points exist.]
17. Suppose the stable dispersion relation satisfies

$$c(P) = c_\infty(1 - \alpha e^{-\beta(P-P_{\min})}),$$

- where $\alpha = (c_\infty - c_{\min})/c_\infty$, $c_\infty > c_{\min} > 0$ and $\beta > 0$. Analyze the kinematics of this type of dispersion curve. What happens to a pair of spikes on an axon? More generally, suppose $c = F(P)$ and F is monotonically increasing. Show that if $F(P) > PF'(P)$, then $D(\phi)$ has no roots. Thus, show that if the dispersion relation is monotonic, there are no double-pulse solutions (see [81]).
18. For many class II axons, the dispersion relation $c(P)$ is oscillatory. For simplicity, suppose

$$\frac{1}{c(P)} = \frac{1}{c_\infty} + \eta e^{-aP} \cos bP,$$

- where a and b are positive constants and $\eta > 0$ is smaller than $1/c_\infty$. Find an equation for the interspike interval of a pair of pulses on the cable. What is the minimal interval? Pick some values of a , b , and η and look at the kinematics of pulse triplets, etc.
19. Consider the simple ring model for excitability:

$$V_t = I - \cos V + V_{xx},$$

where $0 < I < 1$. There are two fixed points of interest: $V_0 = -\arccos(I)$ and $V_1 = 2\pi - \arccos(I)$. For $I = 0.95$, find the velocity of the front joining V_1 to V_0 . Let c_∞ be the velocity of the front. Since the state space for this system is a cylinder (recall Fig. 6.7), we can also look for “periodic” solutions. Take it as a fact that if $c < c_\infty$, then the unstable manifold of V_1 hits the V' -axis before it hits the V -axis. Show that, on the cylinder, the unstable manifold approaches a periodic solution – that is, $V(\xi + P) = V(\xi) - 2\pi$ (see [76]).

20. Show that $\lambda = 0$ is an eigenvalue of the linear system (6.17).

21. *Propagation failure.* Consider the equation

$$\frac{dv_n}{dt} = f(v_n) + D(v_{n+1} - 2v_n + v_{n-1}).$$

Assume f has roots at 0, 1, and $a \in (0, 1)$ such that 0 and 1 are stable fixed points of $v' = f(v)$.

(a) Suppose $U_n(t)$ and $V_n(t)$ are solutions to this equation with initial data such that $V_n(0) > U_n(0)$ for all n . Prove $V_n(t) \geq U_n(t)$ for all $t > 0$.

(b) Part (a) implies that if there is a stationary front (that is, a zero velocity front) with $V_n \rightarrow 1$ as $n \rightarrow \infty$ and $V_n \rightarrow 0$ as $n \rightarrow -\infty$, then there will be no traveling front; this is because the stationary front blocks the propagation. It is clear that if $D = 0$, then such a stationary front exists – just take $V_n = 0$ for $n < 0$, $V_0 = a$ and $V_n = 1$ for $n > 0$. This stationary front persists for small D . (One can show that it is a hyperbolic fixed point.) Thus, we expect that the stationary front exists for D sufficiently small. Keener [146] showed that there is a $D^* > 0$ such that if $D \leq D^*$, there is a stationary front. Suppose $f(v) = -v + H(v - a)$, where H is the Heaviside step function. Find D^* for this model. (Hint: Consult [148], page 280.) Answer: $D^* = a(1-a)/(2a-1)^2$.

Chapter 7

Synaptic Channels

So far, we have restricted our modeling and analysis efforts to single neurons. To begin to develop networks and the theoretical background for networks, we need to introduce an additional class of membrane channels. We have already looked at voltage- and ion-gated channels. However, there are many other channels on the surface of nerve cells which respond to various substances. Among the most important of these, at least in computational neuroscience, are synaptic channels.

The events leading to the opening of synaptic channels involve several steps. The action potential travels down the axon and terminates at many presynaptic sites invading regions called synaptic terminals. These terminals contain calcium channels. When these are depolarized they cause release of calcium. The calcium then activates a calcium binding protein, which promotes transmitter release by binding to vesicles containing the transmitter. These “docked” vesicles release their transmitter into the synaptic cleft. The transmitter diffuses through the cleft, where it binds to various receptors on the postsynaptic neuron (often on protuberances on the dendrites called spines). These receptors open channels which either depolarize or hyperpolarize the neuron depending on the nature of the transmitter.

Transmitter release can become quite complex for there are sometimes presynaptic receptors near the site of transmission which can be modulated by various chemicals. Furthermore, the release of transmitter is probabilistic and occurs in discrete amounts called *quanta*. Presynaptic stimulation can lead to more vesicles becoming docked to the membrane, so on the next presynaptic spike more transmitter is released than on the first spike. This increase is called *potentiation* or *facilitation*. Additionally, after several presynaptic spikes, the transmitter release per spike can decrease through various means (such as depletion) and take some time to recover. Decrease of transmitter over successive firings of action potentials is called *synaptic depression*.

The consequences of synaptic dynamics and short-term plasticity (e.g., depression and facilitation) have not been thoroughly explored in terms of dynamical systems theory. Here, we will develop several models for both synaptic release and the plasticity of synaptic release. In Chap. 11, we will show some interesting behavior which occurs because of synaptic depression.

7.1 Synaptic Dynamics

In this section, we deal with the five most common classes of synaptic dynamics. The main transmitters associated with cortical neurons are glutamate and γ -aminobutyric acid (GABA). A good rule of thumb is that glutamate excites the postsynaptic cell, whereas GABA inhibits it. However, the reversal potential of some GABA receptors is mainly dependent on chloride concentration, so it can be close to rest and even above rest. Thus, (particularly, early in development) some GABA synapses can be excitatory. Like other currents, we model the synaptic currents as the product of a conductance with a voltage difference:

$$I_{\text{syn}} = g(t)(V_{\text{post}} - V_{\text{rev}}).$$

Unlike our previously studied channels, the conductance $g(t)$ depends on the presynaptic neuron.

There are several ways to model the conductance $g(t)$. A popular method among computational neuroscientists is to assume $g(t)$ is the sum of fixed functions which depend only on the times at which that the presynaptic cell has spiked:

$$g(t) = \bar{g} \sum_k \alpha(t - t_k) \equiv \bar{g} z(t), \quad (7.1)$$

where \bar{g} is a constant conductance and $\alpha(t)$ is a prescribed function of time, vanishing for $t < 0$ and positive for $t > 0$. The times t_k are when the presynaptic cell has spiked. The most general form for the function $\alpha(t)$ is

$$\alpha(t) = \frac{a_d a_r}{a_r - a_d} (e^{-a_d t} - e^{-a_r t}). \quad (7.2)$$

The parameter a_r characterizes the rise rate of the synaptic conductance and a_d characterizes the decay. Many modelers assume $a_d = a_r$, in which case the function has the form

$$\alpha(t) = a_d^2 t e^{-a_d t}.$$

Letting $a_r \rightarrow \infty$ reduces the model to a single exponential. The maximum of $\alpha(t)$ occurs at $t^* = \ln(a_r/a_d)/(a_r - a_d)$. The constants multiplying these functions are chosen so that the area under $\alpha(t)$ is 1. Other normalizations are possible; for example, choosing the value of $\alpha(t^*) = 1$ for some $t^* > 0$.

If one uses alpha functions in simulations, then (7.1) implies that it is necessary to keep track of all the incoming spikes at times t_k . Since $z(t)$ in (7.1) is the solution to a second-order linear differential equation,

$$z'' + (a_r + a_d)z' + a_r a_d z = 0, \quad (7.3)$$

we need only solve this equation in time with the proviso that each time t_k that a presynaptic spike arises, $z'(t)$ is increased by an amount $a_d a_r$. Formally, we can write

$$z'' + (a_r + a_d)z' + a_r a_d z = a_r a_d \sum_k \delta(t - t_k).$$

If the spike train is random (say, Poisson) with a time-varying rate, $v(t)$, then we can formally average this equation to obtain

$$z'' + (a_r + a_d)z' + a_r a_d z = a_r a_d v(t). \quad (7.4)$$

The solution to this linear equation provides a formula for the average net synaptic input for a time-varying random stimulus.

Choosing a fixed function $\alpha(t)$ for the synaptic response has some advantages which will become apparent when we study networks. However, from a physical point of view, the use of alpha functions is unsatisfactory. First, as noted above, we need to track the time of a spike which could be ambiguous. Furthermore, this approach does not connect well with our notion of voltage- and ligand-gated channels. We now introduce a simple model for synapses which is identical to the formalism that we previously described for voltage-gated ionic channels. Let $[T]$ denote the concentration of transmitter released into the synaptic cleft by a presynaptic spike. Note that $[T]$ will be time-dependent since synaptic transmitter is rapidly taken up and/or degraded. Then the conductance $g(t) = \bar{g}s(t)$, where $s(t)$ denotes the fraction of open channels. $s(t)$ satisfies

$$\frac{ds}{dt} = a_r [T](1 - s) - a_d s. \quad (7.5)$$

Suppose at $t = t_0$, $[T]$ jumps to T_{\max} and at $t = t_1$, $[T]$ falls back to 0. Then

$$s(t - t_0) = s_\infty + (s(t_0) - s_\infty)e^{-(t-t_0)/\tau_s}, \quad \text{for } t_0 < t < t_1,$$

where

$$s_\infty = \frac{a_r T_{\max}}{a_r T_{\max} + a_d} \quad \text{and} \quad \tau_s = \frac{1}{a_r T_{\max} + a_d}.$$

After the pulse of transmitter has gone, $s(t)$ decays as

$$s(t) = s(t_1)e^{-a_d(t-t_1)}.$$

Although it may appear that, like the alpha function, there is a rise rate and a decay rate, the formula for τ_s shows that the rates are not independent. If $a_r T_{\max}$ is large, the synapse will saturate near 1, so it is not possible to make this rise rate arbitrary. However, by varying the residence time of the transmitter, $t_1 - t_0$, we can mimic the alpha function quite closely. We now must connect the transmitter release $[T]$ with the presynaptic neuron. We assume a model of the form

$$[T](V_{\text{pre}}) = \frac{T_{\max}}{1 + \exp(-(V_{\text{pre}} - V_T)/K_p)}. \quad (7.6)$$

Destexhe et al. [62] suggest $T_{\max} = 1$ mM, $V_T = 2$, and $K_p = 5$ mV. As this synaptic channel is gated by the *presynaptic* spike, there could be some transmission delay due to the propagation of the presynaptic spike down the axon to the postsynaptic receptor. Thus, modelers often include a delay term; that is, the term $V_{\text{pre}}(t)$ is replaced by $V_{\text{pre}}(t - t_{\text{delay}})$ in (7.6). Synaptic delays can be fixed or depend on the distance between the presynaptic and the postsynaptic neuron to account for the finite propagation speed down the axon (see Chap. 6).

We now have a complete model of the conductance changes of a simple synapse connected to the presynaptic voltage. We turn next to the four main classes of synaptic transmission used in models of cortical neurons. Figure 7.1 shows the conductance changes due to each of our four model synapses.

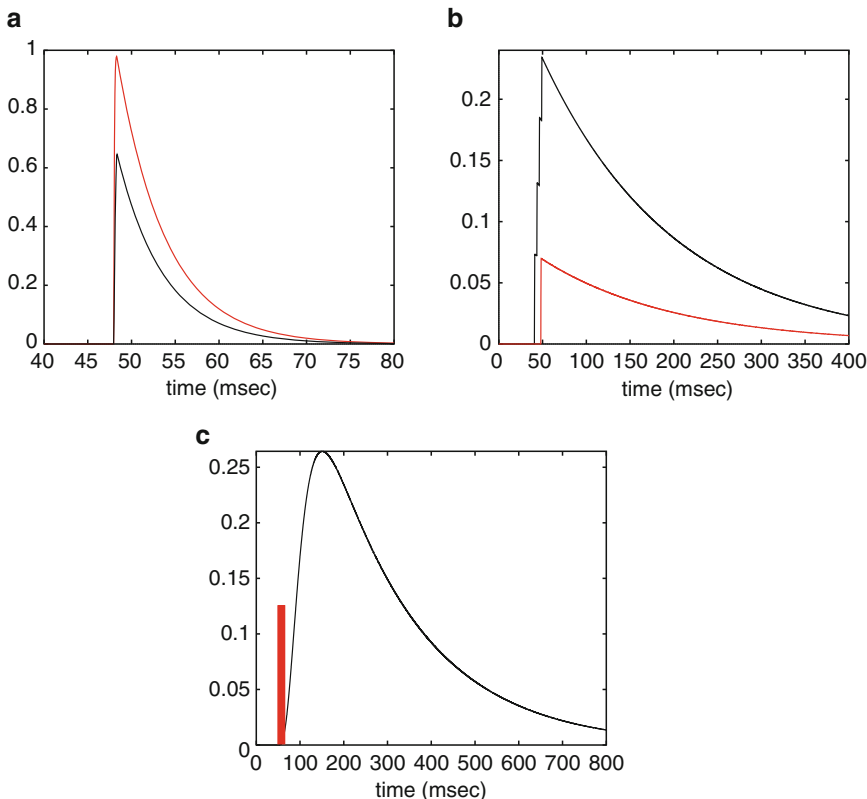


Fig. 7.1 Model synaptic conductances. (a) AMPA (black) and GABA_A (red) conductance due to a single presynaptic spike. (b) NMDA conductance due to a single spike (red) and a burst of four spikes (black). (c) GABA_B conductance due to a burst of eight spikes. Single spike response is negligible

7.1.1 Glutamate

The neurotransmitter glutamate activates two different kinds of receptors: AMPA/kainate, which are very fast, and NMDA, which is implicated in memory and long-term potentiation of synapses. Both of these receptors lead to excitation of the membrane.

7.1.1.1 AMPA/Kainate

The current from a fast AMPA synapse is

$$I_{\text{AMPA}} = \bar{g}_{\text{AMPA}} s(V - V_{\text{AMPA}}), \quad (7.7)$$

where $V_{\text{AMPA}} = 0$ mV. For the synapse shown in Fig. 7.1a, s satisfies (7.5) and (7.6) with $a_r = 1.1 \text{ mM}^{-1} \text{ ms}^{-1}$ and $a_d = 0.19 \text{ ms}^{-1}$.

The AMPA synapses can be very fast. For example, in some auditory nuclei, they have submillisecond rise and decay times. In typical cortical cells, the rise time is 0.4–0.8 ms. Using the above model with a transmitter concentration of 1 mM, the rise time would be $1/(1.1 + 0.19) = 0.8$ ms. The decay is about 5 ms. As a final note, AMPA receptors on inhibitory interneurons have rise and fall times about twice as fast as those on excitatory neurons.

Real AMPA synapses show quite strong depression. That is, the peak amplitude of the AMPA current decreases with each subsequent spike. We will address this short-term plasticity in the next section. Figure 7.1a shows the conductance change for a single presynaptic spike.

7.1.1.2 NMDA

The NMDA receptor is also sensitive to glutamate but has effects that last considerably longer than those of AMPA. However, under normal physiological conditions, the NMDA receptor is partially blocked by magnesium ions. The magnesium block can be removed if the postsynaptic neuron is depolarized and, of course, if the neuron is bathed in a low magnesium medium. Thus, if the postsynaptic cell is already active, then the NMDA receptor opens and the effect of the current will be long-lasting. Because of the property that both the presynaptic and the postsynaptic cells must be active for the NMDA current to flow, the presence of these receptors is believed to be necessary for many types of long-term changes in the synapses which presumably encode memories. Indeed, one of the ions carried by NMDA current is calcium, which is a main player in long-term changes in neurons. This synaptic current is also thought to play a role in maintaining persistent activity required for short-term memory (see [182] and Chap. 12). The NMDA current is modeled as

$$I_{\text{NMDA}} = \bar{g}_{\text{NMDA}} s B(V)(V - V_{\text{NMDA}}), \quad (7.8)$$

where s obeys (7.5) and (7.6) and $B(V)$ represents the magnesium block [138]:

$$B(V) = \frac{1}{1 + e^{-0.062V} [\text{Mg}^{2+}] / 3.57}.$$

It is convenient to rewrite this as

$$B(V) = \frac{1}{1 + e^{-(V - V_T)/16.13}},$$

where V_T is the half activation and is given by

$$V_T = 16.13 \ln \frac{[\text{Mg}^{2+}]}{3.57}.$$

At the physiological concentration of 2 mM, $V_T \approx -10$ mV, so the postsynaptic cell has to be quite depolarized. Even at the relatively low concentration of 1 mM, $V_T \approx -20$ mV. The synaptic parameters for s are well fit by the choices $a_r = 0.072 \text{ mM}^{-1} \text{ ms}^{-1}$, $a_d = 0.0066$, and $V_{\text{NMDA}} = 0$ mV. Figure 7.1b shows the conductance change for a model NMDA synapse when there is a single spike and when there are four spikes. The rise time is fast enough such that each spike can be seen in the model trace.

Sometimes it is desirable to implement the NMDA channel so that there is greater flexibility in the rise time. In this case, the channel is modeled by two variables,

$$\begin{aligned} \frac{dx}{dt} &= \alpha_1 T(V)(1 - x) - \beta_1 x, \\ \frac{ds}{dt} &= \alpha_2 x(1 - s) - s/\tau, \end{aligned} \tag{7.9}$$

so that the first-order s in (7.8) is replaced by the s in (7.9).

7.1.2 γ -Aminobutyric Acid

GABA is the principal inhibitory neurotransmitter in the cortex. There are two main receptors for GABA: GABA_A and GABA_B.

7.1.2.1 GABA_A

GABA_A is responsible for fast inhibition and, like AMPA and NMDA, requires a single presynaptic spike to be evoked. The current is

$$I_{\text{GABA}_A} = \bar{g}_{\text{GABA}_A} s(V - V_{\text{GABA}_A}), \tag{7.10}$$

where s obeys (7.5) and (7.6) with $a_r = 5 \text{ mM}^{-1} \text{ ms}^{-1}$, $a_d = 0.18 \text{ ms}^{-1}$, and V_{GABA_A} varying between -81 and -60 mV . This GABA current is carried by chloride (among other ions) and thus there is a wide range of values depending on the physiological conditions and the developmental stage of the neurons. (Early in development GABA is mainly depolarizing with a reversal potential well above rest.) In many models in the literature, $V_{\text{GABA}_A} = -75 \text{ mV}$. Figure 7.1a shows the conductance change for our model GABA_A synapse.

7.1.2.2 GABA_B

The three synapses described so far (AMPA/kainate, NMDA, and GABA_A) share the common feature that the ion channel and the receptor are the same protein. Thus, the effect of transmitter on these synaptic receptors is *direct*. However, there are other synaptic events which are *indirect* in that the activation of the receptor sets off a cascade of intracellular events which eventually alter the conductivity of an ion channel. The GABA_B receptor is an example of this indirect effect: transmitter binds to a receptor protein which activates an intracellular complex called a G-protein, which in turn activates a potassium channel to hyperpolarize the membrane. Such indirect effects can have several consequences. The responses can be (1) nonlinear, (2) slow to activate, and (3) long-lasting. There are several models for the activation of GABA_B synapses; we will consider only the simplest one. There is a receptor r which is activated exactly as described by (7.5) and (7.6). This receptor activates the ion channel, s , and results in the GABA_B current. The current is a nonlinear saturating function of s . Thus, the model for GABA_B is

$$\begin{aligned} I_{\text{GABA}_B} &= \bar{g}_{\text{GABA}_B} \frac{s^n}{K_d + s^n} (V - E_K), \\ \frac{dr}{dt} &= a_r[T](1 - r) - b_r r, \\ \frac{ds}{dt} &= K_3 r - K_4 s. \end{aligned} \quad (7.11)$$

For the synapse shown in Fig. 7.1c, $a_r = 0.09 \text{ mM}^{-1} \text{ ms}^{-1}$, $a_d = 0.0012 \text{ ms}^{-1}$, $n = 4$, $K_d = 100$, $K_3 = 0.18 \text{ ms}^{-1}$, and $K_4 = 0.034 \text{ ms}^{-1}$. We use the same function (7.6) for the transmitter release, T , as we have in the other synaptic models. The nonlinearity in (7.11) means s must become large enough for the synapse to take effect. GABA_B is more effective when several action potentials occur in a row. Note also that the reversal potential is that of potassium; in a cortical cell this can be around -90 to -105 mV . GABA_B is unambiguously hyperpolarizing. Figure 7.1c shows the effective synaptic conductance, $s_{\text{eff}} = s^4/(s^4 + K_d)$, for a burst of eight spikes. The conductance for a single spike is very close to 0.

7.1.3 Gap or Electrical Junctions

Many cells can directly communicate with each other via tight junctions between their membranes. These act as resistors connecting compartments in two different cells and are called either electrical or gap junctions. The difference between gap junctions and chemical synapses is that the former always keep the cells in communication, whereas the latter occur only when there is a presynaptic action potential. (Although there are some neurons which release transmitter in a graded fashion, these are rare and atypical. The granule cells in the olfactory bulb of mammals are the best known example.) We model the current for this type of synapse as

$$I_{\text{gap}} = \bar{g}_{\text{gap}}(V_{\text{post}} - V_{\text{pre}}), \quad (7.12)$$

where g_{gap} is the conductance. Gap junctions may play an important role in synchronizing the spiking of inhibitory neurons in the cerebral cortex [4, 12, 101, 102].

7.2 Short-Term Plasticity

Our conceptual model for synapses treats them as though there is no history dependence. That is, the magnitude of the postsynaptic current is independent of how many times that it has been invoked in recent history. However, the experimental work of many groups over the years shows that many synapses exhibit *short-term plasticity*. Here, the emphasis is on the phrase *short-term* as opposed to long-term changes that are associated with learning and memory. Short-term plasticity occurs over timescales of the order of milliseconds to minutes and takes the form of short-term depression (the magnitude of successive postsynaptic currents decreases), facilitation (the magnitude of successive postsynaptic currents increases), or possibly both. We point out that the GABA_B model shows facilitation in that several closely timed action potentials lead to a much larger current. Beierlein and Gibson [12], Castro-Alamancos [36], and Markram et al. [191] have quantified synaptic plasticity in mammalian brains. Varela et al. [279] were among the first to recognize the computational consequences of short-term plasticity. Here, we briefly describe some models and some consequences of this plasticity. Later, we will see that the effects on networks or neurons can be much more interesting.

Figure 7.2a shows examples of synaptic depression and synaptic facilitation in cortical neurons. We now describe phenomenological and mechanistic models for short-term plasticity. The phenomenological model is due to Dayan and Abbott but is closely related to many other models. Suppose we want to characterize the magnitude, $M(t)$, of synaptic release per presynaptic spike. We write this magnitude as the product of two factors, the depression $q(t)$ and the facilitation $f(t)$, so that

$$M(t) = q(t)f(t).$$

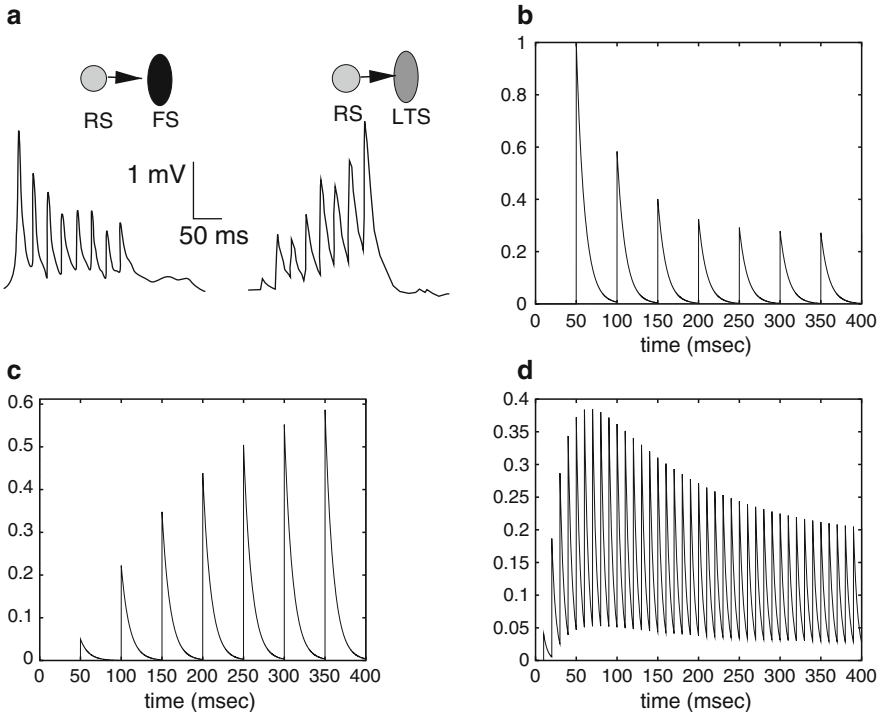


Fig. 7.2 (a) Short-term synaptic plasticity in cortical neurons (from [12]). Connections between cortical excitatory cells (RS) and cortical fast spike units (inhibitory) show synaptic depression for 20-Hz stimuli, whereas connections between cortical excitatory cells and low threshold spike (LTS) inhibitory cells show facilitation. (b-d) Simulations of (7.13) and (7.14) to periodic stimuli. The parameters for (b) are $\tau_d = 300$, $a_d = 0.5$, $d_0 = 1$, $\tau = 10$ and there is no facilitation. The parameters for (c) are $\tau_f = 500$, $a_f = 0.2$, $f_0 = 0$, $\tau = 10$ with no depression. The frequency is 20 Hz. (d) Both depression and facilitation with $f_0 = 0$, $d_0 = 1$, $\tau_f = 50$, $\tau_d = 400$, $a_f = 0.2$, $a_d = 0.05$, and $\tau = 5$. The frequency is 100 Hz

We could also call $M(t)$ the probability of release if we were interested in treating the process stochastically. Both $f(t)$ and $q(t)$ lie between 0 and 1 and each has a resting value of f_0 and d_0 , respectively, to which it returns with time constant τ_f and τ_d , respectively. Thus, in absence of any inputs,

$$\tau_f \frac{df}{dt} = f_0 - f \quad \text{and} \quad \tau_d \frac{dq}{dt} = d_0 - q.$$

Each time there is a spike, $f(t)$ is increased by an amount $a_f(1 - f)$ and $q(t)$ is decreased by an amount $a_d d$. In both cases, the change is multiplied by a factor

which keeps the variables bounded between 0 and 1. We assume both a_f and a_d are less than 1. Formally, we can write the facilitation equation as

$$\frac{df}{dt} = \frac{f_0 - f}{\tau_f} + \left(\sum_j \delta(t - t_j) \right) a_f (1 - f), \quad (7.13)$$

where t_j are the times of the incoming spikes. Similarly, for the depression equation, we have

$$\frac{dq}{dt} = \frac{d_0 - q}{\tau_d} - \left(\sum_j \delta(t - t_j) \right) a_d q. \quad (7.14)$$

We leave the analysis of these equations when stimuli are periodic as an exercise. Figure 7.2b–d shows the results of a simulation of these equations when there is a periodic input. Each time a stimulus comes in, the synaptic variable $s(t)$ is increased by $M(t)$ and both $q(t)$ and $f(t)$ are updated. Between stimuli, $s(t)$ decays exponentially with a time constant of τ .

Suppose the inputs to the synapse are Poisson with rate r . (see Chap. 10, Sect. 4 for a definition of Poisson) Averaging (7.13), we obtain

$$\frac{df}{dt} = (f_0 - f)/\tau_f + a_f r (1 - f).$$

The steady-state value of f is

$$f_{ss} = \frac{f_0 + a_f \tau_f r}{1 + a_f \tau_f r}.$$

A similar calculation for q yields

$$q_{ss} = \frac{d_0}{1 + a_d \tau_d r}.$$

The effective average rate is

$$r_{\text{eff}} = r f_{ss} d_{ss} = r d_0 \frac{f_0 + a_f \tau_f r}{(1 + a_f \tau_f r)(1 + a_d \tau_d r)}.$$

If there is depression, then this function saturates as the true rate goes to infinity.

Varela et al. [279] pointed out that synaptic depression has a useful computational property in that it emphasizes changes in input rates. That is, starting at a low rate and jumping to a high rate results in a huge jump of r_{eff} . Suppose $d_0 = 1$ and the input jumps from r_{lo} to r_{hi} . At the moment before the jump

$$r_{\text{eff}}^- = \frac{r_{\text{lo}}}{1 + a_d \tau_d r_{\text{lo}}}.$$

Right after the jump,

$$r_{\text{eff}}^+ = \frac{r_{\text{hi}}}{1 + a_d \tau_d r_{\text{lo}}}$$

since the depression has not had a chance to take effect. That is, the denominator is still that for the low rate. Over time, the effective rate will decrease to the steady state:

$$r_{\text{eff}} = \frac{r_{\text{hi}}}{1 + a_d \tau_d r_{\text{hi}}}.$$

By the same argument, if the rate is suddenly lowered again, the effective rate will be very small since the denominator is large from the high prior rate. Thus, synaptic depression behaves much like a differentiator of the input rate and allows for very strong temporal contrast. We note that Bertram [14] called our depression model a *vesicle depletion mechanism* as one can regard the variable d as the amount of transmitter available for release.

7.2.1 Other Models

The models discussed so far for plasticity require that one track the time of spikes. In this sense, they are analogous to using alpha functions for synapses rather than the mechanistic models. Manor et al. [190] used a channel-like model for synaptic depression. They combined an activation model like (7.5) with a depression model of the form

$$\frac{dq}{dt} = \frac{q_\infty(V) - q}{\tau_1 + \tau_2 q_\infty(V)},$$

where

$$q_\infty(V) = \frac{1}{1 + e^{k(V - V_{\text{thr}})}}$$

and $k > 0$ and V_{thr} are parameters. The threshold is set close to $V = 0$ and k is somewhat large so that when V is near rest, $q_\infty(V)$ is close to 1 and $q(t)$ will relax to 1 with a time constant roughly like $\tau_1 + \tau_2$. When the neuron spikes, q_∞ is nearly 0 and $q(t)$ will decay to 0 with a time constant of τ_1 . Thus, $1/\tau_1$ is like a_d and τ_2 is like τ_d in the heuristic model. Given the equation for $q(t)$ and a model such as (7.5) for $s(t)$, the total synaptic conductance is $\bar{g}s(t)q(t)$. Similar models can be built for potentiation of synapses, but with $k < 0$ so that at rest the potentiation variable goes to a low value which is increased with each spike. A more direct mapping is

$$\frac{dq}{dt} = (d_0 - q)/\tau_d - a_d(V)q,$$

where

$$a_d(V) = \frac{a}{1 + e^{-k(V - V_{\text{thr}})}}.$$

When the neuron spikes $a_d(V)$ is large, otherwise it is negative.

We close this section with a three-state model for depression which is based on a simple physical model:

$$\begin{aligned} A &\longrightarrow S, \\ S &\longrightarrow U, \\ U &\longrightarrow A. \end{aligned}$$

A is the available transmitter, S is the conducting state which produces the synaptic conductance, and U is the transmitter which is unavailable for release. Since $A + S + U$ is conserved, we can eliminate A and obtain the following pair of differential equations:

$$\frac{ds}{dt} = \alpha(V)(1 - s - u) - \beta s \quad \text{and} \quad \frac{du}{dt} = \beta s - \beta_2 u.$$

By varying β_2 , we can incorporate various degrees of synaptic depression. This simple model does not have the degree of freedom that other models have; there is only one free parameter β_2 since β determines the decay rate of the synapse and $\alpha(V)$ is voltage-dependent.

7.3 Long-Term Plasticity

One of the main hypotheses in neuroscience is that memories are encoded in the strengths of synapses between neurons. There are dozens of “rules” for strengthening the connections between pair of neurons, far more than we can analyze in depth in this book. Dayan and Abbott [53] (Chap. 8) gives a nice summary of so-called Hebb and timing-based rules along with different ways to normalize the synaptic strengths. Hebb rules strengthen or weaken connections depending on whether or not the presynaptic and postsynaptic neurons are active. (For example, in one implementation, if both neurons are active, the synapse is strengthened; if the postsynaptic neuron is silent, nothing is changed and if the postsynaptic neuron is active but the presynaptic is silent, the synapse is weakened.) The problem with many Hebb rules is that they can lead to runaway excitation since strengthening of (excitatory) synapses results in more activity and thus greater strengthening. Thus, in typical implementations of long-term plasticity, some normalization is applied. For example, the total input to a neuron may be constrained to some constant value. This results in competition between inputs. Exercise 9 provides an example of such competition by developing a very simple model.

Timing-dependent inputs strength the synapse if presynaptic spikes precede the spikes of the postsynaptic cell and weaken if vice versa. Such plasticity can be used to develop networks of unidirectionally coupled neurons that can learn sequences.

7.4 Bibliography

Destexhe et al. [62] were the first to systematically derive a set of differential equation models for synapses where they were treated like other channels. Varela et al. [279] devised a number of short-term plasticity models and emphasized several useful computational features of this kind of plasticity.

7.5 Exercises

1. Simulate and recreate all of Fig. 7.1 using the parameters in the text.
2. If inputs come into a synapse periodically, determine the steady-state values of $q(t)$ and $f(t)$ at the moment after a stimulus has arrived.
3. What rate r maximizes the probability of release for a synapse which has both facilitation ($f_0 = 0$) and depression ($d_0 = 1$)?
4. Simulate

$$\frac{dq}{dt} = \frac{1 - q}{\tau_d} - a_d r(t)q$$

with $a_d = 0.4$, $\tau_d = 500$ ms, and $r(t)$ changes as follows: for the first 200 ms, it is 25 Hz, it jumps to 100 Hz for the next 300 ms, then it falls to 10 Hz, and at $t=1,000$ ms it jumps to 40 Hz. Plot the effective firing rate $d(t)r(t)$.

5. Castro-Alamancos [36] described a synapse with the following properties. The ratio of the first spike to the second spike is 0.6 when the time between spikes is 50 ms. If the time between spikes is 25 ms, the ratio is 0.4. Given $d_0 = 1$, find the parameters a_d and τ_d which match this assuming there is no potentiation.
6. Given an alpha function (7.2), compute the steady-state value of $s(t)$ assuming the presynaptic spikes, $t_k = kP$, are periodic with period P .
7. Suppose $v(t)$ in (7.4) is sinusoidal, $v(t) = \sin \omega t$. Find $z(t)$. Find the magnitude of the response.
8. Gullledge and Stuart [113] demonstrated an interesting example of GABA enhancing the postsynaptic response to an excitatory synapse. They recorded from pyramidal neurons in rat somatosensory cortex and produced both dendritic and somatic GABA stimulation. Create a two-compartment passive model with a resting potential of -78 mV, a leak of 0.05 mS/cm 2 , and a capacitance of 1 μ F/cm 2 . Suppose the reversal potential of AMPA is 0 mV and that of GABA is -68 mV. Apply a dendritic inhibitory postsynaptic current (use a synapse model for GABA) and measure the depolarization in the soma. Apply an AMPA excitatory postsynaptic current to the soma. Measure the deviation. Now apply both simultaneously and arrange the parameters so that the sum is bigger than either current by itself. Now apply the inhibitory postsynaptic current in the soma along with the same excitatory postsynaptic current. You should get a smaller net depolarization owing to the shunting effects of the inhibitory postsynaptic current. In other words, try to mimic Fig. 3 in the Gullledge and Stuart [113] paper.

9. *Synaptic competition.* Consider a single linear neuron which receives inputs from two different sources, I_1 and I_2 , with weights w_1 and w_2 :

$$\tau \frac{dV}{dt} = -V + w_1 I_1(t) + w_2 I_2(t).$$

Hebbian learning is a mechanism for strengthening the weights according to whether or not presynaptic and postsynaptic cells are active. In a typical model

$$\Delta w = k I_{\text{pre}} V_{\text{post}},$$

where I is the input and V is the output. Many neural models use such a mechanism to strengthen the weights between two cells or between an input and an output neuron. The problem with this kind of learning rule is that all synapses will grow since there is nothing to reduce the weight of the synapse. Thus, in this simple model, synaptic weights can also decay at a rate that is proportional to the activity of the postsynaptic cell, V . As the inputs change randomly, we will look at the averages and build a model based on them. Look at the averages

$$\langle I_1 V \rangle = \langle I_1 (I_1 w_1 + I_2 w_2) \rangle \approx \langle I_1 I_1 \rangle w_1 + \langle I_1 I_2 \rangle w_2.$$

This approximation is valid if the weights change slowly compared with the inputs. The terms in the brackets are just the correlations between the two inputs; we will call them C_s and C_d , respectively, corresponding to the same and different stimuli, respectively. It should be expected that $C_s > C_d$. On the other hand, the average postsynaptic activity is approximately $\langle I_1 \rangle w_1 + \langle I_2 \rangle w_2$. We assume the average inputs are the same and that the change in weights is a function of the averages:

$$\begin{aligned} \frac{dw_1}{dt} &= f(C_s w_1 + C_d w_2)(1 - w_1) - g(w_1 + w_2)w_1, \\ \frac{dw_2}{dt} &= f(C_s w_2 + C_d w_1)(1 - w_2) - g(w_1 + w_2)w_2. \end{aligned}$$

The first term represents the growth of the weights to a maximum of 1 and the second term represents the decay. (They are thus constrained to lie between $0 < w_j < 1$ when f and g are positive.) Take $C_s = 0.8$, $C_d = 0.2$, and

$$\begin{aligned} f(x) &= 1/(1 + \exp(-\alpha(x - 1/2))), \\ g(x) &= 1/(1 + \exp(-\beta(x - 1))). \end{aligned}$$

- Prove $w_1 = w_2 = 1/2$ is always a fixed point of this system.
- Analyze the stability as a function of α and β .
- Compute the bifurcation diagram as you vary α and hold $\beta = 5$.
- Sketch the nullclines for $\alpha = 10, 12, 15$, and 20 and describe all the possible qualitative behaviors.

Chapter 8

Neural Oscillators: Weak Coupling

This chapter begins the second part of the book. By now, we hope that the reader has a thorough knowledge of single cell dynamics and is ready to move onto networks. There are two main approaches to the analysis and modeling of networks of neurons. In one approach, the details of the action potentials (spikes) matter a great deal. In the second approach, we do not care about the timing of individual neurons; rather, we are concerned only with the firing rates of populations. This division is reflected in the sometimes acrimonious battles between those who believe that actual spike times matter and those who believe that the rates are all that the brain cares about. On these issues, we have our own opinions, but for the sake of the reader, we will remain agnostic and try to present both sorts of models.

If spikes matter, then it is important to understand how the spikes of one neuron affect the timing of the spikes of another neuron to which it is synaptically (or otherwise) connected. *General* theories on the influence of inputs on the dynamics of single neurons do not exist. Here, we have emphasized the word “general” as there has been some work on the influence of transients on firing patterns of cells. In order to say something rigorously, we consider, in this chapter, a very specific situation in which the individual neurons intrinsically oscillate. This is not an unreasonable assumption at least for the short timescale. A neuron receiving a slowly varying current may throw off a few fairly regularly spaced spikes; thus, at least for those few moments it can be regarded as an oscillator. Hence, we are interested in how networks of neural oscillators behave when they are allowed to interact. Such oscillatory (or transiently oscillatory) networks arise in many areas of neuroscience. There is absolutely no doubt that these networks play a critical role in motor patterns for repetitive activity such as locomotion, feeding, breathing, and mating. Such *central pattern generators* (CPGs) consist of networks of neurons which produce robust rhythmic output. Kopell [159] was among the first to recognize the connection between the mathematical theory of coupled oscillators and CPGs. This alone should be sufficient motivation for studying the properties of coupled neural oscillators. However, a more controversial role for neural oscillations and synchrony has emerged over the last 20 years. A major question in cognitive psychology concerns how different sensory modalities are brought together to produce a unified percept. The problem of how such different aspects of, say, an object, are brought together is called the *binding problem*. Von der Malsburg and Schneider [281] were among the

first to suggest neural oscillations could “solve” this problem. That is, different areas of the brain would synchronize when there was a common percept. Wolf Singer’s group [107, 108] found tantalizing evidence for this theory in electrical recordings of the cat visual cortex. So-called gamma oscillations (30–80 Hz) were found to have a high degree of synchrony under certain situations presumably related to perceptual grouping. Thus, an industry was born and there are now hundreds of papers which concern the role of gamma oscillations and synchrony in perception. Our goal here is not to ask whether these synchronous oscillations do in fact play a role, but rather to use this possibility to motivate the study of spike synchronization between neurons.

8.1 Neural Oscillators, Phase, and Isochrons

A single neuron often fires repetitively when it is injected with a constant current. Indeed, we studied the onset of these oscillations in many different neural models in previous chapters. Thus, it is not unreasonable to regard a stimulated neuron as a limit cycle at least in the short term (over a period of several spikes.) Thus, it behooves us to consider some general properties of limit cycles. Unlike a stable fixed point, a stable limit cycle oscillator has a degeneracy associated with it; namely, any solution $X(t)$ can be arbitrarily translated in time and still be a solution. In the first two exercises, we explore the notion of linear stability for limit cycles. In particular, one can never get the same kind of asymptotic stability as with fixed points. Instead, one gets orbital asymptotic stability.

Consider the differential equation in R^n

$$\frac{dX}{dt} = F(X) \quad (8.1)$$

and suppose Γ is a T -periodic limit cycle. Recall that the limit cycle is said to be orbitally asymptotically stable if nearby initial conditions approach Γ as $t \rightarrow \infty$. We can parameterize Γ by time with respect to the period T (see Fig. 8.1a) and thus define a phase, $\theta \in [0, T]$, along the limit cycle. Let $\Theta(x)$ denote the phase of the oscillator for a point x on Γ . When the cycle is asymptotically stable, it is possible to define a phase for points y in a neighborhood of the cycle. Let $X(t; y)$ be the solution to (8.1) with initial condition y . Suppose y is a point in the neighborhood of the limit cycle and x is a point on the limit cycle such that $\|X(t; x) - X(t; y)\| \rightarrow 0$ as $t \rightarrow \infty$. Then we define $\Theta(y) = \Theta(x)$. That is, as $t \rightarrow \infty$, the solutions are indistinguishable. The set of points y which have the same asymptotic phase is called the isochron of the limit cycle (see Fig. 8.1b). We denote the isochron through a point $x \in \Gamma$ as $N(x)$. Isochrons are local invariant sections; that is, for a point $y \in N(x)$, $X(T; y) \equiv y' \in N(x)$. The map $y \rightarrow y'$ is a Poincaré map for the limit cycle which takes time *exactly* T to return. The existence of isochrons (proven

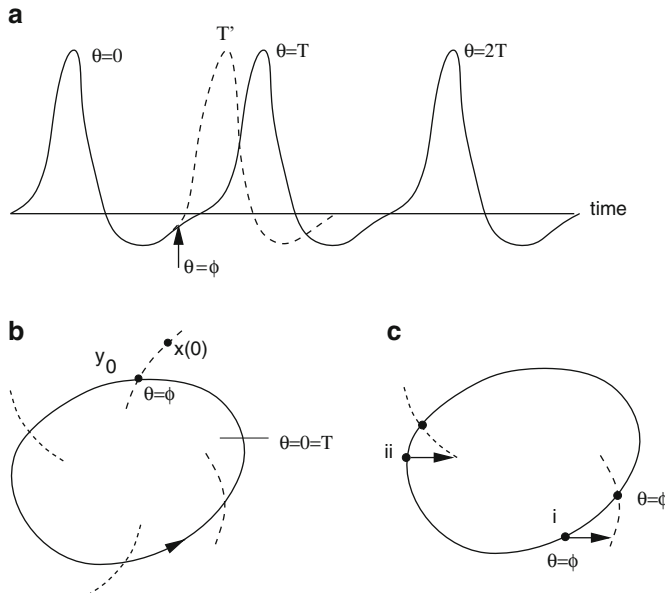


Fig. 8.1 Phase for a limit cycle. (a) Time trace showing the definition of the phase zero as the peak of the potential. (b) Limit cycle in the phase plane showing contours with the same asymptotic phase. These are called isochrons. Initial condition $x(0)$ is mapped to y_0 on the limit cycle with phase ϕ . (c) Geometry of phase resetting. At point i a perturbation along the x -axis at phase ϕ tends to a new asymptotic phase ϕ' which is closer to spiking with respect to the original phase. The same perturbation at point ii delays the next spike time

generally in [110]) allows us to define the phase of any point in the neighborhood of the limit cycle, which as above we call $\Theta(x)$. In most of this chapter, we define the zero phase to be the peak of the voltage, so any point on the limit cycle has a uniquely defined phase lying between 0 and T .

In practice, the isochrons can only be computed numerically. However, for some simple models, an exact formula can be found (cf. Exercise 5). Izhikevich [136] provided MATLAB code for computing isochrons for planar limit cycles. Figure 8.2 shows the color-coded isochrons for the Morris–Lecar model. The function $\Theta(x)$ is not at all isotropic and shows very slow changes near the spike and very rapid changes near the “ghost” of the saddle–node bifurcation. For example, the time difference between the isochrons labeled a and b is about 2.5 ms, whereas the time difference between those labeled c and d is about 40 ms. This says that small changes in the variables near points c and d will have a much greater effect on the phase of the oscillator than similar magnitude perturbations near points a and b. We will see the implications of this next.

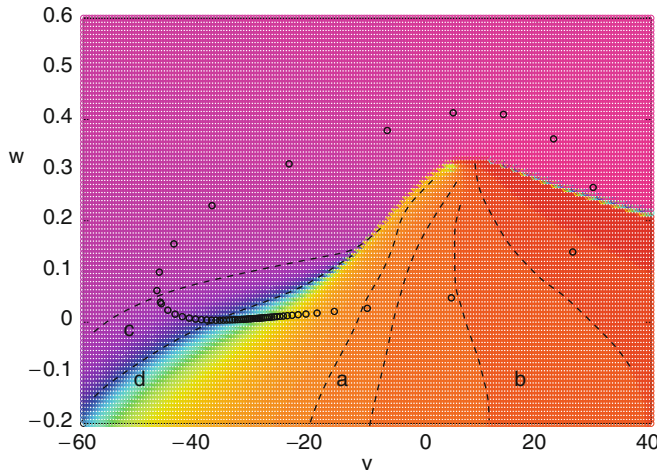


Fig. 8.2 Morris–Lecar oscillator (class I parameters, $I = 42$) showing the asymptotic phase function $\Theta(x)$ and some representative isochrons. Black dots show values on the limit cycle in increments of 2.5 ms. The period of the limit cycle is 145 ms

8.1.1 Phase Resetting and Adjoints

Suppose we are merrily rolling along the limit cycle and a brief stimulus is given. For example, in Fig. 8.1c, we have applied a horizontal perturbation to the vector field at phase ϕ . This perturbation puts us on the isochron for ϕ' so that the phase of the oscillator is reset to a different value which depends on its initial phase. For each phase ϕ at which the stimulus is applied, we get a new phase ϕ' . The map from old phase ϕ to new phase ϕ' is called the *phase transition curve* (PTC), $\phi' = P(\phi)$. Winfree [291] and others have noted that the PTC has two different topological forms that are called type 0 (strong) and type 1 (weak) resetting. In weak resetting, the map $P(\phi)$ is an invertible map of the interval $[0, T]$ to itself. With strong resetting, the map is not invertible. For example, suppose the stimulus is so strong that the phase is always reset to 0 (that is, the neuron spikes immediately). For the classic integrate-and-fire model, any finite increase of the voltage always results in type 0 resetting (see Exercise 6), whereas for the quadratic integrate-and-fire model with infinite reset, all perturbations show type 1 resetting. (Do not confuse type 1 and type 0 phase resetting with class I and class II excitability.) For the normal form at a Hopf bifurcation, resetting can be both type 1 or type 0 depending on the size of the perturbation.

In this chapter, we will be concerned almost exclusively with type 1 resetting, where the function $P(\phi)$ is invertible. In Chap. 9, where strong coupling is applied to relaxation oscillators, we will analyze the opposite extreme, in which essentially all resetting is type 0.

Experimentalists are often interested not in the PTC, but rather in the actual change in phase due to the perturbation. This function, known as the *phase resetting*

curve (PRC), is defined as the difference between the new phase and the old phase:

$$\Delta(\phi) \equiv \phi' - \phi = P(\phi) - \phi.$$

Figure 8.3 shows some examples of experimentally computed PRCs from cortical and related neurons. In each case, if the stimulus is given at the moment of spiking, the PRC is zero. This says that a stimulus given at the moment of the action potential is ignored.

Figure 8.1a shows the time trace of, say, the voltage of a neuron, with and without the brief perturbation given at time (phase) ϕ . Suppose the time of the spike given the perturbation is at T' . We now relate T' to the PRC. Note that the phase of a limit cycle satisfies

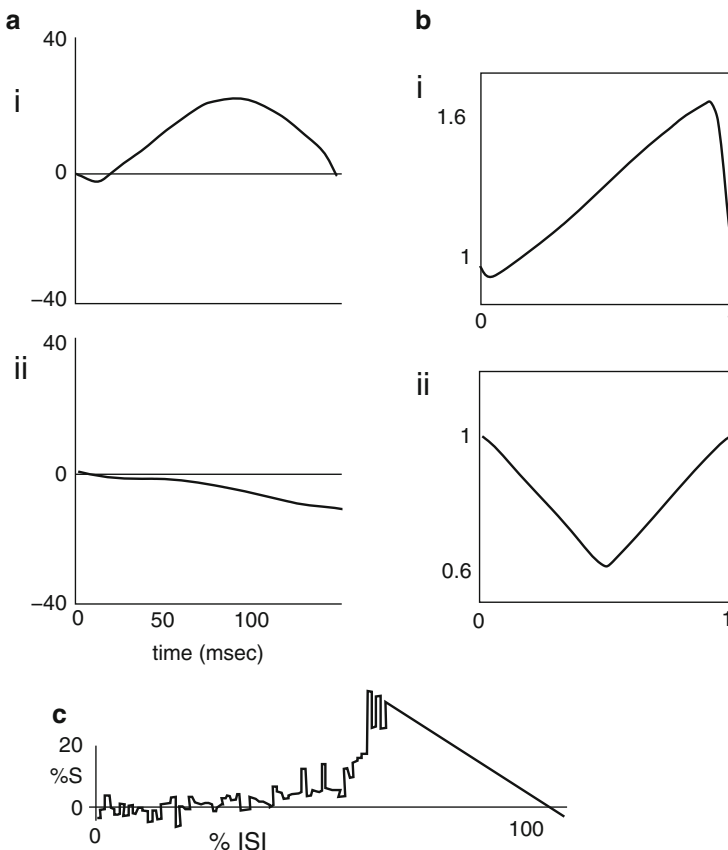


Fig. 8.3 Some experimentally measured phase resetting curves (PRCs) from neurons. (a) Enthorinal cortex cells [207] for excitatory (i) and inhibitory (ii) synaptic perturbations; (b) rat barrel cortex pyramidal cells [252] with excitatory (i) and inhibitory (ii) perturbations; (c) cat motor cortex neurons [225]. Note that in (b), $T'(\phi)/T = g(\phi) = 1 + \Delta(\phi)/T$ is plotted

$$\frac{d\theta}{dt} = 1.$$

Suppose at time ϕ the stimulus is applied and this causes a shift to a new phase ϕ' . Assume for the moment the new phase is less than T , the period of the limit cycle. (This is not an unreasonable assumption for neurons since it says that the perturbation will never cause an immediate spike; rather there is some delay.) The time until the next spike is just $\tau = T - \phi'$, so the time of the next spike is $T' = \phi + \tau = \phi + T - \phi' = T - \Delta(\phi)$. Thus, we have

$$\Delta(\phi) = T - T'. \quad (8.2)$$

Typically, if one is trying to measure a PRC either experimentally or from a numerical simulation, the time of the next event, e.g., is measured as a function of the time of the stimulus. This is just T' . If $T' < T$, then the stimulus advances the phase (speeds up the cycle) and vice versa. Figure 8.3a and b(i) shows that excitatory stimuli can lengthen the time to spiking if they occur very shortly after the spike, but otherwise they shorten the time to spiking. Figure 8.3c essentially shows only lengthening. Inhibitory stimuli (Fig. 8.3a, b(ii)) always appear to lengthen the time to the next spike – they phase-delay the oscillator.

Many people normalize the phase to lie between 0 and 1 or 0 and 2π so that we have to rescale ϕ and Δ , e.g., multiply by $1/T$ or $2\pi/T$. The rescaling is useful if we want to compare the PRCs for oscillators at different frequencies since they then have the same domain and range. Unless otherwise noted, we will not rescale the phase and the PRC.

We now relate the PRC to the phase function $\Theta(x)$ defined by the isochrons of an attracting limit cycle. Let $x = X_0(\phi)$ be the point on the limit cycle, $X_0(t)$, with phase (time) $\phi \in [0, T]$. Note that $\Theta(x) = \phi$ by definition. Consider an arbitrary perturbation, $y \in R^n$, of the vector field. The new phase is

$$\phi' = \Theta(x + y) = \phi + \nabla_X \Theta(x) \cdot y + O(|y|^2).$$

Thus, for small perturbations

$$\Delta(\phi; y) = \nabla_X \Theta(x) \cdot y.$$

(We have included y in the PRC to emphasize that this corresponds to a very general perturbation.) If we suppose the first component of the differential equation is the voltage of the neuron and take $y = (a, 0, \dots, 0)$, where a is the scalar size of the perturbation of the potential, then we see that the PRC is approximately the first component of the gradient of the phase function $\Theta(x)$ evaluated at $X_0(\phi)$. Indeed, for neuroscientists, the PRC comes from some experimental perturbation which typically involves only at most a few of the variables which make up the dynamical systems governing the oscillation. The vector function

$$Z(\phi) \equiv \nabla_X \Theta(X_0(\phi)) \quad (8.3)$$

provides a complete description of how infinitesimal perturbations of the limit cycle change its phase. Kuramoto [166] introduced the function $Z(\phi)$ and Winfree [290] was a long-time proponent of the utility of the PRC. In the correct limit, we see that they are related. The PRC is exactly related to $\Theta(X_0(\phi) + y) - \phi$, but in practice the function $\Theta(x)$ for arbitrary x is very difficult to calculate. However, the gradient evaluated at the limit cycle, the function $Z(\phi)$, is very simple to compute as we will now see.

8.1.2 The Adjoint

As we have noted, the phase function $\Theta(x)$ is not easy to compute. The function $Z(\phi)$ could be computed by applying small stimuli to the limit cycle along each of the n components of the limit cycle and then linearly interpolating the results to zero amplitude. The reader with time on her hands is urged to try this! However, it turns out that the function $Z(\phi)$ is the solution to a linear differential equation which is closely related to the linearization of (8.1) about the limit cycle.

Suppose $X_0(t)$ is a T -periodic limit cycle solution to (8.1). Let

$$A(t) = D_X F(X)|_{X_0(t)}$$

be the $n \times n$ matrix resulting from linearizing (8.1) around the limit cycle. Then solutions to the linearized equation satisfy

$$\frac{dy(t)}{dt} - A(t)y(t) \equiv (Ly)(t) = 0. \quad (8.4)$$

Let

$$(u(t), v(t)) = \int_0^T u(t) \cdot v(t) dt \quad (8.5)$$

be the standard inner product on T -periodic functions in R^n . Recall that if L is a linear operator, then the adjoint linear operator, L^* , satisfies $(u, Lv) = (L^*u, v)$ for all u, v . As shown in Exercise 3, the adjoint L^* is

$$(L^*y)(t) = -\frac{dy(t)}{dt} - A(t)^T y(t). \quad (8.6)$$

We now use Brown et al.'s [25] simple proof that $Z(t)$ satisfies the adjoint equation.

Recall that the asymptotic phase to an infinitesimal perturbation $y(t)$ is given by $Z(t) \cdot y(t)$. By definition, this phase is independent of time. Note that since $y(t)$ is arbitrarily close to the limit cycle, its dynamics are linear, so $Ly = 0$. Thus,

$$\begin{aligned} 0 &= \frac{d}{dt} Z(t) \cdot y(t) \\ &= \frac{dZ(t)}{dt} \cdot y(t) + Z(t) \cdot \frac{dy}{dt} \end{aligned}$$

$$\begin{aligned}
&= \frac{dZ(t)}{dt} \cdot y(t) + Z(t) \cdot A(t)y(t) \\
&= \frac{dZ(t)}{dt} \cdot y(t) + A(t)^T Z(t) \cdot y(t) \\
&= \left[\frac{dZ(t)}{dt} + A(t)^T Z(t) \right] \cdot y(t).
\end{aligned}$$

Note that the operator inside the square brackets is $-L^*$. Since $y(t)$ is arbitrary, we must have that

$$L^* Z(t) = 0.$$

If $X_0(t)$ is a stable limit cycle, then the operator L has a nullspace spanned by scalar multiples of $dX_0(t)/dt$ (see Exercise 1) which is a periodic function. The adjoint has a one-dimensional nullspace (in the space of T -periodic functions in R^n) as well, so $Z(t)$ must be proportional to this eigenfunction. It remains to determine the appropriate normalization. But this follows immediately from the observation that $\Theta(X_0(\phi)) = \phi$. Differentiate this with respect to ϕ and see that

$$Z(\phi) \cdot \frac{dX_0(\phi)}{d\phi} = 1.$$

This uniquely defines $Z(t)$ as the solution of $L^*Z = 0$ and $Z \cdot dX_0/dt = 1$. (Exercise 1 suggests a direct proof of this result.)

Numerically solving $L^*y = 0$ is done by integrating the equation

$$\frac{dy}{dt} = -A(t)^T y$$

backward in time. Since the limit cycle is asymptotically stable, backward integration damps out all components except the periodic one which is the solution of the adjoint equation. Suitable multiplication by a scalar provides the necessary normalization.

8.1.3 Examples of Adjoints

8.1.3.1 Ring Models

Consider the differential equation

$$x' = f(x),$$

where $f(x) > 0$ and $x \in S^1$. Thus, $f(x+1) = f(x)$. This equation has a T -periodic solution $x_0(t)$ with period

$$T = \int_0^1 \frac{dx}{f(x)}.$$

The adjoint is just $z(t) = 1/f(x_0(t))$ since $z(t)dx_0/dt = 1$. For example, consider the function $f(x) = 1 + a \cos 2\pi x$, where $|a| < 1$. This has a period $T = 1/\sqrt{1-a^2}$ and a bit of algebra shows that the adjoint is just

$$z(t) = \frac{1 - a \cos 2\pi t/T}{1 - a^2}. \quad (8.7)$$

In particular, note that $z(t)$ is always positive. One can only phase-advance the oscillator when the stimulus is positive. On the other hand, plotting $-z(t)$ as would be the response to an inhibitory stimulus looks a great deal like the PRC in Fig. 8.3b(ii). In general for any ring model, the PRC/adjoint is always nonnegative, a fact that should be obvious. Exercise 10 asks the inverse problem – given a positive PRC, find a ring model.

8.1.3.2 $\lambda-\omega$ Systems

Kopell and Howard [162] introduced a class of nonlinear oscillators (which is closely related to the normal form for the Hopf and Bautin bifurcations):

$$u' = \lambda(r)u - \omega(r)v; \quad v' = \lambda(r)v + \omega(r)u, \quad (8.8)$$

where $r^2 = u^2 + v^2$. Suppose $\lambda(1) = 0$, $\omega(1) = 1$, and $\lambda'(1) < 0$. Then there is a stable limit cycle solution $(u, v) = (\cos t, \sin t)$. Ermentrout and Kopell [71] were the first to compute the adjoint for this system; we leave it as an exercise to prove

$$z(t) = (u^*(t), v^*(t)) = (a \cos t - \sin t, a \sin t + \cos t), \quad (8.9)$$

where $a = -\omega'(1)/\lambda'(1)$. Note that the normal form of the Hopf bifurcation $\lambda(r) = 1 - r^2$ and $\omega(r) = 1 + q(r^2 - 1)$, so $a = q$.

8.1.3.3 Quadratic Integrate-and-Fire Model

The quadratic integrate-and-fire model with infinite reset,

$$V' = V^2 + I,$$

is a singular example of a scalar “ring” model. The solution to this is

$$V(t) = -\sqrt{I} \cot \sqrt{I}t.$$

The adjoint is thus $z(t) = 1/V'(t)$:

$$z(t) = \sin^2(\sqrt{I}t)/I = (1 - \cos(2\sqrt{I}t))/I.$$

An alternative way to find $z(t)$ is to compute the PTC for a finite perturbation, b (Exercise 8), differentiate with respect to b , and evaluate at $b = 0$.

We note that for a finite reset and finite spike, the model is essentially a ring model. In Exercise 11b, you will compute the adjoint for this case.

8.1.3.4 Singularly Perturbed Systems

In Exercise 9, you find a general formula for the adjoint of any stable planar limit cycle. The result is not particularly transparent. However, for a relaxation oscillator, the singular limit makes the calculation more useful. Izhikevich [133] was the first to do this and we follow his presentation here. Figure 8.4 shows the singular trajectory ($\mu = 0$) for the system

$$\begin{aligned}\mu x' &= f(x, y), \\ y' &= g(x, y).\end{aligned}$$

Let $\Gamma(t)$ be the singular trajectory. The x -component of $\Gamma(t)$ has jumps at $t = t_j$ corresponding to the jumps in the phase plane from a_j to b_j . The linearized equation is

$$\begin{aligned}0 &= f_x(\Gamma(t))x + f_y(\Gamma(t))y, \\ y' &= g_x(\Gamma(t))x + g_y(\Gamma(t))y.\end{aligned}$$

The linearized system has a solution $\Gamma'(t) = (f(\Gamma(t)), g(\Gamma(t)))$ which, because of the jumps at t_j in $\Gamma(t)$, will consist of a smooth part and a singular part (with Dirac delta functions at t_j). The adjoint equation is

$$0 = -f_x(\Gamma(t))u - g_x(\Gamma(t))v, \quad (8.10)$$

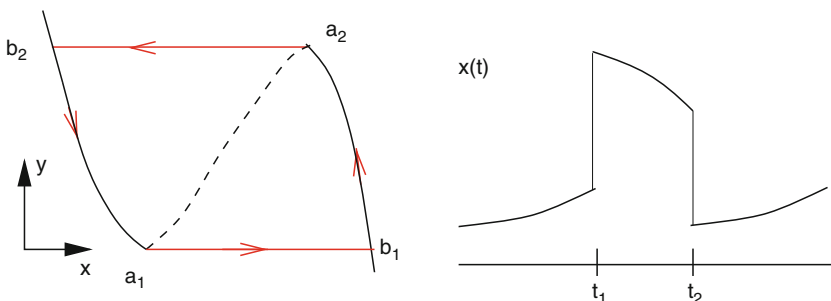


Fig. 8.4 Singular trajectory and the fast variable as a function of time

$$v' = -f_y(\Gamma(t))u - g_y(\Gamma(t))v. \quad (8.11)$$

The normalization is

$$ux' + vy' = uf(\Gamma(t)) + vg(\Gamma(t)) = 1.$$

Consider, first, the smooth parts of the trajectory, $t \neq t_j$. Along the singular trajectory, $f(\Gamma(t)) = 0$, so the normalization yields

$$v = 1/g(\Gamma(t)). \quad (8.12)$$

Since $f_x(\Gamma(t))$ is nonzero away from the jump points, equality (8.10) implies that

$$u = -\frac{g_x(\Gamma(t))}{g(\Gamma(t))f_x(\Gamma(t))}. \quad (8.13)$$

At $t = t_j$, $v(t)$ jumps from $1/g(a_j)$ to $1/g(b_j)$. From (8.11),

$$u(t) = -\frac{1}{f_y(\Gamma(t))} (v'(t) + g_y(\Gamma(t))v(t)).$$

Since v jumps, u must have a Dirac delta function singularity. Integrating across this, we have to have

$$u(t_j^+) - u(t_j^-) = -\frac{1}{f_y(a_j)} \left(\frac{1}{g(b_j)} - \frac{1}{g(a_j)} \right) \equiv c_j.$$

Thus, at $t = t_j$ we have

$$(u, v) = (c_j \delta(t - t_j), 1/g(a_j)). \quad (8.14)$$

Equations (8.12)–(8.14) provide the complete adjoint solution

8.1.4 Bifurcations and Adjoints

In general, except for the few examples described above, it is not possible to find the adjoint explicitly for a limit cycle. Certainly, the minimal condition is that an explicit solution for the limit cycle should be provided and there are very few examples of that. However, several of the examples are suggestive they may be more general than they first appear. For example, in class I excitability, the behavior near the bifurcation is the same as that of the quadratic integrate-and-fire/theta model. Thus, we expect that near the onset of rhythmicity, the adjoint of *any* class I oscillator should look like $1 - \cos t$. How well does this actually work in practice? We can numerically compute the adjoint for any oscillator and compare the shape with that predicted near the bifurcation.

8.1.4.1 Class I Excitability

From (8.7) we expect that near a saddle-node on an invariant circle bifurcation, the adjoint should be proportional to $1 - \cos \theta$. As an example, we will look at the Morris–Lecar model, about which we have already exhausted a great deal of ink.

Figure 8.5 shows the numerically computed adjoint (black) and the approximation (red) for two different currents. When $I = 40$, the model is very close to the bifurcation as can be seen from the length of the period, which is nearly 1,000 ms. The adjoint is quite close to the theoretical value from (8.7). When $I = 50$, the period drops more than tenfold and the approximation is not as good, but remains qualitatively similar.

8.1.4.2 Hopf Bifurcation

Very few neural models actually undergo *supercritical* Hopf bifurcation at least at the onset of the rhythmic behavior. Thus, it is difficult to make comparisons. However, for illustrative purposes, we use a model from [104] which has a supercritical Hopf bifurcation at high applied currents. The normal form for the supercritical Hopf bifurcation is of the form (8.8) and, for this model, each component of the adjoint is a pure sinusoid:

$$u^*(\theta) = \alpha \sin \theta + \beta \cos \theta.$$

We thus compute the adjoint numerically and see how well it is approximated by pure sinusoids. Figure 8.6 shows the results for currents close to the Hopf bifurcation and further away. The key take-home lesson here is that models near a Hopf bifurcation have regimes of phase advance and phase delay in contrast to class I models, which are dominated by phase-advance dynamics.

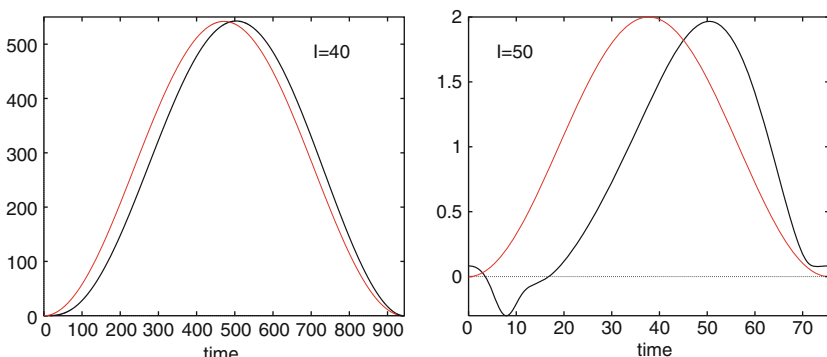


Fig. 8.5 The numerically computed adjoint for the Morris–Lecar model near the saddle–node bifurcation and its comparison with the asymptotic solution. *Left panel*, $I = 40$ and $T = 943$; *right panel*, $I = 50$ and $T = 75.5$

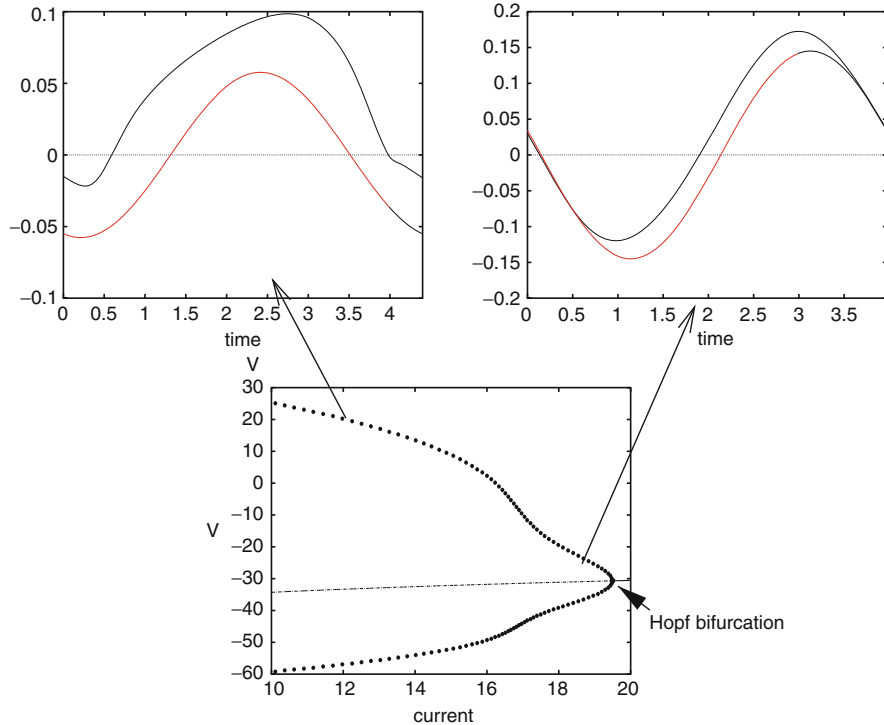


Fig. 8.6 The numerically computed adjoint for the Golomb–Amitai model near the supercritical Hopf bifurcation. *Bottom:* The bifurcation diagram as a function of the current. *Top:* The adjoint (black) and the approximation (red) $a \sin \theta + b \cos \theta$. The choices of a and b come from the Fourier expansion of the numerically computed adjoints

8.1.4.3 Limit Point

In most class II neural models, the Hopf bifurcation is subcritical but the unstable branch folds back to become stable. Thus, there is a saddle-node bifurcation of limit cycles. What can we expect the adjoint to look like in this case? A hint for the behavior can be found in returning to the $\lambda-\omega$ system (8.8) since we can easily obtain this type of bifurcation by choosing

$$\lambda(r) = p + r^2 - r^4,$$

where p is a bifurcation parameter. For $p < 0$ and small, there are two roots of $\lambda(r) = 0$, $r_1 < r_2 < 1$, corresponding to a stable and an unstable limit cycle. They coalesce when $r_1 = r_2$, which occurs when $\lambda'(r_{1,2}) = 0$. From (8.9), we see that the magnitude of the adjoint is dominated by the terms multiplied by $\omega'(r)/\lambda'(r)$ since $\lambda'(r)$ goes to zero as the limit point is approached. Thus, we expect that the magnitude of the adjoint will tend to infinity as the limit point is approached. This

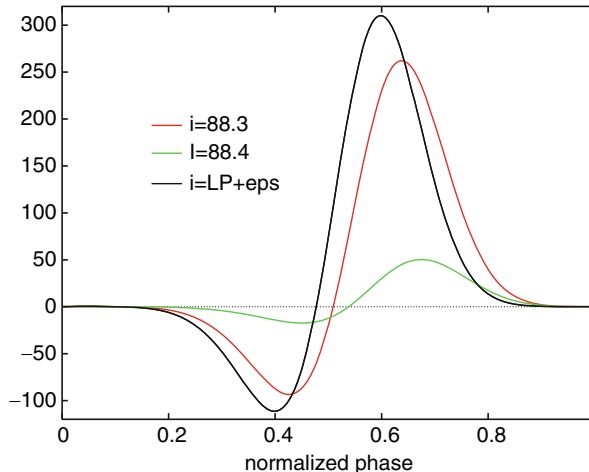


Fig. 8.7 The adjoint for the Morris–Lecar model near the turning point bifurcation. The *black curve* is closest to the limit point and the adjoint has been scaled by a factor of 10 to fit on the same figure. The phase is normalized from 0 to 1 for easier comparison since the periods are different

may seem somewhat counterintuitive since we know that $\mathbf{u}^*(t) \cdot \mathbf{u}'(t) = 1$. Thus, all of the growth of the adjoint is in a direction orthogonal to the limit cycle. Exercise 9 gives an explicit formula for the adjoint to any planar system. The computation depends on solving a scalar equation of the form

$$\frac{dc}{dt} = -(f_u + g_v)c + p(t).$$

For a planar limit cycle the attraction is determined by (see Exercise 1)

$$v = \int_0^T f_u + g_v dt.$$

As a limit point or saddle–node of limit cycles is approached, v tends to zero, so the quantity $c(t)$ will grow like $1/v$. This $c(t)$ multiplies a vector which is orthogonal to the limit cycle, so we expect to see that adjoint grow rapidly as the bifurcation is approached. Figure 8.7 confirms this fact for the Morris–Lecar model. As we approach the bifurcation, the adjoint rapidly increases. Intuitively, this makes sense: if the attraction to the limit cycle is weak, then the motion around the limit cycle will be very fast compared with the motion into the limit cycle so the isochrons will have a very pronounced twist.

8.1.4.4 Takens–Bogdanov

In Chap. 4 we showed that the M-type potassium channel (an outward current which acts at voltages near rest) can convert the transition to oscillations from

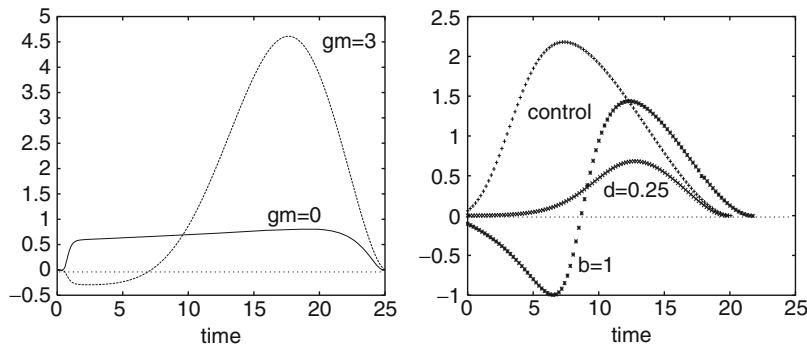


Fig. 8.8 The effects of outward currents on the PRC. **(a)** Adding an M-type potassium current to the Destexhe–Paré model adds a negative component to the adjoint. **(b)** PRCs for the quadratic integrate-and-fire model with adaptation computed by injecting a pulse with amplitude 1 for 0.2 time steps

class I (saddle-node on an invariant circle) to class II (Hopf bifurcation). The mechanism for this transition is organized around the Takens–Bogdanov bifurcation (see Fig. 4.5b). Our results so far suggest this should have a big effect on the shape of the PRC. Figure 8.8a shows the effects of adding an M-type current to the Destexhe–Paré model described in Chap. 4. The PRC (where we have added sufficient current so that the cell fires at about 40 Hz) switches from strict positivity to a substantial negative region.

How can we understand this switch? In Exercise 13 in Chap. 4, you show that the quadratic integrate-and-fire model with adaptation (4.19) is locally equivalent to the normal form for the Takens–Bogdanov bifurcation. We compute a PRC for this model by injecting a brief current (the discontinuous resetting makes the adjoint difficult to compute accurately) at different times in the spike cycle. Recall the equations

$$V' = I + V^2 - u, \quad u' = a(bV - u)$$

with reset of V to c when there is a spike and at the same time the variable u is increased by an amount d . The adaptation is manifested in two ways: the parameter b governs subthreshold effects and the parameter d governs effects due to spikes. Since only the parameter b (which acts at rest) can switch the cell from class I to class II, we expect that this parameter will produce a negative component in the PRC. This is illustrated in Fig. 8.8b. With no adaptation ($b = d = 0$), the PRC is close to the canonical form, $1 - \cos t$. When $b = 1$, the resting state loses stability at a Hopf bifurcation and the excitability class is II. The PRC shows a pronounced negative component. However, if $b = 0$ and d is nonzero, then the PRC stays positive but is flattened in the early part of the cycle. In Exercise 13, you explore this effect more systematically in a biophysical model.

8.1.4.5 Other Currents

Other currents affect the PRC in subtle ways. A good project would be to explore these currents in a systematic fashion. Exercises 13 and 14 explore the roles of adaptation and the sag current. The reader should look at some of the other oscillators from Chap. 4 and examine the adjoints of these models.

8.1.5 Spike-Time Response Curves

With the advent of the *dynamic clamp*, it is possible to add and subtract channels and synapses in real neurons in a slice. (The dynamic clamp is an experimental method in which the potential of a neuron is fed into a computer model for a channel and the resulting current is injected into the cell. Thus, it is possible to add channels to and remove channels from real neurons in real time.) Several experimental groups now use the dynamic clamp to look at the behavior between two or more cells when they are coupled with artificial (that is, computer) synapses. The first step in understanding the behavior of these coupled neurons is to understand how a single neuron responds to a synaptic current. If this current is an infinitesimal perturbation of the membrane potential, then we know that the response is precisely the adjoint. More generally, we can compute a PRC to any stereotypical input. Indeed, we already used this idea to compute the PRC for the quadratic integrate-and-fire model by applying a small rectangular pulse of current at different times.

Let us consider this generally. Let X be the vector of variables satisfying

$$\frac{dX}{dt} = F(X)$$

and let $G(t, t_0)$ be the vector of inputs parameterized by the onset time t_0 . Our system is thus

$$\frac{dX}{dt} = F(X) + G(t, t_0).$$

We assume $X' = F(X)$ has a stable limit cycle. We multiply by the phase gradient function (8.3) and find that the phase of the oscillations satisfies

$$\frac{d\theta}{dt} = 1 + Z(t) \cdot G(t, t_0). \quad (8.15)$$

This is an exact equation for the phase. We start with $\theta = 0$ and ask when $\theta(T') = T$, the period of the unperturbed limit cycle. T' is a function of t_0 and is the time of the spike. When $G(t, t_0) = 0$, $T'(t_0) \equiv T$. We integrate (8.15) and find

$$\theta(T') = T' + \int_0^{T'} Z(t) \cdot G(t, t_0) dt = T.$$

Solving this for T' tells us when the next spike occurs. The PRC for a stimulus $G(t, t_0)$ is just $\text{PRC}(t_0) = T - T'(t_0)$, which tells us how much the stimulus advances or delays the next spike. Suppose $G(t, t_0)$ is small, say, $G(t, t_0) = \epsilon g(t, t_0)$. Then we can expand $T'(t_0)$ as

$$T'(t_0) = T + \epsilon \tau(t_0) + \dots$$

This leads to

$$0 = \tau(t_0) + \int_0^T Z(t) \cdot g(t, t_0) dt,$$

so to lowest order

$$\text{PRC}(t_0) = \int_0^T Z(t) \cdot G(t, t_0) dt. \quad (8.16)$$

This is the time advance/delay due to the input G . Often one expresses it in terms of the fraction of a cycle, in which case we divide by T . Note that if $G(t)$ is a Dirac delta function along one of the components of X , then the PRC is exactly the same as the adjoint as it is just a component of Z .

When $X(t)$ is a membrane equation and $G(t, t_0)$ is a synaptic current generated by an alpha function type of synapse,

$$G(t, t_0) = \alpha(t - t_0)(V_{\text{syn}} - V(t)),$$

then function (8.16) is called the spike-time response curve (STRC). It tells us how the spike time of a neuron is changed by a stereotypical input as a function of when that input arrives. In the reduction to maps and phase equations which follows later in this chapter, we do not distinguish between the STRC and the usual PRC.

8.2 Who Cares About Adjoints?

At long last, we come to the core of this chapter. We have spent several pages extolling the virtues of PRCs, STRCs, and adjoints. There are at least two ways in which these response functions are useful. First, we can use them directly to create systems of pulse-coupled equations which we can reduce to maps. Second, we can use the weak coupling assumption and averaging to reduce arbitrarily coupled networks of neurons to systems of equations on a torus. The most obvious application of a PRC is to study the effects of periodic drive on an oscillator; the subject of the next section.

8.2.1 Relationship of the Adjoint and the Response to Inputs

The adjoint and its cousin the PRC are relevant beyond purely oscillating neurons and they provide information about how a neuron responds to inputs *even when it is*

not a regular oscillator. Clearly, if the neuron is in a stable resting state, then a weak input will, by definition, have no effect on it and only strong inputs will produce a spike. In this case, there is no dependence of the response on the time of the inputs since the cell is at rest. However, if the neuron is subject to sufficient depolarization so that it is firing (irregularly, perhaps), then even “weak” inputs can alter the time of a spike. The amount by which the spike time is altered depends on when the neuron last spiked and thus we can expect that there is some relationship to the PRC. Gutkin et al. [114] numerically showed that the shifting of spikes in a nonstationary system (that is, a nonconstant stimulation, either slowly varying input currents or fast noisy inputs) is determined by the steady-state PRC of the neuron. That is, the PRC can tell us how an input shifts a spike even when the neuron is not a regular oscillator.

One of the most common measurements done by neurophysiologists is the post-stimulus time histogram (PSTH). The PSTH is the probability of a spike occurring at a given time t after the onset of a stimulus. It is measured by collecting the spike times of a neuron over many repetitions of the same stimulus. Implicit in the usefulness of the PSTH is that the dynamics are stationary. For example, the mean firing rate of the neuron before the stimulus is constant and the time between repetitions is long enough so that the effect of the stimulus wears off. A cartoon of the PSTH is shown in Fig. 8.9. A brief stimulus is applied at $t = 0$ causing the probability of firing for the neuron to increase transiently before returning to the baseline uniform probability. Gutkin et al. [114] showed that the PSTH can be related to the PRC, an argument that we now repeat. We assume:

1. The mean firing rate of the neuron is $1/T$ prior to the stimulus and the probability over trials of firing is uniform.
2. The stimulus is sufficiently weak so that *no new spikes are added*. That is, the probability of firing is shifted, but there are no new spikes.
3. The neuron rapidly returns to its baseline mean firing rate after one cycle.

Assumptions 2 and 3 imply that the area between $t = T$ and $t = 2T$ is 1 since no new spikes are added and all the rearranging of spikes is finished within one average period. Consider the spike at time s in the figure. In the absence of the stimulus, the expected time of the next spike is $s + T$ since the mean firing rate is $1/T$. But, because of the stimulus, the expected spike time is shifted to s' . The mean period of the neuron is T , so with respect to the spike at time s , the stimulus comes $T - s$ milliseconds after the neuron last fired. From the definition of the PRC, the expected time of s' is

$$s' = s + T - \Delta(T - s) \equiv F(s).$$

Note that $F(0) = T$ and $F(T) = 2T$. Furthermore, $F'(s) = 1 + \Delta'(T - s) > 0$ since the stimulus is assumed to be weak. Thus, $F(s)$ is an invertible map from

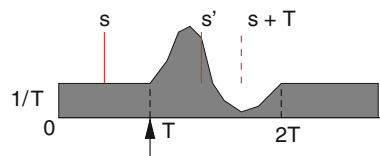


Fig. 8.9 Poststimulus time histogram for a neuron

the interval $[0, T]$ to $[T, 2T]$. The PSTH is the probability that a spike occurs in a given window of time after the stimulus. Thus, the probability that $s' < t$ for some $t \in [T, 2T]$ is just

$$\Pr\{s' < t\} = \int_T^t \text{PSTH}(t') dt'.$$

However,

$$\begin{aligned}\Pr\{s' < t\} &= \Pr\{F(s) < t\} \\ &= \Pr\{s < F^{-1}(t)\} \\ &= \frac{1}{T} F^{-1}(t).\end{aligned}$$

The last equality comes from the fact that the distribution of spikes before the stimulus arrives is uniform. We thus have the relationship between the PSTH and the PRC:

$$F^{-1}(t) = T \int_T^t \text{PSTH}(t') dt'. \quad (8.17)$$

8.2.2 Forced Oscillators

PRCs are directly computable from experimental data; thus, they provide a way of creating a model of a specific biological oscillator without needing a mechanistic basis. Let us first explore how one can use the PRC to develop a map for the dynamics of a single oscillator which is periodically forced by an external pulsatile stimulus. This type of analysis has a long history and the reader should consult the comprehensive book by Glass and Mackey [103] for references and applications to cardiac and other oscillators. Stoop et al. [252, 253] as well as several older references also used PRCs to compute the behavior of forced systems.

Suppose an oscillator $X(t)$ has a PRC, $\Delta(t)$, which describes the advance or delay as a function of the time of the stimulus, $0 \leq t < T$, where T is the period of the oscillator. Suppose a stimulus is applied every T_f time steps and let ϕ_n denote the phase of the oscillator at the instant before the stimulus arrives. Right after the stimulus, the phase is given by $P(\phi_n) \equiv \phi_n + \Delta(\phi_n)$. Recall that $\phi \in [0, T)$. Between stimuli, the oscillator advances by an amount T_f in phase. Thus, at the moment of the next stimulus, we have

$$\phi_{n+1} = \phi_n + \Delta(\phi_n) + T_f = P(\phi_n) + T_f \equiv M(\phi_n), \quad (8.18)$$

where $P(\phi)$ is the PTC. This is a map on the circle and there is a huge literature on such maps. Since PRC theory is valid mainly when stimuli are weak, the size of Δ is assumed to be small. Therefore, $P(\phi)$ is monotonic and its derivative is

$$P'(\phi) = 1 + \Delta'(\phi).$$

Invertible maps on the circle are completely characterized by their *rotation number*, which is defined as the average number of cycles covered per stimulus. We can make this more precise as follows. Instead of considering ϕ_n to be defined with respect to T , we let it evolve on the real line. The rotation number is defined as

$$\rho \equiv \lim_{n \rightarrow \infty} \frac{1}{T} \frac{\phi_n}{n}. \quad (8.19)$$

This quantity has a nice intuitive appeal. For example, if $\rho = 1$, then, on average, the oscillator completes one cycle per stimulus and we say that there is 1:1 locking. On the other hand, if $\rho = 2/3$, then the oscillator completes two cycles for each three cycles of the stimulus and we call this 2:3 locking. The rotation number is described by a beautiful theorem which we state without proof. This version of the theorem appears in Hale and Kocak [115].

Theorem. (Denjoy) *The rotation number is well defined; that is, the limit exists and is independent of the initial condition. Furthermore, if $M(\phi)$ (cf. (8.18)) is twice continuously differentiable, then:*

1. (1) ρ is rational if and only if $M(\phi)$ has a periodic orbit of some period: $\phi_{n+N} = \phi_n \text{ mod } T$.
2. (2) ρ is irrational if and only if every orbit $\{\phi_n\}$ is dense in the circle.
3. (3) ρ is a continuous function of any parameters in the function M .

We turn to the analysis of the map (8.18). We first find conditions for 1:1 locking, 2:1 locking, and 1:2 locking and determine the stability. We then look at the rotation number of two relevant simple maps as a function of T_f , the period of forcing.

For 1:1 locking, we must have $\phi_{n+1} = \phi_n + T$; that is, the oscillator must complete one cycle per stimulus. This means

$$\phi + T = \phi + \Delta(\phi) + T_f,$$

so we must solve

$$\Delta(\phi) = T - T_f \quad (8.20)$$

for ϕ . In class I neurons, the PRC is typically nonnegative everywhere, so to entrain this type of neural oscillator, the period of the forcing stimulus must be smaller than the natural period. On the other hand, for class II firing, the PRC can be both positive and negative, so the period of the forcing stimulus can be both shorter and longer than the natural period. Since $\Delta(\phi)$ is a periodic function, we expect that there will be at least two roots of (8.20) except at bifurcation points. To determine the stability, we linearize and obtain

$$y_{n+1} = (1 + \Delta'(\phi))y_n \equiv cy_n.$$

We know that $c > 0$ since the PTC is monotonic. If $\Delta'(\phi) > 0$, then $c > 1$ and the fixed point is unstable, whereas if $\Delta'(\phi) < 0$, then $0 < c < 1$ and the fixed point

is stable. The only bifurcation that can occur corresponds to $c = 1$ or $\Delta'(\phi) = 0$, which means ϕ is a double root and occurs at a local maximum or minimum of $\Delta(\phi)$.

The 2:1 locking occurs when $\phi_{n+1} = \phi_n + 2T$; that is, the oscillator fires twice for every cycle of the stimulus. In this case, we have to solve

$$\Delta(\phi) = 2T - T_f.$$

Note that if $\Delta(\phi)$ is centered around zero, then we can solve this equation when T is close to $T_f/2$. Stability follows in the same way as the 1:1 case. In general, phase locking of the form $m:1$ is very simple to analyze and is done in a manner similar to the 1:1 case.

The 1:2 locking means the oscillator fires only once for every two stimuli, so

$$\phi_{n+2} = \phi_n + T.$$

We note that $\phi_{n+2} = M(\phi_{n+1}) = M(M(\phi_n))$, where $M(\phi)$ is as in (8.18), so we must solve

$$T = 2T_f + \Delta(\phi) + \Delta[\phi + \Delta(\phi) + T_f]. \quad (8.21)$$

Obviously, this is more difficult to solve than the $m:1$ case. However, we note that if Δ is small, then this can be solved only when $2T_f \approx T$. That is, the stimulus must be roughly twice as fast as the intrinsic period of the oscillator, another intuitively appealing observation. Stability proceeds in a similar manner and we require that $c = M'(M(\phi))M'(\phi)$ be less than 1 for stability. This gives a condition on $\Delta(\phi)$ and its derivatives:

$$c = [1 + \Delta'(\phi)][1 + \Delta'(\phi + \Delta(\phi) + T_f)] < 1.$$

In general, for $m:r$ locking, in which the stimulus fires r times and the oscillator fires m times, we have to solve

$$\phi + mT = M^r(\phi),$$

where M^r is r iterates of $M(\phi)$. We note that

$$M^r(\phi) = \phi + rT_f + \dots,$$

where the remaining terms depend on Δ . Thus, for small PRCs, we want $T_f/T \approx m/r$.

The analysis above hints that whenever T_f/T is near a rational number, m/r , then there can be phase-locking and thus a rational rotation number. If the PRC is nontrivial (that is, it is not constant), then we should be able to solve for ϕ and thus find $m:r$ locked solutions for some open set of forcing periods, T_f . This means if T_f is a parameter, then $\rho(T_f)$ should be constant over the open regions where there

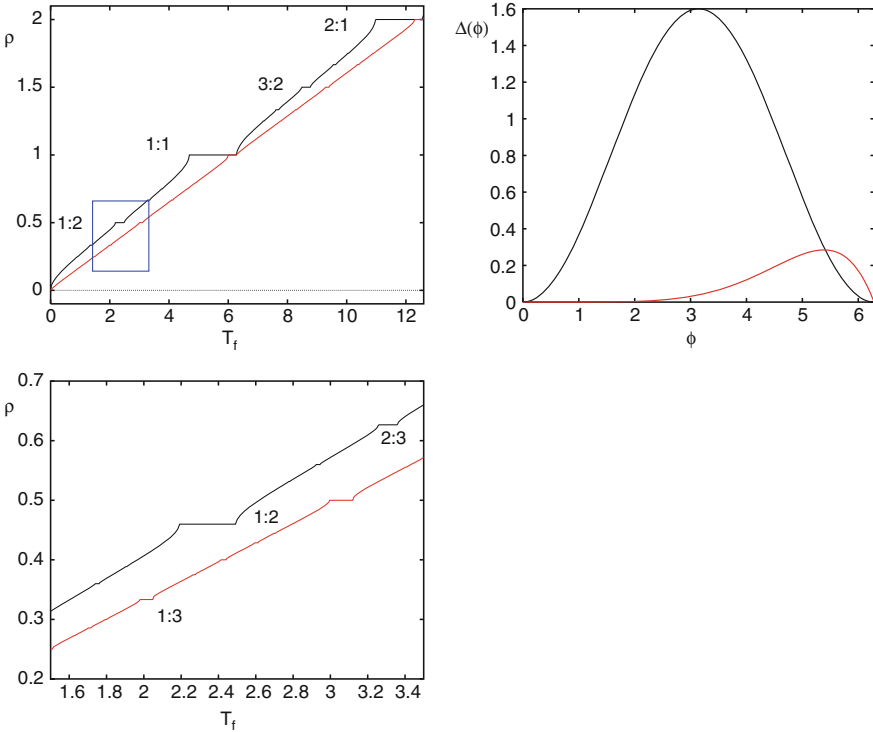


Fig. 8.10 The rotation number for the map $M(\phi) = \phi + \Delta(\phi) + T_f$ for $\Delta(\phi) = 0.8(1 - \cos \phi)$ (black) and $\Delta(\phi) = 0.000013\phi^6(2\pi - \phi)$ (red) as T_f varies. The expanded region is shown at the bottom. Some rational rotation numbers are shown. The right panel shows the relative sizes of the two PRCs. The slope of the red PRC at $\phi = 2\pi$ is the same as that of the black PRC at $\phi = 3\pi/2$

is locking. Figure 8.10 shows the rotation number for (8.18) for two different PRCs: $\Delta_1(\phi) = 0.8(1 - \cos \phi)$ and $\Delta_2(\phi) = c\phi^6(2\pi - \phi)$, where c is chosen so that the maximal magnitude of the slope is the same as Δ_1 . The shape of this PRC is meant to mimic that in Fig. 8.3c. Since the magnitude of Δ_2 is much smaller than that of Δ_1 , the width of the plateaus is much shorter. In both cases, the rotation number increases with T_f and is punctuated with regions where it is constant. This diagram is called “the Devil’s staircase.” We note an interesting pattern in the steps. The largest steps are 2:1, 1:1, and 0:1. The next largest are 3:2 and 1:2. Between any flat regions $a:b$ and $c:d$, the largest regime is always the one obeying the Farey addition rule, $(a + c):(b + d)$. Allen [2] was the first to notice this pattern in the context of neural firing.

If the slope of the PRC becomes more negative than -1 , the invertibility of $M(\phi)$ is violated and it is possible to get very complex behavior in these simple maps, such as chaos. In neural models, a slope of -1 means the neuron fires at the instant of the stimulus. Thus, it is impossible to get slopes more negative than -1 .

8.2.3 Coupled Oscillators

We now turn our attention to the case of two mutually coupled cells where we use the computed PRC to create a dynamical system. The cells are both oscillators and to start, we assume they are identical with the same period, T_0 . Each time one cell spikes, the cycle of the other cell is perturbed according to the PRC. This is the only time there is interaction between the cells. There are at least two ways to derive the dynamics. One is to derive equations for the spike times of the cells. The second is to derive equations for the phase of one cell when the other cell fires. The latter is considerably more convenient and can be formally generalized in a more straightforward manner. So that we can close this section on a good note, we start with the firing time idea.

8.2.3.1 Firing Time Maps

Consider the spike times shown in Fig. 8.11. Our goal is to derive a map for t'_j given t_j . If there was no spike t_2 , then $t'_1 = t_1 + T_0$, since the cell is oscillatory with period T_0 . The spike from cell 2 occurs at time $t_2 - t_1$ after cell 1 spikes, so the time of the next cell 1 spike is shifted according to the PRC. Recalling definition (8.2), we obtain

$$t'_1 = t_1 + T_0 - \Delta(t_2 - t_1).$$

Now, we turn our attention to t'_2 , the time of the next spike from cell 2. As with cell 1, without coupling, $t'_2 = t_2 + T_0$, but the intervening spike at t'_1 produces a phase shift in the cell 2 spike. Thus, we obtain

$$t'_2 = t_2 + T_0 - \Delta(t'_1 - t_2).$$

Note that t'_2 depends on the difference between t'_1 and t_2 , *not* the difference between t_1 and t_2 , since t'_1 is the spike occurring between t_2 and t'_2 . These equations are valid provided that neither cell spikes twice before the other cell spikes. Thus, the spike alternation must be maintained for all finite time. We can reduce this equation to a one-dimensional map for the time difference between the cell 2 spike and the cell 1 spike. Let $\tau = t_2 - t_1$ and let $\tau' = t'_2 - t'_1$. Now,

$$t'_1 - t_2 = t_1 - t_2 + T_0 - \Delta(t_2 - t_1) = T_0 - \tau - \Delta(\tau) \equiv D(\tau),$$

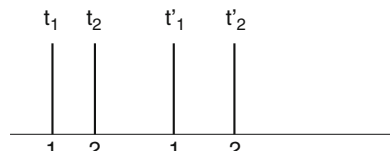


Fig. 8.11 Spike times of two coupled oscillators

so the t'_2 equation is

$$t'_2 = T_0 + t_2 - \Delta[T_0 - \tau - \Delta(\tau)].$$

We subtract the t'_1 equation from the t'_2 equation to obtain

$$\tau_{n+1} = \tau_n - \Delta[T_0 - \tau_n - \Delta(\tau_n)] + \Delta(\tau_n) = D[D(\tau_n)]. \quad (8.22)$$

The new time difference between cell 1 and cell 2 is just the composition of two identical maps, $D(\tau) = T_0 - \tau - \Delta(\tau)$. The map $D(\tau)$ tells us how much longer we have to wait for a spike when a stimulus arrives τ after the previous spike. This map is the “time” equivalent of the PTC. Recall that a fixed point of a scalar map $x \rightarrow M(x)$ satisfies $x = M(x)$ and it is stable provided that $|M'(x)| < 1$. We seek a fixed point for (8.22); thus,

$$0 = \Delta(\tau) - \Delta(T_0 - \tau - \Delta(\tau)).$$

For many of the PRCs which we have encountered (e.g., see Figs. 8.3, 8.5) $\Delta(0) = \Delta(T_0) = 0$. That is, the oscillator is not affected by stimuli at the moment it spikes. In this case, $D(0) = 0$, so synchrony $\tau = 0$ is a fixed point. Synchrony is a stable fixed point if

$$|1 + \Delta'(0) + \Delta'(T_0)(1 + \Delta'(0))| = |[1 + \Delta'(0)][1 + \Delta'(T_0)]| < 1.$$

We have not assumed $\Delta'(T_0) = \Delta'(0)$ since for experimental PRCs (e.g., see Fig. 8.3c) this may not be the case. We can also remove the absolute value since throughout this section we have assumed the phase transition map $\tau + \Delta(\tau)$ is monotonic. Thus, synchrony is stable when

$$[1 + \Delta'(0)][1 + \Delta'(T_0)] < 1. \quad (8.23)$$

For “nice” PRCs such as the adjoint (in which the PRC is continuously *differentiable*), this condition is reduced to $\Delta'(0) < 0$. There may be other fixed points as well. Indeed, since $D^2(\tau)$ is a monotonic map of the circle to itself, there must be at least one other fixed point corresponding to the so-called antiphase solutions in which $\tau \approx T_0/2$. We can see this if, for example, $\Delta(\tau) = a \sin \tau$ (or any odd periodic function for that matter). In this case, it is clear that $\tau = \pi$ is also a fixed point; as with the synchronous case, it is stable if $\Delta'(\pi) < 0$.

In the derivations, we have assumed the oscillators are identical. We leave it as an exercise for the reader to show that, with nonidentical oscillators, the map becomes

$$\tau_{n+1} = T_2 - T_1 + \tau_n + \Delta_1(\tau_n) - \Delta_2[T_1 - \tau_n - \Delta_1(\tau_n)], \quad (8.24)$$

where T_j is the natural period of oscillator j and Δ_j is the PRC.

8.2.3.2 Phase Equations

The firing time methods that we derived above are useful for pairs of oscillators, but it is difficult to generalize them to many oscillators. Instead, we will turn to the phase description of oscillators. The phase of an oscillator is complementary to its firing time in that, for our purposes, the phase is the amount of time since the oscillator last fired. Many researchers define phase so that it is normalized and represents not an absolute time, but rather the percentage or fraction of a cycle covered. As we pointed out earlier in this chapter, normalization of phase makes it easier to compare cells with different frequencies. Since the remainder of this chapter deals with phase equations, we will normalize the PRC. To prevent confusion with the unnormalized PRC, we define the normalized PRC as

$$d(\phi) = \frac{1}{T_0} \Delta(T_0\phi). \quad (8.25)$$

$d(\phi)$ is unitless and is 1-periodic. The derivative of d has the same magnitude as that of Δ .

We now derive equations for a pair of cells coupled by their normalized PRCs:

$$\theta'_1 = \omega_1 + \delta_1(\theta_2)d_1(\theta_1), \quad (8.26)$$

$$\theta'_2 = \omega_2 + \delta_1(\theta_1)d_2(\theta_2). \quad (8.27)$$

$\delta_1(\phi)$ is the “periodized” Dirac delta function – a unit impulse at every integer:

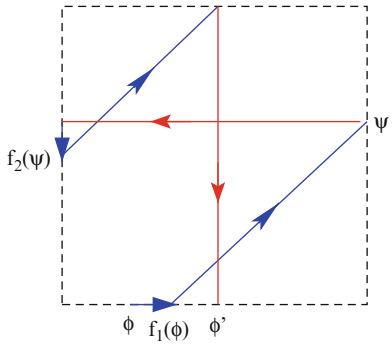
$$\delta_1(t) := \sum_{n=-\infty}^{\infty} \delta(t - n).$$

We interpret this equation to mean that each time θ_2 crosses an integer (completes a cycle), θ_1 is increased by its normalized PRC, $d_1(\theta)$. This equation is a flow on the torus and if the PRCs are not too big and the frequencies are close, then we expect that there will be a cycle of θ_1 for each cycle of θ_2 . Thus, we can define a Poincaré map; we take the Poincaré section to be $\theta_2 = 0$. That is, we let ϕ denote the *phase* of oscillator 1 at the moment that oscillator 2 fires but before oscillator 1 is reset. Figure 8.12 shows the setup. Between spikes, each oscillator runs according to its frequency until it hits 1, is reset, and jolts the other oscillator. Let $d_{1,2}(\phi)$ be the response of oscillator 1 (respectively 2) to a spike from oscillator 2 (respectively 1). Let $f_j(\phi) = d_j(\phi) + \phi$ be the PTC. This is the new phase *after* a stimulus as a function of the current phase. ψ is the phase of oscillator 2 when oscillator 1 reaches 1:

$$\psi = \frac{\omega_2}{\omega_1}[1 - f_1(\phi)].$$

To see this, note that the solution to (8.26) is $\theta_1 = \omega_1 t + f_1(\phi)$, so θ_1 fires at $t_1 = (1 - f_1(\phi))/\omega_1$. In that time, θ_2 has advanced by $\omega_2 t_1$. Oscillator 2 is reset

Fig. 8.12 Coupling of two phase equations



to $f_2(\psi)$ and fires again at $t_2 = (1 - f_2(\psi))/\omega_2$. At this point, θ_1 has advanced to $\phi' = \omega_1 t_2$. Thus, we find that

$$\phi' = \frac{\omega_1}{\omega_2}[1 - f_2(\psi)],$$

where ψ is as above. We can think of the map $\phi \rightarrow \phi'$ as the composition of two maps:

$$\begin{aligned} \phi' &= G_2(G_1(\phi)), \\ G_1(\phi) &= \frac{\omega_2}{\omega_1}[1 - \phi - d_1(\phi)], \\ G_2(\phi) &= \frac{\omega_1}{\omega_2}[1 - \phi - d_2(\phi)]. \end{aligned} \quad (8.28)$$

We must be *very careful* in applying this map and using it since it requires that the spikes of the two oscillators *alternate*. If one oscillator is sufficiently fast compared with the other, then the fast oscillator may spike twice before the slow oscillator can spike. This violates the premise of alternation which we used to derive the map. Thus, we will assume the ratio ω_2/ω_1 is sufficiently close to 1 to guarantee that this happens. In fact, the main role of the map is to examine the existence and stability of fixed points, which we now do. We note that the map (8.28) is quite similar to the time map (8.24) in that it is the composition of the effects of one oscillator on the other. Let us first suppose $\rho \equiv \omega_1/\omega_2 = 1$. As in the rest of this chapter, we assume $d_j(0) = d_j(1) = 0$. Then, $G_j(0) = 1$ and $G_j(1) = 0$, so $\phi = 0$ is a fixed point of the composed map (8.28). A fixed point $\bar{\phi}$ is linearly stable if

$$\lambda = G'_2(G_1(\bar{\phi}))G'_1(\bar{\phi})$$

is less than 1 in magnitude. That is,

$$[1 + d'_1(0)][1 + d'_2(1)] < 1. \quad (8.29)$$

This is exactly the same condition as we saw for stability of the synchronous state for the time map (8.23) since $d(\phi) = \Delta(T_0\phi)/T_0$ [see (8.23) and (8.25)]. Other locking patterns besides 1:1 are possible. In Exercise 18, the reader is asked to derive equations for 2:1 locking in which oscillator 1 fires twice for each firing of oscillator 2.

8.2.3.3 Mirolo and Strogatz

It is possible to analyze larger systems of pulse-coupled oscillators, but owing to the singular nature of the coupling, only special types of solutions can be easily analyzed. In particular, “all-to-all” identical pulse coupling was first analyzed by Mirolo and Strogatz [204]. These authors studied strong coupling between oscillators; that is, the PTC is not invertible. Specifically, they assumed in absence of coupling each oscillator obeys dynamics governed by $x_j(t) = f(t)$, where $f(t)$ is a prescribed function satisfying $f(0) = 0$, $f(1) = 1$, $f'(t) > 0$, and $f''(t) < 0$. When $x_j(t) = 1$, it is reset to 0. For example, if $f(t)$ is a solution to the integrate-and-fire model, then with rescaling of time, $f(t)$ will satisfy the assumptions. Note that the quadratic integrate-and-fire models do not satisfy the concavity assumption, so the Mirolo–Strogatz theorem does not hold. Oscillators communicate with each other by advancing those which have not fired by an amount $\epsilon > 0$. Each oscillator is coupled identically to all the others with the following rules:

1. At time t^- , if m oscillators fire (cross 1), then all other oscillators which are below 1 are increased by $m\epsilon$
2. If this increment is sufficient to cause an oscillator to fire (cross 1), then it is set to 1 but does not contribute a pulse to the others
3. All oscillators at 1 are immediately reset to 0.

Because the oscillators are *identical*, rule 2 implies that once an oscillator joins a group which has fired (by crossing 1 due to the inputs) it is *absorbed* into the group for all times and will remain synchronous with the oscillators in the group. Intuitively, it is clear how this type of strong coupling will lead to synchronization of the entire group by the process of absorption. Indeed, as more and more oscillators become absorbed, their effect on the remaining oscillators becomes very large and will rapidly bring them into the synchronized pool.

Mirolo and Strogatz [204] proved, with the above assumptions regarding $f(t)$ and the coupling, the set of initial conditions for which the oscillators are not completely absorbed has measure zero. We sketch the proof for $N = 2$ as it is the basis for the general proof and it also exposes some problems with basic assumptions of the model. As with the rest of this section, we reduce the analysis of the behavior of a pair of oscillators to a simple map.

Since $f(t)$ is monotonic, $f(0) = 0$, and $f(1) = 1$, $f(t)$ has an inverse, $t = g(x)$, which provides the phase (or time) in the cycle given the value $x \in [0, 1]$. Let ϕ be the phase of oscillator B right after oscillator A fires; that is, after oscillator B has received a kick from oscillator A. If oscillator B is pushed past 1, we are done since

now oscillators B and A are synchronous; we therefore assume $\phi < 1$. Oscillator B will fire at time $1 - \phi$ and at this point oscillator A is at $x_A = f(1 - \phi)$. Oscillator A receives a kick of size ϵ and if this now exceeds 1, we are done since the two are synchronous. Thus, suppose $f(1 - \phi) + \epsilon < 1$. The phase of oscillator A is now $g(f(1 - \phi) + \epsilon) \equiv h(\phi)$. We are exactly where we started before except that the roles of oscillators A and B are reversed. Since the oscillators are identical, the complete map is just two iterates of $h(\phi)$. Thus, our map is

$$\phi \rightarrow h(h(\phi)) \equiv R(\phi).$$

Note that the domain of $R(\phi)$ is not the whole interval $[0, 1]$ because for any finite ϵ , if ϕ is sufficiently close to 0, then $f(1 - \phi) + \epsilon$ will cross 1. Let δ be such that $f(1 - \delta) + \epsilon = 1$. The function $h(\phi)$ is defined for $\phi \in (\delta, 1)$. f and g are monotonically increasing, so $h' < 0$; that is, h is monotonically decreasing. Since $R(\phi) = h(h(\phi))$, we must have $h(\phi) > \delta$ as well. That is, $\phi < h^{-1}(\delta)$ because h is a decreasing function. Thus, the domain of R is the interval $(\delta, h^{-1}(\delta))$. We need to prove this is nonempty. That is, $\delta < h^{-1}(\delta)$ or, equivalently, $h(\delta) > \delta$. But, clearly, $h(\delta) = 1 > \delta$.

We can define the map on the whole of $[0, 1]$ as follows. For $\phi > h^{-1}(\delta)$, we set $R(\phi) = 1$ and for $\phi < \delta$, we set $R(\phi) = 0$. These conditions correspond to absorption, that is, once you hit 0 or 1, you stay there for all time. Since the phase space is the circle, point 1 is identified with 0.

Before continuing with the analysis, it is useful to consider a specific example, say, $f(t) = t(2 - t)$. Then, $g(x) = 1 - \sqrt{1 - x}$. Figure 8.13 shows $R(\phi)$ for this example when $\epsilon = 0.02$. Note that the map is only defined for a subinterval of $[0, 1]$. There is a single fixed point at $\phi = 1/2$ and it is evidently a repeller (since the slope at the fixed point is greater than 1). The red curve shows successive iterates of the map until there is absorption and $\phi = 0$. Any initial condition except the fixed point will be absorbed into either 0 or 1 after a finite number of cycles.

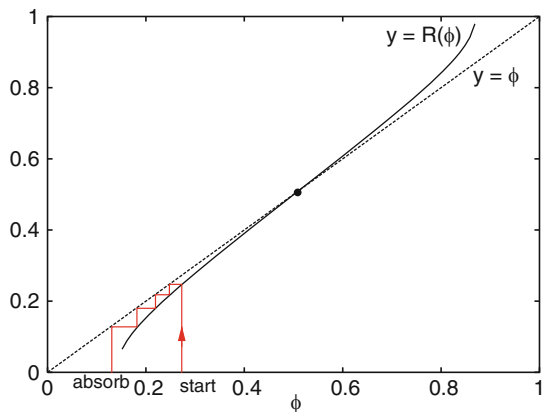


Fig. 8.13 Miroollo–Strogatz map with $f(t) = t(2 - t)$ and $\epsilon = 0.02$

Thus, we can prove almost all initial data are eventually absorbed if we can prove two things about $R(\phi)$: (1) there is a single fixed point and (2) it is unstable. Since $R(\phi) = h(h(\phi))$, we can prove the second of these if we can show that $|h'(\phi)| > 1$ for all ϕ where it is defined. Since f and g are inverses, $f'(y) = 1/g'(f(y))$, so

$$h'(\phi) = -g'(f(1 - \phi) + \epsilon).f'(1 - \phi) = -\frac{g'(f(1 - \phi) + \epsilon)}{g'(f(1 - \phi))}.$$

Let $u = f(1 - \phi)$. Then,

$$h' = -g'(u + \epsilon)/g'(u).$$

By hypothesis, $f'' < 0$, so $g'' > 0$; thus, $g'(u)$ is monotonically increasing. This means $g'(u + \epsilon) > g'(u)$ for $\epsilon > 0$. Thus, the above ratio is less than -1 and we have proven that any fixed points (if they exist) are unstable.

All that is left to do is to prove there is a unique fixed point. If there is a fixed point for $\phi = h(\phi)$, then this is also a fixed point for $\phi = R(\phi)$ since $R(\phi) = h(h(\phi))$. Let $F(\phi) = \phi - h(\phi)$. Note that $F(\delta) = \delta - h(\delta) = \delta - 1 < 0$. On the other hand, $F(h^{-1}(\delta)) = h^{-1}(\delta) - \delta > 0$, so there is root between $(\delta, h^{-1}(\delta))$. Since $F'(\phi) = 1 - h'(\phi) > 2$, this root is unique.

Mirroll and Strogatz prove the all-to-all case for N oscillators in a similar manner. The original motivation for their work was a conjecture by Charles Peskin for the leaky integrate-and-fire model. For the leaky integrate-and-fire model, the profile of $x(t)$ is $1 - \exp(-t)$, so this satisfies the concavity assumption, which is critical. On the other hand, the quadratic integrate-and-fire model and other models like it rise to the spiking threshold in a manner which can be concave up. What happens in this case is for the reader to explore.

8.2.4 Other Map Models

Ermentrout and Kopell [73] studied the circuit shown in Fig. 8.14 in order to understand results from the Whittington laboratory [286]. Specifically, gamma (40 Hz) rhythms were induced in brain slices which contained both halves of the hippocampus. Long fibers connected the two halves and there was consequently a delay in the coupling between the two networks. The experiments showed that for each spike forced by the excitatory cells, the local inhibitory cells fired “doublets” or pairs of spikes. But the doublets only occurred when the two halves were synchronized. The figure shows a simple abstraction of the circuit (Fig. 8.14a) and the spiking pattern of one side near synchrony (Fig. 8.14b). The single excitatory–inhibitory pair is driven by the excitatory cell. That is, without the synaptic excitation, the inhibitory cell would not fire. The feedback inhibition from the inhibitory cell slows the excitatory cell down to about a 40-Hz rhythm. Thus, the first spike, I_1 , is a consequence of the excitation from the local circuit and the second spike, I_2 , comes from the distant excitation.

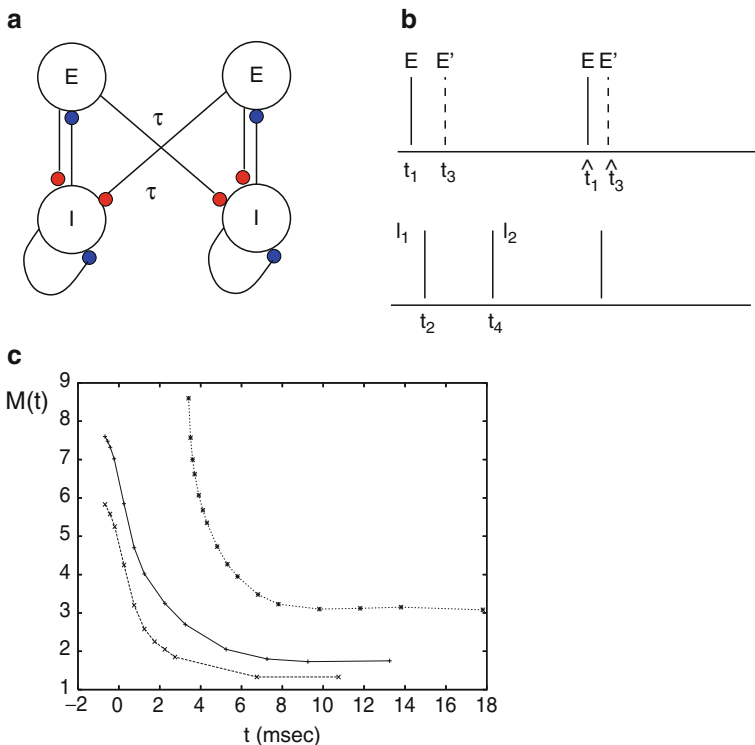


Fig. 8.14 Hippocampal oscillatory circuit. (a) Two “columns” coupled via excitatory (E) to inhibitory (I) synapses with a delay. (b) Times of spikes in the two columns. (c) Spiking time map for inhibitory neuron (see the text)

Let us devise a simple map for this model and then use this to analyze the existence and stability of the synchronous state. To do this, we will make some simplifying assumptions:

- (1) The excitatory cell spikes a *fixed* time after the last inhibitory spike that it received.
- (2) All inhibitory spikes produce the *same* amount of inhibition of their target excitatory cells.
- (3) The second inhibitory spike (I_2) occurs at a time which depends on the time difference between its two excitatory inputs.
- (4) The first inhibitory spike (I_1) occurs a *fixed* time after the local excitatory spike that it received.
- (5) The delay τ between columns is not long compared with the period of the uncoupled system.

Assumption 1 implies the excitatory cells have no memory of when they last spiked and what keeps them from spiking is the inhibition. They can only spike when the

inhibition has worn off sufficiently. Assumption 2 says that each time the inhibitory cell spikes, the total inhibition to the excitatory cell is reset to the maximum where it then decays. Assumption 3 is crucial. It says the inhibitory cell has some memory of when it last fired since a second excitatory input does not necessarily make it spike immediately. Assumption 4 says the effect referred to in assumption 3 wears off quickly. Assumption 5 is a necessary one to make the map well defined.

We now put these assumptions into mathematical terms to derive a simple map for the timing difference between the excitatory cells. In the figure, we have labeled several different times. Assumptions 1 and 2 say the time between \hat{t}_1 and t_4 is a fixed number we will call T_{ie} . Assumption 4 says the time between t_1 and t_2 is fixed at T_{ei} . Thus, the key to the derivation of the map is to determine t_4 . In absence of coupling, the period of the single circuit is $T_{ie} + T_{ei}$ by assumptions 1 and 4. If the distant excitatory cell spikes at time t_3 , then the local inhibitory cell receives the input at time $t_3 + \tau$, where τ is the delay. Assumption 3 says t_4 is a function of the time difference, $t_3 + \tau - t_1$. Call this function $M(t)$; $t_4 = M(t_3 + \tau - t_1) + t_3 + \tau$. That is, the second inhibitory spike occurs with a delay M after its second excitatory input. $M(t)$ is strictly decreasing since the longer we wait, the more time the inhibitory cell has to recover from its prior firing and the less time it takes for a second spike to occur. If t is too small, then it is possible that the inhibitory cell will never fire, so $M(t)$ will tend to infinity as t gets smaller. We are now done, since we can write

$$\begin{aligned}\hat{t}_1 &= T_{ie} + t_4 \\ &= T_{ie} + M(t_3 + \tau - t_1) + t_3 + \tau.\end{aligned}$$

We can write exactly the same type of equation for \hat{t}_3 :

$$\hat{t}_3 = T'_{ie} + M(t_1 + \tau - t_3) + t_1 + \tau.$$

We have put a prime on T_{ie} above to account for possible heterogeneities between the two circuits. For example, if the drive to the right-hand circuit is larger than that to the left-hand circuit, we would expect the right-hand circuit to recover from inhibition more quickly and hence T'_{ie} would be less than T_{ie} . Let $\zeta = t_3 - t_1$, $\hat{\zeta} = \hat{t}_3 - \hat{t}_1$, and $\mu = T'_{ie} - T_{ie}$. Then, subtracting these two equations leads to

$$\hat{\zeta} = \mu - \zeta + M(-\zeta + \tau) - M(\zeta + \tau) \equiv F(\zeta). \quad (8.30)$$

Note that because of the delay, the distant inhibitory input always occurs after the local inhibitory input even if $t_3 < t_1$. This means, unlike our timing maps above, we do not require the excitatory spikes keep the same order. Indeed, with effective inhibition coupling the cells and with the delay, we never have to worry about a distant input making the local excitatory cell fire immediately.

Let us turn our attention to the map $M(t)$. This can be numerically computed as follows. Create the single circuit so that the excitatory and inhibitory cells fire exactly one spike per period. At time t after the excitatory cell spikes, stimulate the inhibitory cell with an excitatory synaptic input and then examine when the inhibitory cell spikes. This sounds, at first, like a PRC since the inhibitory cell fires periodically and receives a stimulus. However, the basic premise of PRC theory is that the stimulus is weak enough to *move* the spike but not strong enough to *add* new spikes. In the present setting, the input from the distant excitatory cell is strong enough to cause the inhibitory cell to produce an extra spike. Thus, this is a large-amplitude theory, rather than an infinitesimal one. What accounts for the shape of this map? A biophysical interpretation is that if the input comes in right after the inhibitory cell has spiked, then the cell will not be able to fire again at all. As the second input is delayed, the inhibitory cell just manages to cross the threshold. Since the inhibitory cell is class I (cf. Chap. 4), the delay to spiking can be arbitrarily large. This accounts for the vertical asymptote. Finally, for long times after spiking, the inhibitory cell has forgotten the previous spike, so it fires at a finite delay after the input. In Exercise 19, we put some mathematical meat on these meager heuristic bones.

Turning back to (8.30), we know that $M(t)$ is a strictly decreasing function which has a rather steep slope for small t . Phase-locking between the two columns occurs if there is a fixed point of the map in (8.30). Let ξ be such a fixed point. It is linearly stable if $|F'(\xi)| < 1$, which from the definition of F (8.30) means

$$-1 < \frac{1}{2}[M'(-\bar{\xi} + \tau) + M'(\bar{\xi} + \tau)] < 0.$$

The right-hand inequality is always true since M' is a decreasing function. However, if M is very steep, then the left hand condition can be violated. Since the slope decreases with large delay τ , increasing τ can stabilize a given fixed point. If the two columns are identical, $\mu = 0$, and $\bar{\xi} = 0$ is the synchronous fixed point. The stability condition reduces to $M'(\tau) > -1$. Thus, the delay must be large enough to prevent the destabilization. However, the delay should also not be too long (see Exercise 20).

8.3 Weak Coupling

We will now analyze a pair of nonlinear oscillators which are coupled in an arbitrary fashion, but the coupling is “weak.” Kuramoto [166] popularized the methods and ideas of weak coupling using a very intuitive geometric concept which employs the gradient of the phase map $\nabla_X \Theta(x)$ – an object which we have seen is the solution to the adjoint.

8.3.1 Geometric Idea

Suppose $X' = F(X)$ has an asymptotically stable limit cycle, $U(t)$. Consider two identical oscillators which are coupled:

$$\frac{dX_j}{dt} = F(X_j(t)) + \epsilon G_j(X_j(t), X_k(t)), \quad (8.31)$$

where $j = 1, 2$ and $k = 3 - j$. Kuramoto suggested a simple approach to this. We make the change of coordinates along the limit cycle, $\theta_j = \Theta(X_j)$, where Θ is the asymptotic phase function as in Fig. 8.1. Then

$$\begin{aligned} \frac{d\theta_j}{dt} &= \nabla_X \Theta(X_j) \cdot \frac{dX_j}{dt} \\ &= \nabla_X \Theta(X_j) \cdot F(X_j(t)) + \epsilon \nabla_X \Theta(X_j) \cdot G_j(X_j, X_k) \\ &= 1 + \epsilon \nabla_X \Theta(X_j) \cdot G_j(X_j, X_k). \end{aligned} \quad (8.32)$$

This equation is exact but quite useless since we do not know what $X_j(t)$ is, so we cannot evaluate the right-hand side. However, if ϵ is small, then $X_j(t)$ is close to $U(t)$, which is close to $U(\theta_j)$. Thus, (8.32) becomes an equation which only involves the phases, $\theta_{1,2}$:

$$\frac{d\theta_j}{dt} = 1 + \epsilon \nabla_X \Theta[U(\theta_j)] \cdot G_j[U(\theta_j), U(\theta_k)]. \quad (8.33)$$

Equation (8.33) is intuitively appealing since it shows that the evolution of the phase is determined by a product of the coupling with the response function. Winfree [290] deduced this equation on first principles. For neurons, the coupling is often only through input currents to the membrane potential of the cell, leading to a simpler pair of equations:

$$\begin{aligned} \frac{d\theta_1}{dt} &= 1 + \epsilon P_2(\theta_2)d_1(\theta_1), \\ \frac{d\theta_2}{dt} &= 1 + \epsilon P_1(\theta_1)d_2(\theta_2), \end{aligned}$$

where $d_j(\theta)$ is the PRC for the oscillator and $P_j(\theta)$ is the synaptic input of the presynaptic oscillator. Note the similarity between this simple equation and (8.26) and (8.27). One can regard (8.33) as a smooth equivalent of the pulsatile coupling we considered above.

We exploit the fact that ϵ is small once more to further reduce (8.33). Let us introduce the variables, $\phi_j = \theta_j - t$. Then (8.33) becomes

$$\frac{d\phi_j}{dt} = \epsilon \nabla \Theta[U(t + \phi_j)] \cdot G_j[U(t + \phi_j), U(t + \phi_k)]. \quad (8.34)$$

All functions involved are smooth and U is itself T -periodic. Thus, we have a system of the form

$$y' = \epsilon M(y, t)$$

and we can apply the method of averaging which says that $y(t)$ is close to \bar{y} , where

$$\bar{y}' = \epsilon \frac{1}{T} \int_0^T M(\bar{y}, t) dt.$$

Recall that $\nabla_X \Theta(X)$ is exactly the solution to the adjoint equation, $Z(t)$. Applying averaging to (8.34) results in the following equations:

$$\begin{aligned} \frac{d\phi_1}{dt} &= \epsilon H_1(\phi_2 - \phi_1), \\ \frac{d\phi_2}{dt} &= \epsilon H_2(\phi_1 - \phi_2), \end{aligned} \quad (8.35)$$

where

$$H_j(\phi) = \frac{1}{T} \int_0^T Z(t) \cdot G_j[U(t), U(t + \phi)] dt. \quad (8.36)$$

The beauty of (8.35) is that the interactions between the two oscillators only show up in the phase differences between them: $\phi_2 - \phi_1 = \theta_2 - \theta_1$. Indeed, let $\psi = \phi_2 - \phi_1$ denote the phase difference between the two oscillators. Then subtracting the two equations in (8.35) results in the following *scalar* equation for the phase difference:

$$\frac{d\psi}{dt} = \epsilon [H_2(-\psi) - H_1(\psi)]. \quad (8.37)$$

Stable (unstable) fixed points of (8.37) correspond to stable (unstable) periodic solutions to the full equations (8.31). For example, if $\psi = 0$ is a stable fixed point of (8.37), then the two oscillators will synchronize.

Equation (8.35) generalizes to N coupled neural oscillators, leading to the following system of differential equations:

$$\frac{d\phi_j}{dt} = \epsilon H_j(\phi_1 - \phi_j, \phi_2 - \phi_j, \dots, \phi_N - \phi_j), \quad j = 1, \dots, N. \quad (8.38)$$

Although (8.38) represents a considerable simplification of a general system of N coupled oscillators, it is by no means a trivial system to analyze and there are many open problems concerning the behavior of this dynamical system on the N -torus. An entire book could easily be devoted to the subject! We define a *phase-locked* state of (8.38) to be a solution of the form

$$\phi_j(t) = \Omega t + \xi_j,$$

where Ω is the *ensemble* frequency, $\xi_1 = 0$, and ξ_j are constants called the relative phases. We pin ξ_1 to zero since you can add an arbitrary constant to all of the phases

$\phi_j(t)$ corresponding to the arbitrary translation in time of any autonomous limit cycle oscillator. Thus, the existence of a phase-locked solution to (8.38) reduces to solving a set of N algebraic equations in the N unknowns, $\Omega, \xi_2, \dots, \xi_N$:

$$\Omega = \epsilon H_j(-\xi_j, \xi_2 - \xi_j, \dots, \xi_N - \xi_j), \quad j = 1, \dots, N. \quad (8.39)$$

If we can find such states, then there is a convenient theorem which provides sufficient (*but not necessary*) conditions for stability.

Theorem [65]. *Let $S = \{\Omega, 0, \xi_2, \dots, \xi_N\}$ be a phase-locked solution to (8.38). Let a_{jk} denote the partial derivative of $H_j(\eta_1, \dots, \eta_N)$ with respect to η_k evaluated at S . Suppose $a_{jk} \geq 0$ and that the matrix $A = (a_{jk})$ is irreducible. Then S is asymptotically stable.*

We provide an intuitive definition for irreducibility. Draw N points on a paper. Draw a directed line from point j to point k if $a_{jk} > 0$. The matrix A is irreducible if and only if it is possible to start at any point n and go to any other point m following the directed lines.

8.3.2 Applications of Weak Coupling

Before proceeding to specific neural examples, we examine (8.36) more closely. Recall that H_j is the average of the interaction with the PRC. Let us break G_j into two parts representing coupling terms and heterogeneity between the oscillators:

$$G_j(X, Y) = B_j(X) + gC_j(X, Y),$$

where g is the strength of the coupling between the two cells and B_j represents intrinsic differences between the two neurons. For membrane models, the main interactions are through the membrane potential, so $B_j(X)$ may be something as simple as a small bias current and $C_j(X, Y)$ is the synaptic current. In this case, (8.39) becomes the equation typically studied:

$$\Omega = \epsilon \left(\omega_j + \sum_k H_{jk}(\xi_k - \xi_j) \right) \quad (8.40)$$

with $\xi_1 = 0$.

We consider two cases for the synaptic current – chemical synapses and electrical synapses:

$$\begin{aligned} C_{\text{syn}}(X, Y) &= -s_Y(V_X - V_{\text{syn}})\mathbf{e}_V, \\ C_{\text{gap}}(X, Y) &= (V_Y - V_X)\mathbf{e}_V, \end{aligned}$$

where \mathbf{e}_V is the vector of all 0's except for a 1 in the voltage component and $s_Y(t)$ is the synaptic response of the presynaptic cell. If we define $V^*(t)$ to be the voltage component of the adjoint solution, $V(t)$ the potential, and assume except for the heterogeneity both cells are identical, then we see that

$$H_j(\phi) = \omega_j + h(\phi),$$

where

$$h(\phi) = h_{\text{syn}}(\phi) \equiv \frac{1}{T} \int_0^T V^*(t)s(t+\phi)[V_{\text{syn}} - V(t)]dt, \quad (8.41)$$

$$h(\phi) = h_{\text{gap}}(\phi) \equiv \frac{1}{T} \int_0^T V^*(t)[V(t+\phi) - V(t)]dt. \quad (8.42)$$

We remark that these equations have a nice intuitive interpretation. The adjoint is (at least for weak perturbations) a scaled version of the PRC of a neuron. When the PRC is computed, it is done by perturbing with a brief *current*. However, chemical synapses between cells are best modeled as *conductances*. Thus, the effect of a presynaptic conductance change on the postsynaptic cell is the product $Q(t) \equiv V^*(t)(V_{\text{syn}} - V(t))$. The presynaptic cell alters the phase of the postsynaptic cell by averaging the effective response, $Q(t)$, with the time course of the synapse. The function $Q(t)$ will not differ substantially from the adjoint, $V^*(t)$, for excitatory conductances since $V_{\text{syn}} - V(t)$ is positive except for a short period when the neuron spikes. (Recall that $V_{\text{syn}} = 0$ mV for excitatory synapses.) However, there can be a rather large difference between $Q(t)$ and $V^*(t)$ for inhibitory synapses since the reversal potential can sometimes be very close to the resting state of the neuron. In Project 3 given later, you can explore how the reversal potential of the inhibition affects the synchronization properties of pairs of cells. Since the reversal potential of inhibition varies a great deal during the development of the nervous system, this could have important implications in setting up local cortical circuits.

8.3.3 Synaptic Coupling near Bifurcations

Equation (8.41) provides a formula for the interaction function between a presynaptic and a postsynaptic neural oscillator. Equation (8.37) provides the equations for the phase difference between two coupled neurons. Suppose both neurons are identical. Then the phase difference, ψ , satisfies

$$\psi' = -2H_{\text{odd}}(\psi), \quad (8.43)$$

where $2H_{\text{odd}}(\psi) = H(\psi) - H(-\psi)$. Any continuous odd periodic function vanishes at $\psi = 0$ and $\psi = T/2$, where T is the period of the function. Thus, a pair of mutually coupled neural oscillators will always have a synchronous and an *antiphase* pattern of behavior. If $\bar{\psi}$ is a zero of $H_{\text{odd}}(\psi)$, then from (8.43), it will be

stable if and only if $H'_{\text{odd}}(\bar{\psi}) > 0$. (Note the minus sign in the equation!) For a pair of mutually coupled identical oscillators, the key function is the odd part of the interaction function. Zeros of this function are phase-locked states. In general computing H and its odd part must be obtained numerically since the explicit form for the adjoint is not generally available. However, near bifurcations, we have a formula for the adjoint and thus we can study some of the effects of frequency and synaptic parameters on the ability of a pair of neurons to synchronize. Furthermore, near bifurcations $V(t)$ is close to a fixed point, so we replace $p_0 - g_{\text{syn}}(V(t) - V_{\text{syn}})$ by I , a constant current j positive for excitatory and negative for inhibitory synapses.

Suppose we choose

$$s(t) = \frac{e^{-\beta[t]_+} - e^{-\alpha[t]_+}}{\alpha - \beta}$$

as our synaptic conductance. Here, $[t]_+$ is the positive part of t ; the alpha-function synaptic conductances vanish for $t < 0$.

$$H(\phi) = \frac{I}{T} \int_0^T V^*(t) \sum_{j=-\infty}^{\infty} s(t + jT + \phi) dt.$$

The sum arises since the synaptic function $s(t)$ is not itself periodic, so we have to “periodize” it by adding the synaptic response for every spike at intervals of the period. We leave it as an exercise to the reader to show that

$$H(\phi) = \frac{I}{T} \int_0^{\infty} V^*(t - \phi) s(t) dt.$$

Since the interval of integration is nonnegative, we can drop the $[]_+$ and just evaluate the integrals. Finally, we can rescale the period of the oscillations, allowing us to express $V^*(t)$ and $H(\phi)$ in simple sines and cosines. Thus, a long-period oscillation is like an oscillation of period 2π , but with very fast synapses: $\alpha \rightarrow \alpha/\omega$ and $\beta \rightarrow \beta/\omega$, where $T = 2\pi/\omega$.

Near bifurcations we have an explicit formula for the adjoint, so we can analyze $H(\phi)$ explicitly by evaluating the integrals. Suppose the neural oscillator is class I so that the adjoint is $V^*(t) = 1 - \cos t$. If the synaptic current is $Is(t)$ with $I > 0$ for excitatory synapses and $I < 0$ for inhibitory, then

$$H_{\text{odd}}(\phi) = -I \frac{\alpha + \beta}{(\alpha^2 + 1)(\beta^2 + 1)} \sin \phi.$$

We recover the well-known result [67, 278] that excitatory coupling ($I > 0$) results in stable antiphase and inhibitory coupling ($I < 0$) results in stable synchrony.

The behavior near a Hopf bifurcation depends on the parameters in the normal form. The adjoint can be written as $V^*(t) = -\sin(t) + q \cos(t)$, where q is a parameter from the normal form. Evaluation of the integral yields

$$H_{\text{odd}}(\phi) = I \frac{q(\alpha + \beta) + \alpha\beta - 1}{(\alpha^2 + 1)(\beta^2 + 1)} \sin \phi.$$

Unlike systems near a saddle–node, the stability of, say, synchrony depends on the timing of the synapses and the parameter q . Even when $q = 0$, it is possible to switch from stable synchrony to stable antiphase as the frequency of the oscillator (the timing of the synapses) changes.

In neither case does there exist bistability between synchrony and antiphase, nor are any other phase-locked patterns possible. The reason for this is that the adjoint has only pure sines and cosines without any higher modes. Looking at, say, Fig. 8.3a(i) or c, it is clear that these two simple models for the adjoint (PRC) are not always good approximations. We can combine the two types and add two more terms to obtain a pretty good approximation for neural PRCs:

$$V^*(t) = a(1 - \cos(t)) + c(1 - \cos(2t)) + b \sin(t) + d \sin(2t). \quad (8.44)$$

With this model, we find

$$\begin{aligned} H_{\text{odd}}(\phi) &= \left(\frac{-a(\alpha + \beta) - b(\alpha\beta - 1)}{(\alpha^2 + 1)(\beta^2 + 1)} \right) \sin \phi \\ &\quad + \left(\frac{-2c(\alpha + \beta) - d(\alpha\beta - 4)}{(\alpha^2 + 4)(\beta^2 + 4)} \right) \sin 2\phi. \end{aligned} \quad (8.45)$$

We remark that since we have normalized the period to be 2π , the parameters α and β should be scaled as $\alpha = \alpha_0 T$ and similarly for β , where α_0 is the true synaptic time scale and T is the period of the oscillator. Note that for T large, the terms b and d dominate.

8.3.4 Small Central Pattern Generators

A CPG is a network of neurons which is able to produce a patterned oscillator output to motor neurons. For example, in Chap. 4, we looked at a model for the respiratory oscillation driven by the so-called pre-Bötzinger complex. Much research has been done on simple locomotor CPGs which govern the different gaits for walking, running, etc. Most mammalian CPGs are poorly understood and their actual location in the brain is not known. However, the story for certain fish and invertebrates is much clearer. There are numerous review articles on CPGs and their modeling. (See Grillner et al. [109] for a recent review with many references to other reviews or Yuste et al. [294] for a call to treat cortical circuits in the way that motor patterns have been treated.) We will consider three examples: finger tapping, hand clapping, and quadrupedal locomotion.

In a clever series of experiments Kelso and collaborators (see his book for a complete discussion and analysis [149]) studied the transition from one pattern to another as the frequency of finger tapping increased. In the experiment (and you can do this yourselves) the subject is asked to tap his fingers in an alternating rhythm. The subject is asked to speed up the rhythm and try to maintain the pattern. However,

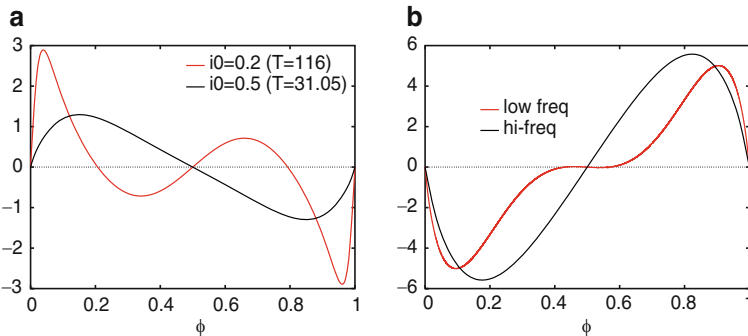


Fig. 8.15 Weakly coupled Wang–Buszaki model for inhibitory (left) and excitatory (right) coupling

at high enough frequencies, the subject tends to switch to synchronous tapping. The subject is able to tap fingers synchronously at all frequencies, thus, there appears to be bistability between the two types of coupling.

Imagine that each finger is controlled by an oscillatory circuit and that the two sides are synaptically coupled. Then we can ask whether this kind of model can explain the bistability and the switch as the frequency increases. Figure 8.15 shows a numerical computation for the Wang–Buszaki model with inhibitory and excitatory synapses as the frequency changes. (The Wang–Buszaki model is a simple conductance-based model used for fast-spiking inhibitory neurons. Its equations are available on the online site). At low frequencies with inhibitory coupling (about 9 Hz) both the synchronous and the antiphase state are stable since the odd part of H has a positive slope. However, at higher frequencies (30 Hz) only the synchronous state is stable. Thus, there is a transition from bistability to monostability at high frequencies. In contrast, with excitatory coupling (Fig. 8.15, right), the synchronous state is unstable for both high and low frequencies. This simple model of mutually coupled inhibitory circuits shows that we can induce a switch from the antiphase state to synchrony as the frequency increases. Van Vreeswijk et al. [278] demonstrated this phenomenon for weakly coupled integrate-and-fire neurons and also showed that a similar effect occurs in the Hodgkin–Huxley model. We can use (8.44) and (8.45) to analytically show this result.

8.3.4.1 Quadruped Gaits

An interesting and well-studied problem is the existence and stability of patterns of movement in four-legged animals (quadrupeds). There are many subtly different gaits; here we present only the so-called primary gaits. Table 8.1 shows the relative phases of the six primary gaits. $x_1(t)$ is the dynamics of a single limb, so all the other limbs can be specified in terms of their relative phase with the left-rear limb. Golubitsky et al. [106] derived minimal circuits which can explain the gaits using symmetry arguments. Their methods are elegant and from them they concluded that the minimal number of oscillators required is eight, corresponding to two oscillators

Table 8.1 Common simple quadruped gaits

Name	Left rear	Right rear	Left front	Right front
Pronk	$x_1(t)$	$x_1(t)$	$x_1(t)$	$x_1(t)$
Rack/pace	$x_1(t)$	$x_1(t + \frac{1}{2})$	$x_1(t)$	$x_1(t + \frac{1}{2})$
Bound	$x_1(t)$	$x_1(t)$	$x_1(t + \frac{1}{2})$	$x_1(t + \frac{1}{2})$
Trot	$x_1(t)$	$x_1(t + \frac{1}{2})$	$x_1(t + \frac{1}{2})$	$x_1(t)$
Jump	$x_1(t)$	$x_1(t)$	$x_1(t \pm \frac{1}{4})$	$x_1(t \pm \frac{1}{4})$
Walk	$x_1(t)$	$x_1(t \pm \frac{1}{2})$	$x_1(t \pm \frac{1}{4})$	$x_1(t \pm \frac{3}{4})$

per limb. Their reasoning goes something like this. Suppose there are only four oscillators and suppose an animal has both a stable walk and a stable trot. Then, by symmetry, it must also have a stable pace. Since no animal both paces and walks, there must be additional structure to break the symmetry. We can see this for ourselves by considering the following network of four coupled oscillators:

$$\begin{aligned}\theta'_1 &= H_a(\theta_2 - \theta_1) + H_b(\theta_3 - \theta_1) + H_c(\theta_4 - \theta_1), \\ \theta'_2 &= H_a(\theta_1 - \theta_2) + H_b(\theta_4 - \theta_2) + H_c(\theta_3 - \theta_2), \\ \theta'_3 &= H_a(\theta_4 - \theta_3) + H_b(\theta_1 - \theta_3) + H_c(\theta_2 - \theta_3), \\ \theta'_4 &= H_a(\theta_3 - \theta_4) + H_b(\theta_2 - \theta_4) + H_c(\theta_1 - \theta_4).\end{aligned}\quad (8.46)$$

Here, $\theta_1, \dots, \theta_4$ are the left-front, right-front, right-rear, and left-rear limb oscillators, respectively. Connections labeled H_a are left-right coupling, those labeled H_b couple “diagonal” limbs, and those labeled H_c couple the same side. Phase-locked solutions have the form

$$\theta_j = \omega t + \phi_j,$$

where $\phi_1 = 0$, Ω is the ensemble frequency, and ϕ_2, ϕ_3 , and ϕ_4 are the phases of the other limbs relative to the left-front limb, θ_1 . We are interested in several types of solutions. The walk corresponds to $W = (0, \pi, 3\pi/2, \pi/2)$, the trot to $T = (0, \pi, 0, \pi)$, the pace to $P = (0, \pi, \pi, 0)$ and the bound to $B = (0, 0, \pi, \pi)$. The “pronk” is a fully synchronous state. If you walk your dog slowly, you will notice that she moves using the walk, whereas as you speed up, she will switch to a trot, the gait used in the show ring. (Hopefully, your dog will have nice long legs to make this evident; my dog, a corgi, makes the observation somewhat difficult.) We leave as an exercise the analysis of this network. If the functions H_a , H_b , and H_c are general and periodic, then there will be a walk state if and only if $H_b = H_c$. From this, you can deduce that there is also a trot and a pace state and that they must have the same stability properties. This result (easily deduced in the present case) actually follows from the symmetry arguments of Golubitsky et al.

8.3.4.2 Excitatory/Inhibitory Coupling

We have already seen that near a saddle-node bifurcation, weak excitatory coupling tends to push pairs of oscillators into antiphase. However, most cortical networks

consist of networks with both excitation and inhibition. Can the inhibition affect the response of coupled networks? Naturally, this depends on the nature of the individual neurons, but, at least near bifurcations, we can explore these questions using simple models such as the theta model. Consider a single “column” consisting of an excitatory and an inhibitory cell:

$$\theta'_e = 1 - \cos \theta_e + (1 + \cos \theta_e)(0.25 - 2s_i), \quad (8.47)$$

$$\theta'_i = 1 - \cos \theta_i + (1 + \cos \theta_i)(-0.2 + 2s_e), \quad (8.48)$$

$$s'_e = 4[1 + \exp(-20(1 + \cos \theta_e))](1 - s_e) - s_e/3, \quad (8.49)$$

$$s'_i = 4[1 + \exp(-20(1 + \cos \theta_i))](1 - s_i) - s_i/8. \quad (8.50)$$

When there is simulation, this produces a nearly 40-Hz rhythm. (In absence of inhibition, the network fires at 200 Hz.) Figure 8.16 shows the results of a weak coupling analysis of the above network. There are several important points. The inset shows the interaction function for a purely excitatory network adjusted so that the frequency is about 40 Hz. $H(\phi)$ has a positive slope at the antiphase solution and a negative slope at $\phi = 0$, so synchrony is unstable but the antiphase state is stable. This, of course, was anticipated from our results above. However, in an excitatory–inhibitory network, the period (at least for strong recurrent inhibition) is largely determined from the decay of the inhibition. In this case, excitatory–excitatory

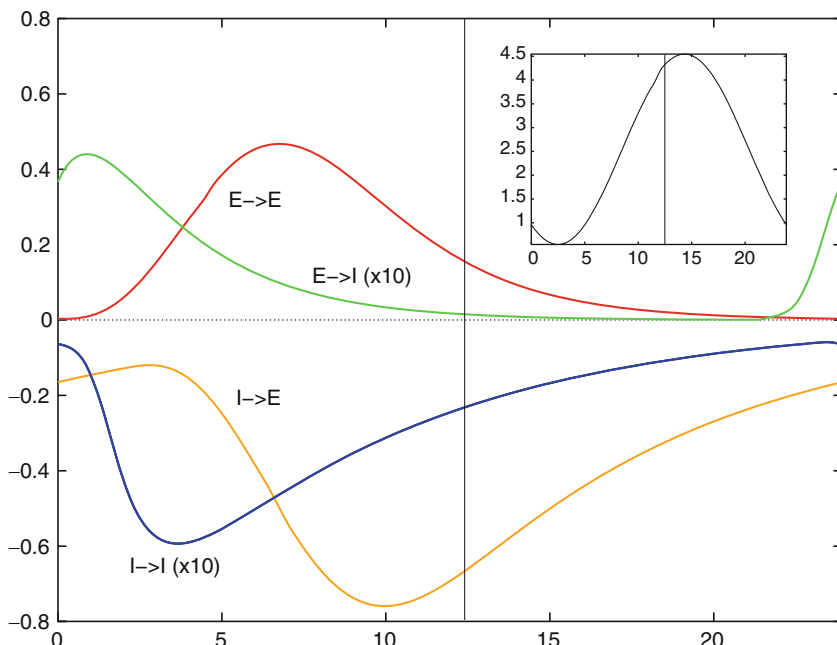


Fig. 8.16 Interaction functions for an excitatory–inhibitory pair. The *inset* shows a pure excitatory network

coupling no longer stabilizes the antiphase state. Instead, there is a near synchronous state which is stabilized. Coupling to the inhibitory cell is an order of magnitude less efficacious than coupling to the excitatory cell. This is because the excitatory cell is really the driver of the rhythm, with the inhibitory cell firing only because of the strong transient excitatory cell input. Note that inhibitory → excitatory coupling is quite strongly synchronizing but also produces a stable antiphase solution. We leave it as an exercise for the reader to simulate a pair of these simple models and show that the weak coupling results predict what happens for the full model.

It should not be surprising to the reader that the effect of, say, excitatory coupling between a pair of cells in isolation is quite different from excitatory coupling between the same pair in the presence of recurrent inhibition. In this case, we can regard the inhibition as a delayed negative feedback – much like an additional outward current. Since the PRC of an oscillator is sensitive to the presence of different currents, these same currents should affect the behavior of coupled pairs of oscillators.

Pfeuty et al. [214] explored how synchrony between neurons coupled with gap junctions depends strongly of the shape of the PRC. We can see this geometrically by recalling that the interaction function for a pair of cells coupled with gap junctions has the form

$$H_{\text{gap}}(\phi) = \frac{1}{T} \int_0^T V^*(t)[V(t + \phi) - V(t)]dt.$$

Here, $V(t)$ is the somatic potential and $V^*(t)$ is the adjoint. Synchrony is stable if $H'_{\text{gap}}(0) > 0$, which we write as

$$H'_{\text{gap}}(0) = \frac{1}{T} \int_0^T V^*(t)V'(t)dt.$$

Figure 8.17 provides a geometric interpretation for how the shape of the PRC can alter synchrony for gap junctions. If the area of the product of $V'(t)$ (the black

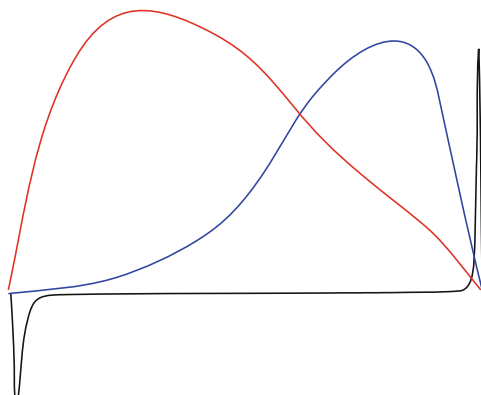


Fig. 8.17 $V'(t)$ and two different adjoints

curve) and the adjoint (red or blue curves) is positive (negative), then synchrony will be stable (unstable). Since the bulk of the PRC is toward the right for the blue curve, the total area is positive and synchrony will be stable, whereas for a PRC like that in the red curve, synchrony will be unstable. Ermentrout and Kopell [?] were the first to make this argument. Pfeuty et al. showed how the addition of a persistent sodium current or removal of some potassium current can shift the PRC from the rightward-leaning to the leftward-leaning case and thus demonstrated how intrinsic membrane properties alter the stability of the synchronous state.

8.3.4.3 Dendritic Structure

All of the results for weak neural coupling have considered only point neurons. The same methods here can be applied to models with active dendrites by discretizing them to a finite number of compartments and then computing the adjoint. However, if the dendrites are nothing more than passive cables, then we can treat the dendrite as a cable with a sealed end at the apical tip and a periodic current at the somatic end due to the oscillating soma. Suppose there is a synapse at a point x on the dendrite (where $x = 0$ is the soma). Then, the synaptic current felt at the soma from a synaptic current $I(t)$ at x is

$$I_{\text{soma}}(t) = \int_0^\infty G(x; s) I(t - s) ds,$$

where $G(x; t)$ is the Green function associated with the dendrite. That is, the dendrite acts as a linear filter. Thus, if $H(\phi)$ is the interaction function for a synapse occurring at the soma, then the interaction function for a synapse a distance x from the soma on a passive dendrite is simply

$$H(x; \phi) = \int_0^\infty G(x; s) H(\phi - s) ds. \quad (8.51)$$

Crook et al. [51] showed how stability of synchrony between two oscillators changes as the position of the synapse is changed. For example, if we take $H(\phi) = \sin \phi$ and $G(x; t) = \exp(-t) \exp(-x^2/t)/\sqrt{\pi t}$ (which is the Green function for an infinite dendrite), then at $x \approx 1.25$, the slope of $H(x; \phi)$ at $\phi = 0$ changes sign. Thus, distal synapses (further away than about 1 space constant) will have synchronization properties opposite to those of proximal synapses.

8.3.5 Linear Arrays of Cells

There are a number of neural systems which can be regarded as a one-dimensional array of oscillators, at least at a crude level. The locomotor pattern generator of the

lamprey (an eel-like fish vampire) is among the best characterized examples of such a model [41]. The leech swim generator is also organized in a linear array [23]. However, some sensory systems are similarly organized, notably the procerebral lobe (“olfactory brain”) of the slug [77]. In both the lamprey and the slug brain, the network of oscillators produces oscillatory waves which propagate down the network. Interestingly, similar waves have been observed in cortical brain slices in which the magnesium is reduced [292]. In all of these systems, the local uncoupled network appears to oscillate, so the idea of a locally coupled network of intrinsic oscillators is a good first approximation. Some jellyfish have swim generators which are organized into a ring, so one-dimensional arrays of oscillators with periodic boundary conditions could also be biologically relevant [199].

For simplicity, we discuss only nearest-neighbor coupling. The more general types of coupling can also be analyzed but not as transparently. Consider a linear array of N oscillators, possibly with heterogeneity in the frequencies:

$$\theta'_j = \omega_j + H_{j+1,j}(\theta_{j+1} - \theta_j) + H_{j-1,j}(\theta_{j-1} - \theta_j). \quad (8.52)$$

These equations are valid for $j = 2, \dots, N - 1$, and at the ends we can impose a number of different boundary conditions. For example, if we identify θ_0 with θ_N and θ_{N+1} with θ_1 , then we have a periodic array. On the other hand, identifying $\theta_0 = \theta_1$ and $\theta_{N+1} = \theta_N$ gives reflecting conditions. Finally, the “cut” conditions assume the interactions with $j = 0$ and $j = N + 1$ do not exist. Both the reflecting and the periodic boundary conditions lead to a homogenization of the network, whereas the cut condition can produce waves even in the absence of any heterogeneities.

8.3.5.1 Homogeneous Networks

Consider the case in which $H_{j,k} = H$ for all j, k and such that there is no heterogeneity: $\omega_j = \omega$. For the reflecting and the periodic boundary conditions, there is a synchronous state, $\theta_j = \Omega t$, where $\Omega = \omega + 2H(0)$, which is stable if and only if $H'(0) > 0$. (Note the “if” follows from the theorem in Sect. 8.3.1, but the “only if” requires explicit calculation of the eigenvalues. Since the linearized matrix is just tridiagonal, this is a relatively simple calculation. See Exercise 27). For periodic boundary conditions, there is also a wave solution of the form $\theta_j = \Omega t + 2\pi j/N$, where $\Omega = \omega + H(2\pi/N) + H(-2\pi/N)$. In the exercises, you are invited to examine this solution in more detail.

8.3.5.2 Cut Ends

The “cut” end case is rather interesting, even when there is no frequency gradient. The oscillators at $j = 1$ and $j = N$ receive less input than the rest of the oscillators. Thus, unless $H(0) = 0$, there will be no synchronous solution. That being the case, what happens? Suppose $H(\phi)$ is positive near the origin. Then, since the end

oscillators receive less input than the middle ones, we expect that they will oscillate faster, so we expect a phase gradient symmetric about the center of the chain such that the phase increases from oscillator 1 until it reaches the middle and then the phase decreases back to zero at oscillator N . If the chain is anisotropic, then we expect to see a traveling wave. To understand why this is so, consider the following model:

$$\begin{aligned}\theta'_1 &= \omega_1 + H_a(\theta_2 - \theta_1), \\ \theta'_j &= \omega_j + H_a(\theta_{j+1} - \theta_j) + H_d(\theta_{j-1} - \theta_j), \\ \theta'_N &= \omega_N + H_d(\theta_{N-1} - \theta_N).\end{aligned}\tag{8.53}$$

Now, set $\omega_j = \omega$ and suppose $H_a(\phi) \equiv 0$ so that there is only coupling from the lower-numbered oscillator. Then, clearly $\theta_1 = \omega t$ and for there to be a phase-locked solution, oscillator 2 must be of the form $\theta_2 = \omega t + \xi_d$. This means $H_d(-\xi_d) = 0$. Continuing down the chain in this manner, we see that $\theta_{j+1} - \theta_j = \xi_d$. If H_d has a nondegenerate zero (that is, one such that $H'(x) \neq 0$), then, since it is continuous and periodic, it must have at least two zeroes and one of these has a positive slope. This stable zero sets the wavelength of the traveling wave, so $\theta_j = \omega t + \xi(j-1)$. If $\xi > 0$, then the wave travels to the left and if $\xi < 0$, it travels to the right. (If oscillator 2 has a positive phase difference with respect to oscillator 1, then it fires earlier, so the wave travels to the left.) So, for unidirectional coupling, if there is a nondegenerate zero for $H_{a,d}(x) = 0$, then this sets the phase difference between successive oscillators in the chain. If the chain is anisotropic but bidirectional, then the two types of coupling will “fight it out.” For large N , it can be shown that the oscillators will form a wave (except near one end) of the form $\theta_j = \Omega t + \xi(j-1)$, where ξ is either ξ_a or ξ_d and $H_a(\xi_a) = 0$ and $H_d(-\xi_d) = 0$. A proof of this result appears in [161]. If the chain is completely isotropic, $H_a(\phi) = H_d(\phi)$, and H has a zero with a positive slope, then for large N the chain will organize into a pattern that consists of a pair of symmetric waves moving toward or away from the center of the chain. Let ξ be such that $H(-\xi) = 0$ and $H'(-\xi) > 0$. Then, the phase-locked solution will look roughly like

$$\theta_j = \Omega t - |(N+1)/2 - j|\xi, \quad j = 1, \dots, N,\tag{8.54}$$

where $\Omega = \omega + H(\xi)$. Figure 8.19a shows the phase-locked solutions for a chain of 50 nearest-neighbor-coupled oscillators along with the above approximation. Since $H(\phi) = \sin \phi + 0.5 \cos \phi$, $\xi = \tan^{-1}(0.5)$. Except near the center, this approximation matches extremely well.

By manipulating the two end frequencies, ω_1 and ω_N , while keeping the middle frequencies the same, we can produce waves of the form $\theta_j = \Omega t + \xi(j-1)$. Choose ξ so that $H'_a(\xi) > 0$ and $H'_d(-\xi) > 0$. Then choose

$$\omega_1 = \omega + H_d(-\xi) \quad \text{and} \quad \omega_N = H_a(\xi).$$

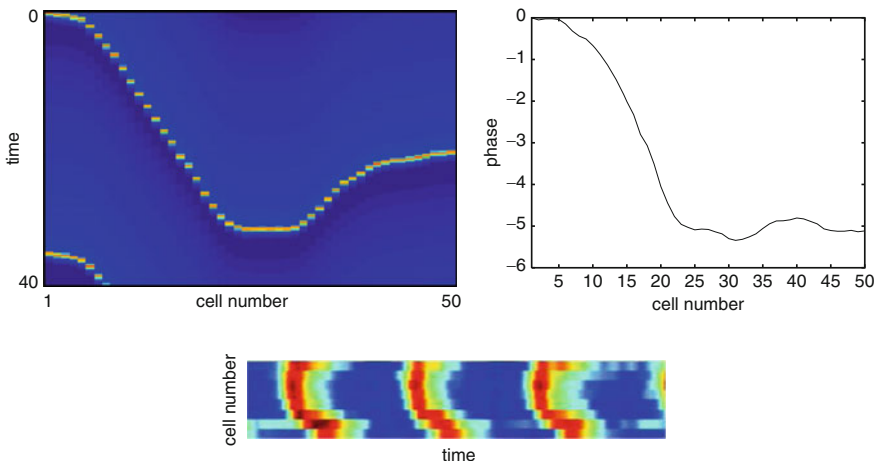


Fig. 8.18 50 Wang–Buszaki neurons coupled to nearest neighbors with inhibitory synapses (reversal potential -80 mV, decay 6 ms). Each oscillator is driven by a constant current of 0.5 plus a small random value (between -0.0035 and 0.0035) to produce heterogeneity. The coupling strength is 0.02. The phase-locked solution to the corresponding phase model is shown on the right. The space–time plot from Bao and Wu [9] for a carbachol-treated slice is shown at the bottom

One must be cautious in using a linear array of oscillators for a cortical slice because of the importance of the boundary effects and the fact that these boundary effects can have global effects on the behavior of the network. For this reason, it is best to use some type of homogeneous condition so as to avoid waves which are driven solely from the boundaries. Weak coupling theory, nevertheless, works quite well and one may be tempted to suggest the organized oscillations seen in pharmacologically treated cortical slice preparations may be a consequence of nothing more than coupled heterogeneous oscillators. Figure 8.18 shows an example of the application of weak coupling to a linear array of cells. Fifty Wang–Buszaki neurons were coupled with nearest-neighbor inhibition and a small degree of heterogeneity was introduced in the form of constant randomly chosen applied currents. The figure shows approximately one period of the cycle after a steady state is reached. Although the currents were random, the network organizes itself into a rather simple pattern which consists of a rightward-moving wave which collides with a leftward-moving wave. Using the single neuron model, we have computed the interaction function $H(\phi)$ and used this to derive the phase model (8.53). The heterogeneous currents become heterogeneous frequencies for the phase model. [In the full model, we have a frequency–current relationship for an individual cell, $\omega = F(I)$. Since I is close to I_0 , we obtain, $\omega \approx F(I_0) + c(I - I_0)$, so the frequency in the phase model is just a scalar multiple of the heterogeneity of the currents.] The phase model produces a pattern very similar to that of the full model. Such colliding waves are seen in experiments as the bottom of the figure shows.

8.3.6 Two-Dimensional Arrays

There are fewer studies (both experimentally and theoretically) of two-dimensional arrays of neural oscillators. Ren and Ermentrout [223] proved phase-locked solutions of two-dimensional arrays coupled to the four neighbors (left, right, above, and below) decomposed into the product of one-dimensional chains. This behavior is only “interesting” if the boundary effects dominate so the one-dimensional chains themselves produce interesting patterns. For example, consider an isotropic two-dimensional array of oscillators with “cut” boundary conditions. Let $H(\phi)$ have a zero with $H'(\phi)$ positive at the zero. Then the Ren theorem says that

$$\theta_{j,k} \approx \Omega t - \xi(|j - (N + 1)/2| + |k - (N + 1)/2|).$$

Figure 8.19b shows an example. The pattern of phases is like a square target pattern. This pattern completely disappears when the boundary condition is homogeneous; it is driven by the boundary. Intuitively, as with the chain, neurons along the edges receive less input than those in the center and if $H(0) > 0$, this means they will lag the oscillators in the middle, producing waves which begin at the center of the array. If $H(0) < 0$, then they will lead the center oscillators and waves start at the edges and propagate to the center.

Patterns such as shown in Fig. 8.19 are derived from the inhomogeneities at the boundaries which act like pacemakers along the edges of the medium. There are, however, patterns which arise from the intrinsic two-dimensional nature of the coupling. Spiral waves are well known in the reaction–diffusion literature and are distinct from the target waves shown in Fig. 8.19 in that they do not require any heterogeneity in the medium. Figure 8.20 shows examples of rotating waves from a variety of neural systems. The first example (that we know of) of rotating electrical activity in the central nervous system was of rabbit cortex treated with penicillin (which makes the network “epileptic”). Petsche et al. [213] reconstructed the spatiotemporal activity from a 4×4 array of electrodes placed on the surface

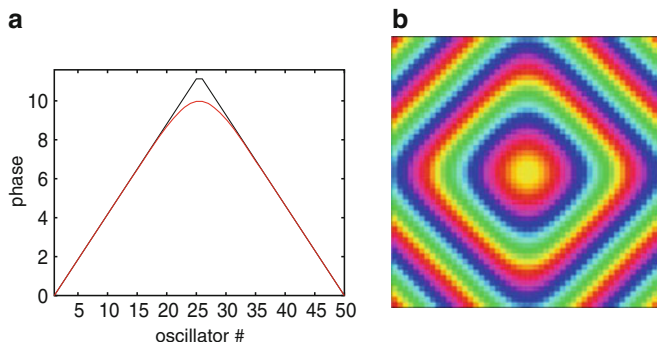


Fig. 8.19 (a) Steady-state phases for a chain of 50 oscillators, $H(\phi) = \sin \phi + 0.5 \cos \phi$, with cut ends. The *black line* is (8.54). (b) An array of 50×50 oscillators with the same H

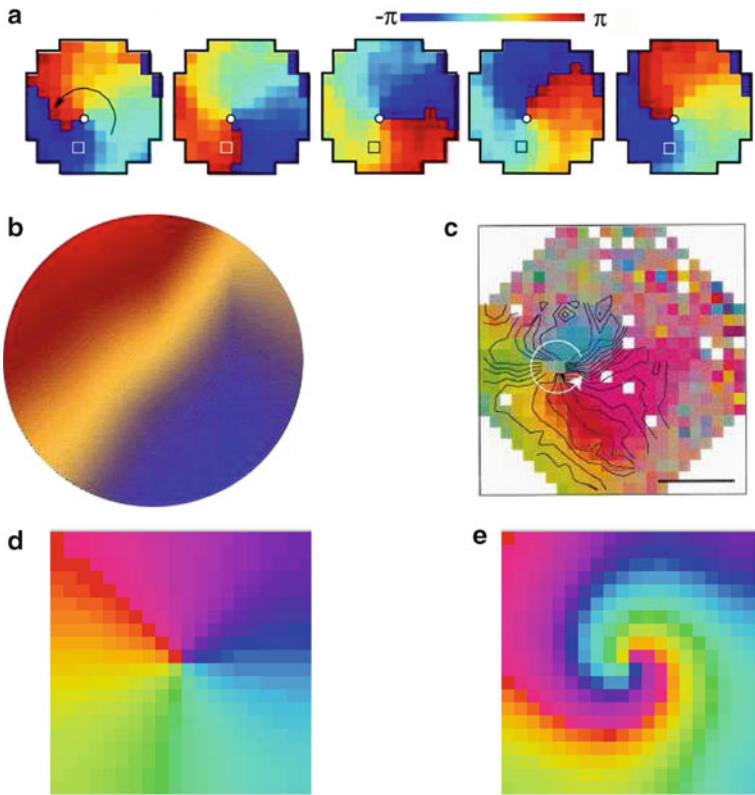


Fig. 8.20 Rotating and spiral wave patterns seen in neural tissue. (a) From [130], in a tangential disinhibited cortical slice. (b) From [195], reconstructed from EEG electrodes in a human during alpha activity. (c) From [70], optical activity in the turtle visual area. (d) Steady-state phases in a 20×20 array of nearest-neighbor phase oscillators ($H(\phi) = \sin \phi$). (e) As in (d) but $H(\phi) = \sin \phi + 0.5(\cos \phi - 1)$

of the occipital lobe (back of the brain). Mayville et al. [195] reconstructed activity from a human electroencephalogram during resting (alpha) activity. Prechtl et al. [220] used voltage-sensitive dyes to extract spatiotemporal activity from turtle cortex when certain stimuli were presented. Most recently, Huang et al. [130] created tangential slices of cortex and using voltage-sensitive dyes, they were able to record over 30 rotations of a spiral wave on the slice.

The classic model for a spiral wave in the reaction–diffusion literature consists of an excitable medium with local coupling. However, there is no need for the medium to be excitable and intrinsically oscillatory media can exhibit rotating waves and spiral waves, as seen in Fig. 8.20d and e. A simple discrete model has the form

$$\theta'_{i,j} = \omega + \sum_{k,l} H(\theta_{k,l} - \theta_{i,j}),$$

where the sum is over the four neighbors. Figure 8.20 shows the phase distribution for $H(\phi)$ as a pure sine and also with a cosine component. The existence and stability of the first pattern was established through a theorem due to Paultet and Ermentrout [210]. For any $2N \times 2N$ array with nearest-neighbor coupling such that $H(\phi)$ is odd and $H'(\phi) > 0$ for $-\pi/2 < \phi < \pi/2$, then Paultet and Ermentrout proved there exists a rotating wave and it is asymptotically stable. The pattern of phases for the wave is such that in the upper-left corner the phase is 0, in the upper-right corner it is $\pi/2$, in the lower-right corner it is π , and in the lower-left corner it is $3\pi/2$. The diagonals from these four corners have the same phase as their respective corners and all meet in the central 2×2 array of oscillators. We leave the 4×4 case as an exercise for the reader. If $H(\phi)$ is not odd, then the behavior can be quite complex. For a small amount of even periodic coupling, the pattern evolves into a spiral wave (see Fig. 8.20e), but as the even component increases, the “core” of the spiral breaks away and complicated (even chaotic) behavior ensues [66, 241]. The existence of stable phase patterns for this case has yet to be proven.

8.3.7 All-to-All Coupling

(Note that this section may be a bit technical and could easily be skipped.) In this section, we consider the so-called Kuramoto model and in so doing introduce a powerful method for analyzing large networks of neurons. We will start with a very general system of phase models with additive noise and heterogeneities in their frequency:

$$\theta'_j = \omega_j + \frac{K}{N} \sum_k H(\theta_k - \theta_j) + \sigma dW_j. \quad (8.55)$$

Here, dW_j is a white noise process (see Chap. 10), K is the strength of the coupling, which we will regard as a parameter, and H is a square-integrable periodic function. We can assume without loss of generality the average value of $H(\phi)$ is zero for if it is nonzero, we can write $H(\phi) = H_1(\phi) + \bar{H}$ (where \bar{H} is the mean of H) and then replace ω_j by $\omega_j + K\bar{H}$. The frequencies ω_j are taken from some distribution (see below). Since we can always replace θ_j by $\theta_j + Ct$, where C is a constant, we can assume the mean frequency is zero.

Rather than looking at the individual neurons, θ_j , the idea of the *population density* method is to consider the distribution of phases, θ , that any randomly chosen neuron might take. Kuramoto [166] studied a particular case when the noise is zero and $H(\phi) = \sin \phi$. His method was formal and we refer the reader to the excellent review by Strogatz [256] to see how Kuramoto proceeded. Matthews et al. [194] devised a method based on the phase density which was more rigorous and can be readily generalized to equations such as (8.55). (Strogatz describes his burst of insight for using the population density method in his popular book [254]. It reminded one of the authors of the present volume of Kekulé’s insight into the

structure of benzene, both occurring in a near dreamlike state.) Neu [208] was the first to introduce the notion of density to coupled oscillators, but he did not take it to the extent that Strogatz and those who followed him did.

We will not attempt to rigorously derive the equations; rather, we write down an equation for the population density which should allow the reader to apply it to her own results and models. We assume $N \rightarrow \infty$ and let $\rho(\theta, \omega, t)$ denote the density of oscillators with uncoupled frequency ω and phase θ at time t . Note that the oscillators cannot change their uncoupled frequency. Let $g(\omega)$ denote the density function for the distribution of frequencies. We will define g on the real line with

$$\int_{-\infty}^{\infty} g(\omega) d\omega = 1.$$

The density, ρ , satisfies the continuity equation:

$$\frac{\partial \rho}{\partial t} = -\frac{\partial}{\partial \theta} J(\theta, \omega, t) \rho.$$

This equation simply says that the phase of a given oscillator evolves in time and that total “mass” of the oscillators, $\int_0^{2\pi} \rho(\theta, \omega, t) d\theta$, is conserved. The flux is given by $d\theta/dt$, so

$$J(\theta, \omega, t) = \omega - \frac{\sigma^2}{2} \frac{\partial \rho}{\partial \theta} + KQ(\theta, t).$$

The first term is pretty obvious; the second is the diffusive flux from the noisy inputs, dW_j , which as usual are independent. The last term is

$$Q(\theta, t) = \lim_{N \rightarrow \infty} \frac{1}{N} \sum_{k=1}^N H(\theta_k - \theta).$$

The reader will recognize this as the average of H over the phases of the other oscillators, so we can write

$$Q(\theta, t) = \int_{-\infty}^{\infty} g(\omega) \int_0^{2\pi} H(\phi - \theta) \rho(\phi, \omega, t) d\phi d\omega. \quad (8.56)$$

Thus, we have the following continuity equation:

$$\frac{\partial \rho}{\partial t} = \frac{\sigma^2}{2} \frac{\partial^2 \rho}{\partial \theta^2} - \frac{\partial}{\partial \theta} ((\omega + KQ(\theta, t)) \rho). \quad (8.57)$$

Equation (8.57) is nonlinear since Q is a functional of the density ρ . Because of the nonlinearity, it is difficult to write down any closed-form solutions. However, one solution is the fully *asynchronous state* in which the distribution of phases is uniform. Substitute $\rho = 1/2\pi$ into (8.56) to see that $Q = \bar{H}$, the average value of $H(\theta)$ over $[0, 2\pi]$. We can always absorb the average value of H into the frequency

and thus we suppose $\bar{H} = 0$. Plugging this into (8.57), we see that the uniform density is in fact a solution. The key to Strogatz's analysis (and, in fact, all other analyses) is that we can linearize (8.57) about this stationary solution and study stability as a function of the coupling strength, K . Let $\rho = 1/2\pi + z$. Then, to lowest order

$$\begin{aligned}\frac{\partial z}{\partial t} &= \frac{\sigma^2}{2} \frac{\partial^2 z}{\partial \theta^2} - \omega \frac{\partial z}{\partial \theta} \\ &\quad + \frac{K}{2\pi} \int_{-\infty}^{\infty} g(\omega) \int_0^{2\pi} H'(\phi - \theta) z(\phi, \omega, t) d\omega d\phi.\end{aligned}$$

Note that the dependence on θ appears through the convolution of z with the derivative of $H(\theta)$. This linear equation is homogeneous with respect to t and to θ and so z must be 2π -periodic in θ . Thus, we can look for solutions of the form

$$z(\theta, \omega, t) = e^{in\theta} e^{\lambda t} f(\omega).$$

$f(\omega)$ is an unknown function which we must compute. Since $H(\theta)$ is periodic and square-integrable, we can expand it in a trigonometric series,

$$H(\theta) = \sum_{n=-\infty}^{\infty} a_n e^{in\theta},$$

and since H is real, $a_{-n} = \bar{a}_n$. Finally, since the average of H is zero, we also assume $a_0 = 0$. If H is differentiable, then

$$H'(\theta) = i \sum_{n=-\infty}^{\infty} n a_n e^{in\theta}.$$

With these preliminaries, we plug the solution z into the linearized equation and obtain

$$\lambda f(\omega) = \left(-in\omega - \frac{\sigma^2 n^2}{2} \right) f(\omega) - in\bar{a}_n K \int_{-\infty}^{\infty} g(\omega) f(\omega) d\omega. \quad (8.58)$$

The last part of the equation follows from the fact that

$$\frac{1}{2\pi} \int_0^{2\pi} e^{im(\phi-\theta)} e^{in\phi} d\phi$$

vanishes unless $n = m$, in which case it is $e^{in\theta}$. We will not worry about the essential spectrum for this problem and instead will focus on the discrete spectrum. Let

$$A = \int_{-\infty}^{\infty} g(\omega) f(\omega) d\omega.$$

Then from (8.58), we can solve for $f(\omega)$:

$$f(\omega) = \frac{-in a_{-n} K A}{\lambda + in\omega + \sigma^2 n^2 / 2}.$$

Recalling how A is defined, we find the equation for A must satisfy

$$A = -inKAa_{-n} \int_{-\infty}^{\infty} g(\omega) \frac{1}{\lambda + in\omega + \sigma^2 n^2 / 2} d\omega.$$

Dividing through by A (since $A = 0$ is the zero solution), we obtain

$$1 = -inKa_{-n} \int_{-\infty}^{\infty} g(\omega) \frac{1}{\lambda + in\omega + \sigma^2 n^2 / 2} d\omega. \quad (8.59)$$

We will study two cases: (1) no noise and (2) no heterogeneity. In the first case, we must have

$$1 = -inKa_{-n} \int_{-\infty}^{\infty} \frac{\lambda - in\omega}{\lambda^2 + n^2\omega^2} g(\omega) d\omega. \quad (8.60)$$

This is an equation for λ , which depending on the function $g(\omega)$ may or may not be possible to evaluate in closed form. Suppose $g(\omega)$ is symmetrically distributed around 0. Then (8.60) becomes

$$1 = -2inKa_{-n} \int_0^{\infty} \frac{\lambda}{\lambda^2 + n^2\omega^2} g(\omega) d\omega.$$

Finally, we make one last simplification. Suppose $H(\phi)$ is an odd function,

$$H(\phi) = \sum_n b_n \sin n\phi,$$

so $a_n = -ib_n/2$ and the eigenvalue equation is then

$$1 = nKb_n \int_0^{\infty} \frac{\lambda}{\lambda^2 + n^2\omega^2} g(\omega) d\omega.$$

Stability of the asynchronous solution occurs as K changes if λ crosses the imaginary axis. Clearly, $\lambda = i\beta$ is impossible, so the only way to lose stability is through a real eigenvalue. (We remark that if H has even components or if the frequency distribution is asymmetric, then the zero eigenvalue will not generally occur and instead stability will be lost through imaginary eigenvalues.) We will let λ tend to zero and use this to compute the critical value of the parameter K . Let $\omega = \lambda\gamma$ be a change of integration variables. Then

$$\int_0^{\infty} \frac{\lambda}{\lambda^2 + n^2\omega^2} g(\omega) d\omega = \int_0^{\infty} \frac{g(\lambda\gamma)}{1 + n^2\gamma^2} d\gamma.$$

As $\lambda \rightarrow 0$, this integral is just

$$g(0) \frac{\pi}{2n}.$$

Thus, we find that for each n ,

$$K_c(n) = \frac{2}{\pi g(0)b_n}.$$

In particular, for Kuramoto's case of a pure sinusoidal coupling, $b_1 = 1$ and all other $b_m = 0$, $K_c = 2/\pi g(0)$. If all the $b_j < 0$, then the asynchronous state is always stable. However, as long as $g(0) > 0$, if there is a single positive b_n , then for strong enough coupling the asynchronous state will destabilize. Since the mode $\exp(in\theta)$ becomes unstable with stronger coupling, standard bifurcation methods (see later chapters when we explore spatial models) predict that the new solutions which bifurcate from the asynchronous state will have the form

$$\rho(\omega, \theta) = \frac{1}{2\pi} + cf(\theta) \cos n\theta,$$

where c is some small parameter.

We will leave the case of noise with no heterogeneity as an exercise for the reader, but we provide a start here. Referring to (8.58), we can set $f(\omega) = 1$, a constant, since there is no frequency dependence. The integral with respect to ω becomes 1 and we have

$$\lambda = \left(-in\omega - \frac{\sigma^2 n^2}{2} \right) - in\bar{a}_n K. \quad (8.61)$$

If stability is lost for $n > 1$, then the solution which emerges will generally have n peaks and is called a clustered state. Noise-free two-clustered states are left as an exercise for the reader.

8.4 Pulse-Coupled Networks: Solitary Waves

The method of phase reduction provides a very general way to reduce systems of coupled oscillatory neurons to simple phase models. However, it presumes that the individual cells are intrinsically oscillatory. In the next chapter, we address the behavior of networks with strong coupling, some of which are not intrinsically oscillating. Recall that when a single nerve cell is stimulated, an action potential propagates down the axon mediated by the diffusion of the potential along the unmyelinated axon. Similar propagation of electrical activity can be found in *networks* of neurons in which a spatially localized region is stimulated and results in the outward spread of activity over distances of several millimeters. Figure 8.21 shows an example of an experimental demonstration of synaptically generated waves in a network of cortical cells with the inhibition blocked. A slice is removed from the brain

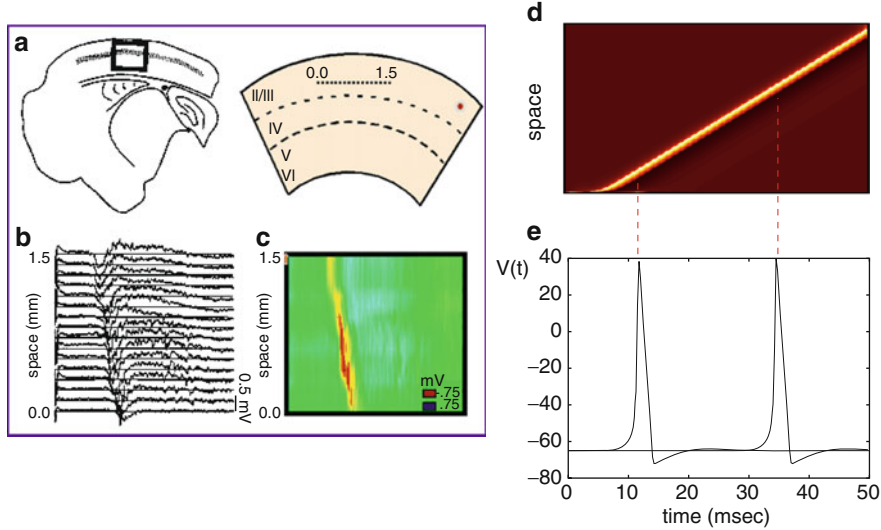


Fig. 8.21 Propagating wave of activity in a brain slice preparation in which the inhibition has been blocked [219]. (a) Where the slice comes from. (b) The extracellular potential recorded from a 16-electrode array. (c) Plot of (b) in pseudocolor. (d) Simulation of an array of 200 Hodgkin–Huxley neurons with excitatory synaptic coupling and exponentially decaying spatial connectivity. (e) The membrane potential from cells at position 25 and 125 in the array

of a rat and bathed in a medium which blocks the effects of synaptic inhibition. A stimulating electrode produces a brief local shock which causes neurons to fire and this activity is transmitted via excitatory synapses to neighboring cells, exciting them and so on. The result is a wave which propagates at 80–150 mm/s. This is slower than axonal propagation (roughly 1 m/s) since the wave depends on the activation of synapses rather than direct diffusive coupling. The figure also shows a simulation of the Hodgkin–Huxley model coupled in a network of 200 neurons with excitatory synapses. In Chap. 12, we study wave propagation in synaptically coupled firing rate models. Because the waves we now explore are related to the precise timing of spikes, and, because the equations we obtain are similar to phase equations, we analyzed pulse coupled networks in this chapter.

We consider the following general system:

$$\begin{aligned} C \frac{\partial V}{\partial t} &= -I_{\text{ion}}(V, z, \dots) - \left(g_{\text{syn}} \int_{-\infty}^{\infty} W(x-y) s(y, t) dy \right) \\ &\quad (V(x, t) - V_{\text{syn}}), \\ \frac{\partial z}{\partial t} &= Z(V, z, \dots), \\ s(x, t) &= \sum_m \alpha(t - t_k(x)), \end{aligned} \quad (8.62)$$

where the sum is taken over all spikes produced by the neuron at spatial location x , and $\alpha(t)$ is a predefined function which vanishes for $t < 0$ and represents the time

course of the synaptic conductance. z represents the possibly many gating variables (such as the activation of potassium current and inactivation of sodium current). $W(x)$ describes the distance-dependent strength of interactions between neurons. We assume W is symmetric, nonnegative, and integrates to 1 over the whole line. For the model in the figure, $\alpha(t) = \exp(-t/5)$ and $W(x) = \exp(-|x|)/2$. We define the time of a spike to be that time at which the potential crosses a predefined threshold, V_T . In Fig. 8.21d each neuron spikes exactly once during the course of the wave. We can exploit this to construct and analyze the propagation of waves. Suppose (as in the simulation, but not in the experiment) each neuron fires exactly once at time $T(x)$. Then that cell contributes $\alpha(t - T(x))$ to the other cells and the total conductance produced by the wave is

$$G(x, t) = g_{syn} \int_{-\infty}^{\infty} W(x - y) \alpha(t - T(y)) dy.$$

A constant-speed traveling wave satisfies, $T(x) = x/v$ where v is the velocity of the wave. The simulations in the figure suggest that we look for traveling wave solutions to the integro-differential equation. That is, we seek solutions of the form, $V(x, t) = Y(x - vt)$, $z(x, t) = U(x - vt)$ where Y, U are functions of the single variable, $\xi = x - vt$. We note that in these coordinates, the conductance, $G(x, t)$ can be written as

$$G(x, t) = g(\xi, v) = g_{syn} \int_{-\infty}^0 W(\xi - \eta) \alpha(-\eta/v) d\eta.$$

The traveling waves start at rest and end at rest. Thus equation (8.62) becomes the non-autonomous ODE:

$$\begin{aligned} -vC \frac{dY}{d\xi} &= -I_{ion}(Y, U) - g(\xi, v)(Y - V_{syn}) \\ -v \frac{dU}{d\xi} &= Z(Y, U). \end{aligned} \tag{8.63}$$

We must solve this for $Y(\xi), U(\xi)$ satisfying:

$$\begin{aligned} (Y(\pm\infty), U(\pm\infty)) &= (V_{rest}, z_{rest}) \\ Y(0) &= V_T. \end{aligned}$$

Here, (V_{rest}, z_{rest}) is the resting state for each neuron. Since traveling waves are translation-invariant, the second condition sets the origin of the wave $\xi = 0$ to be the point at which the neuron crosses the threshold. We note that $g(\xi) \rightarrow 0$ as $\xi \rightarrow \pm\infty$ since $W(x)$ is integrable, $\alpha(t)$ decays as $t \rightarrow \infty$ and vanishes for $t < 0$. If the velocity, v is positive, then the boundary condition at $-\infty$ is simple to achieve since the resting state is asymptotically stable and g decays to zero. On the other hand, it is natural to ask how we can attain the decay of (v, u) to rest as $\xi \rightarrow \infty$ since the resting state is unstable as a solution to (8.63) for $v > 0$ and for $\xi \rightarrow \infty$.

There is no proof for the existence of a wave speed, v , such that $(v(\xi), u(\xi))$ go to the resting state as $\xi \rightarrow \infty$. However, for simple models such as the integrate-and-fire model, the solution can be explicitly computed.

8.4.1 Integrate-and-Fire Model

The analog of (8.62) for an integrate-and-fire model is

$$\tau \frac{\partial V}{\partial t} = V_{\text{rest}} - V + a(V_{\text{syn}} - V)S(x, t),$$

where $a = g_{\text{syn}}R_M$ and

$$S(x, t) = \int_{-\infty}^{\infty} W(x - y) \sum_k \alpha(t - t_k(y)) dy. \quad (8.64)$$

Here, $\alpha(t)$ is the prescribed synaptic gating variable (e.g., it could be a simple exponential, or a difference of exponentials) and $t_k(x)$ represents the firing times of a neuron at spatial point x . This says that the effect of other neurons on a neuron at spatial point x depends on the distance (the function $W(x)$) and the times at which those neurons fire, $t_k(y)$. We note that in this formalism, there could be delays to the synapse and it is clear that we could also introduce delays that depend on the distance. This makes the model more complex, but it remains solvable. We have absorbed any current applied to the model into the constant V_{rest} , which we assume is less than the threshold for firing. (Otherwise, the neuron would spontaneously fire and we are interested in evoked waves, so we do not want spontaneous activity.) We shift the potential by V_{rest} , $\hat{V} = V - V_{\text{rest}}$, so the driving force for the synaptic coupling is

$$V_{\text{syn}} - V_{\text{rest}} - \hat{V}.$$

The equation is still difficult to analyze since the potential \hat{V} is multiplied by the synaptic activity $S(x, t)$, making it difficult to integrate the equation. Thus, we make one more simplification. We replace the voltage-dependent drive by a constant drive, $V_{\text{syn}} - V_{\text{rest}}$. Noting that a is dimensionless, we absorb it into the drive, $V_{\text{drive}} = (V_{\text{syn}} - V_{\text{rest}})g_{\text{syn}}R_M$, and now turn our attention to the simpler problem:

$$\tau \frac{\partial V}{\partial t} = -V + V_{\text{drive}}S(x, t), \quad (8.65)$$

with $S(x, t)$ as defined in (8.64). We have dropped the hats on the voltage for notational simplicity. As in the conductance-based model, we suppose there is only one spike per neuron, so the index k can be dropped from the sum in (8.64). By assuming there is only one spike per wave, we do not have to worry about what happens after

the wave passes through. This makes our work much simpler. Equation (8.65) can be integrated with the integrating factor $\exp(t/\tau)$, leading to the following equation:

$$V(x, t) = C_0 e^{-t/\tau} + V_{\text{drive}} \int_{-\infty}^{\infty} W(x - y) A(t - T(y)) dy, \quad (8.66)$$

where

$$A(t) = \frac{1}{\tau} \int_0^t \alpha(t-s) e^{-s/\tau} ds.$$

(The proof of this statement is left as an exercise.) We take $C_0 = 0$ since we are interested in what happens when the neurons all start from rest. The function $A(t)$ vanishes for $t < 0$ since the function $\alpha(t)$ vanishes for $t < 0$. $A(t)$ is the response of a passive membrane with time constant τ to a synaptic current of the form $\alpha(t)$. An obvious generalization of (8.66) could include passive dendrites between the synapse and the spike-generating zone of the neuron. In this case, $A(t)$ is the convolution of $\alpha(t)$ with the spatiotemporal Green's function for the dendrite evaluated at the spatial location of the synapse (see Chap. 3). Since each neuron fires exactly once, this means the membrane potential of a neuron at $t = T(x)$ must be equal to its firing threshold, V_T (which has been shifted by V_{rest}); thus, we must have

$$V(x, T(x)) = V_T.$$

Evaluating (8.66) at $t = T(x)$, we have the following functional differential equation:

$$V_T = V_{\text{drive}} \int_{-\infty}^{\infty} W(x - y) A(T(x) - T(y)) dy. \quad (8.67)$$

We note that if the neuron fires multiple times, we have to take into account the resetting properties of the integrate-and-fire model and also that there will be a family of firing times, $t_k(x)$. This problem was investigated by Osan et al. [209]

A traveling wave with velocity v satisfies $T(x) = x/v$. Keeping in mind that $A(t)$ is nonzero only if $t > 0$, expression (8.67) reduces to

$$\begin{aligned} \frac{V_T}{V_{\text{drive}}} &= \int_{-\infty}^x W(x-y) A((x-y)/v) dy \\ &= \int_0^\infty W(y) A(y/v) dy \\ &\equiv Q(v). \end{aligned}$$

This is just an algebraic equation for v as a function of V_T/V_{drive} . For example, if $W(x) = \exp(-|x|/\sigma)/(2\sigma)$ and $\alpha(t) = \exp(-\beta t)$, then

$$Q(v) = \frac{1}{2} \frac{\sigma v}{v^2 \tau + \sigma v(1 + \tau \beta) + \beta \sigma^2}.$$

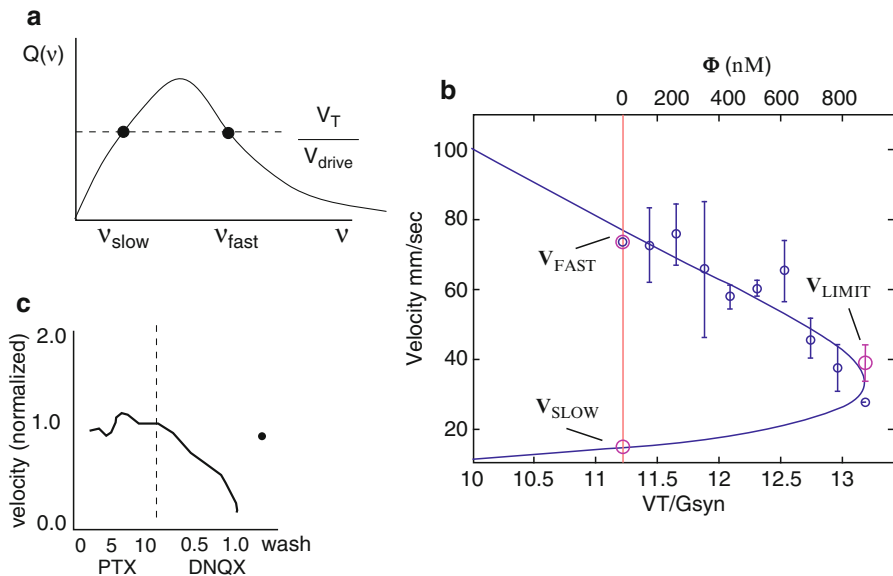


Fig. 8.22 (a) Calculation of the wave speed for single-spike traveling waves as a function of the threshold and drive. (b) Experimental velocity in a one-dimensional cultured network as a function of the amount of excitatory synaptic blocker 6,7-dinitroquinoxaline-2,3-dione (DNQX) (from [85]). (c) Same for a disinhibited slice (from [219])

Notice that $Q(0) = 0$ and as $v \rightarrow \infty$, $Q(v) \rightarrow 0$. Note also that $Q(v)$ has a single maximum. Thus, if V_T / V_{drive} is too big, we cannot solve

$$V_T / V_{\text{drive}} = Q(v)$$

but that if it is small enough, then there are always two roots, v . In Exercise 32, you are asked to draw this function and solve for v . For most functions $W(x)$, one cannot evaluate the integral, Q ; however, it is possible to prove some properties (see Exercise 33). Figure 8.22a shows a typical plot of $Q(v)$ and the calculation of roots of $Q(v) = V_T / V_{\text{drive}}$. As long as this latter quantity is small enough, there are two possible wave velocities, one slow and one fast. Intuition tells us that if we increase the drive, the wave should travel faster; increasing the drive corresponds to lowering the dashed line. The fast wave increases in speed and the slow wave decreases in speed. Thus, we would like to conclude that the fast wave is the one that is observed experimentally and numerically. Indeed, that is the case as would appear from Fig. 8.22b and c, which shows experimentally determined wave velocities in two different preparations as the strength of the recurrent excitatory connections is pharmacologically decreased. In Fig. 8.22b, neurons are grown in a one-dimensional cultured array [85] and the velocity of evoked waves is measured while different concentrations of the excitatory synaptic blocker DNQX are applied. The authors of this paper attempted to fit their data to a curve similar to that in Fig. 8.22a. The slow

velocity is estimated by applying a minimal stimulation, which results in a slow initial propagation that switches to the fast wave after a small transient. Pinto et al. (Fig. 8.22c) observed a similar qualitative dependence of the velocity on the strength of connections in a disinhibited cortical slice preparation [219]. The Wu laboratory [8, 9, 293] examined many aspects of wave propagation in neocortex under a number of pharmacological manipulations. Han et al. [117] suggested wave propagation plays an important role in visual processing.

8.4.2 Stability

The stability problem for the traveling waves is difficult. However, we can explore a simple version of stability called spatial stability. We suppose $T(x) = x/v + b \exp(\lambda x)$, where b is a small deviation. Plugging this into (8.67), we see that

$$0 = b \int_{-\infty}^{\infty} W(x-y) A'((x-y)/v) [e^{\lambda x} - e^{\lambda y}] dy.$$

Factoring out $e^{\lambda x}$ and using the fact that $A(t)$ and therefore $A'(t)$ vanishes for $t < 0$, we must have

$$0 = \int_0^{\infty} W(y) A'(y/v) [1 - e^{-\lambda y}] dy \equiv E(\lambda).$$

This is the ‘‘Evans’’ function and zeros correspond to eigenvalues. Any eigenvalues with positive real parts will lead to an exponential growth of $T(x)$ away from the traveling wave as x increases. In Exercise 36, you show that if $W(x)$ is a monotonically decreasing function of x on the positive real line and if $A(t) \geq 0$, then the slow wave (cf. Fig. 8.22) is unstable. The stability of the fast wave is proven in [20].

8.5 Bibliography

The analysis of neural oscillations goes back to the original work of Hodgkin and Huxley. Most recent work on neural oscillations concerns their behavior in networks.

8.6 Exercises

1. Suppose $X_0(t)$ is a T -periodic solution to the differential equation

$$\frac{dX}{dt} = F(X),$$

where $F(X)$ is C^1 . Show that $X_0(t + t_0)$ is also a solution for any number t_0 . Let $A(t) = D_X F(X_0(t))$ be the matrix formed by linearizing the above ordinary differential equation around the limit cycle. Show that

$$\frac{dY}{dt} = A(t)Y(t)$$

has a nontrivial periodic solution, $Y(t) = dX_0(t)/dt$. Consider the adjoint equation:

$$\frac{dX^*}{dt} = -A(t)^T X^*(t).$$

Show that if $X^*(t)$ is a periodic solution to the adjoint, then

$$X^*(t) \cdot \frac{dX_0}{dt} = \text{constant}$$

for all t .

2. Floquet theory is the periodic analog of stability theory for fixed points. Floquet's theorem states the following. Consider the homogeneous linear periodic system

$$\frac{dx}{dt} = A(t)x, \quad A(t+T) = A(t), \quad T > 0. \quad (8.68)$$

Then every fundamental solution, $X(t)$, to (8.68) has the form

$$X(t) = P(t)e^{Bt},$$

where $P(t)$ is a T -periodic matrix and B is a matrix. The matrix $C = e^{BT}$ is called the monodromy matrix and the eigenvalues of C are called the Floquet multipliers. If the Floquet multipliers are all inside the unit circle, then the origin is an asymptotically stable solution to (8.68).

If $A(t)$ is as in Exercise 1, show that there is always at least one Floquet multiplier with value 1.

A classic result from linear differential equations is

$$\det X(t) = e^{\int_0^t \text{Tr } A(s)ds} \det X(0).$$

Use this to show that a planar limit cycle,

$$u' = f(u, v); \quad v' = g(u, v),$$

is asymptotically stable if

$$\int_0^T f_u(t) + g_v(t)dt < 0.$$

Note that f_u means the partial derivative of $f(u, v)$ with respect to u evaluated along the limit cycle.

3. Show by direct calculation that the adjoint L^* of the operator L in (8.4) under the inner product (8.5) is

$$L^* y = -\frac{dy(t)}{dt} - A(t)^T y(t).$$

4. Let $\Phi(t)$ be a fundamental solution to the differential equation

$$\frac{dX}{dt} = A(t)X(t).$$

Show that $\Psi(t) = (\Phi(t)^{-1})^T$ satisfies the adjoint equation:

$$\frac{dY}{dt} = -A^T(t)Y(t).$$

Suppose $A(t)$ is as in Exercise 1 so that there is a unique (up to a scalar factor) periodic solution to (8.68). Let the first column of $\Phi(t)$ be this periodic solution. Show that the first column of $\Psi(t)$ is also periodic.

5. Consider the normal form for a Hopf bifurcation in polar coordinates:

$$r' = r(1 - r^2); \quad \theta' = 1 + q(r^2 - 1).$$

Suppose $(r(0), \theta(0)) = (r_0, \theta_0)$ and $r(0) > 0$. Find the asymptotic phase and use this to sketch the isochrons. (Hint: Let $R = r^2$ and rewrite the equations in terms of R .) When $q = 0$, this oscillator is sometimes called the radial isochron clock. Why?

6. Consider the leaky integrate-and-fire model:

$$\tau \frac{dV}{dt} = I - V,$$

with $I > 1$ such that when $V = 1$, it is reset to 0. Define phase zero as the moment of reset to 0. Suppose at time (phase) $t < T$ the voltage is increased by an amount a . If $V + a > 1$, the voltage is immediately reset to 0. Compute the PTC for this model and show that for any $a > 0$, the PTC is type 0.

7. Consider the model oscillator

$$r' = r(1 - r); \quad \theta' = 1.$$

The period of this is 2π . In rectangular coordinates, $(u, v) = r(\cos \theta, \sin \theta)$, we define the zero phase to be the peak of $u(t)$. Thus, $\theta = 0$ is the zero phase. Suppose at time (phase) t , $u(t)$ is instantly increased by an amount a . Compute the PTC for this model as a function of a . For what values of a is this type 1 resetting? Can you offer a geometric interpretation of this?

8. Consider the quadratic integrate-and-fire on the whole line:

$$\frac{dV}{dt} = V^2 + I,$$

where $I > 0$ and such that when $V = +\infty$, it is reset to $-\infty$. Define phase zero to be the time of reset. You have already shown that the period of this oscillator is $T = \pi/\sqrt{I}$. Suppose at time (phase) $t \in [0, T)$, the voltage is instantly increased by an amount a . Compute the PTC for this and show that no matter how big a is, it is always type 1 resetting.

9. Davis Cope (personal communication) derived a formula for the adjoint equation for arbitrary nonlinear planar systems, $u' = f(u, v)$, $v' = g(u, v)$. He showed that

$$\begin{pmatrix} u^*(t) \\ v^*(t) \end{pmatrix} = \begin{pmatrix} \frac{u'(t)}{u'(t)^2 + v'(t)^2} \\ \frac{v'(t)}{u'(t)^2 + v'(t)^2} \end{pmatrix} + c(t) \begin{pmatrix} -v'(t) \\ u'(t) \end{pmatrix}, \quad (8.69)$$

where $c(t)$ is periodic and satisfies

$$\frac{dc}{dt} = -(f_u + g_v)c + \frac{2u'(t)v'(t)[f_u - g_v] + (v'(t)^2 - u'(t)^2)[f_v + g_u]}{(u'(t)^2 + v'(t)^2)^2}. \quad (8.70)$$

Here, f_u is the derivative of $f(u, v)$ with respect to u evaluated along the limit cycle. f_v , g_u , and g_v are similarly defined. Prove this formula satisfies the adjoint equation

$$u_t^* = -f_{uu}u^* - g_{uv}v^*, \quad v_t^* = -f_{vu}u^* - g_{vv}v^*$$

along with the condition that $u^*u' + v^*v' = 1$. Also, prove if the limit cycle is asymptotically stable, then the equation for $c(t)$ has a periodic solution.

10. We saw how a ring model has a strictly positive PRC. So, suppose you are given a model with a continuous positive PRC, $\Delta(t)$. Given the positive PRC, does there exist a function $f(x) > 0$ such that the ring model

$$x' = f(x)$$

has the given PRC? (Note that the ring length is unspecified and it depends on the choice of the PRC.) For the most part, you cannot arrive at a closed-form solution for $f(x)$. However, for some problems, it is possible. Try, $\Delta(t) = a + t(1-t)$. Try $\Delta(t) = \exp(t)$.

11. Compute the adjoint for

- (a) The leaky integrate-and-fire model

$$\tau \frac{dV}{dt} = V_0 - V$$

with the condition that if $V(t) = V_{\text{spike}} < V_0$, the voltage is reset to V_{reset} .

- (b) The quadratic integrate-and-fire model with finite reset

$$\frac{dV}{dt} = aV^2 + I$$

with $I > 0$ and such that if $V = V_{\text{spike}}$, then V is reset to V_{reset} .

12. Consider

$$\frac{dV}{dt} = V^2 + I$$

such that at time $\tau < T$ after firing, the voltage is decreased by an amount $b > 0$. If T is the period of the oscillation without the inhibition, compute the period as a function of τ and b . For τ and b fixed, compute the PRC for this model for a stimulus which arrives at time t after the spike and increases V by $a > 0$. How does the shape of this PRC compare with that of the uninhibited PRC.

13. In this exercise, you consider the Traub model for hippocampal pyramidal cells (see online for the equations) in which a small high-threshold calcium current is added (to produce calcium only when the cell spikes) and two types of adaptation are included. There is an M-type voltage-dependent calcium current acting at rest and a calcium-dependent potassium current acting only when there is a spike. The conductances for these are g_m and g_{ahp} , respectively. You should first compute the bifurcation diagram for this model when both are set to zero as the current varies. Now change the adaptation to 0.5, 1.0, 1.5 and compute the bifurcation diagram. Note that the onset of spiking is still via a saddle-node on an invariant circle. Do a similar analysis with g_m and see that the onset of spiking is via a Hopf bifurcation. Pick $g_{ahp} = 0$ and $g_m = 0$ and add sufficient current to get a 40-Hz oscillation. Compute the adjoint. Add $g_{ahp} = 0.5$ and enough current so that the frequency stays at 40 Hz. Compute the adjoint and compare it with the adaptation-free adjoint. Finally, set $g_{ahp} = 0$ and $g_m = 0.5$ and add sufficient current to keep the frequency at 40 Hz. Compute the adjoint. Show that the type of adaptation has a drastic effect on the adjoint.
14. In Exercise 13, you showed how some outward currents can affect the PRC. Use the Traub model from Exercise 13 without the calcium and adaptation currents. Add to this the sag current (which is an inward current – equations are online as the sag+inward rectifier model) using the McCormick parameters and pick $g_h = 4$. Apply current so that the frequency is 40 Hz. Compute the adjoint. You should see that there is a negative region in it. Check the nature of the bifurcation to a limit cycle. Is it now a Hopf? Conclude that like the M-type potassium current (Exercise 13), the sag converts a saddle-node limit cycle to a Hopf limit.
15. Derive the analog of (8.22) when the oscillators have slightly different periods, say, T_0 and $T_0 + c$. Suppose $\Delta(\phi) = a \sin \phi$, with $-1 < a < 0$. Study the

- existence of fixed points as c varies with a held fixed. Use a computer to solve for the fixed points and determine the magnitude of c such that there exists a stable fixed point.
16. Suppose the PRC is $\Delta(\phi) = b(1 - \cos \phi)$. What is the behavior of the map (8.22)? Can you prove the synchronous state is asymptotically stable? (Hint: What is the behavior of the map $x \rightarrow x + cx^2$?)
 17. (a) Consider the map (8.28) and use $d(\phi) = a \sin 2\pi\phi$. For what values of a is synchrony a stable fixed point when $\rho = \omega_1/\omega_2 = 1$. Fix $a = -0.1$ and vary ρ . Plot the map and figure out for what values of ρ there is a saddle-node and locking is lost. You should be able to do this analytically, since a saddle-node occurs when (8.29) is exactly equal to 1. (b) Suppose $d_j(\phi) = a_j \sin 2\pi\phi$. Even though the two PRCs are different, show that synchrony is still a solution and find the conditions for which it is stable.
 18. Derive a map for 2:1 locking of two oscillators satisfying (8.26) and (8.27) with $\omega_1 \approx 2\omega_2$. That is, suppose the firing pattern is oscillator 1, oscillator 1, oscillator 2, and so on. Let ϕ denote the phase of oscillator 2 when oscillator 1 fires the first time. Assume ϕ is close enough to 0.5 so that oscillator 1 fires again before oscillator 2 fires. Use this sequence to devise a map for ϕ . Find a condition like (8.29) for determining stability. Suppose the normalized PRC is an odd periodic function so that $d(0) = d(1/2) = 0$. Show that if the frequency ratio is exactly 2:1, then $\phi = 1/2$ is the fixed point.
 19. To better understand the shape of the map $M(t)$ in Sect. 8.2.3, we will examine the behavior near threshold. Recall that the inhibitory cell is a class I neuron, so at threshold it undergoes a saddle-node bifurcation. Thus, we approximate its dynamics as

$$V' = qV^2. \quad (*)$$

Suppose after it fires, the inhibitory cell is set to $V = -V_0 < 0$. The larger is V_0 , the more refractory the cell is. Now, t^* milliseconds later the second excitatory spike arrives at the inhibitory cell and suppose all it does is increase $V(t)$ by an amount A . If $V(t^*) + A > 0$, then the inhibitory cell will fire (reach infinity) in finite time. Compute this firing time, t_f , and show that it can be written as

$$t_f(t^*) = c + \frac{a}{t^* + b},$$

where c , a , and b are parameters. In particular, parameter b can be positive or negative. This simple function provides a good fit to the map $M(t)$ and each parameter has a nice physical interpretation in terms of the size of the input A and the degree of refractoriness V_0 . [Hint: Solve (*) starting at $t = 0$ with the given initial data up to t^* . Then increase $V(t)$ by A and solve (*) up to the point where $V(t)$ becomes infinite. This is $t_f(t^*)$.]

20. What is the nature of the bifurcation which occurs in the map (8.30) when $M'(\tau) = -1$? (If you need to recall what sorts of bifurcations occur in maps, see Kuznetsov, 2004 [167].) Since we know that for sufficient delay, the synchronous state can be stable, explain why a very long delay (thus, where $M'(\tau)$

is small) might also be bad. (Hint: If $M'(t) = -\epsilon$, where ϵ is a small positive parameter, then the map reduces to

$$z_{n+1} = \mu - z_n + 2\epsilon z_n.$$

What is the fixed point for this and how long does it take to settle into it?)

21. *Mirollo and Strogatz I.* (a) Analyze the map for two coupled Mirollo–Strogatz oscillators when $\epsilon < 0$. (b) Analyze the map for $f''(t) > 0$ for $\epsilon < 0$ and $\epsilon > 0$.
22. *Mirollo and Strogatz II.* Plot $h(\phi)$ and $R(\phi)$ when

(a)

$$f(t) = \frac{1 - e^{-ct}}{1 - e^{-c}}$$

for different values of c and ϵ . This, of course, is the profile for the leaky integrate-and-fire model. Explicitly compute the interval of existence for $R(\phi)$.

(b) Repeat (a) for the firing map:

$$f(t) = \frac{\tan[a(t - 1/2)] + \tan(a/2)}{2 \tan(a/2)},$$

where $0 < a < \pi$. This is the map which occurs for a quadratic integrate-and-fire model with finite reset. It is both concave and convex!

23. Using

$$V^*(t) = 1 - \cos(t) - \sin(t) + \sin(2t)/2$$

for the PRC and $s(t) = I_0 t e^{-\beta t}$ as the synaptic current, compute $H_{\text{odd}}(\phi)$. [Hint: Use formula (8.45) and set $\alpha = \beta$.] Compute the derivative of H_{odd} at $\phi = 0$ and $\phi = \pi$ and plot the result for excitatory ($I_0 = 1$) and inhibitory ($I_0 = -1$) coupling as a function of β . Recalling that β large means low frequency, conclude that this simple model with inhibition could explain the results of the finger-tapping experiment.

24. Find conditions for when the pronk is stable. Prove the walk exists as a solution to (8.46) if and only if $H_b(x) = H_c(x)$. Show that under these assumptions the pace, trot, and bound all exist as phase-locked solutions. Find conditions such that the walk is asymptotically stable. Prove if the trot is asymptotically stable, then so is the pace. Prove it is possible for the bound to be stable, but for the trot and pace to be unstable. Find conditions such that the walk is stable and the trot/pace is unstable and vice versa. (Hint: You will have a 4×4 matrix, but it will have a great deal of symmetry so you should be able to explicitly write down the eigenvalues since the eigenvectors will be chosen from the fourth roots of unity.)
25. Make a model consisting of two sets of the excitatory–inhibitory pair (8.47) and couple them with all four types of coupling (one at a time),

excitatory→excitatory, excitatory→inhibitory, etc., and start with a variety of initial conditions. Describe all the stable states and compare these with the predictions you would get from Fig. 8.16.

26. Consider the nonisotropic chain for $j = 1, \dots, N$:

$$\theta'_j = \omega + H_a(\theta_{j+1} - \theta_j) + H_b(\theta_{j-1} - \theta_j).$$

Suppose the end conditions are either periodic $\theta_0 = \theta_N$ and $\theta_{N+1} = \theta_1$ or reflecting $\theta_0 = \theta_1$ and $\theta_{N+1} = \theta_N$. Prove the synchronous solution is asymptotically stable if and only if $H'_a(0) > 0$ and $H'_d(0) > 0$.

27. Consider the same chain as in the previous problem with periodic boundary conditions. Show that there is a wavelike solution of the form $\theta_j = \Omega t + 2\pi j/N$, determine Ω , and also the stability of this solution. (This leads to a tridiagonal matrix whose eigenvalues are pretty easy to compute.) If synchrony (the previous problem) is stable, then you should be able to prove this traveling wave is also stable if N is sufficiently large.
28. Show that a 4×4 network of nearest-neighbor phase oscillators has the following phase-locked pattern and compute the unknown quantity $0 < \xi < \pi/2$ for sinusoidal coupling. Prove this solution is also asymptotically stable using the theorem in Sect. 8.3.1.

$$\begin{array}{cccc} 0 & \xi & \pi/2 - \xi & \pi/2 \\ -\xi & 0 & \pi/2 & \pi/2 + \xi \\ 3\pi/2 + \xi & 3\pi/2 & \pi & \pi - \xi \\ 3\pi/2 & 3\pi/2 - \xi & \pi + \xi & \pi \end{array}$$

29. Show that the only terms contributing to instability of the asynchronous state for the all-to-all coupled oscillator model with noise and no heterogeneity are the odd parts of $H(\phi)$. Equation (8.61) should provide the crucial clues. Compute the critical values of K for each n .
30. *Two-cluster states.* Suppose there are N all-to-all oscillators with identical frequencies and no noise:

$$\theta'_j = \omega + \frac{1}{N} \sum_{k=1}^N H(\theta_k - \theta_j).$$

Let us look for a solution such that the first m oscillators are synchronized and the remaining $N - m$ oscillators have a phase difference ϕ with respect to the first group. As long as $m < N$ and $\phi \neq 0$, this is called a two-cluster state. Let $p = m/N$. Show that a two-cluster state exists if and only if

$$\begin{aligned} \Omega &= \omega + pH(0) + (1-p)H(\phi), \\ \Omega &= \omega + pH(-\phi) + (1-p)H(0). \end{aligned}$$

Here, Ω is the unknown ensemble frequency. You can parameterize this using p as

$$p = \frac{H(\phi) - H(0)}{H(\phi) + H(-\phi) - 2H(0)}.$$

Show that there is always a solution to this for $\phi = \pi$ and $p = 1/2$. This is a balanced cluster state with half of the oscillators in antiphase with the others. If H is an odd function, show that p can be anything and $\phi = \pi$ [since $H(\pi) = H(0) = 0$]. Stability of the general clustered state is a more difficult problem, but with some decent linear algebra skills you should be able to do it. The stability matrix has a nice simple block form.

31. Derive (8.66) from (8.65).
32. Derive the equation in the text for $Q(v)$ when $W(x) = \exp(-|x|/\sigma)/(2\sigma)$ and $\alpha(t) = \beta \exp(-\beta t)$. Plot the wave speed as a function of the ratio V_T/V_{drive} .
33. Suppose $W(x) \geq 0$ and $A(t) \geq 0$, $A(0) = 0$ and both functions are integrable over $[0, \infty)$. Consider the expression

$$Q(v) = \int_0^\infty W(y)A(y/v)dy.$$

Prove $Q(0) = 0$ and $Q(\infty) = 0$. What happens if you relax the assumption $A(0) = 0$? If $W(y) > 0$ and $A(t) > 0$ except at $t = 0$, where it vanishes, prove $Q(v) > 0$ for $0 < v < \infty$.

34. Suppose $\alpha(t) = \beta \exp(-\beta(t - \tau_d))$, where τ_d is a delay (fixed and space-independent). Analyze the existence and stability of the one-spike waves in this case.
35. Suppose there is a delay due to the conduction velocity so that it depends on distance. Justify the expression for $S(x, t)$ below and analyze the existence of traveling waves in this case when there is an exponential weight $W(x) = \exp(-|x|/\sigma)/(2\sigma)$ and $\alpha(t) = \exp(-\beta t)$.

$$S(x, t) = \int_{-\infty}^\infty W(x - y)\alpha(t - T(y) - |x - y|/c)dy,$$

where $c > 0$ is the conduction velocity.

36. *Instability of the slow wave.* In this exercise, you prove the slow wave is unstable by showing that there is a real positive root of the Evans function:

$$E(\lambda) = \int_0^\infty W(y)A'(y/v)[1 - e^{-\lambda y}]dy.$$

Consulting Fig. 8.22, it is clear that for the slow wave, $Q'(\nu_{\text{slow}}) > 0$. We suppose $W(x)$ is monotonically decreasing for $x > 0$, differentiable, and that $A(t) > 0$ for $t > 0$.

- (a) Clearly $E(0) = 0$. As $\lambda \rightarrow \infty$,

$$E(\lambda) \rightarrow \int_0^\infty W(y) A'(y/\nu) dy \equiv E_\infty.$$

By integrating E_∞ by parts, conclude that $E_\infty > 0$.

- (b) Differentiate $Q(\nu)$ with respect to ν and differentiate $E(\lambda)$ with respect to λ . Show that the sign of $E'(0)$ is the opposite of that of $Q'(\nu)$.
- (c) Use the previous two parts of this exercise to show that at $\nu = \nu_{\text{slow}}$, $E(\lambda) < 0$ for small positive λ and $E(\lambda) > 0$ for large λ . Thus, conclude that there is a real positive value of λ such that $E(\lambda) = 0$ and that the slow wave is unstable.

8.7 Projects

1. Use the Izhikevich model or a similar “integrate-and-fire” model to compute a PSTH for a weak perturbation and then use this to reconstruct the PRC.
2. *Development and synchrony.* During the development of the nervous system, there are two important features of neural communication. First, there are many electrical or gap junctions between cells. Second, the reversal potential of GABAergic synapses is such that they actually act to depolarize rather than hyperpolarize. In this project, you should perform the weak coupling analysis for a pair (or more) of coupled neurons as the reversal potential of the inhibition changes from, say, -40 to -75 mV. You should also apply the weak coupling analysis to a gap junctionally coupled neuron. A good choice for the membrane model is the Wang–Buszaki model (found in the list of models online). Drive the Wang–Buszaki model so that it fires at about 40 Hz and use a fast GABA synapse such as defined in Chap. 7. Vary the reversal potential of the synapse and compute the interaction function $H(\phi)$. Use this to predict whether a pair of synaptically coupled neurons will synchronize or fire in antiphase. With this “prediction,” couple two Wang–Buszaki membrane models with weak inhibition and see if the theoretical results agree. Look at larger networks either using a phase model or the full-blown network.
3. *Kuramoto and coupling.* Suppose instead of heterogeneity in the frequencies of the Kuramoto model, there is instead heterogeneity in the coupling. In general, there is little one can do to analyze this case, but there is one type of coupling which lends itself to rigorous analysis. Suppose $H(0) > 0$ and consider

$$\dot{\theta}_j = \omega + \frac{1}{N} \sum_k C_j C_k H(\theta_k - \theta_j).$$

The coupling coefficients C_j are taken from some distribution with mean μ and variance σ . Develop a population density theory for this and analyze the stability (and existence) of the asynchronous state. (You could probably do this with C_k replaced by E_k taken from author distribution.)

4. *Integrate-and-fire neurons and phase-locking.* Consider a system of integrate-and-fire neurons which we write simply as

$$\frac{dV_j}{dt} + V_j = I_j + \sum_{k,l} C_{jk} \alpha(t - t_k^l) - B \sum_l \delta(t - t_j^l),$$

where C_{jk} are the coupling currents and t_k^l are the firing times. The delta function appearing on the right-hand side represents the reset when the neuron fires. B is the distance between threshold and reset. Let $E(t) = \exp(-\max(t, 0))$ and let $A(t)$ denote the integral

$$A(t) = \int_0^t e^{-t+s} \alpha(s) ds.$$

Show that we can rewrite this equation as

$$V_j(t) = V_j(0)e^{-t} + I_j(1 - e^{-t}) - B \sum_l E(t - t_j^l) + \sum_{k,l} C_{jk} A(t - t_k^l).$$

Now suppose the integrate-and-fire neurons all fire with a period T (unknown) so that they are phase-locked. That is, $t_j^l = lT + \zeta_j$. Let V_{th} denote the threshold for firing; that is, $V_j(t_j^l) = V_{\text{th}}$. Let

$$A_T(t) = \sum_l A(t + lT) \quad \text{and} \quad E_T(t) = \sum_l E(t + lT).$$

Show that a phase-locked solution for the integrate-and-fire model must satisfy

$$V_{\text{th}} = I_j - \frac{B}{1 - e^{-T}} + \sum_k C_{jk} A_T(\zeta_k - \zeta_j).$$

This equation is very similar to (8.40), which provides a set of algebraic conditions for locking in weakly coupled oscillators. The only difference here is that the coupling function A_T depends on the ensemble period. Bressloff and his collaborators have shown that many of the results proven for weakly coupled oscillators also hold for synaptically coupled integrate-and-fire models. As a project, you should evaluate some of these functions and look at, say, a pair of neurons or an array of neurons in a circle and compute the conditions for phase-locking. In the case of neurons in a circular array, you could also find the algebraic conditions for a traveling wave.

5. Solve the identical frequency, noisy, Kuramoto density model numerically as follows. Assume $\rho(\theta, t)$ can be written as a finite number of terms:

$$\rho(\theta, t) = \sum_{n=-N}^N p_n(t) e^{in\theta}.$$

Write

$$H(\phi) = \sum_m h_m e^{im\theta}.$$

Show that

$$\int_0^{2\pi} H(\phi - \theta) \rho(\phi, t) d\phi = 2\pi \sum_n h_{-n} p_n(t) e^{in\theta}.$$

From this, you should be able to write a series of ordinary differential equations for $p_n(t)$ satisfying

$$p'_n(t) = -\sigma^2 n^2 / 2 p_n - 2\pi i n \sum_k h_{-k} p_k p_{n-k}.$$

Write these in real coordinates to get $2N + 1$ differential equations. If, for example, $H(\phi) = K \sin \phi$, then h_k vanishes except when $k = \pm 1$, so this is a very simple set of equations. In the case for which H is the pure sine model, show that the equations reduce to

$$p'_n = -\sigma^2 n^2 / 2 p_n + K \pi n [p_1 p_{n-1} - p_{-1} p_{n+1}].$$

Finally, since H is odd, we can assume the density is symmetric, so $p_{-j} = p_j$ and thus this becomes a set of N ordinary differential equations:

$$p'_n = -\sigma^2 n^2 / 2 p_n + K \pi n p_1 [p_{n-1} - p_{n+1}], \quad n = 1, \dots, N.$$

The end conditions are $p_0 = 1/(2\pi)$ and $p_{N+1} = 0$. The condition at $n = 0$ comes from the fact that

$$\int_0^{2\pi} \rho(\theta, t) d\theta = 1.$$

The condition at $n = N + 1$ is just our truncation. Use whatever methods you have at your disposal (analytic, numerical) to study the stability of the state $p_j = 0$, $j = 1, \dots, N$ and compute the bifurcation diagram for K as a parameter. (Note that this numerical approximation of the partial differential equation is considerably better than simply applying the method of lines to the density model.) If you are ambitious, you can try $H(\phi)$ as a sum of several sines and analyze the emergence of clustered states.

Chapter 9

Neuronal Networks: Fast/Slow Analysis

9.1 Introduction

In this chapter, we consider a very different approach to studying networks of neurons from that presented in Chap. 8. In Chap. 8, we assumed each cell is an intrinsic oscillator, the coupling is weak, and details of the spikes are not important. By assuming weak coupling, we were able to exploit powerful analytic techniques such as the phase response curve and the method of averaging. In this chapter, we do not assume, in general, weak coupling or the cells are intrinsic oscillators. The main mathematical tool used in this chapter is geometric singular perturbation theory. Here, we assume the model has multiple timescales so we can dissect the full system of equations into fast and slow subsystems. This will allow us to reduce the complexity of the full model to a lower-dimensional system of equations. We have, in fact, introduced this approach in earlier chapters when we discussed bursting oscillations and certain aspects of the Morris–Lecar model.

Complex population firing patterns, similar to those described in this and subsequent chapters, are believed to play a critical role in many brain functions. For example, oscillatory behavior has been observed in many systems; it has been implicated in sensory processing, the generation of sleep rhythms, parkinsonian tremor, and motor activity. The spatiotemporal structure of spiking activity can be very complicated. For example, neurons may fire action potentials in a synchronous or partially synchronous manner, or the spiking of different neurons may be uncorrelated. The activity may propagate through the population in a wavelike manner or may remain localized.

We note that population rhythms arise through interactions between three network components. These are (1) the intrinsic properties of cells within the network, (2) the synaptic properties of connections between neurons, and (3) the topology of network connectivity. Each of these may depend on numerous parameters and the first two usually involve multiple timescales. We have described intrinsic properties of cells in the preceding chapters. A cell’s dynamics depends primarily on its channel gating variables. These may activate or deactivate on disparate timescales and a single cell may exhibit a variety of firing patterns, including continuous spiking, bursting oscillations, and even chaotic dynamics. As described in Chap. 7, there are

several classes of synapses. Synapses may be chemical or electrical and chemical synapses may be excitatory or inhibitory. Different types of excitatory or inhibitory synapses have distinct properties that determine how one cell influences another. Finally, there are many possible classes of network architectures. The connectivity may be sparse or dense; that is, each cell may communicate with a small number or a large number of other cells. The connectivity may be random or it may be highly structured. We also note that a given neuronal system may include many different types of cells with different types of synaptic connections.

A goal of this chapter is to consider reduced two-variable neuron models and classify the types of activity patterns that emerge. We also wish to understand how the activity depends on the types of cells and synapses in the network, as well as the network architecture. One traditional view is that excitatory synapses always tend to promote synchronous activity in which different cells fire spikes at the same time. Inhibitory synapses, on the other hand, are thought to promote out-of-phase behavior. This traditional view is, in fact, often true. However, simple examples demonstrate that it may not always be the case. The network behavior may depend not only on whether the synapses are excitatory or inhibitory, but on the rates at which the synapses turn on or turn off. The dynamics also depends on how synaptic properties interact with intrinsic properties of cells within the network.

9.2 Mathematical Models for Neuronal Networks

Recall that a network consists of three components. These are (1) the individual cells within the network, (2) the synaptic connections between cells, and (3) the network architecture. We now describe how each of these components is modeled for the analysis presented in this chapter. We also describe different categories of cells, synapses, and network architectures.

9.2.1 Individual Cells

Throughout this chapter, we consider a general two-variable neuron model of the form

$$\begin{aligned}\frac{dv}{dt} &= f(v, w), \\ \frac{dw}{dt} &= \epsilon g(v, w).\end{aligned}\tag{9.1}$$

We have seen several examples of models that can be written in this form. These includes the Morris–Lecar equations. We write the equations in a rather general form to emphasize that the analysis does not depend on the specific form of the equations.

In (9.1), v is the membrane potential of the cell, w is a channel gating variable, and ϵ is a small positive parameter. Hence, w represents a channel state variable that either activates or inactivates on a timescale slower than the other processes.

We need to make some assumptions regarding the nonlinear functions f and g . We assume the v -nullcline $\{f = 0\}$ defines a cubic-shaped curve and the w -nullcline $\{g = 0\}$ is a monotonically increasing curve. Moreover, $f > 0$ ($f < 0$) below (above) the v -nullcline and $g > 0$ ($g < 0$) below (above) the w -nullcline. Note that these assumptions are satisfied by the Morris–Lecar model for a robust range of parameter values. Throughout this chapter, we will describe a cell as being either in the active or in the silent phase such that v is either on the left (silent) or on the right (active) branch of the cubic nullcline. Since cells will be connected by synapses, we suppose there is a threshold, V_T , for the synapses so that if v is in the active (silent) phase, it will be larger (smaller) than V_T . In other words, unless stated otherwise, we assume this threshold V_T lies between the two “knees” – that is, the local maximum and local minimum – of the v -nullcline.

We would like to understand how firing properties of individual cells influence network behavior. For this reason, it would be useful to somehow classify the firing properties of cells. One simple way to do this is that the cells may be *oscillatory* or *excitable*; that is, a cell may or may not fire intrinsically without any synaptic input. Recall that this depends on whether (9.1) has a fixed point that lies along the middle or left branches of the cubic shaped v -nullcline.

If (9.1) is oscillatory, then there are several possible ways to classify the dynamics. One is in terms of the frequency of oscillations. Another is in terms of the *duty cycle*. This is defined to be the ratio of the time the cell spends in the active phase over the time it spends in the silent phase. We sometimes interpret oscillations with a long duty cycle as corresponding to bursting activity and oscillations with a short duty cycle as corresponding to a spiking neuron.

In the following sections, we will demonstrate that the frequency or duty cycle of a cell may have a significant influence on network behavior. In particular, it may be crucially important in determining whether neurons synchronize or not.

9.2.2 Synaptic Connections

We model the synaptic current as described in Chap. 7. Most of the discussion will be concerned with chemical synapses. In this case, the synaptic current can be written as

$$I_{\text{syn}} = g_{\text{syn}} s(V_{\text{post}} - v_{\text{syn}}), \quad (9.2)$$

where g_{syn} is a constant maximal conductance, V_{post} is the membrane potential of the postsynaptic cell, and v_{syn} is the synaptic reversal potential. The dependent variable s represents the fraction of open channels and depends on the presynaptic membrane potential. We will usually assume s satisfies a first-order equation of the form

$$\frac{ds}{dt} = \alpha(1-s)H_\infty(V_{\text{pre}} - V_T) - \beta s. \quad (9.3)$$

Here, α and β represent the rates at which the synapse turns on and turns off, respectively. Recall that different types of synapses may turn on or turn off at very different rates. For example, GABA_B synapses are slow to activate and slow to turn off, compared with GABA_A and AMPA synapses. We assume H_∞ is a smooth approximation of the Heaviside step function (or actually is the Heaviside step function) and V_T is some threshold.

The model for a pair of mutually coupled neurons is then

$$\begin{aligned}\frac{dv_i}{dt} &= f(v_i, w_i) - g_{\text{syn}} s_j (v_i - v_{\text{syn}}), \\ \frac{dw_i}{dt} &= \epsilon g(v_i, w_i), \\ \frac{ds_i}{dt} &= \alpha(1 - s_i) H_\infty(v_i - V_T) - \beta s_i.\end{aligned}\tag{9.4}$$

Here, i and j are 1 or 2 with $i \neq j$. We are assuming the cells are identical so that the nonlinear functions f and g do not depend on the particular cell. Later, we consider networks with heterogeneities.

Note that the coupling between the cells is through the synaptic variables s_j . In particular, suppose cell 1 is the presynaptic cell. When cell 1 fires a spike, its membrane potential v_1 crosses the threshold V_T . The synaptic variable s_1 then activates at a rate that depends on both α and β and this then changes the membrane potential of cell 2, the postsynaptic cell. When cell 1 is silent, such that $v_1 < V_T$, then s_1 decays at rate β .

We wish to classify different types of synapses to study how synaptic interactions influence network behavior. A traditional way to classify synapses is whether they are *excitatory* or *inhibitory*. This depends primarily on the synaptic reversal potential v_{syn} . For example, the reversal potential of the AMPA receptor is $V_{\text{AMPA}} = 0 \text{ mV}$. This is greater than the postsynaptic cell's resting potential, so the AMPA synapse is excitatory. The principal inhibitory synapses involve the neurotransmitter GABA. Recall that the reversal potential of GABA_A varies between -81 and -60 mV ; this is usually less than the cell's resting potential. However, there are examples of cells in which the GABA_A reversal potential is very near or even above rest and GABA_A synapses may be excitatory.

We can further classify synapses depending on the rates at which they activate or deactivate. For example, GABA_A synapses are often referred to as fast-inhibitory synapses, whereas GABA_B synapses are referred to as slow-inhibitory synapses. As discussed above, the rates at which the synapses turn on or off depend on the parameters α and β .

We will also classify synapses as being *direct* or *indirect*. The synapses we have considered so far are direct synapses since they are activated as soon as a membrane potential crosses the threshold V_T . To more fully represent the range of synapse dynamics observed biologically, it will sometimes be necessary to consider more complicated connections. These will be referred to as indirect synapses, and

they are modeled by introducing a new independent variable x_i for each cell in the network. To model indirect synapses, we replace the third equation in (9.4) with the following equations for each (x_i, s_i) :

$$\begin{aligned}\frac{dx_i}{dt} &= \epsilon\alpha_x(1 - x_i)H_\infty(v_i - V_T) - \epsilon\beta_x x_i, \\ \frac{ds_i}{dt} &= \alpha(1 - s_i)H(x_i - \theta_x) - \beta s_i.\end{aligned}\quad (9.5)$$

The constants α , β , α_x , and β_x are assumed to be independent of ϵ . The variable x corresponds to a secondary process that is activated when transmitters bind to the postsynaptic cell. This form was used to model GABA_B and NMDA in Chap. 7. The effect of the indirect synapses is to introduce a delay from the time one cell jumps up until the time the other cell feels the synaptic input. For example, if the first cell jumps up, a secondary process is turned on when v_1 crosses the threshold V_T . Synapse s_1 does not turn on until x_1 crosses some threshold θ_x ; this takes a finite amount of (slow) time since x_1 evolves on the slow timescale, like the w_i .

9.2.3 Network Architecture

There are many possibilities for network architecture. For example, the architecture may be *global* or *local*, *dense* or *sparse*, *random* or *structured*. In general, we model an arbitrary network as

$$\begin{aligned}\frac{dv_i}{dt} &= f_i(v_i, w_i) - g_{\text{syn}}^i \left(\sum_j W_{ij} s_j \right) \left(v_i - v_{\text{syn}}^i \right), \\ \frac{dw_i}{dt} &= \epsilon g_i(v_i, w_i), \\ \frac{ds_i}{dt} &= \alpha_i(1 - s_i)H_\infty(v_i - V_T) - \beta_i s_i.\end{aligned}\quad (9.6)$$

Here, we are assuming the cells are heterogeneous so that the nonlinear functions f and g may depend on cell i . Moreover, the reversal potential v_{syn} , as well as the rates at which the synapses turn on and turn off, depends on the cell, so some of the cells may be excitatory and some of the cells may be inhibitory. The sum in (9.6) is over all presynaptic cells and the constants W_{ij} represent synaptic weights. They can be viewed as the probability that there is a connection from cell j to cell i .

It is sometimes convenient to consider the limiting equations as the number of cells in the network becomes unbounded. We assume the cells lie in some domain \mathcal{D} and $v(x, t)$ represents the membrane potential of the cell at position $x \in \mathcal{D}$ at time t . We now assume the cells are homogeneous; it is straightforward to generalize this to heterogeneous networks. Then, after an appropriate rescaling, (9.6) becomes

$$\begin{aligned}\frac{\partial v}{\partial t} &= f(v(x, t), w(x, t)) - g_{\text{syn}}(v(x, t) - v_{\text{syn}}) \int_{y \in \mathcal{D}} W(x, y) s(y, t) dy, \\ \frac{\partial w}{\partial t} &= \epsilon g(v(x, t), w(x, t)), \\ \frac{\partial s}{\partial t} &= \alpha(1 - s(x, t)) H_\infty(v(x, t) - V_T) - \beta s(x, t).\end{aligned}\tag{9.7}$$

It will be convenient to introduce some notation that will be used throughout the remainder of this chapter. Let $\Phi(v, w, s) \equiv f(v, w) - g_{\text{syn}}s(v - v_{\text{syn}})$. Then the right-hand side of the first equation in (9.4) is $\Phi(v_i, w_i, s_j)$. If g_{syn} is not too large, then each $\mathcal{C}_s \equiv \{\Phi(v, w, s) = 0\}$ defines a cubic-shaped curve. We express the left branch of \mathcal{C}_s as $\{v = \Phi_L(w, s)\}$ and the right branch of \mathcal{C}_s as $\{v = \Phi_R(w, s)\}$.

For convenience, we will assume $H_\infty(v) = H(v)$, where H is the Heaviside step function. That is, $H_\infty(v) = 0$ if $v < 0$ and $H_\infty(v) = 1$ if $v > 0$. It follows that if the presynaptic membrane potential V_{pre} satisfies $V_{\text{pre}} > V_T$, then we can rewrite (9.3) as

$$\frac{ds}{dt} = (\alpha + \beta) \left(\frac{\alpha}{\alpha + \beta} - s \right). \tag{9.8}$$

In this case,

$$s \rightarrow \frac{\alpha}{\alpha + \beta} \equiv s_A$$

at the rate $\alpha + \beta$. While a cell receives synaptic input, it lies along the cubic \mathcal{C}_{s_A} . We will often write \mathcal{C}_A instead of \mathcal{C}_{s_A} . We denote the positions of the left and right knees of \mathcal{C}_s as $w = w_L(s)$ and $w = w_R(s)$, respectively, and sometimes write $w_L^A = w_L(s_A)$.

9.3 Examples of Firing Patterns

We now describe some of the firing patterns that can arise in a network of the form (9.6). In the following examples, each cell is modeled by the Morris–Lecar equations. We begin by considering a network with just two mutually coupled cells. The model can then be written as

$$\begin{aligned}\frac{dv_i}{dt} &= I - I_{\text{ion}}(v_i, w_i) - g_{\text{syn}}s_j(v_i - v_{\text{syn}}), \\ \frac{dw_i}{dt} &= (w_\infty(v_i) - w_i)/\tau_w(v_i), \\ \frac{ds_i}{dt} &= \alpha(1 - s_i) H_\infty(v_i - V_T) - \beta s_i,\end{aligned}\tag{9.9}$$

where i and j are 1 or 2 and $i \neq j$.

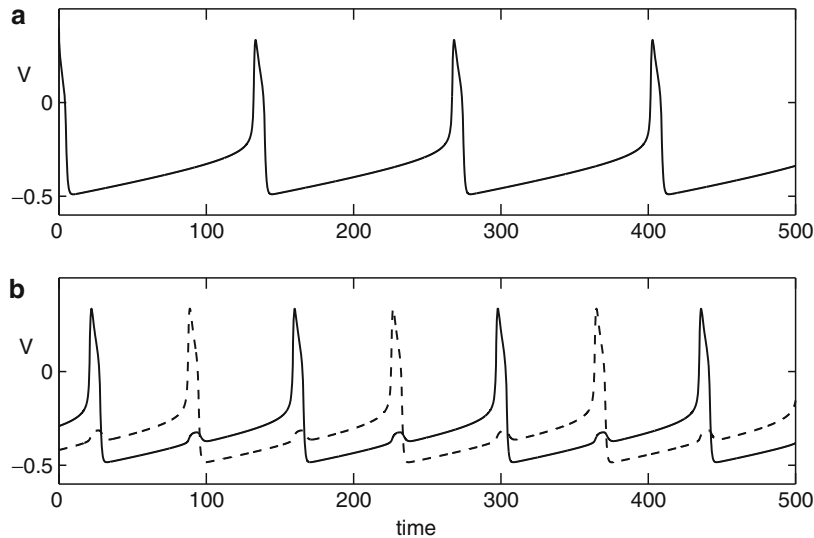


Fig. 9.1 Solutions of a network of two mutually coupled Morris–Lecar neurons with excitatory coupling. (a) Synchronous solution. The membrane potentials are equal so only one is shown. (b) Antiphase behavior. The solutions shown in (a) and (b) are for the same parameter values but different initial conditions. Hence, the system is bistable

Figure 9.1 shows two solutions of (9.9); $v_{\text{syn}} = 0.5$, so the synapses are excitatory. A stable synchronous solution is shown in Fig. 9.1a. Here, $(v_1(t), w_1(t)) = (v_2(t), w_2(t))$ for all t . Figure 9.1b shows a solution with antiphase behavior. This solution is stable; moreover, the synchronous solution is also stable. Hence, for this choice of parameters, the system is bistable. (Note that for Fig. 9.1, dimensionless versions of the Morris–Lecar equations were used, so the actual voltage should be scaled by 120 mV.)

Figure 9.2 shows solutions of (9.9) in which $v_{\text{syn}} = -0.5$, so the synapses are inhibitory. We choose parameters so that a single cell, without any input, is excitable; that is, it does not generate oscillations. Therefore, a network of two cells, which by themselves are silent, can generate oscillatory behavior with inhibitory synaptic coupling. In Fig. 9.2a, the cells take turns firing. The mechanism underlying this rhythm is *postinhibitory rebound*. As one cell spikes, it sends inhibition to the other cell, thereby hyperpolarizing the silent cell’s membrane potential. When the active cell stops firing, it releases the silent cell from inhibition, so the silent cell rebounds and generates an action potential. Mechanisms underlying postinhibitory rebound will be described later.

Figure 9.2b shows a solution in which one of the cells fires shortly after the other; there is then a delay until the first cell fires again. This is sometimes referred to as an *almost-synchronous solution*. We note, in fact, that an inhibitory network can generate a stable synchronous solution. This will be discussed in more detail later. In Fig. 9.2c, one of the cells fires periodically and the other cell never generates

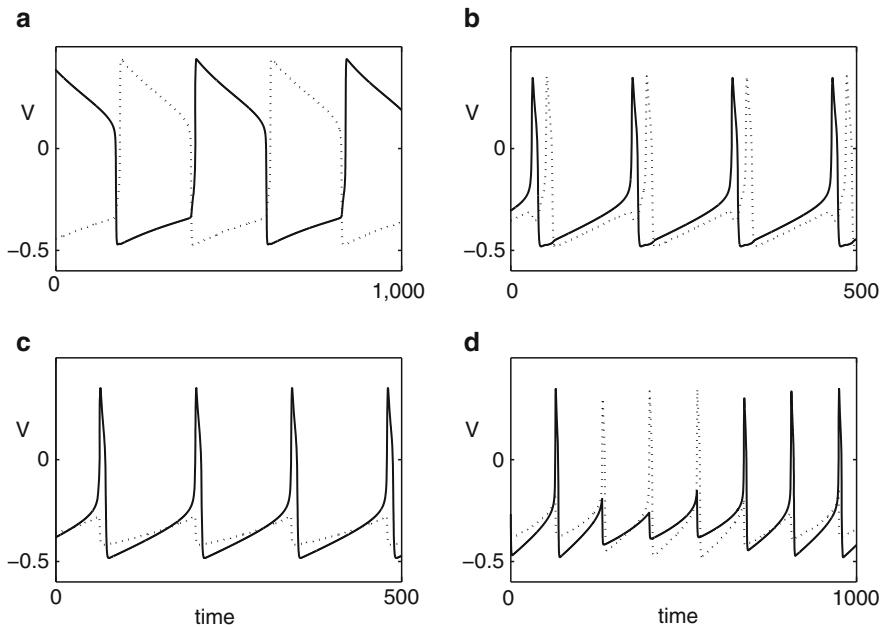


Fig. 9.2 Solutions of a network of two mutually coupled Morris–Lecar neurons with inhibitory coupling. (a) Each cell fires owing to postinhibitory rebound. (b) An almost-synchronous solution. (c) A suppressed solution. (d) The cells take turns firing three spikes while the other cell is silent

an action potential. This is sometimes referred to as a *suppressed solution*. Finally, Fig. 9.2d illustrates a more exotic solution in which one cell generates three spikes while the other cell is silent and then the roles of the cells are reversed. All of the solutions shown in Fig. 9.2 are stable.

We next describe firing patterns in larger networks. An example of *clustering* is shown in Fig. 9.3a and b. Here, a network of four cells with all-to-all inhibitory coupling breaks up into different groups or clusters; cells within each cluster are synchronized but different clusters fire out of phase. We note that these two solutions correspond to the same network with the same parameter values. The only difference between the solutions is the initial conditions. Figure 9.3c shows a solution in which the four cells take turns firing in a wavelike manner. Waves may arise in both excitatory and inhibitory networks. Figure 9.3d shows an example of *dynamic clustering*. Here, there are seven cells in the network and different groups of cells take turns firing. However, the membership of the groups changes, so two different cells may fire together during one episode but not fire together during later episodes.

We note that by “synchrony” we do not necessarily mean “perfect synchrony” in a strict mathematical sense. That is, two cells exhibit perfect synchrony if the dependent variables corresponding to each cell are exactly equal to each other for all time. The cells within each cluster shown in Fig. 9.3 may not be perfectly

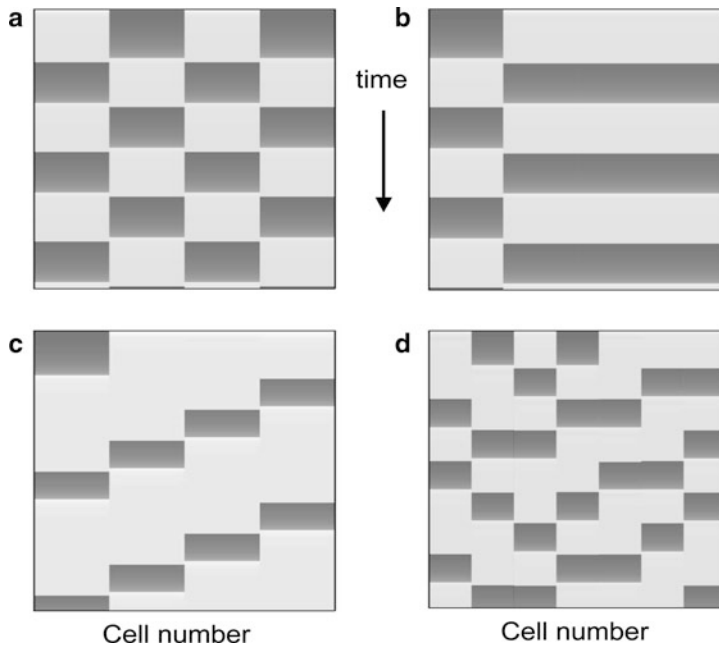


Fig. 9.3 Firing patterns in inhibitory networks. (a) and (b) show examples of clustering. Wavelike behavior is shown in (c) and dynamic clustering in (d). The columns represent the time evolution of a single cell; a *dark rectangle* corresponds to when the cell is active

synchronous; however, they do jump up to the active phase and then jump down at “approximately” the same time. As we shall see, the time difference from when cells within each cluster jump up or jump down is $O(\epsilon)$, where ϵ is the singular perturbation parameter.

9.4 Singular Construction of the Action Potential

The main mathematical tool that will be used throughout this chapter is geometric singular perturbation theory. Here, one exploits the fact that neuronal systems typically involve separate processes that evolve on very different timescales. For example, the membrane potential may jump up or jump down on a much faster timescale than some ionic gating or synaptic variable. By exploiting this discrepancy in timescales, one can often reduce a complicated neuronal system to a lower-dimensional system of equations, one that is easier to analyze and implement numerically. We have, in fact, already seen examples of this method when we considered traveling wave solutions and bursting oscillations. Recall, for example, that for parabolic bursting, we reduced the full four-dimensional system to equations for just the two slow variables. Similar methods will be used to study networks of coupled cells.

In this section, we consider a single neuron modeled by (9.1). By considering a single neuron, we are able to illustrate important features of the geometric singular perturbation method with a rather simple example. We note that (9.1) is an example of a relaxation oscillator. The Morris–Lecar equations will be used for all of the numerics. The analysis, however, is quite general and does not depend on details of the equations. In what follows, we refer to the v -nullcline as “*the cubic*” and the local minimum and local maximum of the cubic as the *left knee* and *right knee*, respectively.

Assume the cubic intersects the w -nullcline at a single point that lies along its middle branch. This fixed point is unstable and there exists a stable periodic orbit. The periodic solution is shown in Fig. 9.4a and its projection onto the phase plane is shown in Fig. 9.4b. Using geometric singular perturbation methods, we will give a rather explicit description of this periodic solution, in the limit $\epsilon \rightarrow 0$.

We dissect the periodic orbit into four pieces; these are referred to as (1) *the silent phase*, (2) *the jump up*, (3) *the active phase*, and (4) *the jump down*. Note that during the silent and active phases, the solution lies close to the left and right branches of the cubic, whereas the jump up and the jump down occur when the trajectory reaches the left and right knees. To obtain a more detailed description of each piece, we consider two timescales: a fast timescale corresponding to the original variable t and a slow timescale defined as $\tau = \epsilon t$. The fast timescale is used to describe the evolution of the solution during the jumps up and down, whereas the slow timescale is used to describe evolution during the silent and active phases.

First consider the slow timescale. If we let $\tau = \epsilon t$ and set $\epsilon = 0$, then (9.1) becomes

$$\begin{aligned} 0 &= f(v, w), \\ \frac{dw}{d\tau} &= g(v, w). \end{aligned} \quad (9.10)$$

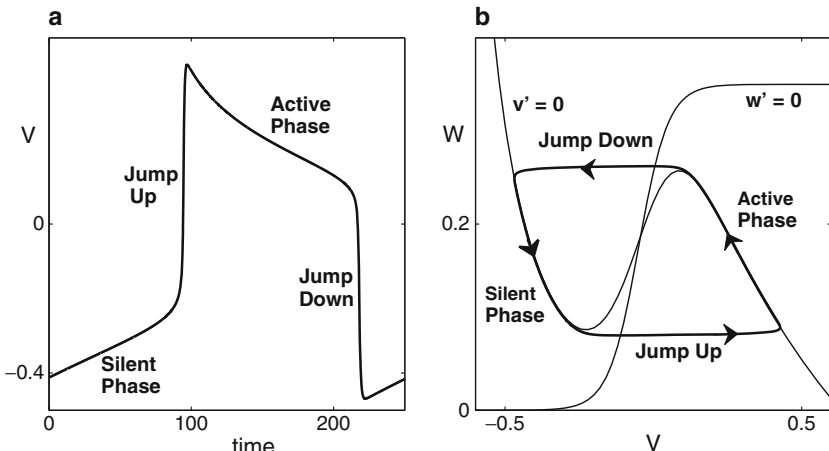


Fig. 9.4 (a) Periodic solution of the Morris–Lecar equations corresponding to an action potential. The projection of this solution onto the (v, w) -phase plane is shown in (b)

The first equation in (9.10) states that a singular periodic orbit lies along the left and right branches of the cubic during the silent and active phases, respectively. The second equation determines the time evolution along these branches. This evolution can be written as a scalar equation for the single (slow) variable w . Suppose the left and right branches can be written as $v = \Phi_L(w)$ for $w > w_L$ and $v = \Phi_R(w)$ for $w < w_R$, respectively. Here, w_L and w_R represent the positions of the left and right knees. Then (9.10) can be written as

$$\frac{dw}{d\tau} = g(\Phi_\alpha(w), w) \equiv \Lambda_\alpha(w), \quad (9.11)$$

where $\alpha = L$ or R .

Now, consider the jumps up and down. These take place on the fast timescale. Let $\epsilon = 0$ in (9.1) to obtain the reduced system:

$$\begin{aligned} \frac{dv}{dt} &= f(v, w), \\ \frac{dw}{dt} &= 0. \end{aligned} \quad (9.12)$$

The second equation in (9.12) implies that w is constant during the jumps. During the jump up, $w = w_L$ and v is a solution of (9.12) that approaches the left knee as $t \rightarrow -\infty$ and approaches the right branch of the cubic as $t \rightarrow +\infty$. During the jump down, $w = w_R$ and v is a solution of (9.12) that approaches the right knee as $t \rightarrow -\infty$ and approaches the left branch of the cubic as $t \rightarrow +\infty$.

An important feature of geometric singular perturbation theory is that it gives a systematic way to reduce complicated models to lower-dimensional systems of equations. In the example illustrated here, the full model (9.1) is two-dimensional, whereas each piece of the singular periodic solution corresponds to a solution of a single differential equation: the jumps up and down satisfy the first equation in (9.12), whereas the silent and active phases correspond to solutions of the second equation in (9.10). We have therefore reduced the original two-dimensional model to four first-order equations. This may not seem like such a big deal, since two-dimensional systems can be easily analyzed using phase-plane methods; however, for larger cell models or networks of cells, such a reduction may be crucially important when analyzing the dynamics.

We conclude this section by considering how the geometric singular perturbation approach can be used to analyze the response of a neuron to a time-varying injected current. This analysis will be very useful when we consider networks of cells. It will illustrate, with a simple example, how a neuron may respond to excitatory or inhibitory input.

Consider the system

$$\begin{aligned} \frac{dv}{dt} &= f(v, w) + I(t), \\ \frac{dw}{dt} &= \epsilon g(v, w). \end{aligned} \quad (9.13)$$

We assume the system is excitable when $I(t) = 0$; that is, the v - and w -nullclines intersect at a stable fixed point along the left branch of the cubic. We further assume there exist I_0 and $T_{\text{on}} < T_{\text{off}}$ such that

$$I(t) = \begin{cases} I_0 & \text{if } T_{\text{on}} < t < T_{\text{off}} \\ 0 & \text{otherwise.} \end{cases} \quad (9.14)$$

We consider two cases: either $I_0 > 0$, in which case the injected current is said to be *depolarizing*, or $I_0 < 0$ and the injected current is *hyperpolarizing*. Figure 9.5 illustrates a Morris–Lecar neuron’s response to depolarizing and hyperpolarizing applied currents. In the depolarizing case, the neuron responds by firing a series of action potentials. The cell returns to rest once the applied current is turned off. In the hyperpolarizing case, the neuron’s membrane potential approaches a more negative steady state until the current is turned off, at which time the neuron fires a single action potential. This last response is an example of *postinhibitory rebound*.

The geometric approach is very useful in understanding these responses. As before, we construct singular solutions in which ϵ is formally set equal to zero. The singular solutions lie along the left or right branches of some cubic-shaped nullcline during the silent and active phases, respectively, as shown in Fig. 9.6. The cubics depend on the value of $I(t)$. We denote the cubic corresponding to $I = 0$ as C_0 and the cubic corresponding to I_0 as C_A . Note that if $I_0 > 0$, then C_A lies “above” C_0 , whereas if $I_0 < 0$, then C_A lies “below” C_0 .

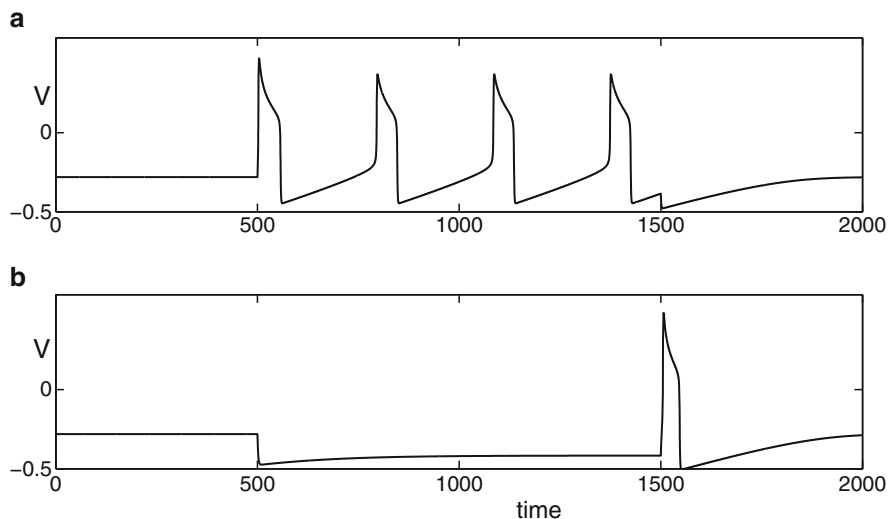


Fig. 9.5 Response of a model neuron to applied current. Current is applied at $t = 500$ and turned off at $t = 1,500$. (a) The current is depolarizing and the neuron fires a series of action potentials. (b) The current is hyperpolarizing and the neuron exhibits postinhibitory rebound

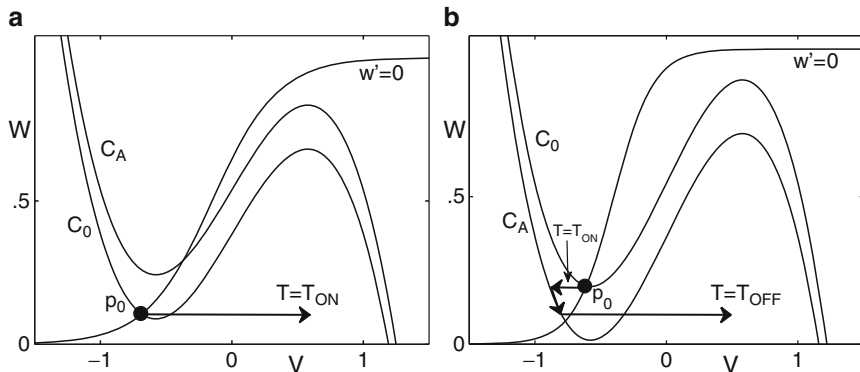


Fig. 9.6 Phase-space representation of the response of a model neuron to applied current. Current is applied at time $t = T_{\text{on}}$ and turned off at $t = T_{\text{off}}$. (a) Depolarizing current. The cell jumps up as soon as the current is turned on. (b) Hyperpolarizing current. The cell jumps to the left branch of C_A when the current is turned on and jumps up to the active phase owing to postinhibitory rebound when the current is turned off

Consider the depolarizing case $I_0 > 0$. This is illustrated in Fig. 9.6a. For $t < T_{\text{on}}$, $I(t) = 0$ and the solution lies at the fixed point p_0 along the left branch of C_0 . When $t = T_{\text{on}}$, $I(t)$ changes to $I_0 > 0$ and the cubic switches from C_0 to C_A . If the left knee of C_A lies above p_0 , then the cell jumps up to the right branch of C_A ; this corresponds to the firing of an action potential. If the w -nullcline intersects C_A along its middle branch – that is, the cell with applied current is oscillatory – then the solution oscillates, generating action potentials, until the input is turned off. The number of action potentials depends on the size of $T_{\text{off}} - T_{\text{on}}$ and the rates at which the solution evolves along the left and right branches of C_A . It is possible that the w -nullcline intersects C_A along its left or right branch. If the w -nullcline intersects C_A along its left branch, then the cell will fire a single action potential and then approach the stable fixed point along the left branch of C_A until the input is turned off at $t = T_{\text{off}}$. If the w -nullcline intersects C_A along its right branch, then the cell will jump up and remain in the active phase until the input is turned off at $t = T_{\text{off}}$.

Next, consider the hyperpolarizing case $I_0 < 0$, shown in Fig. 9.6b. In this case, C_A lies below C_0 and the w -nullcline intersects C_A at a point denoted by p_1 . At $t = T_{\text{on}}$, the solution jumps to the left branch of C_A and then evolves along this branch approaching p_1 for $T_{\text{on}} < t < T_{\text{off}}$. When $t = T_{\text{off}}$, $I(t)$ switches back to 0 and the cell now seeks the left or right branch of C_0 . If, at this time, the cell lies below the left knee of C_0 , then the cell jumps up to the active phase, giving rise to postinhibitory rebound.

Note that to generate postinhibitory rebound, the hyperpolarizing input must be sufficiently large and last sufficiently long. I_0 must be sufficiently negative so that p_1 lies below the left knee of C_0 . Moreover, $T_{\text{off}} - T_{\text{on}}$ must be sufficiently large; the cell needs enough time to evolve along the left branch of C_A so that it lies below the left knee of C_0 when the input is turned off.

9.5 Synchrony with Excitatory Synapses

We now find conditions for when excitatory networks exhibit stable synchronous oscillations. Later we will find conditions for when excitatory connections lead to stable out-of-phase behavior. We begin by considering a simple network of two mutually coupled cells with fast, direct synapses. We assume throughout this section that each cell, without any coupling, is oscillatory.

We use geometric singular perturbation methods to analyze solutions. As before, we formally set $\epsilon = 0$ and construct singular solutions. The singular trajectory corresponding to each cell lies along either the left or the right branch of the cubic shaped v -nullcline during the silent or active phase. The jumps up and down between the silent and active phases occur when a singular trajectory reaches the left or right knee of some cubic. There are now a family of cubic-shaped nullclines, depending on the total synaptic input.

It is straightforward to show that there exists a synchronous solution. This is because along a synchronous solution, $(v_1, w_1, s_1) = (v_2, w_2, s_2) \equiv (v, w, s)$ satisfy the reduced system

$$\begin{aligned}\frac{dv}{dt} &= f(v, w) - g_{\text{syn}}(v - v_{\text{syn}}), \\ \frac{dw}{dt} &= \epsilon g(v, w), \\ \frac{ds}{dt} &= \alpha(1 - s)H_\infty(v - V_T) - \beta s.\end{aligned}$$

The singular trajectory consists of four pieces and is shown in Fig. 9.7a. During the silent phase, $s = 0$ and (v, w) lies along the left branch of C_0 . During the active phase, $s = s_A$ and (v, w) lies along the right branch of the cubic C_A . The jumps between these two phases occur at the left and right knees of the corresponding cubics. A similar construction holds if the synapses are inhibitory, as shown in Fig. 9.7b.

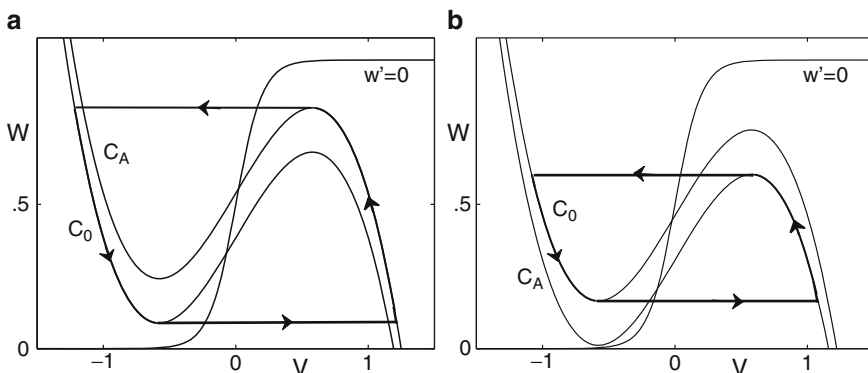
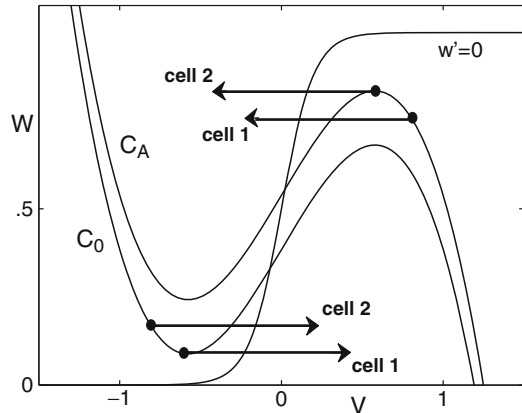


Fig. 9.7 Synchronous singular trajectories corresponding to (a) excitatory synapses and (b) inhibitory synapses

Fig. 9.8 Fast threshold modulation



We next consider the stability of the synchronous solution for small perturbations. We begin with both cells close to each other in the silent phase with cell 1 at the left knee of \mathcal{C}_0 ready to jump up. We follow the cells around in phase space until one of the cells returns to the left knee of \mathcal{C}_0 . We wish to show that the cells are closer to each other after this cycle than they were initially.

The singular solution consists of four pieces. The first piece begins when cell 1 jumps up. When $v_1(t)$ crosses V_T , $s_1(t) \rightarrow s_A$. This raises the cubic corresponding to cell 2 from \mathcal{C}_0 to \mathcal{C}_A . If $w_2(0) - w_1(0)$ is sufficiently small, corresponding to a sufficiently small perturbation, then cell 2 lies below the left knee of \mathcal{C}_A . The fast equations then force cell 2 to also jump up to the active phase, as shown in Fig. 9.8. Note that this piece takes place on the fast time scale. Hence, on the slow time scale, both cells jump up together at precisely the same time.

During the second piece of the singular solution, both oscillators lie in the active phase along the right branch of \mathcal{C}_A . Note that the ordering in which the oscillators track along the left and right branches has been reversed. While in the silent phase, cell 1 was ahead of cell 2. In the active phase, cell 2 leads the way. The oscillators remain on the right branch of \mathcal{C}_A until cell 2 reaches the right knee of \mathcal{C}_A .

The oscillators then jump down to the silent phase. Cell 2 is the first to jump down. When $v_2(t)$ crosses V_T , s_2 switches from s_A to 0 on the fast timescale. This lowers the cubic corresponding to cell 1 from \mathcal{C}_A to \mathcal{C}_0 . If, at this time, cell 1 lies above the right knee of \mathcal{C}_0 , then cell 1 must jump down to the silent phase. This will certainly be the case if the cells are initially close enough to each other.

During the final piece of the singular solution, both oscillators move down the left branch of \mathcal{C}_0 until cell 1 reaches the left knee. This completes one full cycle.

To prove the synchronous solution is stable, we must show that the cells are closer to each other after this cycle; that is, there is compression in the distance between the cells. There are actually several ways to demonstrate this compression; these correspond to different ways to define what is meant by the “distance” between the cells. Here, we consider a Euclidean metric. Sommers and Kopell [163] gave an alternative stability proof using a time metric. They referred to the mechanism by

which one cell fires, and thereby raises the cubic of the other cell such that it also fires, as *fast threshold modulation*. We will use a time metric in later sections when we discuss other types of solutions of (9.9).

By the Euclidean distance between the cells, we mean the following. Suppose both cells lie along the same branch of the same cubic and the coordinates of cell i are (v_i, w_i) . Then the distance between cells 1 and 2 is defined as simply $|w_1 - w_2|$. We wish to demonstrate that this distance decreases along the solutions described above. Since the singular solution consists of four pieces, we need to consider four cases. Note, however, that during the jump up and the jump down, the Euclidean distance does not change. This is because the jumps are horizontal, so the values of w_i do not change. If there is compression, therefore, it must take place as the cells evolve along the left and right branches of the cubics in the silent and active phases. We now show that this is indeed the case if we make some very mild assumptions regarding the nonlinearities f and g .

The first step in the analysis is to reduce the full model to equations for just the slow variables w_1 and w_2 . We introduce the slow timescale $\tau = \epsilon t$ and then let $\epsilon = 0$ in (9.4). This leads to the equations

$$\begin{aligned} 0 &= f(v_i, w_i) - g_{\text{syn}} s_j (v_i - v_{\text{syn}}), \\ \frac{dw_i}{d\tau} &= g(v_i, w_i), \\ 0 &= \alpha(1 - s_i) H_\infty(v_i - V_T) - \beta s_i. \end{aligned} \tag{9.15}$$

The first equation in (9.15) states that each (v_i, w_i) lies on the cubic-shaped nullcline determined by s_j . Let

$$G_L(w, s) = g(\Phi_L(w, s), w) \quad \text{and} \quad G_R(w, s) = g(\Phi_R(w, s), w),$$

where Φ_L and Φ_R were defined earlier. Then, the second equation in (9.15) can be written as

$$\frac{dw_i}{d\tau} = G_\rho(w_i, s_j), \tag{9.16}$$

where $\rho = L$ if cell i is silent and $\rho = R$ if cell i is active. Note that the third equation in (9.15) implies that either $s_i = 0$ or $s_i = s_A$ depending on whether the presynaptic cell is silent or active.

We now return to the stability analysis of the synchronous solution. We demonstrate that the Euclidean distance between the cells decreases as both cells evolve in either the silent phase or the active phase. Here, we consider the silent phase; the analysis for the active phase is similar.

Suppose when $\tau = 0$, both cells lie in the silent phase; hence, each (v_i, w_i) lies on the left branch of C_0 . We assume, for convenience, $w_2(0) > w_1(0)$. We need to prove $w_2(\tau) - w_1(\tau)$ decreases as long as the cells remain in the silent phase. Now each $w_i(\tau)$ satisfies (9.16) with $\rho = L$ and $s_j = 0$. Hence,

$$w_i(\tau) = w_i(0) + \int_0^\tau G_L(w_i(\xi), 0) d\xi$$

and, using the mean value theorem,

$$\begin{aligned} w_2(\tau) - w_1(\tau) &= w_2(0) - w_1(0) \\ &\quad + \int_0^\tau G_L(w_2(\xi), 0) - G_L(w_1(\xi), 0) d\xi \\ &= w_2(0) - w_1(0) \\ &\quad + \int_0^\tau \frac{\partial G_L}{\partial w}(w^*, 0)(w_2(\xi) - w_1(\xi)) d\xi \end{aligned} \tag{9.17}$$

for some w^* . Now $G_L(w, 0) = g(\Phi_L(w, 0), w)$. Hence,

$$\frac{\partial G_L}{\partial w} = g_v \frac{\partial \Phi_L}{\partial w}(w, 0) + g_w.$$

Note that

$$\frac{\partial g}{\partial v} \geq 0 \quad \text{and} \quad \frac{\partial g}{\partial w} \leq 0 \tag{9.18}$$

near the synchronous solution. This follows from our assumption that $g > 0$ ($g < 0$) below (above) the w -nullcline. We now make the additional assumption that there is a strict inequality in (9.18). We further note that $\frac{\Phi_L}{\partial w}(w, 0) < 0$. This is because $v = \Phi_L(w, 0)$ defines the left branch of the cubic C_0 , which has negative slope. It follows that $\partial G_L / \partial w < 0$ and, therefore,

$$w_2(\tau) - w_1(\tau) < w_2(0) - w_1(0).$$

This gives the desired compression. We note that if there exists $\gamma > 0$ such that $\partial G_L / \partial w < -\gamma$ along the left branch, then Gronwall's inequality can be used to show that $w_2(\tau) - w_1(\tau)$ decreases at an exponential rate.

We remark that this analysis generalizes to arbitrarily large networks of homogeneous cells with excitatory synaptic coupling. Suppose initially all of the cells are in the silent phase and are sufficiently close to each other. When one cell, say, cell 1, jumps up, then those cells that receive excitatory input from cell 1 will be induced to jump up as long as they lie below the left knees of the cubics corresponding the excitatory input. These cells will then induce other cells to jump up and so forth. In this way, all of the cells will fire at the same time (on the slow timescale).

9.6 Postinhibitory Rebound

9.6.1 Two Mutually Coupled Cells

We now consider two mutually coupled cells with inhibitory synapses. We continue to assume fast, direct synapses. Figure 9.2 shows that this network can exhibit a wide variety of activity patterns. In this section, we consider the pattern shown in Fig. 9.2a in which the cells take turns firing owing to postinhibitory rebound. In general, an oscillating network with two cells in antiphase is known as a “half-center” oscillator. This type of behavior is found in many applications, including networks governing locomotion and other motor patterns.

As we shall see, the antiphase solution shown in Fig. 9.2a exists and is stable only if certain conditions regarding the nonlinearities and parameters are satisfied. In particular, the coupling strength g_{syn} must be sufficiently strong and the duty cycle must be sufficiently long. Recall that by the duty cycle, we mean the ratio of the times a cell spends in the active and silent phases.

We assume throughout this section the w -nullcline intersects the left branches of both \mathcal{C}_0 and \mathcal{C}_A . We denote these points as p_0 and p_A . In particular, individual cells, without any coupling, are excitable. We also note that the resting state $(v_1, w_1) = (v_2, w_2) = p_0$ is a stable solution of the coupled network. Hence, if the system exhibits stable oscillations, as shown in Fig. 9.2, then the system is bistable.

There does exist a synchronous solution with $(v_1, w_1, s_1) = (v_2, w_2, s_2)$; however, this solution is unstable. The singular trajectory corresponding to the synchronous solution is shown in Fig. 9.7b. During the silent phase, it lies along the left branch of \mathcal{C}_0 and during the active phase, it lies along the right branch of \mathcal{C}_A .

We now step through the construction of the singular solution corresponding to the solution shown in Fig. 9.2a. We begin with cell 1 at the right knee of \mathcal{C}_0 ready to jump down. We further assume cell 2 is silent and lies along the left branch of \mathcal{C}_A below the left knee of \mathcal{C}_0 . When cell 1 jumps down, $s_1 \rightarrow 0$. Since (v_2, w_2) lies below the left knee of \mathcal{C}_0 , cell 2 exhibits postinhibitory rebound and approaches the right branch of \mathcal{C}_0 (Fig. 9.9).

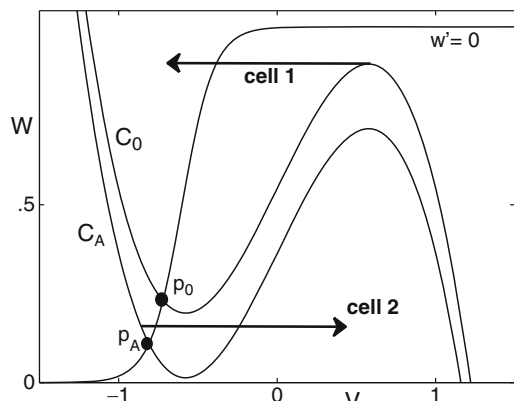


Fig. 9.9 Postinhibitory rebound

Cell 2 then moves up the right branch of C_0 and cell 1 moves down the left branch of C_A toward p_A . Eventually, cell 2 reaches the right knee of C_0 and jumps down. If at this time, cell 1 lies below the left knee of C_0 , then it jumps up owing to postinhibitory rebound. The roles of cell 1 and cell 2 are now reversed. The cells continue to take turns firing when they are released from inhibition.

The preceding construction requires several assumptions. Firstly, the coupling strength g_{syn} needs to be sufficiently large. In particular, the fixed point p_A must lie below the left knee of C_0 . The duty cycle must also be sufficiently large. The active cell must spend enough time in the active phase so that the silent cell can evolve along the left branch of C_A to below the left knee of C_0 . We note that if either g_{syn} or the duty cycle is too small, then the only stable solution will be the resting state $(v_1, w_1) = (v_2, w_2) = p_0$. This last statement depends on our assumption that both cells are excitable.

Wang and Rinzel [284] distinguished between “escape” and “release” in producing out-of-phase oscillations. In the preceding construction, we assumed both cells are excitable for all levels of synaptic input. Then the silent cell can only jump up to the active phase once the active cell has jumped down and released the silent cell from inhibition. This is referred to as the release mechanism. To describe the escape mechanism, suppose each cell is oscillatory for some fixed levels of synaptic input. Then the inactive cell may reach a left knee of its cubic and escape the silent phase. When the silent cell jumps up, it inhibits the active cell. This lowers the cubic of the active cell, so it may be forced to jump down before reaching a right knee, as shown in Fig. 9.10a.

Another mechanism for generating antiphase oscillations is to relax the restriction that the synaptic threshold lies between the active and silent branches (Fig. 9.10b). If the synaptic threshold lies along one of the branches, then the synaptic input given from one cell to the other changes as the cell traverses along its branch, not during its jump between branches. As shown in [249], this may have a large effect on the wave form and frequency of the resulting oscillation.

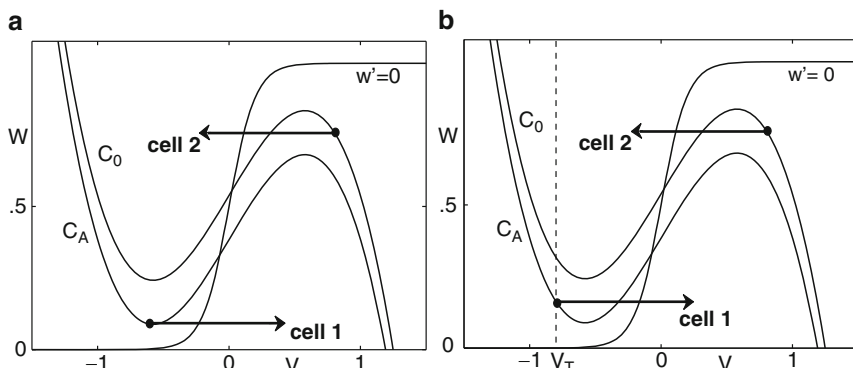


Fig. 9.10 (a) Cellular and (b) synaptic escape mechanisms

9.6.2 Clustering

We now consider larger networks with inhibitory synapses. By a *clustered solution*, we mean one in which the population of cells breaks up into distinct groups or clusters. Cells within each cluster fire in (near) synchrony, whereas cells in different clusters fire out of phase. The basic mechanism underlying clustering is simply postinhibitory rebound. Examples of clustered solutions are shown in Fig. 9.3. These are for a network with four cells and all-to-all coupling. The solution shown in Fig. 9.3a consists of two clusters with two cells within each cluster. The existence of this solution is equivalent to the antiphase solution for a two-cell network described in the previous section. We note that there are subtleties associated with proving the stability of this two-clustered solution. One must demonstrate that cells within each cluster are stable with respect to perturbations along with proving that the different clusters remain separated.

Other types of clustered solutions are possible. For the solution shown in Fig. 9.3b, there are two clusters; one of the clusters consists of three cells, and the other cluster has only one cell. This is very similar to the clustered solution described above; however, note that now cells within a cluster may lie on different nullclines in phase space. This is because the total inhibition that a cell receives depends on the number of cells within the active cluster.

Figure 9.3c shows a solution in which all the cells fire out of phase with each other. This can be viewed as a four-cluster solution. When one of the cells jumps down, another is released from inhibition. The cells then take turns firing. Note that the existence of such a solution depends on the relative times the cells spend in the silent and active phases. The active phase cannot be too long or the network will exhibit a two-clustered solution. To obtain the four-clustered state, the time the cell spends in the active phase must be roughly one third the time it spends in the silent phase.

These considerations carry over to larger networks. There may exist a two-clustered solution in which the entire network breaks up into two groups, which take turns jumping up when released from inhibition. The existence of such a solution clearly requires assumptions regarding the length of the active phase and the strength of synaptic coupling. One can also obtain activity with more than two clusters. The type of clustered solution that a network exhibits depends on the duty cycle along with the strength of coupling. A more detailed analysis can be found in [236].

9.6.3 Dynamic Clustering

Dynamic clustering differs from clustering in that the membership of the active groups may change. That is, two different cells may fire together during one episode, but fire separately during subsequent episodes. An example of such a solution is shown in Fig. 9.3d. Note that cell 2 sometimes fires with cell 3, but sometimes it does not. We now explain a simple mechanism for the generation of dynamic clustering.

The mechanism depends on both postinhibitory rebound and network architecture. We will explain the mechanism with a rather simple example; however, this generalizes in a straightforward manner to larger networks. A complete analysis of this type of solution is given in [267].

The example network consists of seven cells and the network architecture is shown in Fig. 9.11a. All connections are assumed to be inhibitory. Different responses, for the same parameter values, but different initial conditions, are shown in Fig. 9.11b and c. Each response consists of episodes in which some subset of the cells fires in near synchrony. These subsets change from one episode to the next; moreover, two different cells may belong to the same subset for one episode but belong to different subsets during other episodes. After a transient period the response becomes periodic. For example, consider the solution shown in Fig. 9.11b. The cells which fire during the sixth episode are cells 1, 2, and 7. These are precisely the same cells which fire during the eighth episode. This subset of cells continues to fire together every second cycle thereafter. We say that this solution has a periodic attractor

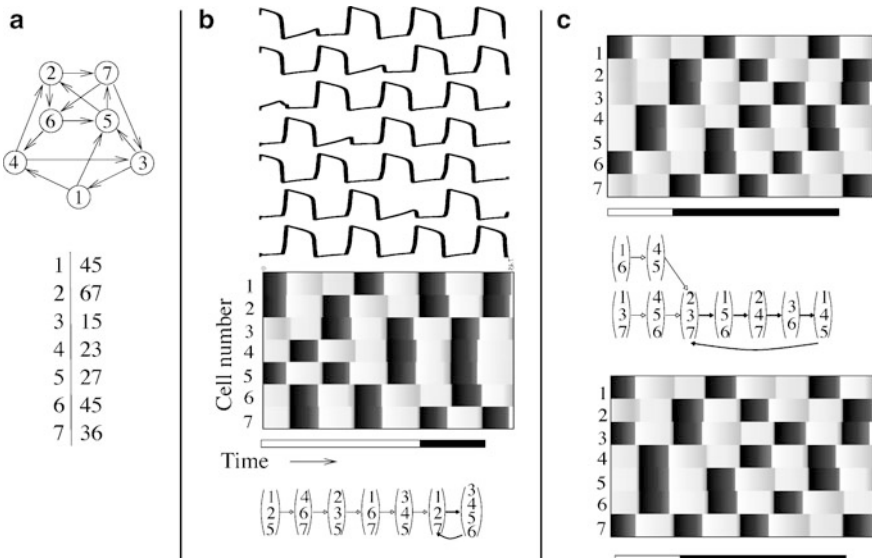


Fig. 9.11 Dynamic clustering. (a) The network consists of 7 cells with connections indicated by arrows. The connectivity is summarized in a table (*bottom*), in which the left column shows the indices of all cells, and the remaining columns show the indices of all cells that receive connections from the cell on the left. (b) An example of network activity. The *top* panel shows the time courses of voltage in all 7 cells over 8 epochs of activity. Grey scale in the checkerboard panels corresponds to the magnitude of voltage, with black areas indicating spikes. After a transient (white part of the time bar under the checkerboard) the response converges to a repeating pattern (black part of the time bar). The bottom panel shows the orbit of the discrete dynamical system corresponding to this example. (c) Solutions of the same network, but with different initial conditions. These solutions have different transients (white parts of the time bars), but they converge to the same attractor (which, in turn, is different from the one in b)

consisting of two episodes (or simply, the period is 2). Different initial conditions produce different transients that may approach the different attractors (Figs. 9.11b, c (top)) or the same attractor (Fig. 9.11c).

We next describe an algorithm which will allow us to determine how the network responds to initial conditions and analyze properties of the periodic attractors. If we know which subset of cells fire during one episode, then the algorithm determines which subset of cells fire during the next episode. To derive the algorithm, we need two assumptions. The first is that if a cell fires during an episode, then every cell that receives input from that cell and which does not fire during that episode must fire during the next episode. The second assumption is that no cell can fire in two subsequent episodes.

Consider the solution shown in Fig. 9.11c (bottom). The cells which fire during the first episode are cells 1, 3, and 7. Because of the two assumptions, these induce cells 4, 5, and 6 to fire during the second episode. Continuing in this way, we can determine which cells fire during each subsequent episode.

Note that if the number of cells is N (in this example $N = 7$), then the cells that fire during an episode represent a subset of $\mathcal{P}_N \equiv \{1, \dots, N\}$. Let \mathcal{S}_N denote the set of all subsets of \mathcal{P}_N . The algorithm represents a map Φ from \mathcal{S}_N to itself. For the example shown in Fig. 9.11c (bottom), we represent the cells which fire during the first and second episodes by indices $\{1, 3, 7\}$ and $\{4, 5, 6\}$, respectively; hence, $\Phi(\{1, 3, 7\}) = \{4, 5, 6\}$. Iterating Φ , we obtain an orbit of subsets; these correspond to those cells that fire during successive episodes. The orbits corresponding to the three solutions illustrated in Fig. 9.11b and c are also shown in that figure. Note that each orbit consists of two components: there is an initial transient until the orbit returns to a subset that it has already visited. The orbit must then repeat itself. We remark that every orbit must eventually become periodic; this is because there are only a finite number of subsets of \mathcal{P}_N .

By considering every subset of \mathcal{P}_N , one obtains a directed graph. This graph has 2^N nodes. Hence, even for the seemingly simple example shown in Fig. 9.11a, there are 128 nodes and the directed graph is quite complicated. The entire graph is shown in Fig. 9.12. Here, we do not include the trivial solutions in which every cell fires or no cells fire during one episode. Examining this directed graph, we find that the model exhibits seven periodic attractors.

Further details and analysis of this algorithm can be found in [267], where precise conditions are given for when the differential equations model can be rigorously reduced to discrete dynamics.

9.7 Antiphase Oscillations with Excitatory Synapses

We have, so far, found conditions for when excitatory coupling leads to synchrony and inhibitory coupling leads to antiphase oscillations. The existence and stability of these patterns depend on various assumptions. For example, to generate antiphase behavior with inhibitory synapses, we required that the active phase, and therefore

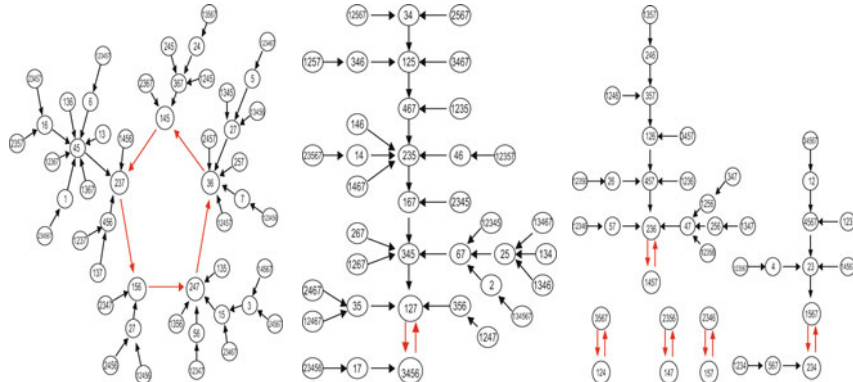


Fig. 9.12 Graph of discrete dynamics associated with the network shown in Fig. 9.11

the duty cycle, is sufficiently long. Note that a cell with a long duty cycle can be viewed as a bursting oscillator; the active phase represents the envelope of spiking activity. In this section, we consider what happens if the duty cycle is short. We also assume each cell, without coupling, is oscillatory. We may, therefore, think of the cell as exhibiting single, periodic spikes instead of bursts. We find conditions for when excitatory coupling leads to stable antiphase behavior. The analysis also demonstrates when the antiphase solution is unstable for inhibitory coupling. Throughout the analysis, we assume the synapses are fast and direct.

We will demonstrate that stable antiphase solutions exist if the synapses are excitatory and both the coupling strength g_{syn} and the duty cycle are sufficiently small. In this case, the antiphase solution will exist but be unstable if the synapses are inhibitory.

9.7.1 Existence of Antiphase Oscillations

We first find conditions for when there exists an antiphase solution. The stability of this solution will be discussed in Sect. 9.7.2.

Figure 9.1b shows an antiphase solution with excitatory synapses. The projection of this solution onto the (v, w) phase plane is shown in Fig. 9.13. We now step through the various pieces of this trajectory. We start with both cells in the silent phase with cell 1 at the left knee of \mathcal{C}_0 ready to jump up. Suppose $w_2(0) = w_*$. When cell 1 jumps up, $s_1 \rightarrow s_A$. If $w_* > w_L^A$, so that cell 2 lies above the left knee of \mathcal{C}_A , then cell 2 approaches the left branch of \mathcal{C}_A . Cell 1 then moves up the right branch of \mathcal{C}_0 and cell 2 moves down the left branch of \mathcal{C}_A . If the active phase is sufficiently brief, then cell 1 reaches the right branch of \mathcal{C}_0 and jumps down before cell 2 reaches the left knee of \mathcal{C}_A . Suppose this happens when $\tau = T_A$. (Here, we are considering the slow timescale.) After cell 1 jumps down, both cells evolve along

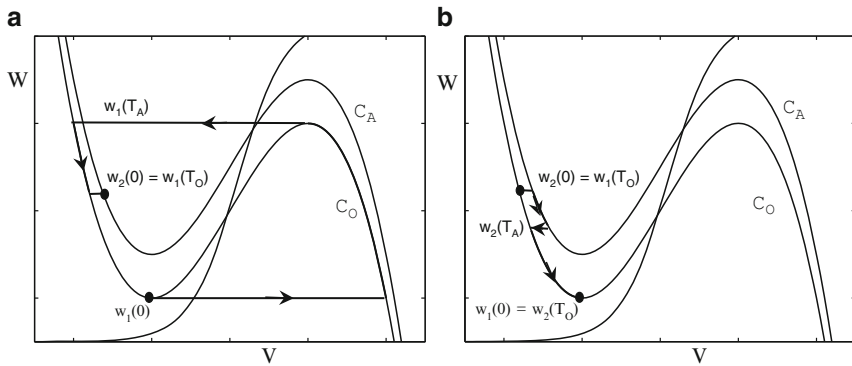


Fig. 9.13 Singular construction of antiphase solution. (a) Cell 1 and (b) cell 2

the left branch of \mathcal{C}_0 until cell 2 reaches the left knee of \mathcal{C}_0 . Suppose this happens when $\tau = T_0$. If $w_1(T_0) = w_*$, then the roles of cell 1 and cell 2 are reversed and this completes half of a complete antiphase cycle.

We prove the existence and stability of an antiphase solution by constructing a one-dimensional map, which we denote as π . The definition of π is simply $\pi(w_*) = w_1(T_0)$, where w_* and T_0 were defined above. Clearly, a stable fixed point of π corresponds to a stable antiphase solution. Note that to define $\pi(w_*)$ we need that cell 1 jumps up to the active phase and then jumps back to the silent phase before cell 2 is able to jump up. This requires a number of assumptions. In particular, the duty cycle cannot be too long, g_{syn} cannot be too big, and $(w_* - w_L)$ cannot be too small. We now derive precise conditions for when π is well defined and has a stable fixed point.

As before, we reduce the analysis to equations for just the slow variables w_1 and w_2 . Each of these variables satisfies (9.16), where $\rho = L$ or R if cell i is silent or active, and $s_j = 0$ or s_A if the presynaptic cell is silent or active. In particular, if both cells are silent, then each w_i satisfies

$$\frac{dw_i}{d\tau} = G_L(w_i, 0). \quad (9.19)$$

If cell i is silent and cell j is active, then

$$\frac{dw_i}{d\tau} = G_L(w_i, s_A) \quad (9.20)$$

and

$$\frac{dw_j}{d\tau} = G_R(w_j, 0). \quad (9.21)$$

Let T_A denote the duration of the active phase. More precisely, this is the time needed for a solution of (9.21) starting at w_L to reach w_R .

We will need to consider the distance between the cells and determine how the distance changes as trajectories evolve in phase space. Here, we use a *time metric*. For now, we only consider the case when both cells are silent; that is, $(v_1(0), w_1(0))$ and $(v_2(0), w_2(0))$ lie along the left branch of \mathcal{C}_0 . Suppose $w_1(0) < w_2(0)$. Then the time metric $\rho_L(w_1(0), w_2(0))$ is defined to be the time it takes for the solution of (9.19) starting at $w_2(0)$ to reach $w_1(0)$. Note that this metric is time-invariant in the following sense. Suppose $w_i(\tau)$, $i = 1, 2$, are solutions of (9.19). Then

$$\rho_L(w_1(\tau), w_2(\tau)) = \rho_L(w_1(0), w_2(0))$$

for all $\tau > 0$, as long as the cells remain on the left branch of \mathcal{C}_0 . The proof of this statement is left as an exercise.

Note that π is not defined for all $w_* \in (w_L, w_R)$. We need that cell 1 jumps up and down before cell 2 jumps up. This will be true if T_A is sufficiently small and $w_* - w_L$ is sufficiently large. We assume, for the moment, this is true. Once we have characterized w_* , we will demonstrate that it is indeed in the domain of π .

We now find the conditions for π to have a fixed point. Since

$$w_L < w_2(T_A) < w_* < w_R,$$

it follows that

$$\rho_L(w_L, w_R) = \rho_L(w_L, w_2(T_A)) + \rho_L(w_2(T_A), w_*) + \rho_L(w_*, w_R).$$

Let $T_S = \rho_L(w_L, w_R)$ be the length of the silent phase. If w_* is a fixed point of π , then $w_2(T_0) = w_L$, $w_1(T_0) = w_*$, and $w_1(T_A) = w_R$. Hence,

$$\begin{aligned} T_S &= \rho_L(w_2(T_0), w_2(T_A)) + \rho_L(w_2(T_A), w_*) + \rho_L(w_1(T_0), w_1(T_A)) \\ &= (T_0 - T_A) + \rho_L(w_2(T_A), w_2(0)) + (T_0 - T_A) \\ &= 2(T_0 - T_A) + \rho_L(w_2(T_A), w_2(0)). \end{aligned} \tag{9.22}$$

Note that the last term tends to 0 as $T_A \rightarrow 0$. Hence, in this limit, the solution of (9.22) is $T_0 = \frac{1}{2}T_S$. It follows that (9.22) has a solution, and there exists a fixed point of π if the duration of the active phase is sufficiently small.

It remains to prove the fixed point w_* lies in the domain of π . Recall that cell 1 must jump up and jump down before cell 2 jumps up. Choose $\omega_D > w_L^A$ so that the time it takes a solution of (9.20) starting at ω_D to reach w_L^A is T_A . Then cell 1 will jump up and jump down before cell 2 jumps up if $w_* > \omega_D$. This will be the case if

$$\rho_L(w_L, w_*) > \rho_L(w_L, \omega_D). \tag{9.23}$$

We show that this is true if the coupling strength g_{syn} and the duration of the active phase T_A are sufficiently small. Note that the right-hand side of (9.23) can be written as

$$\rho_L(w_L, \omega_D) = \rho_L(w_L, w_L^A) + \rho_L(w_L^A, \omega_D).$$

Since $w_L^A \rightarrow w_L$ as $g_{\text{syn}} \rightarrow 0$ and $\omega_D \rightarrow w_L^A$ as $T_A \rightarrow 0$, it follows that the right-hand side of (9.23) is as small as we please if g_{syn} and T_A are small. On the other hand, the left-hand side of (9.23) can be rewritten as

$$\begin{aligned}\rho_L(w_L, w_*) &= \rho_L(w_L, w_R) - \rho_L(w_*, w_R) \\ &= T_S - T_0 \\ &\rightarrow \frac{1}{2}T_S\end{aligned}\quad (9.24)$$

as $T_A \rightarrow 0$. Hence, (9.23) is satisfied if g_{syn} and T_A are sufficiently small. This completes the proof that π has a fixed point corresponding to an antiphase solution.

9.7.2 Stability of Antiphase Oscillations

We now consider the stability of the fixed point w_* . To prove the stability, we must show that $|\pi'(w_*)| < 1$. We demonstrate that this is the case if the synapses are excitatory and some rather natural assumptions regarding the nonlinearities f and g are satisfied. The analysis also demonstrates that the fixed point is unstable if the synapses are inhibitory.

We begin by describing another way to visualize the antiphase solution. Consider the projection of the solution onto the (w_1, w_2) slow phase plane as shown in Fig. 9.14. Note that the solution lies within the rectangular region

$$\mathcal{R} = \{(w_1, w_2) : w_L \leq w_1 \leq w_R, w_L \leq w_2 \leq w_R\}.$$

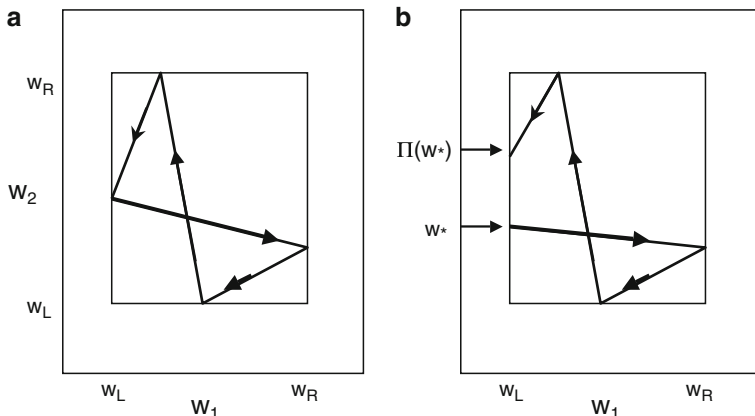


Fig. 9.14 (a) Projection of the antiphase solution onto the slow (w_1, w_2) phase plane. (b) The one-dimensional map

Denote the left, right, top, and bottom sides of \mathcal{R} as $\mathcal{R}_L, \mathcal{R}_R, \mathcal{R}_T$, and \mathcal{R}_B , respectively. These correspond to positions where one of the cells reaches a left or right knee of \mathcal{C}_0 ; that is, where cell 1 jumps up, cell 1 jumps down, cell 2 jumps down, and cell 2 jumps up, respectively.

We now view π as a map defined on \mathcal{R}_L and denote this new map as Π . That is, suppose we start at a point $(w_L, w_*) \in \mathcal{R}_L$. Then cell 1 is ready to jump up and cell 2 is silent. We follow the trajectory until it reaches \mathcal{R}_L again. If the position of cell 2 at this time is w_0 , we let $\Pi(w_*) = w_0$. Since we are now considering a full cycle, and in the definition of π we only considered half of a cycle, it follows that $\Pi(w_*) = \pi^2(w_*)$. It suffices to show that $|\Pi'(w_*)| < 1$. We will, in fact, demonstrate that $|\Pi'(w_*)| < 1$ for each w_* such that $\Pi(w_*)$ is well defined.

Since the antiphase solution consists of four pieces, we can decompose Π into four pieces. We write $\Pi(w_*) = (\Pi_4 \circ \Pi_3 \circ \Pi_2 \circ \Pi_1)(w_*)$, where each Π_k is a flow-defined map from one side of \mathcal{R} to another. Then

$$\Pi'(w_*) = \Pi'_4 \Pi'_3 \Pi'_2 \Pi'_1(w_*). \quad (9.25)$$

Note that $|\Pi'_2| = |\Pi'_4| = 1$. This follows because the time metric ρ_L is time-invariant and each of these maps corresponds to when both cells are silent and lie along the left branch of \mathcal{C}_0 . We leave the details as an exercise. We must, therefore, prove $|\Pi'_1| < 1$ and $|\Pi'_3| < 1$. Here, we consider $|\Pi'_1|$ since the other inequality is similar. Note that Π_1 corresponds to when cell 1 is active and cell 2 is silent. Hence, w_1 satisfies (9.21) and w_2 satisfies (9.20).

To calculate the derivative of Π_1 , we write it as a difference quotient:

$$\Pi'_1(a) = \lim_{b \rightarrow a} \frac{\rho_L(\Pi_1(a), \Pi_1(b))}{\rho_L(a, b)}. \quad (9.26)$$

Here, we are assuming $a < b$. We now need a formula for ρ_L in terms of the nonlinearities f and g . Recall that $\rho_L(a, b)$ is the time for a solution of (9.19) starting at $w = b$ to reach $w = a$. Hence,

$$\rho_L(a, b) = \int_b^a \frac{1}{G_L(w, 0)} dw. \quad (9.27)$$

This formula is not convenient to work with because w_2 does not satisfy (9.19); it satisfies (9.20) instead. For this reason, we define a new time metric $\rho_A(a, b)$ to be the time it takes a solution of (9.20) starting at $w = b$ to reach $w = a$. Changing variables in (9.27), we find that if $w_2(\tau, b)$ is the solution of (9.20) with $w_2(0, b) = b$, then

$$\rho_L(a, b) = \int_0^{\rho_A(a, b)} \frac{G_L(w_2(\tau, b), s_A)}{G_L(w_2(\tau, b), 0)} d\tau. \quad (9.28)$$

Since this holds for all a and b such that $w_L^A < a < b < w_R$, we also have that

$$\rho_L(\Pi_1(a), \Pi_1(b)) = \int_0^{\rho_A(\Pi_1(a), \Pi_1(b))} \frac{G_L(w_2(\tau, \Pi_1(b)), s_A)}{G_L(w_2(\tau, \Pi_1(b)), 0)} d\tau. \quad (9.29)$$

We insert these expressions into (9.26) to conclude that

$$\Pi'_1(a) = \left(\frac{G_L(\Pi_1(a), s_A)}{G_L(\Pi_1(a), 0)} \right) \left(\frac{G_L(a, 0)}{G_L(a, s_A)} \right). \quad (9.30)$$

We find conditions for the nonlinear functions f and g so that if the synapses are excitatory, then $G_L(w, s_A)/G_L(w, 0)$ is an increasing function of w ; that is,

$$\frac{\partial}{\partial w} \left(\frac{G_L(w, s_A)}{G_L(w, 0)} \right) > 0. \quad (9.31)$$

Since $\Pi_1(a) < a$ this, together with (9.30), implies that $|\Pi'_1(a)| < 1$ and the antiphase solution is stable. A similar analysis shows that if the synapses are inhibitory, then $G_L(w, s_A)/G_L(w, 0)$ is a decreasing function of w ; hence, the antiphase solution is unstable.

Let $\Delta(w, s) = G_L(w, s) - G_L(w, 0)$. Then

$$\frac{\partial}{\partial w} \left(\frac{G_L(w, s_A)}{G_L(w, 0)} \right) = \frac{G_L(w, 0)\Delta_w(w, s_A) - G_{Lw}(w, 0)\Delta(w, s_A)}{[G_L(w, 0)]^2}.$$

We derive conditions for the nonlinear functions f and g so that

$$G_L < 0, \quad \frac{\partial G_L}{\partial w} < 0, \quad \Delta > 0 \text{ and } \Delta_w < 0.$$

To do this, we need to express each of these inequalities in terms of f and g and their derivatives.

Recall that $G_L(w, s) = g(\Phi_L(w, s), w)$, where $v = \Phi_L(w, s)$ represents the left branch of \mathcal{C}_s . In particular, $f(\Phi_L(w, s), w) - g_{syn}s(v - v_{syn}) = 0$. Suppose $g(v, w)$ can be written in the usual form $g(v, w) = (h_\infty(v) - w)/\tau_w(v)$. To simplify the analysis, we assume $\tau_w(v) = \tau_w$ is constant while the cell is in the silent phase. For convenience, we assume $\tau_w = 1$.

Clearly, $G_L(w, 0) < 0$; that is, w decreases in the silent phase. Moreover,

$$\frac{\partial G_L}{\partial w} = \frac{\partial g}{\partial v} \frac{\partial \Phi_L}{\partial w} + \frac{\partial g}{\partial w} = h'_\infty(v) \frac{\partial \Phi_L}{\partial w} - 1 < 0$$

if $h'_\infty(v) > 0$ and the left branch of the cubic \mathcal{C}_0 has negative slope. It is not hard to give precise conditions for the nonlinear function f for when this last statement is true.

We next consider Δ and Δ_w . Note that

$$\Delta(w, s_A) = \int_0^{s_A} \frac{\partial G_L}{\partial s}(w, \gamma) d\gamma \text{ and } \Delta_w(w, s_A) = \int_0^{s_A} \frac{\partial^2 G_L}{\partial w \partial s}(w, \gamma) d\gamma.$$

Now

$$\frac{\partial G_L}{\partial s} = \frac{\partial g}{\partial v} \frac{\partial \Phi_L}{\partial s} = h'_\infty(v) \frac{\partial \Phi_L}{\partial s} > 0$$

if $h'_\infty(v) > 0$ and the cubics “increase” as s increases; that is, if $s_1 > s_2$, then the cubic corresponding to s_1 lies above the cubic corresponding to s_2 . This is the case if the synapse is excitatory. Finally, note that

$$\frac{\partial^2 G_L}{\partial w \partial s} = h'_\infty(v) \frac{\partial^2 \Phi_L}{\partial w \partial s}.$$

We assume $h'_\infty(v) > 0$; this is true for most neuronal models, including the Morris–Lecar equations. Hence, it remains to find conditions for f so that $\partial^2 \Phi_L / \partial w \partial s < 0$. We leave this as an exercise.

We remark that the analysis above leads to precise conditions for when the antiphase solution is stable for excitatory synapses and unstable for inhibitory synapses. It is possible to construct nonlinearities so that these conditions are not satisfied, in which case excitatory synapses may lead to unstable antiphase solutions. It is also important to note that the conclusions of this analysis holds only if the singular perturbation parameter ϵ is sufficiently small. It is not at all clear what bifurcations may take place as ϵ increases.

9.8 Almost-Synchronous Solutions

9.8.1 Almost Synchrony with Inhibitory Synapses

We now consider the *almost-synchronous solution* shown in Fig. 9.2b. Note that one of the cells fires shortly after the other and there is then a delay until the cells fire again. Here, we assume the coupling is inhibitory and each cell, without any coupling, is oscillatory. We also assume the duty cycle is small. In this case, we will demonstrate that the almost-synchronous solution exists and is stable. Note that results from the previous section demonstrate that both the synchronous and the antiphase solution exist but are unstable. Here, we consider a network consisting of two mutually coupled cells. The analysis carries over to larger networks.

Figure 9.15 shows the projection of the almost-synchronous solution onto the (v, w) phase plane. We now step through this solution as it evolves in phase space. This description leads to a one-dimensional map, a fixed point of which corresponds to the almost-synchronous solution.

We start with both cells in the silent phase with cell 1 at the left knee ready to jump up. When cell 1 jumps up, cell 2 approaches the left branch of \mathcal{C}_A . Then cell 1 moves up the right branch of \mathcal{C}_0 and cell 2 moves down the left branch of \mathcal{C}_A . We assume the active phase is sufficiently short so that cell 1 reaches the right knee of \mathcal{C}_0 and jumps down before cell 2 reaches the left knee of \mathcal{C}_A . Note that this assumption is not necessary if the w -nullcline intersects the left branch of \mathcal{C}_A .

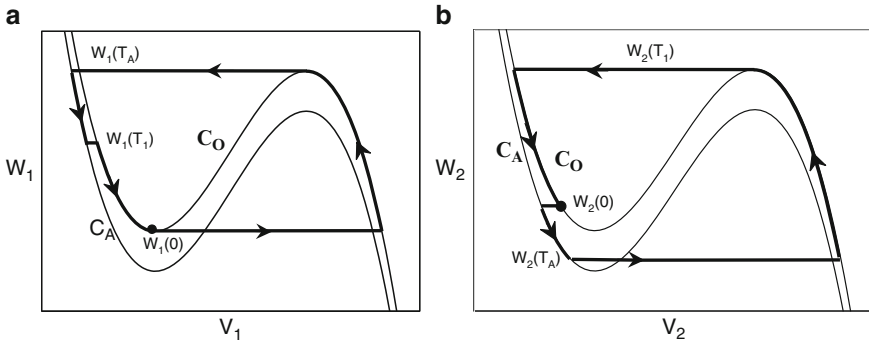


Fig. 9.15 Singular construction of the almost-synchronous solution. Cell 1 is shown in (a) and cell 2 in (b). Both cells begin in the silent phase. Cell 1 jumps up at $\tau = 0$ and jumps down at $\tau = T_A$. When cell 1 jumps down, cell 2 jumps up owing to postinhibitory rebound. Cell 2 jumps down at $\tau = T_1$. The cycle is complete when cell 1 returns to the left knee

at some point p_A . We further assume $w_2(0) - w_1(0)$ is sufficiently small so that when cell 1 jumps down, cell 2 lies below the left knee of \mathcal{C}_0 . Then cell 2 exhibits postinhibitory rebound. Suppose cell 1 jumps down at time $\tau = T_A$.

Cell 2 then moves up the right branch of \mathcal{C}_0 and cell 1 moves down the left branch of \mathcal{C}_A . If the active phase is sufficiently short, then cell 2 jumps down before cell 1 can jump back up. Suppose this happens at time $\tau = T_1$. We assume $w_1(T_1) > w_L$ so that cell 1 does not rebound at this time. This will be the case if the active phase is short enough.

Finally, both cells move down the left branch of \mathcal{C}_0 until cell 1 reaches the left knee. Suppose this happens at time T_2 . If $w_2(T_2) = w_2(0)$, then we have constructed an almost-synchronous periodic solution. We define the one-dimensional map $\pi(w_2(0)) = w_2(T_2)$. We now derive conditions for when this map is well-defined and has a stable fixed point.

We first consider the domain of π . For π to be well defined, three conditions need to be satisfied: (1) cell 2 cannot jump up before cell 1 jumps down; (2) cell 2 must rebound when cell 1 does jump down; and (3) cell 1 cannot rebound when cell 2 jumps down. We consider the time metrics ρ_L and ρ_A defined in the preceding section.

Note that condition 1 must be satisfied if the w -nullcline intersects the left branch of \mathcal{C}_A . If this is not the case, then condition 1 will be satisfied if $w_2(0) > w_L$ and $T_A < \rho_A(w_L^A, w_L)$. We next choose $\omega > w_L$ so that $\rho_A(w_L, \omega) = T_A$. If $w_L < w_2(0) < \omega$, then $w_2(T_A) < w_L$ and condition 2 is satisfied. Finally, condition 3 is satisfied if we assume $T_A < \rho_A(w_L, w_R)$.

We now show that π has a stable fixed point. Recall that a fixed point satisfies $\pi(w_2(0)) = w_2(T_2)$; that is, $\rho_L(w_L, w_2(0)) = \rho_L(w_L, w_2(T_2))$. Now cell 1 and cell 2 both lie on the left branch of \mathcal{C}_0 for $T_1 < \tau < T_2$. Since ρ_L is time-invariant, it follows that

$$\begin{aligned} \rho_L(w_L, w_2(T_2)) &= \rho_L(w_1(T_2), w_2(T_2)) = \rho_L(w_1(T_1), w_2(T_1)) \\ &= \rho_L(w_1(T_1), w_R). \end{aligned}$$

Hence, it suffices to show that

$$\rho_L(w_L, w_2(0)) = \rho_L(w_1(T_1), w_R). \quad (9.32)$$

To do this we consider two limiting cases: $w_2(0) = w_L$ and $w_2(0) = \omega$. If $w_2(0) = w_L$, then $\rho_L(w_L, w_2(0)) = 0$. Clearly, $\rho_L(w_1(T_1), w_R) > 0$. Hence,

$$\rho_L(w_L, w_2(0)) < \rho_L(w_1(T_1), w_R).$$

We will prove if $w_2(0) = \omega$, then $\rho_L(w_L, w_2(0)) > \rho_L(w_1(T_1), w_R)$. It then follows that there must exist $w_2(0) \in (w_L, \omega)$ such that (9.32) is satisfied.

So assume $w_2(0) = \omega$. Then $\rho_A(w_L, w_2(0)) = \rho_A(w_L, \omega) = T_A$ and cell 2 jumps up at $w_2(T_A) = w_L$. Moreover, cell 2 lies in the active phase for $T_A < \tau < T_1$ with $w_2(T_A) = w_L$ and $w_2(T_1) = w_R$. Recall that T_A is the time it takes for a solution of (9.21) to go from w_L to w_R . Hence, $T_1 - T_A = T_A$. Since $w_1(T_A) = w_R$, it follows that

$$\rho_A(w_1(T_1), w_R) = \rho_A(w_1(T_1), w_1(T_A)) = T_1 - T_A = T_A.$$

Therefore,

$$\rho_A(w_L, w_2(0)) = \rho_A(w_1(T_1), w_R) = T_A.$$

Using (9.28), we find that if $w(\tau, b)$ is the solution of (9.20) with $w(0, b) = b$, then

$$\rho_L(w_L, \omega) = \int_0^{T_A} \frac{G_L(w(\tau, \omega), s_A)}{G_L(w(\tau, \omega), 0)} d\tau$$

and

$$\rho_L(w_1(T_1), w_R) = \int_0^{T_A} \frac{G_L(w(\tau, w_R), s_A)}{G_L(w(\tau, w_R), 0)} d\tau.$$

Finally, we showed in Sect. 9.7.2 that $G_L(w, s_A)/G_L(w, 0)$ is a decreasing function of w if the synapses are inhibitory. Moreover, $\omega < w_R$ and, therefore, $w(\tau, \omega) < w(\tau, w_R)$ for each $\tau \in (0, T_A)$. It follows that if $w_2(0) = \omega$, then $\rho_L(w_L, w_2(0)) > \rho_L(w_1(T_1), w_R)$ and this completes the proof that there exists a stable fixed point of π .

9.8.2 Almost Synchrony with Excitatory Synapses

It is also possible that two mutually coupled cells with excitatory coupling exhibit almost-synchronous solutions. This was considered in several papers, including [215]. In [19], it is proved almost synchrony may arise in excitatory networks if we do not assume, as before, cells evolve on the slow timescale while in the active phase. We note that if a cell evolves on the fast timescale while in the active phase,

then the cell's active phase would be shorter; this would then correspond more to a spiking neuron rather than a bursting neuron that we have been considering so far in this chapter.

We now write the equation for each cell as

$$\begin{aligned}\frac{dv}{dt} &= f(v, w), \\ \frac{dw}{dt} &= \epsilon g(v, w)/\tau_\infty(v),\end{aligned}\quad (9.33)$$

where $f(v, w)$ and $g(v, w)$ are as before and the function $\tau_\infty(v)$ is given by

$$\tau_\infty(v) = \begin{cases} 1 & \text{if } v < v_\theta \\ \epsilon/\gamma & \text{if } v > v_\theta. \end{cases}\quad (9.34)$$

Here, the parameter v_θ is the threshold for entering the active phase and γ governs the rate of passage through the active phase. We assume v_θ lies between the knees of C_0 . A singular periodic solution of (9.33) is shown in Fig. 9.16a. While in the silent phase, the singular solution lies along the left branch of the v -nullcline and evolves according to (9.10). Once the singular solution reaches the left knee of C_0 , it begins to jump up according to (9.12). However, this equation is valid only until $v = v_\theta$; at this point the equations become

$$\begin{aligned}\frac{dv}{dt} &= f(v, w), \\ \frac{dw}{dt} &= \gamma g(v, w).\end{aligned}\quad (9.35)$$

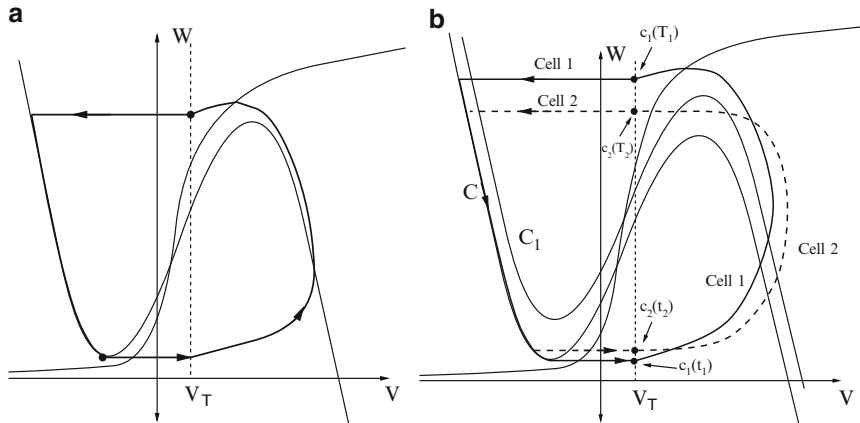


Fig. 9.16 Almost-synchronous solution with excitatory synapses. (a) The synchronous solution. (b) Singular construction for stability proof. Note that the order in which the two cells fire switches after one cycle

These equations determine the evolution of the solution in the active phase. The solution must eventually return to the line $v = v_\theta$ and the jump down corresponds to a horizontal segment in the phase plane whose evolution is determined by (9.12). Note that the singular solution now differs from that shown in Fig. 9.4; in particular, the active phase does not lie on the right branch of the v -nullcline.

We now consider two mutually coupled oscillatory cells and write the model as

$$\begin{aligned}\frac{dv_i}{dt} &= f(v_i, w_i) - g_{\text{syn}} s_j(v_i - v_{\text{syn}}), \\ \frac{dw_i}{dt} &= \epsilon g(v_i, w_i)/\tau_\infty(v_i),\end{aligned}\quad (9.36)$$

where $f(v, w)$ and $g(v, w)$ are as before and $s_j = H(v_j - v_T)$, where H is the Heaviside step function. To simplify the analysis, we will assume $v_T = v_\theta$.

The construction of a synchronous solution for the coupled system is done in the same manner as that for the periodic solution for the uncoupled cell; the only difference is that the dynamics are changed once the voltage passes across v_θ . Thus, if each $v_i > v_\theta$, then (9.35) is replaced by

$$\begin{aligned}\frac{dv_i}{dt} &= f(v_i, w_i) - g_{\text{syn}}(v_i - v_{\text{syn}}), \\ \frac{dw_i}{dt} &= \gamma g(v_i, w_i).\end{aligned}\quad (9.37)$$

Note that the synchronous solution is not the same as the uncoupled periodic solution; this is because they satisfy different equations while in the active phase.

We now explain why the synchronous solution may be unstable and there exists a stable almost-synchronous solution. To do this, we assume both cells lie initially close to each other in the silent phase with cell 1 at the left knee of \mathcal{C}_0 ready to jump up. We step through the construction of the singular solution until one of the cells returns to the left knee of \mathcal{C}_0 . We wish to show that if the cells are initially close enough to each other, then after one cycle they are further apart than when they started. This will demonstrate that the synchronous solution is unstable. The analysis will also demonstrate when there exists a stable almost-synchronous solution.

The singular solution is shown in Fig. 9.16b. The first portion begins as cell 1 leaves the left knee. In this portion, cell 1 is governed by (9.12) and has a trajectory that is horizontal until it crosses v_θ at, say, $t = t_1$. During this time, cell 2 does not move. At time t_1 , s_1 switches from 0 to 1, so cell 2 is then governed by (9.12), whereas cell 1 is governed by (9.35). Cell 2 can now move, and does so horizontally until it reaches v_θ at, say, $t = t_2$. Note that for $t_1 < t < t_2$, cell 1 moves both horizontally and vertically, because it is governed by (9.37). At time t_2 , s_2 switches from 0 to 1; hence, cell 1 is then governed by (9.37). Eventually, both cells reach v_θ . Once a cell crosses v_θ , it moves horizontally to the left branch of either \mathcal{C}_0 or \mathcal{C}_1 , depending on whether the other cell is still active or not. Once both cells are silent, they both evolve along the left branch of \mathcal{C}_0 until one of them reaches the left knee.

Note that there are parts of the trajectories in phase space in which the two cells are governed by different equations. In terms of voltages, let v_F denote the v -value of the trajectory of cell 1 at $t = t_2$. Then for $v_\theta < v < v_F$, the two cells satisfy different equations. Cell 1 does not receive excitation from cell 2, and hence satisfies (9.35). Cell 2 does however receive excitation when it is in that portion of the phase plane, so it is governed by (9.37). As shown in [19], this difference causes a separation between the orbits of the cells which is bounded from below by $k_1\gamma$ and from above by $k_2\gamma$ for some $k_2 > k_1 > 0$, independent of the initial difference, provided that the latter is small enough. It is this separation between the orbits that leads to the instability of the synchronous solution. The analysis in [19] also demonstrates that, because the separation is bounded from above, there must exist a stable solution in which the cells fire at slightly different times: if one cell fires at time 0, then the other cell will fire at t_1 , given above. This then corresponds to the almost-synchronous solution.

We note that the order in which the cells fire may or may not switch from one cycle to the next. This is illustrated in Fig. 9.16b and a complete analysis is given in [19].

9.8.3 Synchrony with Inhibitory Synapses

It may be surprising that networks with only inhibitory synapses can generate stable synchronous oscillations; however, this has indeed been demonstrated, both numerically and analytically, in several studies [100, 265, 278, 284]. The main conclusion of the analytic studies is that synchrony may arise in inhibitory networks if the inhibition is slow, corresponding to GABA_B synapses. We note that if the inhibitory synapses are fast and direct, the synchronous solution must be unstable. This is because when one cell jumps up, the resulting inhibition immediately “steps on” the postsynaptic cell and delays its firing. For the synchronous solution to be stable, there must be a delay from the time one cell fires until the resulting inhibition affects the other cell. One convenient way to do this is to consider indirect synapses. That is, as discussed earlier, we introduce a new synaptic variable x_i and assume (x_i, s_i) satisfy (9.5).

Using the analysis given in the preceding sections, one can show that if the inhibitory synapses are indirect, the cells are oscillatory, and the active phase is sufficiently short, then the synchronous solution is stable. We have shown that in this case the antiphase solution is unstable. If there are direct synapses, then the network will exhibit almost-synchronous solutions. With indirect synapses, the delay in synaptic activation allows the trailing cell to fire shortly after the leading cell fires and before it receives synaptic input. We do not include the details here.

9.9 Slow Inhibitory Synapses

Recall that different types of synapses may turn on or turn off at very different rates. For example, GABA_B synapses are slow to activate and slow to turn off compared with GABA_A synapses. The rates at which synapses turn on or turn off may have a profound affect on the network behavior. For example, the solutions shown in Fig. 9.2c and d were generated by choosing the rate at which the inhibitory synapse turns off to be small.

Note that α and β determine the rates at which the synapse turns on and turns off. We have, so far, considered *fast synapses*. By this we mean that α and β are $O(1)$ with respect to ϵ . When a cell either jumps up or jumps down, the corresponding synaptic variable either approaches s_A or approaches 0 on the fast timescale. In this section, we consider *slow synapses*; that is, either α or β (or both) is $O(\epsilon)$. We will use fast/slow geometric analysis to construct singular trajectories corresponding to synchronous and antiphase solutions.

9.9.1 Fast/Slow Decomposition

The first step in the analysis is to decompose the full network (9.4) into fast and slow equations. Here, we assume $\alpha = O(1)$ with respect to ϵ and $\beta = \epsilon K$, where K does not depend on ϵ ; hence, the synapses activate on the fast timescale and turn off on the slow timescale.

We derive slow subsystems valid when cells lie in either the silent or the active phase. There are several cases to consider and we only discuss two of these in detail. First, suppose both cells are silent. Then each $v_i < V_T$ and $H_\infty(v_i - V_T) = 0$. (Here, we are assuming H_∞ is the Heaviside step function.) Hence, after letting $\tau = \epsilon t$ and setting $\epsilon = 0$, (9.4) becomes

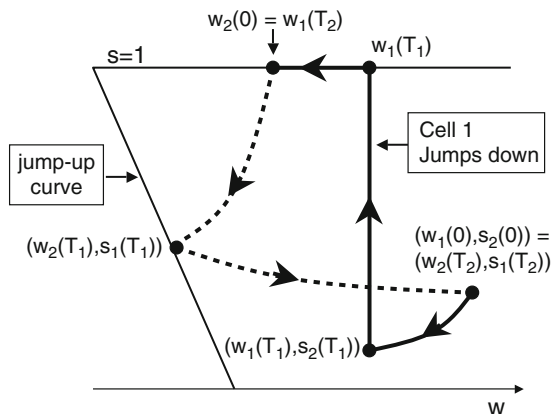
$$\begin{aligned} 0 &= f(v_i, w_i) - s_j g_{\text{syn}}(v_i - v_{\text{syn}}), \\ \frac{dw_i}{d\tau} &= g(v_i, w_i), \\ \frac{ds_i}{d\tau} &= -K s_i. \end{aligned} \tag{9.38}$$

This system can be simplified as follows. As before we write the left branch of C_s as $v = \Phi_L(w, s)$ and let $G_L(w, s) = g(\Phi_L(w, s), s)$. Then,

$$\begin{aligned} \frac{dw_i}{d\tau} &= G_L(w_i, s_j), \\ \frac{ds_i}{d\tau} &= -K s_i. \end{aligned} \tag{9.39}$$

These equations determine the evolution of the slow variables in the silent phase. The equations are well defined as long as each (v_i, w_i) lies along the left branch

Fig. 9.17 Geometric construction of an antiphase solution for slow synapses. The projection of the solution is shown in the (w, s) slow phase plane. Cell 1 is shown with a solid curve, and cell 2 is shown with a dashed curve



of the cubic determined by s_j . Recall that the left knee of the cubic \mathcal{C}_s depends on s and we denote the position of this left knee as $w_L(s)$. This defines a jump-up curve $\mathcal{C}_{\text{JUP}} \equiv (w_L(s), s)$ in the slow phase plane, as shown in Fig. 9.17. The cells remain in the silent phase and each (w_i, s_i) satisfies (9.39) as long as $w_i > w_L(s_j)$. If $w_i(\tau) = w_L(s_j)$, then cell i jumps up to the active phase.

Now suppose cell i is silent and cell j is active. Then s_i is a slow variable, and $s_j \equiv 1$ is a fast variable. In this case, (w_i, s_i) satisfies

$$\begin{aligned} \frac{dw_i}{d\tau} &= G_L(w_i, 1), \\ \frac{ds_i}{d\tau} &= -K s_i \end{aligned} \tag{9.40}$$

and (w_j, s_j) satisfies

$$\begin{aligned} \frac{dw_j}{d\tau} &= G_R(w_j, s_i) \\ s_j(\tau) &= 1 \end{aligned} \tag{9.41}$$

These equations are well defined as long as cell j lies on the right branch of the cubic determined by s_i and cell i is on the left branch of the cubic \mathcal{C}_1 . Cell j will jump down if (v_j, w_j) reaches the right knee of \mathcal{C}_{s_i} – that is, $w_j = w_R(s_i)$.

9.9.2 Antiphase Solution

We now construct singular trajectories corresponding to antiphase and suppressed solutions of (9.4). We assume throughout that the synapses are inhibitory and decay on the slow timescale. Throughout the analysis, we consider the projection of the solution onto the (w, s) slow phase plane. As we shall see, the existence of a particular type of solution depends on the relative sizes of the rate at which the synapse decays and the rate at which the cells evolve during the silent phase.

The projection of an antiphase solution onto the (w, s) phase plane is shown in Fig. 9.17. The curves represent (w_1, s_2) and (w_2, s_1) , since the synaptic input to cell i is determined by s_j , $j \neq i$. We step through the evolution of this solution starting at the time when both cells lie in the silent phase and cell 1 has just jumped down from the active phase. This implies that $s_1(0) = 1$. Both cells then evolve in the silent phase and each (w_i, s_j) satisfies (9.39). This continues until cell 2 reaches the jump-up curve \mathcal{C}_{JUP} . Suppose this occurs at $\tau = T_1$, at which time the inhibition s_2 felt by cell 1 jumps up to the line $s_2 = 1$. Cell 2 then evolves in the active phase; we illustrate the projection of cell 2's trajectory during the active phase with a dotted curve in Fig. 9.17. Note that $s_1(\tau)$ still satisfies the second equation in (9.39); hence, it keeps decreasing while cell 2 is active. During this time, cell 1 lies in the silent phase with $s_2 = 1$. This continues until cell 2 reaches the jump-down curve $w = w_R(s_1)$. We denote this time as T_2 . Cell 2 then jumps down and this completes half of a complete cycle. For this to be an antiphase solution, we must have $w_1(T_2) = w_2(0)$ and $s_2(T_2) = s_1(0)$.

The construction of the antiphase solution requires a number of assumptions. It is not clear, for example, why if we start with both cells in the silent phase one of them will be able to reach the jump-up curve \mathcal{C}_{JUP} . If the cells are oscillatory for fixed levels of synaptic input, then this will certainly be the case. However, it is possible that even if the cells are excitable for fixed levels of synaptic input they are able to reach \mathcal{C}_{JUP} . To explain why this is the case, we assume the cells are excitable for fixed levels of synaptic input. That is, for each s , $0 \leq s \leq 1$, the cubic-shaped nullcline \mathcal{C}_s intersects the w -nullcline along the left branch of \mathcal{C}_s . Denote this point as $(v_{\text{FP}}(s), w_{\text{FP}}(s))$ and let $p_{\text{FP}}(s) = (w_{\text{FP}}(s), s)$. Then $\mathcal{C}_{\text{FP}} \equiv p_{\text{FP}}(s) : 0 \leq s \leq 1\}$ defines a curve in the (w, s) slow phase plane.

Note that \mathcal{C}_{FP} is the w -nullcline of the slow system (9.39). Along \mathcal{C}_{FP} , $dw/d\tau = 0$. If $w < W_{\text{FP}}(s)$, $dw/d\tau > 0$, so w increases, whereas if $dw/d\tau < 0$, w decreases. Moreover, $(w_{\text{FP}}, 0)$ is a fixed point of (9.39).

Solutions of (9.39) may reach the jump-up curve even though the cells are excitable for fixed values of the synaptic input. Trajectories that begin to the “right” of \mathcal{C}_{FP} (as will be the case for all of the cases considered here) will begin to move to left with s decreasing. The trajectory may then cross \mathcal{C}_{FP} vertically, after which w increases, and the trajectory may eventually cross the jump-up curve \mathcal{C}_{JUP} . Note that this will not be possible if the synaptic variable s decays too quickly; that is, if the parameter K is too large. In this case, the trajectory will approach the fixed point $(w_L(0), 0)$. We also note that trajectories cannot reach \mathcal{C}_{JUP} if the synapses decay too slowly. In this case, the trajectories will approach near \mathcal{C}_{FP} and then follow this curve until they approach the fixed point $(w_L(0), 0)$.

These considerations have the following consequences for the existence of an antiphase solution. First, suppose the cells are excitable for each fixed level of synaptic input. If the synapses decay too slowly, then there cannot exist an antiphase solution. If the synapses decay too quickly, then there cannot exist an antiphase solution if the active phase is too short. There will exist an antiphase solution if the active phase is long enough and the synapse decays fast enough. A similar analysis holds if the cells are oscillatory for some (or all) fixed levels of synaptic input.

9.9.3 Suppressed Solutions

We next consider the so-called *suppressed solutions* shown in Fig. 9.2c. In such rhythms, one cell remains quiet while the other oscillates. Here, we assume a single cell, without coupling, is oscillatory. Moreover, the cells are excitable for sufficiently high levels of inhibition. That is, there exists $s_* \in (0, 1)$, so if $0 \leq s < s_*$, then the w -nullcline intersects \mathcal{C}_s along its middle branch, whereas if $s_* < s \leq 1$, then the w -nullcline intersects the left branch of \mathcal{C}_s at some point $p_{\text{FP}}(s)$. Note that $\{p_{\text{FP}}(s) : s_* < s \leq 1\}$ defines a curve \mathcal{C}_{FP} that touches \mathcal{C}_{JUP} when $s = s_*$.

Suppressed solutions arise if the rate at which the synapse turns off is sufficiently slower than the rate at which the cells evolve in the silent phase; that is, the parameter K is sufficiently small. The reason for this is that if the inhibition decays slowly enough, the leading cell can recover and fire again before the inhibition from its previous active phase wears off enough to allow the other cell to fire.

This type of solution cannot exist if the cells are excitable rather than oscillatory, since there is no input from the quiet cell to drive the active one. On the other hand, suppressed solutions only arise if the cells are excitable for some fixed levels of inhibition; i.e., some $s \in (0, 1]$. If this is not the case, then the w -coordinate of the suppressed cell must keep decreasing until that cell eventually reaches the jump-up curve and fires.

If the synaptic inhibition decays at a rate comparable to the recovery of the cell, complex hybrid solutions can occur, in which one cell is suppressed for several cycles, while the other fires, and then fires while the other is suppressed. An example is shown in Fig. 9.2d. In this example, each cell is excitable when uncoupled but is oscillatory for higher levels of inhibition. A cell can fire a number of times while the other cell is suppressed. The inhibition of the firing cell must eventually wear off, such that that cell can no longer fire. This then allows the inhibition of the suppressed cell to wear off to the level from which it can fire. The roles of the two cells are then reversed.

9.10 Propagating Waves

We now consider propagating activity patterns. These may arise in both excitatory and inhibitory (as well as excitatory–inhibitory) networks and there have been numerous theoretical studies of mechanisms underlying both the existence and stability of this phenomenon. Wavelike activity has been observed experimentally in several brain regions (see also Chaps. 8, and 12).

Here, we will consider a conductance-based model of the region of the brain called the thalamus. At its simplest, the network consists of two layers of neurons, the excitatory thalamocortical cells and the inhibitory reticular nucleus cells. These nuclei have been shown to play a key role in the generation of sleep rhythms. Each neuron is modeled with a single- compartment, conductance-based model that

includes the usual potassium and sodium channels for spike generation, as well as a low threshold T-type calcium channel. This last channel allows the cells to produce rebound excitation. Details of the model can be found in [266].

Each cell is modeled as

$$\frac{dv}{dt} = f(v, h),$$

$$\frac{dh}{dt} = \epsilon g(v, h)/\tau(v).$$

The phase plane for an individual cell is shown in Fig. 9.18a. Note that the cubic-shaped v -nullcline is now “upside down” from what we had before. This is because the slow variable h represents the availability of the inward T-current, instead of the outward potassium current activation variable as before. If a cell receives inhibitory input, then this raises the v -nullcline and the cell moves toward the new fixed point. If the inhibition is then rapidly removed, the v -nullcline falls back to the original position ($s = 0$), which leaves (v, h) above h_{\max} , the position of the left knee of the v -nullcline. This causes the voltage to jump to the right branch of the nullcline

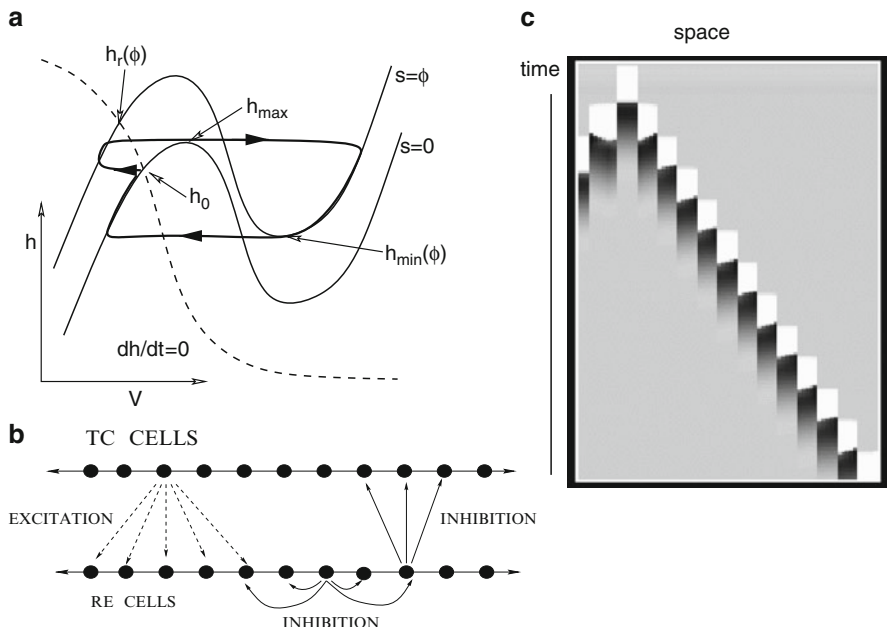


Fig. 9.18 Thalamic network model. (a) Phase plane showing the h -nullcline (dashed line) and v -nullcline at rest ($s = 0$). Several important values of h are shown. The approximate singular trajectory of a lurching wave is drawn in thick lines. (b) The architecture of the full model. (c) A simulation of a lurching wave. The gray scale depicts voltage; white corresponds to -40 mV and black corresponds to -90 mV. TC thalamocortical, RE reticular nucleus

(a rebound spike), before returning to rest. Suppose the two-layer network of these cells is wired up as in Fig. 9.18b. Then, under some circumstance, the result is a wave of activity across the network. Such a wave is shown in Fig. 9.18c. This is not a smooth wave; rather we call this a *lurching wave*. Here is what happens. A group of thalamocortical cells fire. This excites reticular nucleus cells nearby, causing them to fire. They inhibit the thalamocortical cells, including those surrounding the original population of firing cells. The fresh population is inhibited and when the inhibition wears off, the cells fire as a group and so on.

We now use geometric singular perturbation theory to further explain this and find a formula for the wave speed. To do this, we will simplify the situation a bit and consider a single layer of cells with inhibitory coupling. Thus, when a group of cells fire, they inhibit a neighboring group. After the inhibition wears off, the next group of cells fire and so on. The present exposition will be a drastic approximation to a fuller analysis of the model which can be found in [266].

We consider a one-dimensional array of cells coupled through fast and direct inhibition. Each curve \mathcal{C}_s , $0 \leq s \leq 1$, is assumed to be excitable. We assume throughout that there is a square synaptic footprint of unit length; that is, each cell sends the same amount of inhibition to each of its immediate neighbors, as well as itself. One can view each cell as representing the dynamics of an effective footprint of a cluster of cells in a more complicated network. Throughout this analysis, we consider the slow timescale.

We consider a lurching wave propagating to the right and assume the “leading edge” at time $\tau = T_1$ is at cell 1. By this we mean that cell 1 fires at $\tau = T_1$ and none of the cells C_k with $k > 1$ have fired for $\tau < T_1$. We follow the trajectories of cell 1 and cell 2 in phase space until cell 2 fires. Suppose this is at time $\tau = T_2$. For there to be a lurching wave, we require that the position of cell 2 at $\tau = T_2$ is exactly the same as the position of cell 1 at $\tau = T_1$. This will lead to analytic expressions for the time $T_2 - T_1 = T_{\text{tot}}$ between firings; this then determines the velocity of the propagating wave. For convenience, we assume $T_1 = 0$, and thus $T_2 = T_{\text{tot}}$, the total duration of one cycle.

The trajectories of cell 1 and cell 2 are illustrated in Fig. 9.18a. Let \mathcal{C}_0 be the cubic corresponding to a single cell without synaptic input and \mathcal{C}_A , $A = \alpha/(\alpha + \beta)$ the cubic corresponding to a cell that does receive synaptic input. At $\tau = 0$, cell 1 jumps up to the right branch of \mathcal{C}_A . We assume at this time $h_1 = h_J$, where h_J has yet to be determined. Cell 2 lies at the rest point $p_0 = (v_0, h_0)$ for $\tau < 0$ and jumps to the left branch of cubic \mathcal{C}_A when $\tau = 0$. For $\tau > 0$, cell 1 moves down the right branch of \mathcal{C}_A and cell 2 moves up the left branch of \mathcal{C}_A . This continues until cell 1 reaches the right knee of \mathcal{C}_A and jumps down. Suppose this happens at time T_{tot} . For there to be a lurching wave, we require that $h_2(T_{\text{tot}}) = h_J$.

To simplify the analysis, We now make several assumptions concerning the non-linear functions in the model. The simplifying assumptions are the following:

- (1) In the silent phase, $\tau(v) = \tau_L$, a constant.
- (2) In the active phase, $\tau(v) = \tau_R$, a constant, and $h_\infty(v) = 0$.
- (3) The left branches $v = v_L(h, s)$ do not depend on h .

All of these assumptions are nearly satisfied for the model described in [266]. Observe that assumption 2 implies, in the active phase, the equation for h in the slow time $\tau = \epsilon t$ simplifies to

$$\dot{h} = -h/\tau_R. \quad (9.42)$$

From assumption 1, $h(\tau)$ satisfies the following equation in the silent phase:

$$\dot{h} = (h_\infty(v) - h)/\tau_L. \quad (9.43)$$

Since we are assuming the cells are excitable for each fixed value of s , we can define $(v_{FP}(s), h_{FP}(s))$ to be the point where \mathcal{C}_s intersects the h -nullcline. Using assumption 3, we see that on the left branch of \mathcal{C}_s , for any fixed s , v takes a constant value, which must then be $v_{FP}(s)$; therefore, $h_\infty(v)$ is also a constant, namely, $h_{FP}(s)$, and hence we have the following equation describing the behavior in the silent phase:

$$\dot{h} = (h_{FP}(s) - h)/\tau_L. \quad (9.44)$$

We now derive a formula for T_{tot} . Recall that cell 1 jumps up at $h_1 = h_J$, where h_J is yet to be determined. It then follows from assumption 2 that for $0 < \tau < T_{\text{tot}}$, $h_1(\tau)$ satisfies equation (9.42) subject to $h_1(0) = h_J$. Now cell 1 jumps down at the right knee of \mathcal{C}_A at $\tau = T_{\text{tot}}$. Denote the position of this knee as $h_{RK}(A)$. Then $h_1(T_{\text{tot}}) = h_{RK}(A)$. Solving (9.42) together with these two boundary conditions leads to the following expression relating the unknowns h_J and T_{tot} :

$$T_{\text{tot}} = \tau_R \ln \frac{h_J}{h_{RK}(A)}. \quad (9.45)$$

On the other hand, cell 2 lies along the left branch of \mathcal{C}_A for $0 < \tau < T_{\text{tot}}$ and $h_2(\tau)$ satisfies (9.44) with $s = A$, together with the initial condition $h_2(0) = h_0$. Hence,

$$h_2(\tau) = h_{FP}(A) + (h_0 - h_{FP}(A))e^{-\tau/\tau_L}. \quad (9.46)$$

Recall that we also have that $h_2(T_{\text{tot}}) = h_J$; hence, h_J and T_{tot} must also satisfy

$$T_{\text{tot}} = \tau_L \ln \frac{h_{FP}(A) - h_0}{h_{FP}(A) - h_J}. \quad (9.47)$$

Combining (9.45) and (9.46) gives

$$A_1(h_J) \equiv \frac{h_{FP}(A) - h_J}{h_{FP}(A) - h_0} = \left(\frac{h_{RK}(A)}{h_J} \right)^{\frac{\tau_R}{\tau_L}} \equiv A_2(h_J). \quad (9.48)$$

This is a single equation for the unknown h_J . All of the other parameters in this equation can be easily determined by properties of a single cell with constant input. Once we solve for h_J , we can compute T_{tot} , the period of one cycle, from (9.45).

This equation has either two roots or no roots. To see this, note that $A_1(0) < \infty$ while $A_2(h)$ approaches ∞ as $h \rightarrow 0$. Furthermore, $A_1(h_{\text{FP}}(A)) = 0 < A_2(h_{\text{FP}}(A))$. Thus, if there is one (nontangent) root, then there must be another. One of these is close to 0 and the other is close to $h_{\text{FP}}(A)$ and as the ratio τ_R/τ_L increases, the second root approaches $h_{\text{FP}}(A)$. Since no jump to the right branch can occur if $h_{\text{FP}}(A) < h_{\text{LK}}(0)$, we see that if we choose the larger root of (9.48), then (9.45) will be defined.

9.11 Bibliography

Half-centered oscillations, in which two mutually coupled cells can generate antiphase oscillations, were first described by Brown [24]. Another early paper that recognized the importance of postinhibitory rebound was that of Perkel and Mulloney [211].

The geometric singular perturbation approach described here began with papers by Kopell and Somers [163], who introduced the phrase “fast threshold modulation,” and Terman and Wang [264]. Reviews of this and subsequent work can be found in Rubin and Terman [236] and Kopell and Ermentrout [160].

Many papers have addressed the issue of when excitation or inhibition leads to synchrony or antiphase oscillations. Early papers are those of Van-Vreeswijk et al. [278], Gerstner et al. [100], and Wang and Rinzel [284]. Our approach follows most closely the paper of Wang and Rinzel, who recognized the importance of slow inhibitory dynamics in synchronizing the neuronal oscillations.

The issues described in this chapter are motivated by several neuronal systems, including thalamocortical sleep rhythms, olfaction, and rhythmic behavior in the basal ganglia. References include [16, 61, 105, 176, 232, 251].

9.12 Exercises

1. Consider a system of the form (9.1) and assume the system is oscillatory. Moreover,

$$g(v, w) = (w_\infty(v) - w)/\tau(v). \quad (9.49)$$

Assume there are positive constants τ_L and τ_R so that (1) $w_\infty(v) = 0$ and $\tau(v) = \tau_L$ along the left branch of the v -nullcline and (2) $w_\infty(v) = 1$ and $\tau(v) = \tau_R$ along the right branch of the v -nullcline. Finally, assume the left and right knees of the v -nullcline are at $w_L < w_R$, respectively. Compute the period

- of the singular periodic solution, with respect to the slow timescale. The answer should be in terms of the constants τ_L , τ_R , w_L , and w_R .
2. Construct a network of two mutually coupled cells with excitatory synapses that exhibits both a stable synchronous solution and a stable antiphase solution.
 3. Construct a network of two mutually coupled cells with inhibitory synapses that exhibits antiphase (postinhibitory rebound) behavior and, by adjusting a single parameter, an almost synchronous solution. By adjusting another parameter, the network should exhibit a suppressed solution.
 4. Consider a network of two mutually coupled neurons, modeled as in (9.4). Assume each cell, without coupling, is oscillatory and $g(v, w)$ satisfies the assumption described in the first exercise. As before, assume the left knees of the cubics C_0 and C_A are at w_L and w_L^A , respectively, and the right knees are at w_R and w_R^A , respectively. Compute the frequencies of the synchronous solutions corresponding to excitatory and inhibitory synapses. Which is larger? How do these frequencies compare with that of a single cell without coupling?
 5. Consider two cells that satisfy (9.1). Assume one of the cells is excitable so that it has a unique fixed point on the left branch of its v -nullcline, and the other cell has a unique fixed point on the right branch of its v -nullcline. Now suppose we couple them as in (9.4). Under what conditions will the coupled system exhibit stable oscillatory behavior? Are the oscillations synchronous or antiphase, or can one obtain both?
 6. Construct a network of four mutually coupled cells that exhibits (for different values of parameters) (a) synchronous behavior, (b) a two-clustered solution in which there are two clusters with two cells in each cluster, (c) a two-clustered solution in which there are three cells in one cluster and only one cell in the other cluster, (d) a three-clustered solution in which there are two cells in one cluster and only one cell in the other two clusters, (e) a four-clustered solution in which the cells take turns firing and the phase between the firings is constant, (f) an almost-synchronous solution in which the cells take turns firing and the phase between the “trailing cell” and the “leading cell” is longer than the phase difference between other cells, (g) a suppressed solution in which one cell fires periodically but the other cells are suppressed, and (h) a solution in which two of the cells fire in antiphase and the other two cells are suppressed.
 7. Give a detailed construction of the singular solutions corresponding to antiphase solutions arising from postinhibitory rebound for the following cases: (a) cellular escape, (b) synaptic escape, and (c) synaptic release.
 8. Consider the antiphase solutions arising from postinhibitory rebound. How do the frequency and duty cycle depend on g_{syn} and the synaptic threshold V_T ? You should consider separate cases: the cellular escape and release mechanisms and the synaptic escape and release mechanisms. Justify your answers using the singular constructions.
 9. In Sect. 9.7, we constructed the singular antiphase solution for excitatory synapses when the cells have a short duty cycle. Do the same thing for inhibitory synapses. Show that this solution is unstable if the same conditions described at the end of that section are satisfied.

10. Construct a network of two mutually coupled cells with slow inhibitory networks which exhibits a firing pattern in which the cells take turns firing action potentials; during each cycle, one of the cells fires two spikes, whereas the other cell fires only one spike. How does this pattern change as you change the synaptic coupling strength g_{syn} and the rate of synaptic decay β ? Try to find a chaotic solution in which the number of times a cell fires before the other cell takes over appears to be random.
11. Saper et al. [242] suggested the regulation of sleep and wake is due to mutual inhibitory interactions between sleep-active cells in the ventral lateral nucleus and wake-promoting cells in nuclei including the dorsal raphe nucleus, the locus coeruleus, and the tuberomammillary nucleus. Construct a simple model for the sleep–wake cycle that includes just two mutually coupled cells. Say that cell 1 corresponds to the sleep-active nuclei and cell 2 corresponds to the wake-active nuclei. The cells should take turns firing; cell 1 should be active for approximately 8 h and cell 2 should be active for approximately 16 h.
12. In Fig. 9.18c, we show a lurching wave with no activity in its wake. It is also possible that the cells continue to fire repetitively in the wake of the wave. Construct a single-layered inhibitory network and a double-layered excitatory–inhibitory network that exhibits both types of waves. What parameters do you need to change so that the network switches from one type of wave to the other?
13. Prove as cells move along the same left or right branch of a cubic, the time metric between the cells is invariant.
14. Prove $\Pi'_2 = \Pi'_4 = 1$, where Π'_2 and Π'_4 were defined in Sect. 9.7.2.

Chapter 10

Noise

Neurons live in a noisy environment; that is, they are subjected to many sources of noise. For example, we treat ion channels deterministically, but in reality, opening and closing of channels is a probabilistic event. Similarly, there is spontaneous release of neurotransmitter which leads to random bombardment of small depolarizations and hyperpolarizations. In vivo, there is increasing evidence that cortical neurons live in a high-conductance state due to the asynchronous firing of the cells which are presynaptic to them. Noise in neural and other excitable systems has been the subject of research since the early 1960s. There are a number of good books and reviews about the subject. We single out the extensive review [179] and the books [169, 274].

Our goal in this chapter is to look at several aspects of the role of noise in neural models. Most of the analysis that we do will be on scalar models for the firing of action potentials, such as the leaky integrate-and-fire neuron. However, we also look at more general ionic models and stochastic channel dynamics. Since few textbooks in theoretical neuroscience address the issue of noise, we felt that a few words on the subject were warranted. There is no way to introduce a comprehensive theory of stochastic differential equations in the allotted space so we refer the reader to a number of good texts; notably [96] and the first five chapters of [154]. The main point of the analysis in this chapter is to see the effects of noise on the subthreshold properties of neurons. This will allow us to develop heuristics for the firing rates of neurons in networks later in the book.

Since the treatment of noise in this chapter is somewhat informal, we will not describe the beautiful mathematical constructions such as the Ito integral. Our main interest is the Langevin equation:

$$dX = A(X, t)dt + B(X, t)dW(t). \quad (10.1)$$

Here, $X \in R^n$, $A : R^n \times R \rightarrow R^n$, B is an $n \times n$ matrix of functions, $B_{jk} : R^n \times R \rightarrow R$, and $W(t)$ is a vector of independent Wiener processes. (A Wiener process is formally defined below.) To get a feeling for this, it is helpful to solve this numerically:

$$X(n+1) = X(n) + hA(X(n), t_n) + B(X(n), t_n)\sqrt{h}\hat{N}(0, 1), \quad (10.2)$$

where h is the discretization time step and $\hat{N}(0, 1)$ is a vector of normally distributed independent random numbers with unit variance. (We will explain the strange \sqrt{h} scaling below; you will just have to trust us on this for now.)

What does noise do to neurons? One of the main effects is that it allows them to fire in the presence of subthreshold inputs. That is, if a current is applied that will not cause the deterministic model to fire, the addition of zero mean noise can induce the neuron to fire. Figure 10.1a shows a simulation of the integrate-and-fire model with additive noise,

$$dV = (I - V)dt + \sigma dW_t,$$

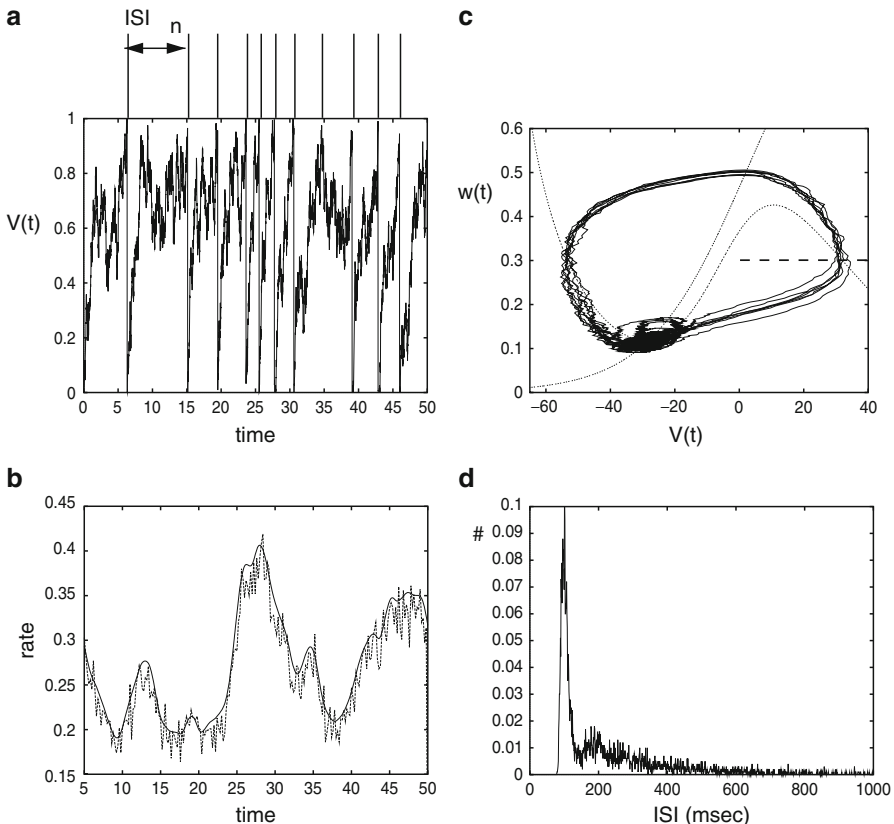


Fig. 10.1 Noisy neurons. (a) Integrate-and-fire model $dV = (I - V)dt + \sigma dW(t)$ with $I = 0.75$ and $\sigma = 0.1$. This numerical solution was computed using (10.2) with $h = 0.01$. Vertical lines represent times at which the model crosses $V = 1$ and is reset to 0. (b) Noise allows a subthreshold stimulus to be encoded. (c) Noisy Morris-Lecar model with class II parameters, $I = 85$, and unit variance noise in the voltage component. (d) Distribution of crossings of $w = 0.3$. ISI interspike interval

which is simulated with the simple scheme

$$V_{n+1} = V_n + h(I - V_n) + \sigma\sqrt{h}\hat{N}(0, 1).$$

In this figure, the threshold is $V = 1$ but $I = 0.75$, so in the deterministic model ($\sigma = 0$), V will never fire. The addition of noise allows the model to fire occasionally. In fact, with sufficient noise, the neuron is able to sample the stimulus and, over many trials, reconstruct it as in Fig. 10.1b (where I is time-varying).

Figure 10.1c shows the effects of noise on the Morris–Lecar model with class II parameters. With $I = 85$, there is only a stable fixed point for the noiseless dynamics. Noise allows the neuron to spike with some regularity. How does one detect a spike in a stochastically driven model? Because the voltage itself is the driven variable, mathematically the trajectory will not be differentiable, so theoretically it could cross a fixed value arbitrarily many times in a given time interval. This is not an issue with the integrate-and-fire model since as soon as it crosses threshold, the voltage is reset far away from threshold. In a simulation, we have access to all of the variables; in particular, the potassium gate. Figure 10.1c shows that crossing level of w is a very reliable indicator of a spike. Thus, we collect all the times at which $w = 0.3$ is crossed from below. The interspike intervals (ISIs) are the times between spikes. Figure 10.1d shows a histogram of the distribution for these times. The distribution shows a sharp peak at about 100 ms and a broader, smaller peak at about 175 ms. In Exercises 1–3 you are asked to look at these distributions more carefully.

The goal of this chapter is to provide some theoretical analysis of the results shown in Fig. 10.1. To set this up, we next provide a rather terse review of the theory of stochastic differential equations.

10.1 Stochastic Differential Equations

Our main interest in this chapter is (10.1). Almost everything that can be done with this both practically and analytically concerns the scalar case where X is one-dimensional. The more general theory is as expected but the equations that we get are not easily solved either numerically or analytically. Thus, we start with the scalar equation. We can rewrite (10.1) as

$$x(t) = x(t_0) + \int_{t_0}^t a(x(s), s) \, ds + \int_{t_0}^t b(x(s), s) dW(s).$$

The first integral is the standard integral that you are probably familiar with, but the second integral is a stochastic integral. Let us briefly discuss some differences in the interpretation since these will come up when we introduce the Fokker–Planck equation.

10.1.1 The Wiener Process

We suppose $W(t)$ is a *Wiener process*. This is just the limiting case of a random walk as the steps and the time between steps get smaller such that $(\Delta x)^2/\Delta t$ tends to the finite limit of 1. That is, $W(t)$ is a simple diffusion process satisfying:

1. $W(0) = 0$.
2. The probability distribution of $W(t)$ is Gaussian; that is, the density function satisfies

$$\frac{\partial p(x, t)}{\partial t} = \frac{\sigma^2}{2} \frac{\partial^2 p(x, t)}{\partial x^2}, \quad p(x, 0) = \delta(x).$$

3. For any finite collection of times $t_1 < t_2 < \dots < t_n$, the random variables $W(t_j) - W(t_{j-1})$ are independent.
4. $E[W(t)] = 0$ and $E[(W(t) - W(s))^2] = \sigma^2(t - s)$ for all $0 \leq s \leq t$.
5. $W(t)$ is a continuous process.

Here, $E[U]$ is the expected value of the random process U . As we pointed out in the introduction to this chapter, you can simulate a standard Wiener process by the iteration

$$W(t + h) = W(t) + \sqrt{h}N(0, 1), \quad (10.3)$$

where $N(0, 1)$ is a normally distributed random variable with zero mean and unit variance. Figure 10.2 shows an example of such a simulation. Property 4 is illustrated in Fig. 10.2a; the mean is zero and the variance grows linearly in time. Figure 10.2b shows that the distribution is a Gaussian and a solution to the diffusion equation

$$p(x, t) = \frac{1}{\sqrt{2\pi t}} e^{-x^2/(2t)}.$$

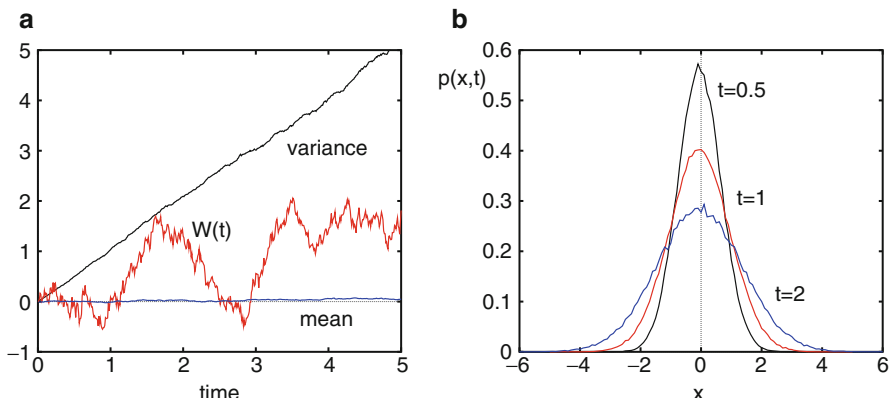


Fig. 10.2 Simulated Wiener process, $h = 0.01$. (a) Sample path and mean and variance of 1,000 sample paths. (b) Probability histogram for 100,000 sample paths starting at $W(0) = 0$

10.1.2 Stochastic Integrals

We now come to the main issue in stochastic calculus, the interpretation of an integral:

$$I = \int_{t_0}^t G(s)dW(s), \quad (10.4)$$

where $G(t)$ is a piecewise continuous function. As with usual integration, we divide the interval $[t_0, t]$ into finitely many points and write the partial sums

$$S_n = \sum_{j=1}^n G(\tau_j)[W(t_j) - W(t_{j-1})],$$

where we choose $t_{j-1} \leq \tau_j \leq t_j$. In Riemann integration, it does not matter how we choose τ_j . However, for stochastic integration, the choice of τ_j matters [96, p. 84]. For mathematical manipulation of the stochastic integrals, it turns out that one should take $\tau_j = t_{j-1}$. In this case, the resulting integral is called the *Itô* integral. The Itô calculus allows one to prove many rigorous results about stochastic integrals and also allows one to evaluate the integrals. An alternative choice of $\tau_j = (t_{j-1} + t_j)/2$ results in the *Stratonovich* integral and regular Stratonovich calculus. There is a relationship between the two integrals in the context of stochastic differential equations and there is a formula relating one to the other. The only reason we bring these technical issues up is that when we define the Fokker–Planck equations for (10.1), the choice of Itô or Stratonovich calculus matters. As far as neural modeling is concerned, some people prefer Stratonovich calculus since it is the appropriate model if we assume the “noise” has correlations and we take the limit as the correlation time goes to zero. *We cannot emphasize enough the point that if B is constant in (10.1), then the two are exactly the same.*

10.1.3 Change of Variables: Itô’s Formula

Later (when we discuss the theta model), we will need to make a change of variables. In ordinary calculus, changing variables is a simple application of the chain rule. However, in stochastic calculus, certain higher-order terms are important. From (10.3), it follows that

$$E[(W(t+h) - W(t))^2] = hE[N(0, 1)^2] = h,$$

since $N(0, 1)$ is a normal random variable with unit variance. Thus, we formally find

$$E[dW(t)^2] = dt.$$

Now suppose x satisfies

$$dx = a(x, t)dt + b(x, t)dW(t).$$

Let $y = f(x)$, where f is twice differentiable. What differential equation does the new variable y satisfy [96, p. 95]?

$$\begin{aligned} dy &= f(x + dx) - f(x) \\ &= f'(x)dx + \frac{1}{2}f''(x)dx^2 + \dots \\ &= f'(x)[a(x, t)dt + b(x, t)dW(t)] + \frac{1}{2}f''(x)b^2(x, t)(dW(t))^2 + \dots \\ &= \left[f'(x)a(x, t) + \frac{1}{2}f''(x)b^2(x, t) \right] dt + f'(x)b(x, t)dW(t) + \dots. \end{aligned}$$

Unlike the standard chain rule, there is an additional term $f''(x)b^2(x, t)/2$ which appears in the deterministic part of the equation for y . We call the equation

$$\begin{aligned} df[x(t)] &= \left\{ f'[x(t)]a(x(t), t) + \frac{1}{2}f''[x(t)]b^2(x(t), t) \right\} dt \\ &\quad + f'[x(t)]b(x(t), t)dW(t) \end{aligned} \tag{10.5}$$

Itô's formula. There is an obvious multidimensional analogue of this equation.

10.1.4 Fokker–Planck Equation: General Considerations

The Fokker–Planck equation is the fundamental method that we have for studying stochastic differential equations. There is a cost to this in terms of practicality. The Fokker–Planck equation is a diffusion equation on R^n , so instead of solving an n -dimensional stochastic differential equation, one has to solve a partial-differential equation. For the scalar case, the trade-off is not too bad and we can learn a lot from the analysis and simulation of the Fokker–Planck equation. Beyond the scalar case, we have to say that it is probably more efficient to simulate the stochastic differential equation.

Let us start with a general continuous scalar random process. Let $P(x, t)$ be the probability that a random variable $X = x$ at time t . We will assume the new state of the system depends only on the current state. (This is called the *Markov property* and such a process is called a Markov process.) Let $M(x', x, t)dt$ denote the rate at which the process whose state is $X = x'$ at time t jumps to x at time $t + dt$. Then,

$$\frac{\partial P}{\partial t} = \int [M(x', x, t)P(x', t) - M(x, x', t)P(x, t)] dx'. \tag{10.6}$$

This is the *master equation* and simply says that the rate of change of P is just the difference between the rate at which X goes from x' to x times the probability of being in state x' and the rate at which the process leaves state x for some other state times the probability of being in state x . If X takes on discrete values, then the integral is replaced by a sum. Let $Q(y, x, t) = M(x, x + y)$ be the rate of making a jump of size y from point x . Equation (10.6) can be written as

$$\frac{\partial P}{\partial t} = \int [Q(y, x - y, t)P(x - y, t) - Q(y, x, t)P(x, t)] dy.$$

The third-order *Kramers–Moyal* expansion is an approximation in which we expand in y to second order:

$$\frac{\partial P}{\partial t} = \int dy \left[-y \frac{\partial Q(y, x, t)P(x, t)}{\partial x} + (y^2/2) \frac{\partial^2 Q(y, x, t)P(x, t)}{\partial x^2} \right]. \quad (10.7)$$

Letting

$$\alpha_1(x, t) = \int dy y Q(y, x, t); \quad \alpha_2(x, t) = \int dy y^2 Q(y, x, t),$$

we get an approximate partial differential equation:

$$\frac{\partial P}{\partial t} = -\frac{\partial \alpha_1(x, t)P}{\partial x} + \frac{1}{2} \frac{\partial^2 \alpha_2(x, t)P}{\partial x^2}.$$

Note that α_1 is the mean jump size and α_2 is the variance. By assuming a diffusion process, all odd moments (y^3 , y^5 , etc.) vanish and the higher even moments turn out to be expressible in terms of the second moment. Thus, for a diffusive process, the Kramers–Moyal expansion is exact.

Let us return to the discretization of the scalar stochastic differential equation:

$$x(t + h) = x(t) + ha(x, t) + \sqrt{hb}(x, t)N(0, 1).$$

We can view this as a jump process in steps of h . The mean jump size is $ha(x, t)$ and the variance is $hb^2(x, t)$. Since the mean and variance in the master equation are defined in terms of the rate per unit time, we divide by h and obtain the Fokker–Planck equation for the scalar Langevin equation (10.1):

$$\frac{\partial P}{\partial t} = -\frac{\partial a(x, t)P}{\partial x} + \frac{1}{2} \frac{\partial^2}{\partial x^2} (b(x, t)^2 P). \quad (10.8)$$

This equation can be more rigorously derived (see [96]), but the present expansion provides the intuition behind it. The general n -dimensional Fokker–Planck equation for (10.1) is

$$\begin{aligned} \frac{\partial P(X, t)}{\partial t} = & - \sum_{i=1}^n \frac{\partial A_i(X, t) P(X, t)}{\partial x_i} \\ & + \frac{1}{2} \sum_{i,j=1}^n \frac{\partial^2}{\partial x_i \partial x_j} \left(B(X, t) B^T(X, t) P(X, t) \right). \end{aligned} \quad (10.9)$$

In general, this partial differential equation is intractable and numerical solutions must be computed. Since it is a partial differential equation, it may be impractical to actually solve this, and instead the best approach is to run the stochastic equation many times and take averages. Below, we introduce a method for obtaining equations for the moments, in particular, the mean and the variance in the small noise case.

10.1.4.1 Derivation from Itô's Formula

Here, we derive the Fokker–Planck equation using Itô's formula and taking averages. This derivation is adapted from [237]. We only derive the scalar model version. Consider the stochastic differential equation

$$dx = f(x, t)dt + g(x, t)dW.$$

Let $y = h(x)$ be a transformation, where h is arbitrary but twice differentiable. From Ito's formula,

$$dh(x) = h'(x)f(x, t)dt + h''(x)g^2(x, t)/2dt + h'(x)gdW.$$

Here, primes mean differentiation with respect to x . Taking the expectation of this, we obtain

$$\frac{d}{dt} E[h(x)] = E[h'(x)f(x, t)] + E[h''(x)g^2(x, t)/2].$$

Let $\rho(x, t)$ be the probability distribution for the variable x . Note that

$$E[U(x, t)] = \int U(x, t)\rho(x, t)dx.$$

The integral is over the domain of x , often the real line, but not always. Using the definition of the expectation, we find

$$\frac{d}{dt} \int h(x)\rho(x, t) dx = \int [h'(x)f(x, t) + h''(x)g^2(x, t)/2]\rho(x, t) dx.$$

If we integrate the right-hand side by parts, we obtain

$$\frac{d}{dt} \int h(x) \rho(x, t) dx = \int [-(f(x, t)\rho(x, t))' + (g^2(x, t)/2\rho(x, t))'']h(x) dx.$$

Since this must hold for any function $h(x)$, we must have

$$\frac{\partial \rho}{\partial t} = \frac{\partial}{\partial x} \left(-f(x, t)\rho(x, t) + \frac{1}{2} \frac{\partial}{\partial x} [g^2(x, t)\rho(x, t)] \right).$$

This is the Fokker–Planck equation.

10.1.5 Scalar with Constant Noise

Here, we are interested in the equation

$$dx = f(x, t)dt + \sigma dW(t), \quad (10.10)$$

where $W(t)$ is the standard Wiener process. We are interested in the distribution of x as well as various rates such as how quickly x leaves a region. We can integrate (10.10) to obtain

$$x(t) = x(0) + \int_0^t f(x(s), s) dt + \sigma \int_0^t dW(t).$$

We start with the Fokker–Planck equation for this process. By assuming *additive* noise, we avoid issues about the interpretation of the stochastic integral. For a full discussion of this topic, see [96]. From (10.8), the *forward* Fokker–Planck equation for (10.10) is

$$\frac{\partial P(x, t)}{\partial t} = -\frac{\partial f(x, t)P(x, t)}{\partial x} + \frac{\sigma^2}{2} \frac{\partial^2 P(x, t)}{\partial x^2}. \quad (10.11)$$

This can also be written as a conservation law for probability,

$$\frac{\partial P(x, t)}{\partial t} + \frac{\partial J(x, t)}{\partial x} = 0,$$

where $J(x, t)$ is the probability current (in dimensions of dx/dt):

$$J(x, t) = f(x, t)P(x, t) - \frac{\sigma^2}{2} \frac{\partial P(x, t)}{\partial x}.$$

The current J consists of two parts: an active transport term $f(x, t)P(x, t)$ and a diffusive term $(\sigma^2/2)\partial P/\partial x$. The probability current is similar to the current we saw earlier in our models of the cable equation. Unlike the axon equations, however, here we have *drift* or transport terms $f(x, t)$ which actively direct the probability flow according to the spatial location. Consider an interval $[a, b]$. The change in probability in the interval must equal the inward current minus the outward current. Thus, we have

$$\frac{\partial}{\partial t} \int_a^b P(x, t) dx = J(a, x) - J(b, x) = - \int_a^b \frac{\partial}{\partial x} J(x, t) dx.$$

Since the interval is arbitrary, we obtain the standard continuity equations:

$$\frac{\partial P(x, t)}{\partial t} = - \frac{\partial J(x, t)}{\partial x}.$$

We note that this simple continuity equation assumes infinitesimal jumps (to write this as a partial *differential* equation), but as we will encounter below, there may be large jumps, so the corresponding conservation equations must be amended.

To solve the Fokker–Planck partial differential equation, we need boundary and initial conditions. If we choose positive initial data, then the maximum principle for the diffusion equation guarantees that $P(x, t) \geq 0$. Furthermore, if

$$\int_{\Omega} P(x, 0) dx = 1,$$

then

$$\int_{\Omega} P(x, t) dx = 1$$

from conservation of probability. (Here, Ω is the domain of x .) There are numerous possible boundary conditions which are physically reasonable. If the domain is the real line, then obviously we want $P(x, t) \rightarrow 0$ as $|x| \rightarrow \infty$. In some examples the domain will be periodic, so $P(a, t) = P(b, t)$ and $J(a, t) = J(b, t)$.

We discuss two particularly important boundary conditions. If $P(x, t) = 0$ at a boundary point, a , we say that the boundary is *absorbing*. A particle reaching the boundary is absorbed. In this case, we lose conservation of probability. So, if this condition occurs, then it is necessary to add other terms to the continuity equations or have the flux out of that end point appear somewhere else to keep the total probability at 1. (In the scalar neuron models, described below, this condition occurs at the “spike” of the cell.) If $J(x, t) = 0$ at a boundary point, a , we say it is a *reflecting* boundary. A particle reaching the boundary cannot cross it (the current is zero), so it bounces back.

Often one is only interested in stationary distributions ($f(x, t)$ is independent of t , for example). Then we obtain

$$\frac{\sigma^2}{2} P'' - (fP)' = 0,$$

where P' is the derivative with respect to x . This is an ordinary differential equation and can be integrated once:

$$-\frac{\sigma^2}{2} P'(x) + f(x)P(x) = J. \quad (10.12)$$

J is just a constant of integration; the current described above. Suppose the domain is the real line. Then, $P(\pm\infty) = P'(\pm\infty) = 0$ since P must be integrable. Thus, $J = 0$ and we can solve for the steady state:

$$P(x) = K \exp \frac{2F(x)}{\sigma^2}, \quad (10.13)$$

where $F'(x) = f(x)$ and K is a normalization constant so that $\int P(x) = 1$. The function $-F(x)$ is called the potential for this process and local peaks in the probability correspond to minima of the potential. Consider, as an example, $f(x) = -x$. Then,

$$P(x) = \frac{1}{\sigma\sqrt{\pi}} e^{-(x/\sigma)^2}.$$

If the domain is not infinite, then J may be nonzero. However, if one of the boundaries is reflecting, then $J = 0$, which means the other boundary must also be reflecting *unless there are additional terms in the continuity equation such as jumps*. Suppose the domain is (a, b) . In general, with $J \neq 0$, we can still solve the steady state. Let

$$\Psi(x) = \exp \left((2/\sigma^2) \int_a^x f(y) dy \right).$$

Then we integrate (10.12) to obtain

$$P(x) = \Psi(x) \left[P(a) - \frac{2J}{\sigma^2} \int_a^x dy / \Psi(y) \right].$$

Suppose, for example, the boundary conditions are periodic. Then we require $P(a) = P(b)$. Then, we obtain

$$J = P(a) \frac{[\Psi(b) - 1]\sigma^2}{2\Psi(b) \int_a^b dy / \Psi(y)}. \quad (10.14)$$

$P(a)$ is found by the normalization condition, $\int_a^b P(x) = 1$.

10.1.6 First Passage Times

Consider (10.10). We now ask the following question: what is the distribution of exit times from the domain $[a, b]$ for the stochastic process? Suppose $x(0) = x$.

Let $p(x', t|x, 0)$ be the probability that the process defined by (10.10) is at x' at time t given it started at x at time 0. Define

$$G(x, t) \equiv \int_a^b dx' p(x', t|x, 0).$$

$G(x, t)$ is the probability that x is still in the interval $[a, b]$ at time t . Thus, if T is the time when x leaves the interval, then $G(x, t) = \text{prob}(T \geq t)$. Why do we care about this function? Below, when we discuss scalar models such as the integrate-and-fire model, we will be interested in when the voltage crosses the threshold. These crossing times correspond to “spikes” and their distribution is the ISI distribution. Gardiner [96] showed that $G(x, t)$ satisfies the *backward* Fokker–Planck equation:

$$\frac{\partial G(x, t)}{\partial t} = f(x, t) \frac{\partial G(x, t)}{\partial x} + \frac{\sigma^2}{2} \frac{\partial^2 G(x, t)}{\partial x^2}. \quad (10.15)$$

What are the initial and boundary conditions? Clearly $G(x, 0) = 1$ if $a < x < b$. The boundary conditions depend on the nature of the problem. We will often take absorbing conditions at $x = b$.

For many problems, we are interested in the mean exit time, $T(x)$, defined as the expected time to leave the interval given a starting value at x . Suppose f is independent of time. The definition of $G(x, t)$ implies that

$$G(x, t) = \int_t^\infty \rho(x, t') dt', \quad (10.16)$$

where $\rho(x, t)dt$ is the probability that x exits the domain in the interval $(t, t + dt)$. The mean first passage time is thus

$$\langle T \rangle(x) = \int_0^\infty t \rho(x, t) dt.$$

Integration by parts (Exercise 6) shows that

$$\langle T \rangle(x) = \int_0^\infty G(x, t) dt.$$

In the same exercise you show that (10.15) implies that $\langle T \rangle$ satisfies the simple ordinary differential equation

$$-1 = f(x) \langle T \rangle' + \frac{\sigma^2}{2} \langle T \rangle''. \quad (10.17)$$

Finally, a closed-form solution is provided in the exercise, although the integrals cannot generally be evaluated except numerically. In addition to the mean first passage time, one is often interested in higher moments such as $\langle T^n \rangle := T_n$. The n th

moment, T_n , satisfies a simple second-order equation like (10.17) depending only on the previous moments (Exercise 6). Since the first passage time is related to the firing rate of a noisy neuron, spike statistics can be found from the solution to the moment equations. For example, the *coefficient of variation* is a measure of the irregularity of a process and is defined as the ratio of the standard deviation to the mean. The standard deviation of the firing rate is just

$$\sigma = \sqrt{E[(T - E[T])^2]} = \sqrt{E[T^2] - E[T]^2},$$

so the coefficient of variation is

$$\text{CV}_T = \sqrt{E[(T/E[T])^2] - 1}.$$

10.1.6.1 Simple Derivation of the First Passage Time

Larry Abbott (personal communication) provided a very simple derivation of the first passage time equation. As above, we let $T(x)$ denote the mean first passage time. On a given trial, x moves from x to $x + \Delta x$ in time Δt . Then on average, $\langle T(x + \Delta x) \rangle = T(x) - \Delta t$. (Note that Δx is a random variable but $T(x)$, x , and Δt are not.) From (10.10), we note that

$$\Delta x = f(x)\Delta t + \sigma\sqrt{\Delta t}\xi,$$

where ξ is a normally distributed random variable with zero mean and unit variance. Thus, the mean of Δx is $f(x)\Delta t$. The mean of $(\Delta x)^2$ is

$$\langle (\Delta x)^2 \rangle = \langle [f(x)\Delta t + \sigma\sqrt{\Delta t}\xi]^2 \rangle = [f(x)\Delta t]^2 + \sigma^2\Delta t = \sigma^2\Delta t + O((\Delta t)^2).$$

Now, expand $T(x + \Delta x)$ in small Δx , to get

$$T(x + \Delta x) \approx T(x) + \Delta x T'(x) + \frac{1}{2}(\Delta x)^2 T''(x) + \dots.$$

Taking the mean, using the above fact that $\langle (\Delta x)^2 \rangle = \sigma^2\Delta t + O((\Delta t)^2)$, and dividing by Δt , we get

$$\frac{\sigma^2}{2} T''(x) + f(x)T'(x) = -1$$

as $\Delta t \rightarrow 0$.

10.1.6.2 Some Comments on the Utility of First Passage Times

First passage time methods are an elegant tool for determining various questions such as the firing rate of a neuron in the presence of noise. However, it is crucial that one be able to actually determine what the crossing threshold is for the model. In one-dimensional neurons, this is very clear – we set a point at which the cell is said to fire and that is that. (Technically, we apply an absorbing boundary condition at the spike, $P(V_{\text{spike}}, t) = 0$.) However, consider a model that actually does produce spikes such as the Morris–Lecar model, for example. The phase space is no longer an interval on the line with a well-defined boundary. Rather, the domain is the whole plane. Given this, what do we mean when we say a neuron produces a spike? We could, for example, look for a peak in the membrane potential and call that a spike. This is what neuroscientists do when they attempt to detect spikes from the extracellular or intracellular recordings of a neurons. However, with additive white noise stimuli, the voltage can cross a set threshold arbitrarily many times in any given interval, so a peak will not make any sense. There are two ways around this difficulty. One way is to use *colored* noise, that is, noise which has been low-pass-filtered so that the right-hand sides of the voltage equation are continuous. In this case, the peak of the voltage is well defined, so we can, at least, run reasonable stochastic simulations. Using colored noise presents a more realistic scenario for the environment of a neuron, but the analysis of this process is far more difficult as we have added an extra dimension, so, e.g., even in a scalar model, the mean first passage time problem becomes a partial differential equation. Another way around the problem (which is not available to an experimentalist) is to consider crossing of one of the other variables in the ordinary differential equation. For example, in the Morris–Lecar model, we could say that a spike is emitted if $w(t)$ crosses some set value, \bar{w} . This was done in the Monte Carlo simulation in Fig. 10.1c. Analytically (but, rather impractically), we could write down the full Fokker–Planck equations on a large enough domain and compute the flux through some region in the domain of the model and call this the firing rate. For example, if the model is planar, $dV = f(V, w)dt + \sigma dW$, $dw = g(V, w)dt$, then we solve the appropriate Fokker–Planck equation

$$P_t = \frac{\sigma^2}{2} P_{VV} - [f(V, w)P]_V - [g(V, w)P]_w$$

on a large rectangle (large enough to ignore the boundaries, since the real problem is actually defined on the whole plane). Suppose we obtain the stationary distribution, $P(V, w)$. We can say that a spike has fired if, for example, w crosses some prescribed value, \bar{w} , while V lies in some specified interval. The total flux is the firing rate:

$$F = \int_{V_1}^{V_2} J_w(V, \bar{w})dV,$$

where $J_w(V, w) = g(V, w)P(V, w)$.

In sum, from a practical viewpoint, most of the noise calculations that are done for neuron models make sense only for simple one-dimensional dynamics. Once we get to biophysical models, it is best to just simulate them as in Fig. 10.1c.

10.2 Firing Rates of Scalar Neuron Models

We now turn to the applications to scalar neuron models of the methods we outlined above. Most scalar neuron models (such as the integrate-and-fire model) have a reset condition when the voltages reaches a particular value, V_{spike} . Often, V_{spike} is the maximum value that the potential can take; thus, the probability of finding the neuron at this value vanishes – there is an absorbing boundary condition. However, the probability current out of that point (which represents the neuron’s firing rate) is “reinjected” at the reset potential, V_{reset} , so the total probability is conserved. We begin with a generic scalar model with additive white noise,

$$dV = f(V, t)dt + \sigma dW(t), \quad (10.18)$$

with the stipulation that when $V(t)$ reaches V_{spike} from below, it is reset to V_{reset} . If $f(V, t) = -aV + I$, then we have the leaky integrate-and-fire model, whereas if $f(V, t) = aV^2 + I$, we have the quadratic integrate-and-fire model. To obtain the mean firing rate, we can solve either the steady-state Fokker–Planck equation (10.11) or the mean first passage time equation (10.17). We can also use the backward equation (10.15) to obtain ISI histograms for these scalar models. In the rest of this section, we apply the theory described above. Unfortunately, the resulting integrals are basically impossible to explicitly evaluate. On the other hand, the fact that the steady-state Fokker–Planck equation and the first passage time equation are ordinary differential equations allows us to find smooth numerical solutions as parameters vary.

10.2.1 The Fokker–Planck Equation

The probability density for (10.18) subject to reset can be formally written as

$$\frac{\partial P(V, t)}{\partial t} = -\frac{\partial}{\partial V} J(V, t) + \delta(V - V_{\text{reset}})J(V_{\text{spike}}, t), \quad (10.19)$$

where

$$J(V, t) = f(V, t)P(V, t) - \frac{\sigma^2}{2} \frac{\partial P(V, t)}{\partial V}. \quad (10.20)$$

This equation is defined on the interval $-\infty < V < V_{\text{spike}}$. The boundary conditions are $P(-\infty, t) = 0$ and $P(V_{\text{spike}}, t) = 0$. The latter condition is *absorbing*. However,

probability is conserved owing to the delta-function term appearing in (10.19). Indeed, the reader can integrate this equation over the interval on which it is defined and see that

$$\frac{\partial}{\partial t} \int_{-\infty}^{V_{\text{spike}}} P(V, t) dV = 0.$$

Stationary solutions satisfy

$$0 = -\frac{d}{dV} J(V) + \delta(V - V_{\text{reset}}) J(V_{\text{spike}}).$$

We integrate this with respect to V to obtain

$$J_0 = -J(V) + J(V_{\text{spike}})H(V - V_{\text{reset}}),$$

where $H(V)$ is the Heaviside step function. Since $P(V)$ and its derivatives must vanish at $V = -\infty$, we conclude that $J_0 = 0$. Since $P(V_{\text{spike}} = 0)$, (10.20) implies that at steady state

$$J(V_{\text{spike}}) = -\frac{\sigma^2}{2} \frac{dP(V_{\text{spike}})}{dV} \equiv v.$$

The firing rate of the neuron is just $J(V_{\text{spike}}, t)$. Thus, we have the simple first-order linear differential equation

$$J(V) \equiv f(V)P(V) - \frac{\sigma^2}{2} \frac{dP(V)}{dV} = vH(V - V_{\text{reset}}).$$

We let $P_{\pm}(V)$ denote the solutions to this equation for $V < V_{\text{reset}}$ and for $V > V_{\text{reset}}$. Then, with normalization we have

$$\begin{aligned} f(V)P_{-}(V) - \frac{\sigma^2}{2} P'_{-}(V) &= 0 & -\infty < V < V_{\text{reset}}, \\ f(V)P_{+}(V) - \frac{\sigma^2}{2} P'_{+}(V) &= v & V_{\text{reset}} < V < V_{\text{spike}}, \\ P_{-}(-\infty) &= 0, \\ P_{-}(V_{\text{reset}}) &= P_{+}(V_{\text{reset}}), \\ P_{+}(V_{\text{spike}}) &= 0, \\ \int_{-\infty}^{V_{\text{reset}}} P_{-}(V) dV + \int_{V_{\text{reset}}}^{V_{\text{spike}}} P_{+}(V) dV &= 1. \end{aligned}$$

The solution to the stationary state depends on a single constant v and this constant is determined by the normalization. Define $F(x)$ as $F'(x) = f(x)$. After a bit of simple manipulation, we find

$$v^{-1} = \frac{2}{\sigma^2} \int_{-\infty}^{V_{\text{reset}}} e^{\frac{2F(x)}{\sigma^2}} dx \int_{V_{\text{reset}}}^{V_{\text{spike}}} e^{\frac{-2F(y)}{\sigma^2}} dy \quad (10.21)$$

$$\begin{aligned}
& + \frac{2}{\sigma^2} \int_{V_{\text{reset}}}^{V_{\text{spike}}} e^{\frac{-2F(x)}{\sigma^2}} \int_x^{V_{\text{spike}}} e^{\frac{-2F(y)}{\sigma^2}} dy dx \\
& = \frac{2}{\sigma^2} \int_{-\infty}^{V_{\text{spike}}} e^{\frac{-2F(x)}{\sigma^2}} \int_{\max(x, V_{\text{reset}})}^{V_{\text{spike}}} e^{\frac{-2F(y)}{\sigma^2}} dy dx.
\end{aligned}$$

This equation and three dollars will get you a small cup of coffee at Starbucks. We can simplify this equation for some particular cases although the evaluation of the resulting expressions is still nontrivial. We note that the flux is always positive *because of the absorbing boundary* at $V = V_{\text{spike}}$. The reason for this is that the flux is proportional to $-\partial_V P(V)$ at V_{spike} . Since P is positive and vanishes at V_{spike} , its derivative at V_{spike} must be negative.

10.2.1.1 Constant Drift

Suppose $f(V) = I$; there is no dependence on the potential. We leave it as an exercise for the reader to show that (10.21) is independent of σ and the firing rate is just

$$v = \frac{I}{V_{\text{spike}} - V_{\text{reset}}}.$$

10.2.1.2 Leaky Integrate-and-Fire Model

For the leaky integrate-and-fire model, $f(x) = I - x$, so $F(x) = Ix - x^2/2$. Fourcaud and Brunel [90] provided the most compact form for the firing rate of the leaky integrate-and-fire model:

$$v^{-1} = \sqrt{\pi} \int_{\frac{V_{\text{reset}}-I}{\sigma}}^{\frac{V_{\text{spike}}-I}{\sigma}} e^{s^2} (1 + \operatorname{erf}(s)) ds, \quad (10.22)$$

where

$$\operatorname{erf}(x) = \frac{1}{\sqrt{\pi}} \int_{-x}^x e^{-s^2} ds.$$

In spite of the simple form, this is not a simple function to compute. Indeed, evaluating the integral numerically requires dealing with the very large $\exp(x^2)$ and the very small $1 + \operatorname{erf}(x)$. In Fig. 10.3, we plot some representative firing curves for the leaky integrate-and-fire model (and other models) by solving an appropriate boundary value problem. We can, however, do some asymptotic analysis in the cases of either large I or large σ . We leave all of this, including the derivation of (10.22), as exercises for the reader.

10.2.1.3 Quadratic Integrate-and-Fire Model

In the quadratic integrate-and-fire model, $f(V) = V^2 + I$, $V_{\text{spike}} = +\infty$, and $V_{\text{reset}} = -\infty$. Sigeti and Horsthemke [248] evaluated the resulting integral exactly for the first passage time in the case in which $I = 0$ (at the saddle-node) and obtained

$$\nu(I=0) = [\Gamma(1/3)]^{-2} \left(\frac{3\sigma}{2} \right)^{1/3} = 0.1595 \dots \sigma^{2/3}.$$

For positive I (the neuron is an oscillator) and for small noise, $\nu \sim \sqrt{|I|}/\pi$, the deterministic firing rate. More interestingly, for $I < 0$ (the excitable neuron), noise-induced firing occurs and the rate is given by

$$\nu = \frac{\sqrt{|I|}}{\pi} \exp \left(-\frac{8|I|^{3/2}}{3\sigma^2} \right)$$

for $\sigma^2 \ll |I|^{3/2}$ [181].

10.2.1.4 Ring Models

In Exercise 10 in Chap. 9, we introduced ring models defined on the unit circle:

$$\frac{dV}{dt} = f(V) + I,$$

where $f(V)$ is continuous and 2π -periodic. We can consider the noisy version of this:

$$dV = (f(V) + I)dt + \sigma dW(t). \quad (10.23)$$

The stationary distribution, $P(V)$, must also be periodic, so it must satisfy

$$J = (f(V) + I)P(V) - \frac{\sigma^2}{2} \frac{dP}{dV}.$$

The constant J is the current and is also the firing rate of the neuron. Unlike the integrate-and-fire models, there is no reset condition, so the current is equal at every point. In particular, if I is large enough, then $f(V) + I$ is positive, so in absence of noise we have

$$J^{-1} = \int_0^{2\pi} \frac{dV}{f(V) + I}.$$

More generally, we can apply (10.14), where

$$\Psi(x) = \exp \left((2/\sigma^2) \int_0^x (f(y) + I) dy \right).$$

We remark that, unlike integrate-and-fire-type models, the current can be either positive or negative. (For I large and negative, the oscillator runs counterclockwise.) Thus, one has to be careful with the interpretation of ring models as neural oscillators. One special case of a ring model was analyzed by Ritt [233]:

$$d\theta = \left[1 - \cos \theta + (1 + \cos \theta)(I - \frac{\sigma^2}{2} \sin \theta) \right] dt + \sigma(1 + \cos \theta)dW(t).$$

Here, firing occurs when $\theta = \pi$. This model is equivalent to the quadratic integrate-and-fire model under the transformation $V \rightarrow \tan(\theta/2)$. Unlike for the ring models with simple additive noise (10.23), the noise is state-dependent and vanishes at $\theta = \pi$. Evaluation of the right-hand side at $\theta = \pi$ shows that the current is always positive. Without the singular noise, we cannot guarantee that the current will always be positive in general ring models.

10.2.2 First Passage Times

The Fokker–Planck equation gives us more than just the firing rate – it also provides the distribution of the potentials. However, it is rare that one would need this information. (Although, Rudolph and Destexhe [237] showed that by measuring the distribution of the noisy subthreshold potential in a neuron, it is possible to extract estimates of the mean and variance of excitatory and inhibitory conductances; see Exercise 13.) Instead, the ISI distribution, the mean firing rate, and the variance of the firing rate are much more useful. In Sect. 10.1.6 we developed equations for the mean time to reach a given point as well as the evolution of those times. We have

$$dV = f(V) + \sigma dW(t),$$

with $V(0) = V_{\text{reset}}$, and we want to determine the distribution of times at which $V(t) = V_{\text{spike}}$. The domain of interest is $-\infty < V < V_{\text{spike}}$. The average time between spikes is just the expected time it takes to go from V_{reset} to V_{spike} and the ISI histogram is just the probability density function for the exit times given that the starting point is V_{reset} . From (10.16), the quantity $\rho(V_{\text{reset}}, t)$ is this probability density function and is just the derivative of the solution to the backward equation (10.15). Because there is no reset involved, it is often the case that the mean first passage time solution results in a simpler, more compact, expression for the firing rate in contrast to (10.21). From (10.17), the mean first passage time equation is

$$\frac{\sigma^2}{2} T''(V) + f(V)T' = -1 \quad (10.24)$$

with appropriate boundary conditions. Recall that $T(V)$ is the expected time to exit some prescribed boundary given that at $t = 0$ the voltage is V . If we are working

with an integrate-and-fire-type model where there is a spike at V_{spike} and a reset to V_{reset} , then one of the boundary conditions is $T(V_{\text{spike}}) = 0$. Gardiner [96, p. 139] showed that the other desired condition is that $T'(V) \rightarrow 0$ as $V \rightarrow -\infty$. However, this does not imply that $T(V)$ itself remains bounded. Equation (10.24) is just a first-order equation in $T'(V)$. We can use asymptotics to examine the large negative V behavior. If $f(V) = KV^p + \dots$, where the remaining terms are lower order in V and $p > 0$, then clearly we must have that

$$T'(V) = -\frac{1}{KV^p} + \dots$$

as $V \rightarrow \infty$. If, as in the case of the leaky integrate-and-fire model, $p = 1$, then $T'(V)$ does go to zero as $V \rightarrow -\infty$, but $T(V)$ diverges. The intuition behind the divergence of T is that with the leaky integrate-and-fire model solutions to the deterministic problem are exponentials which remain finite for all time – a solution with $V(0)$ arbitrarily large and negative reaches firing at a time proportional to $\log(|V(0)|)$, which can be arbitrarily large. In contrast, the quadratic integrate-and-fire model has $p = 2$ and thus $T(V)$ converges as $V \rightarrow \infty$ since the quadratic equation $V' = a + bV^2$ “blows up” in finite time.

With the condition $T(V_{\text{spike}} = 0)$ and $T'(-\infty) = 0$, the solution to (10.24) is

$$T(V) = \frac{2}{\sigma^2} \int_V^{V_{\text{spike}}} e^{-\frac{2F(x)}{\sigma^2}} \int_{-\infty}^x e^{\frac{2F(y)}{\sigma^2}} dy dx, \quad (10.25)$$

where $F(x) = \int f(x)dx$ (see Exercise 8). Analogous expressions for periodic boundary conditions can be found for ring models *as long as the current* is nonzero. The current vanishes if and only if the average of $f(V)$ over the domain is zero. Equation (10.25) allows us (up to actually evaluating the integrals) to compute the F - I curve in the presence of noise. By definition, $T(V_{\text{reset}})$ is the mean time to fire a spike, so the firing rate is just $1/T(V_{\text{reset}})$. We can numerically evaluate the double integral, numerically solve the boundary value problem (10.24), or numerically solve the Fokker–Planck equation (10.19). We find that the solution to the boundary value problem seems to be the simplest choice.

Since we will use the noisy F - I curves later in the book, we illustrate them in Fig. 10.3 for two levels of noise. Both the solutions to the boundary value problem and the solutions to Monte Carlo simulations are shown. (For the Monte Carlo simulations, we solve the equations for a time interval of 2,000 and count the number of spikes.) The main differences between the smaller and larger noise cases is that the F - I curve is more linear with larger noise. This is a classic result: noise linearizes the response. In all cases, the deterministic model is smeared by the noise, resulting in a smoother sigmoidal curve. The firing rate curves will be useful for network models; thus, we will attempt to create easily computed approximations of them. Suppose $F(I)$ is the deterministic F - I curve when there is zero noise. We will approximate the noisy F - I curve by the composition of $F(I)$ with a function $M(I, p)$ which has the following properties. $M(I, p)$ is positive, monotonic, and asymptotically

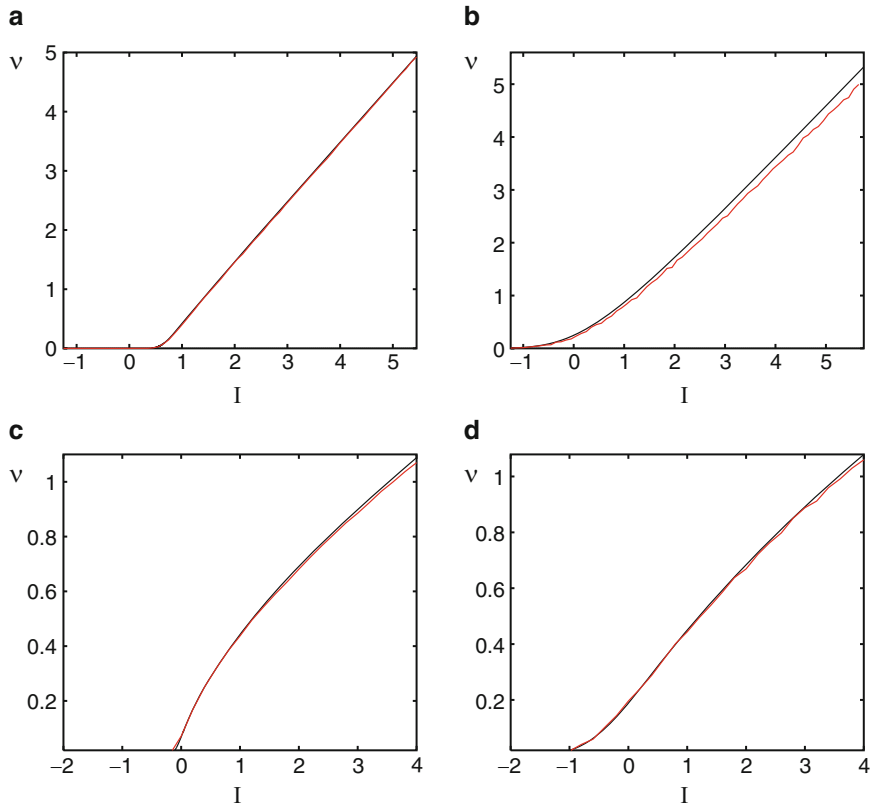


Fig. 10.3 F - I curves for the leaky (spike is at 1 and reset at 0) and quadratic (spike is at 10 and reset at -1) integrate-and-fire models. Solutions to the boundary value problem are shown in black and solutions to the Monte-Carlo simulations are shown in red. Leaky integrate-and-fire model with $\sigma = 0.25$ (a) and $\sigma = 1.0$ (b). Quadratic integrate-and-fire model with $\sigma = 0.25$ (c) and $\sigma = 1$ (d)

approaches I for large I , independent of p . As $p \rightarrow 0^+$, $M(I, p) \rightarrow [I]_+$, the positive part of I . Several choices come to mind:

$$\begin{aligned} M_1(I, p) &= \frac{I}{1 - \exp(-I/p)}, \\ M_2(I, p) &= p \log(1 + \exp(I/p)), \\ M_3(I, p) &= \frac{1}{2} \left[x(1 + \text{erf}(I/p)) + \frac{p}{\sqrt{\pi}} \exp(-(I/p)^2) \right]. \end{aligned} \quad (10.26)$$

The last function is the convolution of a Gaussian with the positive part of I . Thus, we approximate the noisy F - I curve by

$$v(I) = F(M_j(I, p)),$$

where p is chosen to best fit the true F - I curve. We find that the third choice provides a pretty good fit with the F - I curves in Fig. 10.3. The parameter p is roughly linearly proportional to the noise, σ .

10.2.2.1 Other Statistics

There are other statistics besides the mean firing rate which may be useful. For example, one might desire to compute the variance, σ^2 , and thus the standard deviation, σ . A much-used characteristic of the “noisiness” of a neuron is the coefficient of variation, which is σ/T . Recall that the variance is just

$$\sigma^2 = \langle (T - \langle T \rangle)^2 \rangle = \langle T^2 \rangle - \langle T \rangle^2.$$

Exercise 6 shows the second moment $T_2(V)$ obeys a simple second-order ordinary differential equation:

$$\frac{\sigma^2}{2} T_2''(V) + f(V) T_2' = -T(V),$$

where $T(V)$ is the already-determined mean first passage time. The boundary conditions are the same as for $T(V)$.

10.2.2.2 Aside: Solving the Boundary Value Problem

Ideally, we would like to numerically solve (10.24) on the interval $(-\infty, V_{\text{spike}})$; however, this is obviously impossible. Thus, we solve the problem on the interval $(-A, V_{\text{spike}})$, where we pick A large enough. We will use AUTO to do this since it is very efficient and works better than simple shooting. Our estimates above indicate that $T(V) = O(V^{-p})$, where $p = 1$ for the leaky integrate-and-fire model and $p = 2$ for the quadratic integrate-and-fire model. Thus, we expect we will have to make A larger for the leaky integrate-and-fire model to better approximate a reflecting boundary condition $T'(-A) = 0$. Since our asymptotics actually provide an estimate for $T'(-A)$ for large A , we use the boundary condition $T'(-A) = KA^{-p}$ for better accuracy.

10.2.3 Interspike Intervals

Recall that the backward equation (10.15) provides a solution to $G(V, t)$ which is the probability that no spike has fired up to time t given that the initial voltage is at V . Each time there is a spike, V is reset to V_{reset} . Thus, if T is the time to spike

after resetting, $G(V_{\text{reset}}, t) = \text{prob}\{T > t\}$. The ISI histogram is the probability of a spike in a given interval of size Δt . This means in limit as $\Delta t \rightarrow 0$, we have

$$G(V_{\text{reset}}, t) = \int_t^{\infty} \text{ISI}(s) \, ds.$$

So the ISI is found by solving the backward equation and computing the negative t -derivative of $G(V, t)$ at $V = V_{\text{reset}}$. To obtain the ISI distribution for an integrate-and-fire model, we must solve the backward equation (10.15),

$$\frac{\partial G(V, t)}{\partial t} = f(V) \frac{\partial G(V, t)}{\partial V} + \frac{\sigma^2}{2} \frac{\partial^2 G(V, t)}{\partial V^2},$$

along with the boundary and initial conditions $G(V, 0) = 1$ for $V < V_{\text{spike}}$ and $G(V_{\text{spike}}, t) = 0$. Additionally, as with the mean first passage time, we require that $G_V(V, t) \rightarrow 0$ as $V \rightarrow -\infty$. In general, we cannot write down a useable closed-form solution for the backward equation so we must resort to numerical approximations. We solve a discretized version of the backward equation on an interval $(-A, V_{\text{spike}})$, where A is chosen large enough. Figure 10.4 shows some comparisons between the Monte Carlo simulations of (10.18) and the solutions to (10.15). We show both the leaky integrate-and-fire and the quadratic integrate-and-fire models for subthreshold currents/high noise and suprathreshold currents/low noise.

10.2.4 Colored Noise

The sources for noise in neurons are manifold and include both channel noise (see below) as well as *synaptic noise*, which comes about from the constant bombardment of other cells within the same milieu. Our model for white noise is simple and has the advantage of being tractable, at least insofar as providing some simple scalar partial differential equations for the probability density and firing rates. Although the formulae are not exactly useful, they are easy to numerically evaluate as are the partial differential equations which result. The white noise model is a somewhat crude approximation for synaptic noise especially if the time constants of the synapses are not really short. Thus, some researchers replace white noise by the following model:

$$\tau dz = -z dt + \sqrt{\tau} dW. \quad (10.27)$$

Here, $\tau > 0$ approximates the decay properties of the synapses. This stochastic differential equation is called an Ornstein–Uhlenbeck process and has an exact solution; the stationary distribution is Gaussian. Unlike the white noise case, which is uncorrelated in time, Ornstein–Uhlenbeck noise has an autocorrelation function which decays exponentially as $\exp(-t/\tau)$. A natural question to ask is how this can affect the responses of neurons to stimuli, e.g., the *F–I* curve. Lindner [179] computed statistics for the ISIs of a perfect integrator ($dV/dt = I$) when there is

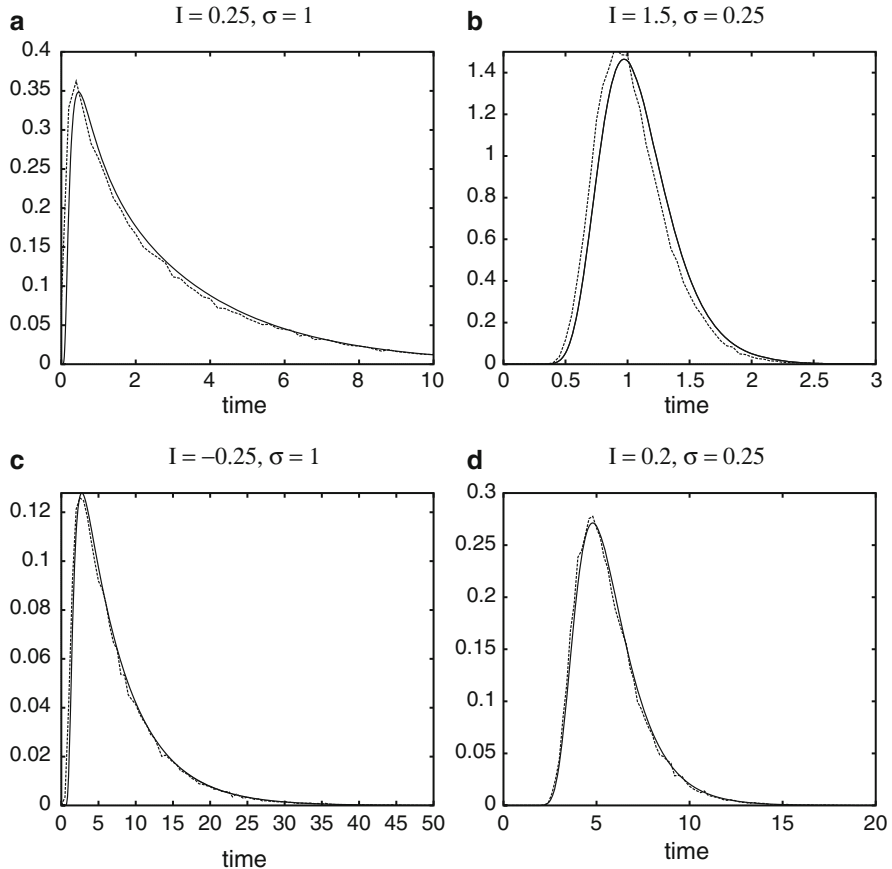


Fig. 10.4 Interspike interval distributions for noisy scalar models. Monte Carlo simulations are shown as *dashed lines* and *solid lines* are solutions to (10.15). The Monte Carlo simulations are 50,000 interspike intervals from a Euler simulation of (10.18). The partial differential equation (PDE) is solved by the method of lines on a finite interval divided into 200 bins. (a, b) Leaky integrate-and-fire model, $f(V) = I - V$. The PDE is solved on the interval $(-4,1)$ with $V = 1$ absorbing and $V = 0$ as the reset value. (c, d) Quadratic integrate-and-fire model, $f(V) = I + V^2$. The PDE is solved on the interval $(-5,5)$ with $V = 5$ absorbing and $V = -1$ as the reset value. Currents and noise are indicated

colored noise. Brunel and coworkers [26, 27] computed the F - I curve for the noisy leaky integrate-and-fire and quadratic integrate-and-fire models, respectively, with this kind of colored noise in the limits of small and large τ as well as a uniformly valid approximation over all ranges of τ . The calculations are heroic, but the bottom line is that colored noise has only a small effect on the steady-state firing rate. For example, if the current applied to the quadratic integrate-and-fire model is 0.5 and $\sigma = 0.5$, then the firing rate varies from 21.5 to 23 Hz for all values of τ . We should point out that colored noise does have a rather important effect on the behavior of these models when periodic stimuli are added.

10.2.5 Nonconstant Inputs and Filtering Properties

So far, we have considered situations in which the inputs to the noisy model are constant. However, real inputs to neurons change in time, so we would like to ask what can be said about the time-dependent firing rate. Figure 10.1b shows that one advantage of noise is that it allows subthreshold inputs to be recovered and a complex stimulus can be accurately encoded in the rates. Contrast this with a noise-free model in which the neuron will not fire at all over a large range of inputs. The analysis of the output from a nonautonomous model is considerably more difficult than that of a stationary distribution. However, both Monte Carlo and numerical solutions of the Fokker–Planck equation provide a good way to study the dynamics of the response of noisy neurons to stimuli. Figure 10.5 shows the response of the

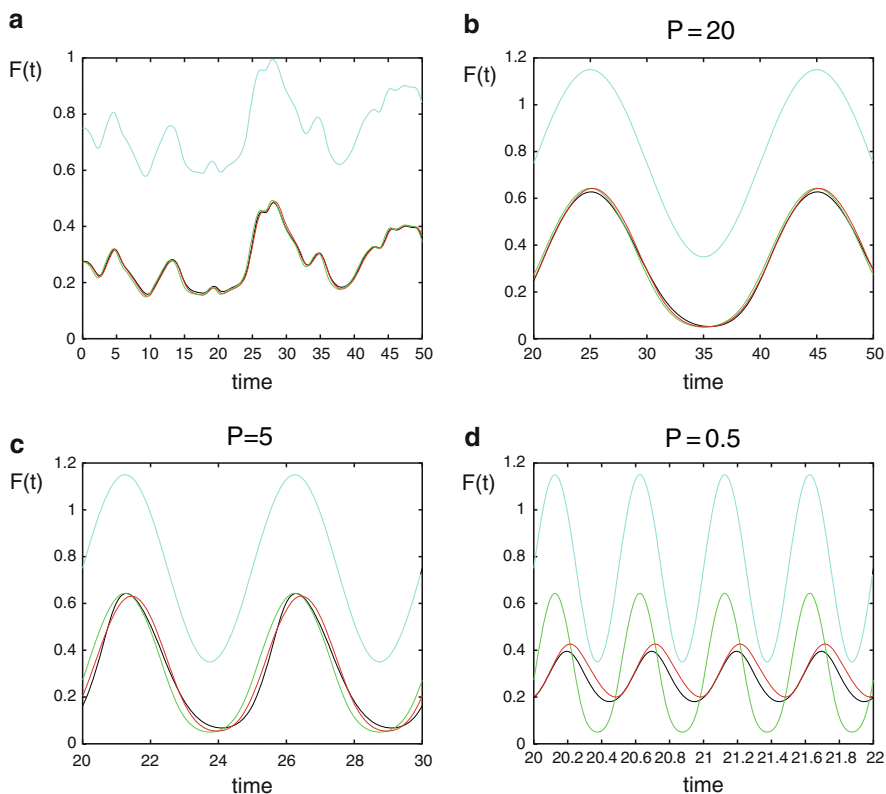


Fig. 10.5 Response of a noisy leaky integrate-and fire model to nonconstant stimuli. The integrate-and fire model has $I = 0.75$, $V_{\text{spike}} = 1$, $V_{\text{reset}} = 0$, and $\sigma = 0.4$. (a) A nonperiodic stimulus. The *blue curve* shows the stimulus. The *lower curves* show the response of the Fokker–Planck equation (*red*) and the instantaneous firing rate (*green*) predicted by the steady-state F – I curve. (b–d) Periodic stimuli at different periods (denoted by P). The *blue curve* shows the stimulus and *red curve* shows the solution to the Fokker–Planck equation. The instant response is shown in *green* and the solution to the simple dynamic model (see the text) is shown in *black* ($\tau = 0.2$)

leaky integrate-and-fire model to aperiodic and periodic stimuli. Brunel et al. [28] and Lindner and Schimansky-Geier [180] provided a formula for the response to weak periodic stimuli which involves various special functions and is well beyond the scope of this book. We point out two conclusions of their work: (1) with white noise the system behaves as a low-pass filter whose magnitude decreases as $1/\sqrt{\omega}$ and the response lags the input by about 45° in phase and (2) with colored noise (e.g., $dx = -x/\tau + dW$) the lag disappears.

In the example shown in Fig. 10.5a, the stimulus is encoded with almost no lag even though the noise is white. One approximation for slowly varying stimuli is to treat them statically and use the steady-state F - I curve. We compute the F - I curve for the level of noise in the model ($\sigma = 0.4$) and fit this to a smooth function, $F(I)$ as in (10.26) so that we can approximate the time-dependent firing rate as

$$\nu(t) = F(I(t)),$$

where we use

$$F(I) = 0.16 \log(1 + \exp((I - 0.51)/0.16)).$$

The red and green curves in Fig. 10.5a show that the static approximation works quite well. Similarly, to periodic stimuli shown in Fig. 10.5b and c, the static response is also very close to the numerically computed response. However, at high frequencies, as shown in Fig. 10.5d, there is a substantial diminution in the amplitude and there is a clear lag. Thus, we introduce a slightly more complicated model for the firing rate:

$$\tau \frac{d\nu}{dt} = -\nu + F(I(t)). \quad (10.28)$$

The results for $\tau = 0.2$ are shown by the black curves – this model provides a much better fit. In Fig. 10.5b and c we also show the results from the dynamic model; they are nearly identical to those from the static model since the frequency is very low compared to τ . We chose τ in an ad hoc manner and expect that its choice will depend on the amount of noise as well as other aspects of the particular neural model. In one of the exercises/projects below, we illustrate that the situation is not so simple with a noisy conductance-based model. Nevertheless, (10.28) is the simplest dynamic model for the responses of neurons to time-varying stimuli and we will use equations like this to model populations of coupled neurons later in the book.

10.3 Weak Noise and Moment Expansions

Rodriguez and Tuckwell [234] developed a clever approximation for analyzing neural models (and any other models) in the presence of small noise. The idea of such methods is to assume the probability distributions are Gaussian, centered at the mean values, $\bar{X}_j = E[X_j]$, with covariances $K_{ij} = E[(X_i - \bar{X}_i)(X_j - \bar{X}_j)]$. (Note that $E[x]$ is the expectation of the process x .) Then one does an expansion and derives

equations for the means and covariances. We briefly outline the idea and then apply it to a simple polynomial neural model. Rodriguez and Tuckwell considered the case of general multiplicative noise. To simplify the description here, we restrict the method to additive noise. We start with

$$dX_j = f_j(X, t)dt + \sum_k g_{jk} dW_k(t). \quad (10.29)$$

The $W_j(t)$ are standard Wiener processes (zero mean, independent, delta-correlated). Of the n^2 quantities, K_{ij} , n of them are variances, $V_i = K_{ii}$, and, the $n(n - 1)/2$ remaining are the distinct covariances between the n variables. Taking the mean of (10.29), we immediately find

$$\frac{d\bar{X}_j}{dt} = E[f_j(X, t)]. \quad (10.30)$$

We note that $E[dW] = 0$, so this is an exact equation for the mean. Unfortunately, we need to approximate the right-hand side to get a closed-system of equations, since X is a random variable which we do not know except through (10.29). Similarly, the covariances satisfy

$$\frac{dK_{ij}}{dt} = E \left[(X_i - \bar{X}_i)f_j(X, t) + (X_j - \bar{X}_j)f_i(X, t) + \sum_k g_{ik}g_{jk} \right]. \quad (10.31)$$

This equation is obtained by differentiating the quantity

$$(X_i - \bar{X}_i)(X_j - \bar{X}_j)$$

with respect to t , taking expectations, and using (10.30). We also use the fact that

$$E[(X_i - \bar{X}_i)E[f_j(X, t)]] = 0$$

since $E[f_j(X, t)]$ is deterministic and $(X_i - \bar{X}_i)$ has zero mean. Equations (10.30) and (10.31) are exact, but of course involve stochastic quantities whose values are not known. (Note that we can also obtain the moment equations by applying Itô's formula to the quantities $(X_i - \bar{X}_i)(X_j - \bar{X}_j)$ and then taking expectations of the resulting differential equation.)

If we make the assumption that the distributions are concentrated near the means and the third and higher moments are small relative to the second moment, we can approximate the right-hand sides of these equations. If $G(x_1, \dots, x_n)$ is a function of n variables, then

$$E[G(X, t)] \approx G(m, t) + \frac{1}{2} \sum_{l=1}^n \sum_{p=1}^n \left\{ \frac{\partial^2 G(m, t)}{\partial x_l \partial x_p} C_{lp}, \right\}, \quad (10.32)$$

where m is the approximation to \bar{X} , and C_{lp} is the approximation to K_{lp} . Applying (10.32) to (10.30), we get

$$\frac{dm_j}{dt} = f_j(m, t) + \frac{1}{2} \sum_{l=1}^n \sum_{p=1}^n \frac{\partial^2 f_j(m, t)}{\partial x_l \partial x_p} C_{lp}. \quad (10.33)$$

We now have an approximate equation for the means. Note that if we ignore the covariances, we correctly recover the noise-free dynamics. The correction term in (10.33) makes intuitive sense since it depends to the sensitivity of the functions f_j to the variables. The approximation for C_{lp} is more difficult to obtain, but can be derived in steps. We replace \bar{X}_j by its approximation, m_j , to obtain

$$E[(X_i - m_i)f_j(X, t)] \approx \frac{1}{2} \sum_{l,p=1}^n \frac{\partial^2}{\partial x_l \partial x_p} [(x_i - m_i)f_j(m, t)] C_{lp}.$$

This partial derivative is just

$$\delta_{il} \frac{\partial f_j}{\partial x_p} + \delta_{ip} \frac{\partial f_j}{\partial x_l},$$

where δ_{jk} is 0 unless $j = k$, when it is 1. We obtain a similar approximation for $E[(X_j - m_j)f_i(X, t)]$ which now leads to our approximation for the covariances:

$$\frac{dC_{ij}}{dt} = \sum_{l=1}^n \left(\frac{\partial f_i}{\partial x_l} C_{lj} + \frac{\partial f_j}{\partial x_l} C_{il} + g_{il}g_{lj} \right). \quad (10.34)$$

It is instructive to apply this to a simple planar model with noise only in the first variable,

$$dV = f(V, U)dt + \sigma dW; \quad dU = g(V, U)dt,$$

such as the Morris–Lecar equations. Let v and u be the approximate means of the two equations and let w , y , and z be, respectively, the variance of V , the variance of U , and the covariance between V and U . Then from (10.33) and (10.34) we get the following equations:

$$\begin{aligned} v' &= f(v, u) + \frac{1}{2}(f_{vv}w + f_{uu}y + 2f_{vu}z), \\ u' &= g(v, u) + \frac{1}{2}(g_{vv}w + g_{uu}y + 2g_{vu}z), \\ w' &= \sigma^2 + 2f_vw + 2f_uz, \\ y' &= 2g_vz + 2g_uy, \\ z' &= (f_v + g_u)z + f_uy + g_vw. \end{aligned} \quad (10.35)$$

Here, f_v means the derivative of f with respect to v , etc. With no noise, $\sigma = 0$, the solution, $(v(t), u(t), 0, 0, 0)$, is an invariant solution, so we can ask if it is a stable invariant solution. It turns out as you will show in an exercise later, that if (\bar{u}, \bar{v}) is a stable fixed point of

$$u' = f(u, v) \quad \text{and} \quad v' = g(u, v),$$

then $(\bar{u}, \bar{v}, 0, 0, 0)$ is also a stable fixed point of (10.35) when $\sigma = 0$. Thus, for small values of σ , the fixed point still exists, is stable, and the covariances are finite. However, if there are periodic orbits for the (u, v) system, then the covariances grow linearly in time for any positive σ . Thus, the moment equations do not admit any bounded periodic solutions if there is noise. They are only valid for a finite amount of time.

The use of the moment equations is limited mainly to fixed points. However, we can use them to see how the stability and the existence of fixed points change as a function of the noise. Figure 10.6 shows an application of (10.35) to the Morris–Lecar model when the dynamics are class I and class II. Consider the noise-free case first. When there is a Hopf bifurcation for the noiseless system, the moment equations have a zero eigenvalue (Exercise 15). Thus, in the computer analysis of the full moment equations, there appears to be a branch point. Solutions along the branch point can often correspond to negative values of w , which is not physically possible; thus, they should be ignored. The same “feature” occurs at the fold point for the class II example (Fig. 10.6b). When there is a small amount of noise, the loss of a stable fixed point occurs at lower values of the current as is intuitively expected. What is surprising is that the branch of solutions for the noiseless system disappears at a fold point in the noisy system (Fig. 10.6a). The fold for class I is shifted to the left in the presence of noise. In Exercise 15, you show that this will be generically the case.

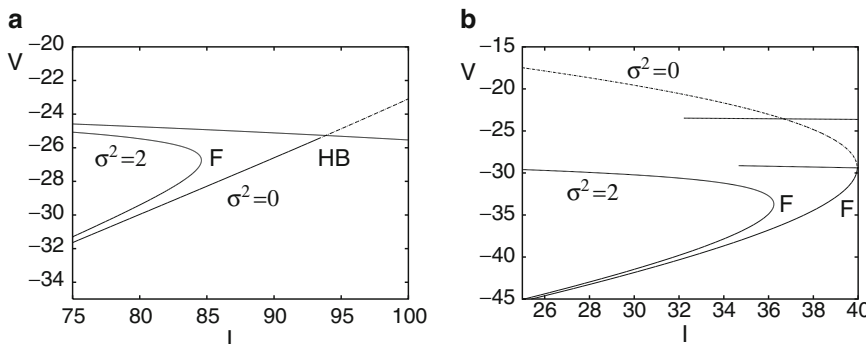


Fig. 10.6 Bifurcation diagram for Morris–Lecar moment expansion for (a) class II and (b) class I excitability as the current varies at zero noise and with large noise ($\sigma^2 = 2$). In each case, the addition of noise shifts the loss of the stable fixed point to a lower value of I

As you will see in Exercise 15, these equations are of limited utility since they generically grow without bound when there are limit cycles for the deterministic equations. However, it has been noted that if higher-order terms are kept in the moment equations (that is, beyond the simple linear dependences), then it is possible to keep solutions bounded even away from stable fixed points [258]. The key point is that in the Gaussian approximation, all moments can be expressed in terms of the variances. For example, $E[x^4] = 3E[x^2]$. For equations with polynomial right-hand sides, then *all* the expressions like $E[f(X)]$ can be expressed in terms of only the means and the variances with a finite number of terms. (For nonpolynomial systems, one can approximate f by a finite number of Taylor series terms.)

10.4 Poisson Processes

Many of the processes which occur at the molecular level in neuroscience are event-related and random. For example, the opening of a single channel is a single event and is random. The release of transmitter from an excited axon is also stochastic. The usual assumption that is made about these processes is that they are Poisson processes:

1. The number of events in nonoverlapping intervals of time is independent for all intervals.
2. The probability of exactly one event occurring in an interval Δt is $P = r\Delta t$, where r is the rate of events and Δt is sufficiently small.
3. The probability of more than one event occurring in a sufficiently small interval is zero.

10.4.1 Basic Statistics

Consider the interarrival times, that is, the times between events. Since the number of events in any nonoverlapping interval is independent, the intervals between events are also independent. Let the events occur at time t_1, t_2, \dots and let $I_1 = t_1$ and $I_k = t_k - t_{k-1}$ for $k > 1$ be the interarrival times. That these are independent means the process has no memory of what has already happened. (This has the following unfortunate consequence: if you have been waiting at the bus stop for a half an hour, then your expected waiting time for the next bus is exactly the same as that of the fellow who has just arrived at the bus stop!). Formally, this means

$$P(I > t + s | I > s) = P(I > t)$$

for all $s, t \geq 0$. The Bayes theorem says

$$P(x|y) = \frac{P(x, y)}{P(y)}.$$

But because the Poisson process “forgets” everything that happens, the joint probability $P(I > t + s, I > s) = P(I > t + s)$. Combining these two equations, we obtain

$$\frac{P(I > t + s)}{P(I > s)} = P(I > t),$$

so

$$P(I > t + s) = P(I > t)P(I > s).$$

Let $G(t) = P(I > t)$. Note that $G(0) = 1$. It is straightforward to show that the only solution to the functional equation $G(t + s) = G(t)G(s)$, $G(0) = 1$ is

$$G(t) = e^{-rt}.$$

Let $F(t) = 1 - G(t) = P(I \leq t)$ be the cumulative probability. Then the density function is the derivative of the distribution function, $f(t) = re^{-rt}$. For this reason, we say that the intervals of a constant-rate Poisson process are exponentially distributed. The mean interevent interval is

$$E[I] = \int_0^\infty tf(t) dt = \frac{1}{r}.$$

The second moment is

$$E[I^2] = \frac{2}{r^2};$$

thus, the variance ($\sigma^2 = E[(I - E[I])^2]$) is $1/r^2$. The *coefficient of variation* is defined as $\sigma/E[I]$ and this is 1 for Poisson process. The ISI distributions for cortical neurons have a coefficient of variation close to 1 [250].

Given we have the density function for the interval arrival times, we can now determine the density of the k th arrival time. Let us approach this inductively. The probability that the second event occurs at time t is the probability that the first event occurs at time $s < t$ and that the ISI is $t - s$. The first probability is $F(s) = 1 - \exp(-rs)$ and the second is $f(t - s)$. Thus,

$$F_2(t) \equiv P(\text{2nd event} < t) = \int_0^t (1 - e^{-rs})re^{-r(t-s)} ds.$$

The density of the second event ($k = 2$) distribution is the derivative of this and is just the convolution of the density function with itself:

$$f_2(t) = \int_0^t f(s)f(t-s) ds.$$

Evaluating this integral, we find

$$f_2(t) = (rt)re^{-rt}.$$

Inductively, we find that the density of the k th event is the so-called gamma distribution:

$$f_k(t) = (rt)^{k-1} r e^{-rt} / (k-1)!.$$

Finally, we can use this result to determine the distribution for the *number* of events in a given interval T . Let N_T denote the number of arrivals by time T . Then clearly $N_t \geq k$ when the k th arrival time is less than or equal to T . That is,

$$P(N_T \geq k) = \int_0^T f_k(s) \, ds.$$

This integral can be readily evaluated to yield

$$P(N_T \geq k) = 1 - e^{-rT} \sum_{j=0}^k (rT)^j / j!.$$

Thus, the density function for k spikes is

$$P(N_T = k) = \frac{(rT)^k}{k!} e^{-rT}.$$

This is called the Poisson distribution. The m th moment for the Poisson distribution is found by evaluating the sum

$$E[N^m] = \sum_{j=1}^{\infty} k^m \frac{(rT)^k}{k!} e^{-rT}. \quad (10.36)$$

This is not an easy task to do directly. Instead, it is easier to use a clever trick called the moment generating function. Consider the sum

$$H(s) = e^{-rT} \sum_{k=0}^{\infty} \frac{(rT)^k}{k!} e^{sk}. \quad (10.37)$$

The m th derivative of $H(s)$ with respect to s evaluated at $s = 0$ is precisely (10.36). The sum in (10.37) can be rewritten as

$$H(s) = e^{-rT} \sum_{k=0}^{\infty} \frac{(rT e^s)^k}{k!} = e^{-rT} \exp(rT e^s).$$

We thus find that $E[N] = rT$, $E[N^2] = rT + (rT)^2$, and the variance is rT . The ratio of the variance in the number of events with the mean is called the *Fano factor* and for a Poisson process is exactly 1.

10.4.2 Channel Simulations

The easiest way to simulate an exponential waiting time with a constant rate r is to draw random numbers from the exponential distribution. That is, let $I_n = -\log(X_n)/r$, where X_n are uniformly distributed numbers in the interval $(0,1)$. This is the key to the so-called Gillespie algorithm which is used to model chemical kinetics. For example, the opening and closing of channels is a simple random process

$$C \rightleftharpoons O$$

between the closed and open states. Let α and β be the respective rates for going from closed to open and vice versa. Let N denote the total number of channels and o the number of open channels. Since the channels are independent, the rate of making a closed to open transition is $r_1 = \alpha(N - o)$ and the rate of making an open to closed transition is $r_2 = \beta o$. The rate of any event occurring is thus $r = r_1 + r_2$. So we can choose a time to the next event as

$$t_{\text{new}} = -\log[X_1]/r,$$

where X_1 is uniform in $(0, 1)$. Now we have to pick which event occurred. We choose another random number, X_2 , uniformly distributed between 0 and r . If $X_2 < r_1$, then the first reaction (closed to open) occurs, otherwise the second reaction (open to closed) occurs. In the former case, o is increased and in the latter o is decreased. The total fraction of channels open is just o/N . Chow and White [39] applied this idea to study the effects of a finite number of channels in the Hodgkin–Huxley equations. We proceed here with a simpler model, the Morris–Lecar model, since all of the channel equations are simple open/close events. Unlike the reduced Morris–Lecar model in which we let the calcium channel have its equilibrium value $m_\infty(V)$, we must retain the temporal dynamics of the channel for a stochastic model. We have four possible events: (1) calcium channel opens, (2) calcium channel closes, (3) potassium channel opens, and (4) potassium channel closes. The rates are dependent on the voltage which satisfies

$$C_m \frac{dV}{dt} = I - g_l(V - E_l) - (g_K w / N_w)(V - E_K) - g_{Ca}(M / N_m)(V - E_{Ca}),$$

where W and M are the total number of open potassium and calcium channels. We divide this by the number of each type of channel since maximal conductances should be defined as conductance per channel. Thus, the total maximal conductance possible will be independent of the numbers of channels. This voltage equation is linear in V for any fixed W and M . Between events, both W and M will be constant, so we can write down the solution to the voltage equation exactly. We can rewrite the V equation as

$$\frac{dV}{dt} = (V_\infty - V)g,$$

where V_∞ and g are functions of the parameters and W and M . Suppose voltage was V_0 at the end of the last event. The next event comes at a time t_{new} later. Thus, the voltage at the beginning of the next event is

$$V(t_{\text{new}}) = V_\infty + (V_0 - V_\infty)e^{-gt_{\text{new}}}.$$

We use this new voltage to update the transition rates and calculate the next event. The only numerical approximation we make is holding the rates constant between events. Chow and White addressed some of these numerical issues. Figure 10.7 shows a simulation of the Morris–Lecar model with 100 potassium and calcium channels and a subthreshold current. The noise due to the fluctuations in channels is enough to cause the neuron to fire sporadically.

Computation of the channel openings and closing as in the above algorithm can be laborious in more complex models or if the number of channels is large. (With a large number, N , of channels, events occur very frequently, so advancing even a

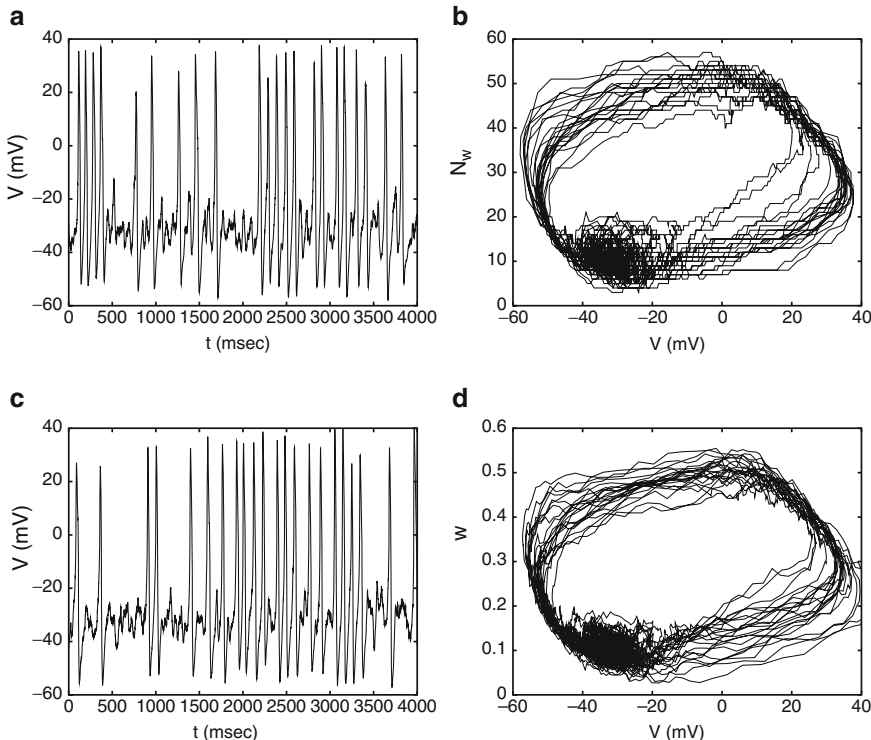


Fig. 10.7 Stochastic simulation of the Morris–Lecar model with 100 potassium and 100 calcium channels. $I = 80 \mu\text{A}/\text{cm}^2$ injected is subthreshold for repetitive firing. (a) Time series of the voltage. (b) Projection onto the (V, W) plane showing the stochastic limit cycle. (c, d) Langevin approximations to the channel dynamics

small amount of time can take thousands of steps – indeed the time step is $O(1/N)$.) Thus, there are a number of approximations often made. The most straightforward is to add noise to the deterministic channel models. That is, solve

$$dx = [a(1 - x) + bx]dt + \sigma_x dW(t). \quad (10.38)$$

The key question is the choice for σ_x . Using methods from statistical physics, [84] in Chap. 11 shows the following approximation:

$$\sigma_x^2 = \frac{a(1 - x) + bx}{N}, \quad (10.39)$$

where N is the number of channels. This has the right behavior for large N ; from the law of large numbers, we expect the standard deviation to scale as $1/\sqrt{N}$. Fox and Lu [92] made this approximation rigorous by (1) producing a master equation for the channels, (2) approximating this by a Fokker–Planck equation, and (3) writing down the corresponding Langevin equation. They made one more simplification of (10.39) by replacing x with $x_\infty = a/(a + b)$ and thus obtained

$$\sigma_x^2 = \frac{1}{N} \frac{ab}{a + b},$$

which is independent of x . Figure 10.7c and d shows the result of a simulation of the Morris–Lecar model using approximation (10.39). One issue that must be dealt with in using these approximations is that the variable x can fall out of the valid range $(0, 1)$; thus, it is necessary cap x when it leaves the interval. Finally, we can ask whether the behavior of these noisy versions of the Morris–Lecar model differ substantially from the model with voltage noise only. A comparison of Fig. 10.7c and d with Fig. 10.1c would lead one to suspect that there is little difference between the figures. We would expect the difference in this physically derived model for stochasticity from the ad hoc additive-noise model to become important only when there are very few channels.

10.4.3 Stochastic Spike Models: Beyond Poisson

Rather than generating spikes with a noisy deterministic model (such as described above) or with a fully deterministic model, sometimes it is desirable to create a completely stochastic model for the spike times. For example, one could simulate the spike times of a neuron with a purely Poisson process. However, biological neurons rarely have perfectly exponential ISI histograms (see, e.g., Fig. 10.1d). One reason for this is that once a neuron fires, the probability of a spike occurring again is very low owing to refractoriness – there is history to the firing pattern. We now derive distributions for such history-dependent models. Let $f(t)$ denote the ISI density function (this is the ISI histogram when defined in discrete time intervals).

The probability of a spike occurring before t is $F(t) = \int_0^t f(s) ds$. The probability that no spike has occurred up to time t is thus $1 - F(t)$. Now, we introduce a notion of history dependence. Let $h(t)\Delta t$ denote the probability that a spike occurs in the interval $[t, t + \Delta t]$ but *not* not at any time before. Let W be the random spike time. Then, formally,

$$h(t)\Delta t = P[t \leq W \leq t + \Delta t | W \geq t].$$

For a pure Poisson process, $h(t) = r$, the spike rate since the probability of the spike occurring is independent of the previous history. The probability of a spike between t and $t + \Delta t$ is just $f(t)\Delta t$ and the probability of no spike before t is $1 - F(t)$; thus, we have

$$h(t) = \frac{f(t)}{1 - F(t)} = -\frac{d}{dt} \log(1 - F(t)),$$

where we use the fact that $F'(t) = f(t)$. Given $h(t)$, we can solve this differential equation to find

$$F(t) = 1 - \exp\left(-\int_0^t h(s) ds\right). \quad (10.40)$$

The density function $F'(t)$ is

$$f(t) = h(t) \exp\left(-\int_0^t h(s) ds\right). \quad (10.41)$$

As a first example, suppose $h(t) = r$ so there is no history dependence. Then we recover the usual exponential function, $f(t) = re^{-rt}$. Suppose when the neuron fires, the rate is set to zero and recovers exponentially. Then $h(t) = r[1 - \exp(-t/\tau)]$ and we get the density function shown in Fig. 10.8a. In this example, the baseline frequency is 40 Hz and $\tau = 50$ ms. Note the peak in the ISI histogram at about 50 ms.

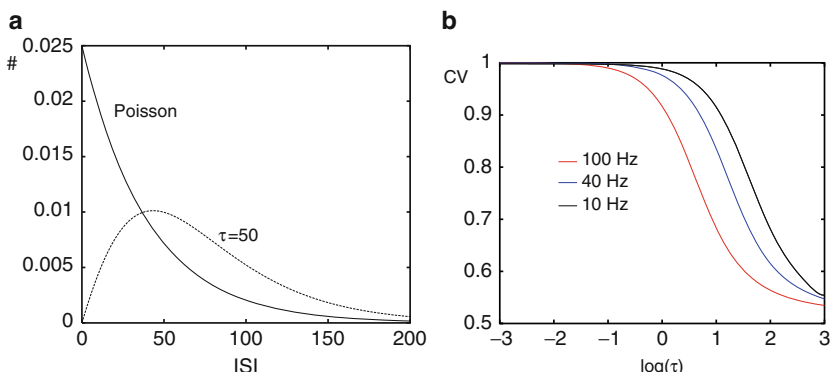


Fig. 10.8 Poisson process with a relative refractory period. $r(t) = r_{\max}(1 - \exp(-t/\tau))$. **(a)** Density function for a pure Poisson process with a 40-Hz rate and one with a refractory period, $\tau = 50$ ms. **(b)** Coefficient of variation (CV) for different rates and refractory periods

The mean ISI is 74 ms and the coefficient of variation is about 0.66. Figure 10.8b shows the coefficient of variation for this model at three different baseline frequencies over 6 orders of magnitude refractory period. Obviously, as $\tau \rightarrow 0$ the process approaches a pure Poisson process. Some more examples are provided as exercises.

Chapter 5 in the book by Gerstner and Kistler [99] provides many examples of stochastic neural models. In particular, there is a very readable discussion of statistics of these generalized point processes such as the spike time autocorrelation function and the spectral power. The interested reader should consult this book as it is beyond the scope of the present text.

10.5 Bibliography

Noise is now recognized as playing a major role in neural dynamics. The lengthy review [179], although not specific to neurons, contains most of the analytically tractable results for the effects of noise on excitable systems. Laing and Lord [169] is a comprehensive set of individual chapters that review noise from the channel level on up to large networks. Whether or not noise is “good” for the nervous system remains a subject of some controversy. Traynelis and Jaramillo [271] argue that it can be very helpful. Indeed, in Fig. 10.1 it is clear that noise allows one to extract many features for a signal that is subthreshold. Ermentrout et al. [79] argue that noise is also good for encouraging synchrony. Faisal et al. [82] suggest the nervous system has to work hard to compensate for the degree of noise. In this chapter, we have briefly reviewed some of the mathematical techniques that can be applied to the study of noise in active nonlinear systems. Unlike deterministic dynamics, the study of noise often leads to high-dimensional partial differential equations. These systems remain an active area of study.

10.6 Exercises

1. Compute the ISI distribution for the Morris–Lecar model with type II dynamics and $I = 95$, which is in the oscillatory regime. Use noise of amplitude 1, i.e., $V' = f(V, w) + \sigma\xi(t)$, $w' = g(V, w)$, where $\sigma = 1$. Show that the bimodality of the ISI is lost. Change I to 85 and set $\sigma = 2$ and then to 0.5. Compare the ISI histograms for these with that in Fig. 10.1d. On the basis of these computations, can you offer an explanation for the bimodality of the distribution?
2. Compute the ISI distribution for the Morris–Lecar model with type I dynamics, unit noise, and $I = 30$. Change the amount of noise. Is the distribution always unimodal?
3. Research problem. Consider the scalar neuron model

$$V' = f(V) + \sigma\xi(t),$$

- where ξ is the usual noise. Let $V = V_{\text{reset}}$ be the reset voltage and let V_{spike} be the voltage for a spike. Can the ISI distribution of this model ever be bimodal?
4. Suppose $f(x)$ has zero mean on the interval (a, b) . Show that $J = 0$ for the Fokker–Planck equation (10.12) with periodic boundary conditions.
 5. Consider the simple model on the circle

$$dx = (I - \cos(x))dt + \sigma dW.$$

- Write down the steady state for the Fokker–Planck equation and numerically compute the flux, J . This is the F – I curve.
6. First passage time. Show that

$$\langle T^n \rangle = \int_0^\infty t^{n-1} G(x, t) dt.$$

Use the fact that $G(x, t)$ satisfies

$$G_t(x, t) = f(x)G_x(x, t) + (\sigma^2/2)G_{xx}(x, t)$$

when f is independent of time to show that the moments $T_n \equiv \langle T^n \rangle$ satisfy

$$-nT_{n-1} = f(x)T'_n + (\sigma^2)/2T''_n.$$

Suppose the domain is $(-\infty, b)$ and the condition at $x = b$ is absorbing ($T(b) = 0$). Show that $T(x)$, the first moment, is given by

$$T(x) = \frac{2}{\sigma^2} \int_x^b dy \int_{-\infty}^y dz e^{(2/\sigma^2) \int_y^z f(s) ds}.$$

7. Provide a complete analysis of the firing rate for the piecewise linear ring model:

$$dV = (I + \text{abs}(V - \pi))dt + \sigma dW.$$

Start with a Monte Carlo simulation on the circle $[0, 2\pi]$ and compute the firing rate as a function of I for several values of σ . Fix the noise and the current I and compute the ISI histogram. Write a closed-form expression for the firing rate. Numerically solve the first passage time equation and use this to compute the ISI histogram. Compare it with the Monte Carlo simulation.

8. Show that v^{-1} from (10.21) is the same as $T(V_{\text{reset}})$ in (10.25). From this, derive the simple expression for the firing rate of the integrate-and-fire model (10.22).
9. For large negative arguments

$$\sqrt{\pi}e^{s^2}(1 + \text{erf}(x)) \sim \frac{1}{s} + O(s^{-3}).$$

Use this to obtain the firing rate for the leaky integrate-and-fire model when I is large. Is this the same as the noiseless value?

10. Provide an approximation to the firing rate of the leaky integrate-and-fire model (10.22) when $1 \ll \sigma$, the large-noise case. The approximation should be valid up to order 1 in σ^{-1} . (Hint: Use Taylor's theorem since both limits of the integral will be small.)
11. Lindner et al. [181] rescaled time and voltage in the quadratic integrate-and-fire neuron with noise,

$$dV = (V^2 + I) + \sigma^2 dW,$$

to eliminate I and absorb this into σ . There are two cases, $I < 0$ and $I > 0$. Do this rescaling to reduce the noisy model to one depending on a single parameter multiplying the noise.

12. Starting with (10.24) with $f(V) = |V|^p + I$, where $p > 1$, find a rescaling analogous to that done with the quadratic integrate-and-fire neuron to reduce the dependence of the firing rate on noise and current to one parameter and two equations for $I > 0$ and $I < 0$. When $I = 0$, show

$$\nu = K\sigma^{2\frac{p-1}{p+1}},$$

where K is some p -dependent constant. Note that for $p = 2$ you recover Sigeti and Horsthemke's result without doing much of anything!

13. *Estimating conductances.* Rudolph et al. [238] described a method for estimating the conductances of excitatory and inhibitory inputs into a neuron by measuring the distribution of the subthreshold voltages. They derived a system of stochastic differential equations and then reduced this to a Fokker–Planck equation for which they could find the stationary distribution. Their method has some flaws [181], but some of the basic ideas still hold. In this exercise, we will use some very simple approximations to perform the estimates. Consider the following stochastic differential equation:

$$CdV/dt = I - g_L(V - E_L) + g_e(t)(V_e - V(t)) + g_i(t)(V_i - V(t)),$$

where $g_{e,i}(t)$ are stochastic conductances of the excitatory and inhibitory neurons. [238] assumed these conductances obey a first-order stochastic differential equation. Here, instead, we assume they are of the form

$$g_{e,i}(t) = \bar{g}_{e,i} + \sigma_{e,i} \frac{dW_{e,i}}{dt},$$

where $W_{e,i}(t)$ are Wiener processes. The problem now is that the noise appears multiplicatively in the voltage equation. Let us avoid this by making a rather crude approximation. Replace $V(t)$ in the conductance terms by \bar{V} , the mean voltage in the absence of the fluctuations. Then we obtain

$$\begin{aligned} CdV &= [I - g_L(V - E_L) - \bar{g}_e(V - V_e) - \bar{g}_i(V - V_i)]dt \\ &\quad + \sigma_e[\bar{V} - V_e]dW_e(t) + \sigma_i[\bar{V} - V_i]. \end{aligned}$$

Now, the noise terms are constant; however, \bar{V} depends on $\bar{g}_{e,i}$. Proceed as follows: (1) Compute \bar{V} , the mean potential as a function of $\bar{g}_{e,i}$ and I . (2) Using two different values of I , find $\bar{g}_{e,i}$ in terms of the mean voltage (experimentally observed) and the other known parameters, V_L , g_L , I , and $V_{e,i}$. (3) Use the fact that the sum of two independent Wiener processes with amplitudes a and b is a Wiener process with amplitude $\sqrt{a^2 + b^2}$ to find the stationary distribution of the voltages at the two different currents. This will be a Gaussian with mean \bar{V} and variance σ^2 . Express σ^2 in terms of the known parameters, the already-determined $\bar{g}_{e,i}$, and the unknowns, $\sigma_{e,i}$. Since σ is experimentally observable for each applied current, I , solve for $\sigma_{e,i}$ in terms of known and experimentally observable quantities using two applied currents.

14. *Colored noise.* Consider the rescaled voltage driven by colored noise:

$$\frac{dv}{dt} = -\beta v + y, \quad \tau dy = -y dt + \sqrt{2D} dW.$$

Verify that the Fokker–Planck equation for this is

$$P_t = [(\beta v - y) P]_v + [y P / \tau + D P_y / \tau^2]_y,$$

where the domain is the plane. Amazingly enough, a steady state for this equation can be found exactly! Show that

$$P(v, y) = N \exp(Av^2 + Bvy + Cy^2),$$

where N is a normalization constant and A , B , and C are unknown constants. Find these constants in terms of β , τ , and D . (It will help a great deal to use a symbolic package such as Maple.)

15. *Analysis of moment equations.* In this exercise, we will examine certain aspects of the moment equations.

- a. As you will show next in this exercise, the only situation in which there is a bounded solution to the moment equations is near a stable fixed point. We will first explore the effects of noise near a fold bifurcation. Consider the following system:

$$\begin{aligned} x' &= x^2 + a + v, \\ v' &= 2xv + \sigma^2. \end{aligned}$$

Find all the stable fixed points and the curve of fold points in the two parameters a and σ^2 . In particular, show that the effect of noise is to make the bifurcation occur at lower values of a . Turn this into an integrate-and-fire model by assuming when x reaches some large number, say, 10, it is reset to a large negative number, say, -10 , and the variance is reset to 0. Numerically find the F – I curve for different values of σ . Show that it is always concave down, so it does not look like the F – I curve computed from the Fokker–Planck equation. Finally, prove $v(t)$ is always nonnegative in this model.

- b. We now consider the general moment equations (10.33) and (10.34) when the noise is zero, that is, $g_{ij} = 0$. The covariance equations are redundant since $C_{ij} = C_{ji}$ is enforced. However, it is much more convenient to work with the full n^2 equations rather than the $n(n + 1)/2$ independent ones. Clearly, $C_{ij} = 0$ is invariant and the first moments obey the deterministic dynamics. We now look at the stability of these equations around some deterministic solution, $(m, C) = (m_0(t), 0)$. Let $A(t) = a_{ij}(t)$ be the linearization of the deterministic system about $m_0(t)$. That is,

$$a_{ij}(t) = \frac{\partial f_i}{\partial x_j}$$

evaluated along the solution $m_0(t)$. The linearization of the full (m, C) system about $(m_0, 0)$ is an $n + n^2$ -dimensional square matrix. However, the lower-left $n^2 \times n^2$ block is all zeros, so the linearized system is block-triangular. Stability is determined solely by looking at the two blocks: the $n \times n$ upper block, which is the matrix $A(t)$, and the lower-right $n^2 \times n^2$ block, which is formed from (10.34). Note that the coefficients multiplying C_{ij} are entries of the matrix $A(t)$, so the lower block is very closely related to the upper block. The linearization of (10.34) can be rewritten as

$$C'_{ij} = \sum_{l=1}^n (a_{il}(t)C_{lj} + a_{jl}(t)C_{il}). \quad (10.42)$$

Suppose $u(t)$ and $v(t)$ are two solutions to $y' = A(t)y$. $u(t)$ and $v(t)$ are vectors with components $u_i(t)$ and $v_i(t)$, $i = 1, \dots, n$. Prove $C_{ij} = u_i(t)v_j(t)$ solves (10.42). Thus, if A is constant, then the solutions, $u(t)$ and $v(t)$, are exponentials, say, $\bar{u}e^{\lambda t}$ and $\bar{v}e^{\nu t}$, where \bar{u} and \bar{v} are constant vectors. This means the solutions to (10.42) are also exponentials with exponent $\lambda + \nu$. Thus, the eigenvalues associated with (10.42) are just sums of the eigenvalues associated with A . From this, you can conclude that the full moment expansion near an asymptotically stable fixed point of the deterministic system is also asymptotically stable.

What about periodic orbits? Suppose the deterministic system has a stable periodic solution, $m_0(t)$. Then the system $y' = A(t)y$ has a periodic solution, $m'_0(t)$. This means (10.42) also has a periodic solution, where we take $u(t) = v(t) = m_0(t)$. All other solutions to $y' = A(t)y$ decay as do those of (10.42). But the existence of a periodic solution to (10.42) is bad since as soon as g_{ij} is nonzero, the solutions to (10.42) will grow. Prove this. That is, suppose we have the system $Z' = B(t)Z$, where $B(t)$ is a periodic matrix. Suppose there is a unique periodic solution, $Z_0(t)$, and all of the other linearly independent solutions to $Z' = A(t)Z$ exponentially decay as $t \rightarrow \infty$. Let P be a constant vector. Show that solutions to

$$Z' = B(t)Z + P$$

- will grow in time unless P is chosen very carefully. (This is a tricky problem related to the Fredholm alternative.)
16. Solve the functional equation $G(0) = 1$ and $G(t + s) = G(t)G(s)$ for all t and s . Assume $G(t)$ is continuously differentiable. (Hint: Take s small and derive a differential equation for $G(t)$.)
 17. Compute the coefficient of variation for spike production in the Morris–Lecar model with class I and class II excitability parameters in both the subthreshold and suprathreshold regimes of current with a fixed strength of additive white noise.
 18. Simulate a Poisson process with an absolute refractory period. That is, let r_{\max} be the maximal rate. Each time a spike occurs, the rate is set to 0 and after τ milliseconds it returns to r_{\max} . Compute the coefficient of variation for this process. Write down the ISI histogram using (10.41) and use this to compute the coefficient of variation exactly.
 19. Create a function $h(t)$ such that the density function $f(t)$ has power-law behavior for large t ; that is, $f(t) \sim 1/t^m$ as $t \rightarrow \infty$. Compute the coefficient of variation for this. Note that m must be larger than 2 in order to compute the coefficient of variation. Show that the coefficient of variation is always larger than 1 for this process.
 20. Consider a renewal process such that $h(t) = r_1$ for $t < 1$ and $h(t) = 1$ for $t > 1$. Compute the coefficient of variation as a function of r_1 . Note that when $r_1 < 1$, the firing rate is diminished right after firing, so it is like a refractory period, whereas if $r_1 > 1$, then the neuron is briefly more likely to spike after it has already fired. This can be likened to an afterdepolarization such as is seen in neurons which produce dendritic spikes. For what value of r_1 is the coefficient of variation maximal?

10.7 Projects

1. Develop computer code to solve the Fokker–Planck equation for the Morris–Lecar model. In particular, compute the noisy F – I curve as follows:

- a. Solve the steady state:

$$0 = -\partial_v(f(v, w, I)P(v, w)) - \partial_w(g(v, w)P(v, w)) + (\sigma^2/2)\partial_{vv}P(v, w).$$

The domain is the plane, but if you choose a large rectangle, $D \equiv (v_{\min}, v_{\max}) \times (w_{\min}, w_{\max})$, this should be sufficient. You should use reflecting boundaries, $J(\partial D) = 0$.

- b. For each I , define the firing rate as

$$f = - \int_{v_{\min}}^{v_{\max}} J(v, w_{\text{th}}) \, dv,$$

where we choose w_{th} as in the Monte Carlo simulations. The reason we do not choose a voltage threshold is that the noise is in the voltage variable and since we are using a Brownian motion, V can cross any specific point infinitely many times in any interval of time. Thus, we use a section which is transverse to the flow in the recovery variable as this is a continuous process.

Compare the result with Monte Carlo simulations.

2. Consider the stochastic differential equation corresponding to the Izhikevich model (normal form for the Takens–Bogdonov bifurcation with finite reset),

$$dV = (I + V^2 - z)dt + \sigma dW; \quad dz = a(bV - z), \quad (10.43)$$

with the reset condition that if $V(t^-) = 1$, then $V(t^+) = c$ and $z(t^+) = z(t^-) + d$ [275]. Explain why the probability density satisfies

$$\frac{\partial P}{\partial t} = -\frac{\partial}{\partial V}(fP) - \frac{\partial}{\partial z}(gP) + \frac{\sigma^2}{2} \frac{\partial^2 P}{\partial V^2} + J[\delta(V - c) + P(V, z - d) - P(V, z)],$$

where

$$J = - \int_{-\infty}^{\infty} dz \frac{\sigma^2}{2} \frac{\partial P(V, z)}{\partial V} |_{V=1}$$

and $f = I + V^2 - z$, $g = a(bV - z)$. This partial differential equation is defined on the domain $(V, z) = (-\infty, 1) \times (-\infty, \infty)$. The stationary distribution will give you the firing rate, J . Try to develop an expansion for the stationary distribution for small a and d . This will be a fast–slow system. Tuckwell et al. [275] developed expansions for the FitzHugh–Nagumo equation that may be of use. Here, we suggest a way to attack the problem. For small a and d , z does not change very much, so we can hold z constant. If z is fixed, suppose one can obtain the steady-state firing rate, J , as well as the density function, $P(V; z, I)$. Then z formally satisfies

$$z' = dv + a(b\langle V \rangle - z) \equiv G(z),$$

where v is the firing rate of the cell and $\langle V \rangle$ is the average potential. Note that both v and $\langle V \rangle$ depend on z . Find a fixed point, $G(z^*) = 0$, and substitute back into $P(V; z, I)$ to obtain the stationary density at the steady state. One can continue this expansion to higher order to get the variance of z as well. We suspect that methods related to the moment expansions in this chapter could be of use for the z dynamics.

Another interesting phenomenon to explore is the ISI distribution for this model. For example, choose $I = 0.05$, $\sigma = 0.015$, $a = 0.03$, $b = 1$, $c = 0.2$, and $d = 0$ and perform a Monte Carlo simulation. You will see that there is a bimodal ISI. (See Exercise 3 for some comments on bimodal ISIs). Is it possible to get a bimodal ISI distribution in the limit as a becomes small but b remains finite?

3. Set some parameters for the Morris–Lecar model with noise. A good choice is to add a modest amount of noise (say, $\sigma = 2$ and $I = 35$) in the class I regime. First, numerically compute the F – I curve for a range of applied currents. Now add a small periodic term as in Sect. 10.2.5 and compute the spike-time histogram. (That is, present the periodic stimulus, say, 10,000 times and count the number of spikes (crossings of $w = 0.3$) in each bin of, say, 2 ms. From this, you get the number of spikes per millisecond, which is the firing rate.) Compare the spike-time histogram with a model for the firing rate as in Sect. 10.2.5:

$$u(t) = L[f(I(t))],$$

where L is some simple linear filter and f is the steady-state firing rate. Can you come up with a simplified firing rate model for the Morris–Lecar system based on these ideas? Repeat the Monte Carlo simulations above, but replace the white noise with the following noise

$$\tau dz = -z dt + \sqrt{\tau} dW$$

for different values of τ . You should find that the lag between the stimulus and the firing rate disappears for τ roughly of the order of 10 ms.

4. *Noisy synchrony.* A model that has been used for a pair of coupled neurons in the presence of noise is

$$\begin{aligned} d\theta_1 &= (\omega_1 + H(\theta_2 - \theta_1))dt + \sigma dW_1, \\ d\theta_2 &= (\omega_2 + H(\theta_1 - \theta_2))dt + \sigma dW_2, \end{aligned}$$

where dW_j is white noise. Subtract these two equations and let $\phi = \theta_2 - \theta_1$ to obtain

$$d\phi = (\delta - 2G(\phi))dt + \sigma \sqrt{2} dW,$$

where $\delta = \omega_2 - \omega_1$ and $G(\phi)$ is the odd part of $H(\phi)$. The $\sqrt{2}$ factor arises because the sum of two Wiener processes with unit variance and zero mean is also a Wiener process with variance 2. Write a Fokker–Planck equation for this Langevin equation. For the case $\delta = 0$, write the steady-state probability density for ϕ . (The more general case is doable but not so compactly.) Pfeuty et al. [214] have shown that this density function is related to the spike-time cross correlation of the two neural oscillators.

5. *Synchrony without coupling.* Two oscillators which are driven with common weak noise can synchronize even if they are not coupled [261]. To see this, start with any two oscillators (for example, the Izhikevich model) and drive them with a common white noise process, started from slightly different initial conditions. Over time, they will converge to a synchronous solution. In this project, you use the results of this chapter to analyze the resulting equations. To simplify the

analysis, we restrict our attention to simple ring model oscillators which are continuous and differentiable:

$$\begin{aligned} dx_1 &= a(x_1)dt + \sigma dW, \\ dx_2 &= a(x_2)dt + \sigma dW. \end{aligned}$$

Assume $a(x) > 0$, $a(x + 2\pi) = a(x)$, and $P = \int_0^{2\pi} \frac{dx}{a(x)} < \infty$. Then we can regard each x as an oscillator

Step 1. Make a change of variables $x = U(\theta)$, where $U' = a(U)$. Since $a(U) > 0$, this is an invertible transformation. Let $f(x)$ be the inverse, so $\theta = f(x)$. Recall Ito's formula when you make the change of variables.

Step 2. Recall that for the scalar oscillator, the adjoint $Z(\theta)$ is given by $Z(\theta) = 1/a(U(\theta))$. Use regular calculus to show that with the change of variables in step 1 the equations are

$$\begin{aligned} d\theta_1 &= \left[1 + \frac{\sigma^2}{2} Z'(\theta_1)Z(\theta_1) \right] dt + \sigma Z(\theta_1)dW, \\ d\theta_2 &= \left[1 + \frac{\sigma^2}{2} Z'(\theta_2)Z(\theta_2) \right] dt + \sigma Z(\theta_2)dW. \end{aligned}$$

Step 3. One solution to this stochastic differential equation is $\theta_1 = \theta_2 = \theta$.

Let $\phi = \theta_2 - \theta_1$. Then ϕ satisfies

$$d\phi = \frac{\sigma^2}{2} [Z'(\theta)Z(\theta)]' \phi dt + \sigma Z'(\theta)\phi dW.$$

Again, using Ito's formula, let $y = \log(\phi)$ and show that y satisfies

$$dy = \frac{\sigma^2}{2} \{[Z'(\theta)Z(\theta)]' - Z'(\theta)^2\} dt + \sigma Z'(\theta)dW.$$

Step 4. The long-time behavior of $y(t)$ determines the stability of the synchronous state. That is, if

$$\lambda \equiv \lim_{T \rightarrow \infty} \frac{1}{T} (y(T) - y(0))$$

is negative, then $\phi(t)$ will decay to zero. λ is the time average of $y(t)$ and we can replace this with the ensemble average:

$$\lambda = \frac{\sigma^2}{2} \int_0^{2\pi} P_{st}(\theta) \{[Z'(\theta)Z(\theta)]' - Z'(\theta)^2\} d\theta.$$

Here, $P_{\text{st}}(\theta)$ is the stationary distribution of θ which satisfies the stochastic differential equation:

$$d\theta = [1 + \frac{\sigma^2}{2} Z'(\theta)Z(\theta)]dt + \sigma Z(\theta)dW.$$

If the noise is small, then θ is nearly uniform and you can approximate $P_{\text{st}}(\theta) = 1/(2\pi)$. Show that with approximation,

$$\lambda = -\frac{\sigma^2}{2} \frac{1}{2\pi} \int_0^{2\pi} Z'(\theta)^2 d\theta.$$

Conclude synchrony is stable.

Supplement the analysis with some numerical simulations. Additionally, add independent noise to each oscillator, say, 10% of the common noise. Solve this numerically and look at the stationary distribution of the phase differences.

Chapter 11

Firing Rate Models

One of the most common ways to model large networks of neurons is to use a simplification called a firing rate model. Rather than track the spiking of every neuron, instead one tracks the averaged behavior of the spike rates of groups of neurons within the circuit. These models are also called population models since they can represent whole populations of neurons rather than single cells. In this book, we will call them rate models although their physical meaning may not be the actual firing rate of a neuron. In general, there will be some invertible relationship between the firing rate of the neuron and the variable at hand. We derive the individual model equation in several different ways, some of the derivations are rigorous and are directly related to some biophysical model and other derivations are ad hoc. After deriving the rate models, we apply them to a number of interesting phenomena, including working memory, hallucinations, binocular rivalry, optical illusions, and traveling waves. We also describe a number of theorems about asymptotic states as well as some of the now classical work on attractor networks.

There are many reasons to use firing rate models. First of all, there is the obvious issue of computational efficiency. Modeling a network of thousands of individual conductance-based neurons can tax even the fastest computers. For this reason, many large-scale simulations use simple spiking models such as the integrate-and-fire model. In many experimental preparations, what is measured is not the intracellular potential of neurons, but instead the probability of firing. This type of recording is done with an extracellular electrode and thus spikes can be detected but the other aspects of the cell are unknown. Hence, to better make better comparisons with experiments, it makes sense to consider the firing rate instead of the potential. Field potential recordings, electroencephalograms, and functional magnetic resonance imaging presumably represent large populations of neurons. Thus, a model at this scale may be better posed in terms of population equations.

Rate models are among the oldest forms of modeling of the brain and the nervous system, going back to the late 1930s. Cowan and Sharp [50] have written a very comprehensive history of the early days of neural network research. A nice oral history of the subject of neural nets can be found in [5].

Rate models are essentially the underlying “biology” in the very popular and useful theory of neural networks. For example, the “connectionist” models developed under the Parallel Distributed Processing program by McClelland and Rumelhart

[196] and the “back propagation” models are all connected to the wet nervous system (albeit, occasionally rather tenuously) via rate models. Massively recurrent attractor networks, perceptrons, hidden layer models, adaptive resonance theory (and its descendants) are all essentially rate models [98]. We will spend little time in this chapter on the more machinelike and abstract ideas of neural network theory and will instead focus on the connection of rate models to biophysics and the usefulness of these networks in modeling biological phenomena.

11.1 A Number of Derivations

11.1.1 Heuristic Derivation

We start with a very simple, somewhat abstract derivation that was advocated in early work of Cowan and later formalized in Ermentrout and Cowan [69]. Figure 11.1 shows a schematic for a pair of neurons with a synapse from one to the other. The measurable output is the firing rate, $u_i(t)$, which depends in a nonlinear way on the somatic potential, $V_i(t)$:

$$u_i(t) = F_i(V_i(t)).$$

Now, the reader might recall that most of our biophysical models produced firing rates as a function of the applied current, so she may be puzzled at the use of voltage as a driver for the output of the cell. We justify this by assuming the current flowing into the axon hillock (which is the site of action potentials) is proportional to the voltage drop between the soma and the resting potential of the hillock compartment. Thus, the somatic potential is passively converted to an axon hillock current via Ohm’s law, that is, $I = V/R_M$, where R_M is the membrane resistance. Each time a presynaptic cell fires a spike, a postsynaptic potential appears at the soma. The size of this potential, as well as the sign, depends on the nature of the synapse, the position on the dendrite, and so on. We define $\Phi_{ij}(t)$ to be the postsynaptic

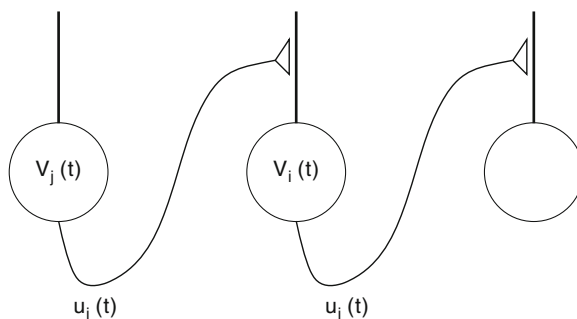


Fig. 11.1 Schematic of a pair of neurons synaptically coupled

potential appearing on postsynaptic cell i due to a single spike from presynaptic cell j . Let t_1, t_2, \dots, t_m be the firing times of the presynaptic cell. By assuming linear summation of the postsynaptic potentials, the total potential received at the soma is

$$G_{ij}(t) = \sum_l \Phi_{ij}(t - t_l).$$

The firing rate $u_j(t)$ determines the instantaneous number of spikes that a neuron fires in an infinitesimal time interval. That is, we can think of $u_j(t)dt$ as the probability of a spike occurring in the time interval $(t, t + dt)$. Thus, the above sum can be rewritten as

$$G_{ij}(t) = \int_{t_0}^t \Phi_{ij}(t-s)u_j(s - \tau_{ij})ds,$$

where τ_{ij} is the possible axonal delay in the spike arising at cell j arriving at cell i . If the effects of each cell linearly sum, then we can close this model, resulting in an integral equation for either V_i or u_i :

$$V_i(t) = \sum_j G_{ij}(t) = \sum_j \int_{t_0}^t \Phi_{ij}(t-s)F_j(V_j(s - \tau_{ij}))ds, \quad (11.1)$$

$$u_i(t) = F_i \left(\sum_j \int_{t_0}^t \Phi_{ij}(t-s)u_j(s - \tau_{ij})ds \right). \quad (11.2)$$

Both of these rather formidable equations can be greatly simplified once we have discussed the postsynaptic potential function $\Phi_{ij}(t)$. To do this, let us consider a passive membrane with a time constant τ_m and into which a presynaptic current is injected:

$$\tau_m \frac{d\Phi}{dt} + \Phi = R_M I(t).$$

For simplicity, suppose $I(t)$ is an alpha function of the form

$$I(t) = \exp(-t/\tau_d) - \exp(-t/\tau_r).$$

Here, τ_d is the decay of the synaptic current and τ_r is the rise time of the current. Assuming $\Phi(0) = 0$, we can solve this simple differential equation to obtain the postsynaptic voltage response:

$$\Phi(t) = \frac{\tau_d}{\tau_d - \tau_m} \left(e^{-t/\tau_d} - e^{-t/\tau_m} \right) - \frac{\tau_r}{\tau_r - \tau_m} \left(e^{-t/\tau_r} - e^{-t/\tau_m} \right). \quad (11.3)$$

This response depends on three parameters: the postsynaptic time constant and the presynaptic rise and decay times. One could make this response function far more complex by including dendritic filtering properties and so on as long as it remains linear. (If the response is nonlinear, then we cannot simply sum the inputs from different neurons, nor can we even sum the individual postsynaptic potentials to form the integral.)

The Volterra integral equations (11.1) and (11.2) are not simple to analyze so one generally attempts to convert them into differential or differential-delay equations. For $\Phi(t)$ represented as a finite sum of exponentials, we can always invert the integral equation to form a set of differential equations. To see this, consider first the simple integral equation

$$x(t) = \int_{t_0}^t e^{-(t-s)/\tau} y(s-r) ds,$$

where r is the possible delay. Differentiate x with respect to t to obtain

$$\frac{dx}{dt} = y(t-r) - \frac{1}{\tau} \int_{t_0}^t e^{-(t-s)/\tau} y(s-r) ds = y(t-r) - x(t)/\tau.$$

Thus, we see that $x(t)$ satisfies

$$\frac{dx}{dt} + x/\tau = y(t-r).$$

If $\Phi(t)$ is the sum of several exponentials, then we can break the Volterra integral equation into a set of differential equations using the above identity.

This approach is not entirely satisfactory since for each connection $\Phi_{ij}(t)$ we need (in the present case) three differential equations. If the network of interest consists of a homogeneous population of neurons, that is, their synaptic time constants are the same and they have the same membrane time constant, then we can write $\Phi_{ij}(t) = w_{ij} \Phi(t)$, where w_{ij} represent the magnitudes of the connections. Suppose the delays, τ_{ij} are the same for all cells, say, $\tau_{ij} = r$. Then the voltage equation (11.1) now becomes

$$(L V_i)(t) = \sum_j w_{ij} F_j(V_j(t-r)), \quad (11.4)$$

where L is a linear homogeneous differential operator. Equation (11.4) is essentially the classical model for a neural network. We can similarly reduce (11.2) to a set of differential equations. Let

$$z_i(t) = \int_{t_0}^t \Phi(t-s) u_i(s-r) ds.$$

Thus,

$$(L z_i)(t) = u_i(t-r) = F_i \left(\sum_j w_{ij} z_j(t-r) \right). \quad (11.5)$$

This is not quite the same as an equation for the firing rate, $u_i(t)$, but this variable is obtained easily from $z_i(t)$ by differentiation [217]. $z_i(t)$ is the *synaptic drive*.

This drastically simplifies the simulation and analysis of single populations of differential equations but we are still stuck with difficulties when we have, say, an excitatory and an inhibitory population. Key to the reduction was the idea that $\Phi_{ij}(t) = w_{ij} \Phi(t)$. However, if we examine (11.1) carefully, we see that we can make a less restrictive assumption that $\Phi_{ij}(t) = w_{ij} \Phi_i(t)$ for then we obtain

$$(L_i V_i)(t) = \sum_j w_{ij} F_j(V_j(t - r)).$$

Similarly, examining (11.2), if we assume $\Phi_{ij}(t) = w_{ij} \Phi_j(t)$, then we obtain

$$(L_i z_i)(t) = F_i \left(\sum_j w_{ij} z_j(t - r) \right).$$

Rather than a system of N^2 differential equations for a network of N neurons, we just have N differential equations. Thus, we now want to examine more closely what these two assumptions entail.

Suppose $\Phi_{ij} = w_{ij} \Phi_i(t)$. This means the response of neuron i to any inputs depends (up to a scalar constant which could be negative or positive) only on the properties of the *postsynaptic* cell. This assumption is valid if the shape and temporal properties of the presynaptic currents are the same no matter what type the presynaptic cell is. This kind of model would fail to distinguish between, say, a slow NMDA current and a fast AMPA current, or even between the fast AMPA and somewhat slower GABA currents. However, looking at (11.3), we see that if $\tau_m \gg \{\tau_d, \tau_r\}$, then $\Phi(t) \approx \exp(-t/\tau_m)/\tau_m$, which is independent of the presynaptic timescales. That being the case, our system of differential equations is first order:

$$\tau_{m,i} \frac{dV_i(t)}{dt} + V_i(t) = \sum_j w_{ij} F_j(V_j(t - r)). \quad (11.6)$$

Equation (11.6) is commonly used as a model neural network and within the scope of our derivation, the timescale associated with each element in the network is that of the *membrane time constant*.

Now, suppose $\Phi_{ij} = w_{ij} \Phi_j(t)$. This means the shape of the postsynaptic potential depends only on the *presynaptic* cell. To us, this is a more reasonable assumption since we can distinguish different types of synapses (and, below, this allows us to incorporate synaptic depression and potentiation). Suppose the rise time of the synapse and the membrane time constant of the postsynaptic cell are small compared with the decay of the synapse. Then $\Phi_j(t) \approx \exp(-t/\tau_d)/\tau_d$ and, as above, we derive the following equation for the *synaptic drive*:

$$\tau_d \frac{dz_i(t)}{dt} + z_i(t) = F_i \left(\sum_j w_{ij} z_j(t - r) \right). \quad (11.7)$$

This model is also a very popular version for neural networks. In this case, the temporal dynamics are dominated by the synaptic decay, τ_d .

Equations (11.6) and (11.7) are often regarded as equivalent, but in the present derivation, they are not. Rather, they represent two distinct assumptions about the dominant timescales.

Before discussing the forms of the firing rate functions, F_i , we turn to a derivation based on the theory of averaging and some assumptions about the types of bifurcation in the conductance-based models.

11.1.2 Derivation from Averaging

Consider the following conductance-based network:

$$C \frac{dV_i}{dt} + I_i(V_i, \dots) = - \sum_j g_{ij} s_j (V_i - V_{\text{syn},j}), \quad (11.8)$$

$$\tau_{\text{syn}} \frac{ds_i}{dt} + s_i = R_i(V_i, s_i). \quad (11.9)$$

Here, I_i represents all the nonlinear conductances which lead to action potentials. To simplify the derivation, we have assumed a synapse from cell j produces the same conductance change regardless of the postsynaptic target. This is not an unreasonable assumption. Weakening this assumption results in more differential equations just as the more general assumptions in the previous section. Suppose $\tau_{\text{syn}} \gg 1$. This means the synapses are slow. If the synapses are slow, then $s_i(t)$ will change very slowly relative to the dynamics of the membrane; thus, we can treat s_i as constant. For ease in exposition, we will suppose all the neurons are excitatory, which means $V_{\text{syn},j} = V_e$. Let $G_i = \sum_j g_{ij} s_j$. Since s_j are roughly constant, so is G_i , so we can treat it as a parameter. Equation (11.8) is now isolated from the rest of the population because G_i is just a constant. We can compute the bifurcation diagram of the membrane potential and obtain

$$V_i(t) = \bar{V}_i(t; G_i).$$

We will assume only two types of behavior: stable fixed points or limit cycles. In the latter case, we assume the period is $T_i(G_i)$. We now return to the synaptic equations (11.9) but substitute $\bar{V}_i(t; G_i)$ for V_i since the potential changes on a faster timescale than the synapses. Thus, (11.9) becomes

$$\frac{ds_i}{dt} = \frac{1}{\tau_{\text{syn}}} (-s_i + R_i(\bar{V}_i(t; G_i), s_i)).$$

If \bar{V}_i is a stable fixed point, then the s_i equation is straightforward since the right-hand side is independent of t . However, if \bar{V}_i is periodic, then we are still safe since we can apply the averaging theorem and obtain

$$\frac{ds_i}{dt} = \frac{1}{\tau_{\text{syn}}}(-s_i + \langle R_i(\bar{V}_i(t; G_i), s_i) \rangle),$$

where

$$\langle R_i(\bar{V}_i(t; G_i), s_i) \rangle = \frac{1}{T_i(G_i)} \int_0^{T_i(G_i)} R_i(\bar{V}_i(t; G_i), s_i) dt \equiv Q_i(G_i, s_i).$$

Thus, since all the quantities involved depend on G_i , we have reduced this conductance-based model to a system of first-order equations for the synaptic gates, s_i :

$$\tau_{\text{syn}} \frac{ds_i}{dt} + s_i = Q_i \left(\sum_j g_{ij} s_j, s_i \right). \quad (11.10)$$

We now explore (11.10), specifically $Q(G, s)$, in more detail. In Chap. 8, we modeled synapses as

$$\frac{ds}{dt} = \alpha(V)(1 - s) - \beta s$$

in much the same way as we model channels. Factoring out the $\beta = 1/\tau_{\text{syn}}$, we see that $R(V, s) = \alpha(V)\tau_{\text{syn}}(1 - s)$. The function $\alpha(V)$ is zero except when the neuron spikes. Let us suppose the width of a spike is independent of the firing rate of the neuron, so

$$\int_0^T \alpha(\bar{V}(t)) \tau_{\text{syn}} dt = \mu,$$

where μ is a constant essentially independent of T , the period. Let us define

$$F(G) \equiv \frac{1}{T(G)}$$

as the firing rate of the conductance-based model given synaptic conductance G . Then, with these approximations

$$Q_i(G_i, s_i) \equiv \frac{1}{T_i(G_i)} \int_0^{T_i(G_i)} R_i(\bar{V}_i(t; G_i), s_i) dt = \mu_i F_i(G_i)(1 - s_i).$$

Putting all these terms together, we can now write (11.10) as

$$\tau_i \frac{ds_i}{dt} = \mu_i F_i \left(\sum_j g_{ij} s_j \right) (1 - s_i) - s_i. \quad (11.11)$$

With the exception of the $(1 - s)$ term, (11.11) is the same as (11.7). This makes sense, for in both cases the timescale is the synaptic decay. Here, the variable $s_i(t)$

is the fraction of open synaptic channels, whereas in (11.7), $z_i(t)$ was called the synaptic drive.

If there are different types of synapses, say, excitatory and inhibitory, the synaptic current is

$$I_{\text{syn}} = G_{\text{ex}}(V - V_{\text{ex}}) + G_{\text{in}}(V - V_{\text{in}})$$

and the period, T , is a function of two variables, G_{ex} and G_{in} . This may seem to be a problem since it is not clear how T should depend on the two conductances; we would like it to be additive or some simple functional. If the conductance-based neuron is operating near a saddle-node bifurcation, then we know that

$$F(I_{\text{syn}}) \approx K \sqrt{I_{\text{syn}} - I^*},$$

where I^* is the critical current at which the saddle-node appears. Let V^* be the potential at the saddle-node. Then (at least near the saddle-node)

$$I_{\text{syn}} = G_{\text{ex}}(V^* - V_{\text{ex}}) + G_{\text{in}}(V^* - V_{\text{in}}),$$

so the firing rate is an *additive* function of the inhibitory and excitatory conductances.

The big advantage of deriving firing rate models from conductance-based models using averaging is that it is simple to incorporate slow currents such as spike-frequency adaptation and also short-term synaptic plasticity. We will introduce some of these models later and others will be provided as exercises.

11.1.3 Populations of Neurons

The derivations above were motivated by considering a single conductance-based neuron and then from this deriving a model for the firing rate. However, the main role of firing rate models is not to mimic single cells, but rather to examine large numbers of neurons in some “average” fashion. We can draw the analogy between intracellular and extracellular recordings in physiology. Intracellular recording enables one to track the membrane potential of a single neuron. Extracellular recordings, such as the local field potential, represent the responses of many neurons. Sharp electrodes (also extracellular) can resolve spikes of individual neurons. However, these spiking events are probabilistic, so experimentalists repeat the same stimulus over many trials to obtain a poststimulus time histogram. The poststimulus time histogram has units in spikes per unit time (often milliseconds), so it is effectively a rate. The intuition behind the poststimulus time histogram is that it is *assumed to be true* that if we were able to record simultaneously from 100 nearby locations, we would get the same result as from recording from one location 100 times. For this to be reasonable, we have to assume the neurons fire largely independently of each other. Once this assumption has been made, then we see that the firing rate of

the population is exactly the same as that of an individual neuron and the equations derived in the previous section can thus be interpreted as the population firing rate. However, in the derivation from averaging, the firing rate function is deterministic. Thus, if every cell were identical, then all cells would fire in perfect concert. Thus, we need to account for differences between neurons when we treat populations. One way to do this is to include the effects of noise. In Chap. 10, we saw that extrinsic noise can smooth the firing rate as a function of the input current. Thus, for example, we could replace a firing rate function $F = \sqrt{I}$ by a smoothed version of this which has a nonzero firing rate even for subthreshold inputs ($I < 0$). Another way to smooth the firing rate function is to assume heterogeneity. For example, suppose the firing rate is $F(I - I^*)$ for $I > I^*$ and zero otherwise as would be the case for a saddle-node on an invariant circle bifurcation. If the threshold values I^* are taken from some distribution, $Q(I)$, then we can write an “average” firing rate function

$$F_Q(I) = \int Q(I^*) F(I - I^*) dI^*. \quad (11.12)$$

We will leave it as an exercise for the reader to explore specific forms for the averaged firing rate.

Let us give a quick derivation of a typical firing rate or population model. Consider N identical neurons which receive (possibly random inputs) and between which there are recurrent connections. We will assume, for simplicity, all the neurons are excitatory (multiple types of neurons are easily generalizable) and the connections are all identical as are the inputs, the strengths of which are scaled by $1/N$. Each neuron undergoes dynamics

$$C \frac{dV_i}{dt} = -I_{\text{ion},i} + \bar{g}s_i(V_i - E_{\text{syn}}),$$

where $\bar{g}s_i$ is the conductance felt by each neuron. Since all inputs are excitatory and we assume the recurrent synapses have dynamics similar to the dynamics of the input synapses, we have

$$(Ls_i)(t) = J_T \sum_k \delta(t - t_k^T) + \sum_{j,k} J_{ij} \delta(t - t_k^j),$$

where L is a linear differential operator which governs the synapse. Alternatively, we could generalize this and write

$$s_i(t) = \int_{t_0}^t \alpha(t - t') \left(J_T \sum_k \delta(t' - t_k^T) + \sum_{j,k} J_{ij} \delta(t' - t_k^j) \right) dt'. \quad (11.13)$$

Here, t_k^T are the spike times from the inputs and t_k^j are the spike times of the j th cell in the network.

Key to the notion of population models is the fact that we assume the neurons are firing independently of each other within the network. Is this a good assumption? If there is a great deal of extrinsic independent noise, then it is likely that there are few correlations between neighboring neurons. A given population of interest often receives inputs from an earlier processing stage. (For example, layer 4 in the cortex receives inputs from the thalamus.) If the incoming action potentials come from randomly chosen subsets of the input layer, then we expect that spiking within the output layer would be uncorrelated. However, it turns out that this seemingly obvious assumption is not true. In recent experiments, Reyes [224] examined the following scenario. From N independent Poisson trains of spikes, a subset of $m \ll N$ was selected and injected into a neuron. The spike times of this neuron were recorded. A different set of m spikes was selected and the experiment was repeated until there were N new spike trains. These formed the basis for a repeat of the first set of experiments; N new spike trains were collected from these spike trains and so on. By layer 10 (ten iterations), there was considerable synchrony between the spike trains, so it was no longer reasonable to assume independence. The reason for this is that even though each trial shared only a few inputs, these inputs were enough to become amplified over multiple layers, leading to synchrony. Thus, the assumption of independence is at best an approximation and at worst is wrong. In the Reyes experiment, there was no recurrent coupling between cells within a layer. Recurrent connections can either increase or decrease the synchrony, depending on the nature of the coupling. Indeed, we saw in Chap. 8 that synaptic timescales, intrinsic currents, and the sign of the coupling can all have dramatic effects on the synchronization between coupled neurons. Since the only theory that has been done on the issue of asynchrony is for very simple models (leaky integrate and fire, quadratic integrate and fire), little more can be said about the assumption of independence for recurrently connected neurons.

There is one last issue that we want to discuss before moving on to applications of firing rate models. This is the issue of time constants. Figure 11.1 showed that a noisy integrate-and-fire model with high noise could follow a stimulus rather robustly if we added a small time constant to the dynamics. Specifically, let $I(t)$ be a time-varying input and let $F(I)$ be the noisy firing rate as a function of the constant input [cf. (11.19) or (11.20)]. Then the firing rate for a time-varying stimulus is

$$\tau_f \frac{df}{dt} = -f + F(I(t)).$$

The parameter τ_f is ad hoc and chosen to be small. It is not related to a membrane or synaptic time constants but depends on all of these as well as the characteristics of the noise [90]. With low noise, then the instantaneous firing rate can be very complicated. In Project 2, we suggest a way to look at these dynamics.

11.2 Population Density Methods

Gerstner and Kistler [99] provided a quick derivation for firing rate models of whole populations of neurons. Cai et al. [32] also derived such models. The equations which result are similar to those that we derived for globally coupled oscillators in Chap. 9. Basically, in all the derivations, the authors start with simple models for neurons such as the leaky integrate-and-fire model and from these derive an equation for the distribution of the potential. The flux of the potential across threshold is the firing rate of the cells. In general, the equations which result from these derivations are difficult to solve and often require special numerical methods. That said, they are still much faster to solve than the full network of spiking neurons. We will eschew a detailed study of the differences between the various derivations and sketch a fairly general equation based on the work of Gerstner and Kistler, which to us is the most transparent derivation. Thus, this section is closely related to Sect. 6.2 in [99]. We will approach it slightly more generally so that the resulting model is not tied to the specific form of the leaky integrate-and-fire neuron. The idea is to consider a one-dimensional neural model with some reset conditions.

We will write

$$\frac{dv_i}{dt} = f(v_i) + g(v_i)I_i(t),$$

where f is the spiking dynamics, g is the response to inputs, and I_i is all the synaptic currents coming into the cell. If the model requires reset, then we have the condition that when $v_i = \theta$, v_i is reset to $v_r < \theta$. For example, the leaky integrate-and-fire model has $f(v) = -v/\tau$ and $g(v) = R/\tau$, where R is the membrane resistance. We define

$$\int_u^{u+\Delta u} p(u, t) du = \lim_{N \rightarrow \infty} \left(\frac{\text{no. of cells with } u < v_i(t) \leq u + \Delta u}{N} \right).$$

The function $p(u, t)$ is the membrane potential density. We have the following normalization:

$$\int_{-\infty}^{\theta} p(u, t) du = 1.$$

This says that the probability is conserved. The firing rate or population activity, $A(t)$, is defined as the flux of cells across the threshold:

$$A(t) = J(\theta, t).$$

We will define this flux shortly. Neurons which cross the threshold reappear at the reset value, v_r , so this must be added to the evolution equations in the form of a source term $A(t)\delta(v - v_r)$. We remark that these discontinuities will disappear if we use a model such as the theta model instead of the leaky integrate-and-fire model since the “threshold” at π is just part of the full cycle. We assume all neurons receive the same external input, $I_{\text{ext}}(t)$, and that there is random background input.

Excitatory and inhibitory synaptic inputs are allowed as well. Synapses of type k occur at rate $v_k(t)$. These could be from external sources or from within the network if it is recurrent. To avoid adding an additional equation, we will assume the synaptic inputs are in the form of delta functions. Consider the single cell

$$\frac{dv}{dt} = f(v) + g(v)w\delta(t - t^*),$$

where t^* is the time of the input and w is the amplitude. If v is the value right before t^* , then $v + wg(v) \equiv G(v, w)$ is the value of the potential right after the input. For the derivation we provide below to be valid, we will assume the function $G(v, w)$ is invertible with respect to v . In Exercise 5, you are invited to show that for small w the inverse of G is

$$H(v, w) \equiv G^{-1}(v, w) = v - g(v)w + g'(v)g(v)w^2 + O(w^3). \quad (11.14)$$

We note that if $g(v)$ is constant, then the inverse is exact. For the theta model, $g(v) = 1 + \cos v$, where $v = \pi$ is the spike. Cai et al. [32] considered $g(v) = (v_s - v)$, where v_s is the synaptic reversal potential. An exact inverse can be found in this case.

With these asides out of the way, we continue the derivation. Each synapse of type k has an amplitude of w_k and occurs at rate $v_k(t)$. The dynamics satisfy

$$\begin{aligned} \frac{\partial p(v, t)}{\partial t} &= -\frac{\partial}{\partial v} ((f(v) + g(v)I_{\text{ext}}(t))p(v, t)) \\ &\quad + \sum_k v_k(t)[p(H(v, w_k), t)H_v(v, w_k) - p(v, t)] + A(t)\delta(v - v_r). \end{aligned} \quad (11.15)$$

The first term on the right-hand side is just the drift due to the uncoupled dynamics of each neuron. The last term is the reinjection of cells which cross through the threshold for spiking. The middle term is the gain of cells which were at $H(v, w_k)$ and jumped to v owing to the synaptic input as well as the loss of those which jump from v to $G(v, w_k)$. The strange term H_v multiplying the probability arises because we want to conserve total probability. Note that it is bounded because G is invertible and thus monotonic. We remark that $p(v, t) = 0$ for $v > \theta$. Right away, we can see that there is trouble lurking about if you are interested in simulation. Equation (11.15) is a functional partial differential equation because of the term H appearing as an argument of the density p . The firing rate is determined from the flux across the threshold. To determine this, we rewrite (11.15) as a continuity equation. Note that

$$v_k[p(H(v, w_k), t)H_v(v, w_k) - p(v, t)] = -\frac{\partial}{\partial v} v_k \int_{H(v, w_k)}^v p(u, t)du.$$

Thus, for any v , (11.15) can be written as

$$\frac{\partial p}{\partial t} = -\frac{\partial J}{\partial v} + A(t)\delta(v - v_r),$$

where

$$J(v, t) = [f(v) + g(v)I_{\text{ext}}(t)]p(v, t) + \sum_k \int_{H(v, w_k)}^v p(u, t) du.$$

Note that $J(v, t) = 0$ for $v > \theta$. If w_k is small, then we can expand this equation in a Taylor series to obtain the diffusion approximation. From (11.14),

$$\int_{H(v, w_k)}^v p(u, t) du \approx \int_{v-w_k}^{v+w_k} p(u, t) du.$$

Applying the fundamental theorem of calculus, this integral is approximately

$$w_k g(v) p(v, t) - \frac{1}{2} [w_k^2 g(v)^2 p(v, t)]_v.$$

With this approximation, the diffusive approximation for the population density equation is

$$\frac{\partial p(v, t)}{\partial t} = A(t)\delta(v - v_r) - \frac{\partial J_D(v, t)}{\partial v}, \quad (11.16)$$

where

$$\begin{aligned} J_D(v, t) &= \left[f(v) + g(v)(I_{\text{ext}}(t) + \sum_k w_k v_k(t)) \right] p(v, t) \\ &\quad - \frac{1}{2} \frac{\partial}{\partial v} \left(\sum_k v_k(t) w_k^2 g(v)^2 p(v, t) \right). \end{aligned} \quad (11.17)$$

Since these are just partial differential equations, they are amenable to numerical solution. If the inputs $v_k(t)$ are external, then we can define

$$\sigma^2(t) = \sum_k v_k(t) w_k^2$$

and

$$r(t) = I_{\text{ext}}(t) + \sum_k v_k(t) w_k.$$

If everything is stationary, then

$$J_D(v, t) = [f(v) + g(v)r]p(v, t) - \frac{\sigma^2}{2} \frac{\partial g^2(v) p(v, t)}{\partial v},$$

where r and σ^2 are constant. Solving the steady-state equations is identical to solving the single noisy integrate-and-fire model we studied in Chap. 10.

If we are using a discontinuous neural model, such as the leaky integrate-and-fire model, then we have $p(\theta, t) = 0$ and the firing rate, $A(t)$, is given by

$$A(t) = J_D(\theta, t) = -\frac{1}{2} \frac{\partial}{\partial v} \left(\sum_k v_k(t) w_k^2 g(v)^2 p(v, t) \right) \Big|_{v=\theta}.$$

However, if we instead use a continuous model on the circle such as the theta model, then the equations are considerably simpler. The term $A(t)\delta(v - v_r)$ no longer appears since the natural flow of the dynamics takes v through π and the domain of the model is $[0, 2\pi]$. In this case, we get

$$A(t) = J_D(\pi, t) = f(\pi)p(\pi, t)$$

since, for the theta model, $g(\pi) = 0$. For time-dependent inputs to the theta model (or other ring models), we can solve the full equations by writing $p(x, t)$ in a finite Fourier series and then writing differential equations for the coefficients. See Project 5 in Chap. 8.

Because the partial differential equations that result from these models can be quite difficult to solve (when the noise is low), we will generally use simple ordinary differential equation forms of population models.

11.3 The Wilson–Cowan Equations

One of the most influential models in the neural network literature is the one developed by Hugh Wilson and Jack Cowan in the early 1970s [287]. The original equations have the following form:

$$\begin{aligned} \tau_e \frac{dE}{dt} &= -E + (1 - r_e E) F_e (\alpha_{ee} E - \alpha_{ie} I + T_e(t)), \\ \tau_i \frac{dI}{dt} &= -I + (1 - r_i I) F_i (\alpha_{ei} E - \alpha_{ii} I + T_i(t)), \end{aligned} \quad (11.18)$$

where T_j is the input from the thalamus and r_e and r_i represent the refractory fraction of the neurons available to fire. The term $(1 - r_e E)$ is an approximation of

$$1 - \int_{t-r_e}^t E(s) ds,$$

which represents the fraction of neurons available to fire given they have an absolute refractory period of r_e . Curtu and Ermentrout [52] analyzed the behavior of the original integrodifferential equations for a single excitatory population. The extra premultiplicative factor $(1 - r_e E)$ does not make too much of a difference in the

analysis of the equations, so we will generally set $r_e = r_i = 0$. We first consider a single scalar model for one recurrent population of neurons. Then we turn to the pair and we will look at mutually excitatory, inhibitory, and mixed populations. The last case is the Wilson–Cowan equations.

A Note on the Gain Functions: What should one use for a gain function, $F(u)$? The traditional form for this is the logistic function, $F(u) = 1/(1 + \exp(-\beta(u - u_T)))$, which we have also encountered in our study of voltage-gated conductances. With the use of a logistic function, we interpret the function F as a probability of firing rather than an actual firing rate. A similar choice for F is $F(u) = 1 + \text{erf}(u)$, where $\text{erf}(u)$ is the error function (integral of a Gaussian). Pinto et al. [219] used this model to study the mean-field approximation for a model of cortex.

If we regard F as an actual firing rate of a single cell, then we could use an approximation for a neuron which undergoes a saddle–node bifurcation of periodic firing; namely,

$$F(u) = A \sqrt{\max(u - u_T)},$$

where u_T is the minimal current needed to induce firing. This gain function is continuous, but not differentiable and so will lead to problems when it comes time to numerically analyze models. In the presence of noise, we saw in Chap. 10 that the function is smoothed out. The following two variants of the above function are good approximations to the noisy firing rate:

$$F(u) = A \sqrt{(u - u_T)/(1 - \exp(-(u - u_T)/\beta))}, \quad (11.19)$$

$$F(u) = A \sqrt{\beta \log[1 + \exp((u - u_T)/\beta)]}. \quad (11.20)$$

Here, β is a measure of the “noise”; as $\beta \rightarrow 0$, both of these functions approach a pure square-root model. There are two more functions which are commonly encountered:

1. The step function, for which the neuron either is not firing at all or is firing at the maximal rate. This turns out to be the easiest to analyze and we will return to it when we get to networks.
2. The piecewise linear function

$$F(u) = \max(u - u_T, 0).$$

Linearity makes it possible to also analyze this function.

For the most part, there is little to recommend for the piecewise linear function other than it can be analyzed. The main objection we have for this function is that the firing rate can become infinite in recurrent networks. The step function and the logistic function, which both saturate, do not suffer from this problem. The square-root model is sublinear for large inputs, so it, too, does not “run away.”

11.3.1 Scalar Recurrent Model

As a warmup problem, we consider the simple recurrent neural network model:

$$\frac{du}{dt} = -u + F(\alpha u + \beta),$$

where β is the input and α is the strength of the connections. We leave as an exercise the analysis of this scalar model. We will assume $F(u) \geq 0$, $F'(u) > 0$, so the firing rate is a monotonic function. If the connections are inhibitory, $\alpha < 0$, then there is a unique asymptotically stable equilibrium point. If the connections are excitatory, then the situation is more interesting. In many firing rate functions, the derivative $F'(u)$ has a single maximum (that is, F has a single inflection point). If this is the case, then you should be able to show that there are at most three fixed points of the scalar neural network. In general, if the nonlinear gain function $F(u)$ has $2m + 1$ inflection points and aside from these $F''(u)$ is nonzero, then it is possible for the recurrent excitatory neural network to have $2m + 3$ fixed points of which $m + 1$ are stable.

To analyze bifurcations in a scalar firing rate model, we consider the current to be a parameter and ask when there is a saddle-node bifurcation. The condition is straightforward:

$$-1 + \alpha F'(\alpha u + \beta) = 0. \quad (11.21)$$

Since $F'(u)$ has a single maximum, if α is sufficiently large, then we can choose u so that (11.21) has two roots. Given such a u , say, \bar{u} , we plug this into the equilibrium condition and solve for β :

$$\bar{u} = F(\alpha \bar{u} + \beta).$$

Since F is invertible, we can solve for β . If α is chosen to be precisely the reciprocal of the maximum of F' , then the two saddle-node roots of (11.21) merge at a codimension-2 cusp point. For more complex functions F with multiple inflection points, it is possible to have even higher codimension bifurcations such as the “butterfly catastrophe” [49].

11.3.2 Two-Population Networks

Beer [11] provided a fairly exhaustive study of two-population networks. Here, we concentrate on a few interesting cases.

We dispense with networks for which the interactions between the cells are the same, excitatory or inhibitory. The following theorem allows us to concentrate on fixed points alone:

Theorem. Consider the planar system

$$\begin{aligned} x' &= f(x, y), \\ y' &= g(x, y), \end{aligned}$$

such that $f_y g_x > 0$ for all (x, y) . Then there are no limit cycles.

With some hints, we leave the proof of this to the reader. We note that this bears a resemblance to Bendixon's negative criterion, which states that if $f_x + g_y$ is of fixed sign in a region, R , then there will be no limit cycles contained wholly in R .

An obvious consequence of this is that for the two-population neural model

$$\begin{aligned}\tau_1 u'_1 &= -u_1 + F_1(w_{11}u_1 + w_{12}u_2), \\ \tau_2 u'_2 &= -u_2 + F_2(w_{21}u_1 + w_{22}u_2).\end{aligned}\quad (11.22)$$

If $F'_j(u) > 0$ and $w_{12}w_{21} > 0$, then there are no limit cycles and there are just fixed points; thus, the entire phase portrait can be worked out by looking at the intersections of the nullclines. We will suppose F_j are saturating nonlinearities with a maximum of 1 and a minimum of 0 without loss of generality. We also assume they are monotonic and have a single inflection point. Let G_j be the inverse of F_j . Let $G_j(x)$ have vertical asymptotes at $x = 0$ and $x = 1$ and be monotonically increasing. The u_1 nullcline has the form

$$u_2 = (G_1(u_1) - w_{11}u_1)/w_{12} \equiv H_1(u_1).$$

If $w_{11} < 0$, then H_1 is a monotonic function much like G_1 . However, if $w_{11} > 0$, then if the self-connection is large enough, the function H_1 has a cubic shape. Similar considerations hold for the u_2 -nullcline: if $w_{22} > 0$, it can have a “cubic” shape. Figure 11.2a and b shows several different possibilities. We can freely shift the u_1 -nullcline up and down by varying the inputs and the u_2 -nullcline left and right as well. Up to nine fixed points are possible or as few as one. Bifurcations are generically saddle–nodes (although below we consider an important symmetric situation which results in a pitchfork). Consider the case when both nullclines are “cubic.” Thus, we can define the outer and middle branches of the cubic. Any fixed point which occurs on the intersection of two outer branches is a stable node. Any fixed point occurring on two inner branches is an unstable node. The rest are saddle points. We leave this as an exercise for the interested reader. Saddle points are important

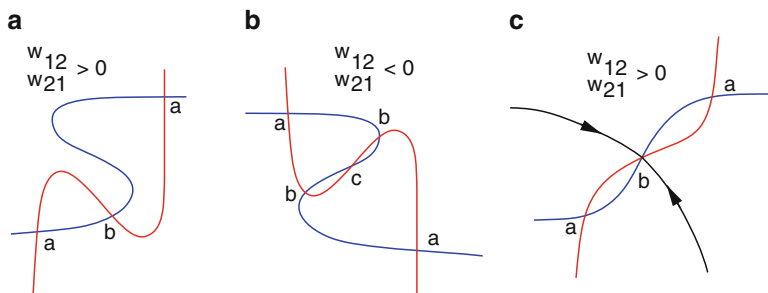


Fig. 11.2 Nullcline configurations for mutually excitatory–inhibitory networks: (a) mutual excitation, (b) mutual inhibition, (c) mutual excitation with weak self-connections

since their stable manifolds form separatrices dividing the plane into the domains of attraction for multiple stable fixed points. Figure 11.2c shows such an example. There are two states of this mutually excitatory network, one where both populations are firing at a low rate and one where both populations are firing at a high rate.

Before turning to the excitatory–inhibitory networks which show the richest dynamics, we consider an important example that will appear throughout this chapter and plays a fundamental role in later sections. Many cognitive and other processes require making a choice between two or more competing sensory inputs. Suppose you have a trusty musket and on your left is a charging lion and on your right a charging pug. To which do you attend? There, the choice is rather obvious. However, suppose instead of the lion, you are confronted by another pug. Then, most likely, unless you like dogs or are afraid of them, you will ignore them. Instead, if you are being charged by two lions, it is likely you will select one of them at random (if one is a bit closer, then there will be a strong bias) and stick with it.

Figure 11.3a shows a model for competition between two neural pools, labeled 1 and 2. Each receives an input and inhibits the other pool. Since this example illustrates many of the mathematical concepts we will encounter later, we will sketch

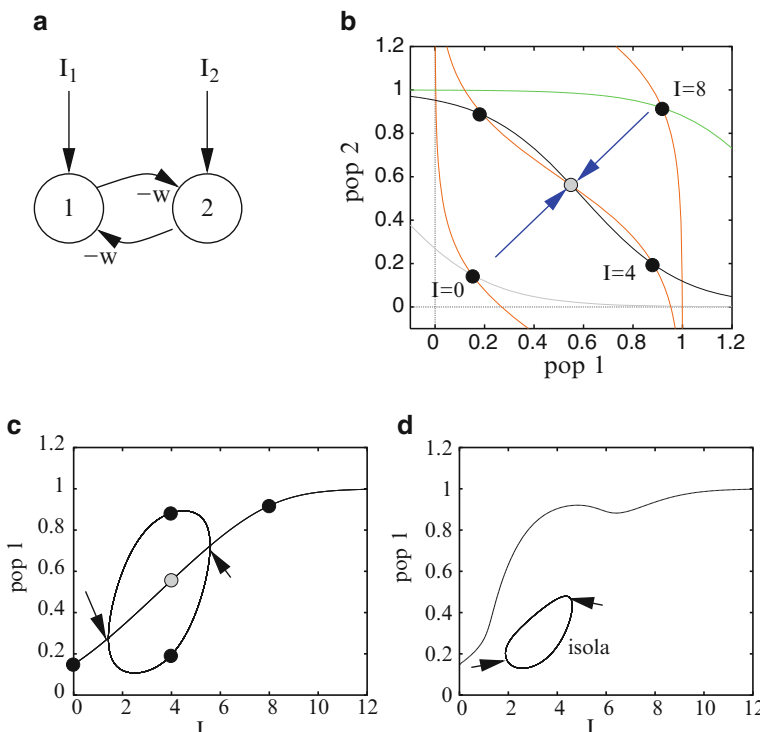


Fig. 11.3 The simplest model for competition between two populations: (a) the circuit, (b) nullclines for identical inputs at three different strengths, (c) bifurcation diagram when the inputs are identical, and (d) same as (c) but there is a small bias in favor of population 1

most of the details. We write $I_1 = I(1 + a)$ and $I_2 = I(1 - a)$, where a is an asymmetry parameter and I is the total input. When $a = 0$, the input is unbiased and does not favor either unit (think of the two charging pugs). The extreme asymmetry case (lion vs. pug) would have $a = \pm 1$. We will restrict our analysis to $a = 0$ and leave the $a \neq 0$ case for numerical analysis. The equations for this case are

$$\begin{aligned} u'_1 &= -u_1 + F(I - wu_2), \\ u'_2 &= -u_2 + F(I - wu_1). \end{aligned} \quad (11.23)$$

We will assume F is a monotonically increasing positive function with $F'(x) \rightarrow 0$ as $x \rightarrow \infty$ and we assume F is bounded as well. The weight $w \geq 0$. *Because of the symmetry*, one solution to this equation is homogeneous, $u_1 = u_2 = \bar{u}$ and

$$\bar{u} = F(I - w\bar{u}).$$

We leave as an exercise the proof that there is a unique homogeneous equilibrium point, that it is positive, and that it is a monotonically increasing function of I and monotonically decreasing function of w . Let $c = F'(I - w\bar{u}) > 0$ be the derivative of F at the equilibrium value. The linearization of (11.23) is

$$\begin{aligned} v'_1 &= -v_1 - cwv_2, \\ v'_2 &= -v_2 - cwv_1. \end{aligned}$$

This is a simple 2×2 matrix, A , but rather than immediately writing down the eigenvalues, we step aside for a moment to discuss matrices of a special form, so-called circulant matrices.

ASIDE.

Let a_0, \dots, a_{n-1} be fixed numbers (real or complex) and consider the matrix A formed as follows:

$$A = \begin{pmatrix} a_0 & a_1 & \dots & a_{n-1} \\ a_{n-1} & a_0 & \dots & a_{n-2} \\ \vdots & \vdots & \ddots & \vdots \\ a_1 & a_1 & \dots & a_0 \end{pmatrix}.$$

Such a matrix is called a *circulant* matrix and the eigenvectors and eigenvalues are easy to write down. Let $z_k = \exp(2\pi ik/n)$ for $k = 0, \dots, n - 1$. Let \mathbf{v}_k be the column vector whose j th entry is z_k^{j-1} . Then \mathbf{v}_k is an eigenvector for A and the eigenvalue is

$$\lambda_k = \sum_{j=0}^{n-1} a_j z_k^j.$$

For example, if $n = 2$, then the eigenvectors are $(1, 1)^T$ and $(1, -1)^T$, with eigenvalues $a_0 + a_1$ and $a_0 - a_1$, respectively.

END ASIDE

Since the linearization A is a circulant matrix, the eigenvectors and eigenvalues are $\{(1, 1), -1 - cw\}$ and $\{(1, -1), -1 + cw\}$. The first of these eigenvalues is always negative; thus, any *homogeneous* perturbation (along the eigenvector, $(1, 1)$) decays to zero. However, if w is large enough, then $-1 + cw$ can become positive for a range of inputs I , which means asymmetric perturbations [along the eigenvector $(1, -1)$] will grow in time. At a critical value of the input, say, I_0 , the asymmetric eigenvalue will be zero and we expect a bifurcation to occur. Since this problem has symmetry, the bifurcation at a zero eigenvalue will not be the generic fold, but rather a pitchfork bifurcation. This is typical in systems in which a circulant matrix is involved (that is, there is a symmetry.) Since the growth will be along the asymmetric eigenvector, the bifurcation solutions will have the form

$$(u_1, u_2) = (\bar{u} + r, \bar{u} - r),$$

where $|r|$ is the amplitude of the solution. r can be either positive or negative, corresponding to u_1 “winning” or u_2 “winning.” Figure 11.3b shows the phase plane and nullclines for (11.23), where $F(u) = 1/(1 + \exp(-(u - 1)))$, $w = 5$, and I is a parameter. At low inputs, both units fire equally at the same value. For intermediate values of the inputs, the homogeneous fixed point is unstable and there are two stable fixed points corresponding to one of the two units “winning.” The saddle point (gray circle) has a stable manifold (blue arrows) which separates the phase plane into two regions; those in the upper-left region tend to the u_2 -dominant fixed point and those in the lower-right region tend to the u_1 -dominant fixed point. Thus, without any input bias, the final outcome of the competition depends on any initial activity of the two units. At high inputs, once again, the homogeneous solution is the only solution and both units fire at high rates. Figure 11.3c shows the bifurcation diagram for the symmetric input case. For I between the two arrows, one or the other population of neurons is dominant. If there is a slight bias in the inputs, then as the input increases, the favored population will always win (Fig. 11.3d), but with a strong enough perturbation it is possible to switch to the less favored population for a limited range of inputs. This figure shows what is called an *isola*, a small island of solutions. The arrows denote a pair of fold bifurcations. As the bias disappears, the isola grows and merges with the main branch of solutions to give the diagram shown in Fig. 11.3c. As the bias a increases, the isola shrinks to a point and disappears.

This example illustrates the basic concept underlying *symmetry-breaking* instabilities and bifurcations and pattern formation. The symmetric solution loses stability owing to the negative interactions and results in new solutions which are no longer so symmetric.

11.3.3 Excitatory–Inhibitory Pairs

We turn our attention to two population models in which one population is excitatory and the other inhibitory:

$$\tau_1 u'_1 = -u_1 + F(w_{11}u_1 - w_{12}u_2 + I_1), \quad (11.24)$$

$$\tau_2 u'_2 = -u_2 + F(w_{21}u_1 - w_{22}u_2 + I_2). \quad (11.25)$$

u_1 (u_2) is the excitatory (inhibitory) population. It is possible to do a fairly comprehensive local bifurcation analysis of this system if the inputs are the main parameters. Borisyuk and Kirillov [18] provided such an analysis when $F(u) = 1/(1 + \exp(-u))$; Hoppensteadt and Izhikevich [128] performed a similar analysis. Choosing this F has the advantage of allowing us to note that

$$\frac{dF}{du} = F(1 - F).$$

Let

$$G(y) = \ln \frac{y}{1 - y}$$

be the inverse of $F(u)$. At an equilibrium point, we can solve for I_j :

$$I_j = G(u_j) - w_{j1}u_1 + w_{j2}u_2. \quad (11.26)$$

Let $B_j = w_{j1}u_1 - w_{j2}u_2 + I_j$ be the total input into each population. The linearization matrix has the form

$$A = \begin{pmatrix} -1 + w_{11}F'(B_1) & -w_{21}F'(B_1) \\ w_{12}F'(B_2)/\tau & (-1 - w_{22}F'(B_2))/\tau \end{pmatrix}.$$

We can rewrite $F'(B_j) = u_j(1 - u_j)$ using the fact that at equilibrium, $F(B_j) = u_j$ and that $F' = F(1 - F)$. There are two types of bifurcations of interest for this model: Hopf and saddle–node bifurcations. Saddle–nodes can be visualized by examining intersections of the nullclines. For the Wilson–Cowan network, there can be up to five different fixed points. Hopf bifurcations can be easily found using the identities above. Recall that a necessary condition for there to be imaginary eigenvalues for A is that the trace of A vanishes:

$$\text{Tr} \equiv -1 + w_{11}u_1(1 - u_1) - 1/\tau - w_{22}u_2(1 - u_2)/\tau = 0.$$

Clearly, since $0 < u_j < 1$, the trace is always negative unless $w_{11} > 4$, so there must be sufficient recurrent excitation. We solve the above equation for $u_1 = U_1^\pm(u_2)$; there are two roots since it is quadratic. Plugging u_1 as a function of u_2 into (11.26), we can parameterize I_1 and I_2 by the single number u_2 . Letting u_2 range between 0 and 1 for each of the two branches, $U_1^\pm(u_2)$, we get curves of Hopf points. This same method is not useful for the curve of folds (where the determinant vanishes) since the determinant is a quartic function of u_1 and u_2 and so not readily solvable.

The easiest way to compute bifurcation diagrams is through numerical methods. Figure 11.4 shows the behavior of this network for a fixed set of weights and time constants. As the excitatory input increases, the resting state increases until it loses stability at a Hopf bifurcation. Since increasing I_1 lifts the u_1 -nullcline up, we can

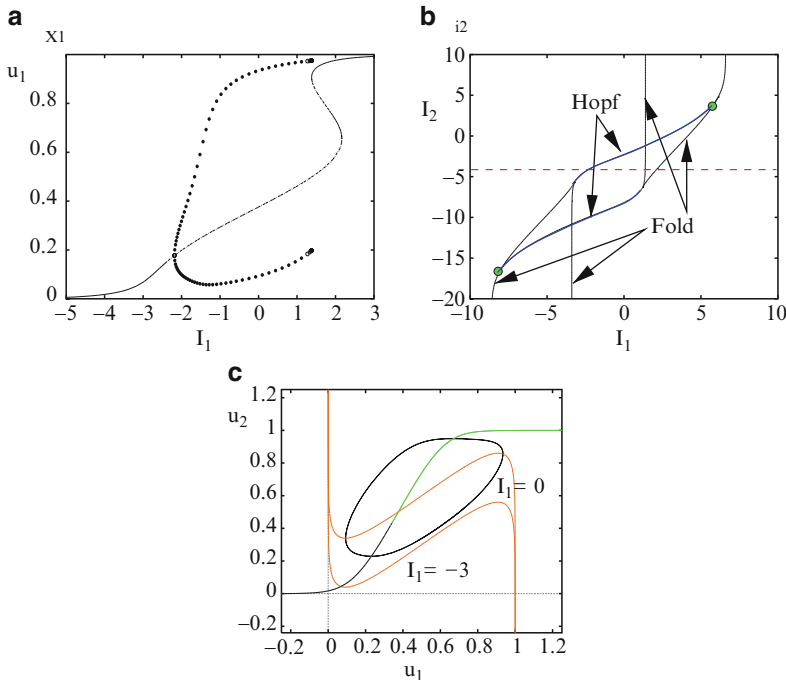


Fig. 11.4 Sample bifurcation diagram for an excitatory and inhibitory population. The parameters are $w_{11} = 12$, $w_{12} = 10$, $w_{21} = 16$, $w_{22} = 4$, and $\tau = 2$. (a) Behavior of u_1 as I_1 increases, $I_2 = -4$. (b) Two-parameter diagram as a function of the inputs, I_1 , I_2 . Green circles indicate Takens–Bogdanov points. (c) Phase plane for $I_2 = -4$, $I_1 = 0$

see the effect by looking at Fig. 11.4c. At negative inputs, the excitatory nullcline intersects at a point where the slope of the nullcline is negative and thus the fixed point is stable. As input increases, the intersection moves to the middle branch and for sufficient input becomes unstable. This leads to a Hopf bifurcation and limit cycle. Note that as the input increases, the excitatory nullcline gets closer and closer to the upper part of the inhibitory nullcline, so the period of the limit cycle increases. For sufficient input, there is an intersection of the nullclines at high values of excitation and inhibition.

11.3.3.1 Up–Down States

Experiments [247] in prefrontal cortical slices show that local recurrent networks of excitatory and inhibitory neurons are able to produce epochs of sustained firing both spontaneously and through stimulation. These two states (firing and quiescent) are observed in extracellular and intracellular recordings of neurons. Figure 11.5a shows an example of a recording from a cortical slice preparation with inhibition and

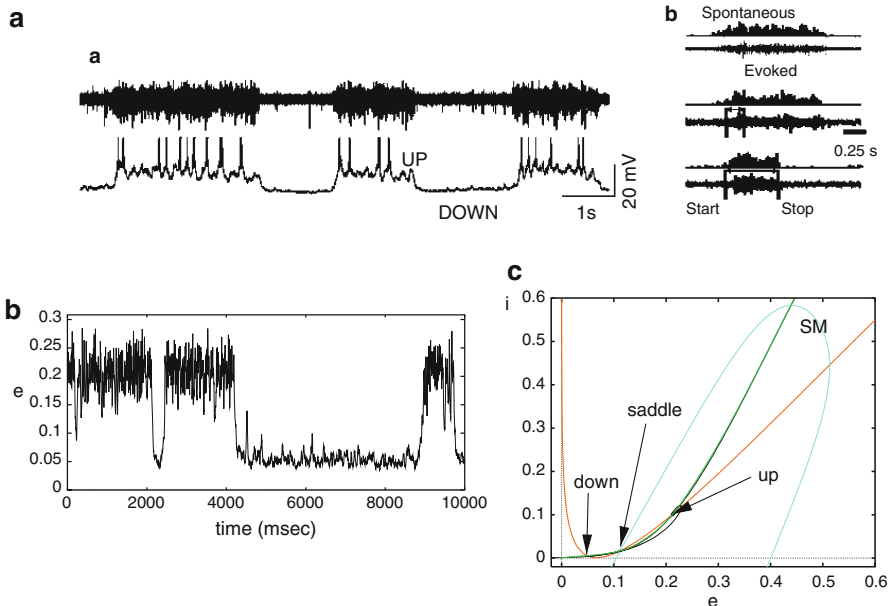


Fig. 11.5 Modeling up and down states in cortex. (a) Experimental data from Shu et al. [247] showing (a) extracellular (*upper curve*) and intracellular (*lower curve*) recordings over about 10 s, and (b) evoked states via external stimuli. (b) Simulation of up-down states in a noisy Wilson–Cowan model showing spontaneous switching. (c) Phase-plane explanation of the balanced bistable state. The parameters are $\tau_1 = 5$, $\tau_2 = 3$, $w_{11} = 16$, $w_{21} = 24$, $w_{12} = 10$, $w_{22} = 6$, $I_1 = -3.7$, and $I_2 = -6.7$. Colored noise is added to the inputs. *SM* stable manifold

excitation intact. The network undergoes bouts of sustained activity lasting up to 4 s followed by quiescence. Intracellular recordings of a pyramidal cell in the network show that during the bouts of activity, the membrane potential is depolarized (“up state”) compared with that during the quiescent period (“down state”). Stimuli allow one to switch from the down to the up state and vice versa. Importantly, depolarizing stimuli can switch the network from the up to the down state. Furthermore, when the network is in the down state, very strong stimuli cause a brief bout of activity immediately followed by a return to the down state. These two properties allow us to make some good guesses as to what the local dynamics must be. Figure 11.5b shows a simulation of (11.24) and (11.25) when there is colored noise added to the inputs. The noise is needed to effect spontaneous switching between states. Holcman and Tsodyks [125] proposed a model for this phenomenon using recurrent excitation and synaptic depression and no inhibition. Here, we suggest a very simple explanation for the properties of up and down states using a combination of excitation and inhibition. Figure 11.5c shows the phase plane in the absence of noise for the simulation shown in Fig. 11.5b. As one would expect, there are two stable fixed points corresponding to the up and down states in the network. Separating these states is a saddle point whose stable manifold acts as a threshold. In bistable systems such as

that shown in Fig. 11.3b, the stable manifold is such that only negative perturbations of state $(1,0)$ can take it to state $(0,1)$. Thus, in the up–down model, the stable manifold must be curved since strong depolarizing inputs can also cause a switch from up to down. Figure 11.5c shows that the stable manifold of the saddle point curves around, so if a stimulus takes the excitatory population beyond about 0.4, then there will be an immediate return to the down state. Modest stimuli will take the system from the down to the up state and vice versa. Other properties of the up–down states follow immediately. For example, a depolarizing shock in the up state can take the system to the down state. Shu et al. [247] observed that there is a delay before going to the down state which is dependent on the amplitude of the stimulus. As can be seen in the figure, a stimulus which is close to the stable manifold but slightly beyond the right-hand branch will take much longer to go to the down state than will a stronger stimulus. Strong stimuli during the down state can induce a brief period of activation followed by a return to the down state as well. Adding a small amount of noise to the model equations can cause spontaneous transitions between up and down states much as is seen in Fig. 11.5a. Because the upper state is closer to instability and has complex eigenvalues, this could explain the fact that the upper state is much noisier than the lower state. Indeed, Volgshev et al. [280] used the large standard deviation of the “up state” as a means of automatically determining when neurons are in the up state.

11.3.3.2 Whisker Barrels

Everyone who has ever had the pleasure of playing with a rat knows that the rat has several rows of whiskers which it uses to feel the world around it. Indeed, the usual white laboratory rats, which are popular with neuroscientists, are virtually blind and use their whiskers to navigate in their environment. Rats’ whiskers are almost as sensitive as human fingers in discriminating textures. Each whisker projects (through the brainstem and then the thalamus) to a well-defined aggregate of neurons in layer 4 of the cortex in the somatosensory area. These discrete areas are called barrels (see Fig. 11.6a, b) and consist of a mixture of excitatory (70%) and inhibitory (30%) neurons which are recurrently connected. Thus, the local circuitry of the barrel is a perfect example of an excitatory–inhibitory network. Inputs to the barrel come from other layers of cortex and from the thalamus. In this example, we restrict our attention to the local recurrent interactions and the thalamic inputs as shown in Fig. 11.6c. Dan Simons [218] and his collaborators have shown that the barrel circuit is exquisitely sensitive to the timing of the inputs from the thalamus. That is, the barrels respond strongly to rapidly increasing inputs and weakly to slow inputs. Figure 11.6d shows a typical example. The left-hand response is very large compared to the right-hand one and the corresponding thalamic inputs show a rapid onset and a more gradual onset. Pinto et al. [217] reduced a large-scale spiking model due to [168] to a network which should be familiar to the reader by now:

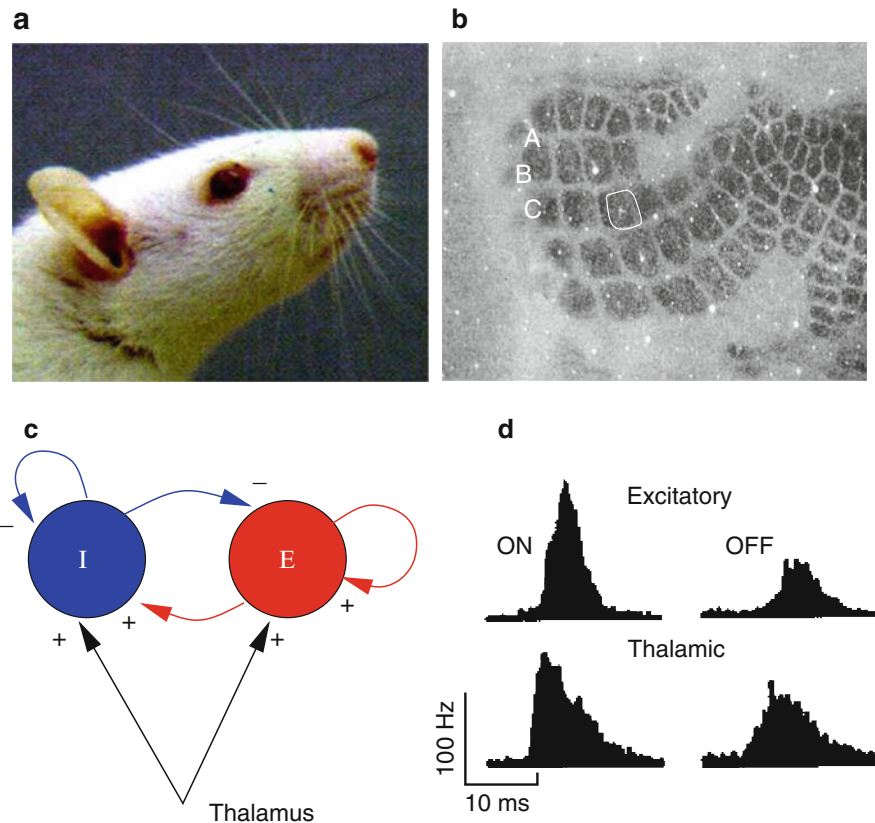


Fig. 11.6 Whisker barrel system of the rat. **(a)** Rat face. **(b)** Layer 4 cortex in the whisker area of the rat showing discrete barrels corresponding to individual whiskers. The C3 barrel is circled. **(c)** Local circuitry within a barrel showing a strongly recurrent excitatory and inhibitory network along with thalamic input. **(d)** Population response of excitatory cells to experimental movement of a whisker. Thalamic response is also shown

$$\begin{aligned}\tau_e \frac{du}{dt} &= -u + F_e(w_{ee}u - w_{ie}v + w_{te}T(t)), \\ \tau_i \frac{dv}{dt} &= -v + F_i(w_{ei}u - w_{ii}v + w_{ti}T(t)).\end{aligned}$$

The thalamic input, $T(t)$, consists of a constant background activity plus a triangle lasting 15 ms. The height of the triangle is constant, but the onset slope can be varied. The question is whether the network responds differently to different slopes of input. The input drives both the inhibition and the excitation, which is crucial. Intuitively, if the slope is too small, then the inhibition can catch up and suppress the excitation. This provides what experimentalists call a “window of opportunity” for the barrel cells to produce a response.

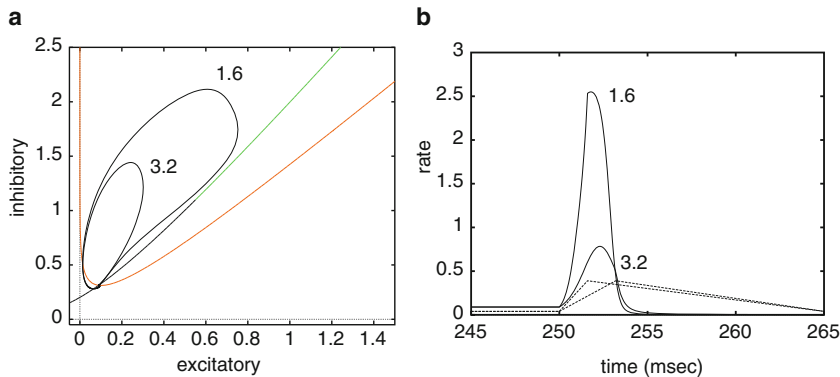


Fig. 11.7 Simulation of the barrel network. **(a)** Phase plane for the barrel network at rest with two responses superimposed corresponding to input peaks at 1.6 and 3.2 ms. **(b)** Firing rate of the excitatory population for the two inputs in (a) along with the inputs themselves (dashed lines). $F_e(x) = 5.12/(1 + \exp(-(x - 15)/4.16))$, $F_i(x) = 11.61/(1 + \exp(-(x - 15)/3.94))$, $w_{ee} = 42$, $w_{ie} = 24.6$, $w_{ei} = 42$, $w_{ii} = 18$, $\tau_e = 5$, $\tau_i = 15$, $w_{te} = 53.43$, $w_{ti} = 68.4$

Figure 11.7a shows that in the absence of inputs, the barrel network has a stable resting state. A perturbation in the excitatory direction past the right (middle) branch of the excitatory nullcline will be greatly amplified before returning to rest (an example of an excitable system). However, in the barrels, inputs come into both the excitatory and the inhibitory cells, so it is not clear what type of response occurs. Two responses are shown in the phase plane and in the accompanying plot in Fig. 11.7b corresponding to triangle inputs which have a width of 15 ms and identical amplitude. The only difference is that they reach the peak amplitude at 1.6 and 3.2 ms, respectively. By rising more quickly, the excitatory cells have a chance to react before the inhibition is engaged. The result is a significantly larger response for the fast-rising inputs compared with the slower-rising ones.

11.3.4 Generalizations of Firing Rate Models

Various bells and whistles can be added to firing rate models to match their architecture with a more biologically realistic one. For example, many cortical neurons are endowed with spike-frequency adaptation which occurs on a much slower timescale than inhibition and is dependent only on the local neuron rather than on other neurons. Another example is short-term synaptic plasticity such as the depression or facilitation of synapses. Adaptation can be introduced as an activity-dependent negative feedback. For example, a single excitatory population with adaptation can be written as

$$\tau \frac{du}{dt} = F(au - cz), \quad (11.27)$$

$$\tau_z \frac{dz}{dt} = R(u, z) - z,$$

where $R(u, z)$ is the activation of adaptation by excitation. There are several different possible models of this. The simplest is that $R(u, z) = u$. This linear adaptation allows for various interesting dynamics. If we recall that F is actually the firing rate, then a more realistic model would be $R(u, z) = \alpha F$ and if there was saturation (as would be the case if the adaptation were based on the conductance of some channel), then

$$R(u, z) = \alpha F(1 - z).$$

This ensures that the adaptation can never exceed 1. The reader should explore this model on her own choosing, for example, $\tau_z \gg \tau$.

Synaptic depression (or facilitation) is more interesting as its effects are multiplicative. Let us recall the model for short-term depression of a synapse (7.14) from Chap. 8 (8.13):

$$\frac{dd}{dt} = \frac{1 - d}{\tau_d} - \left(\sum_j \delta(t - t_j) \right) a_d d,$$

where t_j are the spike times of the presynaptic neuron, a_d is the degree of depression, and τ_d is the rate of recovery back to full strength. If we average this model over many repetitions of the same process, then the spike times are replaced by the firing rate of the presynaptic cell; thus, in terms of the firing rate, the model for synaptic depression is

$$\frac{dd}{dt} = \frac{1 - d}{\tau_d} - a_d F d.$$

We remark that several authors replace F in the above equation by u , which is often also called the firing rate. Depending on the interpretation and derivation of the firing rate, either can be correct. If the firing rate models are derived from synaptic dynamics, then F is the firing rate, but if we are approximating a noisy model neuron response to inputs, then u is the approximation of the firing rate.

We illustrate extended firing rate models by looking at two examples.

11.3.4.1 Binocular Rivalry

When a person looks at two different objects in each of his eyes, such as vertical stripes in the left and horizontal in the right, then he does not perceive a mixture, but rather he sees only one or the other. After a second or two the dominant percept disappears and the other object becomes dominant. Then there is another switch and so on. The switching is random, but there is a peak in the switching time histogram. There have been dozens of models for this kind of behavior, starting with that in [178] and recently reviewed and summarized in [246]. As there is a preferred interval for switching, many models assume the switching is governed by some sort of oscillator. We will start with the competitive model, (11.23), but add the additional adaptation

$$\begin{aligned} u'_1 &= -u_1 + F(I - wu_2 - gz_1), \\ z'_1 &= (u_1 - z_1)/\tau, \\ u'_2 &= -u_2 + F(I - wu_1 - gz_2), \\ z'_2 &= (u_2 - z_2)/\tau. \end{aligned} \tag{11.28}$$

Here, u_1 represents the right-eye pattern and u_2 represents the left-eye pattern. If the degree of adaptation, g , is small enough, then we expect the behavior should be like that of (11.23); for large enough w , as I increases there will be a pitchfork bifurcation from the homogeneous state to a state when one or the other “wins.” Because of symmetry, either left or right can win. As in the competitive model, there will be a homogeneous resting state, $(u_1, z_1, u_2, z_2) = (\bar{u}, \bar{u}, \bar{u}, \bar{u})$. The stability of this state is found by studying the eigenvalues of a 4×4 matrix:

$$M = \begin{pmatrix} -1 & -cg & -cw & 0 \\ 1/\tau & -1/\tau & 0 & 0 \\ -cw & 0 & -1 & -cg \\ 0 & 0 & 1/\tau & -1/\tau \end{pmatrix} = \begin{pmatrix} A & B \\ B & A \end{pmatrix},$$

where A and B are 2×2 matrices and $c = F'(I - (w + g)\bar{u})$. Just like the competition model, the structure of M has symmetry, so we can reduce the computation of the eigenvalues to those of two 2×2 matrices, $C^+ = A + B$ and $C^- = A - B$. These two matrices correspond to eigenvectors of the form (x, y, x, y) and $(x, y, -x, -y)$. The former represents symmetric perturbations of the steady state and the latter represents asymmetric ones. Consider, first, symmetric perturbations:

$$C^+ = \begin{pmatrix} -1 - cw & -cg \\ 1/\tau & -1/\tau \end{pmatrix}.$$

Since C^+ has a negative trace (recall that $F' > 0$, so c is positive and w and g are nonnegative) and a positive determinant, all eigenvalues of C^+ have negative real parts. The asymmetric perturbations are more interesting:

$$C^- = \begin{pmatrix} -1 + cw & -cg \\ 1/\tau & -1/\tau \end{pmatrix}.$$

If we treat c as a parameter (this is related to the intensity of the stimulus and, of course, the shape of F), then the determinant vanishes when $w > g$ and $c = c_0 \equiv 1/(w - g)$ and the trace vanishes when $c = c_H \equiv 1/w(1 + 1/\tau)$. Thus, if g is close to w and τ is large, the trace will become positive at smaller inputs than it takes to make the determinant negative. That is, there will be a Hopf bifurcation as the input increases when the time constant of adaptation is large and the strength of adaptation is also sufficiently large. In contrast, with weak or very fast adaptation, the network

will maintain its winner-take-all behavior. This simple mechanism provides a means by which there will be periodic switching of the dominance of the two percepts. Although this is a somewhat naive model, it is able to explain some aspects of rivalry and, in fact, make some testable predictions [289]. We will leave the full numerical exploration of this model as an exercise for the reader.

11.3.4.2 Synaptic Depression and Oscillations

Many neuronal networks show spontaneous oscillations during development; it is believed that the activity may help strengthen connections between neurons which are important later in the animal's life. A striking example of this is spontaneous episodes of activity in the spinal cord of embryonic chickens. Isolated spinal cord preparations produce bursts of activity every 2–30 min and within these bouts of activity produce 0.1–2-Hz oscillations. Tabak et al. [257] suggested the mechanism underlying this is recurrent excitatory connections coupled to synaptic depression with two different timescales. The slow depression accounts for the long interburst interval and the faster depression accounts for the oscillations within a burst. Here, we will be concerned only with the higher-frequency oscillations. Let $u(t)$ denote the firing rate of the population and $d(t)$ the efficacy of the synapse. Then the equations are

$$\begin{aligned} u' &= -u + f(wdu), \\ \tau d' &= 1 - d - \alpha ud. \end{aligned} \tag{11.29}$$

Our model for d is slightly different from the one in Tabak et al., but the nullclines are qualitatively similar. In the Tabak et al. paper, they used

$$f(x) = 1/(1 + \exp(-(x - \theta)/k)),$$

with $k = 0.05$ and $\theta = 0.18$. By choosing $w = 1$, $\alpha = 5$, and $\tau = 5$, we can obtain sustained oscillations. We leave a complete analysis of this to the reader. A related model and phenomenon is found in [273].

11.3.5 Beyond Mean Field

The Wilson–Cowan equations (11.18) and their kin are meant to represent the mean-field dynamics of networks of many thousands of individual neurons. Often, there is a desire to understand how higher-order statistical fluctuations influence the dynamics. For example in the work reported in [32], some of the dynamics arises from fluctuations rather than from the mean field. A number of authors, notably Buice and Cowan [29] and Bressloff [21], have attempted to include fluctuations

in the mean-field models by creating a stochastic system which has the desired mean-field dynamics. From this model stochastic system, they derived an expansion to include higher-order statistics such as the correlations between populations. As with any noisy nonlinear system, the difficulty arises when computing the moments (mean, variance, etc.) since, for example, the mean depends on second-order, third-order, etc. statistics. We saw in Chap. 10 that approximations could be made in the weak-noise limit for stochastic differential equations. We also saw that it is possible to approximate a Markov channel model by a simple Langevin equation via (10.38) and (10.39). We can combine these two approaches to arrive at a very simple derivation of the system size expansion given in [21]. For simplicity, we will consider just one population of neurons and leave the case of two populations and beyond as an exercise. Let there be N neurons whose state, x_i , can be either be silent (0) or active (1). Each neuron is coupled to all the other neurons in an identical fashion with weight w/N . The transition from active to silent occurs at a constant rate, α , and the transition from silent to active occurs at rate

$$\beta := f \left(\frac{1}{N} \sum_{i=1}^N x_i \right).$$

Thus, we can think of these “neurons” as two-state “channels.” The mean field for the firing neurons (open channels) is

$$\frac{dm}{dt} = -\alpha m + f(m).$$

This equation is like any other mean-field model that we have already considered in this chapter. To get higher-order statistics, we use the Langevin approximation from Chap. 10 [(10.38) and (10.39)]:

$$\frac{dm}{dt} = -\alpha m + f(m) + \left(\frac{\alpha + f(m)}{N} \right)^{\frac{1}{2}} dW(t). \quad (11.30)$$

We assume N is large and apply the Rodriguez–Tuckwell small-noise expansion to this Langevin equation and arrive at the pair of equations

$$\frac{dm}{dt} = -\alpha m + f(wm) + \frac{1}{2} w^2 f''(wm) C, \quad (11.31)$$

$$\frac{dc}{dt} = -2\alpha C + 2wf'(wm)C + \frac{1}{N}[\alpha m + f(wm)]. \quad (11.32)$$

This is equivalent to the system-size expansion in [21].

11.4 Some Methods for Delay Equations

Delay equations do not commonly appear in the curricula of most dynamics courses so we review a number of well-known results mostly from the classic text of Bellman and Cooke [13]. Here, we focus on systems with only one delay and only consider the linear stability theory around equilibria for delay equations. We start with a simple scalar example,

$$\frac{dx}{dt} = f(x(t), x(t - \tau)),$$

and let \bar{x} be a fixed point, $f(\bar{x}, \bar{x}) = 0$. The linearized equation has the form

$$\frac{dy}{dt} = ay(t) + by(t - \tau).$$

Here, a and b are the derivatives of f with respect to the first and second arguments evaluated at the fixed point. As with ordinary differential equations, we look for solutions of the form $y(t) = \exp(\lambda t)$, leading to

$$\lambda = a + b e^{-\lambda \tau}.$$

There are infinitely many roots of this equation; if any of them has a positive real part, then we say the fixed point is unstable. If all roots have negative real parts, then the fixed point is linearly asymptotically stable. For general systems with one delay, if the delay appears only in one variable, then the characteristic equation will take the form

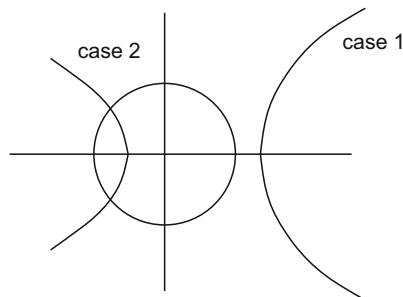
$$M(\lambda) \equiv P(\lambda) + Q(\lambda)e^{-\lambda \tau} = 0.$$

Thus, for many commonly encountered problems, the stability of fixed points relies on solving the polynomial-exponential characteristic equation. Before stating some theorems about stability, we consider a more general question: can a delay destabilize a fixed point which, in the absence of delay, was stable? Stability can be lost via a zero eigenvalue or through complex conjugate eigenvalues. In the former case, one must have $P(0) + Q(0) = 0$, which is clearly independent of the delay. Thus, we focus on determining if it is possible for a delay to cause $M(\lambda)$ to have imaginary eigenvalues. If this happens, then

$$\Gamma(\omega) \equiv \frac{P(i\omega)}{Q(i\omega)} = e^{-i\omega\tau}.$$

The left-hand side of this expression traces out a curve in the complex plane (see Fig. 11.8) and the right-hand side traces out the unit circle. Suppose $\Gamma(0)$ lies outside the unit circle and as ω varies it never crosses the circle (case 1). Then, there will be no delay τ which can change the stability, since the two curves never intersect. If $\Gamma(0)$ is inside the unit circle and never leaves it, then, again, no stability change can

Fig. 11.8 Stability plots for delay equations



occur. However, if $\Gamma(\omega)$ and the unit circle intersect (case 2), then we can always choose τ so that they intersect at the same value of ω . Thus, we can destabilize the equilibrium by changing the delay. Since the critical eigenvalue is $i\omega$, we expect to get a bifurcation to periodic orbits, although the proof of this is much more difficult than that of the ordinary differential equation case. As an example, consider the above scalar problem.

$$\Gamma(\omega) = \frac{i\omega - a}{b}.$$

This traces a vertical line in the complex plane. If $|a/b| < 1$, then $\Gamma(\omega)$ will cross the unit circle and there will be delay-induced instability. Note that for the fixed point to be stable in the absence of a delay, we have $a + b < 0$. For delay-induced instability, the magnitude of b must be larger than a , so these two inequalities imply that b is negative and sufficiently large. We have thus shown a classic result that delayed negative feedback can induce oscillations.

We conclude with a theorem from Bellman and Cooke giving general results for scalar delay equations. We rewrite the characteristic equation as

$$e^{\lambda\tau} P(\lambda) + Q(\lambda) = 0$$

and let $z = \lambda\tau$. Since $\tau > 0$, if z has a positive real part, then so does λ . The following theorem provides necessary and sufficient conditions for stability of the scalar delay equations, which can be written as $H(z) = \tau ae^z + b\tau - ze^z = 0$.

Theorem. (Bellman and Cooke [13], p. 444). *All roots of $pe^z + q - ze^z$ have negative real parts if and only if*

- (a) $p < 1$ and
- (b) $p < -q < \sqrt{r_1^2 + p^2}$,

where r_1 is a root of $r = p \tan r$ such that $0 < r < \pi$. If $p = 0$, we take $r_1 = \pi/2$.

Using this theorem as well as the easy graphical method above, you should have no trouble solving the problems for delay equations.

11.5 Exercises

1. Derive (11.3).
2. We can write (11.3) as

$$\Phi(t) = Ae^{-at} + Be^{-bt} + Ce^{-ct},$$

where a , b , and c are positive numbers. Show that A , B , and C are such that $\Phi(0) = \Phi'(0) = 0$. (Note the first part is by definition. Use the definition of $\Phi(t)$ to prove the second part.) Now that you have done that, suppose

$$x(t) = \int_0^t \Phi(t-s)y(s)ds.$$

What third-order differential equation does $x(t)$ satisfy?

3. Consider the scalar neural network

$$u'' + (a + b)u' + abu = F(u),$$

where a and b are positive. Prove there can be no limit cycle solutions. Suppose $F(0) = 0$. What types of bifurcations are possible?

4. In Exercise 2 you showed that the general $\Phi(t)$ leads to a third-order differential equation. Consider the scalar neural network

$$[(d/dt + a)(d/dt + b)(d/dt + c)]u = F(\alpha u).$$

Suppose $F' > 0$ and a , b , and c are positive. For $\alpha < 0$ show that there exists a unique fixed point and show that a Hopf bifurcation is possible as one of the parameters varies. (Hint: Think about the Routh–Hurwitz criteria.) If $\alpha > 0$, show there cannot be a Hopf bifurcation. We conjecture that there can be no periodic solutions if $\alpha > 0$, but have no proof.

5. Derive (11.14).
6. Consider the delayed excitatory network

$$u_t + u = F(\alpha u(t - \tau)),$$

where we have set $\tau_m = 1$ without loss of generality. Assume $F'(u) > 0$ and $\alpha > 0$. Prove there exists at least one fixed point and prove there can never be a Hopf bifurcation no matter what the delay.

7. Consider the delayed inhibitory network

$$u_t + u = F(-\alpha u(t - \tau)),$$

where $F(u) \geq 0$, $F'(u) > 0$, and $\alpha > 0$. Prove there is a unique fixed point (see the next exercise) and that there can be a Hopf bifurcation. Simulate this

network using $F(u) = 1/(1 + \exp(-(u + I)))$, where I is input to the network. Use $\alpha = 8$ and $I = 1$ and treat τ as a parameter.

8. Suppose $G(u) \geq 0$ and $G'(u) < 0$ for all u . Prove there is a unique root fixed point of

$$u_t + u = G(u)$$

and that it is asymptotically stable.

9. Consider (11.12). (a) If $F(I) = \sqrt{I - I^*}$ for $I > I^*$ and is zero otherwise, compute $F_Q(I)$ when I^* is taken from a uniform distribution $I_{\min} \leq I^* \leq I_{\max}$. (b) If $F(I - I^*) = \max(I - I^*, 0)$ and I^* is taken from a Gaussian distribution with mean \bar{I} and standard deviation σ , compute $F_Q(I)$. (c) Repeat (b) for $F(I - I^*) = 1$ for $I > I^*$ and zero otherwise.
10. Compute the firing rate function for the integrate-and-fire model based on the conductance of the synapse. That is, suppose V satisfies

$$C \frac{dV}{dt} = -g_L(V - E_L) - g(V - E_{\text{syn}}),$$

where $E_L < V_T < E_{\text{syn}}$ is the threshold to spiking and that upon spiking V is reset to $E_r < V_T$. Compute the firing rate as a function of the synaptic conductance, g . What happens as $g \rightarrow \infty$? Can you do some asymptotics of this to get a simple formula for large conductances? Plot the F - g curve for $C = 1$, $g_L = 0.05$, $E_L = -65$, $E_r = -70$, $E_T = -50$, and $E_{\text{syn}} = 0$.

11. Consider a recurrent scalar network with the threshold linear firing rate

$$\frac{du}{dt} = -u + [au - u_T]_+.$$

Show if $a > 1$, then sufficiently large initial conditions grow exponentially. For a fixed positive value of u_T and $a > 1$, find the critical value of u_0 such that if $u(0) > u_0$, $u(t)$ grows exponentially without bound.

12. Suppose $F(u) \geq 0$, $F'(u) > 0$, and $F''(u)$ has a single zero. Assume F and its derivatives are continuous on R . Prove there are at most three fixed points of the neural network equation $u' = -u + F(u)$.
13. *Hard.* Suppose $F'(u) \geq 0$ and $F(u)$ has k inflection points. Show that there can be up to $k + 2$ fixed points of $u = F(u)$. (Hint: Use the previous exercise and proceed inductively.)
14. Find the saddle-nodes and the cusp bifurcation for the scalar model with $F(u) = 1/(1 + \exp(-u))$. (Note that $F' = F(1 - F)$.)
15. Prove if $f_y g_x > 0$ in the plane, there are no limit cycles to $x' = f(x, y)$, $y' = g(x, y)$. Here, is a brief hint to get you started. For there to be a limit cycle, $x'(t)$ must change sign. Suppose, first, $f_y > 0$ and $g_x > 0$. (The other case follows similarly.) Suppose $x'(t)$ is positive and then vanishes at $t = t_1$. We cannot have $y'(t_1) = 0$ since then we would be at a fixed point. Thus, either $y'(t_1) > 0$ or $y'(t_1) < 0$. Suppose we have the first case. Then, $x''(t_1) =$

$f_y y'(t_1) > 0$, so for $t > t_1$ $x'(t) > 0$, so x' does not change sign. Continue to argue in this manner for all the other cases. You will need to use the fact that $g_y > 0$ for this.

16. Prove if $F'(u) > 0$, $F(u) > 0$, and $F(-\infty) = 0$, then there is a unique solution to

$$u = F(I - wu)$$

for all I and $w > 0$. Prove u is a monotonically increasing function of I and that $u > 0$. Prove u is a monotonically decreasing function of w .

17. In the mutual interaction model (11.23), what happens if the interaction is positive (that is, $-w$ is positive)? Show that asymmetric perturbations are always stable.
18. *Disinhibition and epilepsy.* One model for epilepsy is that it arises when the inhibition is partially blocked. Consider the Wilson–Cowan model:

$$\begin{aligned} u'_1 &= -u_1 + F(12u_1 - 12u_2 - 3), \\ 3u'_2 &= -u_3 + F(18u_1 - 4u_2 - 5). \end{aligned}$$

Show through simulation that there is a unique stable equilibrium. Now, suppose a drug such as bicuculline is applied which has the effect of reducing the inhibitory strength. Incorporate a parameter p in the model multiplying the strength of inhibition (do not forget the inhibitory–inhibitory connection) such that when $p = 1$ the inhibition is at full strength and when $p = 0$ it is completely blocked. Compute the bifurcation diagram for the model as p decreases and show that there can be a Hopf bifurcation and for severely reduced inhibition a completely active state.

19. Consider the binocular rivalry model described by (11.28) with $w = 5$, $g = 1$, $\tau = 20$, and $F(x) = 1/(1 + \exp(-(x - 2)))$. Compute the bifurcation diagram of this model as a function of the parameter I . Now set $g = 0.25$ and compute the diagram again. Note that there is no Hopf bifurcation and there is only the pitchfork. Set $g = 0.5$ and compute as much as you can of the bifurcation diagram. Find the curve of branch points and Hopf points as a function of the two parameters g and I .
20. Use the ideas of (11.30) to derive the five-dimensional equivalents of the Wilson–Cowan equations with means and second-order statistics.

11.6 Projects

1. Consider a pair of neurons (excitatory and inhibitory) coupled as

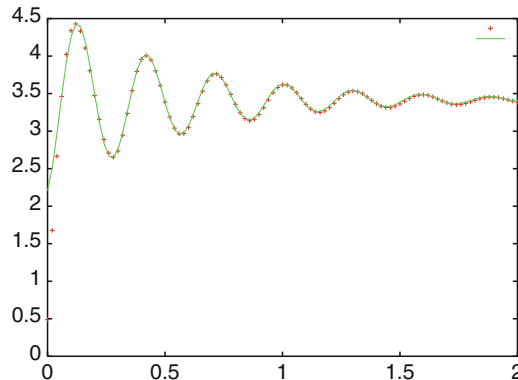
$$\begin{aligned} u_e(t) &= F_e(w_{ee}\Phi_{ee} * u_e(t) - w_{ei}\Phi_{ei}(t) * u_i(t)), \\ u_i(t) &= F_i(w_{ie}\Phi_{ie} * u_e(t) - w_{ii}\Phi_{ii}(t) * u_i(t)), \end{aligned}$$

where $\Phi_{jk}(t) = \exp(-t/\tau_{ij})/\tau_{ij}$ and $U(t) * V(t) = \int_0^t U(t-s)V(s)ds$. If τ_{ij} is independent of i or independent of j , then these can be converted to a pair of first-order differential equations. However, if all τ_{ij} are different, then these integral equations can be converted into four first-order differential equations. Write down these four equations. Is there any behavior (e.g., limit cycles) that occurs for the four-equation model which would not occur for the two-equation model when τ_{ij} is independent of i or j ? For example, can you prove a fixed point for the four-variable model is asymptotically stable if it is stable for the two-variable model?

2. Consider a noisy integrate-and-fire model, $V' = -V + I$, for which the current makes a step from I_1 to I_2 . Using the Fokker–Planck equation, examine the temporal dynamics on the firing rate for this transition in the low- and high-noise regimes ($\sigma = 0.4, 1$). In the low-noise case, the approach to the steady-state rate f is a damped oscillation. For different steps in the current, estimate both the damping and the oscillation rate. The figure below illustrates an example of a step and a fit to a damped oscillation. Use this to suggest a linear model for the firing rate:

$$u'' + 2au' + (a^2 + f^2)(u - f) = 0,$$

where f is the instantaneous firing rate. It may be necessary to also include the derivative of f in the calculation. You will find that for slowly varying stimuli, this does not do any better than the simple ad hoc first-order equation, $\tau_f u' = f - u$.



3. On the basis of the previous exercise, the temporal dynamics of the response of a neuron depends on the steady-state firing rate. Consider the same equation as in the previous exercise, but f now depends on u as

$$f = F(wu - u_{\text{th}}),$$

where F is a nonlinear function as explored in this chapter. Do the dynamics of the scalar recurrent network exhibit anything new? Show that even this second-order model cannot produce limit cycle oscillations.

4. Explore the effects of changing the temporal dynamics of inhibition on the barrel network. For example, quantify how that “window of opportunity” depends on the time constant of the inhibitory response.
5. Volgushev et al. [280] looked at the propagation of down to up and up to down transitions in cortex by recording over a 12-mm spatial area in the cat cortex during sleep. Adapt the population model for up–down states to an array of, say, nearest -neighbor coupled populations and add independent noise to each population sufficient to induce spontaneous switching. Do you see any evidence for propagation of states, e.g., if one group of cells switches from down to up, does this switch propagate across the network? Explore different levels of noise and different degrees of coupling. To couple two networks, you should look at a model of the form

$$\tau_e u'_j + u_j = F_e(w_{ee}\bar{u}_j - w_{ie}\bar{v}_j),$$

where

$$\bar{u}_j = (1 - c)u_j + (c/2)[u_{j+1} + u_{j-1}]$$

and $c \geq 0$ is the degree of coupling. Similar equations for the inhibitory population, v_j , should be written as well with a possibly different coupling strength. Use parameters as in Fig. 11.5.

Chapter 12

Spatially Distributed Networks

12.1 Introduction

In the previous chapters, we focused generally on single neurons, small populations of neurons, and the occasional array of neurons. With the advent of multielectrode recording, intrinsic imaging, calcium imaging, and even functional magnetic resonance imaging, it is becoming possible to explore spatiotemporal patterns of neural activity. This leads to a wealth of interesting fodder for the mathematically inclined and it is the goal of this chapter to provide some examples of this type of analysis. In Chap. 6, we looked at the propagation of action potentials down an axon; this is modeled as a partial differential equation. By looking for traveling waves, we were able to reduce the equations to a set of ordinary differential equations. When neurons are coupled together with chemical synapses, the natural form of coupling is not through partial derivatives with respect to space, but rather through nonlocal spatial interactions such as integral equations. In Sect. 8.4, we also looked at such models under the assumption that there is a single spike wave, much like an action potential. As with the partial differential equations, it is possible to look for specific forms of a solution (such as traveling waves or stationary patterns), but the resulting simplified equations do not reduce to ordinary differential equations. Thus, new techniques must be developed for solving these equations and (if desired) proving their existence and stability.

This chapter begins with a few words on unstructured networks such as random networks and Hopfield networks. Such networks are amenable to various types of analysis and are popular among theoretical physicists owing to their similarity to spin glasses. On the other hand, it is difficult to access their behavior experimentally since they do not produce coherent activity that is easily visualized, measured, or quantified.

We then turn to models for spatially structured networks where the connectivity between neurons depends on their distance from each other. We focus our attention on populations of firing rate models for which the theory is much more developed. We discuss an important existence theorem for traveling fronts and then use this to analyze traveling pulses in networks. We discuss the classic work of Shun-ichi Amari and the relationship between localized stationary activity and working

memory. The Amari model sets the stage for stability analysis when there are delays and other sorts of temporal dynamics. We then turn to so-called ring models for the emergence of tuning curves in the visual system. Finally, we conclude with a bifurcation theory analysis of pattern formation applied to visual hallucinations.

12.2 Unstructured Networks

In this section, we review some general results on “neural networks” or artificial networks. These include some feed-forward models such as those used in the so-called back propagation literature and Hopfield and related attractor networks. We also state and prove the very general Cohen–Grossberg theorem. Specifically, we are interested in networks of the two general forms:

$$\tau_j \frac{du_j}{dt} + u_j = F_j \left(\sum_k w_{jk} u_k \right), \quad (12.1)$$

$$\tau_j \frac{dV_j}{dt} + V_j = \sum_k w_{jk} F_k(V_k). \quad (12.2)$$

The first of these is the so-called ‘firing rate’ formulation, whereas the second is the voltage formulation. Cowan and Sharp [50] reviewed the history of neural networks and provided a guide to the main results.

12.2.1 McCulloch–Pitts

McCulloch–Pitts models [197] consist of “neurons” that have two states, 0 and 1. The next state of neuron i is determined by the quantity

$$\mu_i = H \left(\sum_j w_{ij} \mu_j - \theta_i \right),$$

where H is the step function and w_{ij} and θ_i are real numbers. It is important that $w_{ii} = 0$ for otherwise there may be ambiguity in the value of μ_i . Updating can be done either synchronously (like a discrete dynamical system) or it could be done asynchronously. In the latter case, an index, k , is randomly chosen and neuron k is assigned the value μ_k according to the above quantity. For this network to do something useful, it is necessary to make appropriate choices for the weights. There are a number of learning algorithms which set the weights in such a way as to produce a desired output for a given input. We point the reader to, for example, *Parallel Distributed Processes* [196] as a classic text on learning algorithms for feed-forward networks.

12.2.2 Hopfield's Model

As with the McCulloch–Pitts model, we will consider now a network of asynchronously updated two-state neurons due to Hopfield [126]. Much of which follows in this section is based on the classic text [121]. It is convenient to set their states to be -1 and 1 instead of 0 and 1 . Thus, consider a network of the form

$$S_i(t+1) = \operatorname{sgn} \left(\sum_j w_{ij} S_j - \theta_j \right),$$

where $\operatorname{sgn}(x)$ is $+1$ for nonnegative x and -1 for $x < 0$. If we update asynchronously, then w_{ii} should be zero. To see why, suppose we want to figure out S given

$$S = \operatorname{sgn}(S - 1/2).$$

Clearly, we could choose $S = 1$ or $S = -1$ and satisfy this constraint. Thus, we will assume $w_{ii} = 0$. Furthermore, for simplicity, let us assume $\theta_i = 0$. Hopfield noticed that if $w_{ij} = w_{ji}$, then this dynamical system has an energy function

$$U = -\frac{1}{2} \sum_{ij} w_{ij} S_i S_j.$$

To see that this is an energy function, let S'_k be a new state of the system. The change in energy, $U' - U$, is

$$-\frac{1}{2} (S'_k - S_k) \left(\sum_j S_j w_{kj} + \sum_i S_i w_{ik} \right).$$

However, since $w_{ij} = w_{ji}$, the energy difference is

$$\Delta U = -(S'_k - S_k) \sum_j w_{kj} S_j = -(S'_k - S_k) S'_k.$$

The last equality comes from the fact that $S'_k = \sum_j w_{kj} S_j$. If $S'_k = 1$, then $\Delta U \leq 0$ (with equality only if $S'_k = S_k$) and if $S'_k = -1$, then ΔU is also less than or equal to 0. Thus, the energy U will decrease until a minimum is reached and the dynamics always converges to an equilibrium. Note the importance of the symmetry assumption. If $w_{ij} \neq w_{ji}$, then there is no guarantee that there will be convergence to the steady state.

The ideas of Hopfield can be extended to continuous neural networks as long as there are symmetric connections between the weights. Hopfield proved such a result shortly after his discrete model came out [127]. At roughly the same time, Michael Cohen and Steve Grossberg [40] proved a more general result. We now discuss

the two different models. First consider the continuous network in the “voltage” formulation:

$$C_i \frac{dV_i}{dt} = \sum_j w_{ij} f_j(V_j) - V_i/R_i + I_i, \quad (12.3)$$

where the functions $f_j(V_j) \equiv U_j$ represent the firing rate at the axon hillock of a neuron with somatic potential V_j (see Chap. 11). We assume $w_{ij} = w_{ji}$ and that f_j is a monotonically increasing function. Hopfield formed the following function:

$$E = -\frac{1}{2} \sum_{i,j} w_{ij} U_i U_j + \sum_i \frac{1}{R_i} \int_0^{U_i} f_i^{-1}(U) dU + \sum_i I_i U_i. \quad (12.4)$$

In Exercise 2, you are asked to show the following:

$$\frac{dE}{dt} = - \sum_i \frac{dU_i}{dt} \left(\sum_j w_{ij} U_j - \frac{V_i}{R_i} + I_i \right). \quad (12.5)$$

Note that the term in parentheses is just the dynamics of the individual neuron, that is, $C_i dV_i/dt$. Thus,

$$\begin{aligned} \frac{dE}{dt} &= - \sum_i C_i \frac{dU_i}{dt} \frac{dV_i}{dt} \\ &= - \sum_i C_i (f_i^{-1})'(V_i) (\frac{dV_i}{dt})^2. \end{aligned}$$

As long as f_i are monotonically increasing, then $dE/dt \leq 0$. Thus, solutions to (12.3) will converge to an equilibrium point.

Cohen and Grossberg [40] studied the following class of models:

$$\frac{dx_i}{dt} = a_i(x_i) \left(b_i(x_i) - \sum_{j=1}^N c_{ij} d_j(x_j) \right), \quad (12.6)$$

where

1. $c_{ji} = c_{ij}$
2. $a_i(x_i) \geq 0$
3. $d'_i(x_i) \geq 0$

Suppose, for example, that $a_i = 1/\tau_i$, $b_i = I_i - x_i$, and $c_{ij} = -w_{ij}$. Then (12.6) becomes

$$\tau_i \frac{dx_i}{dt} = I_i - x_i + \sum_{j=1}^N w_{ij} d_j(x_j),$$

which is identical to (12.3) after multiplication by R_i . Thus, the Cohen–Grossberg equations cover the Hopfield model. Consider the following function:

$$E = - \sum_i \int_{d_i}^{x_i} b_i(y) d'_i(y) dy + \frac{1}{2} \sum_{j,k} c_{jk} d_j(x_j) d_k(x_k). \quad (12.7)$$

Then,

$$\frac{dE}{dt} = - \sum_i a_i(x_i) d'_i(x_i) \left(b_i(x_i) - \sum_j c_{ij} d_j(x_j) \right)^2. \quad (12.8)$$

From assumptions 2 and 3, this is nonpositive. This derivative vanishes only when $a_i = 0$, $d'_i = 0$, or the terms in the parentheses vanish. Thus, they proved that E is a Liapunov function and all solutions of (12.6) tend to equilibria.

12.2.3 Designing Memories

Given the unstructured networks we have described so far all converge to fixed points, we can ask some questions about how to design the weights of the network in such a way that they converge to a desired pattern. Many theoreticians (and experimentalists) think of Hopfield networks as a kind of association cortex where memories are stored in the weights and the resulting steady-state patterns are the activities which are retrieved from the memory. That is, a memory is a vector of activities or potentials which should be one of the stable fixed points of network (12.1) or (12.2). If the initial data are close to this vector, then the network dynamics should converge to it. Thus, the network is able to perform *pattern completion* from partial information. Suppose the network has “stored” two memories. Then we want it to be able to retrieve these when initial conditions or inputs are biased toward one or the other. Our question in this section is: How do we choose the weights to get a series of specified vectors as stable equilibria for the neural network?

Consider an N -neuron network which should converge to a single memory specified by a vector ξ . We take as the weight matrix the outer product

$$w_{ij} = \xi_i \xi_j / N.$$

Clearly, $w_{ij} = w_{ji}$. The dynamics satisfy

$$\frac{dV_i}{dt} = -V_i + \xi_i (1/N) \sum_{j=1}^N \xi_j F(V_j).$$

Let $U = (1/N) \sum_j \xi_j F(V_j)$. Then,

$$V'_i = -V_i + \xi_i U.$$

The steady state for this is just $V_i = U\xi_i$. Finally, we see that U must satisfy

$$U = (1/N) \sum_{j=1}^N \xi_j F(\xi_j U).$$

Thus, if this nonlinear equation for U has a solution, then there will be a steady state which is just proportional to the memory, ξ , where the constant of proportionality is U . Exercise 7 asks you to explore the emergence of a stable memory when $F(V) = \tanh(bV)$ and ξ is a vector of -1 and 1 .

Now consider the case of two memories, ξ^1 and ξ^2 , and weights,

$$w_{ij} = (\xi_i^1 \xi_j^1 + \xi_i^2 \xi_j^2)/N.$$

Let

$$U_m = (1/N) \sum_j \xi_j^m F(V_j)$$

for $m = 1, 2$. Notice that the vector V must satisfy

$$V' = -V + \xi^1 U_1 + \xi^2 U_2.$$

Suppose the memory vectors are linearly independent (This may be an unreasonable assumption, but it is one that simplifies the analysis. However, if the network is large and the memory vectors have only a few nonzero components, then the probability of overlap will be small). Any component of the vector V orthogonal to ξ^1 and ξ^2 decays exponentially, so all the dynamics is along the directions corresponding to ξ^1 and ξ^2 . Thus, we can write

$$V(t) = r_1(t)\xi^1 + r_2(t)\xi^2$$

and study the dynamics of $r_1(t)$ and $r_2(t)$. Clearly, we must have

$$\xi^1(r'_1 + r_1 - U_1) + \xi^2(r'_2 + r_2 - U_2) = 0.$$

Since ξ^1 and ξ^2 are linearly independent, we must have

$$r'_1 = -r_1 + (1/N) \sum_j \xi_j^1 F(r_1 \xi_j^1 + r_2 \xi_j^2), \quad (12.9)$$

$$r'_2 = -r_2 + (1/N) \sum_j \xi_j^2 F(r_1 \xi_j^1 + r_2 \xi_j^2).$$

With this choice of weights, we have reduced this N -dimensional dynamical system to a two-dimensional system. If there is a fixed point for this system where $r_1 \gg r_2$, then $V(t)$ will be dominated by ξ^1 , so the first memory is recalled. In the perfect

case, equilibria should be proportional to $(1, 0)$ or $(0, 1)$, implying that there is no mixing of the memories. Exercise 8 explores the dynamics of a two-memory model. In addition, we choose an odd function for F and take the ξ 's from the set $\{-1, 1\}$, then it is possible to show that the recall will be perfect if the two memories are orthogonal. In general, the “contamination” is related to the dot product of the two memories. If the elements in the memories are ± 1 , then $\langle \xi^m, \xi^m \rangle = N$. Consider $\langle \xi^1, \xi^2 \rangle$. If the two memories are independent and randomly chosen from ± 1 , then this dot product is just the result of a random walk of N steps of size ± 1 . The expected value is 0 and the standard deviation is \sqrt{N} . Thus, the relative contamination between the memories scales as $\sqrt{N}/N = 1/\sqrt{N}$. For large N , the contamination is small.

12.3 Waves

Waves of neural activity are commonly seen in a variety of experimental settings ranging from slices to in vivo recordings. Wu et al. [293] provided an extensive and recent review of their putative role in behavior and cognition. We saw in Chap. 8 that a brain slice preparation is able to generate traveling waves of activity in experiments as well as in networks of biophysically based and simple spiking neurons. In this section, we return to a model for neural waves in the context of firing rate models. The mathematical theory developed in Chap. 8 presumed that the wave of activity consisted of only a single-spike traveling wave. Section 9.10 showed how to construct complex wave-like activity in singularly perturbed systems. In Fig. 12.1,

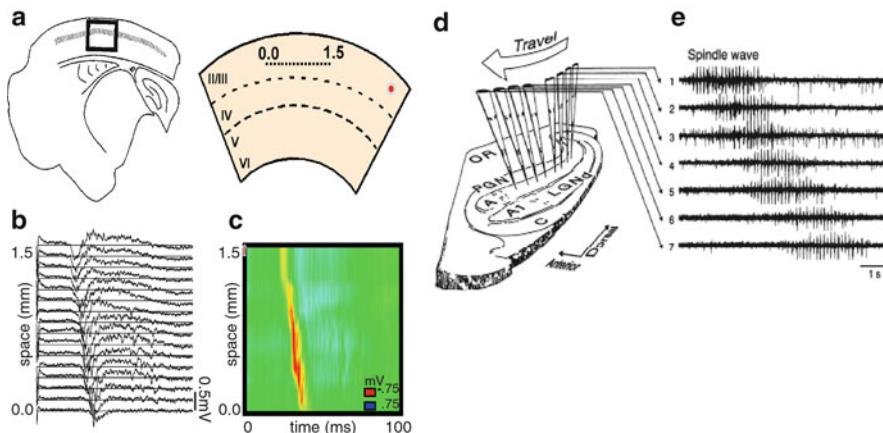


Fig. 12.1 Two examples of propagation in slices. (a–c) A cortical layer 2/3 slice. A multiple-electrode array is placed into the slice in which inhibition is blocked. Local shocking produces an event which propagates along the slice with a characteristic speed. (d, e) Similar experiment in the ferret thalamus showing the propagation of sleep spindles. (a–c From [219], (d) from [152])

we show two examples of traveling waves in brain slices. Figure 12.1e shows that typically there are multiple spikes per wave. Other preparations show similar behavior – the single-spike assumption was to make the mathematical analysis of the spiking models easier and to make a closed-form solution possible for the integrate-and-fire model. In many of the brain slice experiments, the inhibition is blocked, so all that remains is an excitatory population of cells. It should be clear to the reader that the existence of propagation of activity across a slice is not surprising given the large amount of recurrent excitation. Thus, a natural question is how does the activity terminate? In all experimental preparations, the propagating burst of activity stops after a few spikes. Pinto et al. [219] addressed this question experimentally and suggested several plausible mechanisms for the termination of spiking in recurrent networks when the inhibition is blocked. Before turning to the modeling of wave termination, we begin with a simulation and analysis of the propagation of a front of activity.

12.3.1 Wavefronts

In Chap. 8 we saw that it was possible to produce a single-spike traveling wave by “preventing” the cell from producing a spike after it has already spiked. In practice, this is very hard to do without a very strong negative feedback term which prevents the neuron from spiking again. Indeed, if we consider a biophysical model such as the Traub model with excitatory synapses which (1) are strong enough to excite neighboring cells and (2) have realistic decay times (2–3 ms), then the recurrent excitation causes the neurons to fire again after they have spiked owing to neighboring cells firing.

Consider, first, a network of biophysically based neurons with synaptic coupling. The synaptic current is given by

$$I_{\text{syn}}(x, t) = \left(g_{\text{syn}} \int_{-\infty}^{\infty} J(x - y) s(y, t) dt \right) (V(x, t) - V_{\text{syn}}). \quad (12.10)$$

$s(x, t)$ satisfies a differential equation of the form

$$\tau_{\text{syn}} \frac{\partial s}{\partial t} = -s + f(V)h(s). \quad (12.11)$$

The function $f(V)$ is zero unless the voltage is above some threshold (see Chap. 7). If the synapses are saturating, then $h(s) = 1 - s$ (e.g., for NMDA synapses, cf. Chap. 7), otherwise, $h(s) = 1$. Figure 12.2a shows the voltage for a synaptically connected network of 200 neurons which in the absence of synaptic inputs have a unique stable resting state. The synapses have a fast time constant, $\tau_{\text{syn}} = 3$ ms. Figure 12.2b shows the same simulation with a time constant of 10 ms. The synaptic gating variable, $s(x, t)$, for saturating synapses is shown. There appears to be

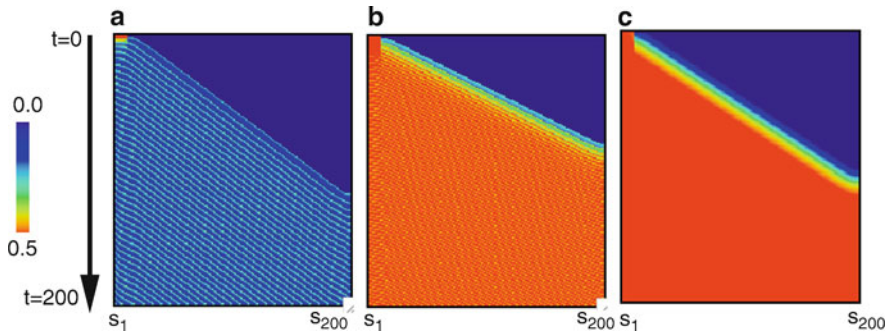


Fig. 12.2 Space–time plots for the simulation of a network of 200 neurons coupled with an exponentially decaying weight function. Time goes down and spatial position is across. Colored according to the synaptic gate, s . (a) Traub model with synaptic decay of 3 ms. (b) Traub model with synaptic decay of 10 ms. (c) Firing rate model derived from the biophysical model

a wavefront with a constant velocity initiated by the first spike (more evident in Fig. 12.2a), with a series of spikes occurring in the wake of the wave apparently persisting forever. This kind of persistence is not biologically realistic; activity eventually terminates and the slice returns to rest as is seen in Fig. 12.1. In the next section, we discuss various slow processes which act to terminate the wavefront activity. We remark that, on the slower timescale, $s(x, t)$ is nearly constant, whereas on the fast time scale, the large variations of s can clearly be seen. The slower timescale simulation suggests we should use the reduction techniques of Chap. 11 to consider a simpler scalar firing rate model.

Consider

$$\tau_{\text{syn}} \frac{\partial s(x, t)}{\partial t} = -s(x, t) + F \left[I_{\text{rev}} \int_{-\infty}^{\infty} J(x - y) s(y, t) dy \right] h(s(x, t)). \quad (12.12)$$

The function $F(I)$ is the average of $f(V(t))$ when the single neuron is provided with a constant current I . For example, at low currents, when the neuron is not firing, $F(I) = 0$. Figure 12.2c shows a simulation of (12.12) when F is chosen to match the Traub model simulated in Fig. 12.2a and b and $\tau_{\text{syn}} = 10$ ms. What is apparent in this picture is that there is a constant-velocity wavefront joining two stable resting states: the inactive state with no firing and $s = 0$ and a tonically firing state with $s > 0$. Without loss of generality, we can assume the integral of $J(x)$ is 1 and, since this is an excitatory network, we suppose $J(x) \geq 0$. As in the simulations, we suppose $J(x)$ is symmetric and monotonically decreasing for $x > 0$. Let

$$g(s) = -s + F(I_{\text{rev}}s)h(s).$$

We suppose $g(s)$ has three roots, $a < b < c$, with $g'(a) < 0$, $g'(c) < 0$, and $g'(b) > 0$. That is, $g(s)$ is our favorite function: cubic-shaped. (The reader may

ask if everything in biology is cubic shaped – the short answer is pretty much, yes!) The simulation of the scalar network suggests there is a traveling wave solution to (12.12) with constant velocity, v , that is a function, $s(x, t) = S(\xi)$, where $\xi = x - vt$, $S(-\infty) = c$, and $S(\infty) = a$. Since any wave is translation-invariant, we set the origin so that $S(0) = b$. With this assumption, we find that $S(\xi)$ must satisfy the integrodifferential equation

$$-\nu \tau_{\text{syn}} \frac{dS}{d\xi} = -S + h(S)F(I_{\text{rev}}J(\xi) * S(\xi)). \quad (12.13)$$

Here, $J(x) * s(x)$ is the spatial convolution over the real line of the function $J(x)$ with $s(x)$. Ermentrout and McLeod [74] proved the existence of such a traveling wave when $h(s) = 1$. Chen [37] generalized this proof to cover the case $h(s) = 1 - s$, a fact which was exploited in [38] for a related model. We briefly sketch the idea of the proof as the method has been used by many other authors to prove existence theorems for nonlocal equations.

Parameterize the functions $J(x)$ and $F(s)$ by functions $J_p(x)$ and $F_p(s)$ where $0 \leq p \leq 1$, $F_1(s) = F(s)$, and $J_1(x) = J(x)$. Each F_p has a corresponding g_p that has three roots with the properties above. Each $J_p(x)$ has the same properties as $J_1(x)$, that is, it is symmetric, integrates to 1, is nonnegative, and is monotonically decreasing for $x > 0$. Choose $J_0(x) = (1/2)\exp(-|x|)$ and $F_0(x)$ so that

$$\int_{a_0}^{c_0} g_0(u)du = 0.$$

Then, it turns out (see Exercise 9) that there is a function $S_0(\xi)$ satisfying (12.13) with $v = 0$ and satisfying the conditions at $\pm\infty$. Using this basic solution, Ermentrout and McLeod [74] applied the implicit function theorem by linearizing (12.13) about $S_0(\xi)$. They obtained a linear operator, L_0 , and proved that this operator has a simple zero eigenvalue (corresponding to the translation invariance of the traveling wave). Thus, for small values of the parameter p , they had to solve

$$L_0\phi(\xi) = r_0(\xi; v_0).$$

In general, since L has a one-dimensional nullspace, there is no hope for solving this. However, the velocity v is not likely to remain at 0 as the function F_p changes, so a judicious choice of v will put $r_0(\xi; v)$ in the range of L_0 so that it is possible to find a traveling wave solution for p sufficiently close to 0. The solution can be continued, say, up to $p = p^*$. If $p^* = 1$, then the desired wavefront has been found. Otherwise, the method is repeated using $S_{p^*}(\xi)$ as the base solution. There are, of course, many technical details, but this is the essence of the proof. If $F(I)$ in (12.12) is chosen to be the Heaviside step function, then an exact expression can be found for the traveling wave solution (this is Exercise 10). We remark that the velocity of the waves is an increasing function of the parameter I_{rev} if the function F is monotonically increasing.

12.3.2 Pulses

Wavefronts are almost never seen in experiments. Instead, pulses are commonly observed in which each neuron involved in the activity produces a number of spikes before returning to rest. Figure 12.3 shows an example of an experiment in which the slice is imaged simultaneously with an intracellular recording of a neuron. The neuron produces a finite number of spikes before returning to rest. What terminates the activity remains an active area of research [219]. In Fig. 12.3b–d, we depict a simulation of the same model which produced Fig. 12.2 but with the addition of a slow outward current which becomes active only when the neuron is firing. (It is much like the high-threshold adaptation described in 4.7.1). This slow current gradually builds up enough to terminate the firing and thus the wavefront is turned into a wave pulse. Here, eight spikes are produced in each neuron as the wave progresses

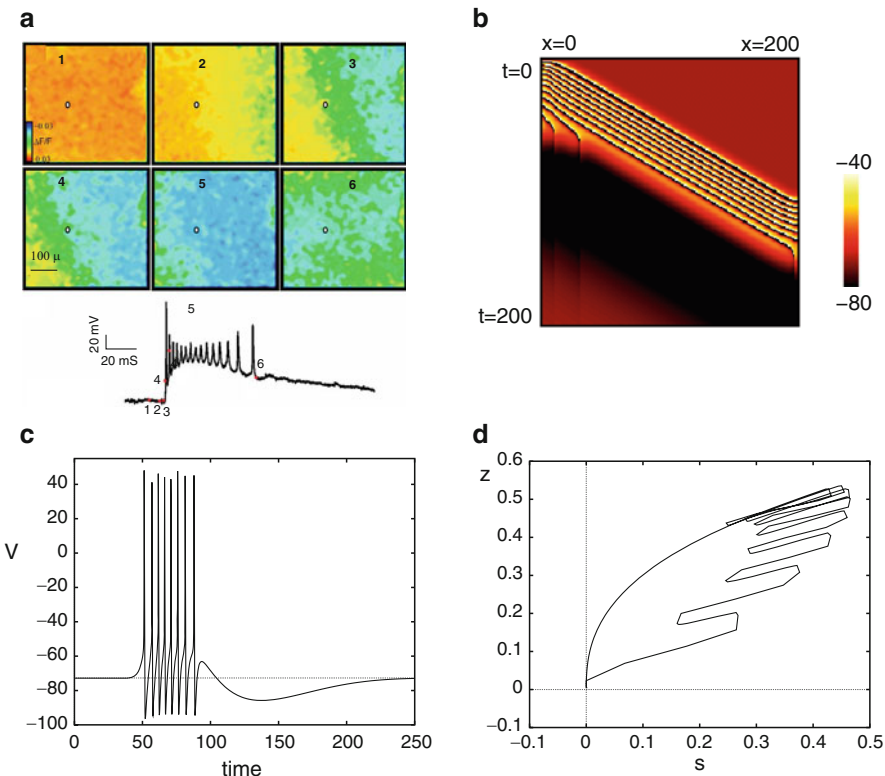


Fig. 12.3 Waves in a slice preparation and simulations. (a) Experimental waves show spatial distribution of potential in an evoked wave (from David Pinto). The *inset* shows the intracellular potential of a single cell as the wave passes through. (b) Simulation of the Traub model with an additional slow potassium current which terminates spikes. (c) Single cell potential as the wave passes through. (d) The synaptic gate against the slow potassium gate

through the one-dimensional domain. Figure 12.3d shows a phase plane of the synapse at a particular location versus the slow outward gate, z . Other mechanisms could also be responsible for the termination of the wave. For example, synaptic depression of the excitatory synapses [151] or inactivation of the sodium channels (depolarization block) [78]. Figure 12.3a is suggestive of either spike adaptation (the interspike interval increases over the duration of the pulse) or depolarization block (the size of the spikes is smallest at the peak of the underlying depolarization). In the subsequent analysis, we will assume the mechanism is adaptation – the slow accumulation of an outward current.

We now describe a simple model for the pulse and sketch how it can be analyzed [216]. We first note that the recovery process, the slow potassium current, is slow compared with the other currents in the model. In the absence of this recovery variable, the model produces a front. If we turn off the slow outward current, the velocity of the front is faster than with the adaptation, but only by about 25%. This suggests an approach like the one we used to construct action potentials in Chap. 6, where we exploited the timescale differences between the upstroke of the action potential and the recovery variables. We start with a general model for a network with slow processes. As in our firing rate model for the fronts, we start with two “slow” currents added to the voltage equations: synaptic excitation and adaptation. In reality, excitatory (AMPA) synapses are quite fast, but if the dominant excitatory current is due to NMDA receptors, then τ_{syn} can be large (cf. Chap. 7). With this conceit, the slow currents are

$$I_{\text{slow}}(x, t) = -g_{\text{syn}}s_{\text{total}}(x, t)(V_{\text{syn}} - V(x, t)) - g_z z(x, t)(V_z - V(x, t)),$$

where the synapses satisfy (12.11) and z satisfies

$$\tau_z \frac{dz}{dt} = -z + f_z(V)(1 - z).$$

Here, $f_z(V)$ is zero unless the neuron is depolarized sufficiently and τ_z is the time constant of the slow recovery process. As in the previous section, we will treat the synapses as if they were slow enough to be considered constant and, in addition, suppose the recovery variable, z , is also slow. The total current into a cell is approximated by

$$I_{\text{slow}}(x, t) \approx I_{\text{rev}}s_{\text{total}}(x, t) + I_z z(x, t),$$

where $I_{\text{rev}} = g_{\text{syn}}(V_{\text{rest}} - V_{\text{syn}}) > 0$ and $I_z = g_z(V_{\text{rest}} - V_z) < 0$. As in the previous section, s_{total} is the total input at x from other cells. We now have a simplified network model identical to (12.12) but with the additional slow recovery process:

$$\tau_{\text{syn}} \frac{\partial s(x, t)}{\partial t} = -s(x, t) + \alpha_s v(x, t)h(s(x, t)), \quad (12.14)$$

$$\tau_z \frac{\partial z(x, t)}{\partial t} = -z(x, t) + \alpha_z v(x, t)(1 - z), \quad (12.15)$$

$$v(x, t) = F[I_{\text{rev}}J(x) * s(x, t) + I_z z(x, t)]. \quad (12.16)$$

The firing rate of a neuron at position x is now a function of both the synaptic activity and the degree of spike adaptation. We define $\epsilon = \tau_{\text{syn}}/\tau_z \ll 1$ to be our small parameter and use singular perturbation to find a traveling pulse solution, $(s(x, t), z(x, t)) = (S(\xi), Z(\xi))$, where $\xi = x - ct$ and c is the velocity of the traveling wave. By rescaling time, we can set $\tau_{\text{syn}} = 1$. Letting U' denote the derivative of U with respect to the moving coordinate ξ , we must solve

$$\begin{aligned} -cS' &= -S + \alpha_s v(S, Z)(1 - S) \equiv f(S, Z), \\ -cZ' &= \epsilon[-Z + \alpha_z v(S, Z)(1 - Z)] \equiv g \epsilon g(S, Z) \\ v(S, Z) &= F(I_{\text{rev}} J(\xi) * S(\xi) + I_z Z(\xi)). \end{aligned} \quad (12.17)$$

That is, we need to find $(S(\xi), Z(\xi))$ such that as $\xi \rightarrow \pm\infty$, (S, Z) tend to the resting state of the network. Notice that $\xi < 0$ corresponds to events which occur *after* the pulse has passed through and $\xi > 0$ corresponds to those before the pulse.

Figure 12.4a shows the time course of the synaptic dynamics and the adaptation at a spatial location in the middle of the one-dimensional medium. Since this plot shows the *time course* and ξ , the moving coordinate is proportional to $-ct$, and

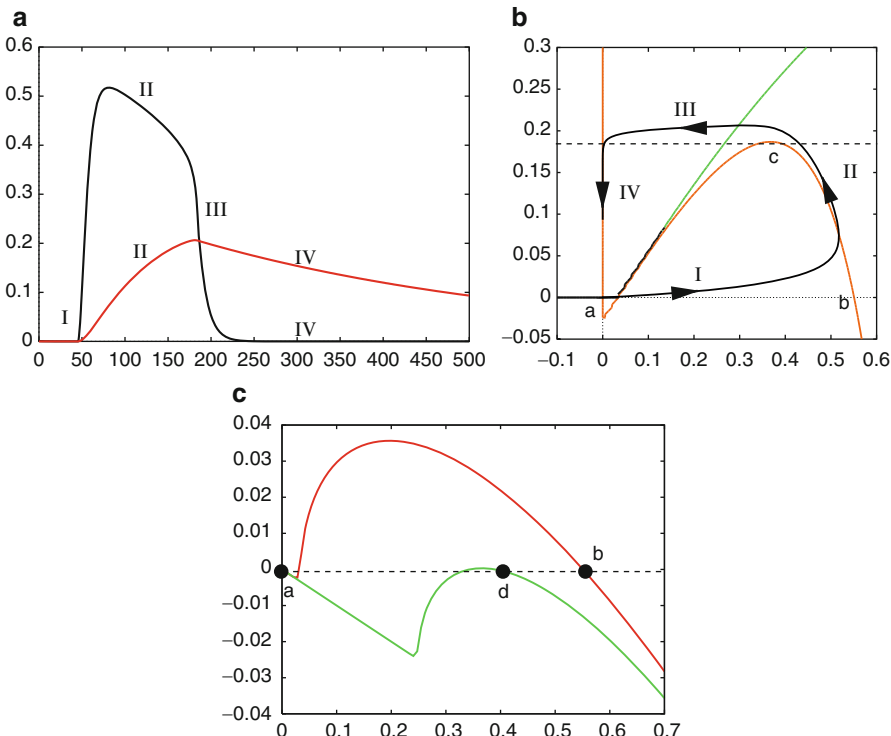


Fig. 12.4 Singular construction of the traveling pulse. (a) Simulation of the network in (12.14) and (12.15) showing four stages in the evolution of the wave. Synaptic activity and adaptation are shown. (b) Phase plane of (a). (c) “Fast” local dynamics showing bistability

the dependent variables (S, z) increase to the left and decrease to the right in this picture. The behavior can be broken into four segments: (1) starting from rest, there is an upstroke to the excited state; (2) there is a slow growth of the adaptation as the excited neuron fires; (3) adaptation reaches a value which forces the synaptic activity to make a fast downstroke to rest; and (4) a slow recovery of adaptation back to rest. Since we assume ϵ is small on the upstroke and downstroke of the pulse, we suppose the adaptation is constant. On the initial upstroke, since the neuron starts from rest, $Z = z_{\text{rest}}$, the resting state of the adaptation. In this example, z_{rest} is essentially 0. At $Z = z_{\text{rest}}$ the S -dynamics is bistable. Figure 12.4c shows that the fast dynamics, $F(S, Z)$ for $Z = z_{\text{rest}}$, has three zeros, with those labeled a and b corresponding to the stable roots. The Ermentrout–McLeod theory for the scalar neural network (or, more precisely, the generalization by Chen) implies that there is a unique traveling wavefront joining the two points a and b . This traveling front travels at velocity $c = c_0$, which is therefore the same velocity as that of the pulse. Once the up jump has been made, the slow dynamics take over and we introduce a new space–time scale: $\xi = \epsilon\eta$. In these coordinates, equations (12.17) become

$$\begin{aligned}\epsilon S_\eta &= f(S, Z), \\ Z_\eta &= g(S, Z),\end{aligned}$$

and the convolution $J(\xi) * S(\xi)$ becomes

$$R(\eta) = \frac{1}{\epsilon} \int_{-\infty}^{\infty} J[(\eta - \eta')/\epsilon] S(\eta') d\eta'.$$

We have assumed $J(x)$ is symmetric, peaked at $x = 0$, nonnegative, and has an integral of 1. Thus, the function $J(x/\epsilon)/\epsilon$ tends to a Dirac delta function as $\epsilon \rightarrow 0^+$. Our equations become

$$\begin{aligned}0 &= -S + \alpha_S F(I_{\text{rec}}S + I_z Z)(1 - S) \equiv f(S, Z), \\ Z_\eta &= -Z + \alpha_Z F(I_{\text{rec}}S + I_z Z)(1 - Z).\end{aligned}$$

Figure 12.4b shows the phase plane for the local S, Z excitable system. The S -nullcline is exactly the points where $f(S, Z) = 0$. For a range of Z (here, between 0.025 and 0.2) there are three roots, S to $f(S, Z) = 0$. Since the solution has jumped to region II, which corresponds to the large value of S , we take the largest root, call it $S^+(Z)$, and plug this into the Z equation:

$$-c_0 \frac{dZ}{d\eta} = g(S^+(Z), Z).$$

The phase plane in Fig. 12.4b shows that along this curve $dZ/d\eta > 0$, so $Z(\eta)$ grows for η decreasing. This is more easily seen in Fig. 12.4a in region II. At what point is a jump made back to the left? In the case of the singular action potential (Chap. 6), this jump occurred at a value of the recovery variable (the equivalent

of Z , here) such that the traveling “back” has the same velocity as the front. For the reaction–diffusion equations, such as the FitzHugh–Nagumo equations, the existence of this jump point is guaranteed. However, there is no guarantee that there will be a similar jump point for the integral equations. Indeed, it appears that for our present wave model, the jump occurs when the recovery Z reaches the maximum of the nullcline. Returning to the ξ coordinates, we have to solve

$$-cS' = f(S, Z_{\max}),$$

where $f(S, Z_{\max})$ has only two fixed points: one corresponding to the point a in Fig. 12.4c and the other, a degenerate point, corresponding to point d in Fig. 12.4c. The existence of a wavefront for this problem was proven by Diekmann [63], who showed that there are infinitely many velocities, c . Assuming that one of these wave velocities is the same as c_0 , we can complete the down jump. The last part of the construction is the return to rest along the left branch of the nullcline, $S^-(Z)$. For our problem, $v(S^-(Z), Z)$ so that Z satisfies

$$c_0 Z_\eta = Z,$$

so

$$Z = Z_{\max} e^{\epsilon \xi / c_0}.$$

Thus, as intuitively expected, once the wave passes by and there is no more neural firing, the recovery variable, Z , decays with a time course of $1/\epsilon$. An explicit solution for a simplified version of this model can be found when the firing rate is a step function. Exercise 12 takes you through the necessary steps.

12.4 Bumps

Working memory refers to the short-term memory that is used for simple tasks such as remembering a phone number as you walk from the phone directory to the telephone. It is memory which you do not need to permanently store and is analogous to the storage in the RAM of a computer during some task as opposed to keeping it on the disk drive. One of several theories of the mechanism for working memory is that it represents a transient but metastable state of neuronal activity. This theory is based on experiments first done over three decades ago by Joachim Fuster [94, 95]. In these experiments, neurons in the prefrontal cortex of a monkey were recorded while the monkey did a simple memory task. The monkey stared at a fixation point on a video monitor. A brief spot of light (*the stimulus*) appeared somewhere in the surrounding area of the screen. Typically, the stimulus lasted at most 1 s and was then turned off. The monkey waited (for a period called the *delay period*). A signal was given and the monkey had to make an eye movement (*saccade*) to the location of the stimulus. Thus, the monkey had to remember the position of the stimulus for up to several seconds after it had been turned off. What Fuster (and many subsequent

experimentalists) found is that certain neurons would begin to fire at a rate above the background level during the delay period and then return to background levels after the monkey had made the saccade. This increased firing, which occurs in a restricted spatial region, is believed to be the neuronal correlate of working memory. There are many other examples of this type of activity in the brain. Brody et al. [235] found neurons in the prefrontal cortex of monkey which fired at a rate that was proportional to the vibration frequency of a brief stimulus to the fingertip during the delay period. That is, not only did the neurons fire during the memory period, but they also coded for one of the stimulus properties.

Theoretically, these local regions of higher neural activity are regarded as stationary spatial patterns in a recurrent neural network often called “bumps” or “bump attractors.” Wilson and Cowan [288] were among the first to try to define working memory in terms of the behavior of firing rate models, mainly through simulations of a two-layer neural network. In an influential paper, Amari [3] created a simplified neural network that was analytically tractable and allowed him to find explicit solutions for stationary patterns as well as to ascertain their stability. Since these papers, there have been hundreds of theoretical and computational models for working memory [43, 46, 170, 172, 182, 283]. Most of the recent work has focused on obtaining local increases in firing in spiking models such as integrate-and-fire and more biophysical models. Although the details differ, the principle for the patterns remains identical to that of the Amari paper.

12.4.1 The Wilson–Cowan Equations

Unlike traveling waves, inhibition plays a major role in the production of spatially localized stationary patterns. We will start our analysis with the following “synaptically” based neural network equations:

$$\tau_e \frac{\partial u_e(x, t)}{\partial t} = -u_e(x, t) + F_e \left(\int_{\Omega} J_{ee}(x - y) u_e(y, t) - J_{ie}(x - y) u_i(y, t) dy + I_e(x, t) \right), \quad (12.18)$$

$$\tau_i \frac{\partial u_i(x, t)}{\partial t} = -u_i(x, t) + F_i \left(\int_{\Omega} J_{ei}(x - y) u_e(y, t) - J_{ii}(x - y) u_i(y, t) dy + I_i(x, t) \right). \quad (12.19)$$

This is a two-layer network model where $u_e(x, t)$ and $u_i(x, t)$ represent the synaptic activity of a population of excitatory and inhibitory neurons. The functions $J(x)$ represent the connectivity between the two populations; these are nonnegative functions which, in general, depend only on $|x - y|$, the distance between two areas. The domain of the model, Ω , can be one- or two-dimensional. Although not strictly true, we will call these the Wilson–Cowan equations. [The published Wilson–Cowan equations have a term $(1 - r_e u_e)$ multiplying S_e and a similar term

for u_i representing the refractory period.] If we pick $r_e = 1$ and $r_i = 1$, then the Wilson–Cowan equations are the same as those that we derived from averaging, e.g., (12.14) in this chapter.

The Wilson–Cowan equations can be transformed into equations similar to those analyzed by Amari in which the nonlinearities are placed inside the spatial integration. We, instead, first make some simple assumptions about the inhibition to reduce (12.18) and (12.19) to a scalar equation and then make the transformation. Suppose $\tau_i \ll \tau_e$, F_i is linear, and $J_{ii} = 0$. The most unreasonable of these assumptions is that inhibition is faster than excitation. (If we suppose the excitation is dominated by the slow NMDA types of receptors, then this is not a bad assumption.) The assumption regarding J_{ii} is unnecessary but simplifies the algebra. We set $\tau_i = 0$ and solve for $u_i(x, t)$:

$$u_i(x, t) = F_i \left(\int_{\Omega} J_{ei}(x - y) u_e(y, t) dy + I_i(x, t) \right).$$

The linearity assumption regarding F_i means we can absorb the slope and the intercept of F_i into J_{ei} and I_i . We substitute $u_i(x, t)$ into (12.18) to obtain

$$\tau_e \frac{\partial u_e(x, t)}{\partial t} = -u_e(x, t) + F_e \left(\int_{\Omega} J(x - y) u_e(y, t) dy + I(x, t) \right),$$

where

$$J(x) = J_{ee}(x) - \int_{\Omega} J_{ei}(x - y) J_{ie}(y) dy$$

and

$$I(x, t) = I_e(x, t) - \int_{\Omega} J_{ei}(x - y) I_i(y, t) dy.$$

The spatial kernel, $J(x)$, is a composite of the excitatory and the inhibitory interactions. If we suppose, for example, the connectivity is a Gaussian and that the space constant (the decay of connectivity) for excitatory (inhibitory) connections is σ_e (σ_i), then $J(x)$ comprises the difference of two Gaussians, one with a space constant of σ_e and the other with a space constant of $\sigma = \sqrt{\sigma_e^2 + \sigma_i^2}$. If recurrent excitation is strong, then $J(x)$ will be positive near $x = 0$ and negative for larger values of x since $\sigma > \sigma_e$. Figure 12.5a shows a typical shape for $J(x)$. Interactions like this are called “Mexican hat interactions” since, in two spatial dimensions, the shape of the interactions resembles a sombrero. We let $v(x, t) = J(x) * u_e(x, t) + I(x, t)$ so that $v(x, t)$ satisfies

$$\tau_e v_t + v = J(x) * F(v(x, t)) + \hat{I}(x, t), \quad (12.20)$$

where

$$\hat{I} = \tau I_t + I.$$

Equation (12.20) is the model that Amari analyzed in his famous 1977 paper when F is the Heaviside step function.

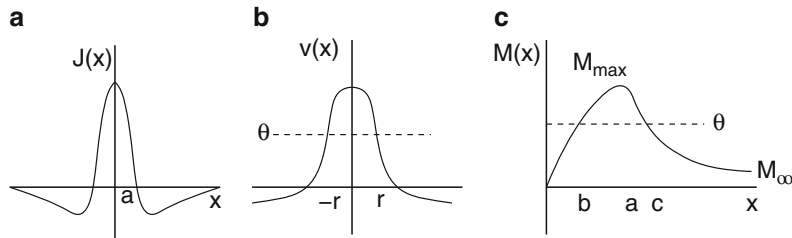


Fig. 12.5 (a) Composite interaction function; (b) “bump” solution; (c) integral of $J(x)$ showing allowable widths of the “bump”

We now suppose $F(v) = H(v - \theta)$ is a step function and that there is no input, $I = \hat{I} = 0$. The spatial domain, Ω , will be the real line. A “bump” is defined as a stationary solution to (12.20) which has a spatially localized peak (Fig. 12.5b). Such a solution satisfies

$$v(x) = \int_{-\infty}^{\infty} J(x - y)H(v(y) - \theta)dy.$$

We construct a bump solution by supposing that $v(x) > \theta$ on an interval $-r < x < r$ and $v(x) < \theta$ outside this interval (see Fig. 12.5b). From the definition of the step function,

$$v(x) = \int_{-r}^r J(x - y)dy = \int_{x-r}^{x+r} J(y)dy = M(x + r) - M(x - r),$$

where $M(x) = \int_0^x J(y)dy$. Continuity of $v(x)$ at $x = \pm r$ implies that $v(\pm r) = \theta$, so we must have

$$\theta = M(2r) = -M(-2r).$$

If $J(y)$ is not symmetric, then we cannot satisfy both of these equations simultaneously and there will be no stationary bump. Instead, there will be motion of the bump much like motion is induced with a transport term in diffusion equations (see Exercise 19). However, if $J(y)$ is an even function, then $M(y)$ is odd and both of these equations reduce to the same equation, $M(2r) = \theta$. We remind the reader that $2r$ is exactly the width of the bump. Figure 12.5c shows that for a Mexican hat interaction as in Fig. 12.5a, there will be one, two, or no roots of this equation. If the threshold, θ , is larger than the maximum of $M(x)$, M_{\max} , then there are no roots and no bumps. If the threshold lies between M_{∞} and M_{\max} , then there are two roots and two different bumps. If $M_{\infty} > 0$, then for $0 < \theta < M_{\infty}$, there is a single root. Laing et al. [172] considered more general functions $J(x)$ which have multiple “wiggles” so that $M(x)$ will oscillate; for example, $J(x) = \exp(-|x|) \cos \omega x$. This means there can many (even infinitely many) roots of $M(2r) = \theta$ and, thus, many different bump widths. We explore the stability below.

12.4.2 Stability

We derived the Amari model from the full Wilson–Cowan equations by assuming that the inhibition was fast so that we could eliminate its dynamics from the equations. Thus, to properly analyze the stability of the bump, we should consider the bump with respect to the full set of (12.18) and (12.19). We will leave a variant of this analysis as an exercise. For ease in exposition, we only examine stability with respect to (12.20). Thus, we suppose

$$v_0(x) = \int_{x-r}^{x+r} J(y) dy$$

is a stationary solution and that r satisfies, $M(2r) = \theta$. We formally linearize about this solution, resulting in the linear equation

$$\tau_e w_t + w = \int_{-\infty}^{\infty} J(x-y) \delta(v_0(y) - \theta) w(y, t) dy.$$

Here, we use the fact that the derivative of the step function is the delta function. Since the linear equation is autonomous, we can look for exponentially decaying solutions, $w(x, t) = \exp(\lambda t)\phi(x)$, where $\phi(x)$ obeys the eigenvalue problem

$$\tau_e \lambda \phi(x) = \int_{-\infty}^{\infty} J(x-y) \delta(v_0(y) - \theta) \phi(y) dy. \quad (12.21)$$

Recall that the delta function satisfies

$$\int_{-\infty}^{\infty} \delta(x-a) \phi(x) dx = \phi(a)$$

for any smooth functions $\phi(x)$. Furthermore, any standard text (see, e.g., [147]) provides the following identity. Suppose $f(0) = 0$ and $f'(0) \neq 0$. Then

$$\int_{-\infty}^{\infty} \delta(f(x)) \phi(x) dx = \frac{\phi(0)}{|f'(0)|}.$$

The argument inside the delta function in (12.21) vanishes at $y = \pm r$, so $\phi(x)$ must satisfy

$$(\tau_e \lambda + 1) \phi(x) = \frac{J(x+r)}{|v'_0(-r)|} \phi(-r) + \frac{J(x-r)}{|v'_0(r)|}.$$

Using the definition of $v_0(x)$, we can easily compute that

$$v'_0(x) = J(x+r) - J(x-r),$$

so $|v'_0(\pm r)| = |J(2r) - J(0)|$. For the case illustrated in Fig. 12.5, $|v'_0(\pm r)| = J(0) - J(2r)$. We let $z^\pm = \phi(\pm r)$ and setting $x = \pm r$ in the eigenvalue equation, we must satisfy

$$\begin{aligned} (\tau_e \lambda + 1)z^- &= \frac{J(0)}{J(0) - J(2r)}z^- + \frac{J(2r)}{J(0) - J(2r)}z^+ \\ (\tau_e \lambda + 1)z^+ &= \frac{J(2r)}{J(0) - J(2r)}z^- + \frac{J(0)}{J(0) - J(2r)}z^+. \end{aligned}$$

Miraculously, the stability reduces to the analysis of a 2×2 symmetric matrix. Because the matrix has the form

$$A = \begin{pmatrix} a & b \\ b & a \end{pmatrix},$$

the eigenvalues are $a + b$ and $a - b$, which for our system translates to $\lambda = 0$ and

$$\lambda = \frac{1}{\tau_e} - 1 + \frac{J(0) + J(2r)}{J(0) - J(2r)}.$$

This eigenvalue is negative if and only if $J(2r) < 0$. Consulting Fig. 12.5a and c, we see that only the wider bump (corresponding to $2r = c$) falls in the region where $J(2r) < 0$. In conclusion, if θ is between M_∞ and M_{\max} , then there are two bumps and the wider one is stable. The narrow bump is unstable and for $0 < \theta < M_\infty$, where there is only one bump; this bump is also unstable.

12.4.3 More General Stability

We transformed the Wilson–Cowan equations and assumed the inhibition was fast and linear to derive the Amari model (12.20). If we take a step back and consider the dynamics of inhibition, then we can obtain some more interesting types of instabilities. Consider the “dynamic” inhibition version of the Amari model where we set the time constant of excitation to 1 and let τ_i be a parameter:

$$u'_e(x, t) = -u_e(x, t) + J_{ee}(x) * H(u_e - \theta) - J_{ie}(x) * u_i, \quad (12.22)$$

$$\tau_i u'_i(x, t) = -u_i(x, t) + J_{ei}(x) * H(u_e - \theta). \quad (12.23)$$

Here, the inhibition is linear and there is no inhibitory–inhibitory interaction. A time-independent solution to these equations satisfies $u_e(x) = U(x)$, $u_i(x) = J_{ei}(x) * H(U(x) - \theta)$, where

$$U(x) = J(x) * H(U(x) - \theta),$$

with

$$J(x) = J_{ee}(x) - J_{ei}(x) * J_{ie}(x).$$

Thus, stationary solutions to (12.22) and (12.23) satisfy the same equations as the simple Amari model, so there will be a bump. We will leave the analysis of the stability of these bumps with respect to the full equations to the reader.

12.4.4 More General Firing Rates

The construction of solutions to the Amari model (12.20) depended on the fact that the nonlinearity was a Heaviside step function. Kishimoto and Amari [153] used a fixed-point theorem to prove there were bump solutions to a smooth version of the equations. Specifically, consider

$$u(x) = \int_{-\infty}^{\infty} J(x-y)F(u(y))dy. \quad (12.24)$$

Suppose $F(u) = 0$ for $u < \theta_1$, $F(u) = 1$ for $u > \theta_2$, and $F(u) = \phi(u)$ for $\theta_1 < u < \theta_2$ with $\phi(u)$ differentiable, monotonic, and satisfying $\phi(\theta_1) = 0$, $\phi(\theta_2) = 1$. This implies that $H(u - \theta_1) \geq F(0) \geq H(u - \theta_2)$. Assume there are bump solutions for $H(u - \theta_j)$, $j = 1, 2$. Then under fairly reasonable conditions placed on the interaction functions, $J(x)$, there is a bump solution for $F(u)$.

Laing and Troy [170, 171] took a somewhat different approach. They chose interaction functions, $J(x)$, whose Fourier transforms are rational functions:

$$\hat{J}(k) \equiv \int_{-\infty}^{\infty} J(x)e^{-ikx}dx = \frac{N(k^2)}{D(k^2)},$$

where N and D are polynomials. For example, the Fourier transform of

$$J(x) = (1 + b^2) \exp(-|x|)(b \cos(bx) + \sin(x))/(4b)$$

is

$$\hat{J}(k) = \frac{(b^2 + 1)^2}{(1 + (k - b)^2)(1 + (k + b)^2)}.$$

Formally, taking the Fourier transform of (12.24), we get

$$\hat{u}(k) = \hat{J}(k)F(\hat{u})(k).$$

Since \hat{J} is a rational function, we unwrap it, obtaining

$$D(k^2)\hat{u}(k) = N(k^2)F(\hat{u})(k).$$

Since N and D are polynomials in k (in fact, even polynomials), we inverse-transform the equation to obtain an ordinary differential equation:

$$L_1 u(x) = L_2 F(u(x)),$$

where L_j are linear differential operators. For example, in the example above, u formally satisfies

$$u_{xxxx} + 2(b^2 - 1)u_{xx} + (1 + b^2)^2 u = (1 + b^2)^2 F(u). \quad (12.25)$$

This is a fourth-order differential equation. Suppose $F(0) = 0$ and so $u = 0$ is a resting state. Then a bump would be a solution to this partial differential equation which is homoclinic to $u = 0$. Krisner [165] proved the existence of homoclinic solutions to (12.25) using a shooting argument (see Exercise 20).

12.4.5 Applications of Bumps

We have thus far regarded bumps as the neural equivalent of working memory and the delayed response task. But, stationary patterns of neural activity might be relevant in many other neural phenomena. Suppose the “ x ” variable in our model represents some other feature of the sensory world other than spatial location, for example, angular preference. Cortical neurons associated with many sensory and motor systems show increased firing rates when presented with oriented stimuli. For example, neurons in the visual cortex show specificity for line segments that depends on their angular orientation. Other visual cells are selective for the direction of motion of a moving grating. In rats, cells in layer 4 of the cortex respond to movements of the whiskers; some of these cells are very specific regarding the direction of movement. Figure 12.6 shows a cartoon of orientation preference for a visual cortical neuron and directional preference for a neuron in the rat somatosensory cortex.

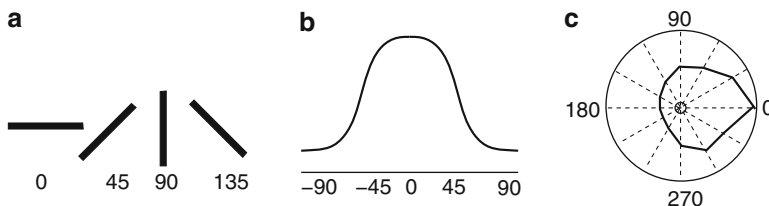


Fig. 12.6 Orientation tuning in neurons. (a) Sample stimuli to the visual system consist of oriented bars. (b) Firing rate of a visual cortex neuron as a function of the stimulus angle. (c) “Polar plot” for a neuron in the somatosensory cortex of the rat showing the strength (radial coordinates) of the response as a function of the direction of the whisker

A number of researchers believe that the strength of these preferences for certain features is a consequence of recurrent excitatory connections coupled with strong inhibition.

When an oriented stimulus is presented, neurons show a *tuning curve* in which their activity depends on the angle of the stimulus with a peak at the preferred angle. Figure 12.6b and c shows two different ways to plot the degree of tuning. An untuned neuron could produce a flat curve instead of the plot shown in Fig. 12.6b and a perfect circle instead of the plot shown in Fig. 12.6c. The mechanism for this tuning sensitivity is controversial, at least in the case of orientation tuning in the visual cortex. The arguments are as to whether this localized activity occurs owing to feed-forward wiring from the thalamus or because recurrent connections and lateral inhibition lead to the amplification, with the feed-forward behavior only biasing the results.

Consider a periodic version of the Amari model:

$$\frac{\partial u(\theta, t)}{\partial t} = -u(\theta, t) + \int_0^{2\pi} J(\theta - \theta') F(u(\theta', t)) + S(\theta, t). \quad (12.26)$$

Here, $u(\theta, t)$ represents the activity of neurons responding to a stimulus moving in the direction θ . (If we wish to consider orientated bars, then the domain is $[0, \pi]$, since there is no difference between a bar which is at 0° and one which is at 180° .) $S(\theta, t)$ is the possible bias due to the inputs to the cortex from the thalamus. In the pure feed-forward model, the recurrent connections $J * F$ play very little role and the activity is dominated by the inputs, S . In the recurrent model, S is small and broadly tuned; the recurrent interactions amplify and sharpen the tuning. Both arguments have experimental evidence to back them up. The Amari-type analysis can be applied to the case where there is a step function nonlinearity with no inputs. A time-independent input, $S(\theta)$, makes the analysis more difficult, but it is quite “doable,” particularly if there is a single local peak. (See [3] for the analysis on the real line.)

For a general nonlinearity, we can exploit the fact that the domain is periodic and thus the function J is also periodic. Suppose, for example, $J(\theta) = A + B \cos \theta$. If $B > |A|$, then $J(\theta)$ has a Mexican-hat-like shape. By approximating $J(\theta)$ by only a few terms of its Fourier series (here only two), we can reduce the infinite-dimensional equation (12.26) to a finite-dimensional one, since

$$K(\theta, t) = \int_0^{2\pi} (A + B \cos(\theta - \theta')) F(u(\theta', t)) d\theta'$$

can be expressed as

$$K(\theta, t) = C_0(t) + \cos \theta C_1(t) + \sin \theta D_1(t),$$

where

$$\begin{aligned} C_0(t) &= A \int_0^{2\pi} F(u(\theta', t)) d\theta', \\ C_1(t) &= B \int_0^{2\pi} \cos(\theta') F(u(\theta', t)) d\theta', \\ D_1(t) &= B \int_0^{2\pi} \sin(\theta') F(u(\theta', t)) d\theta'. \end{aligned}$$

From this, (12.26) becomes

$$u_t = -u + C_0(t) + C_1(t) \cos \theta + D_1(t) \sin \theta.$$

Thus, only the constant and first Fourier modes of $u(x, t)$ are nontrivial; all other modes decay to zero. This allows one to write

$$u(x, t) = c_0(t) + c_1(t) \cos \theta + d_1(t) \sin \theta$$

and, finally, to write

$$\begin{aligned} c'_0 &= -c_0 + C_0, \\ c'_1 &= -c_1 + C_1, \\ d'_1 &= -d_1 + D_1. \end{aligned}$$

This is a *third-order ordinary differential equation*. Furthermore, $d_1 = 0$ is invariant (see Exercise 21) since we can always look for even solutions to this homogeneous translation-invariant set of equations. Thus, (12.26), with a simple choice for a kernel, reduces to a planar differential equation. Finally, if we include an inhomogeneity for the equations, $S(\theta, t)$, and write

$$S(\theta, t) = p_0(t) + p_1(t) \cos \theta + q_1(t) \sin \theta + \dots$$

then we replace the three autonomous ordinary differential equations by

$$\begin{aligned} c'_0 &= -c_0 + C_0 + p_0, \\ c'_1 &= -c_1 + C_1 + p_1, \\ d'_1 &= -d_1 + D_1 + q_1. \end{aligned} \tag{12.27}$$

In Exercise 21, you explore various aspects of this model using the computer.

As a final example of models using bumps, we consider Zhang's model [295] for head direction cells in the hippocampus. Head direction cells signal the head direction of moving animals regardless of the location of the animal in the environment. They have tuning curves very much like those in Fig. 12.6a. That is, they

show a strong preference for particular angles and are therefore often considered as exemplars of bump attractors. Thus, the head direction system is often modeled as a network of recurrently connected neurons and the peaked attractor represents the current angle of the animal's head. As the animal moves around in its environment, its head angle will change relative to its body angle, so we expect the peak of the neural representation to move as well. As you perhaps explored in the exercises on (12.27), it is possible to move a bump with external inputs, but the analytic solution to this problem is not generally possible. An alternative method of shifting the bump is to vary the connection weights by biasing them in one direction or the other. Specifically, Zhang supposed the bump satisfies the equation

$$\frac{\partial u(\theta, t)}{\partial t} = -u(\theta, t) + \int_0^{2\pi} J(\theta - \theta', t) F(u(\theta', t)) d\theta', \quad (12.28)$$

where the weights, $J(\theta, t)$, are not constant in time and, most importantly, not symmetric. The reader may recall that in the Amari model if the weights are not symmetric, then it is impossible to find a stationary bump solution and instead there is a moving solution. In Exercise 19, we created an asymmetric weight matrix by shifting a symmetric matrix. Zhang found a much easier way to make the weights time-dependent and asymmetric. He supposed

$$J(\theta, t) = K(\theta) + \gamma(t) K'(\theta), \quad (12.29)$$

where $K(\theta)$ is a symmetric weight function that leads to stationary bumps and $\gamma(t)$ is an external signal which will serve to shift the bump. When $\gamma(t)$ is nonzero, the interaction, J , is not symmetric, so we expect movement of the bump. Suppose $U(\theta)$ is a stationary solution to

$$U(\theta) = \int_0^{2\pi} K(\theta - \theta') F(U(\theta')) d\theta'.$$

Consider the time-dependent problem (12.28) with $J(\theta, t)$ as in (12.29). Let

$$\phi(t) = \int_0^t \gamma(s) ds$$

be the integrated signal and let $u_0(\theta, t) = U(\theta + \phi(t))$. Then it is easy to see (Exercise 22) that u_0 exactly satisfies (12.28) with J as in (12.29). $\phi(t)$ is the *integrated* phase shift of the bump due to the inputs. Thus, a brief negative input will shift the bump counterclockwise, whereas a brief positive input will shift it clockwise. No matter how fast the inputs vary, the bump will follow them exactly (or at least there is a solution which can follow them – stability has not yet been determined). We remark that models like this are called neural integrators since they integrate the inputs and maintain them. Integrators are found in a variety of neural systems ranging from the oculomotor plant in the goldfish [200, 244] to the brain of an ant [206].

12.5 Spatial Patterns: Hallucinations

Press on your eyeballs with the palms of your hands. After a few seconds, the random light flashes that you see will become organized into faint flickering geometric patterns. Better yet, stare at a diffused strobe light flickering at roughly 20 Hz and your visual field will break up into similar geometric patterns. Even more intense patterns arise upon the ingestion of various hallucinogenic drugs such as lysergic acid diethylamide or mescaline. These simple geometric visual patterns (called *phosphenes*) are ubiquitous in their appearance and their forms seem to be independent of any cultural influences. Kluver [155] noted the relatively few such patterns that subjects report during the early stages of drug intoxication and classified the patterns into four types of *form constants*:

1. Grating, lattice, fretwork, filigree, honeycomb, or chessboard
2. Cobwebs
3. Funnel, tunnel, cone, or vessel
4. Spiral

Typically, during stroboscopic stimulation, human subjects report bull's-eyes (tunnel) and starbursts (funnel/cone), which are examples of the third type of form constant, whereas hallucinogens lead to more varied patterns such as honeycombs and spirals.

Patterns that appear on the retina are transformed in a direct topographic manner to patterns on the cortex, but the mapping is not a simple linear transformation. Think of the retina as having essentially polar coordinates centered at the fovea. If we let r denote the distance from the center of the fovea (in visual science, this is called the eccentricity) and θ denote the angle around the retina, the transformation to the cortex is well approximated by the formula [53]

$$(r, \theta) \rightarrow \lambda \left(\log(1 + r/r_0), -\frac{r\theta}{r + r_0} \right).$$

The parameter λ is called the magnification factor and r_0 is an empirically defined constant. For $r \gg r_0$, this mapping is just the complex logarithm, $z = r \exp(i\theta) \rightarrow (\log r, \theta)$, with the angle reversed. Figure 12.7 shows that the form constants are transformed into even simpler forms under this mapping. Spirals, for example, become diagonal lines away from the fovea.

Ermentrout and Cowan suggested the spatially periodic patterns arose spontaneously in the visual cortex owing to an instability of the resting activity. For example, the hallucinogens are known to enhance cortical excitability by causing the release of glutamate via activation of specific serotonin receptors [173]. Flickering light could interact resonantly with intrinsic oscillatory activity in the cortex to increase overall excitability. Thus, we will explore a simple spatial neural network as some parameter is varied leading to a loss of stability of a uniform state. To simplify the mathematical analysis, we will regard the visual cortex as a two-dimensional sheet with periodic boundary conditions (to avoid boundary effects and to make it possible to compute eigenfunctions as well as to avoid mathematical difficulties

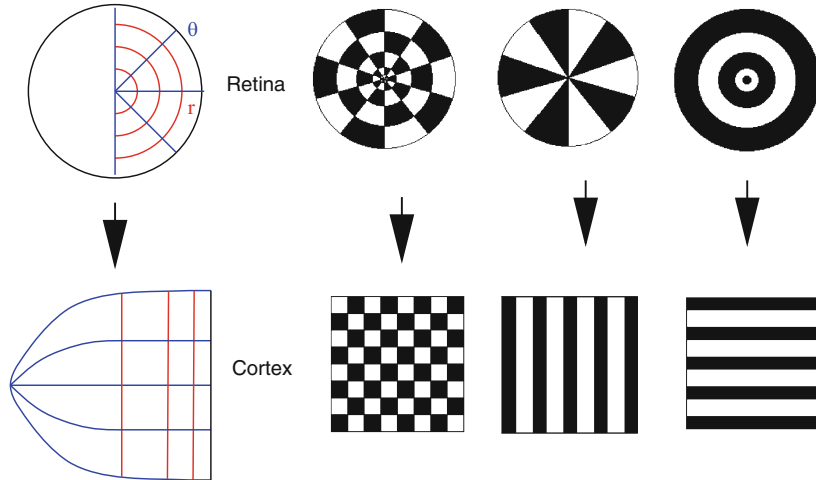


Fig. 12.7 The transformation from retinal to cortical coordinates (*left*) and its effect on three of Kluver's form constants. Most notably, bull's-eyes (starbursts) are transformed into horizontal (vertical) stripes

arising in the infinite plane). The general idea is that we will start with a spatially homogeneous system and study the stability of the spatially uniform state. As we change some parameters, the uniform state loses stability to certain spatially varying modes which grow until the nonlinearities cause them to saturate. We will not go through the complete analysis, but we will touch on the main points, which are (1) linear stability analysis and (2) pattern selection. For simplicity of exposition, we will analyze a scalar neural network with lateral inhibitory connections much like the function shown in Fig. 12.5a in two spatial dimensions and with a smooth nonlinearity. Let $u(x, y, t)$ be the activity of a local region of the cortex and suppose it satisfies

$$\tau \frac{\partial u(x, y, t)}{\partial t} = -u(x, y, t) + J(x, y) * F(u(x, y, t)), \quad (12.30)$$

where

$$J(x, y) * v(x, y) = \int_0^L \int_0^L J((x - x', y - y')v(x', y')dx'dy'.$$

Here, we will exploit two assumptions; the connections between cells are (1) rotationally symmetric and (2) translationally invariant. Since our domain is periodic, we assume $J(x \pm L, y) = J(x, y \pm L) = J(x, y)$ for all $x, y \in [0, L]$. Rotational symmetry means interactions depend only on the distance between neurons. To construct such a $J(x, y)$, we start with a function $w(x)$ which is even and satisfies

$$\int_{-\infty}^{\infty} w(x)dx = C < \infty.$$

For example, $w(x)$ could be like the lateral inhibitory kernel used in the Amari model. Let

$$J(x, y) = \sum_{n=-\infty}^{\infty} \sum_{m=-\infty}^{\infty} w(\sqrt{(x + nL)^2 + (y + mL)^2}).$$

It is clear that $J(x, y)$ is L -periodic in x, y . Furthermore, J depends only on the distance from the origin of (x, y) , so it is rotationally invariant. The reader can verify that $J(x, y)$ is integrable on the square $\Lambda = [0, L] \times [0, L]$. Henceforth, we assume $L = 2\pi$, since we can always rescale the spatial dimensions so that the “cortex” is the unit square. The periodicity of $J(x, y)$, as well as the translation invariance, implies that

$$\int_0^{2\pi} \int_0^{2\pi} J(x - x', y - y') \exp[i(kx' + jy')] dx' dy' = \hat{J}(k^2 + j^2) \exp[i(kx + jy)]$$

for any integers (k, j) and

$$\hat{J}(l^2) = \int_{-\infty}^{\infty} w(x') e^{-ilx'} dx'.$$

This last equality is due to the rotational invariance of the function $w(x)$ and the definition of J . With these necessary preliminaries we turn to the analysis of (12.30). We suppose $F(0) = 0$ and $F'(0) = \alpha > 0$ is a parameter. Think of this as the excitability of the network. For larger α , the network is more excited. We also assume $F(u)$ is at least C^3 . Since $F(0) = 0$, $u(x, y, t) = 0$ is a solution to (12.30) and represents the background state of the cortex. To determine stability, we linearize about $u = 0$ and obtain the linearized equation

$$\tau \frac{\partial v}{\partial t} = -v + \alpha J(x, y) * v(x, y, t).$$

Since J preserves sine and cosines, the general solution to the linear problem is

$$v(x, y, t) = e^{\lambda t} e^{i(kx + jy)},$$

where the eigenvalue λ satisfies

$$\lambda = -1 + \alpha \hat{J}(k^2 + j^2).$$

Note that λ depends only on α and $l^2 = j^2 + k^2$. If α is small enough, then $\lambda < 0$ for all (k, j) . If we suppose the interactions are like those in the Amari model (that is, lateral-inhibitory or “Mexican hat”) such as shown in Fig. 12.8a, the function $\hat{J}(l)$ will look like that shown in Fig. 12.8b. In the figure, we have plotted l as a continuous variable, but in our square domain it takes on discrete values of the form

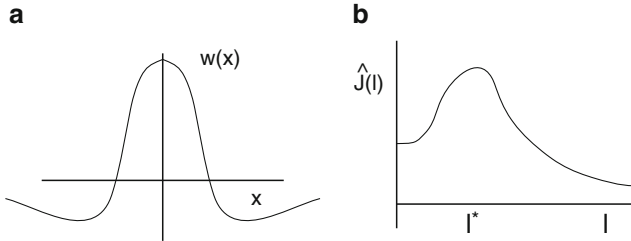


Fig. 12.8 (a) The lateral inhibitory kernel, $w(x)$, and the corresponding Fourier transform (b)

$\sqrt{k^2 + j^2}$, where (k, j) are integers. The important point is that if the interactions are like a Mexican hat, then the function \hat{J} has a maximum value at some $l = l^*$ that is bounded away from 0.

Suppose we increase the excitability parameter, α . Then as soon as α exceeds, $1/\hat{J}(l^*) \equiv \alpha^*$, the resting state will be unstable and spatial perturbations of the form $\exp i(kx + jy)$ with $k^2 + j^2 = (l^*)^2$ will grow at an exponential rate. Since the actual values of l are discrete, there will generically be a small range of values of α such that only modes exactly equal to l^* will grow and all other modes will decay. This phenomenon when a few spatial modes grow and the remainder decay is the essence of what is called the *Turing instability* after Alan Turing's groundbreaking paper on pattern formation in 1952 [276]. This simple mechanism underlies the formation of spatial patterns in hundreds of other biological and physical examples (see [205] for dozens of applications in biology). Of course, this simple analysis is only the beginning. It is also necessary for us to analyze what happens to the full nonlinear problem when α is larger than α^* . The resulting nonlinear analysis (called the *normal form* by mathematicians and *mode* or *amplitude expansion* by physicists) tells us exactly what actual patterns arise. We will sketch this out in the next few paragraphs.

The complexity of the patterns which arise as α increases beyond α^* depends on the value of l^* since this determines how many values of (k, j) satisfy $k^2 + j^2 = (l^*)^2$. For example, suppose $l^* = 7$. The only pairs are $(\pm 7, 0)$ and $(0, \pm 7)$; there are four of them. If $l^* = 5$, then there are many more: $(\pm 5, 0), (0, \pm 5), (\pm 4, \pm 3), (\pm 4, \mp 3), (\pm 3, \pm 4)$, and $(\pm 3, \mp 4)$. If $l^* = \sqrt{2}$, then $\pm(1, -1)$ and $\pm(1, 1)$ are the only four. For larger values of l^* there can be arbitrarily many. For any given l^* , we enumerate all the values of (j_n, k_n) such that $j_n^2 + k_n^2 = l^{*2}$ and write the corresponding functions of x, y as

$$\Phi_n(x, y) = e^{i(j_n x + k_n y)}.$$

The idea of normal form methods is that we seek solutions to (12.30) when the parameter α is close to α^* and thus the solutions are expected to lie close to the homogeneous resting state. Hence, we suppose $\alpha - \alpha^* = \epsilon^2 p$, where ϵ is a small positive-amplitude parameter and p is a scaling factor. We seek solutions to (12.30) of the form

$$u(x, y, t) = \sum_n \epsilon z_n(\eta) \Phi_n(x, y) + \epsilon^2 w_2 + \dots,$$

where $\eta = \epsilon^2 t$ is a slow timescale and w_2, w_3, \dots are orthogonal to $\Phi_n(x, y)$. The complex functions z_n are the so-called amplitude variables and describe the behavior near the resting state in a subspace spanned by the nullspace of the linearized equations. There is a straightforward, but somewhat tedious procedure to go through to get the equations for the z_n , and the interested reader should consult [129]. In general, the resulting equations take the following form:

$$\frac{dz_n}{d\eta} = z_n \left(bp + \sum_m a_{nm} z_m \bar{z}_m \right), \quad (12.31)$$

where a_{nm} and b are real coefficients whose values depend strongly on the details of the model. We remark that in our example system, the loss of stability is at a zero eigenvalue (which is the only possibility for a *scalar* model). However, in more complex models, such as the full Wilson–Cowan equations, it is possible to lose stability at an imaginary pair of eigenvalues. In this case, the coefficients in the normal form equation (12.31) are complex. Here, for simplicity, we study only the emergence of solutions at a zero eigenvalue. We can write $z_n = r_n \exp(i\theta_n)$ and then let $R_n = r_n^2$ to reduce (12.31) to a Lotka–Volterra model,

$$R'_n = 2R_n \left(bp + \sum_m a_{nm} R_m \right),$$

and use this to determine the dynamics of the normal form. There is a great deal of redundancy in (12.31) since the pairs (k_n, j_n) and $(-k_n, -j_n)$ are complex conjugates, so the corresponding z 's have the same values of r and R . Thus, the conversion to r or R has the desirable effect of reducing the dimension by half. Furthermore, the parameters a_{nm} are not independent and are generally related to each other. In particular, $a_{nm} = a_{mn}$. This last condition precludes any complex dynamics such as oscillations and chaos.

Consider, for example, the case when there are just four elements in the nullspace, say, $(\pm 7, 0)$ and $(0, \pm 7)$, which we identify as $n = 1, 2, 3, 4$. Then $z_2 = \bar{z}_1$ and $z_4 = \bar{z}_3$. The amplitude equations are determined solely by R_1 and R_3 :

$$\begin{aligned} R'_1 &= 2R_1(bp - aR_1 - cR_3), \\ R'_3 &= 2R_3(bp - aR_3 - cR_1). \end{aligned} \quad (12.32)$$

Note that in this case, $a_{nn} = a_{mm}$. We are only interested in solutions for which $R_n = r_n^2 \geq 0$. We absorb b into p (so we set $b = 1$ without loss of generality). There are four solutions: $(0, 0)$, $(p/a, 0)$, $(0, p/a)$, and $(p/(a+c), p/(a+c))$. Before continuing, we first interpret these solutions within the context of the patterns for the full model (12.30). Consider, the last solution. Recall that to lowest order

$u(x, y, t)$ is a sum of the $z_n = \sqrt{R_n} e^{i\theta_n}$, so for our particular choice of l^* we have

$$u(x, y) = 2\sqrt{R_1} \cos(7x + \theta_1) + 2\sqrt{R_3} \cos(7y + \theta_3),$$

where the θ 's are arbitrary phase shifts (since we have periodic boundary conditions). The four solutions to the normal form correspond, respectively, to (1) no pattern, (2) vertical stripes, (3) horizontal stripes, and (4) checkerboards. Thus, in one simple example, we can explain several of Kluver's form constants for hallucinations: bull's-eyes, pinwheels, and checkerboards. If instead, we had, for example, $(6, 6)$, $(6, -6)$, $(-6, 6)$, and $(-6, -6)$ as our unstable modes, then the three nonzero patterns for $u(x, y)$ would be two diagonal striped patterns (corresponding to spiral form constants) and checkerboards.

We leave the analysis of the stability as an exercise for the reader, but we summarize it here. The solutions $(p/a, 0)$ and $(0, p/a)$ are stable if and only if $c > a > 0$, whereas the solution $(p/(a+c), p/(a+c))$ is stable if and only if $a > c > 0$. Finally, $(0, 0)$ is stable if and only if $p < 0$.

12.6 Exercises

1. Consider the two-cell network:

$$\begin{aligned} S_1(n+1) &= \operatorname{sgn}(-S_2(n)), \\ S_2(n+1) &= \operatorname{sgn}(S_1(n)). \end{aligned}$$

Does this ever settle down? This shows that the symmetry of weights is absolutely necessary for convergence.

2. Given the energy function (12.4), derive the derivative (12.5).
3. Consider (12.3) for two neurons. Let $R_i = 1$, $C_i = 1$, $I_i = 0$, $f_i(v) = 1/(1 + \exp(-(v - 3)))$, and $w_{21} = w_{12} = 6$. Draw the phase plane for this and compute the energy function, E . Superimpose this on the phase plane.
4. Derive (12.8) from (12.6) and (12.7).
5. Prove the Destexhe et al. [60] shunting model

$$\frac{dx_i}{dt} = -A_i x_i + (B_i - x_i)[I_i + f_i(x_i)] - (x_i + C_i) \left[J_i + \sum_{j=1}^N D_{ij} g_j(x_j) \right]$$

converges to equilibria under the assumptions that $D_{ij} = D_{ji} \geq 0$, A_i , B_i , and C_i are nonnegative, and $g'_j(x_j) \geq 0$. (Hint: Let $y_i = x_i - C_i$ be a simple change of variables and use the Cohen–Grossberg theorem.) Suppose, additionally, I_i , J_i , f_i , and g_i are all positive. Prove if $x_i(0) \in (-C_i, B_i)$, then $x_i(t)$ remains in this interval.

6. Explore the following three-variable model based on (12.6):

$$\begin{aligned}x'_1 &= x_1(1 - x_1 - 2x_2 - x_3/2), \\x'_2 &= x_2(1 - x_2 - 2x_3 - x_1/2), \\x'_3 &= x_3(1 - x_3 - 2x_1 - x_2/2).\end{aligned}$$

This is of the form of the Cohen–Grossberg model but violates the symmetry of interactions. Numerically solve this system and describe the behavior.

7. Consider the single memory network

$$V'_i = -V_i + \xi_i(1/N) \sum_{j=1}^N \xi_j \tanh(bV_j),$$

where ξ_j is either -1 or 1 . Show that if $b > 0$ is too small, the only solution to this is that V_i converge to 0 . Prove as b increases, there is a pitchfork bifurcation and that V_i will converge to a fixed point proportional to the vector ξ . Show that the “antimemory,” proportional to $-\xi$ is also a stable fixed point.

8. Let $F(V) = \tanh(bV)$. Create two random memories of length 100 consisting of -1 and 1 . Numerically study the bifurcation as the gain, b , increases for (12.9). In the perfect recall case of memory 1, $r_2 = 0$. For your simulated example, how small is r_2 as b increases? Suppose the two memories are orthogonal. Can you prove the recall is perfect in this case? (Exploit the fact that F is an odd function and that all the ξ components are ± 1 .)

9. Consider the equation

$$S(x) = f\left(\frac{1}{2} \int_{-\infty}^{\infty} e^{-|x-y|} S(y) dy\right).$$

Suppose $g(u) - u + f(u)$ has three zeros, $a < b < c$, $g'(a) < 0$, $g'(b) > 0$, $g'(c) < 0$, and that

$$\int_a^c g(u) du = 0.$$

Prove there is a bounded solution to this equation satisfying

$$S(-\infty) = c, \quad S(+\infty) = a.$$

Hint: Let

$$z(x) = (1/2) \int_{-\infty}^{\infty} e^{-|x-y|} S(y) dy.$$

Show that

$$z - z_{xx} = S$$

by either using Fourier transforms or directly differentiating. Thus, transform the integral equation to

$$z - z_{xx} = f(z),$$

which is a second-order integrable differential equation which has a solution $z(-\infty) = c$ and $z(+\infty) = a$. Conclude that S also satisfies these conditions.

10. Consider:

$$-\nu \tau S' = -S + \alpha H[J(\xi) * S(\xi) - \theta](1 - S),$$

where $H(u)$ is the step function. Suppose

$$0 < \theta < \frac{\alpha}{2(1 + \alpha)}.$$

Find the unique traveling wave solution joining the states $S = 0$ with $S = \alpha/(1 + \alpha)$.

11. Devise a model similar to (12.14) and (12.15) which uses synaptic depression as the slow recovery instead of adaptation. You should consult Chap. 8 to model the depression. Note that the degree of depression should depend on the firing rate of the neuron, act as a multiplicative factor on the synaptic strength, and have its own dynamics. Draw some representative (s, d) phase planes for the local (spatially homogeneous) case, where d is the depression variable. Find conditions in which the local dynamics admits oscillations. Compare your model and simulations with those in [273]. See also [183].
12. Consider the traveling pulse equations for the analog of (12.17) with step function nonlinearities and no saturation of the synapse and adaptation variables:

$$\begin{aligned} -cS' &= -S + \nu, \\ -c\tau Z' &= -Z + k\nu, \\ \nu &= \text{Heav}\left(\int_{-\infty}^{\infty} J(\xi - \xi')S(\xi')d\xi' - bZ - \theta\right). \end{aligned}$$

Construct a traveling pulse for this equation using $J(x) = \exp(-|x|)/2$. Here is how to proceed. Let

$$U(\xi) = \int_{-\infty}^{\infty} J(\xi - \xi')S(\xi')d\xi' - bZ - \theta.$$

Suppose $U(\xi) > 0$ for $0 < \xi < a$, where a is the width of the pulse. Then for $\xi < 0$ or $\xi > a$, we have

$$-cS' = -S, \quad -c\tau Z' = -Z.$$

As $\xi \rightarrow \pm\infty$, these must be bounded, so the reader should verify that $(S, Z) = (0, 0)$ for $\xi > a$. For $\xi < 0$, the solutions are exponentials with unknown constants. For $0 < \xi < a$, $U > 0$, so the step function is 1 in this region and

$$-cS' = -S + 1, \quad -c\tau Z' = -Z + k.$$

Solutions should be continuous, so that at $\xi = a$, $S(a) = Z(a) = 0$ since (S, Z) vanish for $\xi > a$. This gives a unique solution to (S, Z) in the region $0 < \xi < a$. Furthermore, by continuity, this also provides values for the unknown constants in the region $\xi < 0$. Now, you should have a solution for all ξ which contains two unknown constants, the velocity, c , and the width, a . Since $U(\xi) > 0$ for $0 < \xi < a$ and $U(\xi) < 0$ for $\xi < 0$ and $\xi > a$, it must be the case (by continuity) that $U(0) = U(a) = 0$. These two equations will yield the unknown constants, a and c . Unfortunately, you will probably not be able to solve for a and c explicitly and must resort to a numerical solution. However, the problem has now been reduced to two algebraic equations!

13. Construct spatially periodic solutions to the Amari model (12.20) satisfying $v(x + b) = v(x)$ and $v(x) > \theta$ for $0 < x < a < b$. Can you determine their stability?
14. In this exercise, you will create a numerical model for (12.22) and (12.23) and compare the bump with the solution you construct analytically. After this, do the next exercise to determine the stability of your bump solution. For the simulations, choose $J_{ee}(x) = a \exp(-(x/\sigma_e)^2)/(\sigma_e \sqrt{\pi})$, $J_{ei}(x) = \exp(-(x/\sigma_e)^2)/(\sigma_e \sqrt{\pi})$, and $J_{ie}(x) = \exp(-(x/\sigma_i)^2)/(\sigma_i \sqrt{\pi})$. Choose $\sigma_e = 8$, $\sigma_i = 6$, $a = 1.05$, $\theta = 0.05$, and $\tau_i = 0.1$. First, compute the width of the bump by computing the composite interaction function, $J(x) = J_{ee}(x) - J_{ie}(x) * J_{ei}(x)$. (Note that $*$ means the convolution.) Next, simulate the model by choosing a big enough domain and a suitable discretization. Show that there is a bump that has the same width as the theory predicts. Proceed to the next exercise!
15. Determine the stability of the stationary solution

$$(u_e(x), u_i(x)) = (U(x), J_{ei}(x) * H(U(x) - \theta)),$$

with

$$U(x) = J(x) * H(U(x) - \theta), \quad J(x) = J_{ee}(x) - J_{ie}(x) * J_{ei}(x)$$

as a function of the time constant of inhibition in (12.22) and (12.23). Linearize about the steady solution and use the properties of the Dirac delta function to reduce the stability question to that of a four-dimensional matrix.

16. Suppose $J(x)$ is a Mexican-hat type interaction. That is:
 - a. $J(-x) = J(x)$.
 - b. $J(x) > 0$ on $(-a, a)$ with $a > 0$ and $J(\pm a) = 0$.
 - c. $J(x)$ is decreasing on $(0, a]$.
 - d. $J(x) < 0$ on $(-\infty, -a) \cup (a, \infty)$.
 - e. $J(x)$ is continuous with a finite integral.
 - f. $J(x)$ has a unique minimum on $(0, \infty)$ at a point, $d > a$ and $J(x)$ is strictly increasing on (d, ∞) .

Can you construct a double “bump” solution for (12.20)? That is, $v(x) > \theta$ in the union of two intervals, $(r_1, r_2) \cup (r_3, r_4)$? The answer to this may be no – you have to figure it out. (Hint: Consult [172].)

17. More fun with the Amari model. Consider the linear differential operator

$$Lu \equiv a_m d^m u / dt^m + a_{m-1} d^{m-1} u / dt^{m-1} + \cdots + a_1 du / dt + u$$

and suppose all the roots of the characteristic polynomial have negative real parts (that is, $p(x) = a_m x^m + \cdots + a_1 x + 1$ has roots with negative real parts) Consider the generalized Amari model

$$Lu(x, t) = J(x) * H(u(x, t) - \theta).$$

A time-independent solution satisfies

$$U(x) = J(x) * H(U(x) - \theta),$$

identical to the Amari model. Analyze the stability of the bump. For example, if $m = 1$, this is the case we have done. In particular, for $m = 2$, show that there is still a stable bump solution for all $a_1, a_2 > 0$. What happens when $m = 3$? Can there be a loss of stability?

18. There are many variants to the Amari model incorporating adaptation and dendritic interactions. Coombes and his collaborators have written many papers on the analysis of these variants. In the spirit of Serge Lang’s book on homology, pick any of the papers by Coombes [46, 48] and obtain the same stability criteria without looking at his calculations. A good place to start is the review by [46].

19. *Asymmetric weights.* Consider the Amari model:

$$u_t = -u + W(x) * H(u(x, t) - \theta),$$

where $W(x) = J(x + \alpha)$ with $J(x)$, the usual “Mexican hat” function. When α is nonzero, $W(x)$ is not symmetric, so there will be no stationary bump. However, there may be a traveling bump. Let $u(x, t) = U(x - ct)$, where c is the velocity of the moving bump. Try to construct a moving bump where you try to find c as a function of α . (Hint: Let a be the width of the bump. Then you will have to solve:

$$-cU'(y) = -U(y) + \int_0^a W(y - y') dy',$$

where $y = x - ct$ is the moving coordinate. This linear equation has two parameters (c, a) plus a constant of integration. The condition that $U(y) \rightarrow 0$ as $y \rightarrow \pm\infty$ will determine the integration constant. The other two parameters are determined by the conditions that $U(0) = \theta$ and $U(a) = \theta$.)

20. The bump equation (12.25) contains only even derivatives, so there will be even solutions to it. Thus, to prove the existence of a homoclinic, we need to find a solution $u(x)$ such that $u(0) = \alpha, u''(0) = \beta, u'(0) = u'''(0) = 0$, and u and its derivatives vanish as $x \rightarrow \infty$. This problem is a two-dimensional shooting problem since we have to find the two parameters (α, β) so that the condition at ∞ holds. Two-dimensional shooting is very much more difficult, both numerically and analytically, than one-dimensional (one-parameter) shooting. Thus, the proof would be much simpler if we could somehow reduce it to a one-dimensional shooting problem. Show that if $u(x)$ is a solution to (12.25), then

$$(u''u' - (u'')^2/2 + (b^2 - 1)u'^2 + (1 + b^2)^2 Q(u) = E,$$

where E is a constant and

$$Q(u) = \int_0^u v - F(v)dv.$$

Use the boundary conditions at $x = \infty$ to compute E for the homoclinic and then use this to find an expression for β in terms of α , thus effectively reducing the existence to a one-dimensional shooting problem.

21. *Ring model.* (a) Suppose $q_1 = 0$ in (12.27). Prove $d_1 = 0$ is invariant so that if you start with an even initial condition, the solution will continue to be even. (b) Prove a stable fixed point of (12.27) corresponds to a stable solution to the full integral equation (12.26) for $J(\theta) = A + B \cos \theta$. (c) Use the computer to explore (12.27) when

$$J(\theta) = A + B \cos \theta$$

and $F(u) = \sqrt{\max(u - k, 0)}$ choosing $A = 2$ and $B = 6$. Vary the threshold k and assume the solutions are even functions of θ so that the model reduces to a planar system. How many fixed points are there and what is their stability when $k = 1$ and $k = 0.5$? (d) One point of interest in these models is the contrast dependence of the output relative to the inputs. Consider (12.26) with $S(\theta, t) = a_0 + a_1 \cos \theta$. The ratio a_1/a_0 is called the contrast. The output contrast is c_1/c_0 , where the c_j satisfy (12.27). Explore the bifurcations and the nature of the fixed points as the contrast of the inputs varies. (e) Follow the moving bump. Suppose a stimulus runs through feature space in a periodic manner. That is, in the ring model, we drive (12.26) with a stimulus $S(\theta, t) = a_1 \cos(\theta - \omega t)$. Derive the appropriate version of (12.27) and then numerically study the behavior for $A = 2, B = 6, k = 1$ (with the same non-linearity as in the other parts of this exercise) $a_1 = 0.1$, and $\omega \in [0.02, 0.05]$. Use two different initial conditions, $c_0 = 6$ and $c_0 = 0$, with the other variables set to 0. What is the behavior if you try to drive it too fast.

22. *Zhang's head direction model.* Suppose $K(\theta)$ is a symmetric weight function and $U(\theta)$ is a stationary bump solution to

$$U(\theta) = \int_0^{2\pi} K(\theta - \theta') F(U(\theta')) d\theta'.$$

Show that

$$u(\theta, t) = U \left(\theta + \int_0^t \gamma(s) ds \right)$$

is a solution to

$$\frac{\partial u(\theta, t)}{\partial t} = -u(\theta, t) + \int_0^{2\pi} J(\theta - \theta', t) F(u(\theta', t)) d\theta',$$

where

$$J(\theta) = K(\theta) + \gamma(t) K'(\theta).$$

Simulate the Zhang model using the ring model of Exercise 22 and your choice of inputs $\gamma(t)$.

23. Prove the stability results for (12.32).

References

1. H. Agmon-Snir, C. E. Carr, and J. Rinzel. A case study for dendritic function: Improving the performance of auditory coincidence detectors. *Nature*, 393:268–272, 1998.
2. T. Allen. On the arithmetic of phase locking: coupled neurons as a lattice on \mathbf{R}^2 . *Phys. D*, 6(3):305–320, 1983.
3. S. Amari. Dynamics of pattern formation in lateral-inhibition type neural fields. *Biol. Cybern.*, 27:77–87, 1977.
4. Y. Amitai, J. R. Gibson, M. Beierlein, S. L. Patrick, A. M. Ho, B. W. Connors, and D. Golomb. The spatial dimensions of electrically coupled networks of interneurons in the neocortex. *J. Neurosci.*, 22:4142–4152, 2002.
5. J. Anderson and E. Rosenfeld. *Talking Nets: An Oral History of Neural Networks*. MIT, Cambridge, MA, 1998.
6. D. G. Aronson and H. F. Weinberger. Nonlinear diffusion in population genetics, combustion and nerve pulse propagation. In J. Goldstein, editor, *Partial Differential Equations and Related Topics, Lecture Notes in Mathematics*, pages 5–49. Springer, New York, 1975.
7. S. M. Baer, T. Erneux, and J. Rinzel. The slow passage through a hopf bifurcation: Delay memory effects, and resonances. *SIAM J. Appl. Math.*, 49:55–71, 1989.
8. L. Bai, X. Huang, Q. Yang, and J. Y. Wu. Spatiotemporal patterns of an evoked network oscillation in neocortical slices: Coupled local oscillators. *J. Neurophysiol.*, 96:2528–2538, 2006.
9. W. Bao and J. Y. Wu. Propagating wave and irregular dynamics: spatiotemporal patterns of cholinergic theta oscillations in neocortex in vitro. *J. Neurophysiol.*, 90:333–341, 2003.
10. H. B. Barlow, R. M. Hill, and W. Levick. Retinal ganglion cells responding selectively to direction and speed of image motion in the rabbit. *J. Physiol.*, 173:377–407, 1964.
11. R. Beer. On the dynamics of small continuous-time recurrent neural networks. *Adapt. Behav.*, 3:471–511, 1995.
12. M. Beierlein, J. R. Gibson, and B. W. Connors. Two dynamically distinct inhibitory networks in layer 4 of the neocortex. *J. Neurophysiol.*, 90:2987–3000, 2003.
13. R. Bellman and K. L. Cooke. *Differential-Difference Equations*. Academic, New York, 1963.
14. R. Bertram. Differential filtering of two presynaptic depression mechanisms. *Neural Comput.*, 13:69–85, 2001.
15. R. Bertram, M. J. Butte, T. Kiemel, and A. Sherman. Topological and phenomenological classification of bursting oscillations. *Bull. Math. Biol.*, 57:413–439, 1995.
16. M. D. Bevan, P. J. Magill, D. Terman, J. P. Bolam, and C. J. Wilson. Move to the rhythm: oscillations in the subthalamic nucleus-external globus pallidus network. *Trends Neurosci.*, 25:523–531, 2002.
17. L. J. Borg-Graham. Modeling the nonlinear conductances of excitable membranes. In H. Wheal and J. Chad, editors, *Cellular and Molecular Neurobiology: A Practical Approach*, pages 247–275. Oxford University Press, Oxford, 1991.
18. R. M. Borisyuk and A. B. Kirillov. Bifurcation analysis of a neural network model. *Biol. Cybern.*, 66:319–325, 1992.

19. A. Bose, N. Kopell, and D. Terman. Almost-synchronous solutions for mutually coupled excitatory neurons. *Phys. D*, 140:69–94, 2000.
20. P. C. Bressloff. Traveling waves and pulses in a one-dimensional network of excitable integrate-and-fire neurons. *J. Math. Biol.*, 40:169–198, 2000.
21. P. Bressloff. Stochastic neural field theory and the system-size expansion. *preprint*, 2010.
22. R. Brette and W. Gerstner. Adaptive exponential integrate-and-fire model as an effective description of neuronal activity. *J. Neurophysiol.*, 94:3637–3642, 2005.
23. P. D. Brodfuehrer, E. A. Debski, B. A. O’Gara, and W. O. Friesen. Neuronal control of leech swimming. *J. Neurobiol.*, 27:403–418, 1995.
24. T. G. Brown. The intrinsic factors in the act of progression in the mammal. *Proc. R. Soc. Lond. B*, 84:308–319, 1911.
25. E. Brown, J. Moehlis, and P. Holmes. On the phase reduction and response dynamics of neural oscillator populations. *Neural Comput.*, 16:673–715, 2004.
26. N. Brunel and P. E. Latham. Firing rate of the noisy quadratic integrate-and-fire neuron. *Neural Comput.*, 15:2281–2306, 2003.
27. N. Brunel and S. Sergi. Firing frequency of leaky integrate-and-fire neurons with synaptic current dynamics. *J. Theor. Biol.*, 195:87–95, 1998.
28. N. Brunel, F. S. Chance, N. Fourcaud, and L. F. Abbott. Effects of synaptic noise and filtering on the frequency response of spiking neurons. *Phys. Rev. Lett.*, 86:2186–2189, 2001.
29. M. A. Buice and J. D. Cowan. Statistical mechanics of the neocortex. *Prog. Biophys. Mol. Biol.*, 99:53–86, 2009.
30. R. J. Butera, J. Rinzel, and J. C. Smith. Models of respiratory rhythm generation in the pre-Botzinger complex. I. Bursting pacemaker neurons. *J. Neurophysiol.*, 82:382–397, 1999.
31. R. J. Butera, J. Rinzel, and J. C. Smith. Models of respiratory rhythm generation in the pre-Botzinger complex. II. Populations Of coupled pacemaker neurons. *J. Neurophysiol.*, 82:398–415, 1999.
32. D. Cai, L. Tao, A. V. Rangan, and D. W. McLaughlin. Kinetic theory for neuronal network dynamics. *Commun. Math. Sci.*, 4(1):97–127, 2006.
33. N. Carnevale and M. Hines. *The NEURON Book*. Cambridge University Press, Cambridge, UK, 2006.
34. G. Carpenter. A geometric approach to singular perturbation problems with applications to nerve impulse equations. *J. Differ. Equat.*, 23:335–367, 1977.
35. A. Carpio, S. J. Chapman, S. Hastings, and J. B. McLeod. Wave solutions for a discrete reaction-diffusion equation. *Eur. J. Appl. Math.*, 11(4):399–412, 2000.
36. M. A. Castro-Alamancos. Properties of primary sensory (lemniscal) synapses in the ventrobasal thalamus and the relay of high-frequency sensory inputs. *J. Neurophysiol.*, 87:946–953, 2002.
37. X. Chen. Existence, uniqueness, and asymptotic stability of traveling waves in nonlocal evolution equations. *Adv. Differ. Equat.*, 2(1):125–160, 1997.
38. Z. Chen, B. Ermentrout, and X. J. Wang. Wave propagation mediated by GABA_B synapse and rebound excitation in an inhibitory network: a reduced model approach. *J. Comput. Neurosci.*, 5:53–69, 1998.
39. C. C. Chow and J. A. White. Spontaneous action potentials due to channel fluctuations. *Biophys. J.*, 71:3013–3021, 1996.
40. M. A. Cohen and S. Grossberg. Absolute stability of global pattern formation and parallel memory storage by competitive neural networks. *IEEE Trans. Syst. Man Cybernet.*, 13(5):815–826, 1983.
41. A. H. Cohen, G. B. Ermentrout, T. Kiemel, N. Kopell, K. A. Sigvardt, and T. L. Williams. Modelling of intersegmental coordination in the lamprey central pattern generator for locomotion. *Trends Neurosci.*, 15:434–438, 1992.
42. K. S. Cole, R. Guttman, and F. Bezanilla. Nerve excitation without threshold. *Proc. Natl. Acad. Sci.*, 65:884–891, 1970.
43. A. Compte, N. Brunel, P. S. Goldman-Rakic, and X. J. Wang. Synaptic mechanisms and network dynamics underlying spatial working memory in a cortical network model. *Cereb. Cortex*, 10:910–923, 2000.

44. C. Conley. *Isolated invariant Sets and the Morse Index. CBMS Lecture Notes in Math*, volume 38. AMS Press, Providence, RI, 1978.
45. J. A. Connor and C. F. Stevens. Prediction of repetitive firing behaviour from voltage clamp data on an isolated neurone soma. *J. Physiol. (Lond.)*, 213:31–53, 1971.
46. S. Coombes. Waves, bumps, and patterns in neural field theories. *Biol. Cybern.*, 93:91–108, 2005.
47. S. Coombes and P. C. Bressloff. *Bursting: The Genesis of Rhythm in the Nervous System*. World Scientific, Singapore, 2005.
48. S. Coombes and M. R. Owen. Evans functions for integral neural field equations with heaviside firing rate function. *SIAM J. Appl. Dyn. Syst.*, 3:574–600, 2004.
49. J. Cowan and G. Ermentrout. Some aspects of the eigenbehavior of neural nets. In S. Levin, editor, *Studies Mathematical Biology*, volume 15, pages 67–117. Mathematical Association of America, Providence, RI, 1978.
50. J. Cowan and D. Sharp. Neural networks and artificial intelligence. *Daedalus*, 117:85–121, 1988.
51. S. M. Crook, G. B. Ermentrout, J. M. Bower Dendritic and synaptic effects in systems of coupled cortical oscillators. *J. Comput. Neurosci.*, 5:315–29, 1998.
52. R. Curtu and B. Ermentrout. Oscillations in a refractory neural net. *J. Math. Biol.*, 43:81–100, 2001.
53. P. Dayan and L. F. Abbott. *Theoretical Neuroscience: Computational and Mathematical Modeling of Neural Systems*. Computational Neuroscience. MIT, Cambridge, MA, 2001.
54. P. Dayan and L. F. Abbott. *Theoretical Neuroscience*. MIT, Cambridge, MA; London, England, 2001.
55. C. A. Del Negro, N. Koshiya, R. J. Butera, and J. C. Smith. Persistent sodium current, membrane properties and bursting behavior of pre-btzinger complex inspiratory neurons in vitro. *J. Neurophysiol.*, 88:2242–2250, 2002.
56. A. Destexhe and P. Gaspard. Bursting oscillations from a homoclinic tangency in a time delay system. *Phys. Lett. A*, 173:386–391, 1993.
57. A. Destexhe and D. Paré. Impact of network activity on the integrative properties of neocortical pyramidal neurons in vivo. *J. Neurophysiol.*, 81:1531–1547, 1999.
58. A. Destexhe, A. Babloyantz, and T. J. Sejnowski. Ionic mechanisms for intrinsic slow oscillations in thalamic relay neurons. *Biophys. J.*, 65:1538–1552, 1993.
59. A. Destexhe, D. A. McCormick, and T. J. Sejnowski. A model for 8–10 Hz spindling in interconnected thalamic relay and reticularis neurons. *Biophys. J.*, 65:2473–2477, 1993.
60. A. Destexhe and A. Babloyantz. Pacemaker-induced coherence in cortical networks. *Neural Comput.*, 3:145–154, Dec 1991.
61. A. Destexhe, D. Contreras, T. J. Sejnowski, and M. Steriade. A model of spindle rhythmicity in the isolated thalamic reticular nucleus. *J. Neurophysiol.*, 72:803–818, 1994.
62. A. Destexhe, Z. F. Mainen, and T. J. Sejnowski. Synthesis of models for excitable membranes, synaptic transmission and neuromodulation using a common kinetic formalism. *J. Comput. Neurosci.*, 1:195–230, 1994.
63. O. Diekmann. On a nonlinear integral equation arising in mathematical epidemiology. In W. Eckhaus and E. M. de Jager, editors, *Differential Equations and Applications (Proceedings of Third Scheveningen Conference, Scheveningen, 1977)*, volume 31 of *North-Holland Mathematical Studies*, pages 133–140. North-Holland, Amsterdam, 1978.
64. A. V. Egorov, B. N. Hamam, E. Fransén, M. E. Hasselmo, and A. A. Alonso. Graded persistent activity in entorhinal cortex neurons. *Nature*, 420:173–178, 2002.
65. G. B. Ermentrout. Stable periodic solutions to discrete and continuum arrays of weakly coupled nonlinear oscillators. *SIAM J. Appl. Math.*, 52(6):1665–1687, 1992.
66. B. Ermentrout. A heuristic description of spiral wave instability in discrete media. *Phys. D*, 82:54–164, 1995.
67. B. Ermentrout. Type I membranes, phase resetting curves, and synchrony. *Neural Comput.*, 8:979–1001, 1996.
68. B. Ermentrout. Linearization of F-I curves by adaptation. *Neural Comput.*, 10:1721–1729, 1998.

69. G. B. Ermentrout and J. D. Cowan. Large scale spatially organized activity in neural nets. *SIAM J. Appl. Math.*, 38(1):1–21, 1980.
70. G. B. Ermentrout and D. Kleinfeld. Traveling electrical waves in cortex: insights from phase dynamics and speculation on a computational role. *Neuron*, 29:33–44, 2001.
71. G. B. Ermentrout and N. Kopell. Frequency plateaus in a chain of weakly coupled oscillators. I. *SIAM J. Math. Anal.*, 15(2):215–237, 1984.
72. G. B. Ermentrout and N. Kopell. Parabolic bursting in an excitable system coupled with a slow oscillation. *SIAM J. Appl. Math.*, 46:223–253, 1986.
73. G. B. Ermentrout and N. Kopell. Fine structure of neural spiking and synchronization in the presence of conduction delays. *Proc. Natl. Acad. Sci. U.S.A.*, 95:1259–1264, 1998.
74. G. B. Ermentrout and J. B. McLeod. Existence and uniqueness of travelling waves for a neural network. *Proc. Roy. Soc. Edinburgh Sect. A*, 123(3):461–478, 1993.
75. G. B. Ermentrout and J. Rinzel. Waves in a simple, excitable or oscillatory, reaction-diffusion model. *J. Math. Biol.*, 11(3):269–294, 1981.
76. G. B. Ermentrout and J. Rinzel. Beyond a pacemaker’s entrainment limit: phase walk-through. *Am. J. Physiol. Regul. Integr. Comp. Physiol.*, 246:102–106, 1984.
77. B. Ermentrout, J. Flores, and A. Gelperin. Minimal model of oscillations and waves in the Limax olfactory lobe with tests of the model’s predictive power. *J. Neurophysiol.*, 79:2677–2689, 1998.
78. B. Ermentrout, J. Dutta-Moscato, and D. Pinto. Elliptic bursters, depolarization block, and waves. In P. Bressloff and S. Coombes, editors, *Bursting*, pages 385–396. World Scientific, Hackensack, NJ, 2005.
79. G. B. Ermentrout, R. F. Galán, and N. N. Urban. Reliability, synchrony and noise. *Trends Neurosci.*, 31:428–434, 2008.
80. J. W. Evans. Nerve axon equations. iv. *Indiana Univ. Math. J.*, 24:1169–1190, 1975.
81. J. W. Evans, N. Fenichel, and J. A. Feroe. Double impulse solutions in nerve axon equations. *SIAM J. Appl. Math.*, 42:219–234, 1982.
82. A. A. Faisal, L. P. Selen, and D. M. Wolpert. Noise in the nervous system. *Nat. Rev. Neurosci.*, 9:292–303, 2008.
83. C. P. Fall, E. Marland, J. M. Wagner, and J. J. Tyson. *Computational Cell Biology*. Springer, New York, 2002.
84. C. P. Fall, E. S. Marland, J. M. Wagner, and J. J. Tyson, editors. *Computational Cell Biology*, volume 20 of *Interdisciplinary Applied Mathematics*. Springer, New York, 2002.
85. O. Feinerman, M. Segal, and E. Moses. Signal propagation along unidimensional neuronal networks. *J. Neurophysiol.*, 94:3406–3416, 2005.
86. N. Fenichel. Geometric singular perturbation theory. *J. Diff. Equat.*, 31:53–91, 1979.
87. J. A. Feroe. Existence and stability of multiple impulse solutions of a nerve axon equation. *SIAM J. Appl. Math.*, 42:235–246, 1982.
88. P. C. Fife and J. B. McLeod. The approach of solutions of nonlinear diffusion equations to traveling wave solutions. *Arch. Ration. Mech. Anal.*, 65:355–361, 1977.
89. R. A. FitzHugh. Impulses and physiological states in theoretical models of nerve membrane. *Biophys. J.*, 1:445–466, 1961.
90. N. Fourcaud and N. Brunel. Dynamics of the firing probability of noisy integrate-and-fire neurons. *Neural Comput.*, 14:2057–2110, 2002.
91. N. Fourcaud-Trocmé, D. Hansel, C. van Vreeswijk, and N. Brunel. How spike generation mechanisms determine the neuronal response to fluctuating inputs. *J. Neurosci.*, 23:11628–11640, 2003.
92. R. F. Fox and Y. n. Lu. Emergent collective behavior in large numbers of globally coupled independently stochastic ion channels. *Phys. Rev. E Stat. Phys. Plasmas Fluids Relat. Interdiscip. Topics*, 49:3421–3431, 1994.
93. E. Fransén, B. Tahvildari, A. V. Egorov, M. E. Hasselmo, and A. A. Alonso. Mechanism of graded persistent cellular activity of entorhinal cortex layer v neurons. *Neuron*, 49:735–746, 2006.
94. J. M. Fuster. Unit activity in prefrontal cortex during delayed-response performance: neuronal correlates of transient memory. *J. Neurophysiol.*, 36:61–78, 1973.

95. J. M. Fuster and G. E. Alexander. Neuron activity related to short-term memory. *Science*, 173:652–654, 1971.
96. C. W. Gardiner. *Handbook of Stochastic Methods for Physics, Chemistry and the Natural Sciences*, volume 13 of *Springer Series in Synergetics*. Springer, Berlin, third edition, 2004.
97. K. E. Gavrikov, J. E. Nilson, A. V. Dmitriev, C. L. Zucker, and S. Mangel. Dendritic compartmentalization of chloride cotransporters underlies directional responses of starburst amacrine cells in retina. *PNAS*, 103:18793–18798, 2006.
98. S. Grossberg, G. A. Carpenter. A massively parallel architecture for a self-organizing neural pattern recognition machine. In *Computer Vision, Graphics, and Image Processing*, pages 54–115, Academic, New York, 1987.
99. W. Gerstner and W. M. Kistler. *Spiking Neuron Models: Single Neurons, Populations, Plasticity*. Cambridge University Press, Cambridge, 2002.
100. W. Gerstner, J. L. van Hemmen, and J. Cowan. What matters in neuronal locking? *Neural Comput.*, 8:1653–1676, 1996.
101. J. R. Gibson, M. Beierlein, and B. W. Connors. Two networks of electrically coupled inhibitory neurons in neocortex. *Nature*, 402:75–79, 1999.
102. J. R. Gibson, M. Beierlein, and B. W. Connors. Functional properties of electrical synapses between inhibitory interneurons of neocortical layer 4. *J. Neurophysiol.*, 93:467–480, 2005.
103. L. Glass and M. C. Mackey. *From Clocks to Chaos: The Rhythms of Life*. Princeton University Press, Princeton, NJ, 1988.
104. D. Golomb and Y. Amitai. Propagating neuronal discharges in neocortical slices: computational and experimental study. *J. Neurophysiol.*, 78:1199–1211, Sep 1997.
105. D. Golomb, X.-J. Wang, and J. Rinzel. Synchronization properties of spindle oscillations in a thalamic reticular nucleus model. *J. Neurophysiol.*, 72:1109–1126, 1994.
106. M. Golubitsky, I. Stewart, P. L. Buono, and J. J. Collins. Symmetry in locomotor central pattern generators and animal gaits. *Nature*, 401:693–695, 1999.
107. C. M. Gray, P. König, A. K. Engel, and W. Singer. Oscillatory responses in cat visual cortex exhibit inter-columnar synchronization which reflects global stimulus properties. *Nature*, 338:334–337, 1989.
108. C. M. Gray, A. K. Engel, P. König, and W. Singer. Synchronization of oscillatory neuronal responses in cat striate cortex: temporal properties. *Vis. Neurosci.*, 8:337–347, 1992.
109. S. Grillner and P. Wallén. Cellular bases of a vertebrate locomotor system-steering, inter-segmental and segmental co-ordination and sensory control. *Brain Res. Brain Res. Rev.*, 40:92–106, 2002.
110. J. Guckenheimer. Isochrons and phaseless sets. *J. Math. Biol.*, 1(3):259–273, 1974/75.
111. J. Guckenheimer and P. Holmes. *Nonlinear Oscillations, Dynamical Systems, and Bifurcations of Vector Fields*. Springer, New York, 1983.
112. J. Guckenheimer and R. A. Oliva. Chaos in the Hodgkin-Huxley model. *SIAM J. Appl. Dyn. Syst.*, 1:105–114, 1992.
113. A. T. Gullidge and G. J. Stuart. Excitatory actions of GABA in the cortex. *Neuron*, 37:299–309, 2003.
114. B. S. Gutkin, G. B. Ermentrout, and A. D. Reyes. Phase-response curves give the responses of neurons to transient inputs. *J. Neurophysiol.*, 94:1623–1635, 2005.
115. J. K. Hale and H. Koçak. *Dynamics and Bifurcations*, volume 3 of *Texts in Applied Mathematics*. Springer, New York, 1991.
116. B. J. Hall and K. R. Delaney. Contribution of a calcium-activated non-specific conductance to NMDA receptor-mediated synaptic potentials in granule cells of the frog olfactory bulb. *J. Physiol. (Lond.)*, 543:819–834, 2002.
117. F. Han, N. Caporale, and Y. Dan. Reverberation of recent visual experience in spontaneous cortical waves. *Neuron*, 60:321–327, 2008.
118. S. P. Hastings. On the existence of homoclinic and periodic orbits for the Fitzhugh-Nagumo equations. *Quart. J. Math. Oxford*, 27:123–124, 1976.
119. S. P. Hastings. Single and multiple pulse waves for the Fitzhugh-Nagumo equations. *SIAM J. Appl. Math.*, 42:247–260, 1982.

120. F. Helmchen, K. Imoto, and B. Sakmann. Ca^{2+} buffering and action potential-evoked Ca^{2+} signaling in dendrites of pyramidal neurons. *Biophys. J.*, 70:1069–1081, 1996.
121. A. Hertz, A. Krogh, and R. Palmer. *Introduction To The Theory of Neural Computation, Volume I*. Perseus Books, New York, 1991.
122. B. Hille. *Ion Channels of Excitable Membranes*. Sinauer, Sunderland, MA, second edition, 2001.
123. J. Hindmarsh and R. Rose. A model of neuronal bursting using three coupled first order differential equations. *Proc. R. Soc. Lond., Ser. B*, 221:87–102, 1984.
124. A. L. Hodgkin and A. F. Huxley. A quantitative description of membrane current and application to conduction and excitation in nerve. *J. Physiol.*, 117:500–544, 1952.
125. D. Holcman and M. Tsodyks. The emergence of up and down states in cortical networks. *PLoS Comput. Biol.*, 2:e23, 2006.
126. J. J. Hopfield. Neural networks and physical systems with emergent collective computational abilities. *Proc. Natl. Acad. Sci. U.S.A.*, 79:2554–2558, 1982.
127. J. J. Hopfield. Neurons with graded response have collective computational properties like those of two-state neurons. *Proc. Natl. Acad. Sci. U.S.A.*, 81:3088–3092, 1984.
128. F. C. Hoppensteadt and E. M. Izhikevich. *Weakly Connected Neural Networks*, volume 126 of *Applied Mathematical Sciences*. Springer, New York, 1997.
129. R. B. Hoyle. *Pattern Formation: An Introduction to Methods*. Cambridge University Press, Cambridge, 2006.
130. X. Huang, W. C. Troy, Q. Yang, H. Ma, C. R. Laing, S. J. Schiff, and J. Y. Wu. Spiral waves in disinhibited mammalian neocortex. *J. Neurosci.*, 24:9897–9902, 2004.
131. J. Huguenard and D. McCormick. *Electrophysiology of the Neuron: An Interactive Tutorial*. Oxford University Press, Oxford, 1994.
132. E. M. Izhikevich. Neural excitability, spiking and bursting. *Int. J. Bifurcat. Chaos Appl. Sci. Eng.*, 10(6):1171–1266, 2000.
133. E. M. Izhikevich. Phase equations for relaxation oscillators. *SIAM J. Appl. Math.*, 60(5):1789–1804 (electronic), 2000.
134. E. M. Izhikevich. Simple model of spiking neurons. *IEEE Trans Neural Netw.*, 14:1569–1572, 2003.
135. E. M. Izhikevich. *Dynamical Systems in Neuroscience*. MIT, Cambridge, MA, 2007.
136. E. M. Izhikevich. *Dynamical Systems in Neuroscience: The Geometry of Excitability and Bursting*. Computational Neuroscience, MIT, Cambridge, MA, 2007.
137. J. J. B. Jack, D. Noble, and R. W. Tsien. *Electrical Current Flow in Excitable Cells*. Clarendon Press, Oxford, 1975.
138. C. E. Jahr and C. F. Stevens. A quantitative description of NMDA receptor-channel kinetic behavior. *J. Neurosci.*, 10:1830–1837, 1990.
139. D. Johnston and S. M. Wu. *Foundations of Cellular Neurophysiology*. MIT, Cambridge, MA, 1995.
140. D. Johnston and S. Wu. *Foundations of Cellular Neurophysiology*. MIT, Cambridge, MA, 1999.
141. D. Johnston, J. C. Magee, C. M. Colbert, and B. R. Cristie. Active properties of neuronal dendrites. *Annu. Rev. Neurosci.*, 19:165–186, 1996.
142. D. Johnston, D. A. Hoffman, C. M. Colbert, and J. C. Magee. Regulation of back-propagating action potentials in hippocampal neurons. *Curr. Opin. Neurobiol.*, 9:288–292, 1999.
143. C. K. R. T. Jones. Stability of the traveling wave solution of the fitzhugh-nagumo equations. *Trans. A.M.S.*, 286:431–469, 1984.
144. E. Kandel, J. Schwartz, and T. Jessell. *Principles of Neural Science*. Appleton & Lange, Norwalk, CT, 1991.
145. J. Karbowski and N. Kopell. Multispikes and synchronization in a large neural network with temporal delays. *Neural Comput.*, 12:1573–1606, 2000.
146. J. P. Keener. Proagation and its failure in coupled systems of discrete excitable cells. *SIAM J. Appl. Math.*, 47:556–572, 1987.
147. J. P. Keener. *Principles of Applied Mathematics: Transformation and Approximation*. Advanced Book Program, Perseus Books, Cambridge, MA, revised edition, 2000.

148. J. Keener and J. Sneyd. *Mathematical Physiology*. Springer, New York, 1998.
149. J. Kelso. *Dynamic patterns: The self-organization of brain and behavior*. MIT, Cambridge, MA, 1995.
150. T. B. Kepler, L. F. Abbott, and E. Marder. Reduction of conductance based neuron models. *Biol. Cybern.*, 66:381–387, 1992.
151. Z. P. Kilpatrick and P. C. Bressloff. Spatially structured oscillations in a two-dimensional excitatory neuronal network with synaptic depression. *J. Comput. Neurosci.*, 2009.
152. U. Kim, T. Bal, and D. A. McCormick. Spindle waves are propagating synchronized oscillations in the ferret LGNd in vitro. *J. Neurophysiol.*, 74:1301–1323, 1995.
153. K. Kishimoto and S. Amari. Existence and stability of local excitations in homogeneous neural fields. *J. Math. Biol.*, 7:303–318, 1979.
154. P. E. Kloeden and E. Platen. *Numerical Solution of Stochastic Differential Equations*, volume 23 of *Applications of Mathematics (New York)*. Springer, Berlin, 1992.
155. H. Kluver. *Mescal and the Mechanisms of Hallucination*. University of Chicago Press, Chicago, IL, 1969.
156. C. Koch. *Biophysics of Computation*. Oxford University Press, London and New York, 1999.
157. C. Koch and e. I. Segev. *Methods in Neuronal Modeling: From Synapses to Networks*. MIT, Cambridge, MA, 1998.
158. B. Kocsis and S. Li. In vivo contribution of h-channels in the septal pacemaker to theta rhythm generation. *Eur. J. Neurosci.*, 20:2149–2158, 2004.
159. N. Kopell. Toward a theory of modelling central pattern generators. In A. H. Cohen, S. Rossignol, and S. Grillner, editors, *Neural Control of Rhythmic Movements in Vertebrates*, pages 265–284. Wiley, New York, 1988.
160. N. Kopell and B. Ermentrout. Mechanisms of phase-locking and frequency control in pairs of coupled neural oscillators. In B. Fiedler, G. Iooss, and N. Kopell, editors, *Handbook of Dynamical Systems II: Towards Applications*. Elsevier, Amsterdam, 2002.
161. N. Kopell and G. B. Ermentrout. Symmetry and phaselocking in chains of weakly coupled oscillators. *Comm. Pure Appl. Math.*, 39(5):623–660, 1986.
162. N. Kopell and L. N. Howard. Plane wave solutions to reaction-diffusion equations. *Studies Appl. Mat.*, 52:291–328, 1973.
163. N. Kopell and D. Somers. Anti-phase solutions in relaxation oscillators coupled through excitatory interactions. *J. Math. Biol.*, 33:261–280, 1995.
164. V. I. Krinski and I. u. M. Kokoz. Analysis of the equations of excitable membranes. I. Reduction of the Hodgkins–Huxley equations to a 2d order system. *Biofizika*, 18:506–511, 1973.
165. E. P. Krisner. Homoclinic orbit solutions of a one dimensional Wilson–Cowan type model. *Electron. J. Differ. Equat.*, 107:30, 2008.
166. Y. Kuramoto. *Chemical Oscillations, Waves, and Turbulence*, volume 19 of *Springer Series in Synergetics*. Springer, Berlin, 1984.
167. Y. A. Kuznetsov. *Elements of Applied Bifurcation Theory*, volume 112 of *Applied Mathematical Sciences*. Springer, New York, third edition, 2004.
168. H. T. Kyriazi and D. J. Simons. Thalamocortical response transformations in simulated whisker barrels. *J. Neurosci.*, 13:1601–1615, 1993.
169. C. Laing and G. Lord. *Stochastic Methods in Neuroscience*. Oxford University Press, Oxford, 2009.
170. C. R. Laing and W. C. Troy. PDE methods for nonlocal models. *SIAM J. Appl. Dyn. Syst.*, 2(3):487–516 (electronic), 2003.
171. C. R. Laing and W. C. Troy. Two-bump solutions of Amari-type models of neuronal pattern formation. *Phys. D*, 178(3-4):190–218, 2003.
172. C. R. Laing, W. C. Troy, B. Gutkin, and G. B. Ermentrout. Multiple bumps in a neuronal model of working memory. *SIAM J. Appl. Math.*, 63(1):62–97 (electronic), 2002.
173. E. K. Lambe and G. K. Aghajanian. Hallucinogen-induced UP states in the brain slice of rat prefrontal cortex: role of glutamate spillover and NR2B-NMDA receptors. *Neuropsychopharmacology*, 31:1682–1689, 2006.
174. L. Lapicque. Recherches quantitatives sur l’excitation électrique des nerfs traitée comme une polarization. *J. Physiol. Gen.*, 9:620–635, 1907.

175. P. E. Latham, B. J. Richmond, P. G. Nelson, and S. Nirenberg. Intrinsic dynamics in neuronal networks, I. Theory. *J Neurophysiology*, 83(2):808–827, 2000.
176. G. Laurent. Olfactory network dynamics and the coding of multidimensional signals. *Nat. Rev. Neurosci.*, 3:884–895, 2002.
177. E. Lee and D. Terman. Uniqueness and stability of periodic bursting solutions. *J. Diff. Equat.*, 158:48–78, 1999.
178. S. R. Lehky. An astable multivibrator model of binocular rivalry. *Perception*, 17:215–228, 1988.
179. B. Lindner. Interspike interval statistics of neurons driven by colored noise. *Phys. Rev. E Stat. Nonlin. Soft Matter Phys.*, 69:022901, 2004.
180. B. Lindner and L. Schimansky-Geier. Transmission of noise coded versus additive signals through a neuronal ensemble. *Phys. Rev. Lett.*, 86:2934–2937, 2001.
181. B. Lindner, A. Longtin, and A. Bulsara. Analytic expressions for rate and CV of a type I neuron driven by white gaussian noise. *Neural Comput.*, 15:1760–1787, 2003.
182. J. E. Lisman, J. M. Fellous, and X. J. Wang. A role for NMDA-receptor channels in working memory. *Nat. Neurosci.*, 1:273–275, 1998.
183. A. Loebel and M. Tsodyks. Computation by ensemble synchronization in recurrent networks with synaptic depression. *J. Comput. Neurosci.*, 13:111–124, 2002.
184. Y. Loewenstein and H. Sompolinsky. Temporal integration by calcium dynamics in a model neuron. *Nat. Neurosci.*, 6:961–967, 2003.
185. M. London and M. Häusser. Dendritic computation. *Annu. Rev. Neurosci.*, 28:503–532, 2005.
186. G. Maccaferri and C. J. McBain. The hyperpolarization-activated current (I_h) and its contribution to pacemaker activity in rat CA1 hippocampal stratum oriens-alveus interneurons. *J. Physiol. (Lond.)*, 497(Pt 1):119–130, 1996.
187. G. Mackie and R. W. Meech. Separate sodium and calcium spikes in the same axon. *Nature*, 313:791–793, 1985.
188. J. Magee, D. Hoffman, C. Colbert, and D. Johnston. Electrical and calcium signaling in dendrites of hippocampal pyramidal neurons. *Annu. Rev. Physiol.*, 60:327–346, 1998.
189. K. Maginu. Geometrical characteristics associated with stability and bifurcations of periodic traveling waves in reaction-diffusion systems. *SIAM J. Appl. Math.*, 45:750–774, 1985.
190. Y. Manor, A. Bose, V. Booth, and F. Nadim. Contribution of synaptic depression to phase maintenance in a model rhythmic network. *J. Neurophysiol.*, 90:3513–3528, Nov 2003.
191. H. Markram, Y. Wang, and M. Tsodyks. Differential signaling via the same axon of neocortical pyramidal neurons. *Proc. Natl. Acad. Sci. U.S.A.*, 95:5323–5328, 1998.
192. A. R. Martin, B. G. Wallace, P. A. Fuchs, and J. G. Nicholls. *From Neuron to Brain: A Cellular and Molecular Approach to the Function of the Nervous System*. Sinauer Associates, Sunderland, MA, 2001.
193. R. H. Masland. Directional selectivity in retinal ganglion cells. In L. M. Chalupa and J. S. Werner, editors, *The Visual Neurosciences*, pages 451–462. Cambridge, MIT, 2004.
194. P. C. Matthews, R. E. Mirollo, and S. H. Strogatz. Dynamics of a large system of coupled nonlinear oscillators. *Phys. D*, 52(2-3):293–331, 1991.
195. J. M. Mayville, S. L. Bressler, A. Fuchs, and J. A. Kelso. Spatiotemporal reorganization of electrical activity in the human brain associated with a timing transition in rhythmic auditory-motor coordination. *Exp. Brain Res.*, 127:371–381, 1999.
196. J. McClelland and D. Rumelhart. *Parallel Distributed Processes*. MIT, Cambridge, MA, 1987.
197. W. S. McCulloch and W. Pitts. The statistical organization of nervous activity. *Biometrics*, 4:91–99, 1948.
198. G. Medvedev. Reduction of a model of an excitable cell to a one-dimensional map. *Phys. D*, 202:37–59, 2005.
199. R. W. Meech and G. O. Mackie. Ionic currents in giant motor axons of the jellyfish, *Aglantha digitale*. *J. Neurophysiol.*, 69:884–893, 1993.
200. B. D. Mensh, E. Aksay, D. D. Lee, H. S. Seung, and D. W. Tank. Spontaneous eye movements in goldfish: oculomotor integrator performance, plasticity, and dependence on visual feedback. *Vis. Res.*, 44:711–726, 2004.

201. M. Migliore and G. M. Shepherd. Emerging rules for the distributions of active dendritic conductances. *Nat. Rev. Neurosci.*, 3:362–370, 2002.
202. M. Migliore and G. M. Shepherd. Dendritic action potentials connect distributed dendrodendritic microcircuits. *J. Comput. Neurosci.*, 24:207–221, 2008.
203. M. Migliore, L. Messineo, and M. Ferrante. Dendritic Ih selectively blocks temporal summation of unsynchronized distal inputs in CA1 pyramidal neurons. *J. Comput. Neurosci.*, 16:5–13, 2004.
204. R. E. Mirollo and S. H. Strogatz. Synchronization of pulse-coupled biological oscillators. *SIAM J. Appl. Math.*, 50(6):1645–1662, 1990.
205. J. D. Murray. *Mathematical Biology. II*, volume 18 of *Interdisciplinary Applied Mathematics*. Spatial models and biomedical applications. Springer, New York, third edition, 2003.
206. M. Muller and R. Wehner. Path integration in desert ants, *Cataglyphis fortis*. *Proc. Natl. Acad. Sci. U.S.A.*, 85:5287–5290, 1988.
207. T. I. Netoff, M. I. Banks, A. D. Dorval, C. D. Acker, J. S. Haas, N. Kopell, and J. A. White. Synchronization in hybrid neuronal networks of the hippocampal formation. *J. Neurophysiol.*, 93:1197–1208, 2005.
208. J. C. Neu. Large populations of coupled chemical oscillators. *SIAM J. Appl. Math.*, 38(2):305–316, 1980.
209. R. Osan, R. Curtu, J. Rubin, and B. Ermentrout. Multiple-spike waves in a one-dimensional integrate-and-fire neural network. *J. Math. Biol.*, 48:243–274, 2004.
210. J. E. Paulet and G. B. Ermentrout. Stable rotating waves in two-dimensional discrete active media. *SIAM J. Appl. Math.*, 54(6):1720–1744, 1994.
211. D. H. Perkel and B. Mulloney. Motor pattern production in reciprocally inhibitory neurons exhibiting postsynaptic rebound. *Science*, 145:61–63, 1974.
212. L. Perko. *Differential Equations and Dynamical Systems*. Springer, New York, 1996.
213. H. Petsche, O. Prohaska, P. Rappelsberger, R. Vollmer, and A. Kaiser. Cortical seizure patterns in multidimensional view: the information content of equipotential maps. *Epilepsia*, 15:439–463, 1974.
214. B. Pfeuty, G. Mato, D. Golomb, and D. Hansel. Electrical synapses and synchrony: the role of intrinsic currents. *J. Neurosci.*, 23:6280–6294, 2003.
215. P. Pinsky and J. Rinzel. Intrinsic and network rhythmogenesis in a reduced traub model of ca3 neurons. *J. Comput. Neurosci.*, 1:39–60, 1994.
216. D. J. Pinto and G. B. Ermentrout. Spatially structured activity in synaptically coupled neuronal networks. I. Traveling fronts and pulses. *SIAM J. Appl. Math.*, 62(1):206–225 (electronic), 2001.
217. D. J. Pinto, J. C. Brumberg, D. J. Simons, and G. B. Ermentrout. A quantitative population model of whisker barrels: re-examining the Wilson-Cowan equations. *J. Comput. Neurosci.*, 3:247–264, 1996.
218. D. J. Pinto, J. A. Hartings, J. C. Brumberg, and D. J. Simons. Cortical damping: analysis of thalamocortical response transformations in rodent barrel cortex. *Cereb. Cortex*, 13:33–44, Jan 2003.
219. D. J. Pinto, S. L. Patrick, W. C. Huang, and B. W. Connors. Initiation, propagation, and termination of epileptiform activity in rodent neocortex in vitro involve distinct mechanisms. *J. Neurosci.*, 25:8131–8140, 2005.
220. J. C. Prechtl, L. B. Cohen, B. Pesaran, P. P. Mitra, and D. Kleinfeld. Visual stimuli induce waves of electrical activity in turtle cortex. *Proc. Natl. Acad. Sci. U.S.A.*, 94:7621–7626, 1997.
221. W. Rall. Core conductor theory and cable properties of neurons. In E. R. Kandel, editor, *Handbook of Physiology*, volume 1, pages 39–97. American Physiology Society, Bethesda, MD, 1977.
222. W. Rall and J. Rinzel. Branch input resistance and steady attenuation for input to one branch of a dendritic neuron model. *Biophys. J.*, 13:648–688, 1973.
223. L. Ren and G. B. Ermentrout. Monotonicity of phaselocked solutions in chains and arrays of nearest-neighbor coupled oscillators. *SIAM J. Math. Anal.*, 29(1):208–234 (electronic), 1998.
224. A. D. Reyes. Synchrony-dependent propagation of firing rate in iteratively constructed networks in vitro. *Nat. Neurosci.*, 6:593–599, 2003.

225. A. D. Reyes and E. E. Fetz. Effects of transient depolarizing potentials on the firing rate of cat neocortical neurons. *J. Neurophysiol.*, 69:1673–1683, 1993.
226. J. Rinzel. On repetitive activity in nerve. *Fed. Proc.*, 37:2793–2802, 1978.
227. J. Rinzel. Bursting oscillations in an excitable membrane model. In B. D. Sleeman and R. J. Jarvis, editors, *Ordinary and Partial Differential Equations; Proceedings of the 8th Dundee Conference, Lecture Notes in Mathematics 1151*. Springer, New York, 1985.
228. J. Rinzel. A formal classification of bursting mechanisms in excitable systems. In E. Teramoto and M. Yamaguti, editors, *Mathematical Topics in Population Biology, Morphogenesis and Neurosciences*, volume 71 of *Lecture Notes in Biomathematics*. Springer, New York, 1987.
229. J. Rinzel. Electrical excitability of cells, theory and experiment: Review of the Hodgkin–Huxley foundation and an update. *Bull. Math. Biol.*, 52:3–23, 1990.
230. J. Rinzel and G. B. Ermentrout. Analysis of neural excitability and oscillations. In C. Koch and I. Segev, editors, *Methods in Neuronal Modeling*. MIT, Cambridge, MA, 1989.
231. J. Rinzel and K. Maginu. Kinematic analysis of wave pattern formation in excitable media. In C. Vidal and A. Pacault, editors, *Nonequilibrium Dynamics in Chemical Systems (Bordeaux, 1984)*, volume 27 of *Springer Series Synergetics*, pages 107–113. Springer, Berlin, 1984.
232. J. Rinzel, D. Terman, X.-J. Wang, and B. Ermentrout. Propagating activity patterns in large-scale inhibitory neuronal networks. *Science*, 279:1351–1355, 1998.
233. J. Ritt. Evaluation of entrainment of a nonlinear neural oscillator to white noise. *Phys. Rev. E Stat. Nonlin. Soft Matter Phys.*, 68:041915, Oct 2003.
234. R. Rodriguez and H. C. Tuckwell. Statistical properties of stochastic nonlinear dynamical models of single spiking neurons and neural networks. *Phys. Rev. E Stat. Phys. Plasmas Fluids Relat. Interdiscip. Topics*, 54:5585–5590, 1996.
235. R. Romo, C. D. Brody, A. Hernandez, and L. Lemus. Neuronal correlates of parametric working memory in the prefrontal cortex. *Nature*, 399:470–473, 1999.
236. J. Rubin and D. Terman. Analysis of clustered firing patterns in synaptically coupled networks of oscillators. *J. Math. Biol.*, 41:513–545, 2000.
237. M. Rudolph and A. Destexhe. Characterization of subthreshold voltage fluctuations in neuronal membranes. *Neural Comput.*, 15:2577–2618, 2003.
238. M. Rudolph and A. Destexhe. On the use of analytical expressions for the voltage distribution to analyze intracellular recordings. *Neural Comput.*, 18:2917–2922, 2006.
239. M. E. Rush and J. Rinzel. The potassium A-current, low firing rates and rebound excitation in Hodgkin–Huxley models. *Bull. Math. Biol.*, 57:899–929, 1995.
240. H. Sakaguchi and S. Tobiishi. Spindle oscillation in noisy integrate-and-fire-or-burst neurons with inhibitory coupling. *Prog. Theor. Phys.*, 79:1069–1079, 2005.
241. S. Sakaguchi, H. Shinimoto, and Y. Kuramoto. Mutual entrainment oscillator lattices with nonvariational coupling. *Prog. Theor. Phys.*, 1988.
242. C. B. Saper, T. C. Chou, and T. E. Scammell. The sleep switch: hypothalamic control of sleep and wakefulness. *Trends Neurosci.*, 24:726–731, 2001.
243. I. Segev, J. Rinzel, and G. Shepherd. *The Theoretical Foundation of Dendritic Function: Selected Paper of Wilfrid Rall with Commentaries*. MIT, Cambridge, MA, 1994.
244. H. S. Seung, D. D. Lee, B. Y. Reis, and D. W. Tank. Stability of the memory of eye position in a recurrent network of conductance-based model neurons. *Neuron*, 26:259–271, 2000.
245. A. L. Shilnikov and G. Cymbalyuk. Transition between tonic spiking and bursting in a neuron model via the blue-sky catastrophe. *Phys. Rev. Lett.*, 94:048101, 2005.
246. A. Shpiro, R. Curtu, J. Rinzel, and N. Rubin. Dynamical characteristics common to neuronal competition models. *J. Neurophysiol.*, 97:462–473, 2007.
247. Y. Shu, A. Hasenstaub, and D. A. McCormick. Turning on and off recurrent balanced cortical activity. *Nature*, 423:288–293, 2003.
248. D. Sigeti and W. Horsthemke. Pseudo-regular oscillations induced by external noise. *J. Stat. Physics*, 54:1217–1222, 1989.
249. F. Skinner, N. Kopell, and E. Marder. Mechanisms for oscillation and frequency control in networks of mutually inhibitory relaxation oscillators. *J. Comput. Neurosci.*, 1:69–87, 1994.
250. W. R. Softky and C. Koch. The highly irregular firing of cortical cells is inconsistent with temporal integration of random EPSPs. *J. Neurosci.*, 13:334–350, 1993.

251. M. Steriade. *Neuronal Substrates of Sleep and Epilepsy*. Cambridge University Press, Cambridge, 2003.
252. R. Stoop, L. A. Bunimovich, and W. H. Steeb. Generic origins of irregular spiking in neocortical networks. *Biol. Cybern.*, 83:481–489, 2000.
253. R. Stoop, K. Schindler, and L. A. Bunimovich. When pyramidal neurons lock, when they respond chaotically, and when they like to synchronize. *Neurosci. Res.*, 36:81–91, 2000.
254. S. Strogatz. *Sync*. Hyperion Books, New York, 2003. How order emerges from chaos in the universe, nature, and daily life.
255. S. H. Strogatz. *Nonlinear Dynamics and Chaos*. Addison-Wesley, Readings, MA, 1984.
256. S. H. Strogatz. From Kuramoto to Crawford: exploring the onset of synchronization in populations of coupled oscillators. *Phys. D*, 143(1-4):1–20, 2000. Bifurcations, patterns and symmetry.
257. J. Tabak, W. Senn, M. J. O’Donovan, and J. Rinzel. Modeling of spontaneous activity in developing spinal cord using activity-dependent depression in an excitatory network. *J. Neurosci.*, 20:3041–3056, 2000.
258. S. Tanabe and K. Pakdaman. Dynamics of moments of FitzHugh–Nagumo neuronal models and stochastic bifurcations. *Phys. Rev. E Stat. Nonlin. Soft Matter Phys.*, 63:031911, 2001.
259. T. Tateno, A. Harsch, and H. P. Robinson. Threshold firing frequency-current relationships of neurons in rat somatosensory cortex: type 1 and type 2 dynamics. *J. Neurophysiol.*, 92:2283–2294, 2004.
260. J. N. Teramae and T. Fukai. A cellular mechanism for graded persistent activity in a model neuron and its implications in working memory. *J. Comput. Neurosci.*, 18:105–121, 2005.
261. J. N. Teramae and D. Tanaka. Robustness of the noise-induced phase synchronization in a general class of limit cycle oscillators. *Phys. Rev. Lett.*, 93:204103, 2004.
262. D. Terman. Chaotic spikes arising from a model of bursting in excitable membranes. *SIAM J. Appl. Math.*, 51:1418–1450, 1991.
263. D. Terman. The transition from bursting to continuous spiking in an excitable membrane model. *J. Nonlinear Sci.*, 2:133–182, 1992.
264. D. Terman and D. L. Wang. Global competition and local cooperation in a network of neural oscillators. *Phys. D*, 81:148–176, 1995.
265. D. Terman, N. Kopell, and A. Bose. Dynamics of two mutually coupled inhibitory neurons. *Phys. D*, 117:241–275, 1998.
266. D. Terman, G. Ermentrout, and A. Yew. Propagating activity patterns in thalamic neuronal networks. *SIAM J. Appl. Math.*, 61:1578–1604, 2001.
267. D. Terman, S. Ahn, X. Wang, and W. Just. Reducing neuronal networks to discrete dynamics. *Phys. D*, 237:324–338, 2008.
268. J. Touboul. Bifurcation analysis of a general class of nonlinear integrate-and-fire neurons. *SIAM J. Appl. Math.*, 68(4):1045–1079, 2008.
269. R. Traub and R. Miles. *Neuronal Networks of the Hippocampus*. Cambridge University Press, Cambridge, 1991.
270. R. D. Traub, R. K. Wong, R. Miles, and H. Michelson. A model of a ca3 hippocampal pyramidal neuron incorporating voltage-clamp data on intrinsic conductances. *J. Neurophysiol.*, 66:635–650, 1991.
271. S. F. Traynelis and F. Jaramillo. Getting the most out of noise in the central nervous system. *Trends Neurosci.*, 21:137–145, 1998.
272. W. Troy. The bifurcation of periodic solutions in the Hodgkin–Huxley equations. *Quart. Appl. Math.*, 1:73–83, 1979.
273. M. Tsodyks, A. Uziel, and H. Markram. Synchrony generation in recurrent networks with frequency-dependent synapses. *J. Neurosci.*, 20:RC50, 2000.
274. H. C. Tuckwell. *Introduction to Theoretical Neurobiology. Vol. 2, Nonlinear and Stochastic Theories*, volume 8 of *Cambridge Studies in Mathematical Biology*. Cambridge University Press, Cambridge, 1988.
275. H. C. Tuckwell, R. Rodriguez, and F. Y. Wan. Determination of firing times for the stochastic Fitzhugh-Nagumo neuronal model. *Neural Comput.*, 15:143–159, Jan 2003.

276. A. M. Turing. The chemical basis of morphogenesis. 1953. *Bull. Math. Biol.*, 1953;1990:52:153–197, 1990.
277. D. Ulrich. Dendritic resonance in rat neocortical pyramidal cells. *J. Neurophysiol.*, 87:2753–2759, 2002.
278. C. Van Vreeswijk, L. F. Abbott, and G. B. Ermentrout. When inhibition not excitation synchronizes neural firing. *J. Comput. Neurosci.*, 1:313–321, 1994.
279. J. A. Varela, K. Sen, J. Gibson, J. Fost, L. F. Abbott, and S. B. Nelson. A quantitative description of short-term plasticity at excitatory synapses in layer 2/3 of rat primary visual cortex. *J. Neurosci.*, 17:7926–7940, 1997.
280. M. Volgushev, S. Chauvette, M. Mukovski, and I. Timofeev. Precise long-range synchronization of activity and silence in neocortical neurons during slow-wave oscillations [corrected]. *J. Neurosci.*, 26:5665–5672, 2006.
281. C. von der Malsburg and W. Schneider. A neural cocktail-party processor. *Biol. Cybern.*, 54:29–40, 1986.
282. X. J. Wang. Calcium coding and adaptive temporal computation in cortical pyramidal neurons. *J. Neurophysiol.*, 79:1549–1566, 1998.
283. X. J. Wang. Synaptic basis of cortical persistent activity: the importance of NMDA receptors to working memory. *J. Neurosci.*, 19:9587–9603, 1999.
284. X.-J. Wang and J. Rinzel. Alternating and synchronous rhythms in reciprocally inhibitory model neurons. *Neural Comput.*, 4:84–97, 1992.
285. X.-J. Wang and J. Rinzel. Oscillatory and bursting properties of neurons. In M. A. Arbib, editor, *Brain Theory and Neural Computation*. MIT, Cambridge, MA, 1995.
286. M. A. Whittington, R. D. Traub, and J. G. Jefferys. Synchronized oscillations in interneuron networks driven by metabotropic glutamate receptor activation. *Nature*, 373:612–615, 1995.
287. H. R. Wilson and J. D. Cowan. Excitatory and inhibitory interactions in localized populations of model neurons. *Biophys. J.*, 12:1–24, 1972.
288. H. R. Wilson and J. D. Cowan. A mathematical theory of the functional dynamics of cortical and thalamic nervous tissue. *Kybernetik*, 13:55–80, 1973.
289. H. R. Wilson, R. Blake, and S. H. Lee. Dynamics of travelling waves in visual perception. *Nature*, 412:907–910, 2001.
290. A. T. Winfree. Biological rhythms and the behavior of populations of coupled oscillators. *J. Theor. Biol.*, 16:15–42, 1967.
291. A. T. Winfree. *The Geometry of Biological Time*, volume 12 of *Interdisciplinary Applied Mathematics*. Springer, New York, second edition, 2001.
292. J. Y. Wu, L. Guan, and Y. Tsau. Propagating activation during oscillations and evoked responses in neocortical slices. *J. Neurosci.*, 19:5005–5015, 1999.
293. X. Wu, J. Y. Huang, and C. Zhang. Propagating waves of activity in the neocortex: what they are, what they do. *Neuroscientist*, 14:487–502, 2008.
294. R. Yuste, J. N. MacLean, J. Smith, and A. Lansner. The cortex as a central pattern generator. *Nat. Rev. Neurosci.*, 6:477–483, 2005.
295. K. Zhang. Representation of spatial orientation by the intrinsic dynamics of the head-direction cell ensemble: a theory. *J. Neurosci.*, 16:2112–2126, 1996.
296. L. Zhang. On stability of traveling wave solutions in synaptically coupled neuronal networks. *Differ. Integral Equat.*, 16:513–536, 2003.
297. B. Zinner. Existence of traveling wavefront solutions for the discrete Nagumo equation. *J. Differ. Equat.*, 96(1):1–27, 1992.

Index

- $\lambda-\omega$ oscillators, 179
action potential, 17, 25
activated state, 22
activation curves, 26
active dendrites, 142
adjoint, 177
 $\lambda-\omega$, 179
 bifurcations and, 181
 Hopf bifurcation, 182
 limit point of a cycle, 183
 quadratic integrate and fire, 179
 ring models, 178
 saddle-node on an invariant circle, 182
 Takens–Bogdanov, 184
adjoint:singularly perturbed oscillators, 180
all-or-none behavior, 25
almost-synchronous solution, 249, 271
alpha functions, 158
antiphase oscillations, 249
antiphase oscillator, 260
Aplysia R-15 neurons, 111
associative memory, 375
asynchronous solution, 223
asynchronous state, 221
averaging, 116, 124
- bifurcation diagram, 56
bifurcation theory, 56
binocular rivalry, 359
bistability, 86, 106, 111
bistable, 55, 61
blue-sky catastrophe, 123
Bump attractors, 385
bursting oscillations, 103
 classification of bursters, 117
 elliptic bursting, 111
- cable equation, 13, 15, 33
calcium-dependent potassium channels, 103
central pattern generator, 208
channels
 A-type potassium, 83
 calcium, 80
 calcium-activated nonspecific cation, 93
 calcium-dependent potassium, 90
 calcium-gated, 90
 CAN, 93
 inward rectifier, 86
 L-type calcium, 80
 M-type potassium, 85
 persistent sodium, 79
 potassium, 82
 sag, 87
 sodium, 78
 synaptic, 160
 T-type calcium, 80
chaotic dynamics, 110, 118
circle maps, 189
circulant matrices, 351
class I and class II dynamics, 62, 143
closed orbits, 52
clustering, 250, 262
Cohen–Grossberg theory, 374
colored noise, 300, 309
Conley index, 151
constant-field equation, 5, 6
coupled oscillators, 193
current
 synaptic, 205
- delay equations, 363
dendritic spike, 44

- Denjoy's theorem, 190
 depolarized, 1, 17
 depolarizing current, 254
 Devil's staircase, 192
 diffusion, 4
 direct synapses, 246
 dispersion relation, 139, 140
 dispersion kinematics, 141
 temporal dispersion relation, 140
 distal dendrite, 45
 drift, 4
 driving force, 9
 duty cycle, 245, 260
 dynamic clamp, 186
 dynamic clustering, 250, 262
 dynamical systems, 49
- eigenvalue, 52
 electric field, 4
 electrotonic length, 35, 37
 Elementary constant, 8
 elliptic bursting, 111
 ensemble frequency, 205
 equivalent circuit model, 8
 equivalent cylinder, 38
 Ermentrout–Rinzel model, 144
 escape mechanism, 261
 Evans function, 145, 147
 Evans, J., 145
 excitable, 50, 53, 245
 excitatory synapses, 246
 excitatory–inhibitory neural networks, 352
- fast spiking neurons, 62
 fast threshold modulation, 258
 finger tapping, 209
 firing rate models
 method of averaging, 338
 firing rate models
 heuristics, 334
 firing time maps, 193
 first passage times, 297
 FitzHugh–Nagumo equations, 69, 132
 FitzHugh–Rinzel model, 126
 fixed point, 52
 Fokker–Planck equation, 292, 301
 boundary conditions, 296
 forced oscillators, 189
 form constants, 396
- GABA, 158
 gain functions, 347
- gaits, 209
 gamma rhythms, 199
 gap junctions, 164
 generalized firing rate models, 358
 global bifurcation, 58
 Goldman–Hodgkin–Katz equation, 3, 5, 7, 11
- half-center oscillator, 260
 hallucinations, 396
 head direction, 394
 Hebbian learning, 170
 heteroclinic orbit, 133, 145
 Hill exponent, 108
 Hindmarsh–Rose model, 126
 hippocampus, 199
 Hodgkin–Huxley model, 17, 18, 20, 25, 129
 homoclinic orbit, 59, 60, 106, 129, 130, 144
 Hopf bifurcation, 56
 subcritical Hopf bifurcation, 57
 supercritical Hopf bifurcation, 57
 Hopf bifurcation theorem, 56
 Hopfield networks, 373
 hyperpolarized, 1
 hyperpolarizing current, 254
- I – V plot, 6
 inactivated state, 22
 indirect synapses, 246
 infinite cable, 34
 inhibitory synapses, 246
 input conductance, 37
 input resistance, 12, 16, 31, 36, 37
 integrate-and-fire, 199
 interspike intervals, 308
 inward current, 1
 ionic concentrations, 88
 isochron, 172, 176
 isolated junction, 40
 isopotential, 11
 Itô calculus, 291
 Ito's formula, 291
- Langevin equation, 287
 leak current, 20
 limit cycle, 55
 linearization, 52
 linearization by adaptation, 91
 longitudinal current, 30, 33
 lumped soma, 36
 lurching wave, 282

- master equation, 293
McCulloch–Pitts networks, 372
membrane capacitance, 8, 32
membrane potential, 1, 9, 25
membrane resistance, 32
membrane space constant, 35
membrane time constant, 12, 15
Mexican hat interactions, 387
Mirollo–Strogatz, 197
mobility, 4, 5
moment expansions, 312
Morris–Lecar model, 49, 107
multiple compartments, 29
myelinated axons, 149
- Nernst equation, 3, 5
Nernst potential, 2, 17, 18
Nernst–Planck equation, 3, 4, 6
Neural waves, 377
NEURON, 32
nodes of Ranvier, 149
nullcline, 52
- orientation selectivity, 392
Ornstein–Uhlenbeck process, 309
oscillations
 subthreshold, 82
oscillators
 phase-locking, 204
 two-dimensional arrays, 216
 weak coupling theory, 202
oscillatory, 245
outward current, 1
- pancreatic β cells, 105
parabolic bursting, 111
passive cell, 11
passive membrane, 10
permeability, 1, 6, 11
phase, 172
phase equations, 195
phase plane, 51
phase resetting curve, 175
phase space, 49
phase transition curve, 174
phosphenes, 396
Pinsky–Rinzel model, 43
pitchfork bifurcation, 352
Poincaré map, 118
population density, 220
population density equations, 343
- populations of neurons, 340
postinhibitory rebound, 249, 254, 260
poststimulus time histogram, 188
postsynaptic potentials, 29
potential difference, 1
pre-Botzinger complex, 79, 103
propagating action potentials, 129
propagating waves, 280
- Rall model, 38
Rall, W., 45
reaction–diffusion equations, 129, 132, 145
rebound, 81
rectifying, 6
regular spiking neurons, 62
release mechanism, 261
resistivity, 13
resting potential, 1, 3, 10, 17
reversal potential, 2
ring models, 304
rotation number, 190
Routh–Hurwitz criterion, 65
- saddle–homoclinic bifurcation, 60
saddle–node bifurcation, 59, 60, 106
saddle–node on an invariant circle, 114, 117
saddle–node on an invariant curve, 58
scalar recurrent networks, 348
sealed end, 36
Shilnikov dynamics, 142
shooting method, 131, 133, 135
singular construction of traveling waves, 382
singular solution, 251
slow synapse, 277
slow–fast analysis, 92
Smale horseshoe, 142
Smale–horseshoe map, 121
solitary waves, 224
space constant, 15
space-clamp, 20
specific membrane capacitance, 9
specific membrane conductance, 9
specific membrane resistance, 9, 10
spike-frequency adaptation, 85
spike-time response curves, 186
spines, 29
spiral waves, 218
square-wave bursters, 105
squid axon, 17
stability of bumps, 389
stable and unstable manifolds, 58
steady-state equation, 36, 37

- steady-state potential, 11
- stochastic differential equations, 289
- stochastic integrals, 291
- Stratonovich calculus, 291
- subthreshold response, 50
- suppressed solution, 250, 280
- symbolic dynamics, 121
- symmetry breaking, 352
- synapse
 - AMPA, 161
 - delay, 160
 - excitatory, 161
 - GABA, 162
 - GABA_A, 162
 - GABA_B, 163
 - glutamate, 161
 - NMDA, 161
- synapses
 - electrical, 164
 - plasticity, 164
- synaptic depression, 166, 361
- synaptic facilitation, 166
- synchrony, 206, 249, 256
 - dendrites, 213
 - gap junctions, 212
- target patterns, 217
- temperature factor, 25
- tetrodotoxin, 21
- theta model, 60, 143
- time metric, 267
- tonic spiking, 110
- top hat bursting, 118
- traveling pulses, 381
- traveling wave solution, 129, 130
- traveling waves, 226, 229
 - stability, 229
- tuning curve, 393
- Turing instability, 399
- Two-population neural networks, 348
- up–down states, 354
- van der Pol equation, 69
- voltage clamp, 20, 22, 36
- voltage-gated channels, 1, 17
- wave trains, 139
- wavefronts, 378
- whisker barrels, 356
- Wiener process, 287, 290
- Wilson–Cowan equations, 346, 386
- working memory, 385